



AFRL-RQ-WP-TR-2013-0239

**HIGH WORK, HIGH-EFFICIENCY TURBINES FOR
UNINHABITED AERIAL VEHICLES (UAVs)**

Addendum to AFRL-RQ-WP-TR-2013-0198

Rolf Sondergaard

Turbomachinery Branch

Turbine Engine Division

SEPTEMBER 2013

Final Report

Approved for public release; distribution unlimited.

See additional restrictions described on inside pages

STINFO COPY

**AIR FORCE RESEARCH LABORATORY
AEROSPACE SYSTEMS DIRECTORATE
WRIGHT-PATTERSON AIR FORCE BASE, OH 45433-7542
AIR FORCE MATERIEL COMMAND
UNITED STATES AIR FORCE**

NOTICE AND SIGNATURE PAGE

Using Government drawings, specifications, or other data included in this document for any purpose other than Government procurement does not in any way obligate the U.S. Government. The fact that the Government formulated or supplied the drawings, specifications, or other data does not license the holder or any other person or corporation; or convey any rights or permission to manufacture, use, or sell any patented invention that may relate to them.

This report was cleared for public release by the USAF 88th Air Base Wing (88 ABW) Public Affairs Office (PAO) and is available to the general public, including foreign nationals.

Copies may be obtained from the Defense Technical Information Center (DTIC)
(<http://www.dtic.mil>).

AFRL-RQ-WP-TR-2013-0239 HAS BEEN REVIEWED AND IS APPROVED FOR
PUBLICATION IN ACCORDANCE WITH ASSIGNED DISTRIBUTION STATEMENT.

*//Signature//

ROLF SONDERGAARD
Project Engineer
Turbomachinery Branch
Turbine Engine Division

//Signature//

CHARLES W. STEVENS
Branch Chief
Turbomachinery Branch
Turbine Engine Division

//Signature//

JEFFREY M. STRICKER
Chief Engineer
Turbine Engine Division
Propulsion Directorate

This report is published in the interest of scientific and technical information exchange, and its publication does not constitute the Government's approval or disapproval of its ideas or findings.

*Disseminated copies will show “//Signature//” stamped or typed above the signature blocks.

REPORT DOCUMENTATION PAGE				Form Approved OMB No. 0704-0188	
<p>The public reporting burden for this collection of information is estimated to average 1 hour per response, including the time for reviewing instructions, searching existing data sources, gathering and maintaining the data needed, and completing and reviewing the collection of information. Send comments regarding this burden estimate or any other aspect of this collection of information, including suggestions for reducing this burden, to Department of Defense, Washington Headquarters Services, Directorate for Information Operations and Reports (0704-0188), 1215 Jefferson Davis Highway, Suite 1204, Arlington, VA 22202-4302. Respondents should be aware that notwithstanding any other provision of law, no person shall be subject to any penalty for failing to comply with a collection of information if it does not display a currently valid OMB control number. PLEASE DO NOT RETURN YOUR FORM TO THE ABOVE ADDRESS.</p>					
1. REPORT DATE (DD-MM-YY) September 2013		2. REPORT TYPE Final		3. DATES COVERED (From - To) 01 May 2005 – 30 June 2013	
4. TITLE AND SUBTITLE HIGH WORK, HIGH-EFFICIENCY TURBINES FOR UNINHABITED AERIAL VEHICLES (UAVs) Addendum to AFRL-RQ-WP-TR-2013-0198				5a. CONTRACT NUMBER In-house	
				5b. GRANT NUMBER	
				5c. PROGRAM ELEMENT NUMBER 61102F	
6. AUTHOR(S) Rolf Sondergaard				5d. PROJECT NUMBER 2307	
				5e. TASK NUMBER	
				5f. WORK UNIT NUMBER Q0EB	
7. PERFORMING ORGANIZATION NAME(S) AND ADDRESS(ES) Turbomachinery Branch (AFRL/RQTT) Turbine Engine Division, Air Force Research Laboratory, Aerospace Systems Directorate Wright-Patterson Air Force Base, OH 45433-7542 Air Force Materiel Command, United States Air Force				8. PERFORMING ORGANIZATION REPORT NUMBER AFRL-RQ-WP-TR-2013-0239	
9. SPONSORING/MONITORING AGENCY NAME(S) AND ADDRESS(ES) Air Force Research Laboratory Aerospace Systems Directorate Wright-Patterson Air Force Base, OH 45433-7542 Air Force Materiel Command United States Air Force				10. SPONSORING/MONITORING AGENCY ACRONYM(S) AFRL/RQTT	
				11. SPONSORING/MONITORING AGENCY REPORT NUMBER(S) AFRL-RQ-WP-TR-2013-0239	
12. DISTRIBUTION/AVAILABILITY STATEMENT Approved for public release; distribution unlimited.					
13. SUPPLEMENTARY NOTES Report contains color. Public Affairs (PA) Office clearance case numbers (if available) appear with the respective publications in 14. ABSTRACT. Most of the publications are post-print, while dissertations appear in their original, pre-print version. On many of the papers, the U.S. Government is joint author and has the right to use, modify, reproduce, release, perform, display, or disclose the work.					
14. ABSTRACT This series of publications document the activities and results of an AFOSR-funded, in-house, basic research effort. The effort was focused on the fluid mechanics and heat transfer that is associated with advanced turbine aerodynamic designs, particularly for small engines. The objectives of this task were to identify and evaluate loss mechanisms for very highly loaded turbines and turbines intended to operate at low Reynolds number, and investigate passive and fluidic techniques for the control of separation, reattachment, blade row outlet air angle deviations, secondary flows, and similar loss producing phenomena. The results are applicable to both military and civil applications of gas turbine engines. The following titles published in professional journals and conference proceedings (or unpublished) are provided in this addendum to AFRL-RQ-WP-TR-2013-0198: <ul style="list-style-type: none"> • “PIV Investigation of a Highly-Loaded LPT Blade Using a Curved Laser-Sheet” (88ABW-2008-1431) • “High Lift LPT Blade Suction Surface Flow Investigation Using Surface Stress Sensitive Film” (88ABW-2009-3033) • “Turbulence Model Comparisons for Mixing Plane Simulations of a Multistage Low Pressure Turbine Operating at Low Reynolds Numbers” (88ABW-2009-3036) • “Predicting Separation and Transitional Flow in Turbine Blades at Low Reynolds Numbers” (WPAFB 2007-0314) • “A CFD and Experimental Investigation of Unsteady Wake Effects on a Highly Loaded Low Pressure Turbine Blade at Low Reynolds Number” (88ABW-2009-5080) • “Curved laser-sheet for conformal surface flow diagnostics” (88ABW-2010-4706) • “CFD Modeling of Separation and Transitional Flow in Low Pressure Turbine Blades at Low Reynolds Numbers” (dissertation, 88ABW-2009-4567) • “Design and Validation of a High-Lift Low-Pressure Turbine Blade” (dissertation) • “Characterization of Internal Wake Generator at Low Reynolds Number with a Linear Cascade of Low Pressure Turbine Blades” (thesis, 88ABW-2010-2046) 					
15. SUBJECT TERMS turbine aerodynamics, turbine pressure loss, turbine efficiency, turbine end-wall flows, low Reynolds number, turbine flow control					
16. SECURITY CLASSIFICATION OF:			17. LIMITATION OF ABSTRACT: SAR	18. NUMBER OF PAGES 622	19a. NAME OF RESPONSIBLE PERSON (Monitor) Rolf Sondergaard 19b. TELEPHONE NUMBER (Include Area Code) N/A
a. REPORT Unclassified	b. ABSTRACT Unclassified	c. THIS PAGE Unclassified			

APPENDIX A

PIV Investigation of a Highly-Loaded LPT Blade Using a Curved Laser-Sheet

Christopher Marks¹, Rolf Sondergaard², Mitch Wolff³
Air Force Research Laboratory, WPAFB, OH, 45433

and

Jordi Estevadeordal⁴
Innovative Scientific Solutions, Dayton, OH, 45440

Low Reynolds number flow around a highly loaded LPT blade (the L1A) was investigated by Particle Image Velocimetry (PIV) at the blade midspan. PIV data was acquired in both the blade normal and spanwise direction planes. Measurements in the spanwise direction planes were taken near the airfoil suction surface using a curved laser-sheet that closely matched the curvature of the aft portion of the blade profile. Images in the blade normal plane over a range of Reynolds numbers clearly show the shear layer and transition length, while images in the spanwise direction plane show the three-dimensional nature of the transition region. The experiment was performed on a linear cascade of seven blades mounted in the Air Force Research Lab Low Speed Wind Tunnel facility. Images were taken at two different freestream turbulence levels across a Reynolds number range between 25,000 and 125,000.

Nomenclature

C_p	=	coefficient of pressure
C_x	=	axial chord
d	=	image length in the horizontal direction
$FSTI$	=	freestream turbulence intensity
H	=	shape factor
M	=	magnification factor
n	=	coordinate in the surface normal direction
P_s	=	static pressure
P_t	=	total pressure
S	=	distance between blades (pitch)
u_1	=	velocity component in the x_1 direction
u_2	=	velocity component in the x_2 direction
v	=	velocity component in the y direction
w	=	velocity component in the z direction
δ	=	boundary layer thickness
λ_{int}	=	integrated wake loss coefficient

I. Introduction

Particle Image Velocimetry (PIV) is one of the strongest diagnostic tools for probing complex flow fields. Traditional techniques such as hot-wire anemometry or LDV are limited to point measurements and insufficient in providing instantaneous flow-field data in two-dimensional planes. Experimentally obtained two-dimensional

¹ Graduate Student, Propulsion Directorate, 1950 Fifth St, Member AIAA.

² Aerospace Engineer, Propulsion Directorate, 1950 Fifth St, Associate Fellow AIAA.

³ Scientific Advisor, Propulsion Directorate, 1950 Fifth St., Associate Fellow AIAA.

⁴ Formerly Senior Research Scientist, at ISSI Inc., currently at GE Global Research, Associate Fellow AIAA.

velocity flow-fields are useful for both qualitative and quantitative understanding of complex flow. Data can be obtained quickly and in a large spatial area providing experimental data that can be directly compared to CFD results. Two-dimensional planar PIV is most common and the simplest to setup, but provides velocity components in only two directions. In an attempt to better understand the three-dimensional nature of complex flows, and obtain the third velocity component, a variety of techniques have been devised and are summarized in a book by Raffel et al.¹ Examples include: stereoscopic PIV, volumetric PIV and dual-plane PIV. Most of the abovementioned techniques require specialized calibration or image correlation methods beyond those typically required for 2-D single plane PIV.

The focus of studies on transitional flow around cylinders, aircraft wings, and linear turbine blades is on the flow behavior in the viscous region near the wall. The walls are curved in shape and attached laminar, transitional, and turbulent boundary layer streamlines primarily follow the shape of the curved wall. Curved walls make it difficult to use flat planar PIV in the spanwise plane (see Fig. 1 for definition of image planes) near the wall. Several researchers^{2, 3, 4} have successfully applied 2-D planar PIV in the spanwise direction plane parallel to the suction side of an airfoil (or flat plate with adverse pressure gradient²) by taking advantage of the low curvature of the blade in the region of interest. Burgmann et al.³ obtained spanwise scanning PIV near the wall and through a separation bubble on the suction side of a SD7003 airfoil at Reynolds numbers of 20,000-60,000. The area of interest on the suction side of LPT blades, which have large turning angles, is often near the point of highest curvature which makes imaging in the spanwise direction using a flat planar sheet difficult. The technique used in the current study makes use of traditional 2-D blade normal imaging as well as a curved laser-sheet that allows spanwise imaging very near the surface of a highly loaded LPT blade at low Reynolds number. Curving the laser to closely match the flow streamlines provides additional flow details in the spanwise direction while still using existing 2-D PIV analysis techniques. Experiments were performed at several Reynolds numbers between 25,000 and 125,000, and with FSTI of 0.5% and 3.4%. In addition to PIV and flow visualization, integrated wake total pressure loss coefficient and C_p distributions were recorded in order to better understand the blade performance under low Reynolds number conditions.

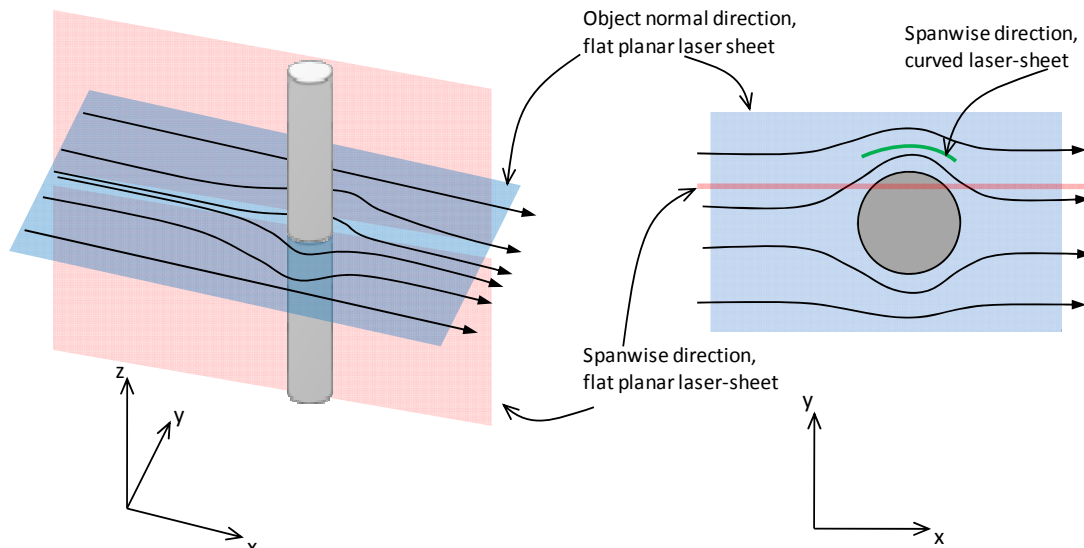


Figure 1. 2D PIV around a cylinder showing object normal, spanwise planar, and spanwise direction using a curved laser sheet.

II. Experimental Setup

A. Experimental Facility

The facility used in this project was the AFRL Low Speed Wind Tunnel (LSWT), which has been described by Sondergaard et al.,⁵ Bons et al.,⁶ and Rivir et al.⁷ The wind tunnel and a schematic of the test section are shown in Figure 2 & Figure 3. The wind tunnel test section is 0.85m tall by 1.22m wide at the inlet and houses the linear turbine cascade. A 125-hp electric motor drives an axial flow fan which draws air through the test section at up to

80m/s. The wind tunnel flow uniformity is better than 1% with a FSTI of approximately 0.5%. An optional turbulence generation grid can be used to increase the freestream turbulence up to a maximum of approximately 12%. In this study data was taken with and without a turbulence grid giving a FSTI of 3.4% and 0.5% respectively⁸.

The linear cascade has 7 blades with a span of 0.88m and an axial chord of 0.18m. The L1A profile studied was designed by John Clark of AFRL⁹ and is described by Bons et al.¹⁰ It is a highly loaded, slightly more aft-loaded version of the L1M profile⁹ with a design Zweifel coefficient of 1.34. The cascade has a solidity of 0.99 and a design inlet flow angle of 55° and design exit angle of 30°. Wake loss coefficient, surface pressure coefficient, and PIV images in the blade normal and spanwise directions were recorded for a variety of Reynolds numbers and freestream conditions. Reynolds number was calculated based on inlet velocity and blade axial chord length. Blade normal direction images were taken on blade 3 and spanwise direction images were recorded on blade 4. Pressure taps were located on blade three and four. An upstream Pitot-static probe and a downstream total pressure Kiel probe were used to measure static and total pressure upstream and total pressure in the wake of the blades. A -0.2 to 0.8 in-H₂O Druck pressure transducer was used for wake loss measurements, and 0 to 2.0 in-H₂O Druck pressure transducer for Cp calculations. A single element hotwire was used to measure inlet velocity and calculate Reynolds number based on axial chord. Cascade periodicity across the blade set was checked by pressure measurement upstream and approximately one and one-half chord lengths downstream of the turbine blades.



Figure 2. AFRL Low Speed Wind Tunnel Facility

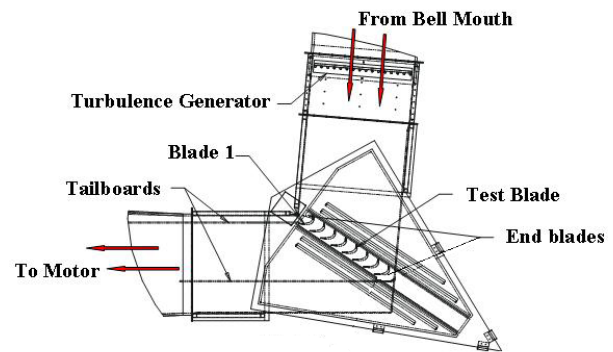


Figure 3. Top view of LSWT test section.

B. PIV Technique

The PIV technique involves two main steps. First, a selected plane or surface within the flow field is created by illuminating seeding particles with a powerful, thin, laser-light sheet. The laser-light sheet is typically formed by means of a combination of spherical and cylindrical lenses. The light scattered by the seeding particles in the illuminated plane is recorded using double-exposure photographs. In the second step, the local fluid velocity is obtained from the ratio of the measured displacement between two images of the same particle ensembles to the time between exposures, which is a preset parameter¹.

Once the PIV images were captured and digitized, the velocity field was obtained using cross-correlation techniques over interrogation domains of the images and PIV software developed by Innovative Scientific Solutions Inc. (ISSI). The present results were obtained with two and three passes with interrogation domains of 128, 64, and 32 pixels with an overlapping of 75%. Overlapping domains (by three-quarters the domain size) yields more vectors and is not merely interpolation since it includes new particles in every domain subregion^{11,12}. A parallel computing code for Linux clusters from ISSI was used for added processing speed¹³.

1. PIV Experimental Setup

A single-color PIV system implemented in the LSWT facility for various configurations is shown schematically in Figure 4, including 2D flat planar and curved laser setups. The laser and cameras for the PIV system were mounted on optical breadboards located directly underneath and adjacent to the cascade. The laser was a dual-head

(532-nm), frequency doubled, flashlamp-pumped Nd:YAG laser (New Wave Solo - 120). The laser was capable of delivering dual 120 mJ pulses at repetition rates of up to 15Hz. The temporal delay between the two lasers was controlled by a pulse generator. The settings of the pulse generator were a function of flow velocity, optical magnification, and interrogation spot size. The spanwise and blade normal direction images were recorded during independent tests.

Mie scattering from the seed particles was recorded on commercial, high-resolution CCD digital camera sensors (PCO1600) with a resolution of 1600 by 1200 pixels and a maximum framing rate of 30 frames per second (fps). These cross-correlation cameras are capable of acquiring double exposures at a rate of 15 Hz. The two frames can be recorded sequentially within one hundred nanoseconds. Images were recorded at a frequency of 10Hz. This PIV technique has been successfully applied to a variety of flows and the results have demonstrated the resolution necessary for exploring flow features in complex flow fields¹⁴. The camera recording images in the blade normal direction was mounted underneath the test section looking through a 1.25cm

thick clear plexiglass cascade bottom plate, approximately 50cm from the plane of the light sheet. The camera was fitted with a 35-70mm f2.8 lens set to a focal length of ≈ 40 mm, which provided a field of view of 119mm by 158mm. The camera recording images in the spanwise direction was mounted adjacent to test section facing the aft portion of the blade 4 suction surface. The camera view was through two, 1.25cm thick plexiglass sheets (the test section wall and tailboard). A 105mm f2.8 lens was used for the spanwise images. The camera and lens were located approximately 100 cm from blade 4 which gave a field of view of 93mm by 124 mm.

Images were correlated using PPIV¹³ at a 32x32 pixel correlation window, and 75% overlapping of the domain which provided a vector at every 8 pixels or 0.8 mm for the streamwise images and ≈ 0.6 mm in the downstream area of the spanwise images. Points along the blade to surface interface were extracted from the PIV images and then a polynomial curve fit was used to identify the location of the surface of the blade in the streamwise PIV images. The area of the blade was blanked during post processing. Instantaneous series of images were averaged using DPIV software and then post processed into vector plots, or contour plots. Select instantaneous flow fields have been further analyzed using Reynolds or Galilean decomposition following the process summarized and demonstrated by Adrian et al¹⁷. Velocity profiles were extracted normal to the blade surface for select Reynolds numbers.

2. Curved Laser-Sheet for Conformal Surface Diagnostics

A novel technique that generates curved laser-sheets of arbitrary wrappable 3D shapes has been developed. The technique employs standard optical components such as a combination of cylindrical lenses or curved mirrors. Customized design optics can also be used to deliver certain curved laser shapes, which requires fewer optical elements. As an example of how the technique functions, a flat laser sheet such as those typically used in PIV can be bent or curved by adding cylindrical lenses at various angles in the optical path. The cylindrical-lens inclinations, distances, and physical properties (such as thickness and focal length) determine the shape and thickness of the curved sheet and can generate any wrappable laser-sheet shape with constant or variable thickness. This is similar to having a flat laser sheet incident to optical windows with curvature. A single customized optical element can also be designed to deliver any wrappable curved-sheet shape. Since these curved laser sheets allow tracking of any curved shape in space, they can be used for 3D illumination of flow regions such as boundary-layer or wall flows in conformal 3D surfaces and airfoil and circumferential planes in turbomachinery. Moving the optical elements can produce changes in the laser curvature, and the motion of surfaces such as wing motions in flying insects or UAV (unmanned air vehicles) can be tracked in time. An example of the use of these curved laser sheets is flow

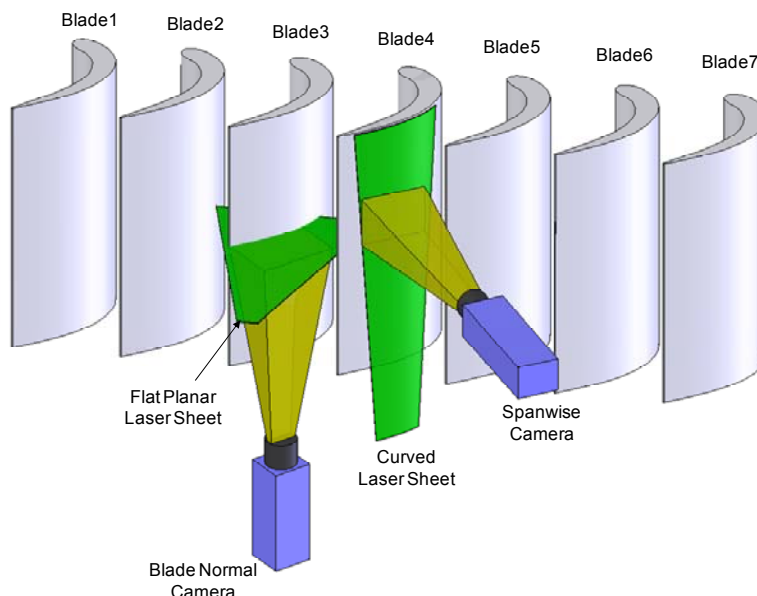


Figure 4. Schematic of the PIV experiments and laser and camera

diagnostics around curved walls using PIV. In the present application for the 2D turbine cascade blades, the laser sheet was curved to be parallel to the wall profiles of the turbine-blade and PIV data acquired for boundary-layer, wall-flow, and flow-separation diagnostics; in this case the curved laser sheet was brought into focus in the camera by employing a large F-number (small aperture) and a grid on the blade profile was used for magnification calibration across the field of view. For a general distorted 3D shape, the camera optics path could include optical elements that compensate for the otherwise out-of-focus image plane at the expense of magnification distortions; this is similar to an extension of the Scheimpflug arrangement used in stereo PIV or when viewing object planes at an angle.

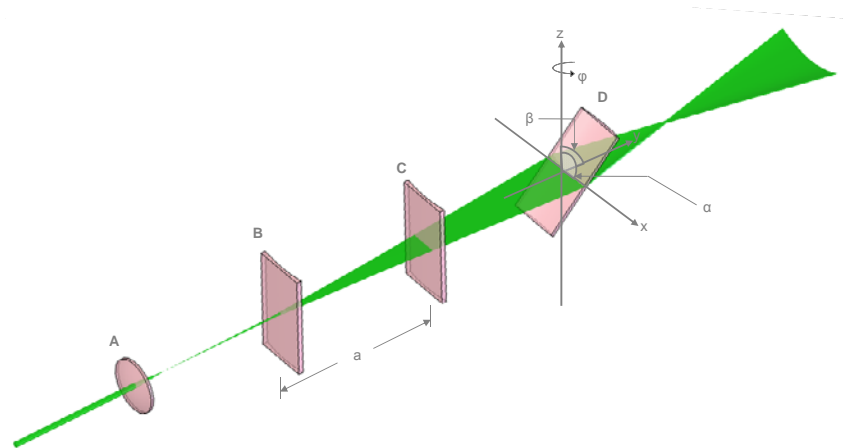


Figure 6. Example of curved laser-sheet forming optics.

An example of an optical system using off-the-shelf lenses used for curving the laser sheet is shown in Figure 5. The first three lenses shown are similar to configurations typically used to generate a planar laser sheet for PIV experiments. A bi-convex spherical lens (A) is used to reduce the diameter of a laser beam; next a series of negative focal length cylindrical lenses (B and C) expand the laser into a planar sheet. In a planar PIV experiment adjusting the focal lengths and placement of lenses A, B, and C sets the laser sheet thickness and width. In order to generate a curved sheet, an additional tilted convex cylindrical lens (D) was added to the system as shown in Figure 5. The orientation of the additional lens determines the shape of the sheet. Tilting the lens by an angle β in the x-axis will generate a curve in the sheet related to the geometry of the cylindrical lens. Rotating the already tilted lens by an angle ϕ about the z axis will adjust the area of the curve that is illuminated and allow limited manipulation of the curvature of the sheet. The rotation of the lens about the z-axis does not adjust the actual curvature, it creates an area of lower curvature which could be illuminated and used as needed. This is shown by modeling in a ray tracing program and demonstrated with a two cylindrical lens setup in Figure 6. Figures 6a and 6b show a curved sheet created by tilting the last cylindrical lens by 45 degrees in the x-direction. Notice that curve in Figure 6a is parabolic so that the rate of curvature is not constant along the entire curve. By rotating the lens in the z-axis as shown in Figure 6c, the area illuminated is shifted to the right to an area with high curvature at the left portion of the sheet, and less curvature on the right. The image shown in Figure 6c, if flipped vertically is much closer to the shape of an airfoil.

Generating a curved sheet is somewhat trivial as demonstrated above; however, creating a sheet that exactly matches the profile of an aerodynamic shape such as a turbine blade involves optical design work. Additional discussion on the development of a curved sheet that closely matches an aerodynamic shape

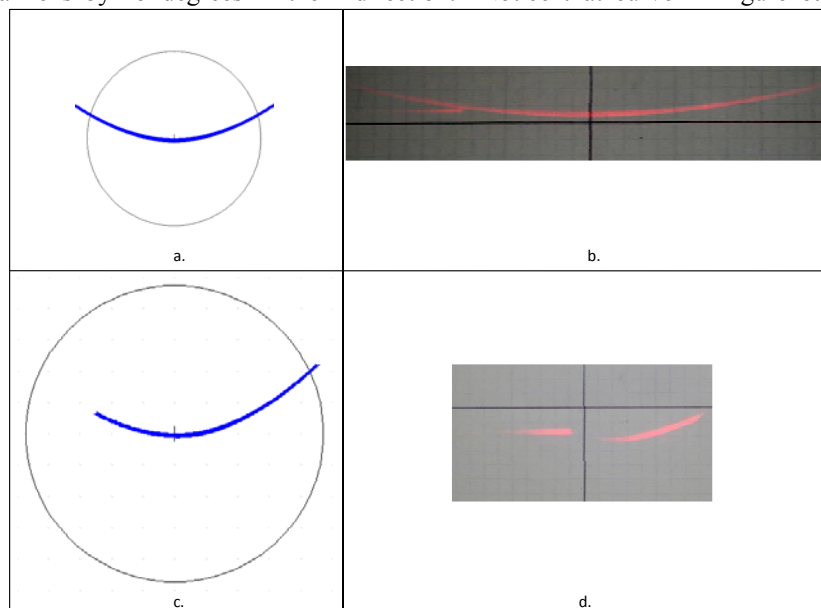


Figure 5. Example of a two lens curved laser sheet modeled in a ray tracing program (a and c) and demonstrated with a class 3a laser. The second lens has orientation: a.) & b.) $\phi = 0^\circ$, $\beta = 45^\circ$; c.) & d.) $\phi = 45^\circ$, $\beta = 45^\circ$

will be included later in the paper.

The field of view of each camera used is shown in Figure 7 as well as the coordinate systems. The following relationship relates the magnitude of velocity in each view, assuming two dimensional flow through the linear cascade and that the curved laser sheet approximates a stream surface:

$$|\vec{V}| = \sqrt{u_1^2 + v^2} = \sqrt{u_2^2} \quad (1)$$

In the spanwise FOV, magnification (M) is a function of x_2 due to the curved laser sheet. This is discussed further in the results section.

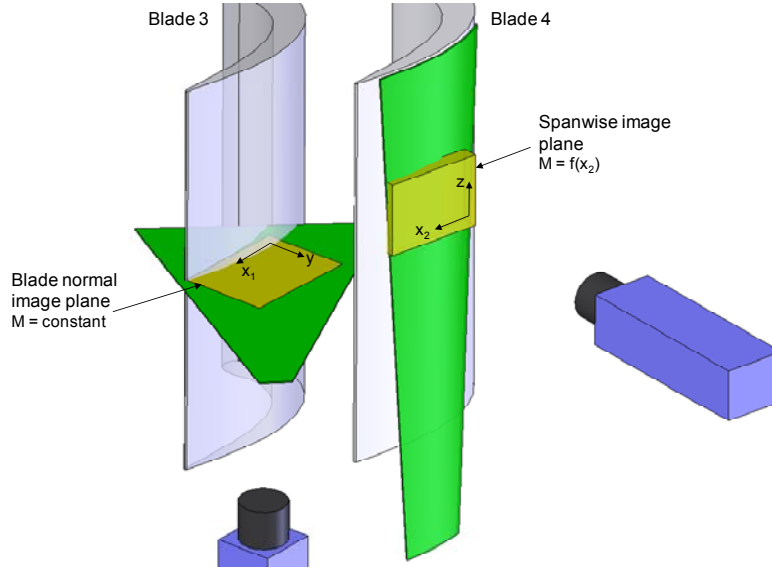


Figure 7. Camera view and coordinate system definition.

3. Uncertainty of velocity calculation from DPIV

The velocity u (m/s) is computed using the formula:

$$u = \frac{\Delta x}{\Delta t \cdot M} \quad (2)$$

where Δx is the displacement (pixels) of each interrogation domain during Δt (sec), the time interval between the two exposures, and M is the magnification of the digital image relative to the object (pixels/m). The displacement in pixels is obtained by using peak locator algorithms (e.g. a centroid method) that finds the location of the peak on the correlation map obtained from cross-correlating the two images and corrects for various biases and yields to sub-pixel accuracy (< 0.1 pixels). The algorithm includes multipass with cell shifting for increased accuracy. The maximum uncertainty in the Δt is calculated from the time interval between the two laser pulses. It has been found that this uncertainty increases with lower laser power and with lower Δt .¹¹ A conservative number for the typical PIV experiments was found to be 1%. Magnification is measured using images of targets located in the laser sheet plane and it is read to better than 1%. Combining these three conservative measurements the uncertainty for typical displacements yields to a maximum error of $< 2\%$.¹¹ The uncertainty added by the curved laser-sheet in the present investigation is reduced to the magnification variation since the present setup did not produce out of focus effects that required special optical corrections.

For successful PIV measurements the selection and implementation of the proper seeding strategy is a major factor. The seeding particles must be extremely small (typically $< 1 \mu\text{m}$) to track accelerations in the fluid effectively and faithfully and to avoid the impact of viscous and inertia forces. The seeding particles must also be efficient light scatterers to ensure that exposure of the recording media occurs. The method implemented used submicron sized propylene glycol smoke generated by a theatrical fog generator. The smoke was injected into the flow at the wind tunnel inlet. These particles were appropriate for tracking the flow in the areas of interest which include shear layer, wake, separation and recirculation areas. The small size of the particles ($< 0.5 \mu\text{m}$) is the main parameter that assured faithful flow tracking in the areas of interest.

In the present investigation, analyses are presented using flow visualizations, instantaneous, and averages from the PIV velocity fields. Averaging the instantaneous velocity fields has the effect of eliminating the fluctuations due to incoherent unsteadiness that are associated with noise and turbulence and permitting a good comparison with CFD predictions. The velocity field is averaged using routines that allow removal of outliers beyond any number of standard deviations and other filtering techniques. Robust statistics for removal of outliers using the median can also be used. PIV is instantaneous in nature but cannot provide temporal evolution of the flow field because of the relatively slow repetition rate of the lasers that are suitable for this type of PIV application requiring relatively large areas be illuminated and imaged.

III. Results

The results presented in this section describe the aerodynamic characteristics of the L1A. The integrated wake loss coefficient and C_p distribution will be presented first, for both low and high freestream turbulence conditions. The pressure data will be followed by flow visualization images and PIV results in both the blade normal direction and spanwise direction.

A. Wake Loss and C_p Distribution:

The integrated wake loss coefficient was calculated using Equation 3 across one blade pitch and is shown in Figure 8 for both FSTI levels along with flowfield predictions. The predictions were made in advance of testing with the RANS solver of Dorney and Davis¹⁵ using point-wise trips defined by the separated-flow transition model of Praisner and Clark¹⁶ (See also Clark et al.⁹). A gradual rise in loss coefficient with decreasing Reynolds number is predicted down to 50,000, followed by rapid rise and then plateau as Reynolds number is decreased further. The shape is similar to the loss knee found for other highly loaded LPT blades (e.g. Pack-B) and the rapid increase in loss is due to flow separation without reattachment on the suction surface⁵. With the exception of the steep rise in loss at Reynolds number of 50,000, the predicted loss profile follows the trends of the higher FSTI experimental results. The CFD predicted loss profile is similar in shape to the low FSTI experimental results, yet has a shift in loss knee of negative 40,000 Reynolds number compared to experiment. At both FSTI conditions and low Reynolds numbers (below 50,000), the experimental loss coefficient was lower than the predicted loss coefficient.

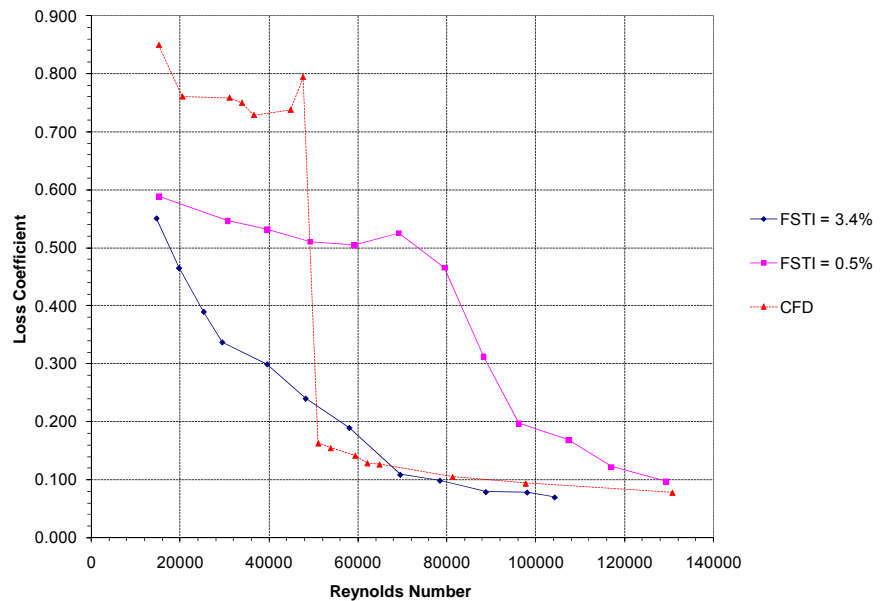


Figure 8. Integrated wake pressure loss coefficient.

$$\gamma_{int} = \frac{1}{S} \int_{-S/2}^{S/2} \left(\frac{P_{t,in} - P_{t,ex}}{P_{t,in} - P_{s,in}} \right) dS \quad (3)$$

The higher FSTI experimental loss versus Reynolds number profile has a gradual lapse compared to the profound knee of the low FSTI case, which indicates the development of a closed reattaching separation bubble. The maximum loss coefficient at the lowest Reynolds number tested was $\approx 65\%$ of that predicted by CFD. The experimental loss profile found during this work varies considerably from that given by Bons et al.¹⁰ whose experimental results (at a FSTI of 3%) showed a minimal increase in loss down to a Reynolds number of 50,000 followed by a sharp nearly constant increase in loss down to a Reynolds number of 20,000, with peak loss of nearly 4 times that found in the AFRL wind tunnel. Bons et al. assumed the drastic difference in their experimental results

versus the CFD prediction they were comparing results with to be due to not fully capturing the periodicity of the CFD model, in their two passage experimental cascade.

Experimental and CFD predicted C_p distributions are shown in Figures 9 & 10 for the low FSTI conditions and high FSTI conditions respectively. For all low FSTI Reynolds numbers tested the C_p distribution indicates a separated non-reattaching boundary layer. The separated region is identified by a plateau in the slope of the surface pressure distribution on the suction side starting between 57% and 62% axial chord for flow Reynolds numbers below 90,000, and $\approx 62\%$ for higher Reynolds numbers. The maximum suction location is consistently located at $\approx 53\%$ axial chord for all Reynolds numbers tested below 117,000, but shifts downstream to $\approx 57\%$ axial chord at a Reynolds number of 117,000. The value of peak C_p stays relatively consistent from a Reynolds number of 15,000 up to 79,000, and then gradually increases as Reynolds number increases. The predicted C_p distribution at Reynolds number of 15,000 agrees well with the experimental results. At the higher Reynolds number of 59,000 the predicted C_p distribution indicates higher loading and a closed reattaching separation bubble on the suction side compared to separated flow measured during experiment.

The experimentally measured C_p distributions for tests run with a FSTI of 3.4% indicate a reattaching separation bubble (identified by the brief plateau in suction side C_p) for the highest value of Reynolds number tested, $Re=80,000$ down to $Re=50,000$. The separation bubble begins near $\approx 62\%$ and reattaches between 78% and 83%. At Reynolds numbers of 25,000, and 15,000 the flow is fully separated as the C_p profile does not recover at the trailing edge of the blade. The separation point for these conditions is between $\approx 57\%$ and $\approx 62\%$. Peak suction location is consistently at 57% axial chord for all Reynolds numbers tested at high FSTI except at Reynolds number of 15,000, where it has shifted upstream to 53% axial chord. This is consistent with the results for the low FSTI separated case in which the peak suction point shifted slightly downstream at the highest Reynolds number tested. The predicted C_p distribution at a Reynolds number of 15,000 has the same shape, but lower loading compared to the experimental results. At higher Reynolds numbers the predicted C_p distribution is of the same shape, but lower overall loading. The predicted C_p distribution at Reynolds numbers of 51,000 and 81,000 both indicated the presence of a closed reattaching separation bubble which agrees with experimental results.

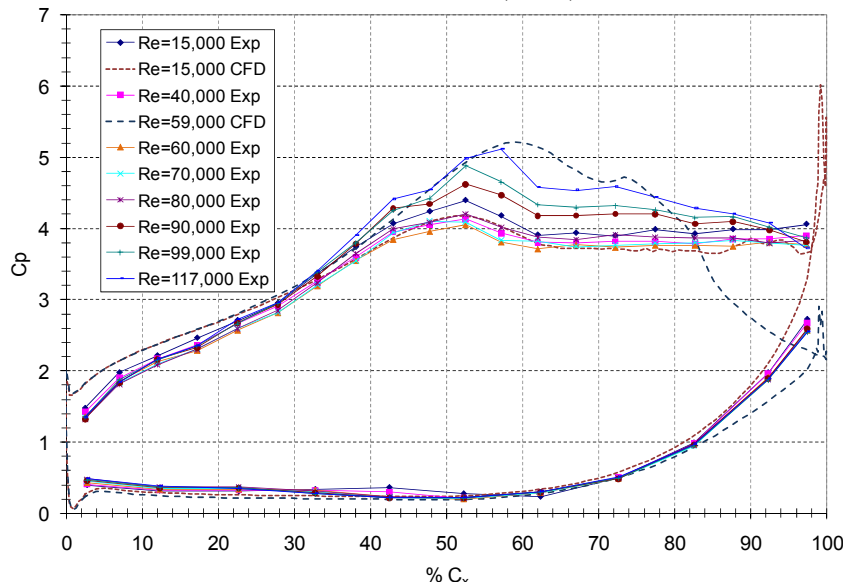


Figure 10. Pressure Coefficient, FSTI=0.5%.

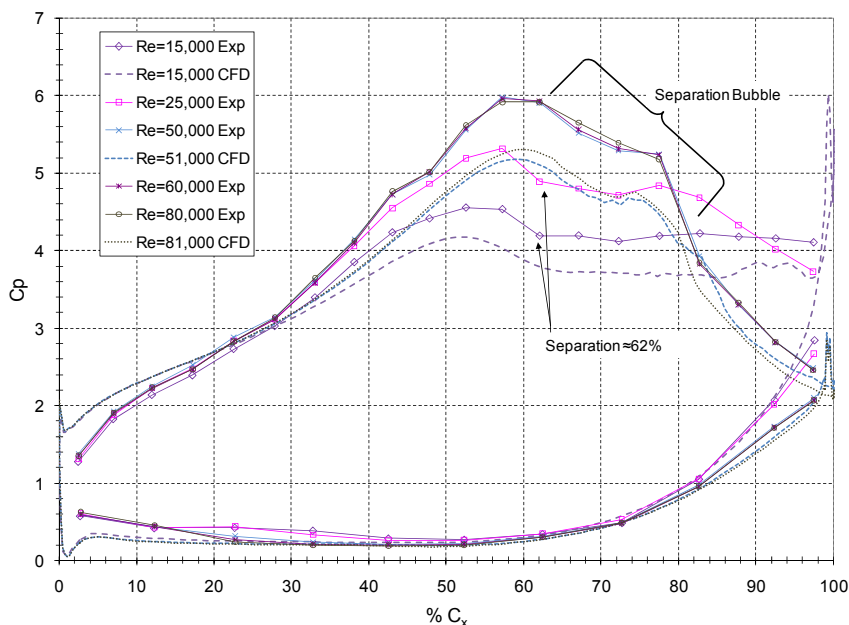


Figure 9. Pressure Coefficient, FSTI=3.4%.

B. PIV and flow visualization

1. $FSTI = 0.5\%$

Figure 11 shows flow visualizations of the separated shear layer above the aft portion of the L1A profile with low values of FSTI (no turbulence grid). At a low Reynolds number of 25,000 the shear layer is separated without reattachment and well defined laminar eddies traveling downstream along the shear layer can be identified. As Reynolds number increases, eddies form in the shear layer closer to the separation point and travel a short distance downstream before they transition to turbulent eddies. At a Reynolds numbers of 110,000 and 125,000 the transition length in the shear layer is very short and eddies maintain a laminar coherent structure for a very short period of time before becoming fully turbulent.

Averaged velocity fields for these conditions are shown in Figure 12. Since the PIV was not synchronized (phase-locked) to the shear layer frequency, the shear layer eddies are washed out by the averaging. The recirculations for high Reynolds numbers in these averages are indication of constancy of the recirculation region motion in the separated area.

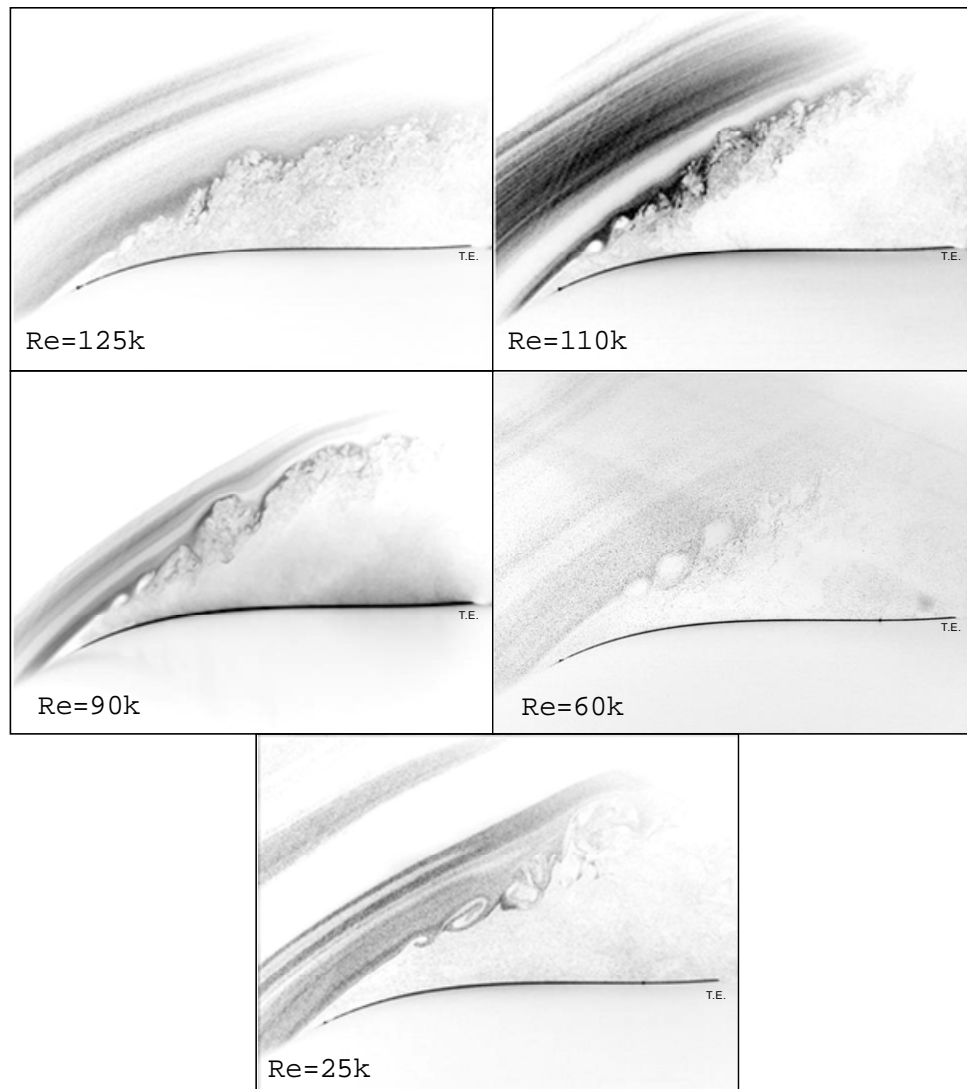


Figure 11: Select instantaneous flow visualizations in the blade normal field of view for $FSTI = 0.5\%$. The blade location on the left edge of the images corresponds to $C_x=52.5\%$ (42.0% SSL) and the trailing edge (marked T.E.) is located near the right side of the image.

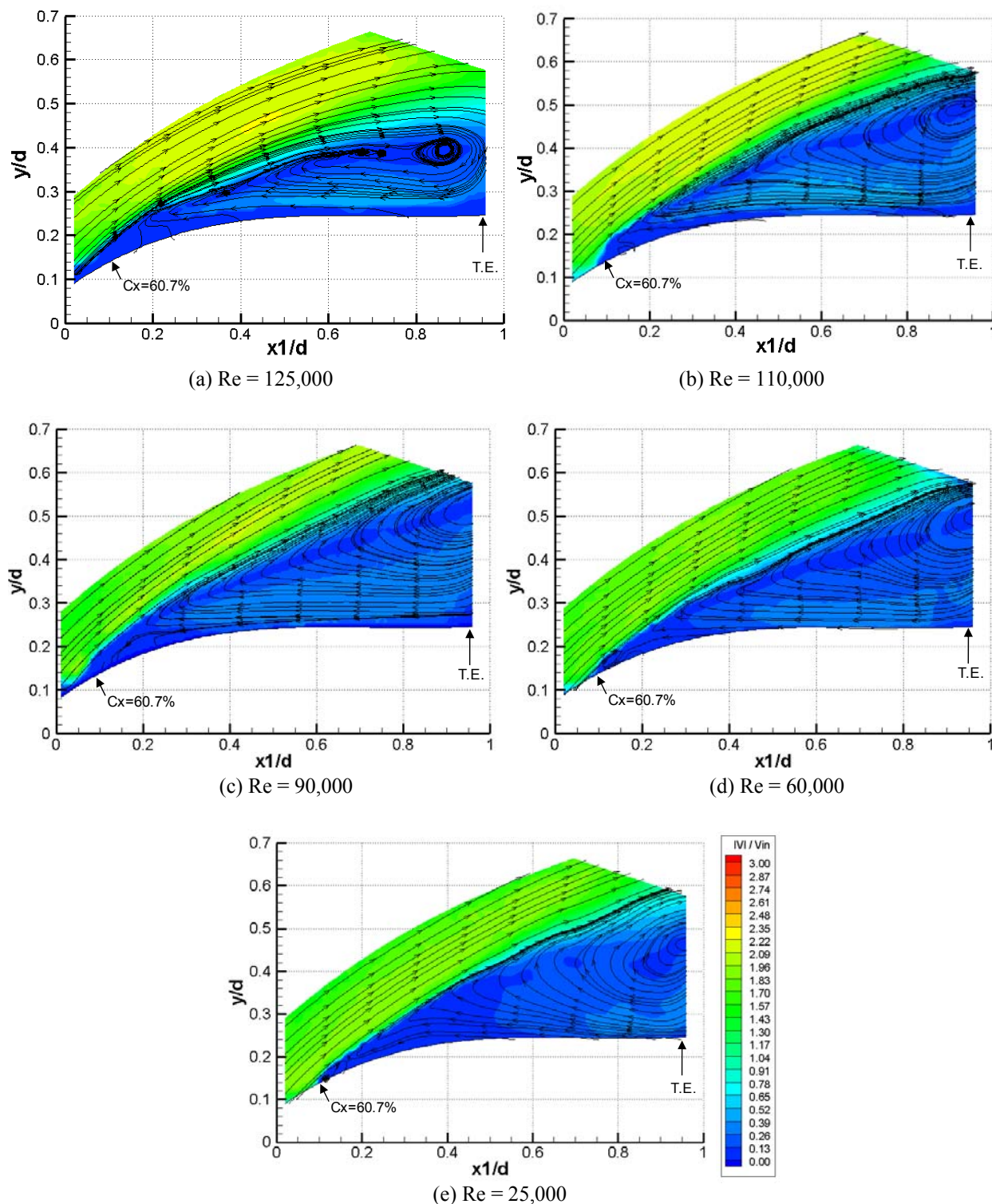


Figure 12. Averaged, non-dimensional velocity contour plots in the blade normal direction.

2. $FSTI = 3.4\%$

PIV and flow visualization was carried out at six flow speeds in the blade normal PIV plane corresponding to Reynolds numbers of 90k, 70k, 60k, 50k, 40k, and 25k. In the spanwise direction, PIV using a curved laser sheet was completed at Reynolds numbers of 60k, 40k, and 25k.

Blade Normal PIV Plane

Flow visualization, non-dimensional velocity contour, and non-dimensional RMS velocity magnitude for each Reynolds number are shown in Figures 13- 15. Flow is from left to right in each image. The instantaneous images show the effect of Reynolds number on transition. At a Reynolds number 90,000 the flow visualization shows a laminar boundary layer growing and transitioning to turbulent. The laminar boundary layer appears dark in the image due to lack of seeding mixing into the viscous layer. The existence of a separation bubble at this flow speed is not obvious from the flow visualization, but the PIV velocity plot shows an area of low velocity between $Cx \approx 60\%$ and $\approx 85\%$. This is consistent with the separation bubble observed in the C_p plots. As Reynolds number decreases to 70,000 the separation bubble thickens and in the instantaneous image it appears an eddy is shed from the separation bubble and transitions to turbulent downstream. The time averaged PIV velocity contour plot shows a separation bubble that has grown in thickness and appears more coherent in structure than the Reynolds number of 90,000 plot. For both flow speeds the time averaged PIV images show a region of near zero flow velocity just before the trailing edge. This is most likely due to a lack of seeding in this area. At a Reynolds number of 60,000 the separation location appears to move slightly downstream to $\approx 60\%$ chord. The turbulent boundary layer downstream from the separation bubble shows much better mixing and no signs of coherent structures such as those observed at Reynolds number of 70,000. As Reynolds number decreases to 50,000 the separation bubble increases in thickness and the flow transitions to a turbulent boundary layer downstream from the bubble. At a Reynolds number of 40,000, the instantaneous image shows a separated transitioning shear layer. Other instantaneous images taken at this flow number showed a shear layer that was fluctuating and nearly reattaching. The time averaged velocity plots show a circulation region below the separated shear layer with the streamlines indicating nearly reattaching flow. At a Reynolds number of 25,000 the flow is separated without reattachment with a separation location near $Cx = 59\%$. This is consistent with the location found by Bons et al.¹⁰. The instantaneous flow visualization shows eddies form in the separated shear layer and then transition to turbulence. A circulation region is present at Reynolds number of 25,000 in the time averaged PIV results. The separation point varies less than $\approx 2\%$ axial chord for each Reynolds number studied. The reattachment point, which is more difficult to locate precisely did not vary considerably across Reynolds number and was consistently located at $Cx \approx 85\%$. This is consistent with the location observed in the C_p plots.

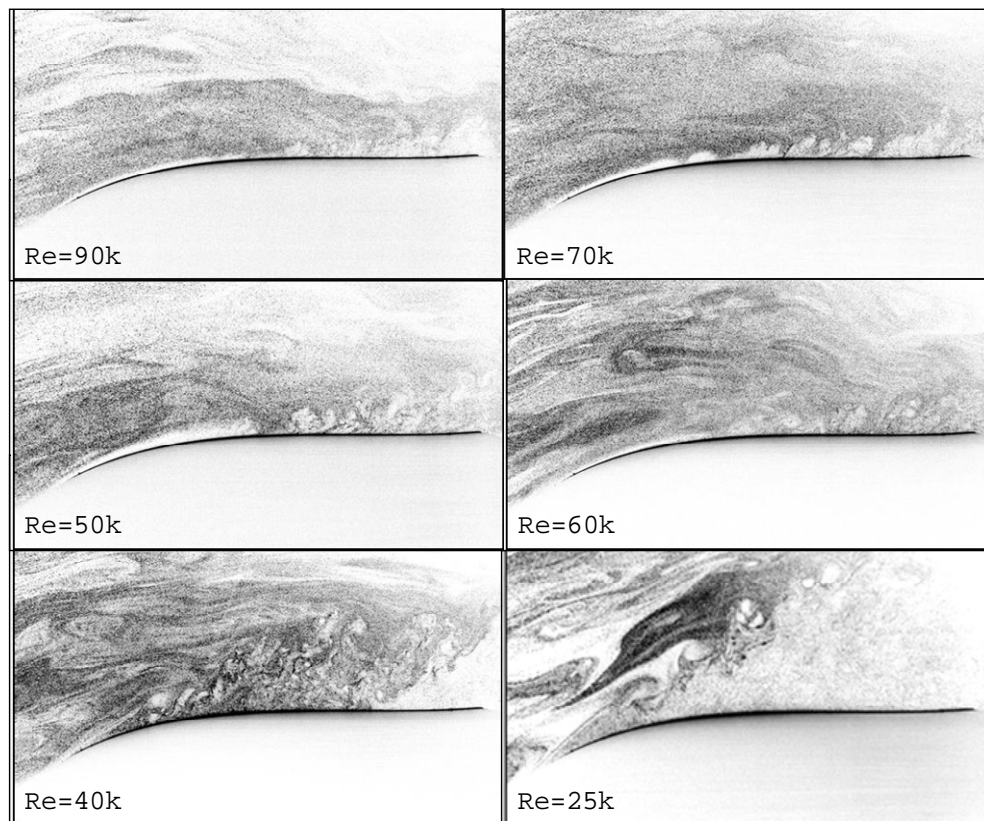


Figure 13. Flow visualizations with FSTI=3.4%.

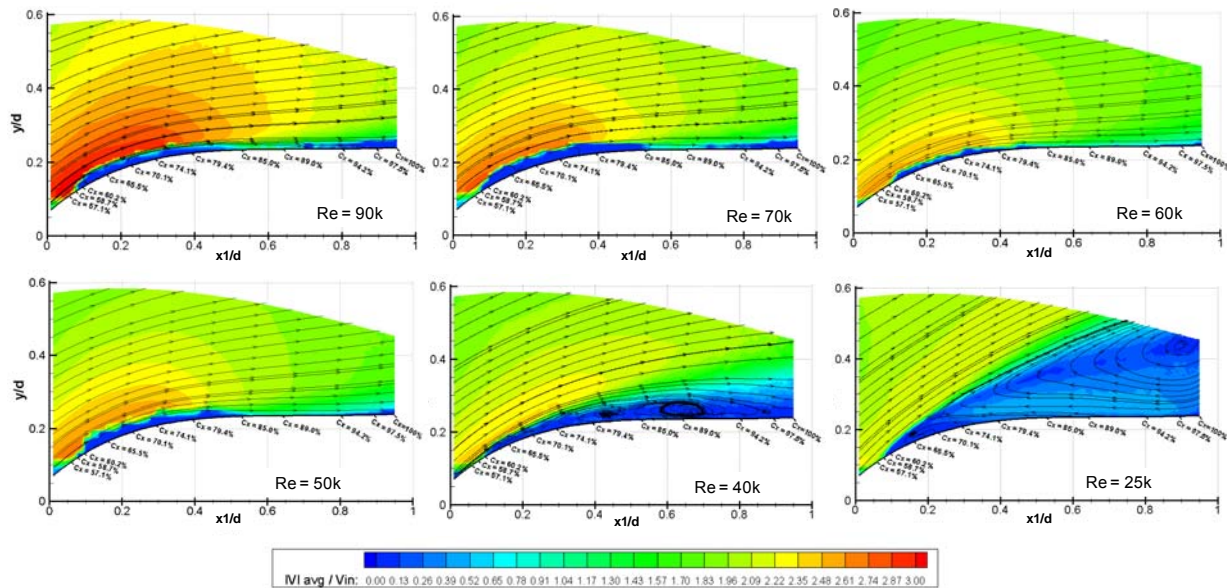


Figure 14. Non-dimensional velocity contours for FSTI=3.4%.

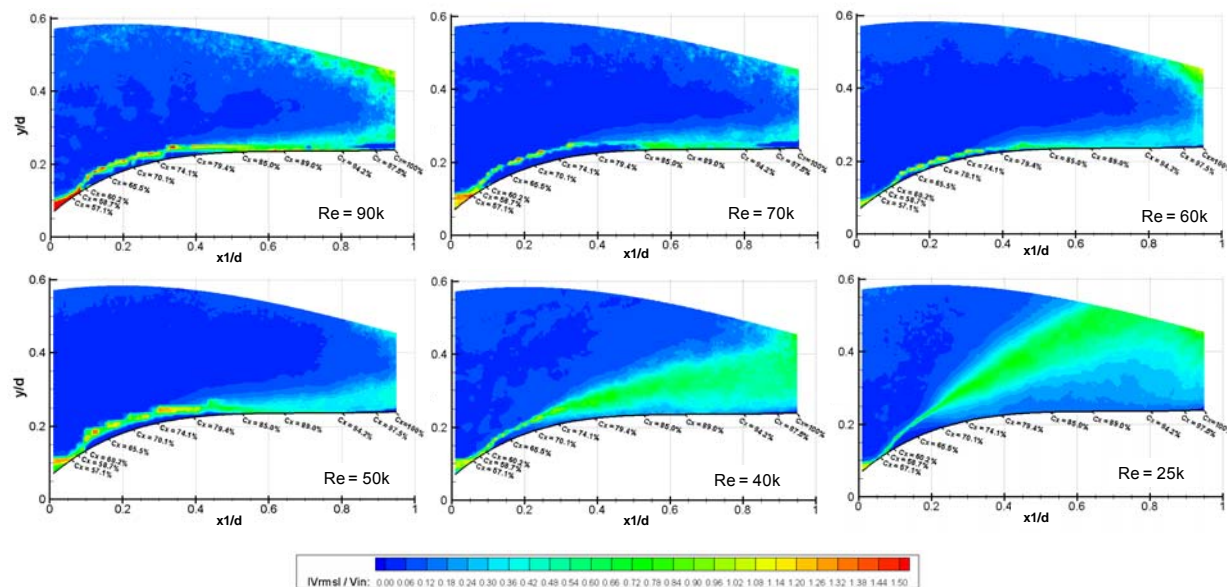


Figure 15. Non-dimensional RMS velocity magnitude for FSTI=3.4%.

Velocity profiles were extracted at the surface normal locations shown in Figure 16. Boundary layer height, δ , and shape factor, H were calculated from the profiles. The shape factor is calculated using Equation 4. Non-dimensionalized velocity profiles at Reynolds number of 60,000 are shown in Figure 17 spaced by %SSL. Figure 18-19 show the boundary layer thickness and shape factor for $Re=25,000, 60,000$ and $90,000$.

$$H = \int_0^{\delta} \frac{|V|}{|V|_{@ \delta}} dn \quad (4)$$

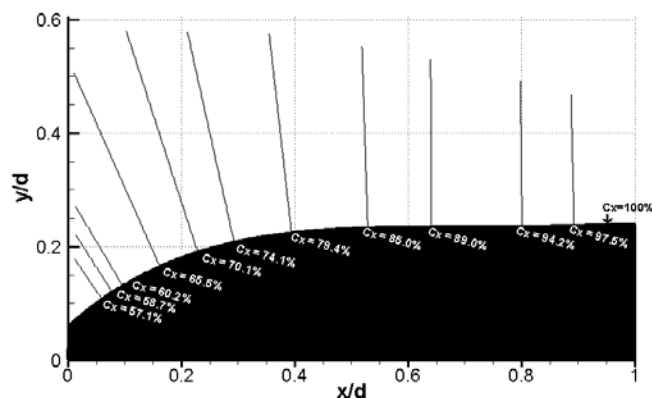


Figure 16. Surface normal velocity extraction locations.

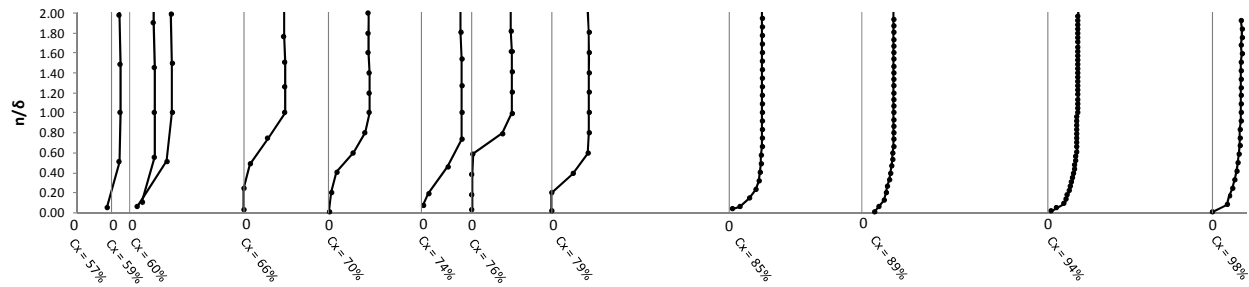


Figure 18. Surface normal non-dimensional velocity profiles at various surface locations for Re=60,000, FSTI ≈3.4%.

For flow over a flat plate, shape factor can be used as an indicator of adverse pressure gradient, transition, and conditions in which separation could occur. Flow over a curved surface can be approximated by flat plate flow if the boundary layer thickness is small compared to the radius of curvature of the wall¹⁸. The L1A blade suction surface radius of curvature is ≈50 times larger than the boundary layer thickness, so the flow over the suction surface of a LPT in a linear cascade meets this criterion, but care must be taken since the flow conditions are not the same. As pointed out by Schlichting¹⁹, there is a large drop in shape factor during transition and measurements by Schubauer and Klebanoff showed a drop in shape factor from 2.6 to 1.4 in the transition region of a flat plate. Shape factor increases as adverse pressure gradient increases and a variety of shape factors for which separated flow can occur are listed in literature. Based on Karman's general two-dimensional boundary layer integral relation, White^{18,20} lists shape factor values of ≈3.5 and ≈2.4, for laminar flow and turbulent flow respectively, above which separation can occur. Schlichting¹⁹ also summarizes different values of shape factor for turbulent boundary layers in which separation can occur and they vary from shape factors greater than $H \approx 4$ to as little as $H \approx 2$.

The boundary layer thickness is constant at the two most upstream surface location for both Reynolds number of 90,000 and 60,000. A gradual rise in boundary layer begins at $Cx=59\%$ for Reynolds number of 90,000 which corresponds to the location of a thin separation bubble. The separation bubble begins slightly further downstream, after $Cx=60\%$ at Reynolds number of 60,000. For both Reynolds numbers of 90,000 and 60,000 the separation bubble reattaches between $Cx=79\%$ and $Cx=85\%$. It is unclear why there is a dip in boundary layer thickness near $Cx \approx 74\%$. The boundary layer is only about 4mm thick in the area of the separation bubble and the limited resolution of PIV near the wall must be considered to add uncertainty to the boundary layer thickness calculation near the wall. In addition, the stair stepped pattern near the wall in the PIV velocity plots in the area of the separation bubble is believed to be due to a

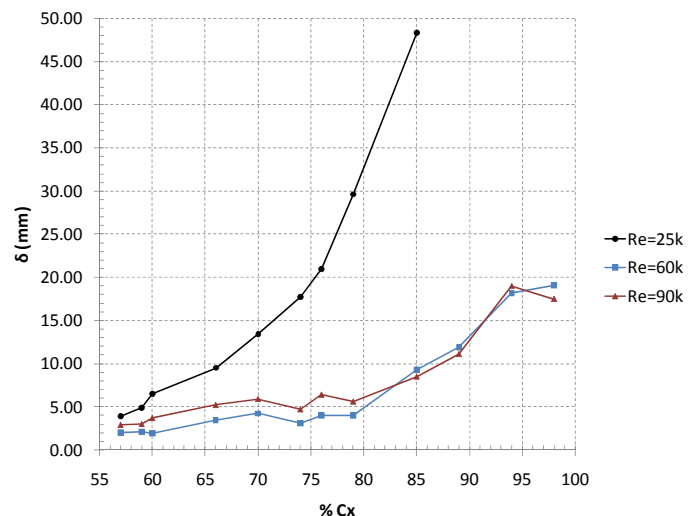


Figure 17. Boundary layer thickness for three Reynolds numbers.

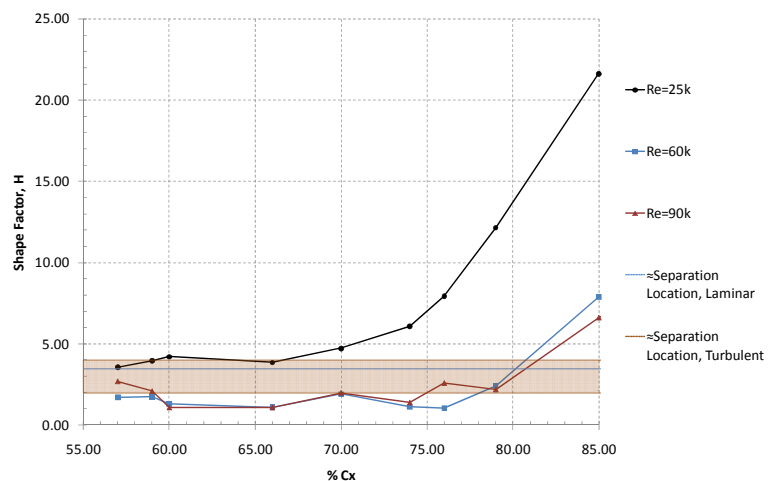


Figure 19. Shape factor for three Reynolds numbers.

combination of factors including the use of a square shaped interrogation region, curvature of the blade, noise due the reflection of the laser near the wall, and large gradient of velocity in the separation bubble versus freestream. The shape factor shown in Figure 19 shows a significant drop in shape factor at the separation location for both Reynolds numbers of 90,000 and 60,000. As discussed above, a sudden drop in shape factor is a characteristic of transitional flow. The shape factor remains low until $C_x=70\%$ where it recovers to a value approximately equal to the attached value, and then decreases again at $C_x=74\%$, followed by a gradual increase after $C_x=76\%$. The fluctuation in shape factor between $C_x=66\%$ and $C_x=76\%$ is likely due to the limitations of PIV near the wall mentioned above. The gradual increase after $C_x=76\%$ is an indicator of a turbulent boundary layer and increasing adverse pressure gradient.

At Reynolds number of 25,000 the boundary layer thickness grows significantly after the separation location of $C_x \approx 59\%$. This is consistent with separated flows that do not reattach. The shape factor at separation point ($H \approx 4$) is consistent with shape factors in literature that are reported to be prone to separation. Shape factor decreases slightly after the separation location until $C_x=70\%$ where it then increases exponentially.

Spanwise Curved PIV Sheet

The location of the spanwise curved laser sheet is shown in Figure 20. Since the laser sheet was formed by off-the shelf cylindrical lenses it does not match the surface curvature exactly, yet matches fairly well from $C_x \approx 60\%$ to 90% . As the sheet diverges from the surface upstream of $C_x=60\%$ streamlines cross the laser sheet decreasing the accuracy of the velocity calculation in the upstream region. Due to the curvature of the laser sheet, magnification factor is not constant and is a function of coordinate x_2 . The measurement of magnification factor adds additional uncertainty to the velocity field calculation. In this study the

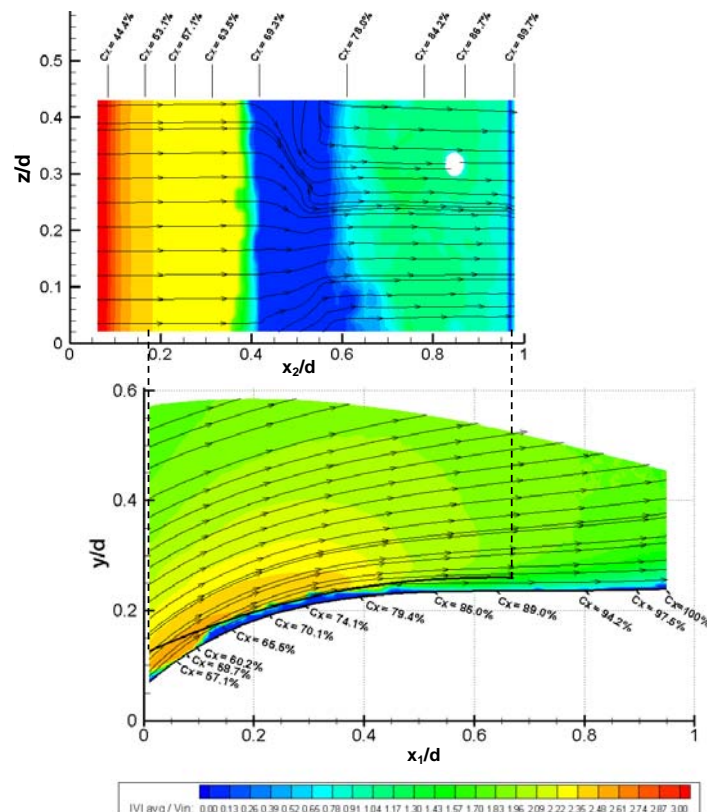


Figure 21: Time averaged, nondimensional velocity in the spanwise (top) and blade normal direction at $Re=60k$.

Reynolds number. At an inlet Reynolds number of 60,000, the spanwise plot shows that the curved laser sheet slices

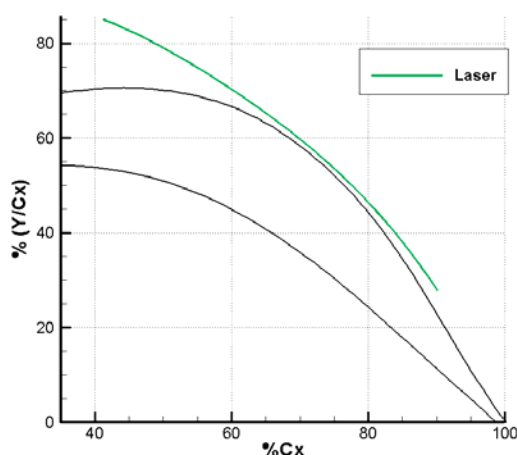


Figure 20: Location of spanwise laser sheet.

magnification was measured from a grid fixed to the blade surface, so the accuracy of the velocity calculation also drops off as the laser sheet diverges from blade surface upstream of $C_x=60\%$. A method of placing a grid that exactly lines up with the curved sheet would increase the accuracy of the magnification factor variation measurement and would decrease the overall uncertainty of the method. A grid placed on a deformable polymer or similar material that could be shaped to match a given laser sheet shape would be ideal.

Images taken in the spanwise FOV have been labeled with the surface location based on axial chord. These locations correspond to the location of the surface of the blade as viewed from the spanwise FOV camera. The optical axis of the spanwise FOV camera was perpendicular with the x_1 axis of the blade normal images.

Figures 21-23 show average spanwise velocity plots placed directly above blade normal direction velocity plots taken at the same

through a separation bubble. The location where the laser cut through the separation bubble is near $C_x \approx 68\%$, the location where velocity drops suddenly to nearly zero in the top image of Figure 21. The flow in the separation bubble is primarily downstream in the region imaged. This is consistent with flow at the top of a separation bubble.

Average velocity plot at Reynolds number of 40k shows a sudden decrease in velocity beginning at $C_x \approx 57\%$ followed by a region of reversed flow downstream of $C_x \approx 60\%$. It is unclear why the separation region begins at a location further upstream in the spanwise image than the blade normal image. The velocity magnitude of the reversed flow increases in the x_2 direction towards the trailing edge.

At a Reynolds number of 25k the spanwise images cut through the separated shear layer at $C_x \approx 60\%$, followed by a region of nearly stagnant flow followed by reversed flow that gradually increases in magnitude towards the trailing edge.

3. Discussion of spanwise instantaneous data

At a Reynolds number of 60,000, with FSTI of 3.4% the spanwise images slices through the top of thin separation bubble. One of the

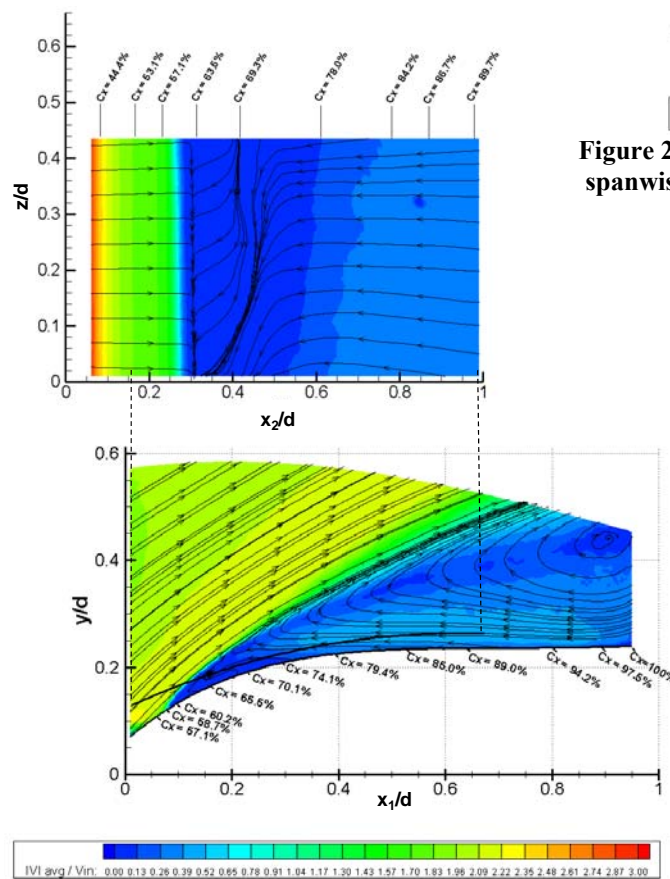


Figure 23. Time averaged, non-dimensional velocity in the spanwise (top) and streamwise (bottom) FOV at Re=25k.

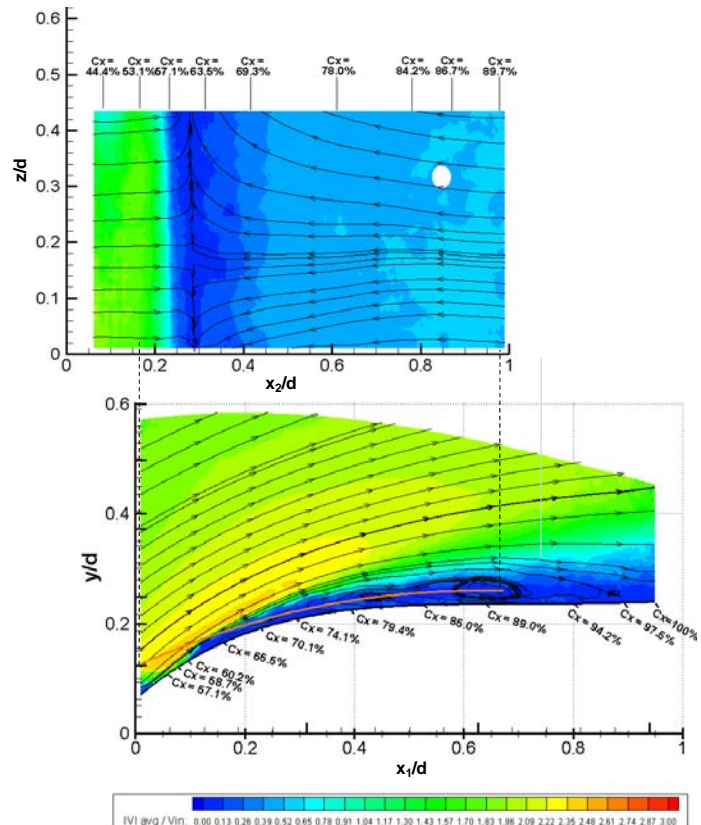


Figure 22. Time averaged, non-dimensional velocity in the spanwise (top) and streamwise (bottom) FOV at Re=40k.

instantaneous images was further analyzed as an example of the flow visualization and velocity data that is obtainable using the curved laser sheet PIV technique. Figure 24 (note: the image is mirrored and the freestream velocity is moving from right to left) includes the instantaneous velocity field in the spanwise direction and a zoomed in velocity vector plot of an area with a mushroom shaped flow feature. The instantaneous velocity shows that the flow in the separation bubble is complex and chaotic, and suggests the area may be a transitional shear layer at this instant in time. The flow appears turbulent directly downstream of the bubble area.

A zoomed in area of the flowfield with the mushroom structure has been further analyzed by using Reynolds and Galilean decomposition following the procedure demonstrated Adrian et al.¹⁷. The Reynolds and Galilean decomposition vector fields are shown in Figures 25 and 26 respectively. The decomposition technique aids in the visualization of vortical structures by subtracting the averaged or vorticity convection speed from the flowfield. The mushroom shaped

feature just downstream from the separated region is a pair of counterrotating vortices, surrounded by several other single vortices circled in Figures 25 and 26. Based on the boundary layer thickness obtained in the blade normal direction images and the location of the curved laser sheet, the spanwise flow field is located inside the boundary layer. The type of flow structures highlighted in the decomposed flowfields warrants further investigation.

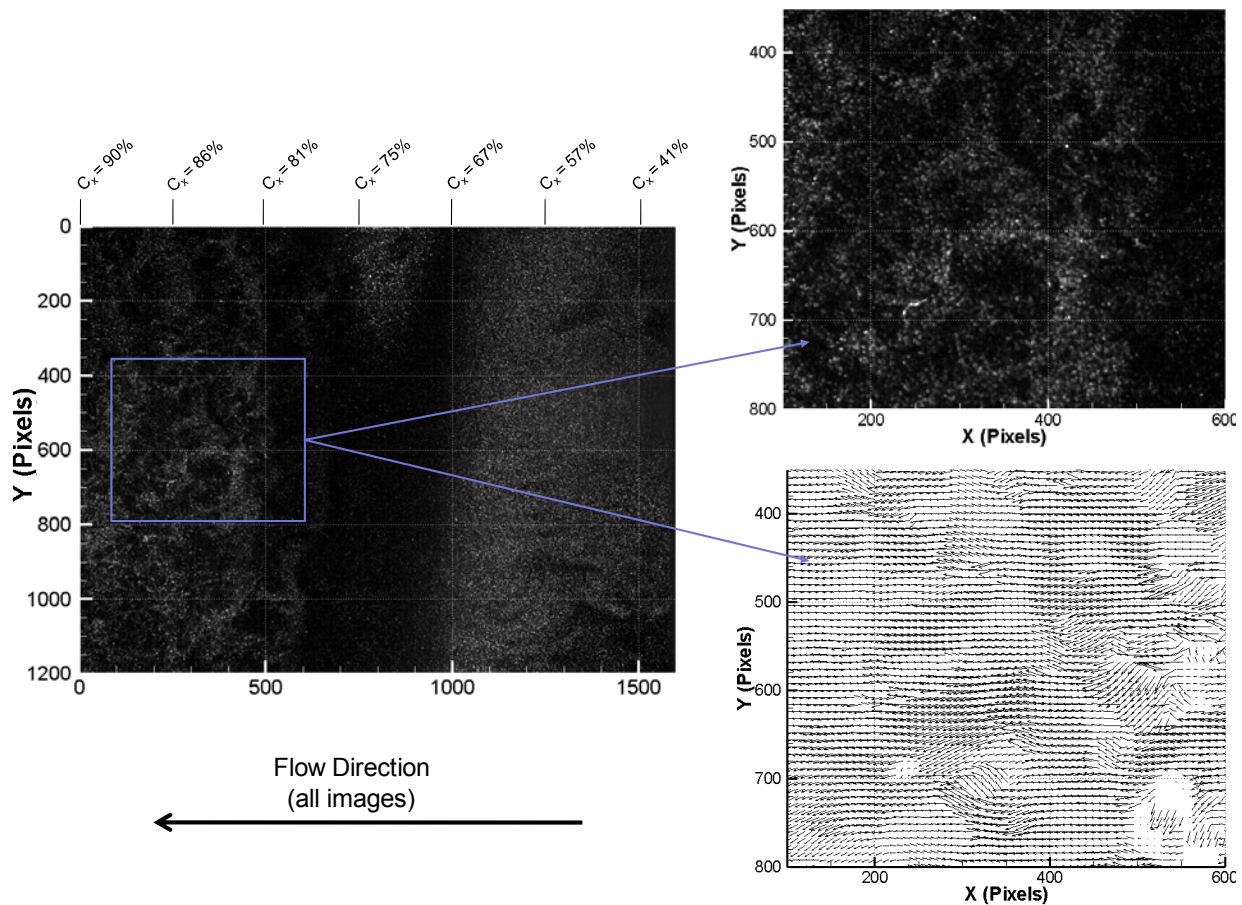


Figure 24. Instantaneous flow visualization in the spanwise field of view (left), zoomed in flow visualization (top right) and velocity vector field (bottom right). $Re=60k$, Image 21, $FSTI=3.4\%$.

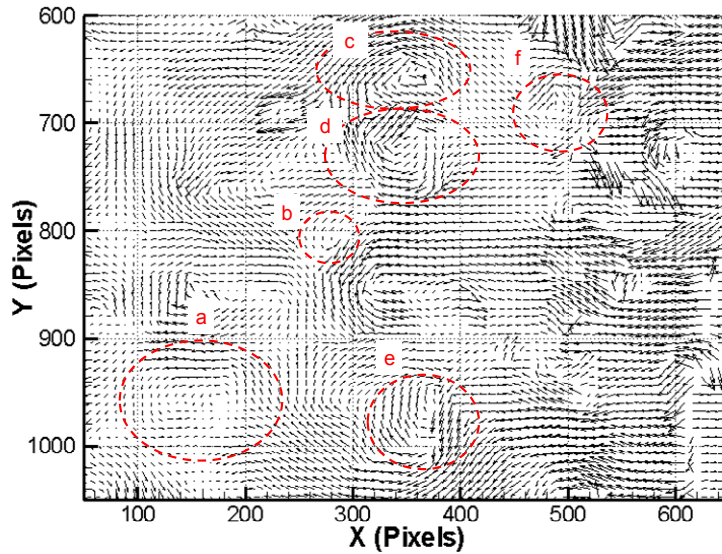


Figure 25. Reynolds decomposition of portion of instantaneous spanwise flowfield at Reynolds number of 60,000.

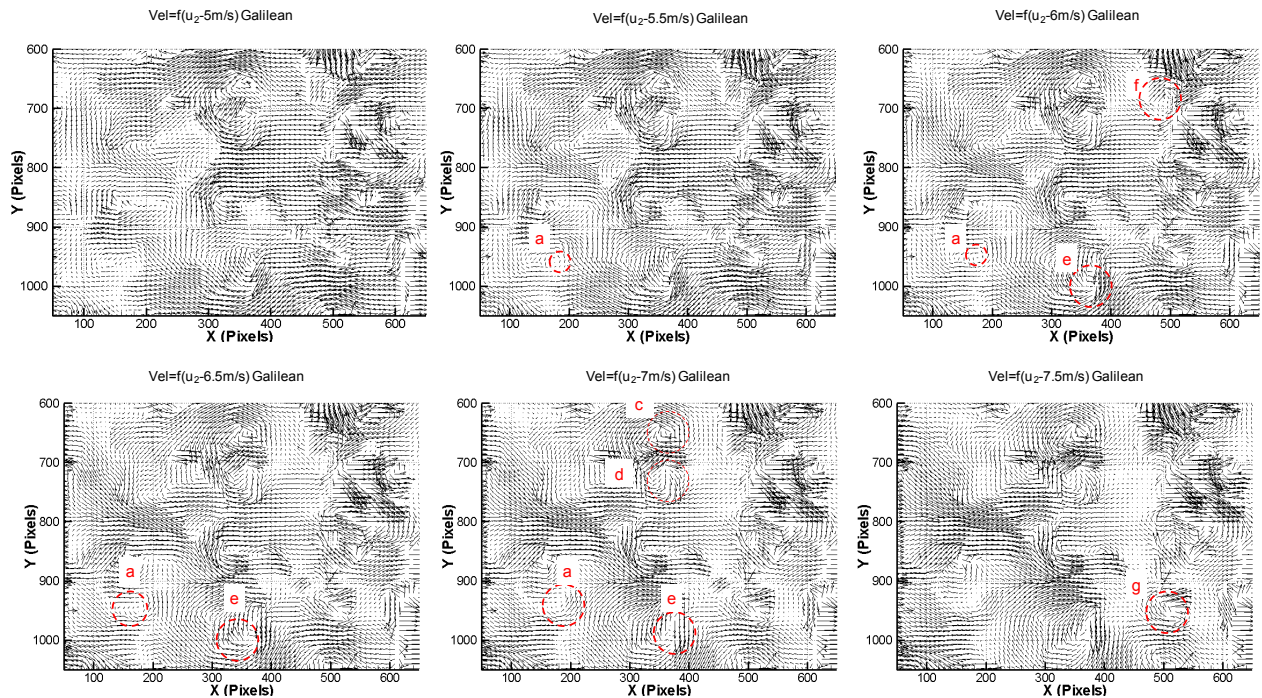


Figure 26: Galilean decomposition of a portion of the instantaneous spanwise flowfield, at Reynolds Number of 60,000.

IV. Conclusion

A novel technique for generating a curved laser sheet around an arbitrary wrappable shape was explained and demonstrated on a highly-loaded linear turbine blade to obtain PIV flowfield data in the spanwise direction. The spanwise direction PIV data was recorded using a curved laser sheet, which closely matched the blade curvature from $Cx \approx 60\%$ to 90% . Instantaneous images obtained with the curved laser sheet parallel to the curved suction surface indicated vortical flow structures in the boundary layer that warrant further investigation and demonstrate the flow visualization and data obtainable using the curved laser PIV technique. In addition wake averaged loss

coefficient and surface pressure coefficient were measured over inlet Reynolds numbers ranging from 15,000-130,000, and FSTI of 0.5% and 3.4%. For a FSTI of 0.5% the loss profile shows a loss knee with a top that begins at Reynolds number of approximately 70,000. The C_p distribution indicates separated flow up to the highest inlet Reynolds number measured with a FSTI of 0.5%. Flow visualization and PIV confirmed separated flow up to Reynolds number of 125,000 for the low FSTI condition. As Reynolds number increases, the separated shear layer transitions from laminar to turbulent much closer to the separation point. This is accompanied by a decrease in separated shear layer height as Reynolds number increases and transition length decreases. At FSTI of 3.4% the wake loss coefficient increases approximately exponentially as Reynolds number is decreased. C_p distribution at the higher turbulence level indicated separation at Reynolds number of 25,000 and below and a separation bubble for inlet Reynolds numbers between 50,000 and 80,000, which was the highest Reynolds number measured. PIV and flow visualization indicated a separation bubble at Reynolds number down to 50,000. At Reynolds number of 40,000 the averaged velocity field indicated separated flow with multiple circulation regions present below the separated shear layer. At a Reynolds number of 25,000, PIV indicated separated flow without reattachment.

Acknowledgments

This work was performed under the sponsorship of the Air Force Office of Scientific Research. The authors would like to thank John Clark, designer of the LPT blade studied in this work, for his support and guidance.

References

1. Raffel, M., Willert, C., Wereley, S., and J. Kompenhans, *Particle Image Velocimetry: A Practical Guide*, Springer, New York, 2007.
2. Lang, M., Rist, U., and Wagner, S., "Investigations on controlled transition development in a laminar separation bubble by means of LDA and PIV", *Experiments in Fluids*, Vol. 36, No. 1, Jan. 2004, pp. 43-52.
3. Burgmann, S., Brucker, C., and Schroder, W., "Scanning PIV measurements of a laminar separation bubble," *Experiments in Fluids*, Vol. 41, No. 2, Aug. 2006, pp. 319-326.
4. Zhang, W., Hain, R., and Kahler, C., "Scanning PIV investigation of the laminar separation bubble on a SD7003 airfoil", *Experiments in Fluids*, Vol. 45, No. 4, October, 2008, pp. 725-743.
5. Sondergaard, R., Rivir, R., Bons, J., "Control of Low-Pressure Turbine Separation Using Vortex Generator Jets", *Journal of Propulsion and Power*, Vol 18, No. 4, pp. 889-895, 2002.
6. Bons, J., Sondergaard, R., Rivir, R., "Control of Low Pressure Turbine Separation Using Vortex Generator Jets", AIAA 2004-2201, June 2004.
7. Rivir, R., Sondergaard, R., Bons, J., Yurchenko, N., "Control of Separation in Turbine Boundary Layers", AIAA 2004-2201, June 2004.
8. McQuilling, M., "Design and Validation of a High-Lift Low-Pressure Turbine Blade," Ph.D. Dissertation, Mechanical and Material Engineering Dept., Wright State Univ., Dayton, OH, 2007.
9. Clark, J. P., Koch, P. J., Ooten, M. K., Johnson, J. J., Dagg, J., McQuilling, M. W., Huber, F., and Johnson, P. D., 2009, "Design of Turbine Components to Answer Research Questions in Unsteady Aerodynamics and Heat Transfer," ASME Paper No. GT2009-60158 (to be published).
10. Bons, J., Pluim, J., Gompertz, K., Bloxham, M., Clark, J., "The Application of Flow Control to an Aft-Loaded Low Pressure Turbine Cascade with Unsteady Wakes", ASME Paper No. GT2008-50864.
11. J. Estevadeordal, S. Gorrell, W. Copenhaver, "PIV study of wake-rotor phenomena in a transonic compressor under various operating conditions", *AIAA J. of Propulsion and Power*, Volume 23, No. 1, January-February 2007, pp. 235-242.
12. Hart, D., "Super-Resolution PIV by Recursive Local-Correlation," *Journal of Visualization*, Vol. 3, No. 2, Sept. 2000, pp.187-194.
13. McCray, T.W., Estevadeordal, J. and Puterbaugh, S. L., "Parallel Computing for Linux Clusters—Application to Particle Image Velocimetry." AIAA Paper 2005-1385, Reno, NV, Jan 10-13, 2005.

14. Estevadeordal, J., Gorrell, S., Puterbaugh, S., "PIV Measurements of Blade-Row Interactions in a Transonic Compressor for Various Operating Conditions," AIAA Paper 2008-4700 44th AIAA/ASME/SAE/ASEE Joint Propulsion Conference & Exhibit, Connecticut 20-23 July 2008.
15. Dorney, D. J. and Davis, R. L., 1992, "Navier-Stokes Analysis of Turbine Blade Heat Transfer and Performance," *ASME Journal of Turbomachinery*, Vol. 114, pp. 795-806.
16. Praisner, T. J. and Clark, J. P., 2007, "Predicting Transition in Turbomachinery, Part I – A Review and New Model Development," *ASME Journal of Turbomachinery*, Vol. 129, pp. 1-13.
17. Adrian, R., Christensen, K., and Liu, Z.-C., "Analysis and interpretation of instantaneous turbulent velocity fields", *Experiments in Fluids*, V. 29, 2000, pp. 275-290.
18. White, F., *Fluid Mechanics*, 4th Ed., McGraw-Hill, 1999.
19. Schlichting, H., *Boundary Layer Theory*, 7th Ed., McGraw-Hill, 1979.
20. Von Karman, T., "On Laminar and Turbulent Friction," *Z. Angew. Math. Mech.*, V. 1, 1921, pp. 235-236.

APPENDIX B

High Lift LPT Blade Suction Surface Flow Investigation Using Surface Stress Sensitive Film

Christopher Marks¹, Chase Nessler², Rolf Sondergaard³, Mitch Wolff⁴,
Air Force Research Laboratory, WPAFB, OH, 45433

Jim Crafton⁵, Sergey Fonov⁶
Innovative Scientific Solutions Inc., Dayton, OH 45440

This paper presents the first in a series of experiments using surface stress sensitive film (S3F) applied to a highly loaded low pressure turbine blade (L1A) developed at the United States Air Force Research Laboratory (AFRL). This effort builds upon previous work that investigated the use of S3F in low speed flows below 7 m/s. The tests were carried out in a linear cascade facility in which the low speed flow environment along with a high degree of flow turning over the blades pushes the limits of the S3F technique. In this initial work, two different film thicknesses were applied to the blade suction surface in order to investigate the film sensitivity and determine a more precise region of interest for follow-on work. Flow visualization was used to evaluate the effect of the film on the suction surface flow. Data was acquired at Reynolds numbers of 6.0×10^4 and 2.5×10^4 . Shear displacement data acquired with S3F indicated regions of separated and attached flow. In addition, shear displacement was obtained at a Reynolds number of 2.5×10^4 in an unsteady flow environment created by a periodic wake generator. The S3F responded to the impingement of periodic wakes across the suction surface and S3F shows promise as an experimental tool for studying LP turbine blade unsteady flow characteristics.

Nomenclature

C_x	= axial chord
F_x	= Force in the x direction (tangential)
h	= S3F thickness
P	= Normal Stress, or Pressure
Re	= Reynolds number, $Re = \rho V_{in} C_x / \mu$
R_x	= tangential reaction of the film
R_y	= normal reaction of the film
u	= shear displacement in the streamwise direction
V	= velocity magnitude
V_{in}	= inlet velocity
w	= shear displacement in the cross-stream direction
ρ	= density
τ	= wall tangential shear stress
μ	= shear modulus, or viscosity

¹ Graduate Student, Propulsion Directorate, 1950 Fifth Street, Member AIAA.

² Graduate Student, Propulsion Directorate, 1950 Fifth Street, Member AIAA

³ Aerospace Engineer, Propulsion Directorate, 1950 Fifth St, Associate Fellow AIAA

⁴ Scientific Advisor, Propulsion Directorate, 1950 Fifth St., Associate Fellow AIAA.

⁵ Research Scientist, 2766 Indian Ripple Road Dayton OH 45440, Member AIAA.

⁶ Research Scientist, 2766 Indian Ripple Road Dayton OH 45440, Member AIAA.

I. Introduction

Low pressure (LP) turbine blades are prone to separation and reduced efficiency when operating at high altitude where the Reynolds number drops to values that allow separated flow across the suction side surface. In an effort to increase LP turbine efficiency it is necessary to understand the flow phenomena associated with transition and separation over the blade. The current paper is the first in a new series of efforts to investigate the use of surface stress sensitive film (S3F) to examine the flow structure on the suction surface of LP turbine blades. This series of work will build upon previous investigations that utilized S3F to investigate flow over the suction surface of similar highly loaded LP turbine blades at low Reynolds number.¹⁻³

S3F is a relatively new method of measuring surface shear stress that utilizes an elastic film which deforms under the action of applied loads. The displacement of markers in the film are optically measured, then spatially cross-correlated with a wind-off image, and converted to forces using a physical stress/strain model of the film. The S3F technique is sensitive to both skin friction and pressure gradient, however, the film response can be designed such that response to shear forces is significantly larger than its response to normal forces (pressure). This behavior allows the S3F to operate as a skin friction sensor, even in the presence of much stronger pressure forces.⁴

Previous investigations have demonstrated the potential of S3F in flow velocities below 7 m/s ,¹ applied to a Pack-B airfoil in a linear wind tunnel. It was found that the sensitivity of the film is critical due to an order of magnitude variation of shear stress gradients from leading edge to trailing edge in the streamwise direction. McQuilling et al. demonstrated the use of S3F applied to a L2F highly loaded LP turbine blade in a linear cascade, to establish the separation location for CFD transition model validation.² The studies by McQuilling et al.^{2,3} demonstrated the potential of S3F for identification of flow features along the suction side surface of a blade at low velocity and also identified measurement uncertainties that need further investigation. Two different applications of S3F film resulted in two different shear stress profiles along the surface of the blade. Sensitivity to tunnel vibration and deformation of the turbine blades in the wind tunnel was identified as a potential source of uncertainty with the technique.² In addition, S3F was applied in a cavity along the suction surface and irregularities in the data were observed that may have been due to disturbance of the flow by the S3F not being perfectly flat or flush with the blade surface.

A. Current Study

The current study is the first in a new series of investigations; it involves the application of several different S3F to the suction surface of a highly loaded LP turbine blade to check the installation method, film sensitivity, and identify a more precise region of interest for future studies. In addition, shear displacement field measurements were acquired in the unsteady flow environment created by a periodic wake generator to investigate the use of S3F for future LP turbine blade unsteady flow investigations. In order to address sources of uncertainty identified by McQuilling et al.,¹⁻³ markers were used to compensate for error introduced by blade deformation, and flow visualization was used to quantify the effect of the film installation on suction side flow characteristics.

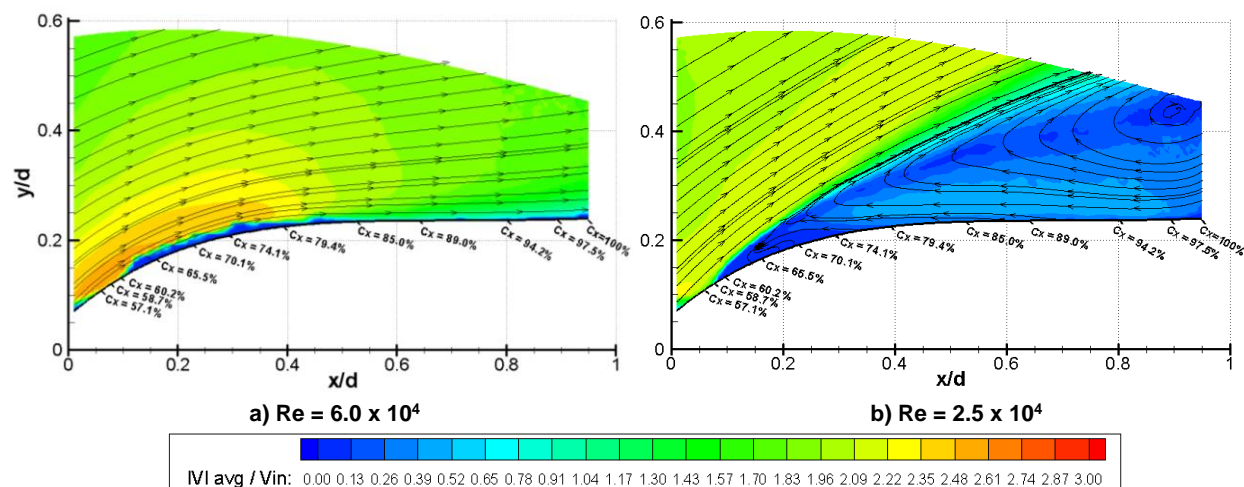


Figure 1. Time averaged velocity field of flow over the suction surface of L1A LP turbine blades at the Reynolds numbers studied in this paper.⁵

Experiments were performed at two different Reynolds numbers in a linear cascade of seven L1A LP turbine blades. The two Reynolds numbers analyzed, 6.0×10^4 and 2.5×10^4 , were chosen for their two different suction side

flow features. A previous experimental investigation of the L1A by Marks et al.⁵ identified a closed reattaching separation bubble on the suction side surface at a Reynolds number of 6.0×10^4 , and fully separated flow when Reynolds number was reduced to 2.5×10^4 . Time averaged PIV velocity contour plots (Figure 1) show the flow over the suction surface of the L1A at the two Reynolds numbers investigated in this work. At the higher Reynolds number tested (Figure 1b), a thin reattaching laminar separation bubble is present on the suction surface, indicated by the region of low velocity along the suction surface from approximately $C_x=60\%$ to 85% . At the separation point the laminar boundary layer detaches from the surface due to an adverse pressure gradient. The separated shear layer transitions to turbulence and then reattaches. At the lower Reynolds number tested (Figure 1b) the boundary layer separates and does not reattach. In between the separated shear layer and the blade surface is a large vortex in which the flow is reversed along the blade surface.

A schematic of the flow features inside a closed reattaching laminar separation bubble is shown in Figure 2. Just aft of the separation point is a “dead air region” of near zero velocity, and just forward of the reattachment point is a vortex of reversed flow.

By definition of wall shear stress in a boundary layer (eq. 1), streamwise shear is greater than zero in regions of attached flow, zero at separation points, and negative in areas of reversed flow.

$$\tau_w \approx \mu \left(\frac{\partial u}{\partial y} \right)_{y=0} \quad (1)$$

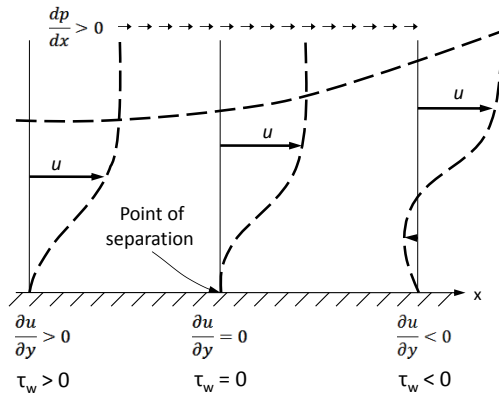


Figure 3. Wall shear stress direction based on streamwise, wall normal velocity gradient. Image modified from White⁷.

The current study uses a surface stress sensor made of an elastic polymer film to obtain the film shear displacement field and shear stress along the blade suction surface, which provides visualization of the surface flow features discussed above. S3F's ability to measure a surface's shear stress field makes it a useful sensor for both qualitative and quantitative indication of surface flow features and separation.

II. Surface Stress Sensitive Film

S3F is an elastic polymer film that deforms to applied normal and tangential forces. Film displacement is measured optically, then spatially cross-correlated with a wind-off image to obtain the two dimensional tangential displacement field. The normal force can be measured using the fluorescence signal emitted from a fluorescent probe embedded in the S3F. The shear stress and pressure gradients are calculated from the displacement field by solving the inverse problem using a finite element model of the elastic film.⁴

The film is sensitive to both tangential and normal stresses, but the film can be designed to be more sensitive to stresses in one direction than the other. At spatial frequencies (thickness/contact surface) below 0.1 (thin films) film response can be modeled mathematically by equation 2.

$$R_x = \frac{h}{\mu} \left(\tau_x - \frac{h}{2} \frac{\partial P}{\partial x} \right) \quad R_y = \frac{h}{\mu} \left(\frac{h^2}{3} \frac{\partial^2 P}{\partial x^2} - \frac{h}{2} \frac{\partial \tau_x}{\partial x} \right) \quad (2)$$

In equation 2, the surface normal (R_y) and tangential (R_x) reaction of the film is written in terms of the film thickness (h), shear modulus (μ), tangential stress (τ_x), and normal stress (P). Note that the x-direction reaction of the film is a function of the applied tangential force and the pressure gradient. Furthermore, the pressure gradient is weighted by the film thickness. These equations may be used as a design tool for the films. If one is interested in skin friction, a thin film will mitigate the response to pressure gradients relative to shear forces. For example a 100- μm film with a 1-kPa/m pressure gradient and a 1-Pa shear would respond to the shear force with an amplitude that is 20X larger than the amplitude of the response to the pressure force. Conversely, pressure forces would be more significant in the response of a thick film.⁴

Quantifying and improving upon the sources of uncertainty of S3F measurements is an on-going effort. Crafton et al.⁴ identified the dominant error sources of shear stress measurement using S3F as tangential displacement and film thickness. Experiments using fully developed channel flow resulted in skin friction measurements with an error of about 6% full scale, demonstrating that S3F is a powerful quantitative tool.

III. Experimental Setup

B. Experimental Facility

The facility used in this project was the AFRL Low Speed Wind Tunnel (LSWT), which has been described by Sondergaard et al.,⁸ and Bons et al.⁹ A photograph of the wind tunnel and a schematic of the test section are shown in Fig. 1 & 2. The wind tunnel test section is 0.85m tall by 1.22m wide at the inlet and houses the linear turbine cascade. A 125-hp electric motor drives an axial flow fan which draws air through the test section at up to 80m/s. The wind tunnel flow uniformity is better than 1% with a FSTI of approximately 0.5%. An optional turbulence generation grid can be used to increase the freestream turbulence up to a maximum of approximately 12%. In this study data was taken with a turbulence grid providing a FSTI of 3.4%³.

In addition to control of isotropic freestream turbulence the facility has a unique internally mounted periodic wake generator described in Nessler et al.¹⁰ The wake generator creates periodic wakes that traverse across the linear cascade row to simulate the periodic unsteadiness found in a real turbine environment. In this work the wake generator speed was adjusted to obtain a flow coefficient of 0.8. Cylindrical rods 3.2 mm in diameter were used to generate the wakes. This rod diameter was chosen because it matches the turbine blade trailing edge diameter. The wake generating rods were spaced 0.178 m apart. Data measured with the periodic wake generator is presented by phase, each phase corresponding to one wake passing period (76 ms) divided into 12 phases.

The linear cascade has 7 blades with a span of 0.88m and an axial chord of 0.18m. The L1A profile studied was designed by John Clark of AFRL and is described by Bons et al.¹¹ It is a highly loaded, slightly more aft-loaded version of the L1M profile with a design Zweifel coefficient of 1.34. The cascade has a solidity of 0.99 and a design inlet flow angle of 55° and design exit angle of 30° from the plane of the cascade. Wake loss coefficient, surface pressure coefficient, and PIV images in the blade normal and spanwise directions were recorded for a variety of Reynolds numbers and freestream conditions by Marks et al.⁵



Figure 4. AFRL Low Speed Wind Tunnel Facility.

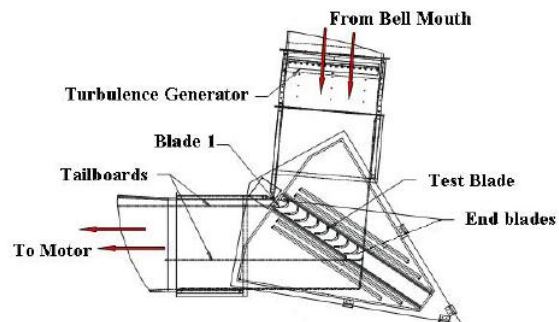
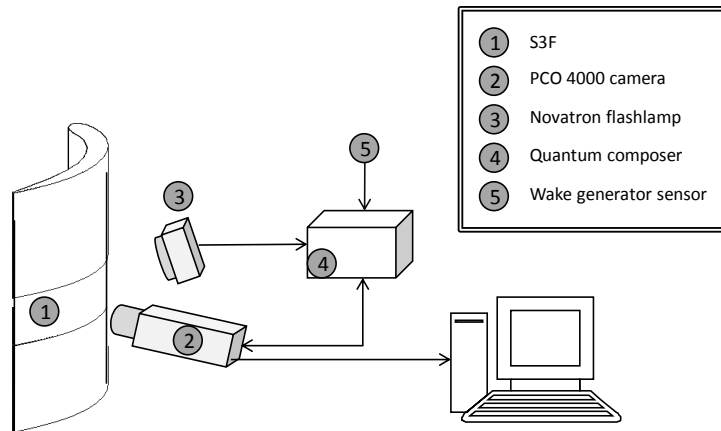


Figure 5. Top view of LSWT test section.

C. S3F Technique

The S3F experimental setup is shown in Figure 6. S3F was installed on blade 4 of the LP turbine cascade. Images were acquired with a commercial, high resolution CCD camera (PCO 4000) with a resolution of 4008 x 2680 pixels. A Nikkor 105 mm f2.8 lens set to an aperture of f8 was fitted to the camera. The camera was mounted between the tailboard and the wind tunnel outer wall which provided a view from $C_x = 50\%$ to 90% . A Novatron flashlamp with flash-on time on the order of several hundred microseconds was used to illuminate the S3F. Data was obtained for two different film thicknesses. The first film was 1.5 mm thick, and the second film was 0.3 mm thick, both on a 2.5 mil substrate. The thinner, 0.3 mm thick film had a shear modulus of 120 Pa, and the thicker 1.5mm thick film had a shear modulus of 110 Pa. Film calibration was determined by harmonic excitation in which the film shear modulus is determined by placing a small weight on the film and determining the first tangential oscillation frequency. This method of film calibration is dependent on oscillation frequency, film thickness, and film density.



The 1.5 mm thick film (Fig. 7) covered the full length of the suction surface and the ends of the film were wrapped around the leading edge and trailing edge of the blade in order to minimize the impact of the film on the suction surface flow structure. The 0.3 mm thick film extended from approximately $C_x=20\%$ and wrapped around the blade trailing edge. The two film installations are shown in Figure 7 and Figure 8. Both films were glued to the surface of the blade. These two different installations provided a check as to whether either film had an effect on the gross flow structure across the blade suction surface. Flow visualization was used to compare the suction surface

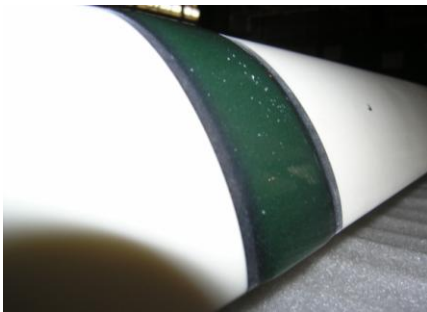


Figure 7. 1.5 mm thick S3F installed on blade suction surface. The leading edge area is shown.



Figure 8. 0.3 mm thick S3F installed on blade suction surface. The leading edge of the film is shown.

flow structure without S3F installed, to the flow with 1.5 mm thick S3F, and 0.3 mm thick S3F installed.

Planned follow-on work will utilize alternative S3F application techniques such as spray-on films, or small cavities filled with S3F placed in areas of interest on the suction side of the blade. Examples of S3F applied by filling a cavity with S3F, and by spraying the polymer components on to the surface of the model are shown in Figure 9. These application methods are expected to have minimal effect on the suction side flow. In addition to minimizing flow perturbation, forming the film in cavities provides good control of the film thickness and physical properties, and control of these parameters is necessary for quantitative measurement of pressure and skin friction.⁴

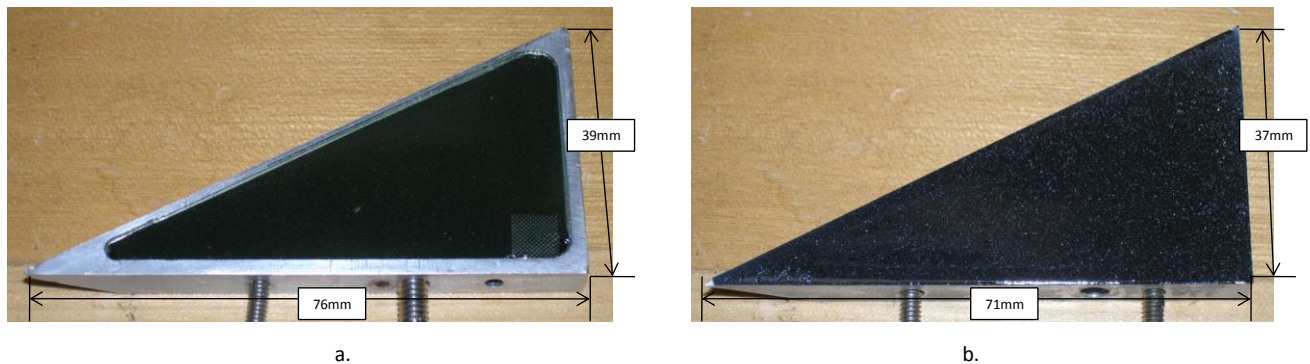


Figure 9. Samples of S3F applied by a.) filling a cavity, and b.) spray-on with an airbrush.

D. Flow Visualization Technique

The flow visualization technique involved illuminating seeding particles with a thin, laser-light sheet and recording the light scattered by the seeding particles in a series of instantaneous images. The laser-light sheet was formed by a combination of spherical and cylindrical lenses. The flow was seeded with a fog mixture of propylene glycol and water.

The laser and camera were mounted on optical breadboards located directly underneath and adjacent to the cascade. The laser was a dual-head (532-nm), frequency doubled, flashlamp-pumped Nd:YAG laser (New Wave Solo - 120). The laser was capable of delivering dual 120 mJ pulses at repetition rates of up to 15Hz.

Mie scattering from the seed particles was recorded on commercial, high-resolution CCD digital camera sensors (PCO1600) with a resolution of 1600 by 1200 pixels. Images were recorded at a frequency of 10Hz. The camera was mounted underneath the test section looking through a 1.25cm thick clear plexiglass cascade bottom plate, approximately 40cm from the plane of the light sheet. The camera was fitted with a 35-70mm f2.8 lens which provided a field of view of 152mm by 113mm.

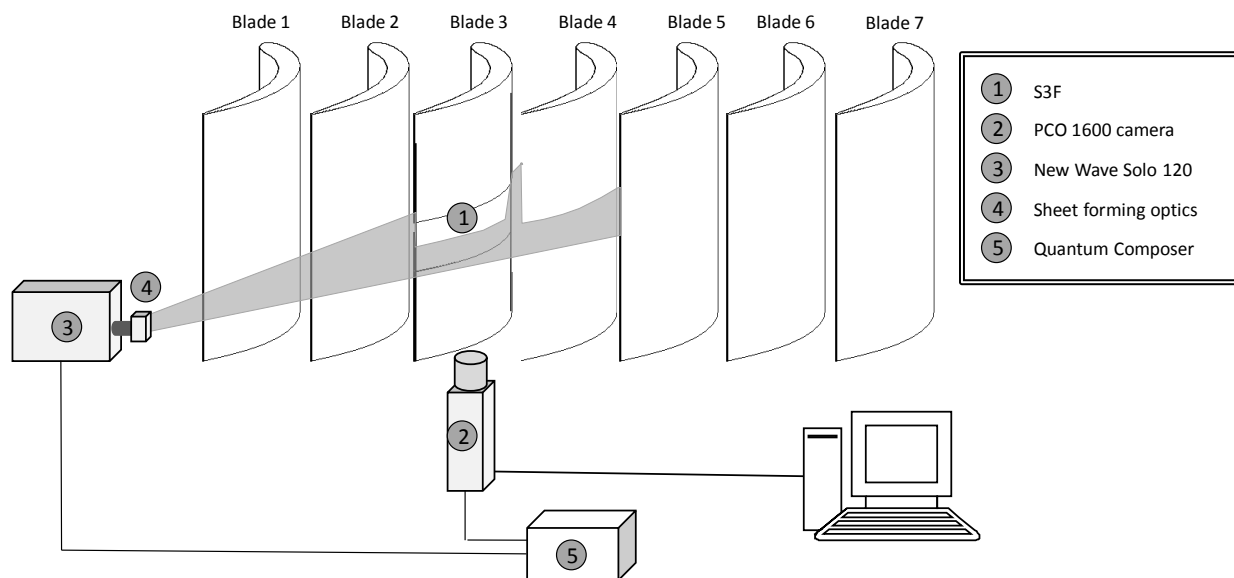


Figure 10. Flow visualization experimental setup.

IV. Results

A. S3F, Steady Flow

Instantaneous wind-off and wind-on images of the S3F were spatially cross-correlated to obtain two dimensional shear displacement fields. Markers on the edge of the S3F substrate were used to cancel out sources of error during the cross-correlation process. In the presence of low pressure gradients, and when film thickness is small, shear displacement relates to shear stress by a linear transformation (see eq. 2). The accuracy of the calculation of shear stress from the shear displacement field is highly dependent on the measurement of the S3F material properties. For this initial work, the majority of the data is presented as shear displacement. Time averaged shear stress was calculated for the 1.5mm thick film at a Reynolds number of 6.0×10^4 and compared to wall shear stress calculation using Cole's law of the wake downstream from the separation bubble reattachment point, and as described in refs. 2 and 7.

Data was obtained at two different Reynolds numbers for each of the two films tested. Instantaneous and mean contour plots of the shear displacement field are presented in Figure 11 & Figure 12, and a line plot of the u and w component of shear displacement in Figure 13. The camera was mounted so that the image plane was parallel to the aft portion of the blade. From the trailing edge to approximately $C_x = 65\%$ the relationship between wall distance and the x-dimension of the image plane is constant. Forward of $C_x = 65\%$ the high curvature of the blade profile results in a nonlinear relationship between wall distance and the x-direction of the image plane. Shear displacement results listed with units of pixels corresponds to shear displacement in the image plane. Shear stress results were calculated in the wall tangential direction by converting displacement from pixels to surface length using a scale glued to the blade surface.

A small area of erroneous data is present in the plots at $x/d = 0.7$ and $y/d = 0.35$ that could not be compensated for due to physical constraints on the experimental setup. Future work will be able to eliminate this erroneous area.

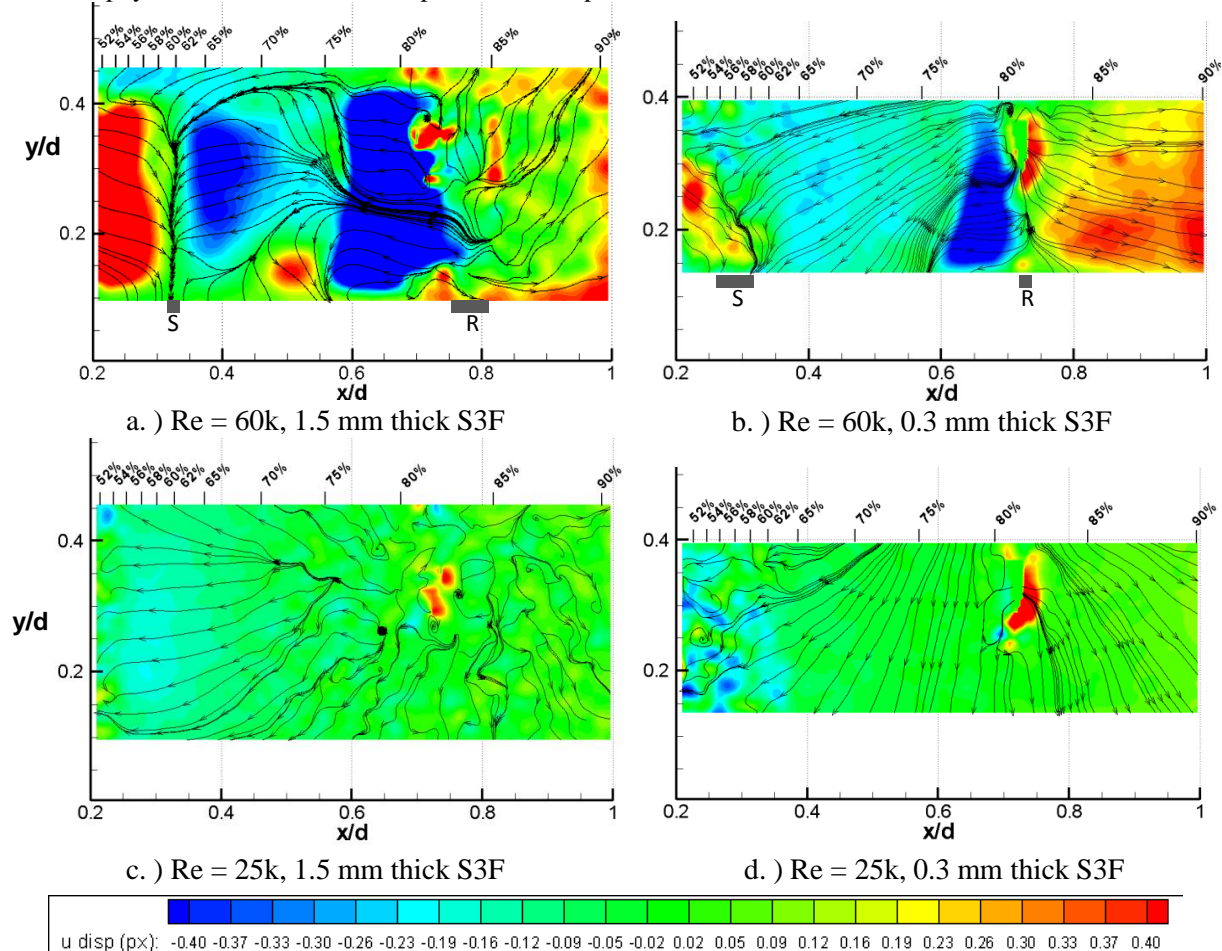


Figure 11. Streamwise instantaneous shear displacement field at two different Reynolds numbers for each S3F film tested. Separation and reattachment areas are labeled with an S or R.

The instantaneous shear displacement field at a Reynolds number of 6.0×10^4 is very interesting (Figs 11a and 11b). The data indicates a vertical line of zero shear corresponding to a separation point at $C_x \approx 60\%$ for the 1.5mm thick S3F. The direction of shear force is in the downstream direction prior to the separation point and then reverses direction downstream of the separation point up to $C_x \approx 84\%$. Another location of zero shear is located at $C_x \approx 84\%$ corresponding to reattachment. A similar flow behavior is observed for the instantaneous shear displacement field of the thinner film. The most noticeable difference between the two different films is a less uniform separation location, and a shift in the reattachment location upstream several percent for the thinner film. In addition the thinner film displacement field has a much stronger spanwise (vertical) component at the upstream side of the view. It is not clear as whether this is due to a flow interaction with the film installation, or perhaps uncertainty in the calculation of the tangential velocity component.

The instantaneous shear displacement field of the thinner film at a Reynolds number of 2.5×10^4 has a significant spanwise component through much of the view. The separation location cannot be clearly identified in the instantaneous image and may have moved several percent chord upstream. The shear displacement in the separated region is very small for the thinner film tested, which increases the uncertainty of the measurement. The thicker film (Fig. 11c) indicates an area of reversed flow on the upstream side of the image view, followed by very small streamwise and spanwise displacement from $C_x=75\%$ to the end of downstream side of the image view. It appears the separation point has moved to the edge of the image view, or upstream out of the view.

It is important to note that in the view shown, the blade surface curves away from the camera starting at about $x/d = 0.3$. At the lowest flow conditions studied, the shear displacement of the S3F is on the order of 0.1 pixels. The curvature of the blade reduces displacement in the image plane towards the left edge of the view, decreasing the signal to noise ratio. If the camera was moved closer to the test article, or a larger zoom lens was used, pixel displacement would increase, and the effect of the blade curvature would be reduced. Future studies will address methods of increasing shear displacement by zooming in on the region of interest.

The mean shear displacement field is shown in Figure 12 for $Re=6.0 \times 10^4$. A relatively uniform separation line is located at $C_x \approx 57\%$ for the thicker S3F, and less spanwise uniform separation location between $C_x \approx 55-60\%$ for the thinner S3F. At $Re=6.0 \times 10^4$ both the instantaneous and mean shear displacement plots qualitatively agree with the laminar separation bubble flow structure shown in Figure 2. An area of reversed flow is observed just downstream of the separation line, followed by a region of relatively constant magnitude reversed shear, followed by an area of larger magnitude reversed shear just upstream of the reattachment location. The area of high increased shear magnitude just prior to the reattachment location corresponds to the reversed flow vortex that was illustrated in Figure 2.

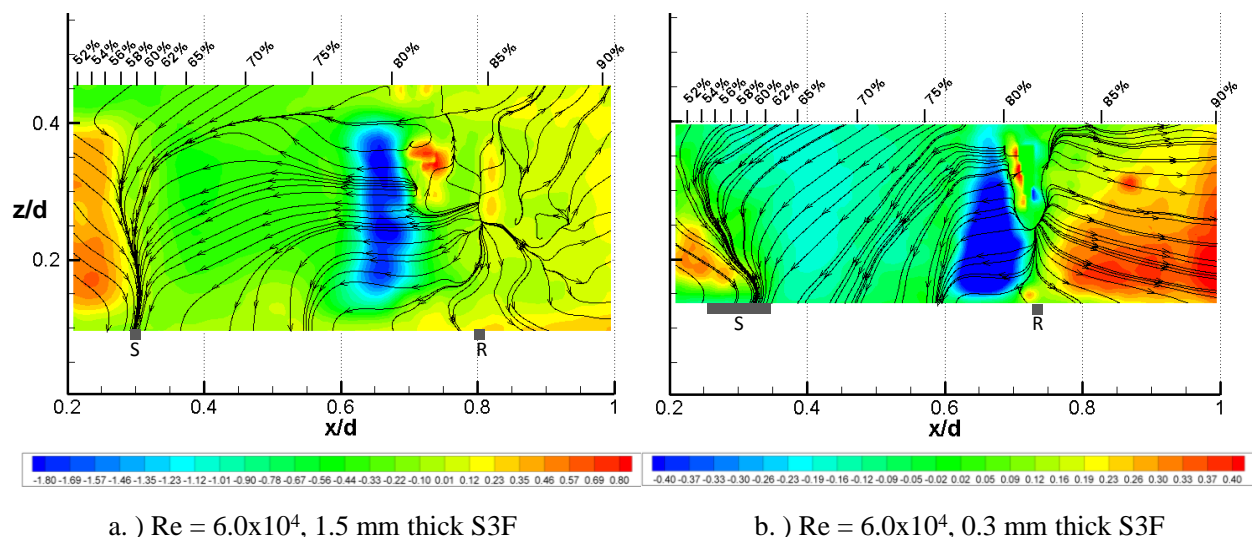


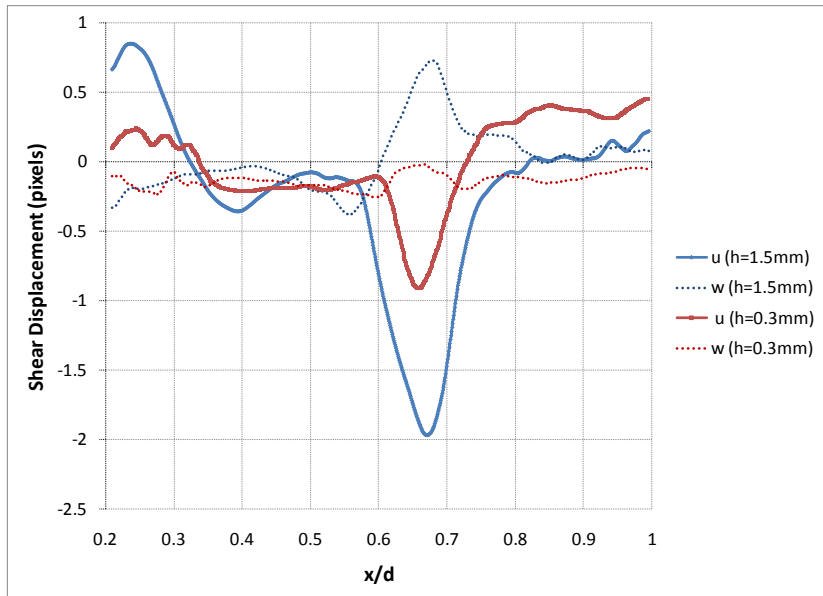
Figure 12. Mean shear displacement at $Re = 6.0 \times 10^4$ colored by stream-wise direction displacement. Separation and reattachment areas are labeled with an S or R.

Line plots extracted at $y/d = 0.2$ are shown in Figure 13. Comparing the shear displacement along $y/d=0.2$ at $Re=6.0 \times 10^4$ measured by the two films, both films indicate a separation bubble, with a small shift in separation point, and a larger shift in reattachment point. This is likely due to an effect of the two different film installations on the suction side flow.

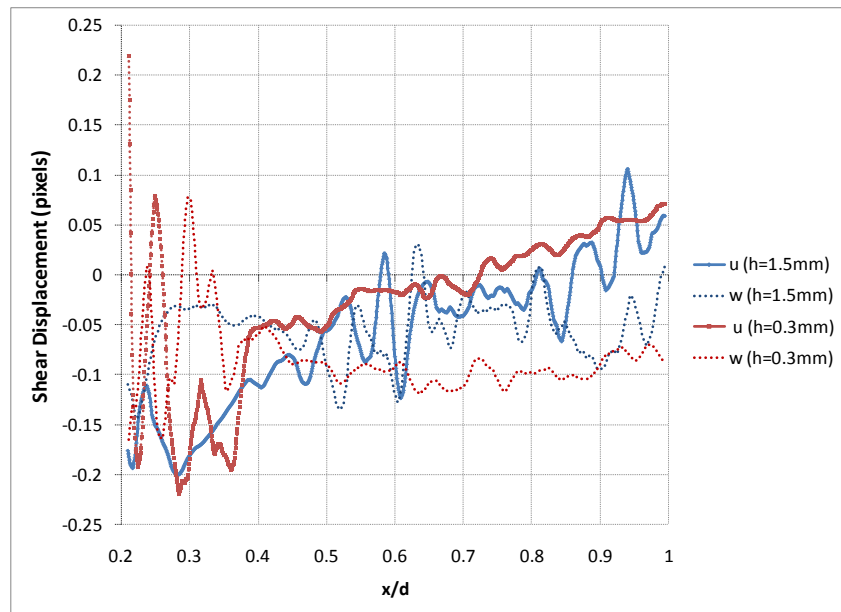
At the lower flow speed tested (Fig. 13b) shear displacement is much lower increasing the uncertainty of the results. Both films indicate a large cross-stream displacement, potentially an indicator of error due to the lower overall pixel displacement.

Pressure coefficient presented in Marks et al.⁵ along the blade surface is shown in Figure 14 compared to S3F obtained instantaneous shear forces in the stream-wise (x-dir) and cross-stream (z-dir) at $Re=6.0 \times 10^4$. The pressure coefficient measurements indicated a separation bubble which is evident by the plateau in the suction surface pressure distribution located between $C_x=62\%$ to 78% . The flow reattaches somewhere between $C_x=78\%$ and 83% . The spatial resolution of the pressure coefficient data with respect to locating separation and reattachment points is limited to the spacing of pressure taps located on the suction surface. S3F offers an additional sensor with greater spatial resolution to identify areas of separated flow. The location of flow separation obtained with the S3F is consistent with the pressure coefficient data. The mean wall shear displacement shown in Figure 12 & Figure 14 indicated the separation point is between $C_x \approx 55-60\%$ with reattachment between $C_x \approx 82-84\%$. This agrees to within a few percent chord with the separation bubble location indicated by pressure coefficient measurement by Marks et al.⁵

The mean streamwise shear force measured with the thicker S3F at $Re=6.0 \times 10^4$ was compared to calculation of wall shear stress by Coles' law of the wake⁷. The turbulent boundary layer velocity distribution measured by PIV and reported in Marks et al. was used to calculate shear force. The calculated shear force and measured shear force agree very well, however, additional work needs to be done to quantify the uncertainty of both experimental calculations.



a.) $Re = 60k$ displacement field



b.) $Re = 25k$ displacement field

Figure 13. Shear displacement components extracted along $y/d = 0.2$.

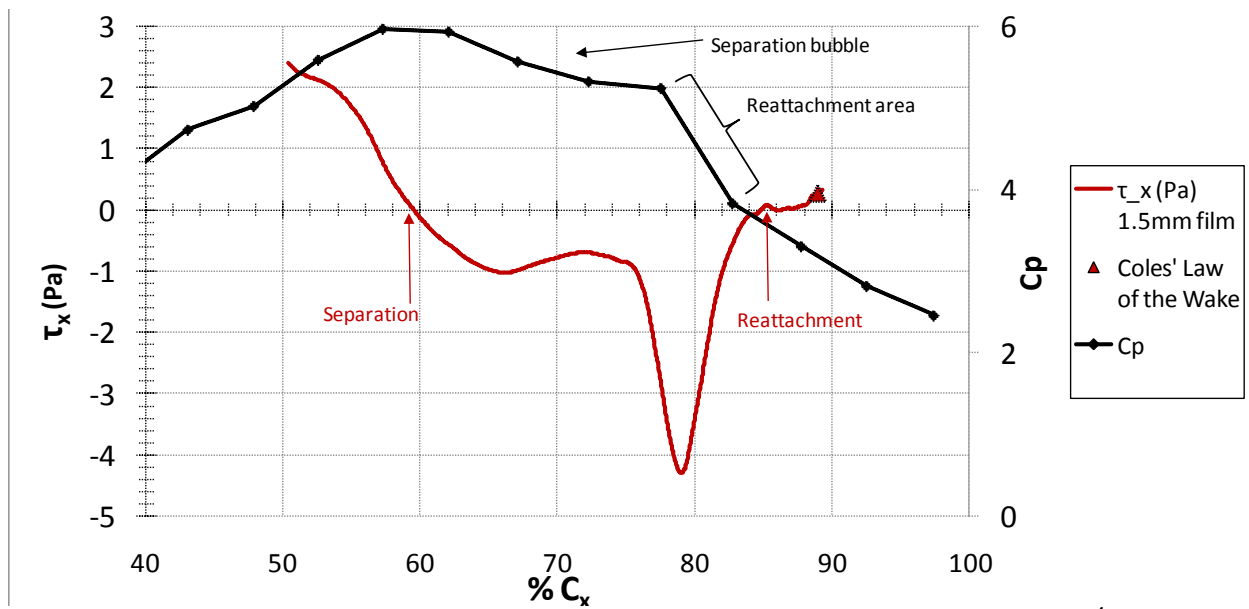


Figure 14. Comparison of surface pressure coefficient profile with S3F results at $Re=6.0 \times 10^4$.

B. S3F with Periodic Wakes

S3F data was also obtained at a Reynolds number of 2.5×10^4 using the 0.3mm thick S3F in the presence of periodic wakes. The range of the linear frequency response of an elastic layer is limited by the first natural frequency (f_0) of tangential oscillation.⁴ This can be estimated by modeling a mass on an elastic surface as

$$f_0 = \frac{1}{2\pi} \sqrt{\frac{\mu}{\rho h^2}} \quad (3)$$

where ρ is the film density, h is the film thickness, and μ is the shear modulus. For a constant shear modulus, and film density, frequency response is proportional to the inverse of thickness as in equation 3.⁴ The frequency response of the thinner film is several times higher than the thicker film, and thus was used for surface stress measurement in the presence of the periodic wake generator. The frequency response of the 0.3mm thick S3F was estimated to be 197 Hz. The wake passing frequency was 13 Hz, which means the S3F had sufficient temporal response to resolve the periodic unsteadiness of the wake passing.

The wake generator was configured to provide a flow coefficient of 0.8. Data was acquired with

both S3F films at 12 phases of wake passing. Nessler et al.¹² has used PIV to examine the effect of wake passing at these flow conditions for one wake passing period split into 6 phases. The 6 phases used by Nessler et al. were formed by dividing one wake passing period into 6. In this paper one wake passing was divided into 12 phases as shown in Figure 15. Phases 1-6 of Nessler et al. correspond to phases 1,3,5,7,9,11 of this paper.

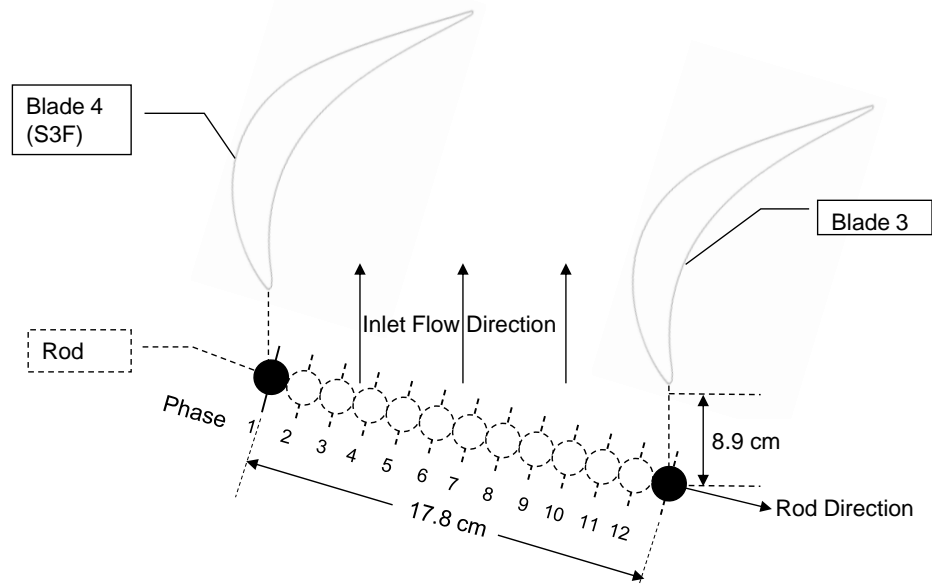


Figure 15. Location of wake generating rod at each phase.

The non-dimensional velocity fields obtained by Nessler et al. are shown in Figure 16 for reference. The wake has a significant effect on the suction side flow, and reattaches the boundary layer.

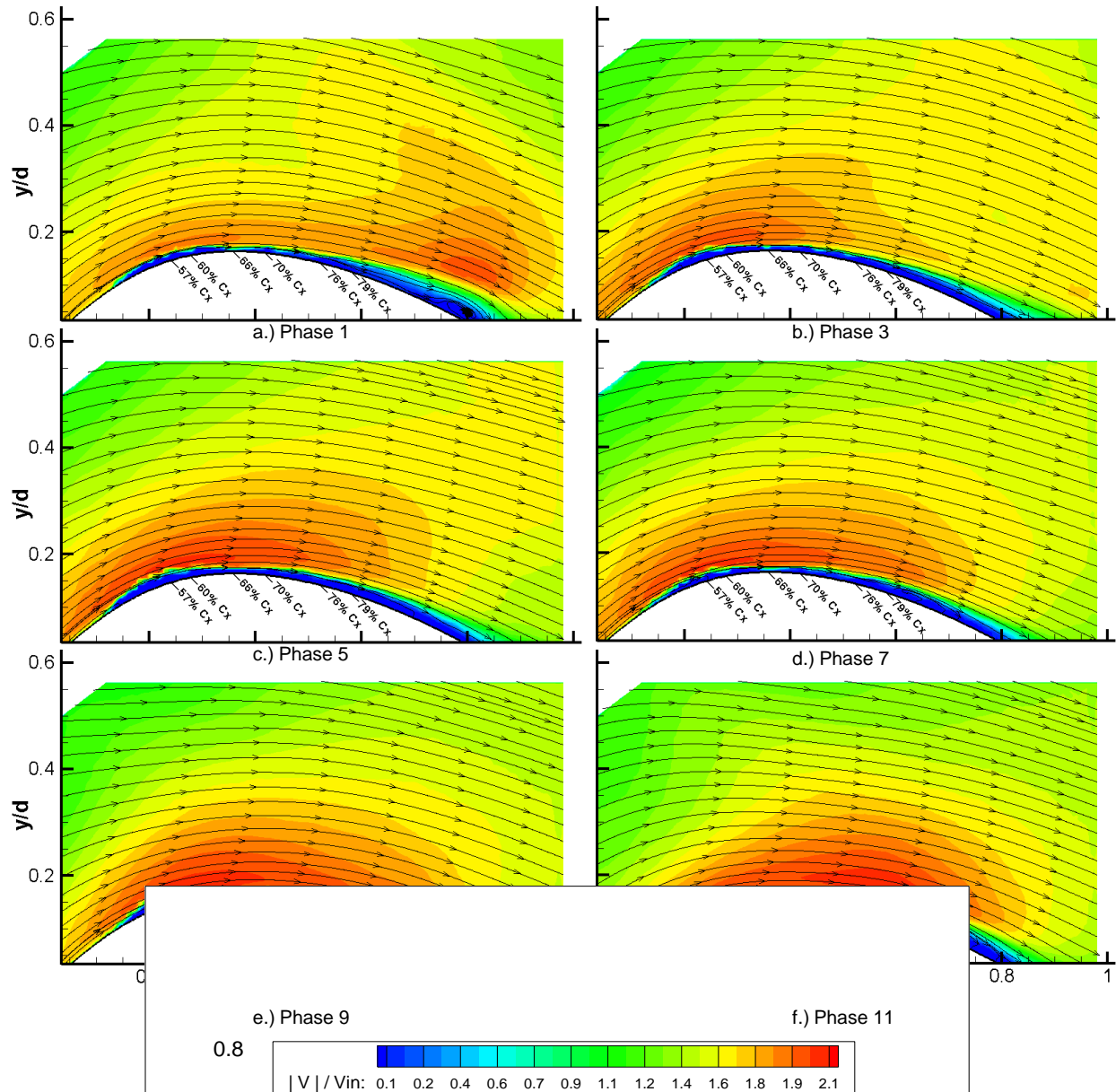


Figure 16. Non-dimensional velocity profile for 6 phases of wake passing, $Re = 2.5 \times 10^4$, flow coefficient = 0.8.¹²

The velocity fields of Figure 16 show the effect of a wake traversing through the passage. Phase 1 shows the wake pushing a separation bubble (at $x/d = 0.8$) down the length of the suction surface. The separation bubble has moved out of the view by phase 3, or at least decreased in height. A separation bubble is not immediately obvious in the velocity fields of phases 5-7, but fidelity near the surface of the wall is limited in the large fields of view. In phase 9 the boundary layer appears to have reattached and a closed separation bubble has reformed. Phase 11 shows the separation bubble in roughly the same location as phase 9, but two phases later, during Phase 1, the bubble has been pushed down the suction surface by an approaching wake.

Shear displacement fields for each phase of wake passing are shown in Figure 17 for flow conditions comparable to the velocity fields presented in Figure 16. Approximate reattachment points are labeled with an 'R'.

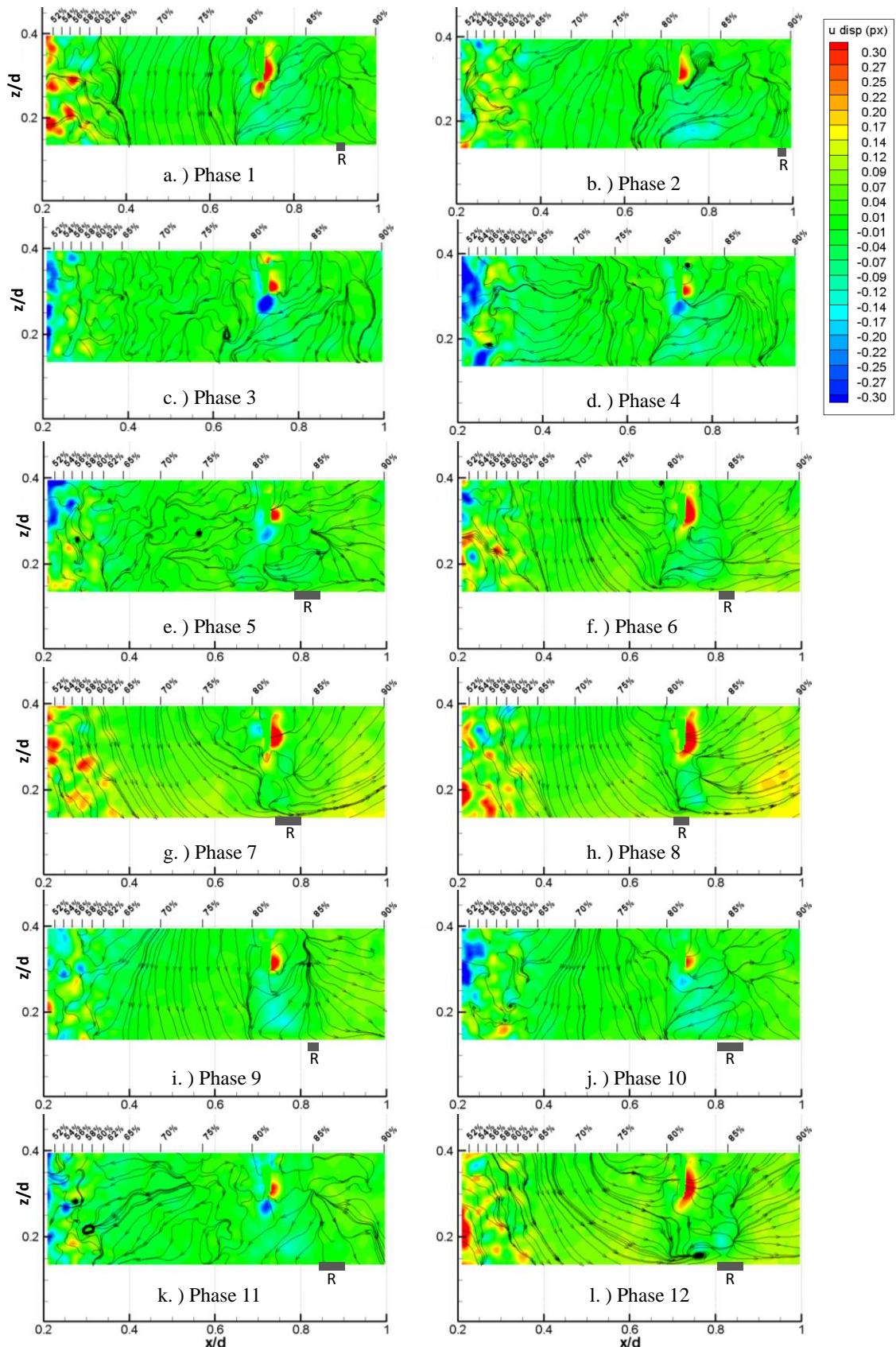


Figure 17. 0.3mm thick S3F film u displacement (streamwise direction) for 12 phases of wake passing at a $Re=2.5 \times 10^4$.

The shear displacement field data indicates the S3F responded to the changes in suction side flow due to wake passing. In phase 1, the shear displacement field indicates a likely separation point near $C_x=62-65\%$, followed by an area of relatively large vertical velocity content, then reattachment at $C_x \approx 87\%$. By phase 2, a reattachment point is not obvious and may have moved to the right edge or off the downstream side of the view. Looking at the sequence of phase 3-4 the flow is gradually less uniform, and no reattachment point is obvious in the view. By phase 5 the flow is disorganized from $C_x=50\%$ to $C_x \approx 85\%$, after which the shear stress changes directions to point downstream, due to boundary layer reattachment. Phases 5-9 all indicate the reformation and presence of a separation bubble with flow reattachment between $C_x=80-85\%$.

The trends of shear displacement in Figure 17 agree well with the PIV data taken by Nessler et al.¹² (Fig. 16) at the same flow conditions. The wake passing pushes the separation bubble towards the trailing edge during phases 1-4. The shear field indicates reattachment by phase 5, and through phase 12. Reattachment was not obvious in the non-dimensional velocity fields obtained with PIV until phase 9. This could be due to an effect of the S3F on the suction surface flow, or a result of the limited fidelity of the PIV near the surface.

C. Comparison of S3F installations using flow visualization

Flow visualization was used to look for an effect of the film on the suction side flow characteristics at each Reynolds number tested. The two S3F films analyzed differed in thickness and installation location. The thicker, 1.5mm thick film was wrapped around the leading edge and trailing edge of the blade to ensure there was no large protrusion on the suction surface to trip the boundary layer. It was expected that the relatively large thickness of the film could however, still have an effect on the suction surface flow. The thinner, 0.3mm thickness film was placed from approximately $C_x=20\%$ to the trailing edge of the blade. In addition, the leading edge of the 0.3 mm film was created with a small slope in order to minimize perturbation of the boundary layer. Instantaneous flow visualization is presented in Figure 18- Figure 19 at each Reynolds number tested.

The flow visualization proved useful for identification of separation location. At a Reynolds number of 2.5×10^4 (Figure 18) the separation location varied slightly between instantaneous images, but overall the separation location did not shift significantly with the 0.3mm thick film, but did shift slightly downstream with the thicker film. By inspection of several images, the separation point at $Re\ 2.5 \times 10^4$ was at $C_x \approx 58\%$, 60% and 58% for the cases of no film, 1.5 mm thick film, and 0.3 mm thick film respectively.

At a Reynolds number of 6.0×10^4 the separation point moved slightly upstream with the thicker film installed. The separation point was at $C_x \approx 61\%$, 59% , and 61% for the cases of no film, 1.5 mm thick film, and 0.3 mm thick film respectively. The flow visualization indicate that the thicker 1.5mm film had an effect on the flow. The most noticeable effect is movement of the separation location. The 0.3mm film had very little effect on the flow when viewed in a blade normal plane. The separation line however, did not look uniform in the spanwise direction of the S3F measured shear displacement field.

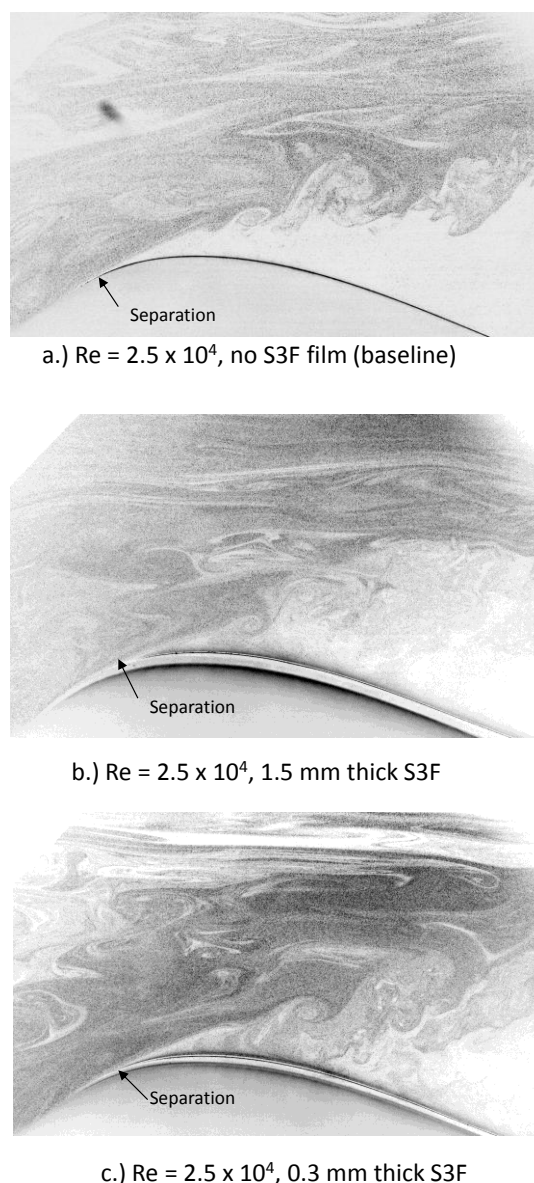


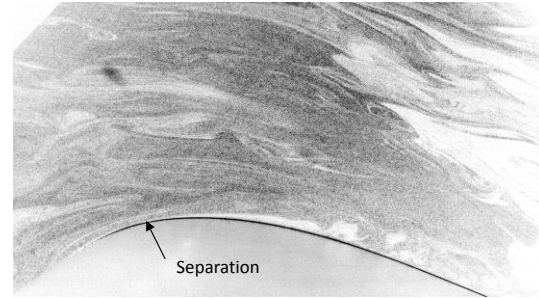
Figure 18. Instantaneous flow visualization at $Re=2.5 \times 10^4$ for each film tested.

V. Conclusion

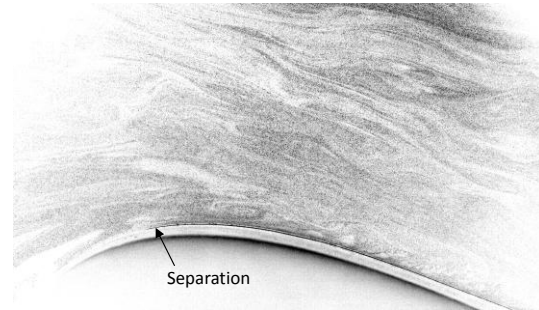
The two S3F sensors tested in this work were used to check that film sensitivity and locate a more precise region of interest for follow-on tests. At a Reynolds number of 6.0×10^4 , shear displacement fields obtained with each S3F film tested indicated a separation bubble on the suction surface of the blade which agreed with previous experiments. As Reynolds was decreased to 2.5×10^4 , the suction surface flow separates and does not reattach. The thicker 1.5mm film had larger shear displacement magnitude than the thinner 0.3mm film, but flow visualization indicated the film shifted the separation location several percent axial chord. The flow visualization indicated the thinner 0.3mm film had little effect on separation location, but the shear displacement field indicated a non-uniform separation location in the spanwise direction. The discrepancy between the flow visualization and S3F indicated separation point requires further investigation. It may be due to a three dimensional effect from the film installation, or experimental uncertainty. The 0.3mm film captured the unsteady effects of the moving wake generator and shear displacement field agreed well with PIV data taken by Nessler et al.¹² The shear measurements could be improved in future experiments by moving the camera closer to the film, or using a larger focal length lens. This work demonstrates that S3F is a powerful sensor for both qualitative and quantitative studies of both steady and unsteady flows found in low pressure turbines.

Acknowledgements

This work was performed under the sponsorship of the Air Force Office of Scientific Research. The first author would like to thank Lauren Lobosky and Derek Miller for their help in setting up the experiments and data acquisition.



a.) $Re = 6.0 \times 10^4$, no S3F film (baseline)



b.) $Re = 6.0 \times 10^4$, 1.5 mm thick S3F

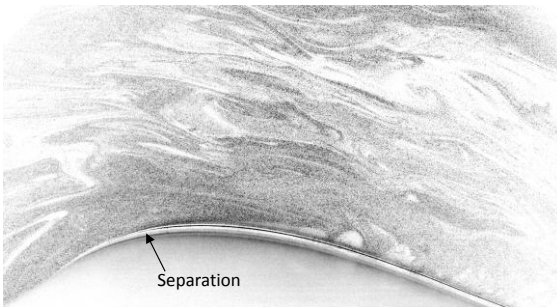


Figure 19. Instantaneous flow visualization at $Re=6.0 \times 10^4$ for each film tested.

References

- ¹ McQuilling, M., Wolff, M., Fonov, S., Crafton, J., Sondergaard, R., "An Experimental Investigation of a Low-Pressure Turbine Blade Suction Surface Using a Shear and Stress Sensitive Film", *Experiments in Fluids*, V. 44, No. 1, pp. 73-88.
- ² McQuilling, M., Wolff, M., Fenov, S., Crafton, J., and Sondergaard, R., "An Experimental Investigation of Suction Surface Flow Features on a High-Lift LPT", AIAA Paper No. 2008-79.
- ³ McQuilling, M., "Design and Validation of a High-Lift Low-Pressure Turbine Blade," Ph.D. Dissertation, Mechanical and Material Engineering Dept., Wright State Univ., Dayton, OH, 2007.
- ⁴ Crafton, J., Fonov, S., Forlines, A., Goss, L., "Skin Friction Measurements Using Elastic Films", *AIAA Aerospace Sciences Meeting*, AIAA, Orlando, FL, 2010. (to be published)
- ⁵ Marks, C., Sondergaard, R., Estevadeordal, J., Wolff, M., "A Spanwise and Streamwise PIV Investigation of Transitional Flow Around a Highly Loaded LPT Blade Using a Curved Laser Sheet", AIAA Paper No. 2009-301, *AIAA Aerospace Sciences Meeting*, AIAA, Orlando, FL, 2009.
- ⁶ Horton, H. P. 1968 Laminar separation in two and three-dimensional incompressible flow. PhD Dissertation, University of London.
- ⁷ White, F., *Viscous Fluid Flow*, 2nd ed., McGraw-Hill, Inc., 1991.

⁸ Sondergaard, R., Rivir, R., Bons, J., “Control of Low-Pressure Turbine Separation Using Vortex Generator Jets”, *Journal of Propulsion and Power*, Vol 18, No. 4, pp. 889-895, 2002.

⁹ Bons, J., Sondergaard, R., Rivir, R., “Control of Low Pressure Turbine Separation Using Vortex Generator Jets”, AIAA 2004-2201, June 2004.

¹⁰ Nessler, C., Marks, C., Sondergaard, R., Wolff, M., “An Investigation of Losses on a Highly Loaded Low Pressure Turbine Blade with Unsteady Wakes”, AIAA Paper No. 2009-302, *AIAA Aerospace Sciences Meeting*, AIAA, Orlando, FL, 2009.

¹¹ Bons, J., Pluim, J., Gompertz, K., Bloxham, M., Clark, J., “The Application of Flow Control to an Aft-Loaded Low Pressure Turbine Cascade with Unsteady Wakes”, ASME Paper No. GT2008-50864.

¹² Nessler, C., Marks, C., Sondergaard, R., Wolff, M., “PIV Investigation of Periodic Unsteady Wakes over a Highly Loaded Low Pressure Turbine Blade”, AIAA Paper No. 2009-5107, *AIAA Joint Propulsion Conference*, AIAA, Denver, CO, 2009.

APPENDIX C

Turbulence Model Comparisons for Mixing Plane Simulations of a Multistage Low Pressure Turbine Operating at Low Reynolds Numbers

Darius D. Sanders¹ and Walter F. O'Brien²

Mechanical Engineering Department, Virginia Tech, Blacksburg, VA, 24061 USA

Rolf Sondergaard³, Marc D. Polanka⁴, and Douglas C. Rabe⁵

Air Force Research Lab, Propulsion Directorate, Wright-Patterson AFB, OH, USA

There has been a need for improved flow prediction methods for low pressure turbine (LPT) blades operating at high altitudes with a reduced inlet Reynolds number. These conditions present an increased amount of laminar-to-turbulent transitional flow within the boundary layers on the LPT blade surfaces. Also, boundary layer separation is more likely to occur within the flowfield of the LPT stages due to the lower freestream velocities in the regions of adverse pressure gradients on the suction surfaces. More accurate predictions of aerodynamic losses due to low Reynolds effects are needed for CFD to provide more accurate input to the design process for LPT stages operating at high altitudes. Steady flow CFD simulations of flow in a multistage LPT geometry were completed at nominal and high altitude conditions with the conventional Spalart-Allmaras turbulence model and a recently-developed three-equation eddy-viscosity type transitional flow model. These models were used in combination with a mixing plane model for the simulation of flow through a three stage low pressure turbine. Flow visualizations were completed using surface flow and streamline calculations to help identify vortical structures present within the flowfield. Also, the total pressure loss coefficient was calculated for each blade row. Qualitative comparisons indicate the amount and the location of the flow separation differed significantly depending on the chosen turbulence model. Overall, the high altitude condition had an increased amount of separated flow compared to the nominal altitude condition resulting in an increase in the loss coefficient. The altitude effect on the laminar-to-turbulent transition location was studied using the three-equation model. The model provided a more detailed understanding of the aerodynamic loss mechanisms present in low Reynolds number flows, since it accounted for transitional boundary layer flow effects. Based on these results, the CFD using the three-equation model has the potential to be a more effective method for turbine flow prediction at low Reynolds numbers compared to conventional RANS turbulence models.

Nomenclature

d	= wall distance
D	= kinetic energy near-wall dissipation
k	= kinetic energy
l_m	= inlet turbulent length scale
P	= pressure; production term
r	= radius
R	= bypass transition production term

¹ Graduate Student, Virginia Tech, Mechanical Engineering, AIAA Student Member

² J. Bernard Jones Professor, Virginia Tech, Mechanical Engineering; AIAA Associate Fellow

³ Research Engineer, AFRL/RZTT, 1950 Fifth St. Bldg 18 WPAFB, OH 45433, AIAA Associate Fellow

⁴ Research Engineer, AFRL/RZTE, 1950 Fifth St. Bldg 18 WPAFB, OH 45433, AIAA Associate Fellow

⁵ Turbine Engine Research Center Director, AFRL/RZTE, 1950 Fifth St. Bldg 18 WPAFB, OH 45433, AIAA Associate Fellow

R_{NAT}	=	natural transition production term
Re	=	Reynolds number based on axial chord
t	=	time
LPT	=	low pressure turbine
TPLC	=	total pressure loss coefficient
Tu	=	freestream turbulent intensity
u	=	velocity magnitude
u'	=	streamwise fluctuation
x	=	directional component
y^+	=	nondimensional wall distance
α_T	=	turbulent diffusivity
δ_{ij}	=	Kronecker delta
λ_{eff}	=	effective length scale
λ_T	=	integral turbulent length scale
μ	=	molecular viscosity
ν	=	kinematic viscosity
$\tilde{\nu}$	=	modified kinematic viscosity
ρ	=	density
ω	=	specific dissipation rate
Subscripts		
0	=	total
i,j	=	indices
in	=	inlet
L	=	laminar
$exit$	=	exit
T	=	turbulent
θ	=	circumferential direction

I. Introduction

THERE is a need to increase the range and endurance of turbine engines operating at high altitudes. Many factors limit the use of turbine engines operating at high altitude, including the operational efficiency of the low pressure turbine. As aircraft altitude increases, the operational Reynolds number decreases due to the change in density. These low Reynolds numbers change the aerodynamics of the low pressure turbine blades and cause the development of laminar flow boundary layers and longer transitional flow regions on the blade suction surface. These laminar and transitional flow boundary layers are more susceptible to separation within the region of adverse pressure gradients located on the aft portion of the blade than a turbulent boundary layer flows found at higher Reynolds numbers. Boundary layer separation results in aerodynamic losses which lowers engine efficiency and reduces the aircraft range and maximum altitude. To understand how to improve designs, better capability for prediction of low Reynolds number turbine flows is needed.

The challenge to improve low pressure turbine designs requires improved computational prediction of aerodynamic loss mechanism such as boundary layers, blade trailing edge wakes, and secondary flows. Also, interactions between adjacent blade rows cause an inherently unsteady flowfield within the turbine stages due to wake and potential effects. Wake effects are caused by the shedding of boundary layer vorticity and momentum deficit by blades located upstream. Potential effects originate from unsteady variations in the pressure field that propagate both upstream and downstream. Accurate prediction of aerodynamic losses due to separation and laminar-to-turbulent transitional boundary flow is required to account for low Reynolds number effects. CFD simulations of multistage geometries must be able to model these effects accurately. Fully unsteady simulations are required to accurately model these effects where the flowfield of each blade row is solved simultaneously in a time-accurate

manner, and meshes for blade rows that involve rotation are moved relative to stationary blade rows. Also, most sliding mesh CFD simulations require the section of the annulus being modeled to remain constant. So, multiple blade passages may have to be modeled due to changes in the number of blades per row, which often results in meshes containing a large number of cells. This type of simulation requires a significant amount of computational resources.

An alternative method is to employ the “mixing plane” numerical method¹. The mixing plane is a method for simulating flow through domains with one or more regions in relative motion. The fluid zone for each blade was treated as a steady state solution using circumferentially averaged or “mixed” profiles of dependent variables. These profiles, usually specified as a function of the radial coordinate, are used to update the boundary conditions along the flow zones between adjacent blade rows during each local iteration. Unsteady effects that would normally occur due to circumferential variations in the flowfield between blade rows, such as, passing wakes, potential effects from shock waves, and separated flow were neglected as a result of the steady-state circumferential averaging being employed. Performance predictions made using the mixing plane model have been shown to produce reasonable results^{2,3}.

The Reynolds Averaged Navier-Stokes (RANS) CFD method using statistical turbulent models is typically used for simulations involving three-dimensional rotating turbomachinery. Currently, Large-Eddy Simulation or Direct Numerical Simulation CFD methods require impractically long simulation times to be applied to modeling flow in multiple stage geometries. Yet, the RANS CFD method when applied to low pressure turbine blade geometries do not adequately predict low Reynolds numbers flows. This limitation has generally been a result of the turbulence model employed in the RANS CFD method. Most conventional turbulence models assume fully turbulent flow and do not account for the laminar-to-turbulent transitional flow and laminar flow separation associated with lower Reynolds numbers.

Several studies have been done where conventional turbulence models have been modified to account for transitional flow effects and separation. Suzen *et al.*⁴ used the turbulent viscosity expression from Mentor’s $k-\omega(SST)$ model and a transport equation was used to solve for the intermittency function. The intermittency transport equation was used to obtain the distribution of intermittency in the transitional flow region, while the onset of attached and separated flow transition is determined by correlations. The Suzen *et al.*² model was applied to two different cascade grid topologies and compared well with three different experiments with differences in separation and reattachment locations. Menter *et al.*⁵ used transport equations for intermittency and the momentum thickness Reynolds number. The intermittency equation was coupled with Mentor’s $k-\omega$ SST model and used to trigger the production of turbulent kinetic energy beyond the turbulent transition region. The second transport equation was formulated in terms of the momentum thickness Reynolds number at transition onset. An empirical correlation was used to control the transition onset criteria in the intermittency equation. The Menter *et al.*⁵ model has been applied to several 2D and 3D geometries by Langtry *et al.*⁶ including the Pack-B cascade, a 3D GE low-pressure turbine vane, and the T106 blade undergoing passing wakes. All simulations agreed well with experiments for all test cases at a wide range of Reynolds numbers and freestream turbulent intensities. Another approach by Praisner *et al.*^{7,8} used correlations developed from an experimental database for attached flow transition, laminar separation with turbulent attachment, and separated-flow transition. These correlations were implemented in a RANS solver using the Wilcox $k-\omega$ turbulence model. The model showed significant improvement in the predicted accuracy of the total pressure loss for both linear cascades and multistage LPT rigs over a conventional fully turbulent flow model.

The recent development of a three-equation eddy-viscosity type model by Walters and Leylek⁹ for modeling transitional flow effects offers the possibility of improved accuracy of flow predictions using the RANS CFD method. Transport equations are used to address the development of pre-transitional fluctuations in the boundary layer and the breakdown to turbulence to predict both natural and bypass transition. The capability of the new model to predict transitional flow behavior has been demonstrated on a highly loaded turbine blade airfoil with and without film cooling and on a flat plate with pressure distribution similar to an axial compressor undergoing passing wakes by Walters and Leylek^{10,11}. Work has been completed by the current authors^{12,13} using the Walters and Leylek transitional flow model. The ability to predict aerodynamic losses due to low Reynolds numbers effects was demonstrated for two-dimensional cascade CFD models on two low pressure turbine blade airfoils¹². Additionally, the Walters and Leylek transitional flow model was applied to a flow simulation of the 1st stage of a multistage low pressure turbine geometry¹³ at inlet Reynolds number of 135,000. The results were compared to those obtained with the Spalart-Allmaras turbulence model and differences were observed in the prediction of aerodynamics losses. Since, the Walters and Leylek model accounted for transitional flow effects; it should provide a more effective method for performance predictions compared to conventional RANS turbulence models.

This present study continues the work initially presented by Sanders *et al.*¹³ where the flowfield of a three-dimensional multistage LPT geometry has been investigated for low Reynolds number flow effects. CFD simulations were completed using the mixing plane numerical method in combination with the Spalart-Allmaras(*S-A*) and Walters and Leylek $k_T-k_L-\omega$ transitional flow model. Steady flow simulations were completed at both nominal and high altitude inlet conditions corresponding to two different inlet Reynolds numbers. The $k_T-k_L-\omega$ model results were compared to the *S-A* model at both altitude conditions to determine the difference in the flowfield predictions each method provided. The flowfield for each blade row was investigated using streamlines and surface flow visualizations at each altitude condition to identify the sources of aerodynamic losses. These results showed the capability of Walters and Leylek $k_T-k_L-\omega$ transitional flow model for prediction of the boundary layer behavior and performance at low inlet Reynolds numbers. This model can potentially provide the type of prediction method needed for design improvement of turbine engines operating at high altitudes.

II. CFD Numerical Methods

A. Computational Grid Technique

The multistage LPT geometry used for this present study consisted of three stator-rotor stages. A structured grid was designed for the LPT multistage geometry because of the requirement for a high degree of control and accuracy with lower amount of computational memory. The same grid O-H topology was used for all six blade flowpaths. The three-dimensional O-grid was made using a hyperbolic extrusion method normal to the blade surface. The first cell wall distance had a $y^+ < 1$ in accordance with the transitional model wall spacing tolerance. Typical O-grid dimensions for each blade row are given in Table 1. A cutting plane grid of approximately (35×151) cells was constructed to control the grid point distribution within the H-grid flowpath. The hub and shroud grid surfaces with nominally (333×35) cells were created based on the node connectors from the cutting plane, blade O-grid, and main flowpath. The elliptic structured grid solver was used so that the minimum-angle cell skewness was above 45°. This cell skewness tolerance was set to make sure the cell shape would not affect the CFD solver accuracy and performance. The grid point distribution of the H-grid boundaries was made so that periodic boundaries can be applied across the blade passage. The flowpath H-grid block dimensions for each of the six blade rows is given in Table 1 including the total number of cells for each blade row. Typically 151 grid points were distributed along the spanwise direction with an initial wall spacing, $\Delta s = 3.81\mu\text{m}$. A grid independence study was performed using the 1st stage of the multistage LPT geometry. It was determined the baseline grid provided adequate resolution of the spanwise flowfield and sufficient initial spacing for endwall effects¹³. Figure 1 shows the grid topologies for each of the three stages of the multistage LPT geometry.

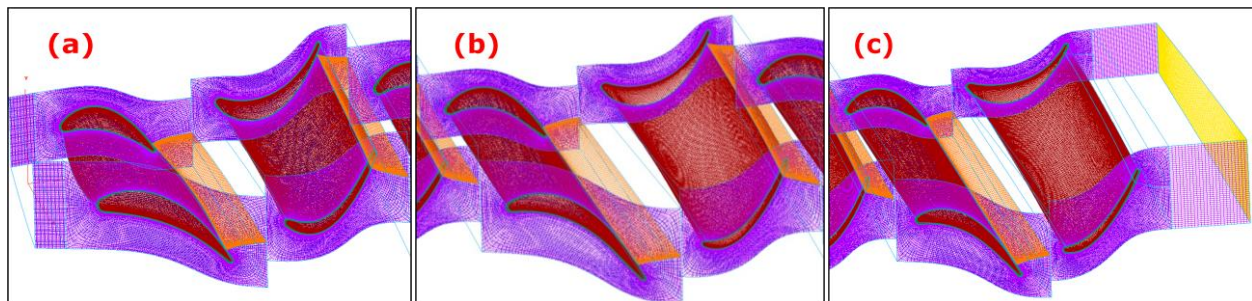


Figure 1. Structured Grid for the Multistage LPT Geometry.
View of the (a) 1st Stage, (b) 2nd Stage, and (c) 3rd Stage Vane and Rotor

	O-Grid Dimensions	H-Grid Dimensions	Cells		O-Grid Dimensions	H-Grid Dimensions	Cells
Inlet		25×41×151	154,775	2nd Rotor	346×14×165	346×35×165	2,797,410
1st Vane	333×17×151	333×35×151	2,614,716	3rd Vane	339×18×165	339×31×165	2,740,815
1st Rotor	335×16×151	335×37×151	2,681,005	3rd Rotor	342×16×168	342×31×168	2,705,640
2nd Vane	333×17×153	333×31×153	2,445,552	Outlet		25×43×168	180,600

Table 1. Blade Row Grid Dimensions and Cell Count for Multistage LPT Geometry

B. CFD Numerical Scheme

CFD simulations were performed using ANSYS® Fluent 12.0 CFD software which was based on a finite volume method. The domain was discretized onto a finite set of control volumes and the general conservation equations mass, momentum, and energy were solved on this set of control volumes. All solution variables represent ensemble or time averaged values. The Reynolds stress term $-\rho \overline{u'_i u'_j}$ was resolved according to the chosen turbulence model to close the equation. Both the Spalart-Allmaras and Walters and Leylek $k_T-k_L-\omega$ models were included and implemented in the Fluent 12.0 CFD software. The RANS equations were discretized using the pressure-based coupled algorithm which solved a coupled system of equations comprising the momentum and energy equations with the pressure-based continuity equation. The convergence rate significantly improved when compared to the pressure-based segregated algorithm.

The mixing plane numerical method employed in ANSYS® Fluent 12.0 was used for all simulations. In the mixing plane method each fluid zone for each blade was solved as a steady state solution. The flowfield parameters were passed as boundary conditions from adjacent stator-rotor zones and were spatially averaged at the mixing plane interface. Mass-weighted averages in the circumferential direction at specified radial locations of the total pressure, total temperature, directional cosines of the local flow angles in the radial, tangential, and directions, and turbulence properties (k_L , k_T , ω , μ_t) were computed from the vane exit and passed to the downstream rotor inlet. Likewise, the profiles of static temperature and pressure, and cosines of the local flow angles were used as boundary conditions on the stator exit. A mixing plane interface was made between an upstream exit boundary zone and downstream inlet boundary zone.

This type of model provided several computational advantages by giving a steady-state approximation to the time-averaged flowfield at a reduced computational solution completion time. Unsteady calculations involving rotation require significant amount of computational time to achieve a time-periodic solution. The mixing plane model does not require a common periodic angle to be maintained for each blade row. This allowed a geometry configuration of one blade passage per row without modifying the blade count. So, the modeling of a large number of blade passages was avoided which reduced the overall grid size. In addition, the grid for each blade inlet and exit boundary does not have to be conformal and can be of different types (i.e., a vane can be an unstructured grid while a downstream blade can be a structured grid). The main limitation of the mixing plane numerical method is the neglect of unsteady effects due to passing wakes and the potential flowfield due to steady-state circumferential averaging.

C. Solution Convergence Procedure

The numerical scheme used in the mixing plane numerical method with the Spalart-Allmaras turbulence model was initialized based on the inlet boundary conditions in the absolute frame of reference with a first-order upwind scheme for density, turbulence, and pressure with a second-order upwind discretization scheme for energy and momentum. Several hundred iterations were performed with turbulence and energy equations disabled to help establish the main flowfield after which the turbulence and energy equations were re-enabled, respectively. Once solution stability was achieved, the CFL was increased to speed the local time stepping while maintaining stability. The solutions were run until convergence tolerance of 10^{-5} for global flow variables was achieved. Second-order upwind discretization for all flow parameters and equations were set and the simulation was ran again until a convergence tolerance of 10^{-5} was achieved for global flow properties.

A specific solution convergence procedure using the Walters and Leylek's transitional flow model was developed in order to maintain solution stability and prevent divergence. A converged solution using the $k-\varepsilon$ model was run with second-order upwind numerical scheme in order to provide an initial approximation of the flowfield. The $k_T-k_L-\omega$ model was enabled and ran sequentially with the first and second-order upwind numerical scheme until convergence of 10^{-5} global flow properties was reached. The flowfield was held "frozen" by disabling the continuity, momentum, and energy equations during this process. The frozen flow solution was used as the initial condition while all equations including continuity, momentum, and energy were re-enabled with $k_T-k_L-\omega$ model equations and run sequentially with the first and second-order numerical scheme. The same residual convergence tolerance of 10^{-5} was attained for all simulations using the $k_T-k_L-\omega$ model.

D. Spalart-Allmaras Turbulence Model

The Spalart-Allmaras model is a one-equation turbulence model specifically developed for aerodynamic external flow applications. It uses a single transport equation for the eddy viscosity. The model was developed to

remove the incompleteness of algebraic and one-equation turbulent kinetic energy models and to be more computationally simpler than more advanced turbulence models. Overall the Spalart-Allmaras model performs well for transonic and mildly separated flows and is widely used in turbomachinery applications although, its accuracy is known to suffer for flows with massive separation and free shear flows. The model equations are based on the transport of a parameter proportional to the turbulent viscosity given in Eq. (1)-(2)

$$\mu_t = \rho \tilde{\nu} f_{v1} \quad (1)$$

$$\rho \frac{D\tilde{\nu}}{Dt} = \rho c_{b1} \tilde{S} \tilde{\nu} + \frac{1}{\sigma_{\tilde{\nu}}} \left[\frac{\partial}{\partial x_j} \left\{ (\mu + \rho \tilde{\nu}) \frac{\partial \tilde{\nu}}{\partial x_j} \right\} + c_{b2} \rho \left(\frac{\partial \tilde{\nu}}{\partial x_j} \right)^2 \right] - c_{w1} \rho f_w \left(\frac{\tilde{\nu}}{d} \right)^2 \quad (2)$$

A full description of all the model constants and source terms are discussed in Wilcox¹⁴.

E. Walters and Leylek's Transitional Flow Model

The Walters and Leylek's k_T - k_L - ω model is a three-equation eddy-viscosity type, with transport equations for the turbulent kinetic energy (k_T), laminar kinetic energy (k_L), and the specific dissipation rate (ω) which are given in Eqs. (3)-(5).

$$\frac{Dk_T}{Dt} = P_{k_T} + R + R_{NAT} - \omega k_T - D_T + \frac{\partial}{\partial x_j} \left[\left(\nu + \frac{\alpha_T}{\sigma_k} \right) \frac{\partial k_T}{\partial x_j} \right] \quad (3)$$

$$\frac{Dk_L}{Dt} = P_{k_L} - R - R_{NAT} - D_L + \frac{\partial}{\partial x_j} \left[\nu \frac{\partial k_L}{\partial x_j} \right] \quad (4)$$

$$\frac{D\omega}{Dt} = C_{\omega 1} \frac{\omega}{k_T} P_{k_T} + \left(\frac{C_{\omega R} \lambda_T}{\lambda_{eff}} - 1 \right) \frac{\omega}{k_T} (R + R_{NAT}) - C_{\omega 2} \omega^2 - C_{\omega 3} f_{\omega} \alpha_T \left(\frac{\lambda_{eff}}{\lambda_T} \right)^2 \frac{\sqrt{k_T}}{d^3} + \frac{\partial}{\partial x_j} \left[\left(\nu + \frac{\alpha_T}{\sigma_{\omega}} \right) \frac{\partial \omega}{\partial x_j} \right] \quad (5)$$

The influence of the laminar and turbulent kinetic energy on the Reynolds stress term was included through the prescription of the total eddy viscosity as given in Eq. (6). A brief summary of the current transitional flow model functionality is presented below.

$$-\overline{u'_i u'_j} = \nu_{TOT} \left(\frac{\partial u_i}{\partial x_j} + \frac{\partial u_j}{\partial x_i} \right) - \frac{2}{3} k_{TOT} \delta_{ij} \quad (6)$$

The laminar kinetic energy was used to describe the low frequency, high amplitude fluctuations that originated from the pre-transitional boundary layer. These fluctuations primarily occurred at one scale and almost all energy was contained in a single streamwise component. The production of laminar kinetic energy was assumed to occur due to a “splat mechanism” which redirected the normal fluctuations of the freestream turbulence into a streamwise component while creating local pressure gradients in the boundary layer, thus increasing the low frequency fluctuations. These fluctuations grow to the development of turbulent spots and then to full turbulence. A local transition parameter that depended on the turbulent energy, effective length scale, and fluid viscosity determined when this occurred. Once this parameter reached a threshold value, a transfer of energy began from streamwise fluctuations (k_L) to turbulent fluctuations (k_T).

Both natural, mixed, and bypass transition were resolved in the current model. Natural transition occurred when orderly laminar flow broke down to turbulent flow in the presence of small perturbations. This process was very slow and was observed when no external forcing was applied and when very small perturbations were present. Bypass transition evolved when those perturbations were large enough to bypass the exponential growth of Tollmien-Schlichting (TS) waves. The mixed transition regime involved elements of both natural and bypass transition. The production terms in the current model controlled the transfer from streamwise fluctuations to full turbulence which depended on the laminar kinetic energy and the local mean velocity in order to include natural and mixed transition. A full description of all model variables and dependences was presented by Walters and Leylek⁹.

F. Boundary Conditions

The CFD boundary conditions for the mixing plane model were set to simulate the actual engine operation at both nominal and high altitude conditions. Inlet conditions to the 1st stage vane were based on the typical inlet profiles seen by multistage LPT. Radial variations of the total pressure, total temperature, and tangential and radial flow angles were specified with an estimated inlet static pressure. The radial and tangential flow angles were converted to directional velocity components using spherical coordinate transforms. The initial inlet turbulent viscosity ratio was set as $\mu_t/\mu = 7.364$ for all simulations, and an inlet turbulent intensity, $Tu = 1\%$ was set for only the $k_T-k_L-\omega$ model simulations. The initial outlet static pressure was defined with a radial equilibrium pressure distribution using Eq. 7.

$$\frac{\partial P}{\partial r} = \frac{\rho v_\theta^2}{r} \quad (7)$$

Radial equilibrium pressure distribution was set for the pressure exit boundary condition to define the radial distribution of the back pressure. The fluid zone for the rotor stages was set in the moving reference frame with a rotational speed with respect the x-axis direction, while the vane fluid zones were set in the stationary or absolute reference frame. The blade speeds for the nominal and high altitude conditions were 7700 rpm and 7900 rpm, respectively. All hub and shroud endwalls and blade surfaces were set as stationary no-slip walls relative to the motion of the adjacent fluid zone. The mixing plane interface zones placed between inlet and exit of each blade row used a 151 point radial profile for circumferential averaging. Periodic boundary conditions were assigned to the mid-passage flow boundaries to model the approximate time-averaged operation of a full annulus blade row.

G. Inlet Reynolds Number Flow Conditions

The low Reynolds number flow effects were investigated using a multistage LPT geometry. Table 2 shows the decrease in the inlet Reynolds number to the multistage LPT geometry compared to the nominal and high altitude condition. These calculations were based on mass-weighted averages of fluid flow properties. The Reynolds number was calculated using the mid-radius true chord for each blade row as the characteristic length. The Spalart-Allmaras and $k_T-k_L-\omega$ model were used in simulations at both altitude conditions.

	Altitude Condition	Inlet Re No.		Altitude Condition	Inlet Re No.
1 st Stage Vane	Nominal	135,000	2 nd Stage Rotor	Nominal	108,000
	High	20,000		High	16,000
1 st Stage Rotor	Nominal	123,000	3 rd Stage Vane	Nominal	85,000
	High	19,000		High	12,000
2 nd Stage Vane	Nominal	110,000	3 rd Stage Rotor	Nominal	86,000
	High	16,000		High	12,000

Table 2. Inlet Reynolds Numbers for each Blade Row at Nominal and High Altitude Conditions

H. CFD Post-Processing and Analysis

Intelligent Light® FieldView 12.0 CFD post-processing and visualization software was the primary tool used for flow visualizations. Fluid flow quantities and vectors were exported from Fluent using native FieldView file formats once CFD simulations were complete. Surface flow and flowfield streamlines were created in order to help visualize any vortical structures present in the flowfield for each stage. The presence of these vortical structures was used as an indicator of sources of aerodynamics losses which cause an increase in the total pressure loss coefficient for each blade row. The streamlines were created by arbitrarily placing seed points on iso-surfaces based on a constant value of the Mach number. The seed points were used to calculate the particle paths by integrating through the velocity vector using a second order Runge-Kutta method. Surface flows are defined as special streamlines which are restricted to lie in the plane of the blade surface. The surface flow streamlines were calculated using the velocity gradient on the surface. Also, radial profiles of circumferentially-averaged flow quantities were calculated using a 150 point computational rake using Fluent's post-processing capability.

III. Turbulence Model Results Comparisons for the First Stage

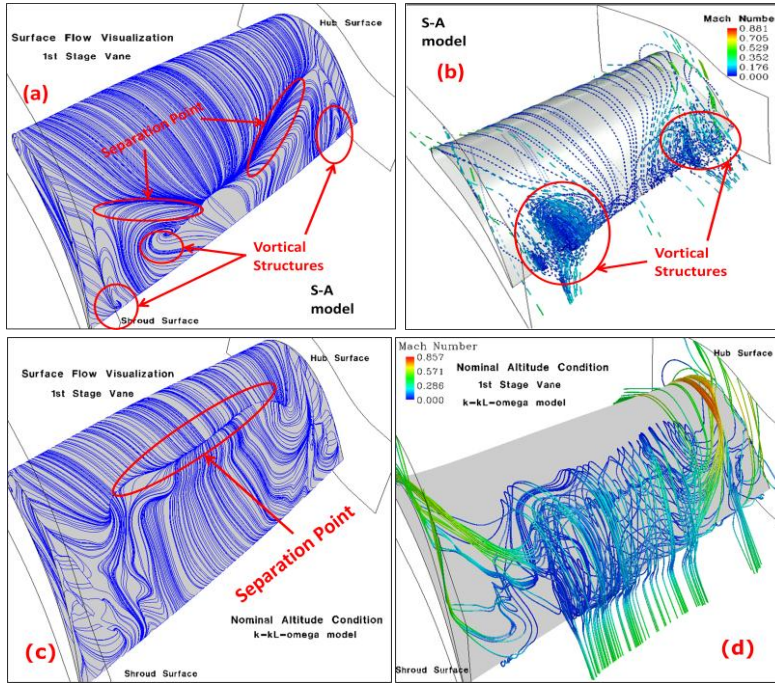


Figure 2. Turbulence Model Comparison of the Surface Flow and Flowfield Streamlines for the 1st Stage Vane at the Nominal Altitude Condition. (a)Surface Flow and (b)Flowfield Streamlines for the S-A Model, (c)Surface Flow and (d)Flowfield Streamlines for the $k-k_L-\omega$ Model

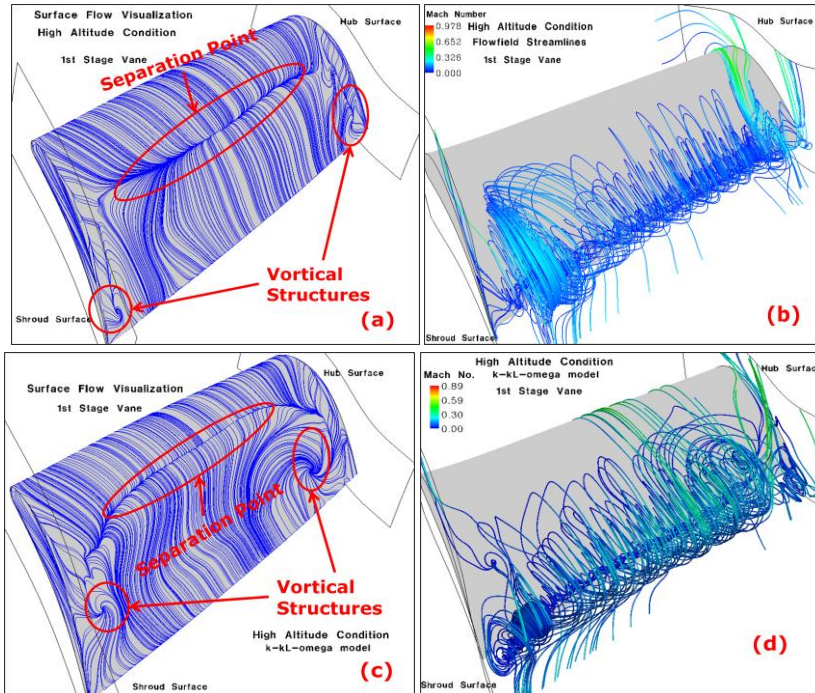


Figure 3. Turbulence Model Comparison of the Surface Flow and Flowfield Streamlines for the 1st Stage Vane at the High Altitude Condition. (a)Surface Flow and (b)Flowfield Streamlines for the S-A Model, (c)Surface Flow and (d)Flowfield Streamlines for the $k-k_L-\omega$ Model

Turbulence model results comparisons were made for the first stage using the multistage LPT geometry at both altitude conditions. Comparisons were evaluated based on the flowfield visualizations using surface flow, flowfield streamlines, and total pressure loss coefficient with subsequent discussions on the inlet flow angle. The laminar-to-turbulent transition region was also investigated using contours of the turbulence quantities on the blade surface.

A. Surface Flow and Flowfield Streamlines

1st Stage

Figure 2 shows the comparison of the surface flow and flowfield streamlines for 1st stage vane using the S-A and $k_T-k_L-\omega$ models. The surface flow results for the S-A model (Fig. 2(a)) revealed that the flow from the endwalls was predicted to move toward the blade mid-span and meet the main streamwise flow which resulted in a foci of separation near the trailing edge of the suction surface. Similar secondary flow effects were observed in the vane for each stage. Downstream of the separation point, two large vortices located at 10% and 75% of the blade span are clearly evident. A third small counter-clockwise vortex close to the shroud endwall was also apparent as shown in Fig. 2(b). The surface flow results using the $k_T-k_L-\omega$ model in Fig. 2(c) showed the foci of separation to be further upstream than observed with the S-A model. A large recirculation region was present on the suction surface due to the joining of the streamwise and endwall flow as shown in Fig. 2(d). The distinct vortical structures predicted with the S-A model were not observed in the $k_T-k_L-\omega$ model results. The difference in prediction of the flowfield was attributed to the transitional boundary layer

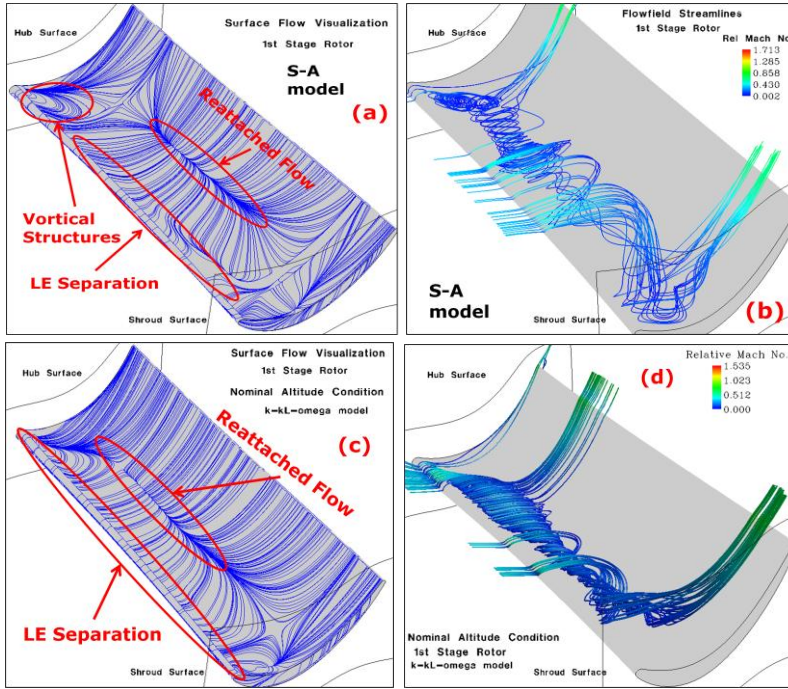


Figure 4. Turbulence Model Comparison of the Surface Flow and Flowfield Streamlines for the 1st Stage Rotor at the Nominal Altitude Condition. (a)Surface flow and (b)Flowfield Streamlines for the S-A Model, (c)Surface Flow and (d)Flowfield Streamlines for the $k-k_L-\omega$ Model

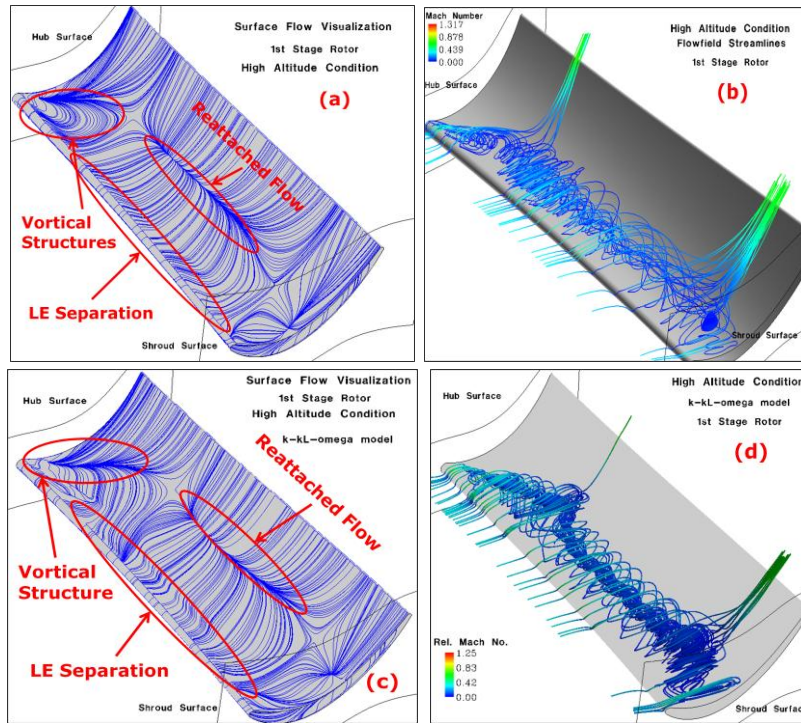


Figure 5. Turbulence Model Comparison of the Surface Flow and Flowfield Streamlines for the 1st Stage Rotor at the High Altitude Condition. (a)Surface Flow and (b)Flowfield Streamlines for the S-A Model, (c)Surface Flow and (d)Flowfield Streamlines for the $k-k_L-\omega$ Model

predicted with the $k_T-k_L-\omega$ model which is discussed in greater detail in Section V.

The surface flow for the high altitude condition using the S-A turbulence model is shown in Figure 3(a). The main foci of separation moved more upstream on the suction surface compared to the nominal altitude result (Fig. 2(a)). In Figure 3(b), the flowfield streamlines indicated the flow was largely separated along the entire blade span. The vortices identified in Fig. 2(b) at the nominal altitude condition have increased in size. For the $k_T-k_L-\omega$ model (Fig. 3(c)), the separation point was located more upstream as compared to the S-A model result at the high altitude, thus producing a larger separation region as seen in Fig. 3(d). The separated flow which was initially restricted to mid-span at the nominal altitude condition (Fig. 2(d)) now extends over the entire blade span at the higher

altitude, similar to the S-A model altitude prediction. The order of magnitude decrease in the Reynolds number at the high altitude condition contributed to the increase in the separation present for all blade rows within each stage as the flow could not successfully turn around the vane suction surface at these lower freestream velocities.

For the 1st stage rotor blade surface, both the S-A and $k_T-k_L-\omega$ models showed similar surface flow and flowfield streamline patterns as indicated in Fig. 4(a)-(d). The surface flow patterns (Fig. 4(a) & 4(c)) indicated that the streamwise flow separated from the blade pressure surface at the leading edge and reattached to the blade surface further downstream. Also, a saddle point was present indicating the presence of small vortical structures near both endwalls for both models. The S-A model predicted the reattachment position to be more downstream

than the $k_T-k_L-\omega$ model result. For the $S-A$ model, this resulted in a relatively large reattachment region (Fig. 4(b)), whereas the $k_T-k_L-\omega$ model predicted a tighter streamwise region of separation that rolled up and was directed outward in the radial direction (Fig. 4(d)).

For the high altitude condition, the reattachment location was slightly more downstream in the $k_T-k_L-\omega$ model (Fig. 5(a) & 5(c)) prediction resulting in a larger separation region than the $S-A$ model. The change in altitude condition did not significantly affect the separation and reattachment locations in the $S-A$ model results as seen when comparing Fig. 4(a) and Fig. 5(a). Yet, the higher altitude condition in the $k_T-k_L-\omega$ model result caused the pressure surface reattachment location to move further downstream with a larger separation region. There was not any evidence of a separation on the suction surface rotor blades in any stages at either altitude conditions for either turbulence model predictions.

B. Total Pressure Loss Coefficient Comparisons

1st Stage

The circumferentially averaged total pressure loss coefficient was calculated for both the 1st stage vane and rotor (Fig. 8) to determine the effect caused by the vortical structures produced by the secondary flow. The loss coefficient was calculated with Eq. (8) by taking the difference between the inlet and exit total pressure and dividing by the difference between the mass-weighted averaged inlet total and static pressure.

$$TPLC = \frac{(P_{0,in} - P_{0,exit})}{(P_{0,in} - P_{in})} \quad (8)$$

The loss coefficient was plotted as a function of the normalized radial location from the hub to shroud surface. Also, Table 3 shows a turbulence model comparison of the mass-weighted average loss coefficient for each blade row at the two altitude conditions. The peaks in the loss coefficient predicted from the $S-A$ model were due to the suction side vortical structures and the endwalls from the hub and shroud for the 1st stage vane. The presence of vortical structures on the pressure side of the 1st rotor, along with the endwall effects, caused a reduction in the outlet relative total pressure at the exit plane. This led to higher peak values of the loss coefficient where the vortical structures at the endwalls were located. There was a 143% increase in the mass-weighted average loss coefficient in the 1st stage rotor when compared to the 1st stage vane. The circumferential averaged wake from the upstream vane calculated by the mixing plane method caused a significant amount of total pressure loss. Additionally, the contributed total pressure loss from the secondary flow in the rotor caused the much higher loss coefficient seen in the 1st stage rotor compared to the 1st stage vane. The loss coefficient results predicted with the $k_T-k_L-\omega$ model showed a 15% reduction in the mass-weighted average loss coefficient compared to $S-A$ model for the 1st stage vane. This was due to the absence of the three distinct vortical structures in the 1st stage vane as predicted with the $S-A$ model. This presented a more uniform inlet flow with less total pressure loss from the upstream vane secondary flow and led to a reduced loss coefficient near the hub and shroud radial locations. The mass-weighted average loss

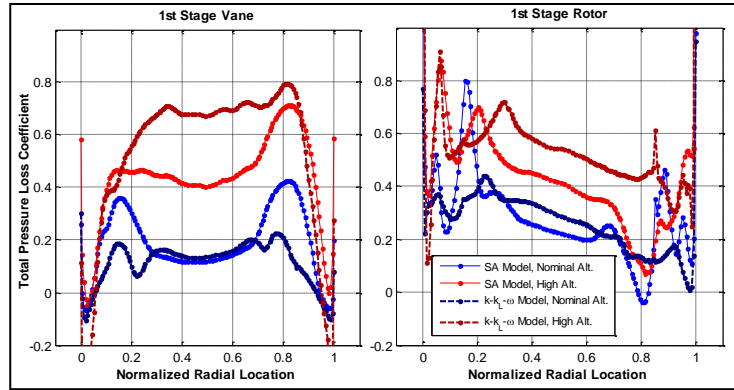


Figure 6. Turbulence Model Comparison of the Circumferentially Averaged Total Pressure Loss Coefficient for the 1st Stage at the Nominal and High Altitude Condition

Nominal Altitude						
	1 st Vane	1 st Rotor	2 nd Vane	2 nd Rotor	3 rd Vane	3 rd Rotor
<i>S-A model</i>	0.1135	0.2763	0.1217	0.2646	0.1220	0.2261
<i>k-k_L-ω model</i>	0.0961	0.2785	0.1709	0.3487	0.1801	0.3025
High Altitude						
<i>S-A model</i>	0.2241	0.4209	0.1974	0.4446	0.1991	0.3966
<i>k-k_L-ω model</i>	0.2187	0.5312	0.3454	0.6376	0.2940	0.5783

Table 3. Turbulence Model Comparison of the Mass-Weighted Average Loss Coefficient for each Blade Row at the Nominal and High Altitude Conditions

coefficient remained constant in the $k_T-k_L-\omega$ model prediction due to higher losses present near the mid-span as compared to the $S-A$ model prediction. This could be attributed to a thicker and more turbulent boundary layer in the $k_T-k_L-\omega$ model prediction which is discussed in greater detail in Section V.

The circumferentially averaged loss coefficient distribution for the 1st stage at the high altitude condition is also shown in Fig. 6. The local loss coefficient peak in the $S-A$ model predictions was due to the increase in the shroud vortex size compared to the nominal altitude condition for the 1st stage vane. The increase in altitude resulted in a 97% and 127% increase in the mass-weighted average loss coefficient for the 1st stage vane in the $S-A$ and $k_T-k_L-\omega$ model results, respectively. There was an overall higher loss coefficient distribution predicted from the $k_T-k_L-\omega$ model compared to the $S-A$ model for the 1st stage vane. This was due to the foci of separation being located more upstream with a larger separation region in the $k_T-k_L-\omega$ model prediction. The loss in the 1st stage rotor showed the same trend because of the higher secondary flow loss in addition to the inlet total pressure loss distortion from the upstream vane. The higher altitude caused a 52% and 90% increase in the mass-weighted average loss coefficient for the 1st stage rotor in the $S-A$ and $k_T-k_L-\omega$ model results, respectively. Both turbulence models predicted an increase in the loss coefficient from the change an altitude condition as result of a reduction in inlet Reynolds number for all blade rows.

IV. Turbulence Model Comparisons for the Second and Third Stages

A. Surface Flow Streamlines and Loss Coefficients for the Second Stage

As shown in Fig. 7, the results for the nominal attitude condition using both models predicted the flow to be relatively attached with only minor secondary flow losses for the 2nd stage vane flowfield. The $S-A$ model results shown in Fig. 7(a) reveal a mostly attached flow to the airfoil surface for the majority of the blade span with only small vortical structures at 10% of the span near the hub surface, and a pattern due to the motion of the flow from the shroud endwall at 85% of the span. In contrast, the $k_T-k_L-\omega$ model prediction did not show any evidence of vortical structures near the trailing edge. Instead, it revealed endwall flow patterns at the hub and shroud surface. Also, a localized separation and reattachment region was predicted near the vane leading edge at 40% of the span

and a vortical structure was shown near the shroud surface at the vane leading edge as shown in Fig. 7(c).

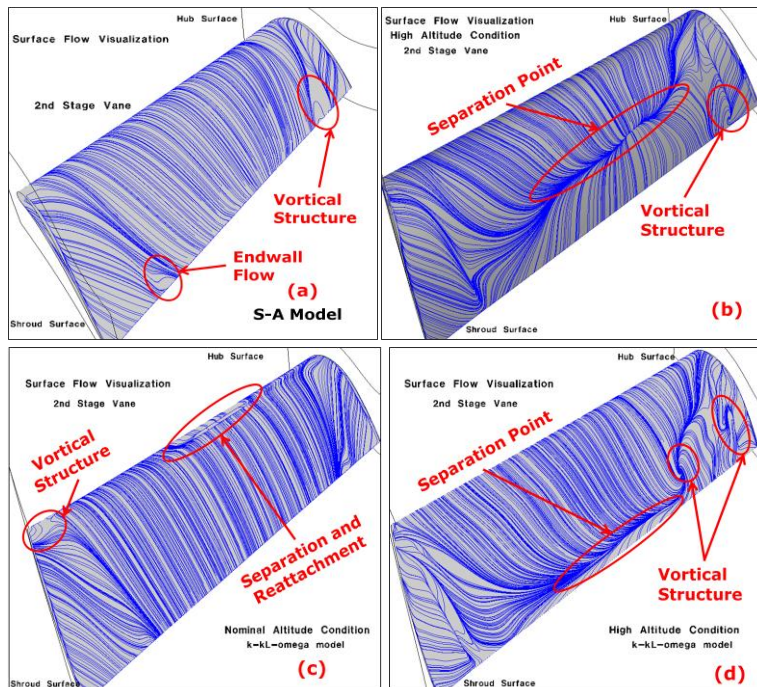


Figure 7. Turbulence Model Comparison of the Surface Flow Streamlines for the 2nd Stage Vane at the Nominal and High Altitude Condition. (a) Nominal and (b) High Altitude for the $S-A$ Model, (c) Nominal and (d) High Altitude for the $k_T-k_L-\omega$ Model

When the multistage LPT flow was simulated at higher altitude, the $S-A$ model showed a foci of separation present on the suction surface in Fig. 7(b) with a large separation region present along a major portion of the 2nd stage vane surface caused by the reduced inlet Reynolds number. The vortical structure was still present near the hub surface. In contrast, the $k_T-k_L-\omega$ model result indicated the separation region was more downstream while still maintaining the hub vortical structure. This indicated the predicted momentum of the main flow was higher with the $k_T-k_L-\omega$ model than the $S-A$ model, which kept the flow more attached to the blade surface.

The surface flow patterns for the 2nd stage rotor (not shown) revealed a similar flow behavior to that seen in the 1st stage rotor. The dominant flow feature was the leading edge separation quickly reattaching on the pressure surface and forming a recirculation region. The k_T-k_L-

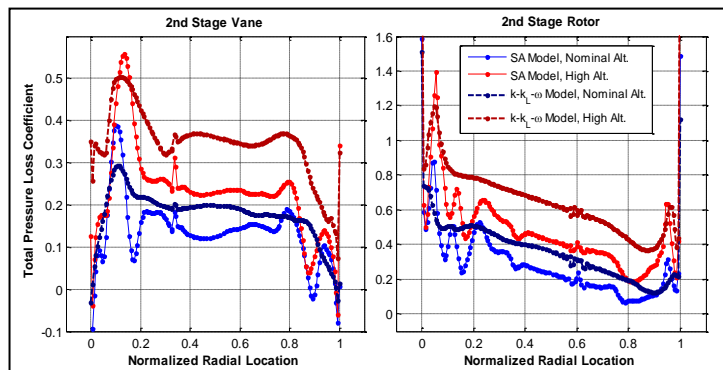


Figure 8. Turbulence Model Comparison of the Circumferentially Averaged Total Pressure Loss Coefficient for the 2nd Stage at the Nominal and High Altitude Condition

hub and shroud endwalls. Also, the loss coefficient distribution was predicted higher in the main streamwise flow normalized radial location ($r \approx 0.2-0.78$) which was due to the presence of the recirculation region observed in Fig. 7(c). This resulted in a 40% increase in the mass-weighted average loss coefficient for the $k_T-k_L-\omega$ model compared to the $S-A$ model prediction for the 2nd stage vane. The loss coefficient results for the 2nd stage rotor revealed smaller peaks due to the smaller vortical structures located close to each endwall surface. For the $k_T-k_L-\omega$ model, the loss coefficient was uniform, yet 32% higher in the mass-weighted average value than the $S-A$ model prediction at the nominal altitude condition. The increased amount of recirculation on the pressure side of the blade coupled with the higher total pressure loss seen in the upstream vane caused the higher loss coefficient in the 2nd stage rotor.

At the higher altitude, the loss coefficient plot for the 2nd stage vane showed a 62% and 102% higher mass-weighted average loss coefficient than the nominal altitude condition for the $S-A$ and $k_T-k_L-\omega$ model predictions, respectively. This was consistent with the separation present at the lower inlet Reynolds number. The two models contained similar peaks near the hub surface consistent with the locations of the vortices. The $k_T-k_L-\omega$ model predicted an 11% decrease in the loss coefficient peak compared to the $S-A$ model. Yet, the distribution of loss coefficient outside of the hub vortex region was higher in the $k_T-k_L-\omega$ model result. The loss coefficient plot for the 2nd stage rotor revealed a 68% and 83% increase in loss at the higher altitude for the $S-A$ and $k_T-k_L-\omega$ model predictions, respectively, compared to the nominal altitude condition. The substantial increase in the loss at the higher altitude was a result of the increased amount of upstream vane total pressure distortion and higher secondary flow losses in the 2nd stage rotor. The $k_T-k_L-\omega$ model prediction showed a higher and a more uniform loss coefficient distribution in the main streamwise flow normalized radial locations ($r \approx 0.15-0.9$) compared to the $S-A$ model prediction as observed in the 1st stage rotor. The higher distribution in the $k_T-k_L-\omega$ model prediction resulted in a 43% increase over the $S-A$ model result in the mass-weighted average loss coefficient for the 2nd stage rotor.

B. Surface Flow Streamlines and Loss Coefficients for the Third Stage

$S-A$ model surface flow results at the nominal altitude condition shown in Fig. 9(a) for the 3rd stage vane indicated separation on the suction surface due to secondary flow effects. Figure 9(c) shows that for the $k_T-k_L-\omega$ model the separation region is no longer present near the vane mid-span but instead a large separation and reattachment region has developed near the vane leading edge. Further downstream, separate recirculation regions formed due to secondary endwall flow. At the high altitude case, the $S-A$ model revealed the presence of a localized separation and reattachment region relatively close to the blade leading edge on suction surface as seen in Fig. 9(b). Also, a foci of separation was located significantly more upstream on the blade surface than the nominal altitude condition result in Fig. 9(a). The $k_T-k_L-\omega$ model result (Fig. 9(d)) predicted a similar flowfield as the 2nd stage vane, where the higher momentum flow from the endwall caused a separation region near the trailing edge that extended the entire blade span. There was no presence of a separation and reattachment region near the leading edge as observed at the nominal altitude condition in Fig 9(c).

The surface flow comparisons for the 3rd stage rotor using the $S-A$ and $k_T-k_L-\omega$ model (not shown) were again similar to that seen in the 1st stage rotor. The $k_T-k_L-\omega$ model prediction revealed that the separation and reattachment region extended even more downstream and further along the blade span than the $S-A$ model prediction, similar to the 2nd stage rotor results. Walters and Leylek's⁹ $k_T-k_L-\omega$ model predicted the least separated flow for the 1st stage

ω model prediction showed an extended recirculation region further along the blade span than the $S-A$ model prediction. Neither model suggested evidence of separation on the suction surface. Nearly identical surface flows occurred at high altitude (not shown) as at the nominal altitude for the 2nd stage rotor.

The total pressure loss coefficient plots for the 2nd stage are shown in Fig. 8. The $S-A$ model results for the 2nd stage vane showed the loss coefficient peaks present near hub were due to the smaller vortices observed in Fig. 7(a) & 7(c) for the nominal altitude condition. The local loss coefficient reduced in size in the $k_T-k_L-\omega$ model as a result of lower momentum flow originating from the

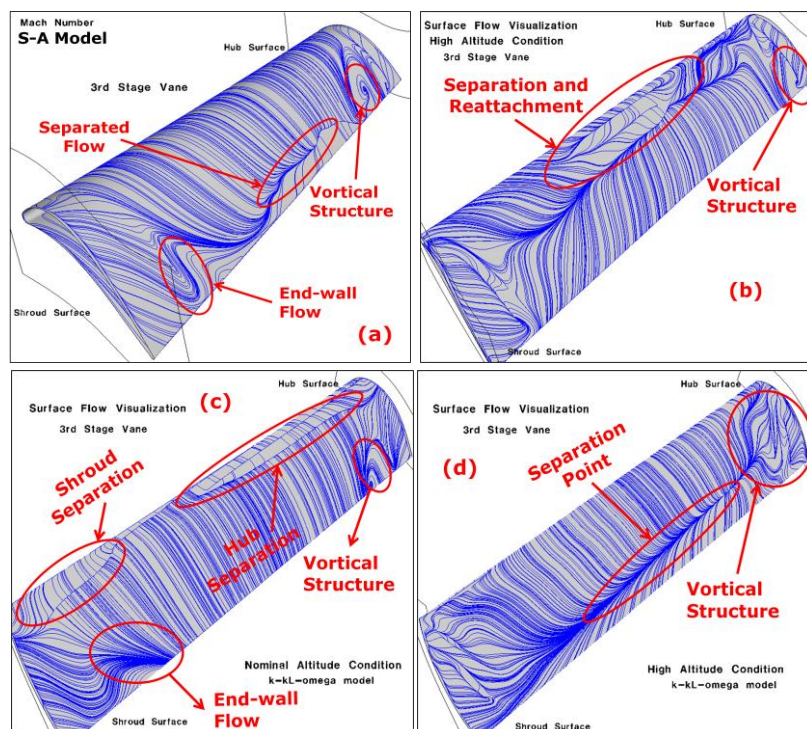


Figure 9. Turbulence Model Comparison of the Surface Flow Streamlines for the 3rd Stage Vane at the Nominal and High Altitude Conditions. (a) Nominal and (b) High Altitude for the S-A Model, (c) Nominal and (d) High Altitude for the $k-k_L-\omega$ Model

at the nominal altitude condition. Similar trends, profiles, and values of the loss coefficient were observed in the 3rd stage as for the 2nd stage. The distribution of the loss coefficient was higher in the $k_T-k_L-\omega$ model results due to the increased amount of separated flow with a 48% increase in the mass-averaged value compared to the S-A model. For the 3rd stage rotor, several smaller vortices were present, causing more localized loss coefficient peaks in S-A model prediction. These localized loss coefficient peaks were absent in the $k_T-k_L-\omega$ model prediction resulting in more uniform loss coefficient distribution with a 34% higher mass-weighted average loss coefficient value. Again the magnitudes of the loss coefficient were similar for the 2nd and 3rd stage rotors.

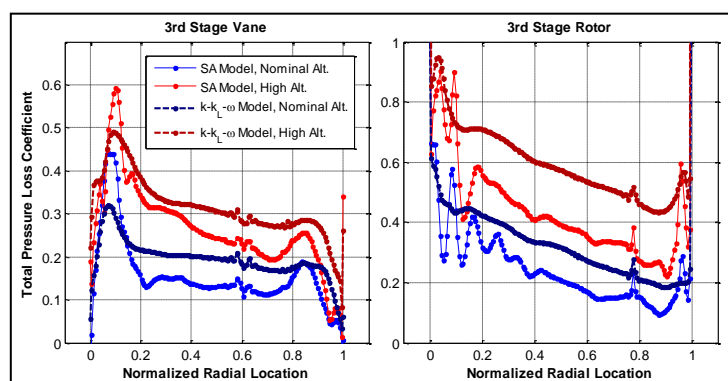


Figure 10. Turbulence Model Comparison of the Circumferentially Averaged Total Pressure Loss Coefficient for the 3rd Stage at the Nominal and High Altitude Condition

In summary, the prediction of the flowfield for the multistage LPT geometry was shown to be heavily dependent on the turbulence model implemented with the mixing plane method. The Walters and Leylele $k_T-k_L-\omega$ transitional flow model predicted lower aerodynamic losses in the 1st stage but higher losses for the 2nd and 3rd stages compared

compared to the S-A model, whereas more separated flow was predicted in the 2nd and 3rd stage at the nominal altitude condition.

At the higher altitude (not shown), the 3rd stage rotor pressure side separation and reattachment region extended from the hub to approximately 70% of the span for both turbulence models, whereas the nominal altitude condition predicted most of the blade span to be influenced by the separated flow. Also the boundary layer reattachment location was more downstream in the high altitude condition. The decrease in Reynolds number largely affected the flowfield in the 3rd stage vane compared to the rotor. This trend was found in all stages and suggests that improvements could be made to the vane in order to control separation and improve efficiency.

In Figure 10, the loss coefficient plot showed peaks near the hub surface due to the vortical structures identified in Fig. 9(a) and 9(c) for both turbulence model predictions at

the nominal altitude condition. Similar trends, profiles, and values of the loss coefficient were observed in the 3rd stage as for the 2nd stage. The distribution of the loss coefficient was higher in the $k_T-k_L-\omega$ model results due to the increased amount of separated flow with a 48% increase in the mass-averaged value compared to the S-A model. For the 3rd stage rotor, several smaller vortices were present, causing more localized loss coefficient peaks in S-A model prediction. These localized loss coefficient peaks were absent in the $k_T-k_L-\omega$ model prediction resulting in more uniform loss coefficient distribution with a 34% higher mass-weighted average loss coefficient value. Again the magnitudes of the loss coefficient were similar for the 2nd and 3rd stage rotors.

At high altitude, a significant increase in the loss was encountered for both models. Similar to the 2nd stage, this was believed to be due to the increased amount of upstream vane total pressure distortion and higher secondary flow losses. The $k_T-k_L-\omega$ model result showed a further 48% increase in the mass-weighted averaged loss coefficient due the 17% decrease on the local peak from the hub vortex and overall higher distribution compared to the S-A model for the 3rd stage vane. The same trend was observed for the 3rd stage rotor with the $k_T-k_L-\omega$ model resulting in more uniform loss coefficient distribution with an increase in the mass-weighted averaged loss coefficient of 46%.

to the *S-A* turbulence model at the nominal altitude condition mainly due to the increased amount of separated flow. At the higher altitude condition, the $k_T-k_L-\omega$ model predicted overall higher aerodynamic losses than the *S-A* model for all three stages, although both models did show that the higher altitude caused an increase in the amount of separated flow due to the order of magnitude decrease in the inlet Reynolds number. Since the $k_T-k_L-\omega$ model accounts for transitional flow effects, it is asserted based on the results presented that the $k_T-k_L-\omega$ model provides more effective prediction of the flowfield at these Reynolds numbers ranges. This is supported by experimental comparisons done on a cascade LPT blade airfoil based on the multistage LPT geometry reported Sanders *et al.*¹² at similar inlet Reynolds numbers. The Walters and Leylek $k_T-k_L-\omega$ transitional flow model demonstrated the ability to predict the transitional flow behavior and performance more effectively than conventional turbulence models such as the Spalart-Allmaras model.

V. Flowfield Comparisons at the Nominal and High Altitude Conditions

An additional altitude comparison was made in greater detail using the Walters and Leylek $k_T-k_L-\omega$ transitional flow model to further investigate the low Reynolds number effect on the predicted flowfield. Only this model was used based on the more representative results of the actual flowfield found in the preceding sections for the multistage geometry. The altitude effect on laminar-to-turbulent transition location was studied for each blade row. Also, the circumferentially-averaged inlet and exit flow angles were studied for the $k_T-k_L-\omega$ model predictions.

A. Laminar-to-Turbulent Transition Altitude Comparisons

1st Stage

Figure 11 shows an altitude comparison of the turbulent kinetic energy (TKE) contours on the 1st stage vane suction surface. Also, a line plot of the vane surface TKE was made at the 1st stage vane mean radius. A white line was drawn to show the position of the mean radius relative to the vane surface. The sudden increase in the turbulent kinetic energy was used as an indicator of the turbulent transition point. At the nominal altitude condition in Fig 11(a), the flow was initially laminar, separated from the blade surface, and became turbulent due the recirculation region observed in Fig 2(d). Also, the flow originating from the endwall onto the blade surface was largely laminar and vortex generation near the endwall surfaces caused local increases in the TKE. Figure 11(b) showed the boundary layer flow to be laminar and only a small increase in the TKE was observed near the trailing edge for the high altitude condition. The large separation region seen in Fig. 3(d) did not cause an increase in turbulence production as in the nominal altitude result. This could be due the flow in the recirculation region having a lower amount of momentum causing a dampening effect to the production of turbulence.

For the 1st stage rotor, the mean radius profile of the TKE indicated the separated flow pressure side of the rotor caused an increase in the TKE starting at $x/r_m \approx 0.215$ as show in Fig. 11(c) at the nominal altitude condition. This resulted in a turbulent boundary layer reattachment. The suction surface boundary layer was turbulent from the leading edge and the turbulent production began to decrease further downstream. At $x/r_m \approx 0.29$ the TKE increased again due to the slowing velocity near the blade trailing edge needed to match the static pressure. A similar behavior on both sides of the rotor was observed for the high altitude condition in Fig. 11(d) but, the magnitude of the TKE has reduced at the higher altitude condition because of a lower amount of turbulence present in the mean flow. Also, the increased separated flow on the pressure surface served to delay turbulent reattachment to further downstream.

2nd Stage

The nominal attitude condition for the 2nd stage vane in Fig. 12(a) highlights the separation region that existed on the suction side for this vane. The separation region caused an instability increasing the TKE production at $x/r_m \approx 0.345$ as the boundary layer reattached and became turbulent. The regions near in the endwalls showed a reduction in the TKE due the hub vortex and the laminar flow from the shroud surface. At the high altitude, figure 12(b) shows a significant reduction in the TKE indicative of the laminar boundary layer flow present on both surfaces. The laminar boundary layer flow in combination with the adverse pressure gradient resulted in higher momentum endwall flow which led to separation and large vortex production as seen in Fig. 7(d). The 2nd stage rotor had similar results at both altitude conditions similar to the 1st stage rotor as shown in Fig. 12(c)-(d). The only significant difference was the growth of the TKE on the pressure side due to the increase in size of the separation and reattachment region at the higher altitude condition.

3rd Stage

The separation and reattachment region extending the entire blade span of the 3rd stage vane suction surface caused the mean radius TKE trend evident at $x/r_m \approx 0.64-0.66$ in Fig. 13(a) at the nominal attitude condition. This

region hindered the transition to turbulence on the blade surface. The boundary remained attached at the blade mid-span as confirmed in the surface flow results (Fig. 9(c)) even though the TKE decreased in this region. The endwall flow and hub vortex caused a reduction in the turbulent production as observed for the 2nd stage vane. Also, Figure 13(b) revealed similar behavior to the 2nd stage vane at the high altitude condition. The lower TKE on suction surface was due to the decrease in the 3rd stage vane separation region compared to the upstream vanes. The distribution of TKE for the 3rd stage rotor was similar to the 2nd stage rotor at both altitude conditions and is not shown. This supports the similar results obtained in the surface flow results for both rotors.

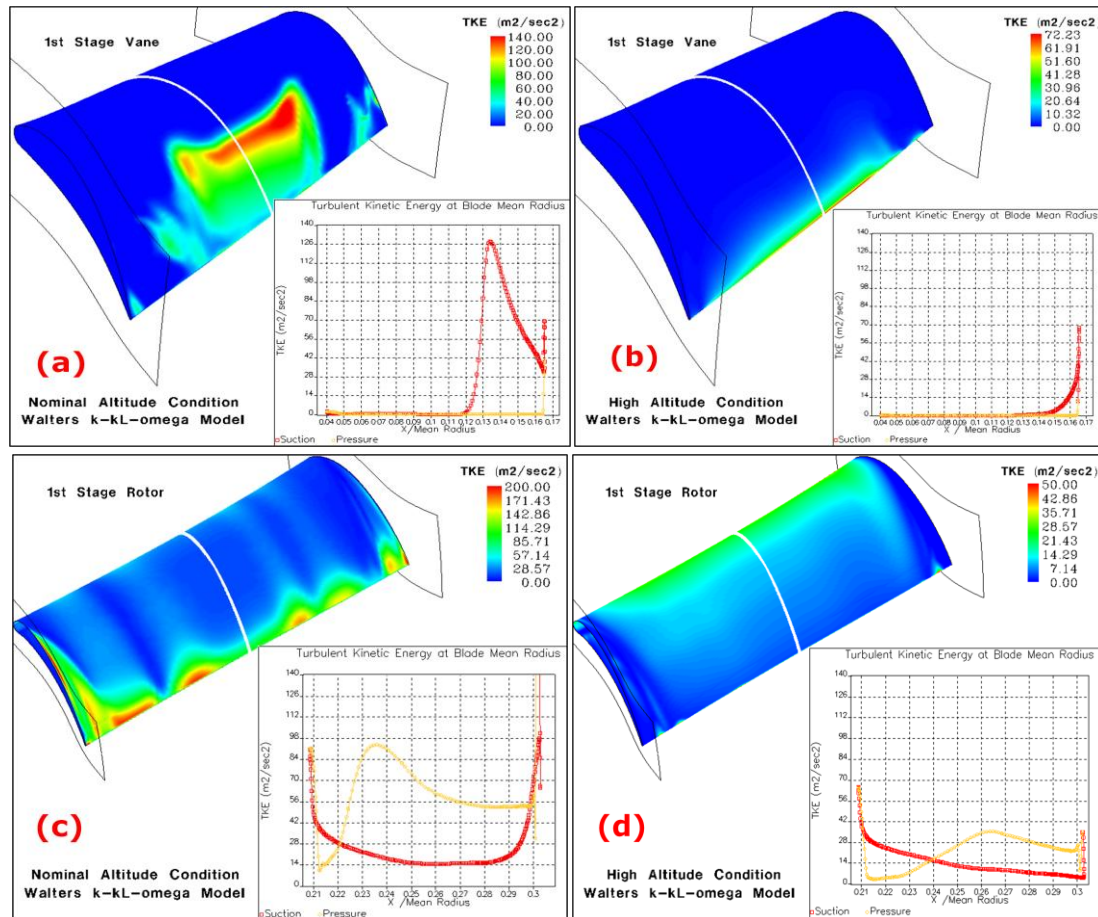


Figure 11. Altitude Comparison of the 1st Stage Surface Turbulent Kinetic Energy Contours using the Walters and Leylek k_T - k_L - ω model. (a) 1st Stage Vane and (b) Rotor at the Nominal Altitude Condition, (c) 1st Stage Vane and (d) Rotor at the High Altitude Condition

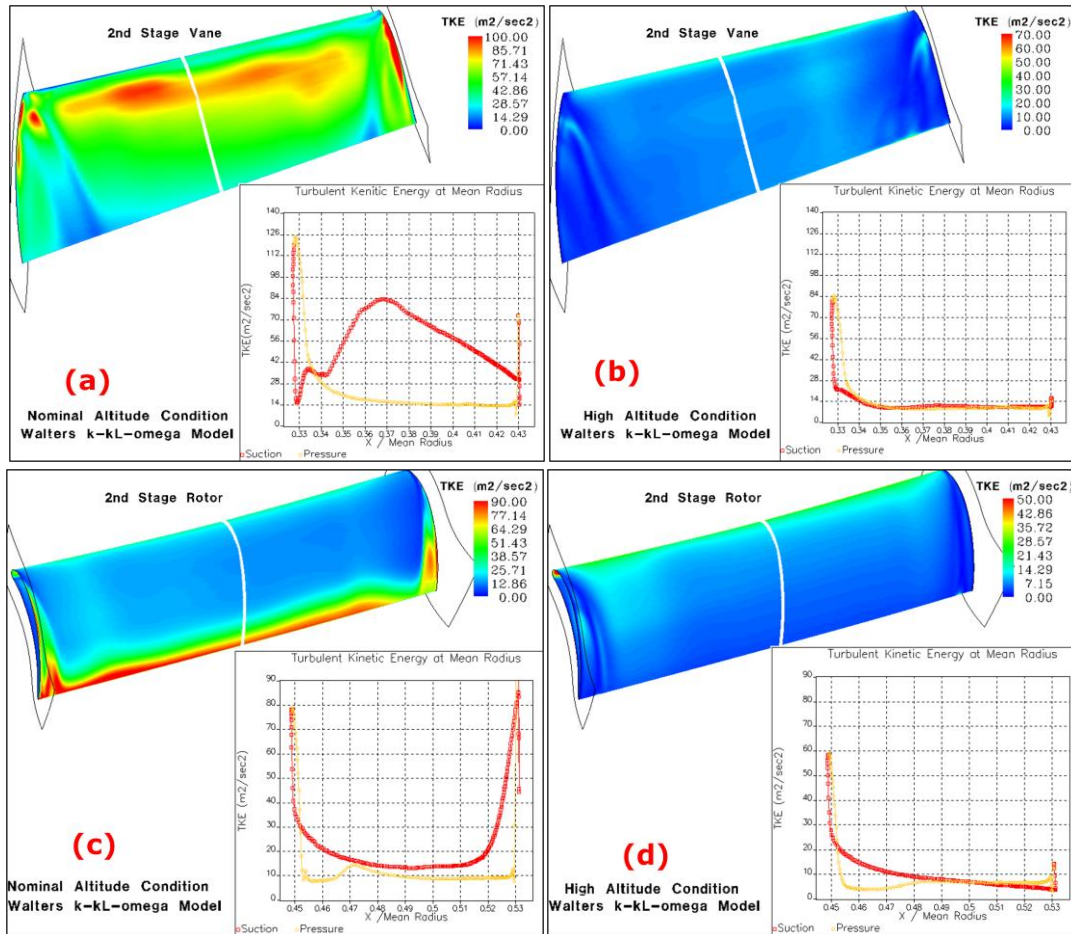


Figure 12. Altitude Comparison of the 2nd Stage Surface Turbulent Kinetic Energy Contours using the Walters and Leylek k_T - k_L - ω model. (a) 2nd Stage Vane and (b) Rotor at the Nominal Altitude Condition, (c) 2nd Stage Vane and (d) Rotor at the High Altitude Condition

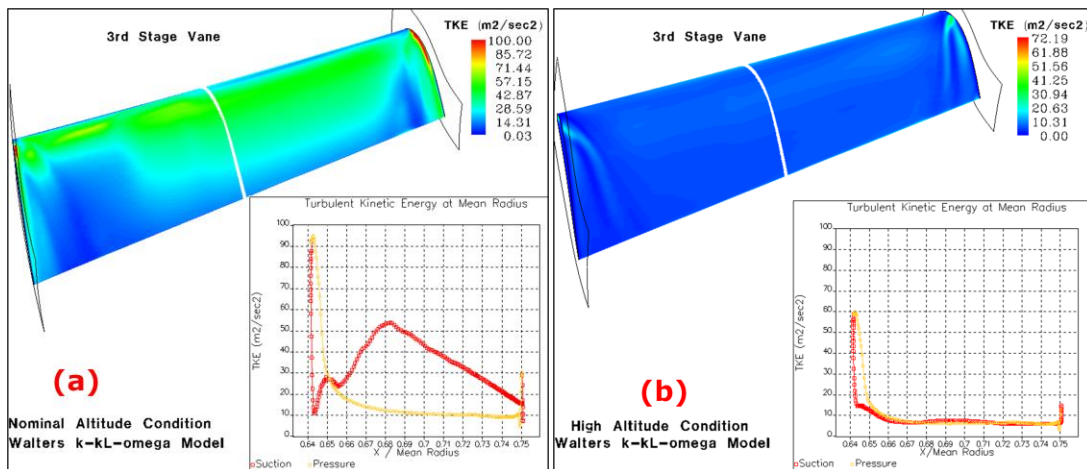


Figure 13. Altitude Comparison of the 3rd Stage Vane Surface Turbulent Kinetic Energy Contours using the Walters and Leylek k_T - k_L - ω model. 3rd Stage Vane at the (a) Nominal and (b) High Altitude Condition

B. Altitude Comparison of the Inlet and Exit Flow Angles

The circumferential relative/absolute flow angles were investigated to determine the altitude effect on the blade turning for each stage. Figure 14(a) shows the normalized absolute flow angles for the 1st vane inlet and exit. Flow angles were normalized with respect to the mean flow angle at the nominal altitude condition. The distribution of the inlet flow angle for 1st vane was specified as an inlet boundary condition at both altitude conditions. The increase in separated flow in the vane at the higher altitude reduced the vane exit flow angle leading directly to a decrease in the relative flow angle of the downstream 1st stage rotor inlet (Fig. 14(b)). This flow angle change was believed to be the cause of the increase in the separation region on pressure side of the blade. Figure 14(b) shows the relative exit flow returned to the same range suggestive that the rotor could compensate for some off angle inlet flow.

Figure 15 shows that the downstream 2nd and 3rd stage did not have a significant change in exit flow angle as a result of the 1st stage rotor exit relative flow angle having a similar range for both altitude conditions. Although, the loss coefficient was observed to increase for the high altitude cases of both these stages due to an increased amount of separated flow. This indicated that the higher losses did not affect the flow angles through the 2nd and 3rd stage.

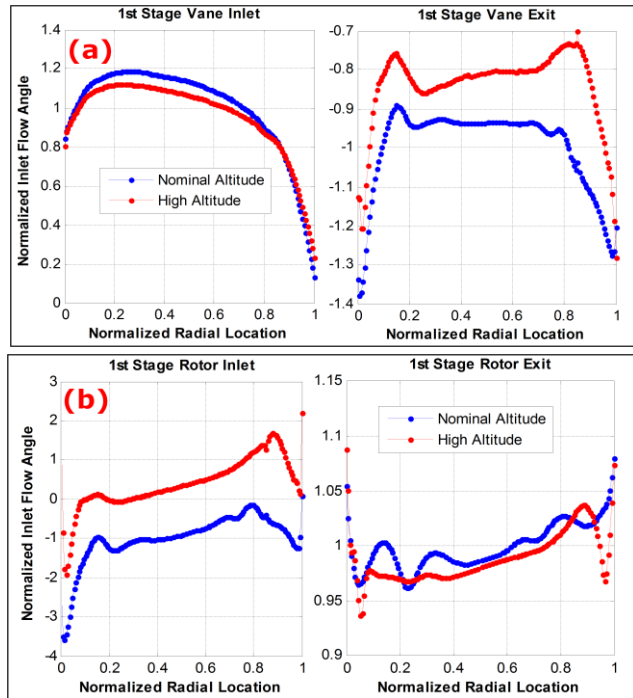


Figure 14. Altitude Comparison of the Normalized Inlet and Exit Flow Angles. 1st Stage (a) Vane and (b) Rotor

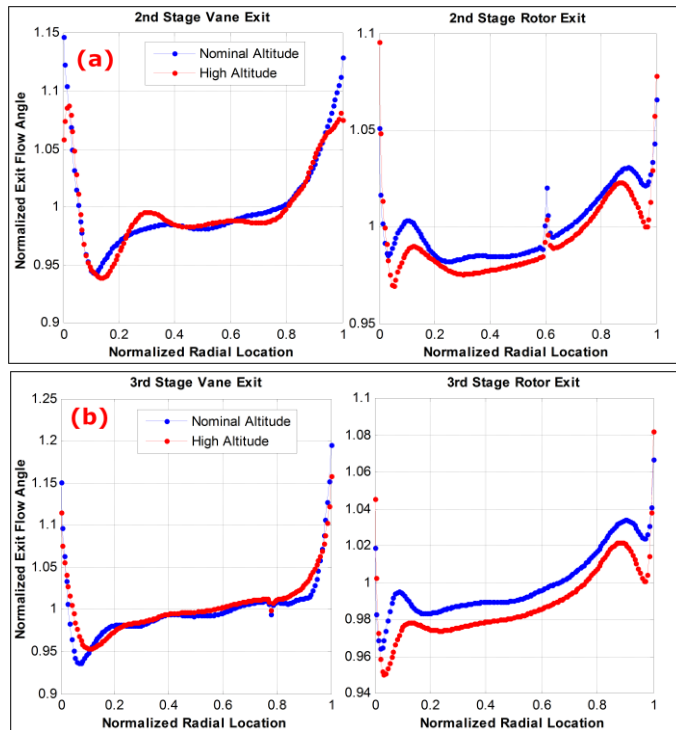


Figure 15. Altitude Comparison of the Normalized Exit Flow Angles. (a) 2nd Stage and (b) 3rd Stage Vane and Rotor

VI. Conclusions

Flows in a multistage low pressure turbine geometry were simulated at a nominal and high altitude condition. The high altitude condition represents a low Reynolds number regime where laminar boundary layers are more likely to exist. In order to accurately predict this flowfield, transition and separation must be modeled accurately. A new three-equation laminar-to-turbulent transitional flow model developed by Walters and Leylek was used in combination with the mixing plane numerical technique to approximate the time-averaged flowfield using a steady-state simulation. The Walters and Leylek k_T - k_L - ω model flowfield predictions were compared to those obtained with the Spalart-Allmaras turbulence model at both altitude conditions.

Surface flow and flowfield streamline visualization was used to investigate vortical structures and separation regions present within the flowfield as sources of aerodynamic losses. The prediction of the amount and the location of the flow separation differed significantly depending on the turbulence model. Overall, less separated flow was predicted with the k_T - k_L - ω model for the 1st stage, whereas the 2nd and 3rd stages more

separated flow observed in the k_T - k_L - ω model predictions compared to the S - A model at both altitude conditions. Some similarities observed for both model predictions were the higher altitude condition had significantly more aerodynamic losses from separated flow than the nominal altitude condition. Also, the vane for each stage had significantly more separated flow compared to the rotor blades. The flowfield behavior was similar in the rotor blades for each stage with only small separation regions at the leading edge. However, the extent of the separation and reattachment region differed depending on the chosen turbulence model and altitude condition. Also, higher loss coefficient was observed for each rotor stage because of the inlet total pressure distortion from the upstream vane in addition to its secondary flow losses. This was observed for both turbulence model predictions at each altitude condition.

A previous investigation by Sanders *et al.*¹² suggested the boundary layer within the multistage LPT geometry was either laminar or transitional dependent on the inlet conditions at this inlet Reynolds number range. Since the k_T - k_L - ω model accounted for transitional flow effects, it is considered to provide a more effective prediction of low Reynolds number effects than the fully turbulent Spalart-Allmaras model for the multistage LPT geometry. An investigation of the growth of the turbulent kinetic energy was used as an indicator of the state of the boundary layer. The boundary layer was mostly transitional on the blade suction surface at the nominal altitude condition whereas the boundary layer was mostly laminar on the vane suction surface for each stage which resulted in more separated flow present at the higher altitude condition. Based on the results presented here, the Walters and Leylek k_T - k_L - ω transitional flow model is considered to provide a superior method for flow prediction in low pressure turbines at low Reynolds numbers compared to conventional RANS turbulence models. This model also provided a more detailed understanding of the aerodynamic loss mechanisms present in low Reynolds number flows. Experimental results are needed to fully validate the CFD predictions using the k_T - k_L - ω model technique for the multistage LPT geometry. Unsteady CFD simulations are also needed to compare with steady-state predictions using the mixing plane CFD technique. This methodology will be used to suggest methods to control separation and improve performance at low Reynolds numbers for future needs.

Acknowledgments

The work presented was sponsored by the Air Force Research Laboratory, Propulsion Directorate, Turbine Engine Division. Computing resources were provided by the U.S. Department of Defense AFRL Distributed Computing Research Center, High Performance Computing facility at Wright-Patterson AFB, OH. The authors are grateful to H. Thornburg for assistance with mesh generation and helpful discussions. Also, C. Hah from NASA Glenn Research Center and F. Kececy from ANSYS® are acknowledged for their helpful advice with CFD simulation set-up and analysis.

References

- ¹ Dawes, W.N., "Towards Improved Throughflow Capability: The Use of 3D Viscous Flow Solvers in a Multistage Environment", ASME Journal of Turbomachinery, Vol. 114, January 1992, pp 8–17.
- ² Dorney, D.J., and Sharma, O.P., "Evaluation of Flow Field Approximations for Transonic Compressor Stages", ASME Journal of Turbomachinery, Vol. 119, July 1997, pp 445–452.
- ³ Wiess, J.M., and Kececy, F.J., "Numerical Simulation of Steady-State Flow Through a Multi-Stage Turbine using Unstructured Meshes" ASME Paper No. FEDSM-99-6862.
- ⁴ Suzen, Y.B., Huang, P.G., Volino, R.J., Corke, T.C., Thomas, F.O., Huang, J., Lake, J.P., and King, P.I., "A Comprehensive CFD Study of Transitional Flows in Low-Pressure Turbines Under a Wide Range of Operating Conditions", AIAA Paper No. 2003-3591.
- ⁵ Menter, F.R., Langtry, R.B., Likki, S.R., Suzen, Y.B., Huang, P.G., and Volker, S., "A Correlation-Based Transition Model Using Local Variables- Part I: Model Formulation", Journal of Turbomachinery, Vol. 128, July 2006, pp 413 – 422.
- ⁶ Langtry, R.B., Menter, F.R., Likki, S.R., Suzen, Y.B., Huang, P.G., and Volker, S., "A Correlation-Based Transition Model Using Local Variables- Part II: Test Cases and Industrial Applications", Journal of Turbomachinery, Vol. 128, July 2006, pp 423 – 434.
- ⁷ Praisner, T.J., and Clark, J.P., "Predicting Transition in Turbomachinery, Part I – A Review and New Model Development", ASME Paper No. GT-2004-54108.
- ⁸ Praisner, T.J., Grover, E.A., Rice, M.J., and Clark, J.P., "Predicting Transition in Turbomachinery, Part II – Model Validation and Benchmarking", Journal of Turbomachinery, Vol. 129, January 2007, pp 14 – 22.

- ⁹ Walters, D.K., and Leylek, J.H., “A New Model for boundary Layer Transition Using a Single Point RANS Approach”, Journal of Turbomachinery, Vol. 126, January 2004, pp 193–202.
- ¹⁰ Walters, D.K., and Leylek, J.H., “Prediction of Boundary-Layer Transition on Turbine Airfoil Profile Losses”, ASME Paper No. IMECE 2003-41420.
- ¹¹ Walters, D.K., and Leylek, J.H., “Computational Fluid Dynamics Study of Wake-Induced Transition on a Compressor-Like Flat Plate”, Journal of Turbomachinery, Vol. 127, January 2005, pp 52–63.
- ¹² Sanders, D.D., O’Brien, W.F., Sondergaard, R., Polanka, M.D., and Rabe, D.C., “Predicting Separation and Transitional Flow in Turbine Blades at Low Reynolds Numbers”, ASME Paper No. GT-2008-50283.
- ¹³ Sanders, D.D., O’Brien, W.F., Sondergaard, R., Polanka, M.D., and Rabe, D.C., “A Mixing Plane Model Investigation of Separation and Transitional Flow at Low Reynolds Numbers in a Multistage Low Pressure Turbine”, AIAA Paper No. 2009-1467.
- ¹⁴ Wilcox, D.C., “*Turbulence Modeling for CFD*”, 3rd Edition, DCW Industries, Inc., 2005.

APPENDIX D

GT2008-50283

PREDICTING SEPARATION AND TRANSITIONAL FLOW IN TURBINE BLADES AT LOW REYNOLDS NUMBERS

Darius D. Sanders

Graduate Student
Department of Mechanical Engineering
Virginia Tech
Blacksburg, VA 24061, USA

Walter F. O'Brien

J. Bernard Jones Professor
Department of Mechanical Engineering
Virginia Tech
Blacksburg, VA 24061, USA

Rolf Sondergaard

Marc D. Polanka

Air Force Research Lab, Propulsion Directorate
Wright Patterson AFB, Dayton, OH, USA

Douglas C. Rabe

ABSTRACT

There is increasing interest in design methods and performance prediction for aircraft engine turbines operating at low Reynolds numbers. In this regime, boundary layer separation may be more likely to occur in the turbine flow passages. For accurate CFD predictions of the flow, correct modeling of laminar-turbulent boundary layer transition is essential to capture the details of the flow. To investigate possible improvements in model fidelity, CFD models were created for the flow over two low pressure turbine blade designs. A new three-equation eddy-viscosity type turbulent transitional flow model originally developed by Walters and Leylek was employed for the current RANS CFD calculations. Previous studies demonstrated the ability of this model to accurately predict separation and boundary layer transition characteristics of low Reynolds number flows. The present research tested the capability of CFD with the Walters and Leylek turbulent transitional flow model to predict the boundary layer behavior and performance of two different turbine cascade configurations. Flows over the Pack-B turbine blade airfoil and the midspan section of a typical low pressure turbine (TLPT) blade were simulated over a Reynolds number range of 15,000-100,000, and predictions were compared to experimental cascade results. The turbulent transitional flow model sensitivity to turbulent flow parameters was investigated and showed a strong dependence on free-stream turbulence intensity with a second order effect of turbulent length scale. Focusing on the calculation of the total pressure loss coefficients to judge performance, the CFD simulation incorporating Walters and Leylek's turbulent transitional flow model produced adequate

prediction of the Reynolds number performance for the TLPT blade cascade geometry. Furthermore, the correct qualitative flow response to separated shear was observed for the Pack-B blade airfoil. Significant improvements in performance predictions were shown over predictions of conventional RANS turbulence models that cannot adequately model boundary layer transition.

INTRODUCTION

The range and endurance of aircraft cruising at high altitude is limited by multiple factors, including the operational efficiency of the low pressure turbine (LPT). As aircraft elevation is increased, the operational Reynolds number decreases due to the change in density. The low Reynolds number causes the development of transitional and laminar flow boundary layers on the suction surface of the low pressure turbine blades. Laminar boundary layers cause the flow to be susceptible to separation due to the presence of adverse pressure gradients on the suction side of the blade. Loss in efficiency due to the aerodynamic losses from boundary layer separation causes loss in engine efficiency, which reduces the aircraft range and maximum altitude. To improve designs, improved capability for prediction of low Reynolds number turbine flows is needed.

The most widely used CFD method for simulations involving three-dimensional rotating turbomachinery is the Reynolds Averaged Navier-Stokes (RANS) method using statistical turbulence models. Currently, Large-Eddy Simulation or Direct Numerical Simulation CFD methods promise improved accuracy for flow predictions, but can require impractically

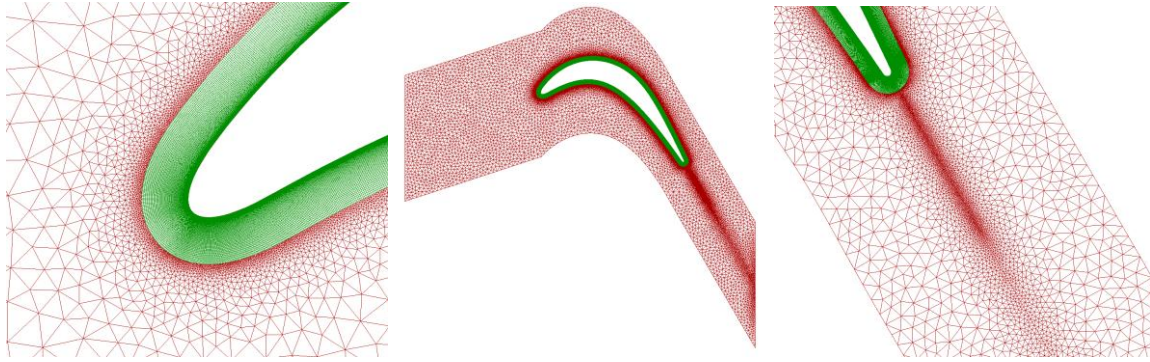


Figure 1. Hybrid O-H Grid of Pack-B Blade Airfoil

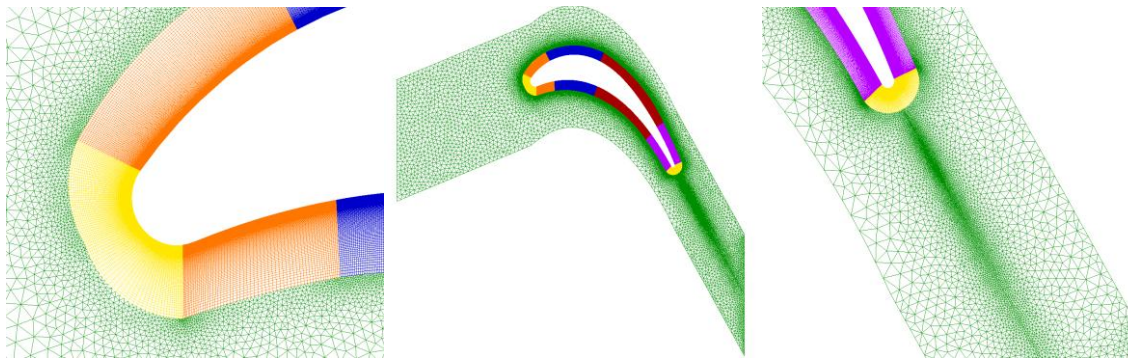


Figure 2. Hybrid O-H Grid of TLPT Blade Airfoil

long simulation times for these types of flows especially for multiple stage configurations as eventually planned as part of the current program. For RANS CFD solvers, all flow quantities are expressed as the sum of mean and fluctuating parts where the whole range of turbulent scales is being modeled.

Successful modeling of low Reynolds number flows involving laminar to turbulent transition and separation has been limited when using conventional RANS turbulence models. Most conventional turbulence models assume fully turbulent flow with no transitional effects, and fail to predict separation with any accuracy. However, several studies have been done where conventional RANS turbulence models have been modified to include transitional flow effects and separation. Choi and Yoo[1] used the low Reynolds number form of Menter's $k-\omega$ turbulence model to study the rotor-stator interactions of a single stage axial turbine. Although the model did not predict the onset of transition or wake-induced transition properly, it did represent the general trend of the transitional flow adequately with satisfactory agreement with experimental results. Both the Baldwin-Lomax and $k-\varepsilon$ turbulence models were modified to include a natural transition model and a separation bubble correlation and flow was simulated at three inlet Reynolds numbers of 43,000, 86,000, and 172,000 for the Pack-B blade airfoil by Dorney *et al* [2]. The predicted total pressure losses using both of the modified turbulent flow models were greater than the experimental values at all three

Reynolds numbers due to the difference in the separation and reattachment locations and the size of the separation region.

The eddy viscosity expression from Menter's $k-\omega$ model was modified with an intermittency factor in a study by Suzen *et al* [3]. This intermittency factor was modeled with a transport equation while the onset of transition was defined by correlations for attached and separated flow transition. The simulations were completed using two different cascade grid topologies and compared well with three different experiments with differences in separation and reattachment locations. Another approach by Praisner *et al.* [4,5] used correlations developed from an experimental database for attached flow transition, laminar separation with turbulent attachment, and separated-flow transition. These correlations were implemented in a RANS solver using the Wilcox $k-\omega$ turbulence model. The model showed significant improvement in the predicted accuracy of the total pressure loss for both linear cascades and multi-stage LPT rigs over a conventional fully turbulent flow model. A correlation-based transitional flow model developed by Menter *et al.* [6] used transport equations for intermittency and the momentum thickness Reynolds number. The intermittency equation is used to trigger transition and is coupled with Menter's $k-\omega$ SST model used to turn on the production of turbulent kinetic energy beyond the turbulent transition region. The second transport equation is formulated in terms of the momentum thickness Reynolds number at transition onset. An empirical correlation is used to control the transition

onset criteria in the intermittency equation. This model has been applied to several 2D and 3D geometries by Langtry *et al.* [7] including the Pack-B cascade, a 3D GE low-pressure turbine vane, and the T106 blade undergoing passing wakes. All simulations agreed well with experiments for all test cases at a wide range of Reynolds numbers and freestream turbulent intensities.

Recently, a new three-equation eddy-viscosity type model has been developed by Walters and Leylek [8] for modeling transitional flow effects to improve loss prediction capability using RANS solvers. Transport equations are used to address the development of pre-transitional fluctuations in the boundary layer and the breakdown to turbulence to predict both natural and bypass transition. This model has been applied to the cases of a zero-pressure-gradient flat plate at various freestream turbulent intensities [8] and a circular cylinder at subcritical, critical, and supercritical Reynolds numbers [9] with good results. Also, the capability of the new model to predict transitional flow behavior has been demonstrated on a highly loaded turbine blade airfoil with and without film cooling [10] and a flat plate with pressure distribution similar to an axial compressor undergoing passing wakes [11]. The intent of this new model is to provide the same ease-of-use as conventional turbulence models. It is independent of integral and non-local inputs, as well as intermittency factors.

The present study examines the ability of the Walters and Leylek laminar-to-turbulent transitional flow model to predict the boundary layer behavior and performance of two different turbine cascade configurations. Parametric studies of laminar-to-turbulent transitional flow model sensitivity to inlet freestream turbulent intensity and turbulent length scale were conducted to investigate how the inlet turbulence parameters affect transition and total pressure loss. Flows over the Pack-B research airfoil and the midspan airfoil of a typical low pressure turbine blade were simulated over a Reynolds number range of 15,000-100,000. The simulation results are compared to available data from experimental studies and other fully turbulent flow models to determine if total pressure loss prediction is improved. The ultimate intent is to use the Walters and Leylek model to predict low Reynolds number effects in three-dimensional geometries involving multiple turbine stages with rotation. This study provides the initial step to baseline a methodology that properly captures separation and transition characteristics for the future needs.

CFD NUMERICAL METHODS

Gridding Technique

The two-dimensional grid of the cross sections of the Pack-B blade airfoil and the TLPT blade airfoil was based on an experimental cascade configuration. The inlet and outlet of the computational domain was placed one axial chord length upstream and one axial chord downstream of the blade leading and trailing edge, respectively. The axial chord length for both blade airfoils was 17.78cm. The mid-passage flow around the blade airfoil was modeled with the passage length equal to the

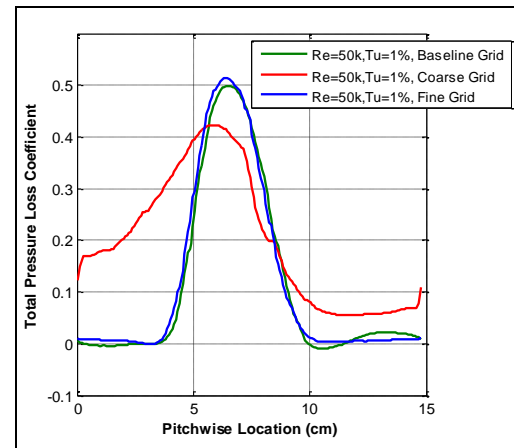


Figure 3. Comparison of the Total Pressure Loss Coefficient for the TLPT Blade Airfoil at Different Grids

blade pitch. Periodic boundaries were applied to model an infinite cascade. The axial solidity for the TLPT blade airfoil was 1.20 and 1.13 for the Pack-B blade.

The computational meshes used consisted of a hybrid O-H grid topology created with Gridgen® 15 mesh generation software (Figure 1 & 2). A structured O-grid was extruded normal to each blade surface in order to provide the resolution needed to resolve the boundary layer. The first cell wall distance was such that the y^+ was less than unity at every grid point around the blade airfoil surface satisfying the y^+ tolerance for the current transitional flow model. The O-grid dimensions were (1749×67) and (1749×110) for the Pack-B mesh and the TLPT blade mesh, respectively. The average aspect ratio for both grid topologies was 6.5:1 but was as high as 30:1 in cells close to the blade surface. An unstructured mesh was placed in the main flowpath consisting of triangles generated by a modified Delauney method. There were 33,209 cells and 44,091 cells in the main flowpath for the Pack-B blade airfoil and the TLPT blade airfoil, respectively. Triangular cell clustering was increased to provide enough resolution for the wake region generated by the trailing edge.

A grid independence study was completed on the TLPT blade mesh to determine if the current meshing scheme provides enough spatial resolution to capture the features of the flowfield within the computational domain. Two grid topologies were created by increasing and decreasing the number of nodes on the blade surface and in the main flowfield by 50% while maintaining the same hybrid O-H grid topology. The coarse and fine grids contained 94,846 and 451,866 cells, respectively while the baseline grid contained 238,230 cells. All three grid topologies were simulated at inlet Reynolds number of 50,000 at an inlet freestream turbulent intensity of 1% and average turbulent length scale of 5 mm using a 2nd order spatial accurate steady flow pressure-based solver in Fluent 6.3®. The y^+ was less than unity around the blade surface and the turbulent transition point was the same for all three grid topologies. The wake total pressure loss coefficient in Figure 3 shows the effect

of the wake distribution at the different grid spatial resolutions. The results from the coarse grid showed a distorted total pressure loss coefficient due to the low cell count in the wake region while the baseline and fine grid indicated a similar total pressure loss coefficient distribution. This indicated that the baseline grid provided enough spatial resolution to capture the effects of the flowfield in the boundary layer and within the wake.

CFD Numerical Scheme

CFD simulations were performed using ANSYS Fluent 6.3[®] which is based on a finite volume method. The domain was discretized onto a finite set of control volumes and the general conservation equations mass, and momentum were solved on this set of control volumes. The partial differential equations based on the RANS equations shown in Eq.(1) and Eq. (2) were discretized algebraically and solved for the mapping of the flowfield.

$$\frac{\partial \rho}{\partial t} + \frac{\partial}{\partial x_i}(\rho u_i) = 0 \quad (1)$$

$$\begin{aligned} \frac{\partial}{\partial t}(\rho u_i) + \frac{\partial}{\partial x_j}(\rho u_i u_j) = -\frac{\partial p}{\partial x_i} + \\ \frac{\partial}{\partial x_j} \left[\mu \left(\frac{\partial u_i}{\partial x_j} + \frac{\partial u_j}{\partial x_i} - \frac{2}{3} \delta_{ij} \frac{\partial u_k}{\partial x_k} \right) \right] + \frac{\partial}{\partial x_j} (-\rho \overline{u'_i u'_j}) \end{aligned} \quad (2)$$

All solution variables represent ensemble or time averaged values. The Reynolds stress term $-\rho \overline{u'_i u'_j}$ is resolved according to the chosen turbulence model in order to close the equation. The RANS equations were discretized using the pressure-based coupled algorithm which solved a coupled system of equations comprising the momentum equations and the pressure-based continuity equation. The convergence rate significantly improved when compared to the pressure-based segregated algorithm. The two-dimensional double-precision parallel version of Fluent 6.3[®] was run on a HP XC Oteron high performance super-computer. A total of 8-10 processors were used for the steady simulations and 16-24 processors for transient simulations.

Steady flow solutions were initialized based on the inlet boundary conditions and iteratively run with a first-order upwind scheme until the residual tolerance for continuity, linear momentum, and turbulence variables were below 10^{-4} . Then the second-order upwind discretization scheme was used until the minimum convergence tolerance for all flow parameters was below 10^{-5} . Also, the drag and lift coefficients were monitored to determine if the steady state solution was adequately converged. Unsteady flow cases were initialized with the first-order discretization steady flow solutions and run using a second-order upwind spatial discretization with a second-order implicit temporal solver. Time steps were chosen in order to obtain enough temporal resolution to allow the solution to converge locally within 20-30 iterations per time step.

Transitional Flow Model Description

The model is a three-equation eddy-viscosity type, with transport equations for the turbulent kinetic energy (k_T), laminar kinetic energy (k_L), and the specific dissipation rate (ω) which are given in Eqs. (3)-(5).

$$\frac{Dk_T}{Dt} = P_{k_T} + R + R_{NAT} - \omega k_T - D_T + \frac{\partial}{\partial x_j} \left[\left(\nu + \frac{\alpha_T}{\sigma_k} \right) \frac{\partial k_T}{\partial x_j} \right] \quad (3)$$

$$\frac{Dk_L}{Dt} = P_{k_L} - R - R_{NAT} - D_L + \frac{\partial}{\partial x_j} \left[\nu \frac{\partial k_L}{\partial x_j} \right] \quad (4)$$

$$\begin{aligned} \frac{D\omega}{Dt} = P_\omega + C_{\omega R} \frac{\omega}{k_T} (R + R_{NAT}) - C_{\omega 2} \omega^2 - \\ C_{\omega 3} f_\omega \alpha_T \left(\frac{\lambda_{eff}}{\lambda_T} \right)^{4/3} \frac{\sqrt{k_T}}{d^3} + \frac{\partial}{\partial x_j} \left[\left(\nu + \frac{\alpha_T}{\sigma_\omega} \right) \frac{\partial \omega}{\partial x_j} \right] \end{aligned} \quad (5)$$

The influence of the laminar and turbulent kinetic energy on the Reynolds stress term was included through the prescription of the total eddy viscosity as given in Eq. (6). A brief summary of the current transitional flow model functionality is presented below.

$$-\overline{u'_i u'_j} = \nu_{TOT} \left(\frac{\partial u_i}{\partial x_j} + \frac{\partial u_j}{\partial x_i} \right) - \frac{2}{3} k_{TOT} \delta_{ij} \quad (6)$$

The laminar kinetic energy was used to describe the low frequency high amplitude fluctuations that originate from the pre-transitional boundary layer. These fluctuations primarily occur at one scale and almost all energy was contained in a single streamwise component. The production of laminar kinetic energy was assumed to occur due to a “splat mechanism”. This “splat mechanism” redirected the normal fluctuations of the freestream turbulence into a streamwise component while creating local pressure gradients in the boundary layer, increasing the low frequency fluctuations. These fluctuations grow to the development of turbulent spots and then to full turbulence. A local transition parameter that depended on the turbulent energy, effective length scale, and fluid viscosity determined when this occurred. Once this parameter reached a threshold value, a transfer of energy began from streamwise fluctuations (k_L) to turbulent fluctuations (k_T).

Both natural, mixed, and bypass transition were resolved in the current model. Natural transition occurred when orderly laminar flow broke down to turbulent flow in presence of small perturbations. This process was very slow and was observed when no external forcing was applied and when very small perturbations were present. Bypass transition evolved when those perturbations were large enough to bypass the exponential growth of Tollmien-Schlichting (TS) waves. The mixed transition regime involved elements of both natural and bypass transition. The production terms in the current model controlled the transfer from streamwise fluctuations to full turbulence which depends on the laminar kinetic energy and the local mean velocity in order to include natural and mixed transition. A full

description of all model variables and dependences are presented by Walters and Leylek [14].

Boundary Conditions

CFD boundary conditions mirrored experimental cascade test conditions as described in the next section. The inlet boundary condition for the steady flow cases was specified as a total pressure inlet where static pressure was set according to an experimentally determined value of 98870 Pa. The inlet total pressure reflected the chosen Reynolds number based on the axial chord. Unsteady cases used a mass flow inlet boundary condition permitting the total pressure to be calculated from the interior solution which aided the local convergence per time step. The mass flow was calculated based on the normal component of the velocity and inlet domain length (kg/sec·m). Simulations were run for a Reynolds number range of 10,000-100,000. The axial and tangential component of the flow direction was given based on the design inlet flow angle for each blade. The inlet angle for the Pack-B blade and the TLPT blade airfoil was 35° and 30.94°, respectively. The experimental cascade blade airfoil geometries were scaled-up causing the inlet Mach number to be less than 0.03 for a given inlet Reynolds number. The flow was assumed to be incompressible in the CFD simulations because of this low Mach number. The inlet turbulent intensity and turbulent length scale were chosen based on user specification or experimental values, when available. The inlet laminar kinetic energy was set to $10^{-6} \text{ m}^2/\text{sec}^2$ in accordance with specifications of the turbulence model. No-slip conditions were assigned to the blade surface and turbulence parameters used a zero-flux boundary condition. The initial static pressure boundary condition at the outlet was estimated using conservation of mass of the axial velocity and ideal outlet flow angle and the assumption that no total pressure loss occurred between the inlet and outlet planes following Eqs. (7) and (8).

$$u_{out} = u_{in} \left[\frac{\cos(\alpha_{in})}{\cos(\alpha_{out})} \right] \quad (7)$$

$$P_{out} = P_0 - \frac{1}{2} u_{out}^2 \quad (8)$$

This calculation of the outlet static pressure provides an initial guess for the pressure-based solver and was adjusted during the calculation. The target mass flow rate option was implemented at the pressure outlet for the steady flow solutions in order to adjust the pressure at the outlet to meet the mass flow rate. The target mass flow rate option was not used for the unsteady cases because the mass flow was set in the inlet boundary condition.

EXPERIMENTAL CONFIGURATION

The experimental work used for comparisons with the CFD results was conducted at the Air Force Research Laboratory (AFRL) low speed linear cascade tunnel at Wright Patterson Air Force Base (WPAFB) [2,12-17]. The wind tunnel was a

modified Aerolab Corporation drawdown tunnel capable of operating air speeds from 3 m/sec to 20 m/sec. The inlet bell-mouth was 305 cm wide and 267 cm tall. A honeycomb flow

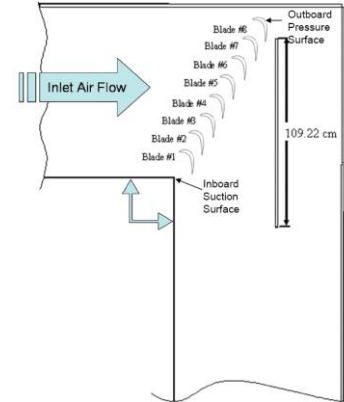


Figure 4. Air Force Research Lab Low Speed Cascade Wind Tunnel View of Test Section [14]

straightener led to a convergent nozzle reducing the flow area by 87%. Stryofoam inserts were placed in the flow straightener to help minimize corner vortices and provide freestream turbulent intensity less than 1%. A passive turbulence grid can be installed yielding freestream turbulence levels up to 4%. Turbulent length scales with these grids have been characterized by both Lake [12] and McQuilling [13].

The test section of the cascade wind tunnel (Figure 4) had a central hinge pivot joint that allowed the inlet and outlet flow angles to be set for the referenced tests involving both the Pack-B blade airfoil and the TLPT blade airfoil studied in this research. Eight blade airfoils with an outboard pressure surface blade were bolted to steel runners and placed in the test section. The blade span was 78.63 cm to further enhance the two-dimensional flow over the midspan region of the blade. The cascade test section exhibited good uniformity and periodicity as confirmed by Lake [12].

Flow measurements from several different experimental studies were used for comparison with the CFD results. All experimental measurements were done on blade #5 to reduce end-wall effects from the cascade. For the TLPT blade airfoil, experiments were performed by Garmoe [14] at an inlet Reynolds numbers of 15,000 to 100,000. Measurements of the inlet total and static pressure were made one axial chord length upstream of the blade airfoil leading edge using a pitot-static probe mounted on a pitchwise traverse. This measurement was used to confirm the inlet Reynolds number. Also, measurements of the outlet total pressure were made one axial chord downstream of the blade trailing edge using a Kiel probe suspended on a pitchwise traverse. These traverses were placed in the same locations for both the TLPT and Pack-B blade airfoil cascade configurations. These measurements were used to calculate the total pressure loss coefficient. The local total pressure was calculated using Eq. (9) by taking the time-averaged difference between the inlet and outlet total pressure

and dividing by the difference between the time-averaged inlet total and static pressure.

$$TPLC = \frac{(P_{0,inlet} - P_{0,outlet})}{(P_{0,inlet} - P_{inlet})} \quad (9)$$

Performance of the blade airfoil was evaluated based on the total pressure loss coefficient, which is an indirect measurement of the entropy generation. As entropy is generated the total pressure at the outlet decreases due to the blade airfoil trailing edge wake and the loss coefficient increases leading to lower stage efficiency. Inlet and outlet turbulent intensity measurements were made at the same locations using a single element hot film.

The Pack-B blade airfoil flow was selected for primary comparisons to the CFD simulation because of the many experimental studies that have been documented. Total pressure loss coefficient calculations based on experimental measurements of Casey [15] and Garmoe [14] were used for comparison with the CFD results. Boundary layer velocity measurements from the Particle Image Velocimetry (PIV) experiments of Woods et al. [16] were used for comparisons. These measurements were extracted normal to the blade surface at 67.2%, 73%, 79.3%, 84.8%, 89.8%, and 95% axial chord locations. Bons et al. [17] measured the blade pressure coefficient using forty static pressure taps around the Pack-B blade suction and pressure surface. The static pressure coefficient is calculated using Eq. (10).

$$C_p = \frac{(P_{0,i} - P_s)}{q_i} \quad (10)$$

$\overline{P_{0,i}}$ is the average inlet total pressure, $\overline{q_i}$ is the average inlet dynamic pressure, and P_s is the static pressure on the surface of the blade. All measurements were taken at inlet Reynolds numbers of 25,000, 50,000, and 100,000. Flow property predictions for both blade airfoil CFD configurations were extracted from the simulations using a mathematical 200 point rake located one axial chord length upstream and downstream of the blade leading and trailing edges, respectively.

TLPT BLADE RESULTS

Comparisons with Other Turbulence Models

The flow over the TLPT blade airfoil was simulated at an inlet Reynolds number of 100,000 using three turbulence models; the Realizable $k-\varepsilon$ [18] model with enhanced wall treatment, Menter's $k-\alpha(SST)$ turbulence model [19] using a low Reynolds number correction to the turbulent viscosity, and with the Walters and Leylek [8] $k_T-k_L-\omega$ transitional flow model. The simulations were run using the steady flow solver in Fluent® 6.3. The inlet turbulent intensity was set to 1% with an inlet turbulent length scale of 10.4 mm. The transition to turbulence, the boundary layer integral parameters, and the wake total pressure loss coefficient were compared for all three turbulence models. Figure 5 shows the turbulent kinetic energy around the

blade surface for the three RANS models. A sudden increase in the magnitude of the turbulent kinetic energy was used as an indicator of the turbulent transition point. On the pressure side of the blade, the flow remains largely laminar until the 70% axial chord position for all three turbulence models. The shape

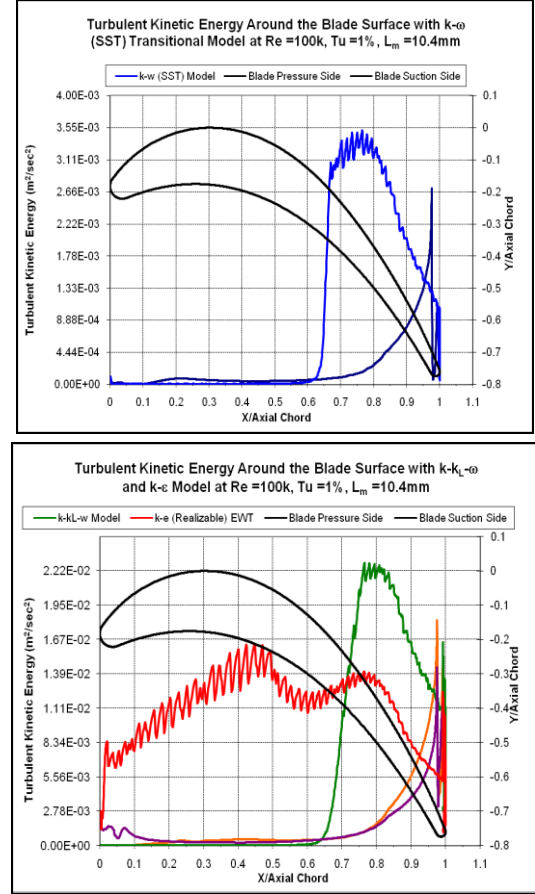


Figure 5. Comparison of Transition Location at Re=100,000, Tu=1% for the TLPT Blade Airfoil

of the plots is also similar for each case, but there is a noticeable magnitude difference between the $k_T-k_L-\omega$ and $k-\alpha(SST)$ model which is due to the formulation of the turbulent kinetic energy and specific dissipation rate for each model.

The difference in the transition behavior for the three turbulence models is seen on the suction side. The $k-\alpha(SST)$ and the $k_T-k_L-\omega$ model both produced transition at 65% axial chord. The $k-\alpha(SST)$ model generated much less turbulent kinetic energy after the transition point on both the pressure and the suction side of the blade when compared to the $k_T-k_L-\omega$ model. It was discovered that the specific dissipation rate around the blade surface was higher for the $k-\alpha(SST)$ model than the $k_T-k_L-\omega$ model. So, the turbulent kinetic energy that was being generated in the boundary layer was being converted into viscous losses at a much higher rate than with the $k_T-k_L-\omega$ model. In contrast, the $k-\varepsilon$ model became turbulent from the leading edge and exhibited no transition behavior. This demonstrates the inherent limitation of conventional RANS

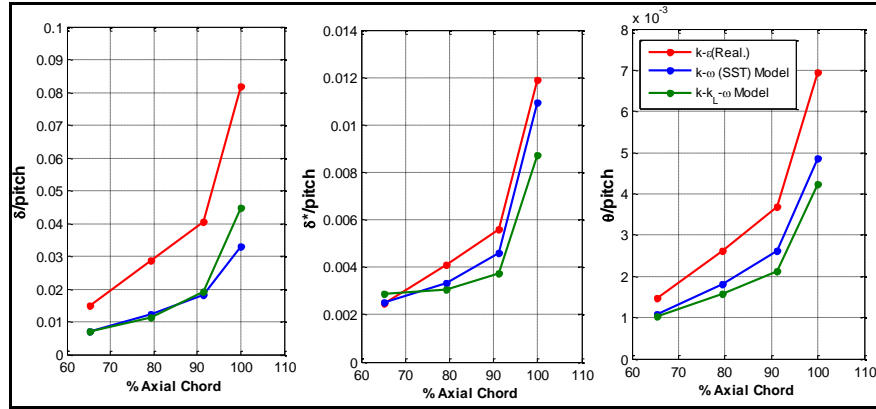


Figure 6. Comparison of the Boundary Layer Integral Parameters of all Three Turbulence Model at Re=100,000 for the TLPT Blade

turbulence models in the inability to model transitional flow effects.

Boundary layer integral parameters were calculated from the velocity profiles at four axial chord locations of 65.3%, 79.4%, 91.3%, and 100% normal to the TLPT blade surface. Figure 6 compares the predicted boundary layer thickness, displacement thickness, and momentum thickness for all three turbulence models. The $k-\varepsilon$ model result has the largest boundary layer thickness because the boundary layer was fully turbulent from the leading edge. This resulted in a faster growth of the boundary layer thickness than for boundary layers undergoing transition as with the $k-\alpha(SST)$ and $k_T-k_L-\omega$ model. The momentum thickness plot showed that $k-\varepsilon$ model yielded a higher momentum loss than both the $k-\alpha(SST)$ and $k_T-k_L-\omega$ models, indicating a more turbulent boundary layer. The boundary layer thickness for the $k-\alpha(SST)$ and $k_T-k_L-\omega$ models were in good agreement with each other until the 100% axial chord location, where the boundary layer for $k_T-k_L-\omega$ model grew at a higher rate after transitioning to turbulence. The $k-\alpha(SST)$ model exhibited a higher displacement and momentum thickness which indicated a larger mass deficit in the boundary layer with a slightly higher momentum loss as compared to the $k_T-k_L-\omega$ model. This was attributed to the high amount of specific dissipation produced in the boundary layer from the $k-\alpha(SST)$ model. Even though the flow was transitional, the high specific dissipation rate produced more viscous losses in the boundary layer which resulted in larger mass deficit and momentum loss than the $k_T-k_L-\omega$ model.

The total pressure loss coefficient plot shown in Figure 7 indicated that $k-\varepsilon$ model produced the highest amount of total pressure loss because the flow was predicted as fully turbulent. The high momentum loss observed in the boundary layer created a larger total pressure loss in the wake region, which was over-predicted compared to the experimental results [14]. The most interesting result was for the case using the $k-\alpha(SST)$ model. The total pressure loss was as high as the fully turbulent $k-\varepsilon$ model even though the boundary layer was transitional and momentum loss was slightly higher in the boundary layer than

with the $k_T-k_L-\omega$ model. This again can be attributed to the specific dissipation present in the wake for the $k-\alpha(SST)$ model which was observed as about 20 times larger than the $k_T-k_L-\omega$ model. The total pressure loss prediction made with the $k_T-k_L-\omega$ model achieved excellent agreement experimental results [14]. The $k_T-k_L-\omega$ transitional flow model demonstrated the ability to better predict transitional behavior associated with low Reynolds number flows than conventional RANS turbulence models.

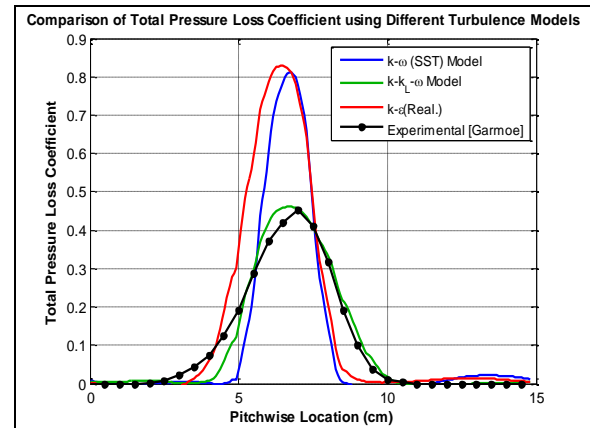


Figure 7. Comparison of Total Pressure Loss Coefficient for Turbulence Models at Re=100,000, Tu =1% for the TLPT Blade
Effect of Inlet Turbulence Parameters on Transition and Performance Prediction

Experimental data for the inlet turbulent length scale was unavailable for the TLPT blade airfoil, so an estimation of the inlet turbulent length scale range was needed for the boundary condition specification. The sensitivity of the transitional $k_T-k_L-\omega$ transitional flow model to the inlet turbulent length scales was investigated in order to determine the accuracy tolerance of the inlet turbulent length scale. The turbulent length scale specification in Fluent 6.3[®] was used to describe the average size of the energy-containing eddies. The transition to turbulence on the suction side of the blade and the wake total pressure loss coefficient was used to study this effect. The inlet

Table 1. Summary of Inlet Turbulence Parameters on Transition Location and Maximum TPLC for the TLPT Blade

Re = 50,000, Tu = 1%			Re = 50,000, $l_m = 5mm$		
l_m (mm)	X_{trans}/C_x	Max. TPLC	Tu (%)	X_{trans}/C_x	Max. TPLC
2	0.831	0.471	0.724	0.879	0.455
3.5	0.761	0.495	0.75	0.862	0.457
4	0.753	0.498	1	0.747	0.499
5	0.747	0.499	1.5	0.615	0.546
6	0.749	0.497			
8	0.765	0.488	Experimental		
20	0.975	0.464	0.724		0.5765
l_m (mm)	St	Max. TPLC	Tu (%)	St	Max. TPLC
30	0.0148	1.040	0.5	0.0139	0.718
40	0.0150	1.000			
50	0.0148	1.015			

Reynolds number for these steady flow simulations was set to 50,000 with a 1% inlet turbulent intensity. The turbulent length scale was varied over a range of 2 – 50 mm. The results are shown in Table 1 and Figure 8. This range of inlet turbulent length scales is typical of what was later measured by McQuilling [13] in the AFRL low speed linear cascade tunnel after this turbulent length scale CFD study was performed. Over a range of $l_m = 3.5 - 8mm$, Table 1 shows that the location of the transition region does not vary significantly. For the $l_m = 2mm$ case, the transition region moved further downstream to the 83% axial chord position, indicating that as the length scale becomes very small the transition region will move downstream. This is consistent with the fact that the magnitude of the disturbance that couples with the boundary layer will be reduced as the turbulent length scale decreases. The transition location was also found further downstream at the 95% axial chord location for the $l_m = 20mm$ case. At a turbulent length scale of $l_m = 30mm$ and above, the flow within the boundary layer becomes laminar and separates. The turbulent scale has grown large enough that the freestream eddies no longer couples to the boundary layer through the turbulence model, hence the boundary layer does not transition to turbulence. Thus for the TLPT blade airfoil there was a range of length scales in which the flow will transition from laminar to turbulent, but above or below which the boundary layer remains largely or completely laminar.

The maximum value of the wake total pressure loss coefficient shown in Figure 8 also shows no significant variation for the $l_m = 3.5 - 8mm$ range. The lowest value of the maximum total pressure loss coefficient is calculated for the $l_m = 2mm$ and $20mm$ cases due to the transition region being located far downstream in comparison to the other cases. This results in a lower momentum loss in the boundary layer. The total pressure loss is increased and remains constant at turbulent length scales above 30 mm because the separation within the laminar flow boundary layer causes vortex shedding within the wake region. The turbulent length scale must be within a range of $l_m = 2 - 20mm$ in order to couple with the boundary layer and affect turbulent transition.

Sensitivity of the inlet turbulent intensity level on turbulent transition location and the total pressure loss coefficient was

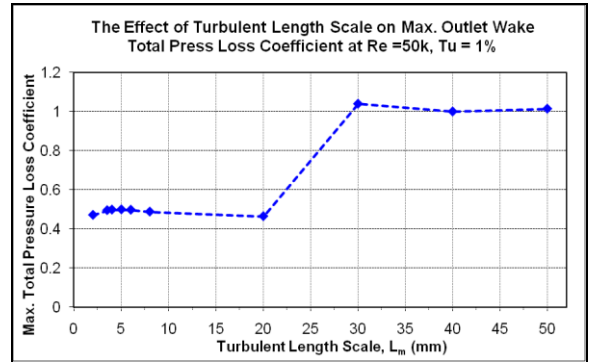


Figure 8. Maximum Wake Total Pressure Loss Coefficient Verses Inlet Turbulent Length Scale at for the TLPT Blade

investigated. Steady flow simulations at $Re = 50,000$ for the TLPT blade airfoil were also completed at inlet turbulent intensities of 0.75%, 1%, and 1.5%. Unsteady flow simulations were completed at inlet turbulent intensities of 0.5% and the experimentally [14] measured inlet turbulent intensity of 0.724%. All these cases used a constant turbulent length scale of 5mm. Figure 9 shows the effect of varying the inlet turbulent intensity on transition. The location of turbulent transition on the suction side moves downstream as inlet freestream turbulent intensity was decreased, while the transition on the pressure side remained unchanged. The low-frequency high amplitude fluctuations in the pre-transitional boundary layer took longer to develop because the freestream turbulence was reduced, causing transition on the suction surface to be further delayed. In the 0.5% inlet turbulent intensity case, the boundary layer did not transition along the blade surface and flow remained laminar. The presence of laminar flow caused vortex shedding at a frequency of 325Hz and explained the origin of the increase in the turbulent kinetic energy at the trailing edge. A Strouhal number of 0.0139 was calculated based on the observed vortex shedding frequency, freestream velocity, and momentum thickness at separation with Eq. (11).

$$St = \frac{f_{shed} \theta_{sep}}{U_{\infty}} \quad (11)$$

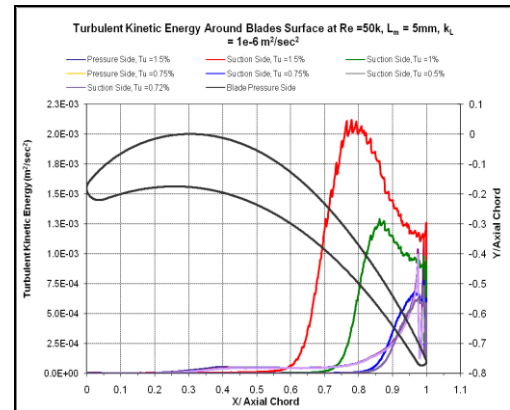


Figure 9. Turbulent Kinetic Energy around the Blade at Different Inlet Turbulent Intensities for the TLPT Blade

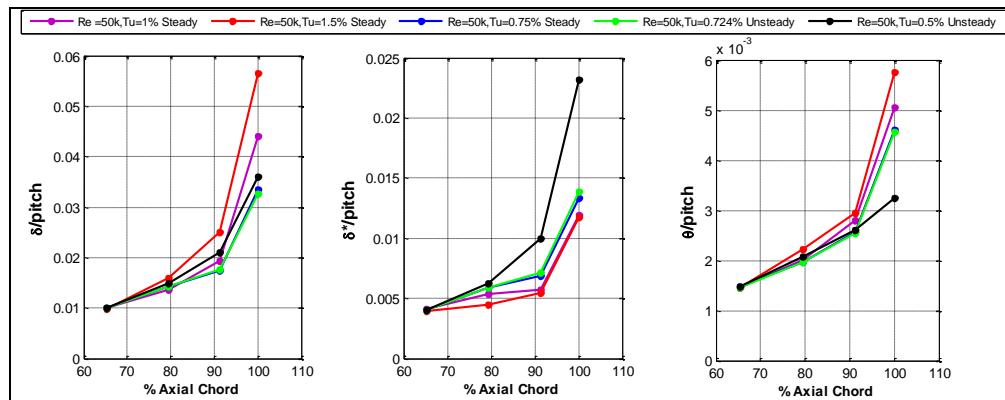


Figure 10. Comparison of Boundary Layer Integral Parameters at Different Inlet Freestream Turbulent Intensities at Re =50,000 for the TLPT Blade Airfoil

Boundary layer velocity profiles were then obtained at four axial locations of 65.3%, 79.4%, 91.3%, and 100% normal to the TLPT blade surface. The profiles (not shown) revealed the flow remains attached for all four measured locations except for the 0.5% inlet turbulent intensity case. The flow separated at the 100% axial chord location due to the initial creation of vortices from the shear layer on suction side. The boundary layer thickness, displacement, and momentum thickness shown in Figure 11 were calculated from the velocity profiles. The largest boundary layer thickness was found in the $Tu = 1.5\%$ case because the boundary layer transitioned to turbulence farthest upstream of all the cases and underwent more of the exponential growth associated with turbulent boundary layers. It also contained the highest momentum thickness because of the larger amount of turbulence present in the mean flow. At the 65.3% axial chord location, the boundary layer thickness was approximately the same for all cases. The smallest boundary thickness was found for the $Tu = 0.75\%$ and $Tu = 0.724\%$ cases, because the transition locations are more downstream than the 1% and 1.5% cases. The displacement thickness at the four axial chord locations increased as the inlet turbulent intensity decreased. The largest displacement thickness was found in the $Tu = 0.5\%$ case because the flow around the suction side of the blade was laminar and separated at the 100% axial chord location.

The behavior of the boundary layer at the various inlet turbulent intensities was reflected in the calculation of the total pressure loss coefficient. In Table 1, the total pressure loss coefficient at the several freestream inlet turbulent intensities simulated are compared to the $Tu = 0.724\%$ experimental result and show the best agreement with the $Tu = 1.5\%$ case. The $Tu = 0.5\%$ and $Tu = 1.5\%$ cases show that large values of the total pressure losses can be produced by two different types of flow behaviors. High values of turbulent intensity cause turbulent transition further upstream of the blade resulting in higher momentum loss in the boundary layer. This high momentum flow leads to a higher total pressure loss. In contrast, at low turbulent intensity the flow remains laminar and separates, causing a von Kármán vortex street. The vortices shed from the trailing edge increases the total pressure loss in the wake. The

$Tu = 0.724\%$ CFD result predicted the flow to transition furthest downstream of all the cases. The total pressure loss coefficient was under-predicted because the momentum loss within the boundary layer was the lowest of all the cases where the flow transitioned. Experimental total pressure loss indicated that the flow was more laminar than predicted with the CFD. So if the inlet turbulent intensity was set in the CFD result between 0.5% and 0.724% such that the flow did not transition but remained laminar, better agreement might be achieved with the experimental results.

Table 1 summarizes the results of the predicted turbulent transition point and maximum value of the total pressure loss coefficient as inlet turbulent length scale and turbulent intensity was varied. The $k_T-k_L-\omega$ transitional flow model does show that the inlet turbulent intensity has a first order effect on transition and prediction of the total pressure loss coefficient. Clearly, setting the correct inlet turbulent intensity was crucial to being able to predict performance at low Reynolds numbers when using current transitional flow model. The CFD simulation demonstrated that high total pressure loss can originate from high freestream turbulence or laminar flow with the presence of vortex shedding. The inlet turbulent length scale had a second order effect on transition and total pressure loss coefficient and needs to be in the correct range in order to penetrate the boundary layer to affect transition and allow for successful performance prediction.

Performance Prediction at Different Inlet Reynolds Numbers

The TLPT blade airfoil flow was simulated at individual Reynolds numbers of 100,000, 75,000, 50,000, 40,000, and 15,000 to determine if the $k_T-k_L-\omega$ transitional flow model could adequately predict the varying Reynolds number performance. Also, sensitivity to changing inlet Reynolds numbers was evaluated. The inlet freestream turbulent intensity for the CFD simulations was set to the average inlet turbulent intensities measured in the experimental [14] results with the turbulent length scale, $l_m = 5mm$. The steady and time-mean velocity contour plots at each inlet Reynolds number are shown in Figure 11. The flow around the TLPT blade airfoil behaved similarly at Reynolds number from 100,000 to 50,000. When

the Reynolds number decreased below 50,000, the flow around the suction side of the blade became laminar and began to separate causing a von Kàrmàn vortex street in the wake region of the blade. At the inlet Reynolds number of 15,000, the steady

flow simulation (Figure 11e) predicted a very large separation region beginning at the 70% axial chord on the suction side of the blade.

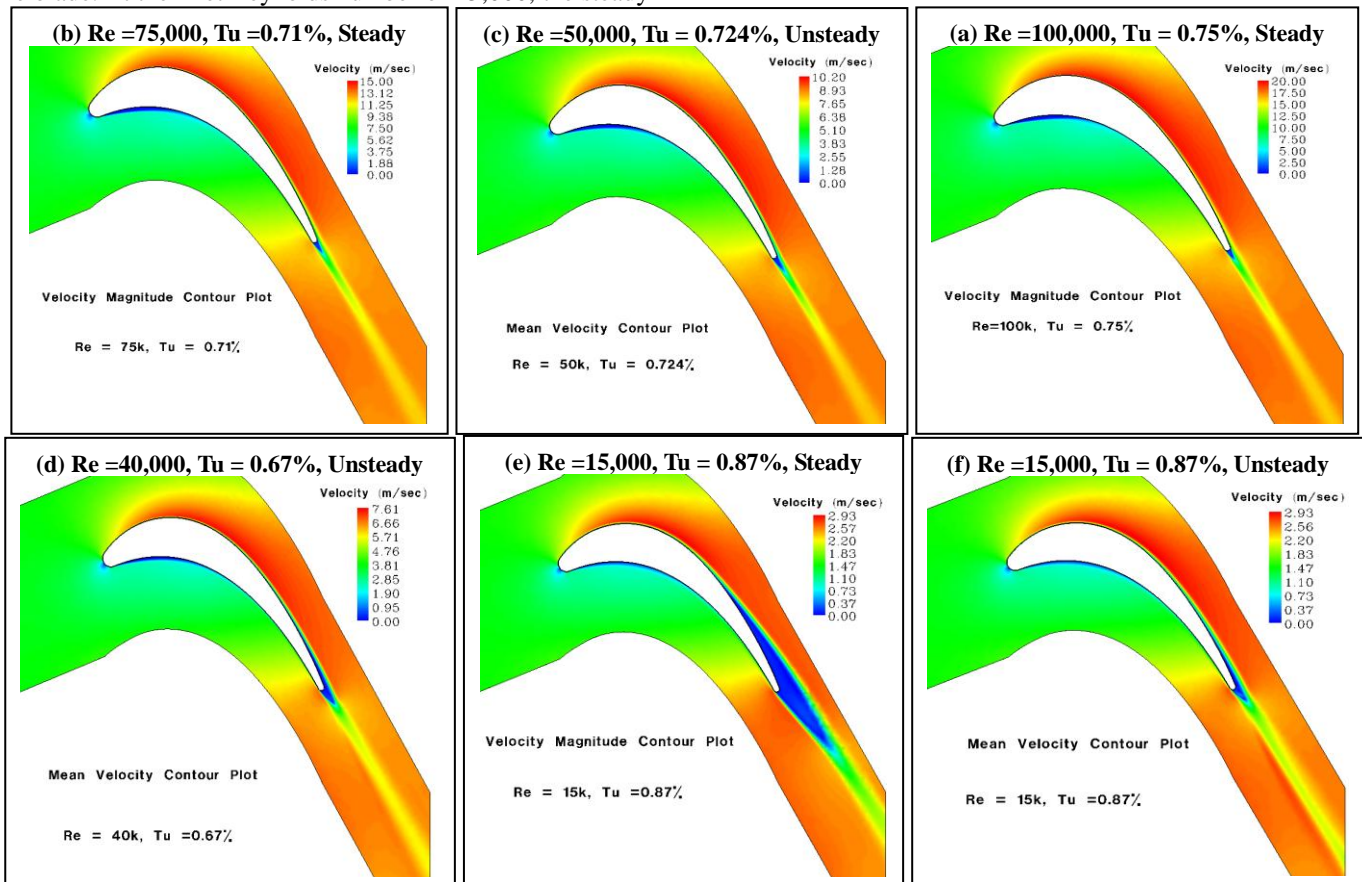


Figure 11(a)-(f). Velocity Magnitude Contour Plots of TLPT Blade Airfoil Simulated at a Range of Inlet Reynolds Numbers

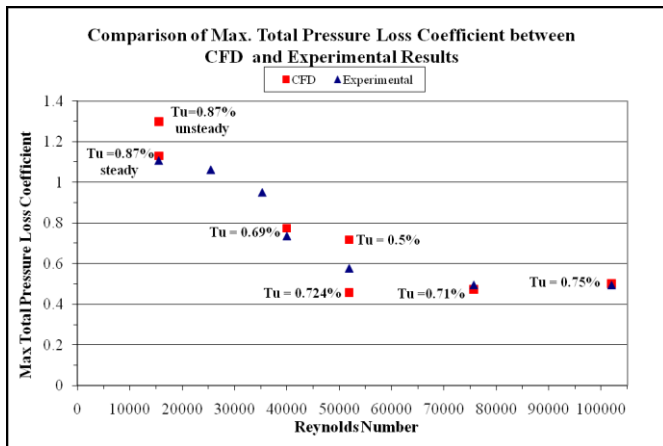


Figure 12. Comparison of the CFD and Experimental [14] Maximum Total Pressure Loss Coefficient at a Range of Inlet Reynolds Numbers for the TLPT Blade Airfoil

However, the unsteady simulation (Figure 11f) predicts a separation beginning at approximately 90% axial chord with the presence of von Kàrmàn vortex shedding at a frequency of 75Hz in the wake region corresponding to a $St = 0.0220$ based

on Eq. (11). The presence of the vortex shedding caused the boundary layer to remain attached an additional 20% further than for the steady flow solution. The separation region was reduced due to the generation of vortices from the trailing edge of the blade.

The maximum value of the wake total pressure loss coefficient is plotted in Figure 12 versus the inlet Reynolds number for both the experimental and the CFD results to show the Reynolds number performance of the TLPT blade airfoil. The maximum value of the total pressure loss coefficient was used instead of the integrated value because the integrated total pressure loss coefficient was affected by the width of the wake region. The width of the wake region was always larger than the experimental value in the CFD simulation due to the higher numerical dissipation inherent in the specific dissipation transport equation. The maximum total pressure loss coefficient was used in order to improve comparisons of the total pressure loss coefficient with experimental results. The CFD results show excellent agreement with the experimental results [14] at inlet Reynolds numbers of 100,000, 75,000, and 40,000. Discrepancies existed between the experimental and CFD

predictions at 50,000 and 15,000. As explained in the previous section with the $Re = 50,000$, $Tu = 0.724\%$ case, the CFD results predicted that the flow does not transition until 85% axial chord, causing the total pressure loss coefficient to be predicted lower than the experimental result [14]. At a Reynolds number of 15,000, the steady flow simulation showed the best agreement with the experimental result [14] even though a large amount of separation was predicted on the suction side. The unsteady case resulted in 20% over-prediction of the total pressure loss coefficient due to the presence of vortex shedding, causing an increased amount of turbulence in the wake. Overall, the CFD simulations using the $k_T-k_L-\omega$ model demonstrated the ability of the model to adequately predict the inlet Reynolds number performance trend of the TLPT blade airfoil. Based on the prediction of performance results, the $k_T-k_L-\omega$ model shows the potential to provide improved prediction of transitional flow on a separated airfoil. This yields confidence in its capability of providing the same type of results for full three-dimensional multistage turbine airfoils.

PACK-B BLADE AIRFOIL RESULTS

Surface Static Pressure Coefficient

The Pack-B blade airfoil flow was simulated at an inlet Reynolds number of 25,000, 50,000, and 100,000. The

unsteady simulations were run with an inlet freestream turbulent intensity of 0.6% and an inlet turbulent length scale of 5cm. In Figure 13, the mean static pressure coefficient distributions on the blade airfoil suction and pressure side were compared to the measurements of Bons *et al* [17] and three-dimensional LES results of Rizzetta and Visbal [20]. The current CFD result predicted a higher static pressure on the suction side of the blade for the $Re = 100,000$ case, but it did predict the flow separation and reattachment and followed the same trend as the experimental [17] results. The flow separated at 70% axial chord location and then underwent turbulent reattachment at approximately the 93% axial chord location. The experiment showed separation to begin more downstream at 75% axial chord and reattach at 88% axial chord. On the pressure side of the blade, the predicted values are in excellent agreement with the experimental values. At 50,000, the current CFD results were in good agreement with the experimental results on both sides of the blade. The flow at 60% axial chord remained separated all the way to the trailing edge of the blade. The surface static pressure on the suction side was predicted lower than the experimental result for the $Re = 25,000$ case. The location where the separation first began was the 60% axial chord location for both the experimental result and the current CFD prediction. The CFD was able to adequately reproduce the

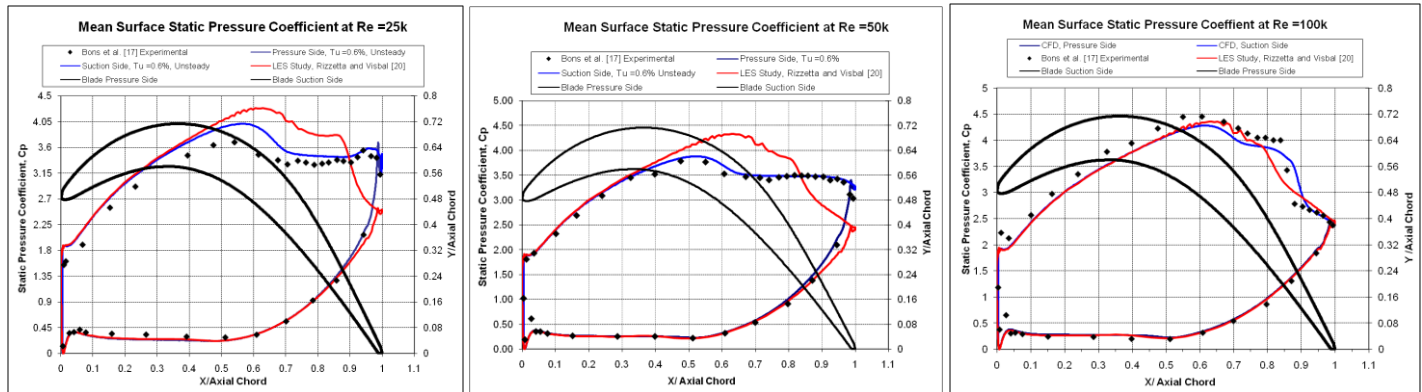


Figure 13. Comparison of Surface Static Pressure Coefficient with 3D LES [20] Simulations and Experimental Results [17] at Inlet Reynolds Numbers of a) 100,000, b) 50,000, and c) 25,000 for the Pack-B Blade Airfoil

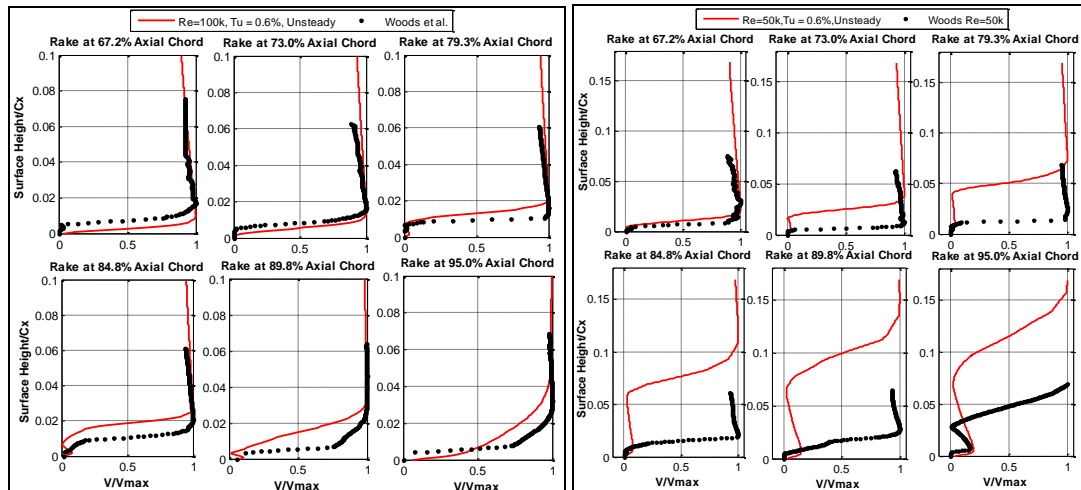


Figure 14. Comparison of the Boundary Layer Velocity Profiles at Inlet Reynolds Numbers of a) 100,000 and b) 50,000 with the Experimental Results [16] for the Pack-B Blade Airfoil

static pressure distribution on the pressure side of the blade. There is a large amount of unsteadiness present in $Re = 25,000$ case due to vortex shedding from the separation bubble, which causes a small static pressure increase beginning at 95% axial chord.

The LES results from Rizzetta and Visbal [20] predicted separation and turbulent reattachment for all simulated inlet Reynolds numbers. At $Re = 100,000$, the separated and turbulent reattachment region was smaller and located more upstream of the blade than compared to the Bons *et al.* [17] experimental result. The separation and reattachment region increased as inlet Reynolds number decreases from 100,000 to 25,000 which was not observed in the experimental results. In summary, this shows the $k_T-k_L-\omega$ transitional flow model was very suitable for the prediction of the location of flow separation and reattachment in separated shear layers in low Reynolds number turbine flows. It was able to capture the qualitative flow response better than a similar three-dimensional LES computation reported by Rizzetta and Visbal [20].

Boundary Layer Velocity Profiles

Time-averaged values of the boundary layer velocity profiles obtained at six axial chord locations of 67.2%, 73.0%, 79.3%, 84.8%, 89.8%, and 95.0% normal to the blade surface are shown in Figure 14 and 15, with the experimental results of Woods *et al* [16]. At the $Re = 100,000$, the rake locations of 79.3%, 84.8%, and 89.8% in Figure 14a show a larger separation region in the CFD prediction than in the experimental results. The high Reynolds number caused the separated shear layer to re-energize and undergo transition to turbulence, causing the flow to reattach to the blade surface. The CFD predicted the flow to be reattached before the 95% axial chord location, while the experiments show turbulent flow reattachment to occur before the 89.8% axial chord location. For the $Re = 50,000$ case, the velocity profile before the 73% axial chord location in the CFD prediction was in good

agreement with the experimental results. The size of the separation region was over-predicted for the CFD results beginning at the 73% axial chord location. The experimental results indicated the separation region remains small with a recirculation region beginning before the 95% axial chord location.

Figure 15 shows the $Re = 25,000$ case where the shape of velocity profiles were in good agreement with experimental results at the 67.2% and 73% axial chord locations. Downstream of those locations, the CFD predicted a larger separation region than experimental results. The time-averaged behavior of the recirculation region caused by the separation bubble was shown to be similar for both the CFD and experimental results. The CFD results did not follow the same trend as the experimental results [16] in that the separation grew as the Reynolds number was decreased. The effect of neglecting the spanwise dimension could be the reason for the discrepancy. The vortical structures being produced are three-dimensional and would be expected to be weaker if the effect of added spanwise dimension was included [20]. The $k_T-k_L-\omega$ transitional flow model demonstrated that it can show a qualitative response to separated boundary layers. There were inaccuracies using the $k_T-k_L-\omega$ transitional model in the prediction of the size of the separation region for all Reynolds number cases. It is noted that the $k_T-k_L-\omega$ flow model was not specifically designed to model boundary layer transition in separated shear layers [10]. It was intended to model attached transitional flows.

Unsteady Features of the Flowfield

The features of the unsteady flowfield have been investigated to gain insight on the behavior of the unsteady flow separation and vortex generation. Instantaneous “snapshots” of the predicted flowfield were taken for all three Reynolds number simulations. For the $Re = 100,000$ case, a total of 44,700 time-steps were utilized for averaging of mean-flow quantities with a flow time-step of $5\mu\text{sec}$. Upon investigation of the unsteady flow features, separation and reattachment were seen to occur at every time step as shown in Figure 16. The separated shear layer on the suction side produces two clockwise vortical structures that move downstream. These vortical structures break down and reduce in magnitude when the separated boundary layer becomes reattached to the surface of the blade. For the $Re = 50,000$ simulation, unsteady averaging was completed for 65,534 time-steps using a flow time-step of $50\mu\text{sec}$. Figure 17 shows contour plots of the RMS velocity magnitude and the instantaneous vorticity magnitude for one time step. The RMS velocity magnitude contour shows a negligible amount of unsteadiness was present in the flowfield and in the separation region. Most of the unsteadiness and vorticity was being produced in the shear layers for both the pressure and suction sides.

In Figure 18, vorticity contour plots for two instantaneous time steps show the unsteady nature of the $Re = 25,000$ case. The flow time-step was $10\mu\text{sec}$ and 43,000 time-steps were completed for mean flow averaging. The separated shear layer

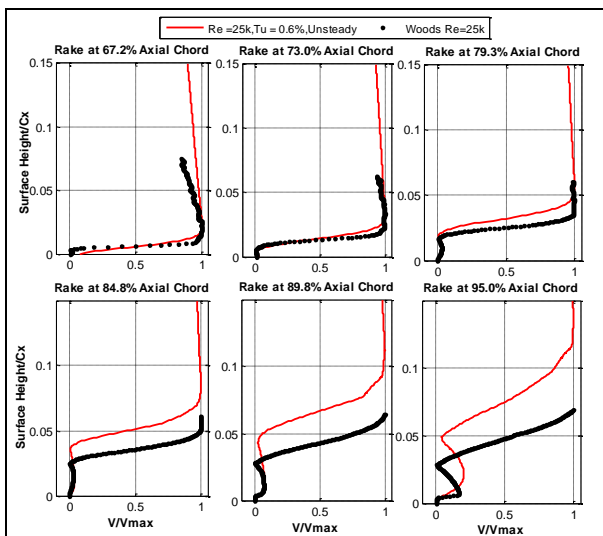


Figure 15. Comparison of the Mean Boundary Layer Velocity Profiles at 25,000 with the Experimental Results [16] for the Pack-B Blade Airfoil

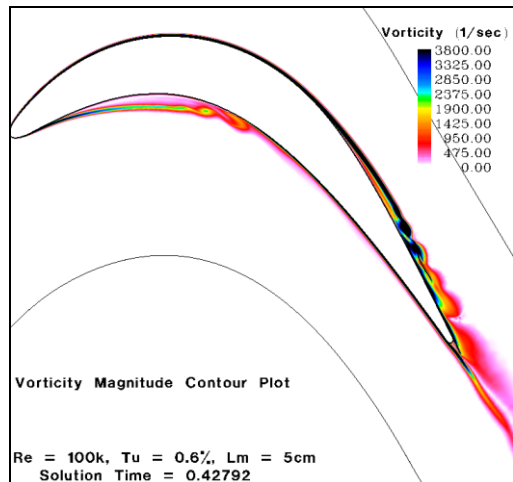


Figure 16. Instantaneous Vorticity Contour Plot at Re = 100,000 for the Pack-B Blade Airfoil

on the suction side produced a clockwise vortex, while the pressure side shear layer produced a counterclockwise vortex that moved from the trailing edge to the wake region. The shedding vortices produced were time periodic. The time signal of the drag coefficient (Figure 18) was calculated by summing the dot product of the pressure and viscous forces with force vector along wall boundary. A FFT calculation was performed to examine the frequency content present in the time signal of the drag coefficient. The frequency resolution based on the time-step and averaging time interval was 1.25Hz. Three dominant frequencies of 12.5Hz, 20Hz, and 45Hz were present in the FFT calculation. These frequencies originated from the vortex generation on the pressure and suction side caused by the separated shear layer. The 12.5Hz and 20Hz frequency content found in the drag coefficient originated from the two vortices generated on the suction side, while the 45Hz signal started from the trailing edge vortex generated by the pressure side shear layer.

Total Pressure Loss Coefficient Predictions

The total pressure loss coefficient predictions using the k_T - k_L - ω transitional model for all three Reynolds number simulations are shown in Figure 19. The CFD results are compared to

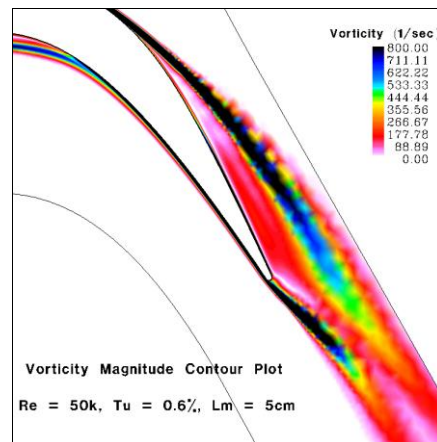
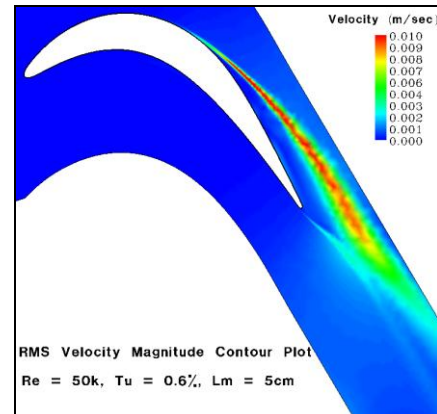


Figure 17. RMS Velocity Magnitude and Instantaneous Vorticity Magnitude Contour Plot, Re =50,000 for the Pack-B Blade Airfoil

experimental wake measurements taken by Garmoe [14] and Casey [15] for a total of two pitch lengths. The major difference in the experimental measurements at Re = 100,000 was in the average inlet turbulent intensity, which was reported as 0.785% for the Garmoe [14] measurements and 0.437% for the Casey [15] measurements. The difference in the location of the wake between the experimental measurement and the CFD predictions was artificial because the traversing Kiel probe had a different starting location for each of the experimental results. For the Re = 100,000 case, CFD prediction under-predicts the

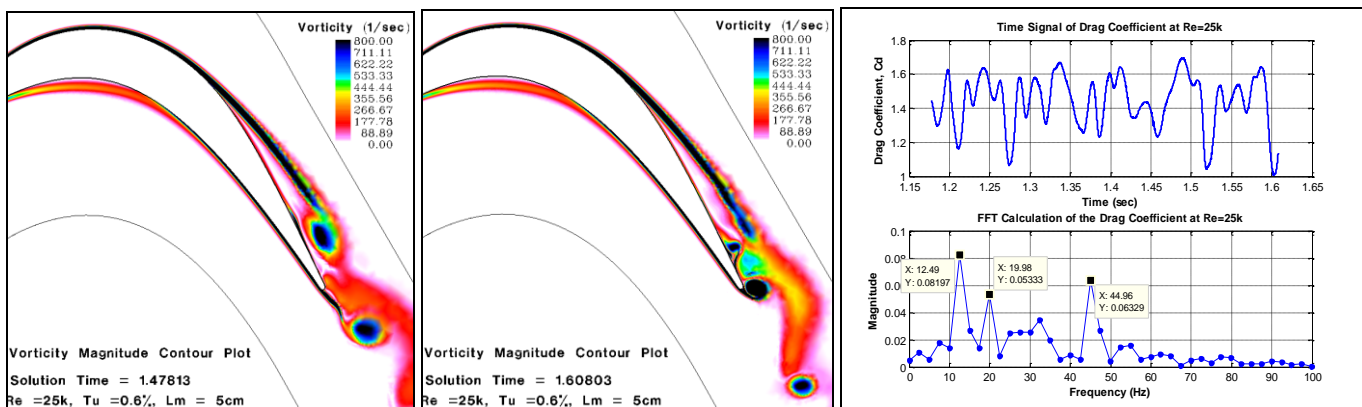


Figure 18. Instantaneous Vorticity Contour Plots including Time Signal and FFT Calculation of Drag Coefficient at Re = 25,000 for the Pack-B Blade Airfoil

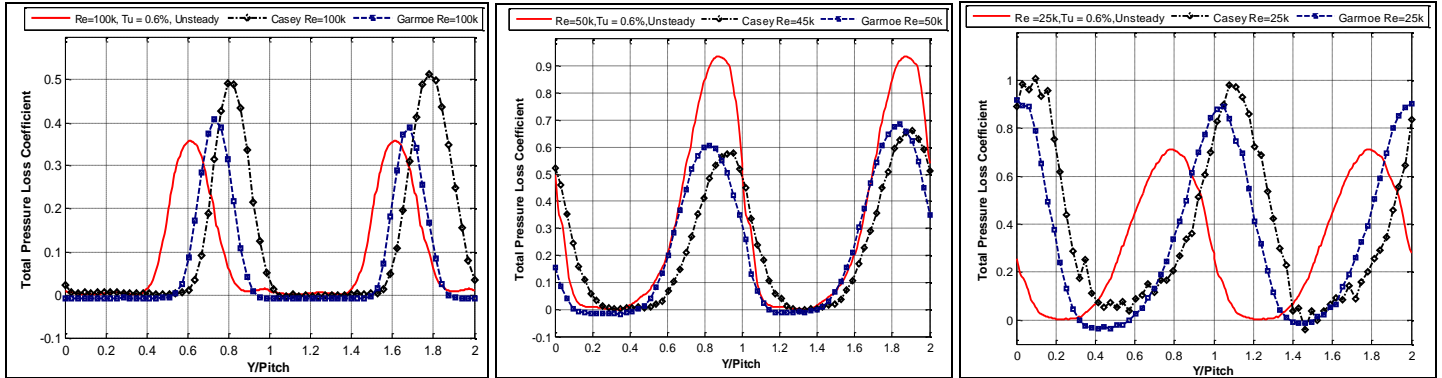


Figure 19. Comparison of Total Pressure Loss Coefficient with Experimental [14,15] Results for the Pack-B Blade Airfoil at Inlet Reynolds Numbers of a) 100,000, b) 50,000, and c) 25,000 for the Pack-B Blade Airfoil

loss coefficient, with 88% and 60% percent agreement with the Garmoe [14] and Casey [15] measurements, respectively. It was expected that the CFD prediction would lie between the two experimental results since the computational inlet turbulent intensity was 0.6%. The reason for the under-prediction was due to the turbulent boundary layer reattachment point being located further downstream on the blade than the experimental measurements, resulting in a lower predicted momentum loss than experimentally measured.

The total pressure loss coefficient prediction at $Re = 50,000$ was over-predicted with respect to both Casey's [15] measurement made at an inlet Reynolds number of 45,000 and inlet turbulent intensity of 0.34%, and Garmoe's [14] measurement at $Re = 50,000$ with turbulent intensity of 0.84%. The over-prediction of the loss coefficient was because the size of the separation bubble in the CFD results was larger than what was observed experimentally, resulting in a large total pressure loss. For the $Re = 25,000$ case, the size of the separation region was over-predicted by the CFD, yet the total pressure loss prediction was lower than both experimental results. This could be due to the behavior of the transport equations in the $k_T-k_L-\omega$ transitional model. The specific dissipation rate in the wake region may be too low, causing a reduced rate of transfer of turbulent kinetic energy to small scale eddies. If the specific dissipation rate were increased, the turbulence being generated from the boundary layer would be transferred at a higher rate due to viscous losses, thus increasing the total pressure loss prediction.

Compared to the TLPT blade airfoil, the flowfield for the Pack-B blade airfoil was very complex involving unsteady separated shear layers. The separated flow produced three-dimensional vortical structures, so the current two-dimensional computation was unable to account for the spanwise distribution of these three-dimensional vortical structures. The shed vortices were expected to be weaker due to the effect of the added spatial dimension, but the vortices will break apart due to spanwise instabilities [20]. A three-dimensional simulation using the $k_T-k_L-\omega$ transitional flow model might provide better performance prediction for the Pack-B blade airfoil. A future

simulation will consist of increasing the spanwise dimension of the two-dimensional Pack-B cascade model to determine the effect of three-dimensionality on the separation and transition development of the Walter's model. Simulation methods of DNS [21,22] and LES [23] have been applied to Pack-B cascade configuration and demonstrated better agreement with experimental results than the current study. However, both the DNS and LES methods are currently computational expensive to be applied to multistage geometries. The RANS method has been the conventional means of simulating flow in multistage rotating turbomachinery. Based on the results reported here, the future plan is to apply Walters and Leylek's [8] $k_T-k_L-\omega$ transitional flow model to a multistage geometry based on the TLPT blade airfoil operating at low Reynolds numbers of the same order of magnitude as simulated in the current study. The present study provides a baseline evaluation of how well the $k_T-k_L-\omega$ transitional flow model captures separation and transition characteristics. The $k_T-k_L-\omega$ transitional flow model accuracy was judged sufficient for an understanding of what was happening within the flow passage, and can identify when and where a separation event occurs which will be the main criteria for the future investigations.

CONCLUSIONS

A new three-equation eddy-viscosity type turbulent transitional flow model developed by Walters and Leylek [8] was tested to predict the performance of two different turbine cascade configurations. A typical LPT blade airfoil was simulated for inlet Reynolds numbers from 15,000 to 100,000. Walters and Leylek's [8] $k_T-k_L-\omega$ transitional flow model showed the ability to predict the transitional flow behavior associated with low Reynolds number flows. The $k_T-k_L-\omega$ transitional flow model provided a more accurate method for performance predictions compared to conventional RANS turbulence models. Sensitivity of the inlet turbulence boundary conditions to the turbulent length scale and freestream inlet turbulent intensity was investigated to determine the effect on prediction of the total pressure loss coefficient. The turbulent transition point and total pressure loss coefficient showed strong sensitivity to changes in the inlet freestream turbulent intensity,

and second order sensitivity effect to the inlet turbulent length scale. Good agreement was obtained for the effect of Reynolds number sensitivity with the experimental results. The ability to adequately predict the Reynolds number effect was demonstrated for the TLPT blade airfoil.

Flows over the Pack-B blade airfoil were simulated at an inlet Reynolds numbers of 100,000, 50,000, and 25,000. The unsteady features of separation and vortex generation of the flowfield were qualitatively investigated. Boundary layer velocity profiles, surface static pressure distributions, and the wake total pressure loss coefficient were compared to the available experimental data. The CFD simulations showed good agreement with the experimental results in prediction of separation and reattachment. When compared to a three-dimensional LES simulation done by Rizzetta and Visbal [20], the k_T - k_L - ω transitional flow model showed a better qualitative response to separated shear layers as seen in the experimental measurements, but quantitative inaccuracies in the size of the separation region were observed. This caused the prediction of the total pressure loss coefficient to differ from the experimental results. The behavior of the transport equations inherent in the k_T - k_L - ω transitional flow model could be the cause of the discrepancy. Also, the absence of spanwise distribution of three-dimensional structures present in separated shear layers observed could lead to inaccuracies. Future work involving three-dimensional CFD simulations of Pack-B blade using Walters and Leylek's [8] k_T - k_L - ω transitional flow model will be considered. However it is noted that this model's results were comparable to more refined three-dimensional LES investigations for this highly separated geometry. The k_T - k_L - ω transitional model demonstrates the potential to provide performance prediction of transitional flow for low Reynolds number airfoils. This model will be applied to the more complex conditions of multistage turbomachinery geometries operating at low inlet Reynolds numbers. This future modeling would be presently cost prohibitive using DNS or LES methods.

ACKNOWLEDGMENTS

The work presented was sponsored by the Air Force Research Laboratory, Propulsion Directorate, Turbine Engine Division. Computing resources were provided by the U.S. Department of Defense Major Shared Resource Center, High Performance Computing facility at Wright Patterson AFB, OH. The authors are grateful to H. Thornburg for assistance with mesh generation, CFD simulation set-up, and helpful discussions. D.P. Rizzetta from Air Vehicles Directorate, AFRL and C. Hah from NASA Glenn Research Center are acknowledged for their helpful advice.

NOMENCLATURE

C_p	=	pressure coefficient
C_x	=	axial chord
d	=	wall distance
D	=	kinetic energy near-wall dissipation
f_{shed}	=	vortex shedding frequency

k	=	kinetic energy
l_m	=	average turbulent length scale
P	=	pressure; production term
q	=	dynamic pressure
R	=	bypass transition production term
R_{NAT}	=	natural transition production term
Re	=	Reynolds number based on axial chord
St	=	Strouhal number
T	=	time interval
t	=	time
TLPT	=	typical low pressure turbine
TPLC	=	total pressure loss coefficient
Tu	=	freestream turbulent intensity
u	=	velocity magnitude
u'	=	streamwise fluctuation
x	=	directional component
y^+	=	nondimensional wall distance
α	=	flow angle
α_T	=	turbulent diffusivity
δ_{ij}	=	Kronecker delta
λ_{eff}	=	effective length scale
λ_T	=	integral turbulent length scale
μ	=	molecular viscosity
ν	=	kinematic viscosity
ρ	=	density
ω	=	specific dissipation rate

Subscripts

0	=	total
i, j	=	indices
in	=	inlet
L	=	laminar
out	=	outlet
T	=	turbulent

REFERENCES

- [1] Choi, C.H., and Yoo, J.Y., "Unsteady Blade-Row Flow Calculations Using a Low-Reynolds-Number Turbulence Model", *Journal of Propulsion and Power*, Vol. 16, No. 5, Sept. - Oct. 2000.
- [2] Dorney, D.J., Lake, J.P., King P.I., and Ashpis, D.E., "Experimental and Numerical Investigation of Losses in Low Pressure Turbine Blade Rows", AIAA 2000-0737.
- [3] Suzen, Y.B., Huang, P.G., Volino, R.J., Corke, T.C., Thomas, F.O., Huang, J., Lake, J.P., and King, P.I., "A Comprehensive CFD Study of Transitional Flows in Low-Pressure Turbines Under a Wide Range of Operating Conditions", AIAA Paper No. 2003-3591.
- [4] Praisner, T.J., and Clark, J.P., "Predicting Transition in Turbomachinery, Part I – A Review and New Model Development", ASME Paper No. GT-2004-54108.
- [5] Praisner, T.J., Grover, E.A., Rice, M.J., and Clark, J.P., "Predicting Transition in Turbomachinery, Part II – Model Validation and Benchmarking", *Journal of Turbomachinery*, Vol. 129, January 2007, pp 14 – 22.

- [6] Menter, F.R., Langtry, R.B., Likki, S.R., Suzen, Y.B., Huang, P.G., and Volker, S., "A Correlation-Based Transition Model Using Local Variables- Part I: Model Formulation", *Journal of Turbomachinery*, Vol. 128, July 2006, pp 413 – 422.
- [7] Langtry, R.B., Menter, F.R., Likki, S.R., Suzen, Y.B., Huang, P.G., and Volker, S., "A Correlation-Based Transition Model Using Local Variables- Part II: Test Cases and Industrial Applications", *Journal of Turbomachinery*, Vol. 128, July 2006, pp 423 – 434.
- [8] Walters, D.K., and Leylek, J.H., "A New Model for boundary Layer Transition Using a Single Point RANS Approach", *Journal of Turbomachinery*, Vol. 126, January 2004, pp 193–202.
- [9] Holloway, D.S., Walters, D.K., and Leylek, J.H., "Prediction of Unsteady, Separated Boundary Layer over a Blunt Body for Laminar, Turbulent, and Transitional Flow", *International Journal for Numerical Methods in Fluids*, Vol. 45, March 2004, pp 1291-1351.
- [10] Walters, D.K., and Leylek, J.H., "Prediction of Boundary-Layer Transition on Turbine Airfoil Profile Losses", ASME Paper No. IMECE 2003-41420.
- [11] Walters, D.K., and Leylek, J.H., "Computational Fluid Dynamics Study of Wake-Induced Transition on a Compressor-Like Flat Plate", *Journal of Turbomachinery*, Vol. 127, January 2005, pp 52–63.
- [12] Lake, J.P., "Flow Separation Prevention on a Turbine Blade in Cascade at Low Reynolds Number" *PhD Dissertation*, Air Force Institute of Technology, AFIT/DS/ENY/99-01, 1999.
- [13] McQuilling, M., "Design and Validation of a High-Lift Low-Pressure Turbine Blade", *PhD Dissertation*, Wright State University, Dayton, OH, August 2007.
- [14] Garmoe, T.L., "Characterization of the GH1R Low Pressure Turbine" *Master Thesis*, Air Force Institute of Technology, AFIT/DS/ENY/05-S02, 2005.
- [15] Casey, J.P., "Effect of Dimple Pattern on the Suppression of Boundary Layer Separation on a Low Pressure Turbine Blade", *Master's Thesis*, Air Force Institute of Technology, 2004. AFIT/GAE/ENY/04-M05.
- [16] Woods, N., Sondergaard, R., McQuilling, M., and Wolff, M., "Investigation of Separation Control in Low Pressure Turbine using Pulsed Vortex Generator Jets", AIAA 2006-4450.
- [17] Bons, J.P., Sondergaard, R., and Rivir, R.B., "Control of Low-Pressure Turbine Separation Using Vortex Generator Jets", AIAA 1999-0367.
- [18] ANSYS Fluent® User's Manual Version 6.3.26, 2006.
- [19] Wilcox, D.C., "Turbulence Modeling for CFD", DCW Industries, Inc., 1993.
- [20] Rizzetta, D.P., and Visbal M.R., "Numerical Investigation of Transitional Flow through a Low Pressure Turbine Cascade", AIAA 2003-3587.
- [21] Enomoto, S., Hah, C., and Loelbach, J., "Numerical Investigation of a Low Reynolds Number Flow Field in a Turbine Blade Row", AIAA 2001-0524.
- [22] Singh, N., Ghia, K., and Ghia, U., "Simulation of Separated Flow inside a Low-Pressure Turbine Cascade", AIAA 2005-1273.
- [23] Gross, A., and Fasel, H.F., "Turbulence Modeling for Low Pressure Blades", AIAA 2005-5292.

APPENDIX E

GT2010-22977

A CFD AND EXPERIMENTAL INVESTIGATION OF UNSTEADY WAKE EFFECTS ON A HIGHLY LOADED LOW PRESSURE TURBINE BLADE AT LOW REYNOLDS NUMBER

Darius D. Sanders Chase A. Nessler Rolf Sondergaard

Marc D. Polanka Christopher Marks
Air Force Research Lab, Propulsion Directorate
Wright Patterson AFB, OH 45433, USA

Walter F. O'Brien
J. Bernard Jones Professor, Department of Mechanical Engineering
Virginia Tech, Blacksburg, VA 24061, USA

ABSTRACT

The flowfield of the L1A blade airfoil subjected to traversing upstream wakes was experimentally and computationally investigated at an inlet Reynolds number of 25,000. The L1A blade airfoil represented a high-lift aft-loaded low pressure turbine blade design that was designed to separate at low Reynolds numbers making it an ideal airfoil for use in flow separation control studies. This study applied a new two-dimensional CFD model to the L1A low pressure (LP) turbine blade design using a three-equation eddy-viscosity type transitional flow model developed by Walters and Leylek. Velocity field measurements using two-dimensional planar Particle Image Velocimetry were obtained and comparisons were made to the CFD predictions using the Walters and Leylek [13] $k-k_L-\omega$ transitional flow model and the Menter's [24] $k-\omega(SST)$ model. Hotwire measurements and pressure coefficient distributions were also used in comparison of each models ability to predict the wake produced from the wake generator and the loading on the L1A LP turbine blade profile with unsteady wakes. These comparisons were used to determine which RANS CFD model could better predict the unsteady L1A blade flowfield at low inlet Reynolds number. This research also provided further characterization of the Walters and Leylek transitional flow model for low Reynolds number aerodynamic flow prediction in low pressure turbine blades.

INTRODUCTION

Low Reynolds numbers are often encountered in low pressure turbines especially at high altitude cruise environments. The use of unmanned aerial vehicles has pushed the altitude limits even further, resulting in extremely low Reynolds number flows through the LP turbine. This can result in a component efficiency drop on the order of 7 percent between takeoff and cruise conditions for small military engines at high altitude [1]. Also, current trends in gas turbine engine development have been toward decreasing the number of blades in the LP turbine while maintaining the same amount of stage work. Since almost one third of the total engine weight in a modern high-

bypass-ratio engine comes from the LP turbine [2], blade count reductions can have a substantial effect on weight. Reduced blade numbers also benefit the manufacturer as it results in a reduced part count, reduced manufacturing costs, and an increase in reliability.

Low Reynolds number flows through the LP turbine can result in a laminar boundary layer forming on the suction surface of the blade. Reductions in blade count have increased the aerodynamic loading on these blades along with the adverse pressure gradient that is present. If the laminar boundary layer is unable to overcome the adverse pressure gradient, the boundary layer will separate. It has been shown that a conventional LP turbine blade can have up to 60 percent of the losses generated by the suction surface boundary layers [3].

Extensive research on reducing the profile loss due to separated boundary layers at low Reynolds number has shown that the effect of unsteady wakes shed from upstream stages can have a profound influence on profile loss. Curtis et al. [3] showed that the inclusion of wakes caused an attached transitional boundary layer to develop on the blade surface which was previously laminar for steady inflow. In a study by Haselbach [2], the inclusion of wakes over an "ultra-high" lift blade showed comparable losses to the previous generation of blades while generating 11% more lift. Work by Schobeiri [4] at low Reynolds number demonstrated that for unsteady inflow the C_p distribution on a blade surface displayed increased loading with a shorter separated region compared to steady inflow, indicating lower losses had also been achieved. Schulte and Hodson [5] used hot film measurements on a LP turbine blade to show that a turbulent patch developed downstream of an impinging wake with increased levels of shear stress. This turbulent spot was observed to prevent the boundary layer from separating and was followed by laminar or "becalmed" region. The becalmed region is said to also prevent the boundary layer from separating due to its relatively elevated shear stress and more developed velocity profiles. Similar studies [6-9] have shown the importance of including unsteady wake flow in addition to elevated levels of free-stream turbulence to develop highly loaded LP turbine airfoils with increased performance at low Reynolds number.

With recent advances in numerical techniques and increased computational resources, CFD is being widely applied to further advance turbomachinery designs. Higher order CFD methods of direct numerical simulation (DNS) and large eddy simulation (LES) have been successfully applied to the simulation of flow in a LP turbine blade cascade with incoming passing wakes. Wissink [11] applied upstream artificial turbulent wakes to a LP turbine blade at a high angle of attack using the DNS method. It was stated that longitudinal vortices were found on the blade pressure and suction surfaces due to the straining of the passing wakes by the freestream flow. Sarkar [12] demonstrated that LES can be used to characterize the flow instabilities during transition of a separated boundary layer under the influence of periodic wakes similar to the DNS method at a reduced computational cost. Spectral analysis showed the shear layer instability downstream of the separation occurred due to a Kelvin-Helmholtz mechanism and caused the periodic shedding of coherent vortices.

Currently, the LES and DNS CFD methods promise improved accuracy for flow predictions, but require long simulation times. These methods are thus not suitable for the turbomachinery design process and simulations of complicated multiple stage geometries. The most widely used CFD method for simulations involving three-dimensional rotating turbomachinery is the Reynolds Averaged Navier-Stokes (RANS) method. Accurate prediction of aerodynamic losses due to separation and laminar-to-turbulent transitional flow is required for RANS CFD method to continue to play an integral role in the design process, particularly for optimization. Previous studies have been completed where conventional statistical turbulence models have been modified to predict separation and transitional flow effects using additional transport equations in combination with empirical correlations [13-16]. These modified RANS models showed significant improvement in the prediction of aerodynamic flow effects at low Reynolds numbers in LP turbine blade geometries over conventional turbulence models [17,18].

The recent development of an improved turbulent transition model by Walters and Leylek [13] appears to offer the possibility of improved accuracy for low Reynolds number LP turbine flow predictions using the RANS CFD method. Transport equations are used to address the development of pre-transitional fluctuations in the boundary layer and the breakdown to turbulence to predict both natural and bypass transition. The capability of the new model to predict the unsteady transitional flow behavior has been demonstrated on a flat plate with a pressure distribution similar to an axial compressor undergoing passing wakes by Walters and Leylek [19]. Work has been completed by the current authors [20-22] in characterizing the Walters and Leylek transitional flow model for aerodynamic flow predictions at low Reynolds number in LP turbine geometries. The ability to predict aerodynamic losses at low inlet Reynolds number was demonstrated for two-dimensional cascade CFD models on three low pressure turbine blade airfoils [20,21] and a multistage low pressure turbine geometry [22,23]. The model provided a more effective prediction of the aerodynamic loss mechanisms present in low Reynolds number flows compared to conventional turbulence models.

A prerequisite of improving the performance of LP turbine blades is efficiently and accurately predicting their performance during the design phase. Researchers at the U.S. Air Force Research Labs (AFRL) have developed a design tool that has been used to create a series of new LP turbine blade profiles that push the aerodynamic loading and low Reynolds number performance capabilities of LP turbines [10]. As part of the design and validation process, new blade profiles have been studied post-design by academia and AFRL using experimental facilities and commercial computational codes.

This present post-design study presents an experimental and computational comparison of the AFRL designed L1A low pressure turbine blade profile behavior in periodic unsteady conditions. Measurements were taken using two-dimensional planar Particle Image Velocimetry (PIV) and velocity field data was generated for

six phases of wake passing. This paper applies the Walters and Leylek [13] laminar-to-turbulent transitional flow model to predict the unsteady aerodynamic flow behavior of the highly loaded L1A blade airfoil cascade configuration subjected to upstream passing wakes. The purpose was to determine if the proposed model can predict unsteady flow behavior similar to the periodic disturbances from wakes shed from upstream vane impinging on the downstream rotor blade found in multistage turbine flows. A Reynolds number of 25,000, based on inlet velocity and blade axial chord was used in both the CFD and experimental results. The simulations were compared to experimental cascade results and CFD simulations completed using the fully turbulent Menter's [24] $k-\omega(SST)$ model at low inlet freestream turbulence intensities. The effect on the upstream wake was investigated on the unsteady flowfield, the separation region, and the blade loading compared to L1A blade baseline cascade configuration without upstream wakes. This model can potentially provide the same prediction capability for more complicated unsteady flowfields found in multistage LP turbine blade geometries.

EXPREMINENTAL METHODS

The experimental measurements were performed on a linear cascade of highly loaded LP turbine blades in the AFRL low speed wind tunnel (LSWT) at Wright-Patterson Air Force Base. A more detailed description of this facility is found in Sondergaard *et al.* [25] and Rivir *et al.* [26]. The wind tunnel is an open circuit type with a 0.85m tall by 1.22m wide test section containing the linear turbine cascade. The inlet is a 3.0m by 2.7m rectangular bell-mouth with an 8:1 gradual reduction in cross-sectional area. Air enters through a series of honeycomb flow straighteners which produce flow uniformity better than 1% and a free-stream turbulence intensity (FSTI) of approximately 0.5% at the cascade test-section inlet [27].

The linear cascade consists of seven fully immersed L1A blade profiles and two partial blade profiles on either end. These blades were designed by Clark and Koch [28] and were manufactured using cast polyurethane. The cascade blade profile has an axial chord (C_x) of 0.178m, a span of 0.88m, and a solidity of 0.99. This aft loaded blade has the same design inlet and exit angle as the Pack B, 60 and 30 degrees respectively. The L1A profile is a very highly-loaded low pressure turbine blade with a calculated incompressible Zweifel coefficient of 1.23 based on Eq. (1).

$$Z_w = 2 \frac{S}{C_x} \cos^2 \alpha_{out} (\tan \alpha_{in} - \tan \alpha_{out}) \quad (1)$$

The L1A profile generates 17% more lift than the Pack B, which correlates to a 17% blade count reduction. The L1A profile is an aft loaded design making it prone to separation under steady flow conditions due to the axial location of the peak velocity and strong adverse pressure gradient on the blade suction surface. This blade was designed for use in flow control studies in which separation may be suppressed while maintaining the benefits of both very high loading and aft loading [29]. In a previous study performed in the same facility, it was shown for Reynolds numbers less than 40,000 (based on inlet velocity and axial chord) and a FSTI of 3.4%, the L1A profile exhibits a non-reattaching separation zone with high losses [30]. These characteristics were desired for the current study to demonstrate the capability of the model under steady and unsteady inflow. A schematic of the linear cascade and the wind tunnel is shown in Fig. 1.

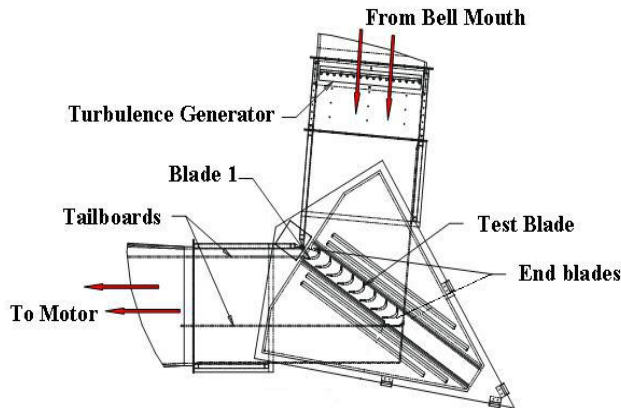


Figure 1. Schematic of linear cascade wind tunnel with turbulence generator

The LSWT at AFRL houses a moving bar wake generator that is used to produce periodic unsteadiness in the flow impinging upon the linear cascade to simulate the effect of upstream vane row wake shedding. A more detailed description of the wake generator design and characterization is found in Nessler *et al.* [31]. The wake generator configuration is such that the entire structure is enclosed inside the wind tunnel upstream of the cascade and is confined within the tunnel wall boundary layer flow to minimize flow disturbances. Similar to other squirrel cage designs, cylindrical rods are used as the wake generating mechanism. Eighteen rods were oriented vertically and fastened to a hollow pin chain running along the top and bottom of the wind tunnel. Chain speeds over 5.0m/s can be obtained with acceptable rod vibrations allowing the rod speed to match the inlet flow velocity for Reynolds numbers below 50,000.

In this investigation, 3.2mm (1/8 inch) diameter unidirectional carbon fiber rods with a spacing of 17.8cm were used to match the diameter of the trailing edge and the blade spacing of the L1A profile. The wake generator was placed with the rods 8.89cm, half of an axial chord length, upstream of the linear cascade. The rod passing frequency was chosen such that it yielded a flow coefficient of 0.8 resulting in a rod velocity that approximately equaled the free-stream velocity. The 18 cylindrical rods span across 36% of the total chain length so that secondary wakes generated from rods making the upstream traverse back across the wind tunnel would not interfere with the primary wakes. A schematic of the wake generator track configuration in reference to the linear cascade is shown in Fig. 2(a) and a complete CAD drawing of the wake generator installed in the wind tunnel is shown in Fig. 2(b). In order to ensure the wake generator structure did not disturb the flow, cascade periodicity across the blade set was verified by total pressure measurements upstream and one chord length downstream of the turbine blades. The periodicity was checked at a Reynolds number of 50,000 with and without the wake generator running.

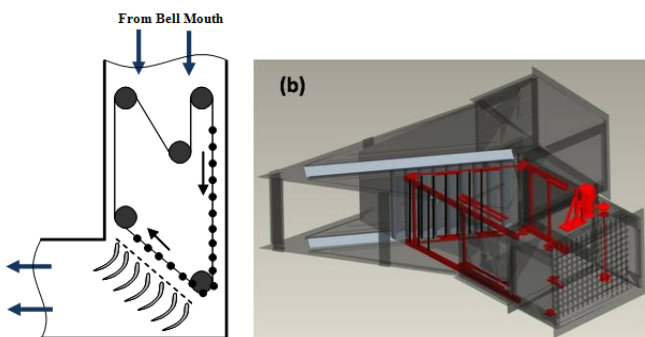


Figure 2. (a) Wake generator track configuration (b) CAD model of wake generator installed in wind tunnel

Phase-locked two-dimensional planar PIV measurements were taken above the suction surface of the L1A profile for six different phases of wake passing. Details of the PIV setup can be found in Nessler *et al.* [32]. Seed particles were illuminated through a thin laser sheet along the flow direction of the suction surface at approximately mid-span of blade three. A high-resolution cross-correlation digital camera was used with a resolution of 1600 by 1200 pixels and the field of view covered approximately 90% to 45% axial chord (C_x). Seeding of the flow was done using a commercial fog generator which produces atomized particle sizes on the order of micro-meters. Data was analyzed using PIV analysis commercial software Flowmanager. Results were obtained through cross-correlation with multiple passes using interrogation domains of 128, 64, and 32 pixels with an overlapping of 50%. Since turbulence statistics were not needed, each phase consisted of 150 image pairs.

Phase locking of the PIV measurements was done using quick response phototransistor optical sensors placed along the wake generator chain which externally triggered the pulse generator. The wake passing event was split into six phases with the first phase nominally beginning with a rod positioned directly upstream from the leading edge of blade four. The temporal delay between the two laser pulses was a function of flow velocity, optical magnification, and interrogation spot size. The delay for each phase however, was based on rod velocity and the distance the rod needed to travel from the sensor. A diagram of the different phases is shown in Figure 3. The black filled rods in this figure demonstrate the placement for the first phase, while the dotted circles are rod locations for the next five phases.

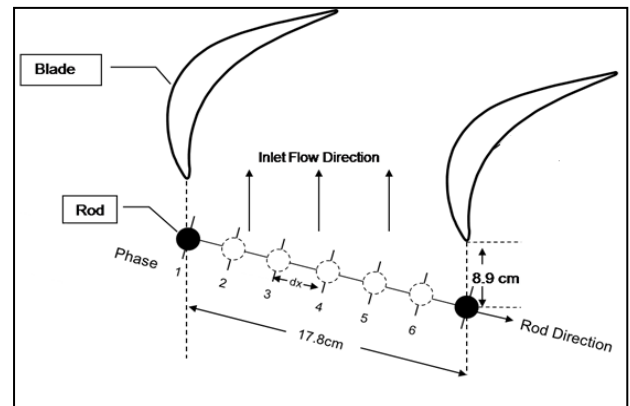


Figure 3. Diagram of the different wake generator locations for each of the six phases [32]

CFD NUMERICAL METHODS

Computational Grid Technique

The two-dimensional grid of the cross section of the L1A blade airfoil with and without upstream wake generators was based on the experimental cascade configuration. The computational meshes shown in Fig. 4 consisted of a hybrid O-H grid topology created in Gridgen[®] 15 mesh generation software. A structured O-grid was extruded normal to each blade surface in order to provide the resolution needed to resolve the boundary layer. The O-grid dimensions were (1099x71) for the L1A blade mesh. The first cell wall distance was such that the y^+ was less than unity at every grid point around the blade airfoil surface, satisfying the y^+ tolerance requirement for the transitional flow model. The average aspect ratio for each grid topology was 6.5:1, but was as high as 30:1 in cells close to the blade surface. An unstructured mesh was placed in the main flowpath consisting of 16,399 and 23,018 triangular cells for the L1A blade baseline and L1A blade with upstream wake generators grids, respectively. The clustering of the unstructured H-grid cells was increased to provide enough resolution for the wake region

generated by the trailing edge. The inlet domain was located 22.9cm from the L1A blade leading edge in the baseline grid. The inlet domain was reduced to 1.87cm in the streamwise direction from the leading edge in the L1A blade with upstream wake generators grid. The outlet of the L1A blade domain was placed 2 axial chord lengths downstream of the trailing edge in the streamwise direction to encompass any experimental wake measurement locations. A formal grid independence study was completed using this type of grid methodology on turbine blades similar to the L1A blade. This grid methodology provided enough spatial resolution to capture the effects of the flowfield in the boundary layer and within the wake region [20].

Another hybrid O-H grid for a circular cylinder (Fig. 4(c)) was placed upstream of the L1A blade. The center of the cylinder was placed a distance of 19.3cm ($60D_{cyl}$) in the streamwise direction from the leading edge of the L1A blade consistent with the experimental configuration. The cylinder was used to generate unsteady wakes similar to the actual wakes generated from an upstream LP turbine vane. The inlet boundary was placed upstream 22.9cm ($72D_{cyl}$) in the streamwise direction from the cylinder center. The shape of the cylinder domain was based on the inlet relative flow angle, $\beta = 62.5^\circ$, which corresponded to a flow coefficient and cylindrical rod speed as set in the experimental configuration. The wake-passing frequency based on wake generator traversing speed was 12.8Hz. A structured O-grid with dimensions of (249x46) was placed around the cylinder and the unstructured H-grid with 20,999 cells was placed in the flowpath and the cylinder wake region. The y^+ was less than unity at every grid point around the wake generator surface. The unstructured cell count and clustering was made fine enough to resolve the small vortical structures produced from the cylinder within the wake region.

CFD Numerical Scheme

CFD simulations were performed using ANSYS Fluent 12.0[®] which was run on a SGI Altix 4700 high performance super-computer using a total of 32 processors for the unsteady simulations. Unsteady flow cases were initialized with the first-order discretization steady flow solutions. The steady flow solutions were initialized based on the inlet boundary conditions and iteratively run with a first-order upwind scheme until the residual tolerance for continuity, linear momentum, and turbulence variables were below 10^{-4} . The unsteady flow case was run using a second-order upwind spatial discretization with a second-order implicit temporal solver. A minimum convergence tolerance of 10^{-5} was used for continuity and momentum equations whereas the turbulence variables used a convergence tolerance of 10^{-4} in order to reduce the number local iterations per time step. Time steps were chosen in order to obtain enough temporal resolution to allow the solution to converge locally within 40-50 iterations per time step.

The translating motion of the wake generators placed upstream of the L1A blade airfoil was modeled using the sliding mesh technique within ANSYS[®] Fluent 12.0. It is the most accurate method for simulating flows in multiple moving reference frames and yet the most computationally demanding. Unsteady interactions due to the potential flowfield, and convecting wakes needed to be accounted for, so a time-dependent solution procedure was required. The two cell zones will move relative to each other along the grid interface in discrete steps during the calculation. Interface zones were set up at the inlet and outlet of the circular cylinder domain at the points where the domain was moved relative L1A blade airfoil domain.

Walters and Leylek Transitional Flow Model Description

The model used in this study is a three-equation eddy-viscosity type, with transport equations for the turbulent kinetic energy (k_T), laminar kinetic energy (k_L), and the specific dissipation rate (ω) which are given in Eq. (4)–(6).

$$\frac{Dk_T}{Dt} = P_{k_T} + R + R_{NAT} - \omega k_T - D_T + \frac{\partial}{\partial x_j} \left[\left(\nu + \frac{\alpha_T}{\sigma_k} \right) \frac{\partial k_T}{\partial x_j} \right] \quad (4)$$

$$\frac{Dk_L}{Dt} = P_{k_L} - R - R_{NAT} - D_L + \frac{\partial}{\partial x_j} \left[\nu \frac{\partial k_L}{\partial x_j} \right] \quad (5)$$

$$\begin{aligned} \frac{D\omega}{Dt} &= C_{\omega 1} \frac{\omega}{k_T} P_{k_T} + \left(\frac{C_{\omega R} \lambda_T}{\lambda_{eff}} - 1 \right) \frac{\omega}{k_T} (R + R_{NAT}) - \\ &C_{\omega 2} \omega^2 - C_{\omega 3} f_{\omega} \alpha_T \left(\frac{\lambda_{eff}}{\lambda_T} \right)^2 \frac{\sqrt{k_T}}{d^3} + \frac{\partial}{\partial x_j} \left[\left(\nu + \frac{\alpha_T}{\sigma_{\omega}} \right) \frac{\partial \omega}{\partial x_j} \right] \end{aligned} \quad (6)$$

The influence of the laminar and turbulent kinetic energy on the Reynolds stress term was included through the prescription of the total eddy viscosity as given in Eq. (7). A brief summary of the current transitional flow model functionality is presented below.

$$-\overline{u_i' u_j'} = \nu_{TOT} \left(\frac{\partial u_i}{\partial x_j} + \frac{\partial u_j}{\partial x_i} \right) - \frac{2}{3} k_{TOT} \delta_{ij} \quad (7)$$

The laminar kinetic energy was used to describe the low frequency, high amplitude fluctuations that originated from the pre-transitional boundary layer. These fluctuations primarily occurred at one scale and almost all energy was contained in a single streamwise component. The production of laminar kinetic energy was assumed to

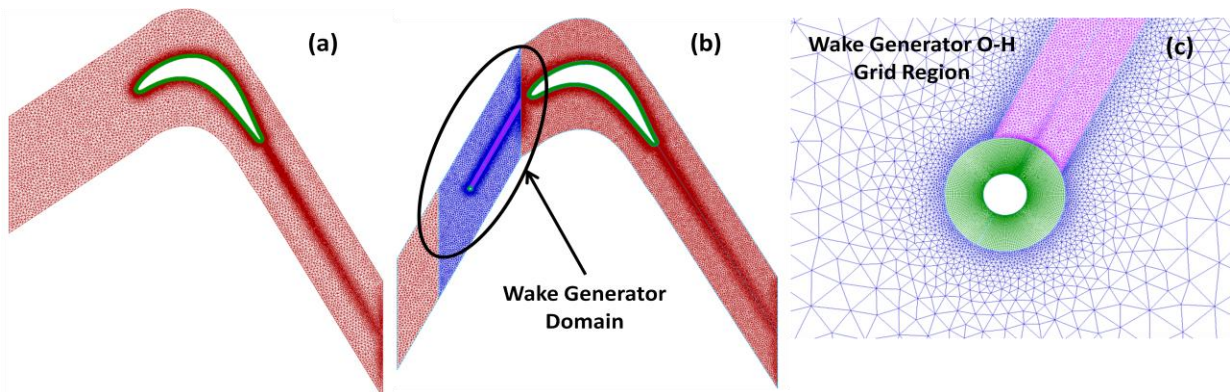


Figure 4. Two-dimensional hybrid O-H grid of the (a) L1A blade baseline, (b) L1A blade with upstream wake generators, and (c) magnified view of wake generator O-H grid region

occur due to a “splat mechanism” which redirected the normal fluctuations of the freestream turbulence into a streamwise component while creating local pressure gradients in the boundary layer, thus increasing the low frequency fluctuations. These fluctuations grow and develop into turbulent spots and then to full turbulence. A local transition parameter that depended on the turbulent energy, effective length scale, and fluid viscosity determined when this occurred. Once this parameter reached a threshold value, a transfer of energy began from streamwise fluctuations (k_L) to turbulent fluctuations (k_T).

Both natural, mixed, and bypass transition were resolved in the Walters and Leylek [13] transitional flow model. Natural transition occurred when orderly laminar flow broke down to turbulent flow in the presence of small perturbations. This process was very slow and was observed when no external forcing was applied and when very small perturbations were present. Bypass transition evolved when those perturbations were large enough to bypass the exponential growth of Tollmien-Schlichting (TS) waves. The mixed transition regime involved elements of both natural and bypass transition. The production terms in the current model controlled the transfer from streamwise fluctuations to full turbulence which depended on the laminar kinetic energy and the local mean velocity in order to include natural and mixed transition.

The fully turbulent Menter’s [24] $k-\omega(SST)$ model was simulated using the L1A blade with upstream wake generators in order to compare with the prediction of the flowfield using the $k-k_L-\omega$ transition model. This model was chosen due to its ability to predict fully turbulent flow due to adverse pressure gradients. It was developed to blend accurate standard $k-\omega$ model in the near wall region with the freestream independence of the $k-\varepsilon$ model in the free shear region. The low Reynolds correction was enabled where a coefficient dampens the turbulent viscosity in the flowfield. A full description of each model variables and dependences was presented in the Fluent 12.0 User Manual [33].

Boundary Conditions

The CFD boundary conditions mirrored experimental cascade test conditions. The inlet boundary condition for the steady flow cases was specified as a total pressure inlet where static pressure was set according to an experimentally determined value of 97900 Pa. The inlet total pressure reflected the chosen Reynolds number of 25,000. A mass flow inlet boundary condition was used in order to permit the total pressure to be calculated from the interior solution which aided the local convergence per time step. The mass flow was calculated based on the normal component of the velocity and inlet domain length (kg/sec-m). The axial and tangential component of the flow direction was given based on the design inlet flow angle of 35°. The experimental cascade L1A blade airfoil was scaled-up causing the inlet Mach number to be less than 0.03 for a given inlet Reynolds number. The flow was therefore assumed to be incompressible in the CFD simulations. The inlet turbulent intensity, $Tu = 0.5\%$, and inlet turbulence length scale, $l_m = 50\text{mm}$, were chosen based on experimental values. The inlet laminar kinetic energy was set to $10^{-6} \text{ m}^2/\text{sec}^2$ in accordance with specifications of the turbulence model. No-slip conditions were assigned to the blade surface and turbulence parameters used a zero-flux boundary condition. The initial static pressure boundary condition at the outlet was estimated using conservation of mass of the axial velocity and ideal outlet flow angle and the assumption that no total pressure loss occurred between the inlet and outlet planes following Eq. (8)–(9).

$$u_{out} = u_{in} \left[\frac{\cos(\alpha_{in})}{\cos(\alpha_{out})} \right] \quad (8)$$

$$P_{out} = P_0 - \frac{1}{2} \rho u_{out}^2 \quad (9)$$

This calculation of the outlet static pressure provides an initial guess for the pressure-based solver and was adjusted during the calculation.

FLOWFIELD COMPARISONS WITH EXPERIMENTAL RESULTS

The CFD predictions of the L1A blade airfoil flowfield with and without upstream wake generators were compared to the experimental measurements presented in this current study and in Marks *et al.* [30]. All frequency and time quantities were normalized with respect to the wake passing frequency, $f_{wake} = 12.8\text{Hz}$, and period. The $k-k_L-\omega$ and $k-\omega(SST)$ model simulations of L1A blade airfoil with wake generators was run for 3 and 10 wake passing periods for averaging of mean-flow quantities, respectively. The L1A blade airfoil baseline predictions used a $t_{norm} = 12.67$ for averaging of mean-flow quantities using at the $Re = 31,000$ using the $k-k_L-\omega$ model. The flow characteristics of the wake generator were investigated with comparisons to single point hotwire velocity measurements. Also, the upstream wake effect on the unsteady flowfield was studied including comparisons of the mean blade pressure distribution. Direct comparisons were made with PIV measurements of the velocity flowfield and perturbation vectors. The difference in the prediction of the flowfield is discussed for each chosen turbulence model.

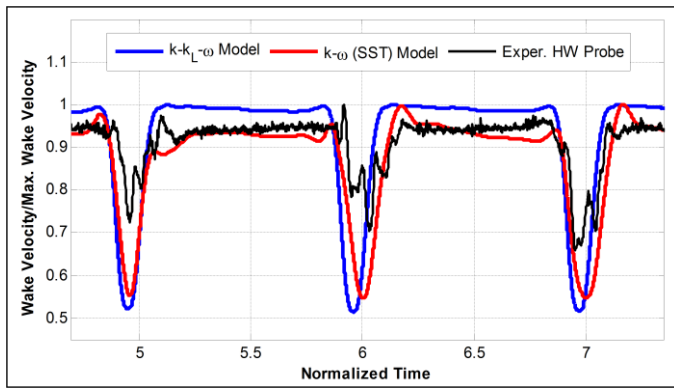
Wake Generator Characteristics

The flowfield of the upstream wake generator was investigated in order to characterize the wake produced by the circular cylinder that impinged upon the downstream L1A blade profile. The inlet Reynolds number based on the cylinder diameter and the inlet relative velocity was 794. The separation point was predicted as 103.5° for both the $k-k_L-\omega$ and $k-\omega(SST)$ model results. This location corresponded to a laminar flow separation point and was within 99% agreement with classical theory [34]. The fully turbulent $k-\omega(SST)$ model predicted the same separation location as the $k-k_L-\omega$ model due to the low Reynolds number correction feature that dampened the production of the turbulent viscosity in the flowfield. The separated shear layers produced a vortex shedding pattern known as the von Kàrmàn vortex street [34]. The FFT calculation of the dynamic drag coefficient indicated that the normalized shedding frequency, $f_{norm} = 23$, for both the $k-k_L-\omega$ and $k-\omega(SST)$ model predictions.

Several single point measurements of the velocity were made downstream of the wake generator. The first hotwire velocity probe (HW #1) was located at mid-span between blades 3 and 4, half an axial chord length downstream of the wake generator. This allowed for the measurement of the velocity deficit produced by the rod just before it impinges upon the cascade. Data was recorded at 10 kHz for three cycles of wake passing. Figure 5 shows the instantaneous single point velocity probe measurement for the CFD and experimental results. The wake was quantified using the peak velocity deficit, u_p , calculated using Eq. 10

$$u_p = \frac{U - u_0}{U} \quad (10)$$

where U is the average velocity outside the wake region and u_0 is the minimum velocity within the wake region as given in Fig. 5. The experimental result showed multiple fluctuations of the velocity within the wake region which could be attributed to vibrations caused by wake generator traversing through the wind-tunnel. The $k-k_L-\omega$ and $k-\omega(SST)$ model had a 60% and 38% higher peak velocity deficit to the experimental results. This could be attributed to the surface of the actual wake generator not being perfectly cylindrical and smooth.



	U_p
$k-k_L-\omega$ Model	0.476
$k-\omega$ (SST) Model	0.409
Exp.	0.296

Figure 5. CFD and experimental comparison of the unsteady wake generator velocity at the HW location #1

The boundary layer of the real hardware may have also been more turbulent, and thus reduced the wake peak velocity deficit in the experimental results. The velocity deficit in the $k-\omega$ (SST) model results had more velocity variations compared to the $k-k_L-\omega$ model result due to the behavior of the vortices as they dissipate within the wake region. The vortices in the $k-\omega$ (SST) model remained coherent further downstream compared to the $k-k_L-\omega$ model due to the lower dissipation rate in the calculated in the $k-\omega$ (SST) model.

Figure 6 shows a comparison between the CFD and experimental results for HW #2 placed at the 64.2% C_x position, 1.86cm above and normal to the blade surface and HW #3 which was placed at the 80.63% C_x position, 1.37cm above and normal to the blade surface. The locations of these measurements allowed for the comparison of the wake as it convected through the blade passage becoming strained and elongated. The CFD predictions showed a higher amplitude change of velocity compared to the experimental results for both probe locations with the $k-k_L-\omega$ model having the largest amplitude change. This was due to a higher peak velocity deficit produced by the upstream wake generator in the $k-k_L-\omega$ model result. The periodic velocity variation of the wake in the blade passage was similar to the experimental results indicating that both turbulence models provided adequate prediction of wake characteristics produced by the wake generator.

Unsteady Features of the Flowfield

The unsteady features of the flowfield were investigated to understand the behavior of the upstream wake on the separation and vortex shedding. The upstream wake traversing event was divided into six phases with the first phase beginning with the rod positioned directly in front of the blade leading edge and in line with the inlet flow direction. Instantaneous contour plots of z -vorticity were used to visualize the features of the flowfield for each of the six phases. The z -vorticity (Ω_z) was calculated using Eq. (11)

$$\Omega_z = (\nabla \times \vec{W}) \cdot \hat{k} \quad (11)$$

where \hat{k} is the unit vector in the z -direction and \vec{W} is the relative velocity vector. Figure 7 presents a magnified view of the vortices produced by suction surface separated shear layer for the $Re = 31,000$, $Tu = 0.5\%$ baseline case (Fig. 7(a)-(c)) compared to the $Re = 25,000$, $Tu = 0.5\%$ with the addition of wakes (Fig. 7(d)-(i)). The baseline case was divided into six phases corresponding to the same time interval as the $Re = 25,000$ case with the wakes. Phase #1 and #2 (Fig. 7(d)-(e)) shows the traversing wake affecting the boundary

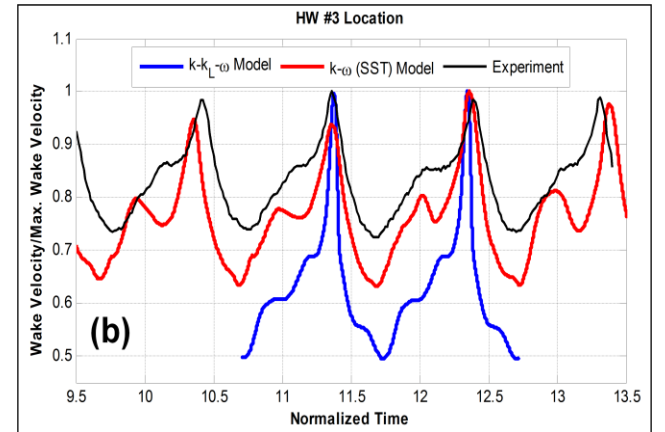
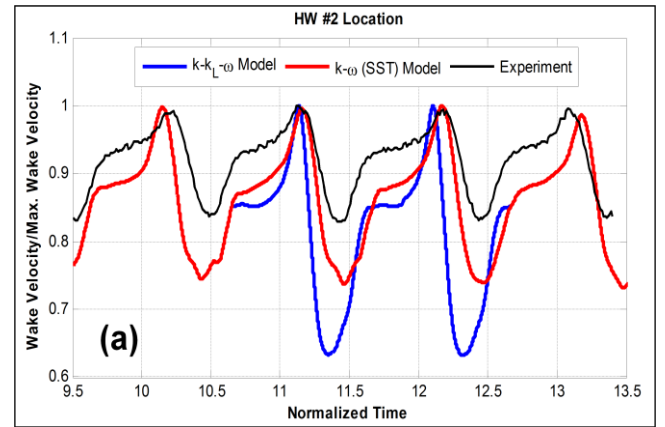


Figure 6. CFD and experimental comparison of the unsteady wake generator velocity (a) HW #2, (b) HW #3

layer separation of the pressure side of the blade. The vortex created on the pressure side was counterclockwise in direction as indicated by positive z -vorticity. The freestream pressure field in the blade passage caused the traversing wake to form into the V-shape as shown in Fig. 7(f)-(h) for Phases #3-#5. The vortices shed from the separated shear layer remained relatively small for these phases until the wake approached separation region in Phase #6. The momentum from the upstream wake forced the separated shear layer to shed another relatively larger vortex as seen in Phase #6 and #1.

The normalized vortex shedding frequencies were calculated using Eq. (12).

$$f_{norm} = \frac{f_{shed}}{f_{wake}} \quad (12)$$

The coherent vortices were significantly smaller in extent compared to the baseline case for all six phases (Phase #1, #3, #5 only shown in Fig. 8). The traversing wake reduced the separation region compared to the baseline case. The separated shear layers produced clockwise vortices that were lifted off the blade surface by the traversing wake at $f_{norm} = 5.9$ which as shed at a higher frequency compared to the baseline case at $f_{norm} = 3.9$. The separated shear layer from the trailing edge produced a similar counter-clockwise vortex ($f_{norm} = 3.1$) as in the baseline case with a normalized shedding frequency of 7.9.

Figure 8 shows z -vorticity contours of the L1A blade airfoil with upstream wake using the $k-\omega$ (SST) model for Phase #1, #3, and #5. The behavior of the wake traversing through the blade passage was similar to the $k-k_L-\omega$ model prediction including the shedding frequencies of the main vortices produced by the separated shear layers. The main difference was the behavior of the vortices produced by the separated shear layer on the blade suction surface. In Phase #1, the coherent vortex found on the suction surface (Fig. 8(a)) quickly

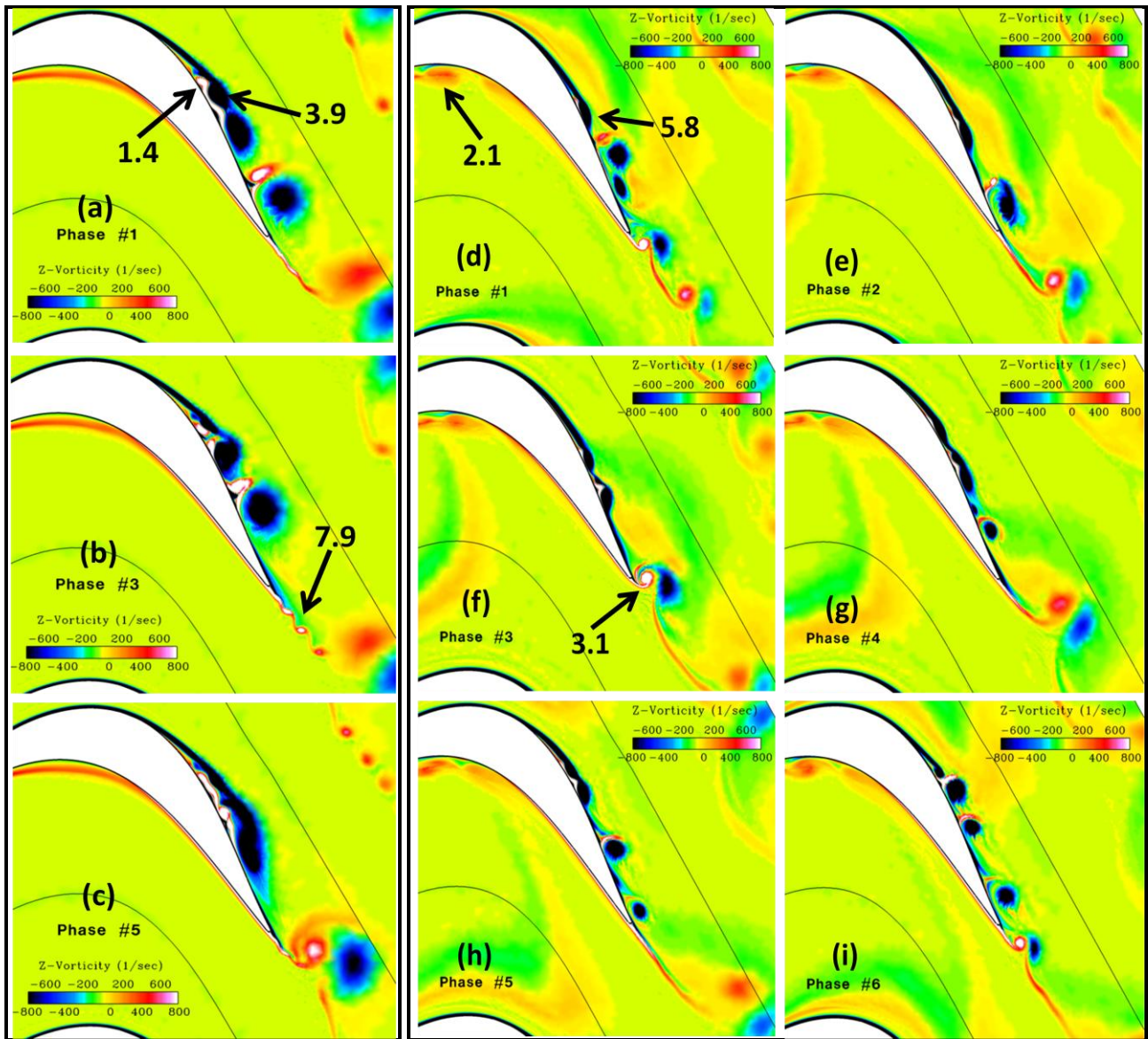


Figure 7. Comparisons of the instantaneous z-vorticity contours of the separation region at ((a)-(c)) Phase #1, #3, and #6 for the L1A blade baseline at $Re = 31,000$ and the addition of upstream wakes at $Re = 25,000$ using the $k-k_L-\omega$ model, ((d)-(i)) for Phase #1 - #6 including vortex shedding frequencies

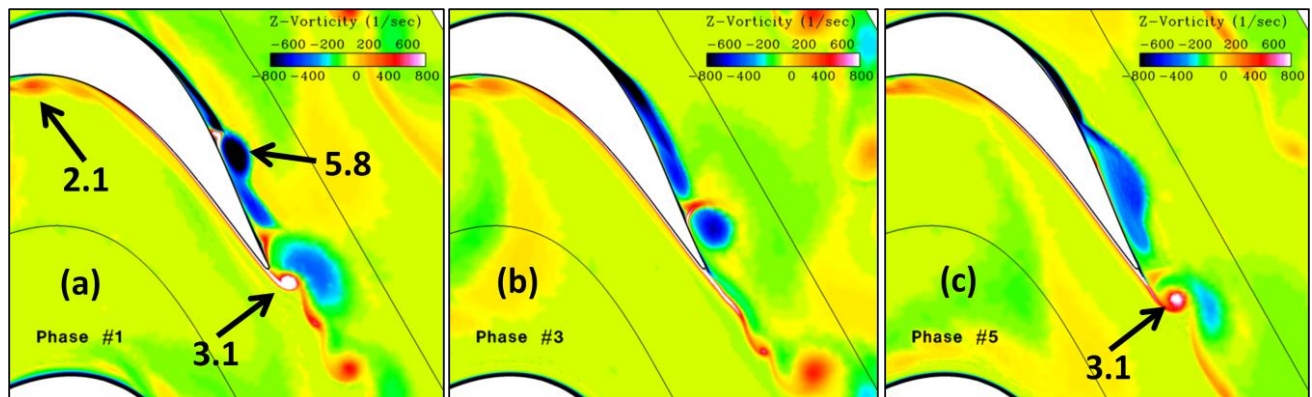


Figure 8. The instantaneous z-vorticity contours of the separation region at Phase (a) #1, (b) #3, and (c) #5 for the L1A blade with the upstream using the $k-\omega(SST)$ model wakes including vortex shedding frequencies

dissipated by Phase #3 as shown in Fig. 8(b) whereas the suction surface vortices in the $k-k_L-\omega$ model prediction remained coherent as it traversed to the wake region. The specific dissipation within the flowfield was an order of magnitude higher in the $k-\omega(SST)$ model compared to the $k-k_L-\omega$ model. Investigations of the turbulent kinetic energy (TKE) on the blade suction surface showed very little growth in TKE when the wake has already passed (Phase #3 & #4) indicating a laminar flow boundary layer in the $k-k_L-\omega$ model prediction. Transition to a turbulent boundary layer occurred when the wake passed over the blade surface reducing the size of the coherent vortices. A higher amount TKE was present on the blade suction surface in the $k-\omega(SST)$ model prediction for all phases and this attributed to the behavior of the shedding and dissipation of the vortices.

Velocity Contours

For the six phases of wake passing, velocity contours are plotted with overlaid streamlines of the velocity components. All velocity data has been made non-dimensional with respect to the inlet velocity. Presented first are the results from the PIV measurements which are shown in Fig. 9. The wake passing event can best be described by beginning with Phase #3. In this phase a very small separation bubble is present, indicated by the dark blue color, starting around 70% C_x . In this phase the wake has just entered the blade passage upstream, and is outside the field of view. Towards the tail end of the view, the contour levels are showing increased velocity indicating a closed bubble is present. This is verified with surface pressure measurements presented in the next section. Progressing to Phase #4, the separation bubble has grown in height and the streamlines indicate a small recirculation region or vortex has formed. By Phase #5, the separation bubble has grown in height and length covering a much larger region of the suction surface. The center of the recirculation has moved further downstream but the separation location has moved slightly upstream to about 67% C_x . Based on hotwire data, the wake is located roughly between 60-65% C_x in Phase #6. In this phase the separation bubble has grown to its full height and length, extending further down the suction surface. The center of the circulation region has moved upstream from the previous phase and the separation point has appeared to move downstream to 70% C_x . A change of events occurs in Phase #1 as the separation bubble appears to have shed a vortex with the location of the wake trailing behind it. The vortex is observed to roll down the blade surface in Phase #2 with the vortex partially out of the field of view and a very small separation bubble remains as shown in Phase #3.

A CFD comparison of the velocity contours for each wake phase was compared to the PIV measurements of the flowfield. Figure 10 shows Phase #1, #3, and #6 for the Menter's [24] $k-\omega(SST)$ model and the Walters and Leylek [13] $k-k_L-\omega$ model. Both models show good agreement for Phase #1 (Fig. 10(a) & 10(d)) with the PIV results where a coherent vortex formed downstream of the 80% C_x . Also, the presence of the two small vortices were shown at the 90% C_x in the $k-k_L-\omega$ model prediction whereas, the $k-\omega(SST)$ model results indicated one relatively large vortex at the 85% C_x . For Phase #3, the separation region began further upstream at approximately the 65% C_x in the $k-k_L-\omega$ model (Fig. 10(b) prediction due to the presence of a laminar flow boundary layer. In the $k-\omega(SST)$ model prediction as shown in Fig. 10(e), the separation region began near the 75% C_x and a delay in flow separation indicating a more turbulent boundary layer. As the upstream wake reached the shear layer in Phase #6 (Fig. 10(c) & 10(e)), a relatively larger vortex was shed and resulted in a reduction of the separation region compared to other phases. The affect of the negative jet from the upstream wake caused the vortex observed in Phase #6 to accelerate and coalesce with the vortex further downstream as shown in Phase #1 at 90% C_x . The wake interaction with the shed vortices was consistent with what was reported by Sarkar [12]. The coalescing of vortices was not observed

in the PIV results because it occurred out of the field of view. The $k-\omega(SST)$ model predictions showed a larger vortex present at the 95% C_x compared to the $k-k_L-\omega$ model prediction with no apparent acceleration of the vortices due the dissipation behavior as discussed previously.

Surface Static Pressure Coefficient

The CFD prediction of the static pressure coefficient distribution was compared to experimental measurements using static pressure taps around the L1A blade airfoil surface shown in Figure 11 and 13. Pressure measurements were obtained using a differential pressure transducer with a range of -50 to 200 Pa. At each pressure tap location, 60 seconds of data was acquired for the average pressure coefficient measurement. The static pressure coefficient is calculated using Eq. (13)

$$C_p = \frac{(\overline{P_{0,i}} - P_s)}{q_i} \quad (13)$$

where $\overline{P_{0,i}}$ was the average inlet total pressure, $\overline{q_i}$ was the average inlet dynamic pressure, and P_s was the static pressure on the surface of the blade. The unsteady vortex shedding observed in the CFD predictions had a significant effect on the pressure coefficient. Because of this, the unsteady envelope of the minimum and maximum pressure coefficient was included with the mean pressure coefficient distribution and the experimental results. For the L1A baseline case shown in Fig 11(a), the $k-k_L-\omega$ model result at $Re = 31,000$ over-predicted the mean peak pressure coefficient compared to the experimental results taken at $Re = 15,000$ and 40,000 by Marks *et al.* [30]. Downstream of the peak static pressure location, the CFD result predicted that the flow would separate at 62.8% C_x . This was in excellent agreement with the experimental results of approximately 62% C_x . The unsteady envelope showed a 12% variation in the peak pressure coefficient and an even greater variation starting at 80% C_x which was due to the motion of the vortices as they lifted off the blade surface and traveled downstream to the wake region. This unsteady variation caused a local pressure peak at 82% C_x in mean pressure distribution. The experimental results showed separated flow to the trailing edge. Yet, there was no evidence of the local pressure peaks within the separated flow region. This could be due to frequency response limitations and the time-averaging of the pressure transducers used in the experimental measurements. On the pressure surface of the blade, the unsteady variation due to the separated flow region near the blade leading and the trailing vortex identified in Fig. 7(b).

In Fig. 11(b), the addition of the upstream wakes on the L1A blade caused an increase in the mean peak pressure value compared to the baseline case, which resulted in a higher blade loading for both the CFD and experimental results. The CFD over-predicted the mean peak pressure coefficient by 14% compared to the experimental results, which was similar to the baseline case. The separation point was located further downstream at 69.9% C_x with the addition of the upstream wakes, compared to the baseline separation point at 62.8% C_x for the CFD predictions. This is consistent with the experimental results which show separation occurring approximately at 67%-68% C_x . Both the CFD predictions and experimental measurements show a similar trend downstream of the peak pressure location. First, the region of constant pressure due to the separation region was smaller with the upstream wakes compared to the baseline case, which indicates a reduction in losses. Secondly, in both of the experimental and CFD results, the pressure coefficient at 78% C_x slightly increased due to the motion of the vortices as they lifted off the blade surface. A similar trend was seen in Stieger *et al.* [35] using fast response Kulite transducers. This spike was smaller and located more upstream compared to the baseline CFD case. This was due to the reduction in size of the vortices created by the separated shear with the addition of

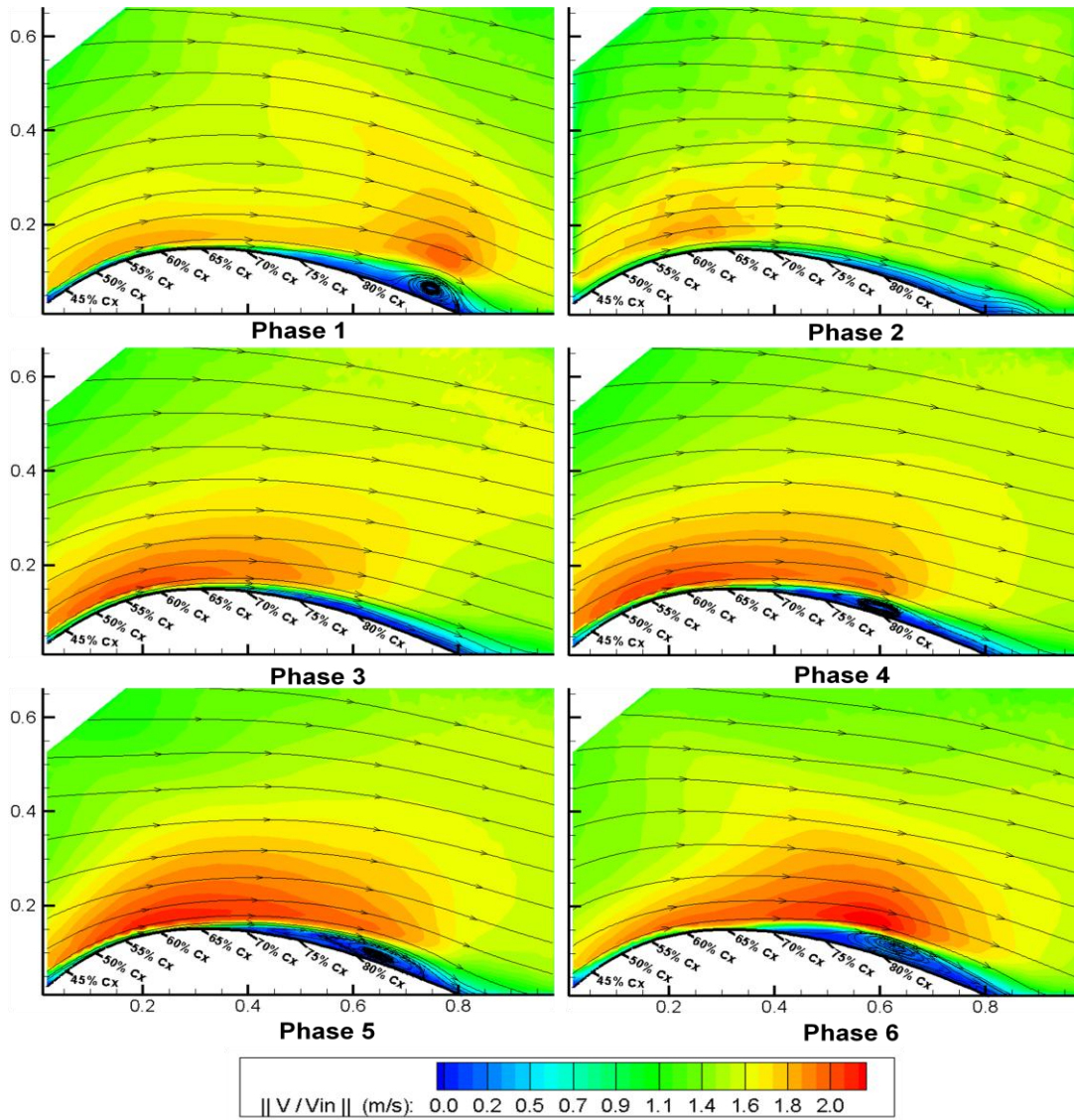


Figure 9. PIV contours of non-dimensional average velocity for six phases of the wake passing

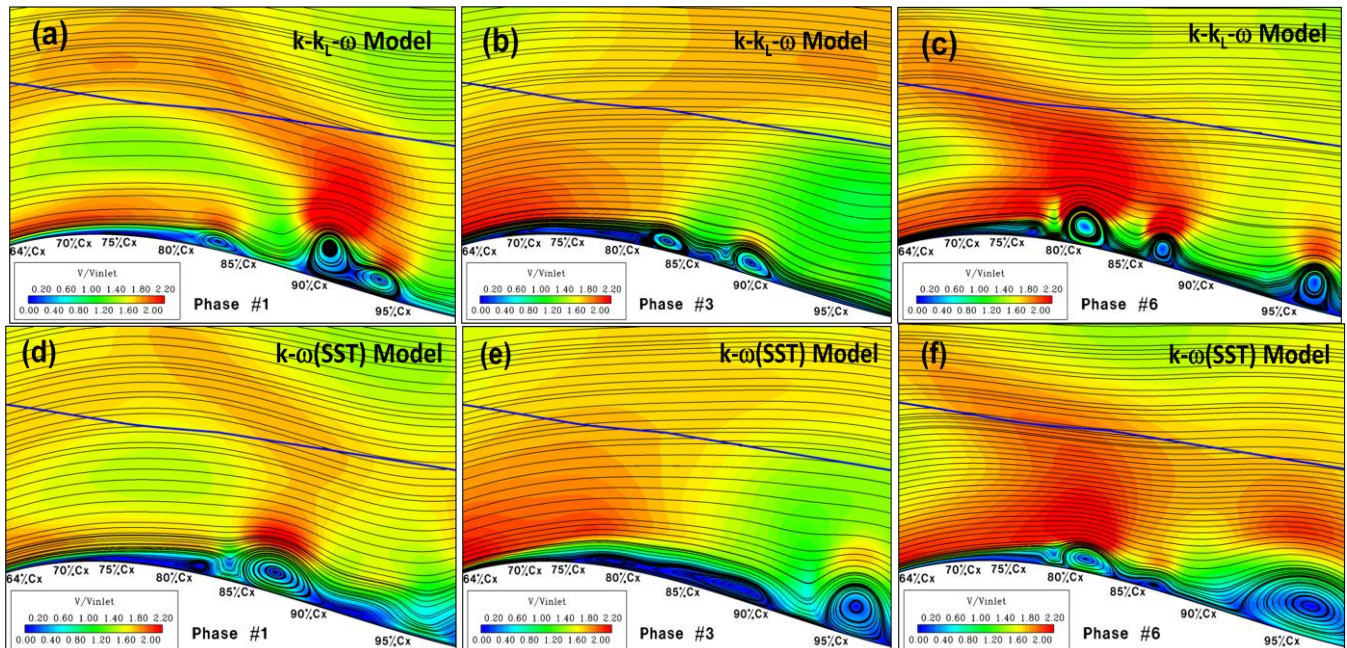


Figure 10. CFD comparison of the velocity magnitude with superimposed streamlines for the (a)-(c) $k-k_L-\omega$ model and (d)-(f) $k-\omega$ (SST) model predictions. View of the flowfield oriented similar to PIV measurements

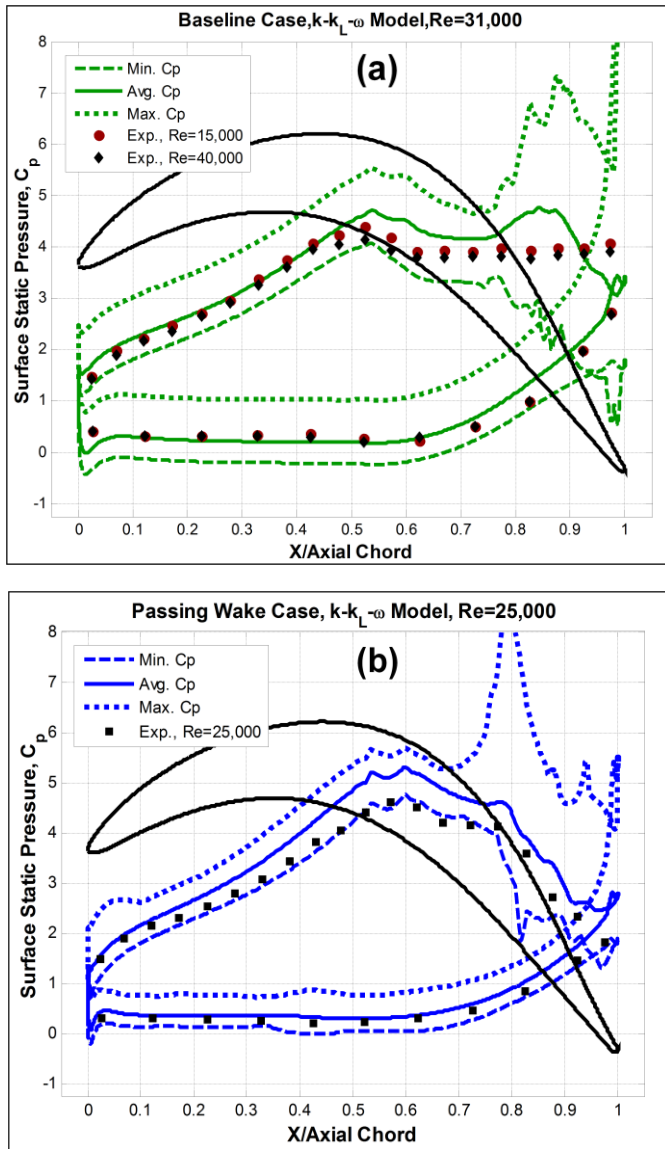


Figure 11. Comparison of the predicted surface static pressure coefficient with experiments for the L1A blade (a) baseline at 31,000 and (b) the addition of upstream wakes at Re = 25,000 using the $k-k_L-\omega$ model including unsteady C_p envelope

the upstream wakes. The unsteady envelope showed a variation of 6% in the peak pressure coefficient with experimental peak pressure value contained within the unsteady envelope range. The increased momentum from the upstream wakes caused significantly higher local peaks of the maximum pressure compared to the L1A baseline case starting downstream of 70% C_x . Similar trends in the L1A baseline case for the unsteady pressure envelop were observed where, unsteady variation originated from the separation region and trailing edge vortex. Investigations of the freestream turbulence, shown in Fig. 12, reveal the upstream wake produced an elevated freestream turbulence intensity greater than 10% (Fig. 12(b)). This turbulence intensity was significantly higher compared to the baseline case and convected through the blade passage to the separation region. This re-energized the boundary layer and caused a decrease in the separated flow present on the blade suction surface.

The $k-\omega(SST)$ model prediction of the mean static pressure distribution indicated the peak pressure distribution was over-predicted by 16% compared to the experimental result as shown in Fig. 13. Yet, the experimental pressure distribution remained within the unsteady envelop as the $k-k_L-\omega$ model predictions. Downstream of the peak pressure coefficient, $k-\omega(SST)$ model prediction did not show an indication of a closed separation bubble on the blade suction surface unlike the $k-k_L-\omega$ model result. The unsteady envelope showed a peak at 78% axial chord location due to the vortical structures from the separated shear layer. As Figure 9 indicated, those vortical structures did not remain coherent and quickly dissipated on the blade surface. Figure 12(c) shows the $k-\omega(SST)$ model predicted the highest level of freestream turbulence in the blade passage due to the passing wake. The flow directly below the quickly dissipating vortex was relatively well attached to the blade surface as a result the mean pressure distribution showed no indication of a flow separation. This higher level of turbulence contributed to the vortices quickly dissipating on blade suction surface. The Walters and Leylek [13] $k-k_L-\omega$ model provided the most effective prediction of the upstream wake generator effect on the L1A blade airfoil pressure loading compared to the Menter's [24] $k-\omega(SST)$ model.

Phase-Averaged Behavior

Certain flow features of the velocity field can be made apparent through the use of perturbation velocity. The perturbation velocity is defined as the difference between the ensemble averaged and time-averaged velocity fields [36-39]. Figure 14 shows the PIV and CFD comparison of the perturbation velocity and streamlines for Phases #1 and #6. In this figure, the location of the wake was apparent and emerged as a negative jet described by Meyer [40] and confirmed using the same perturbation velocity technique by Stieger and Hodson [36]. For Phase #6, both the PIV and CFD results showed

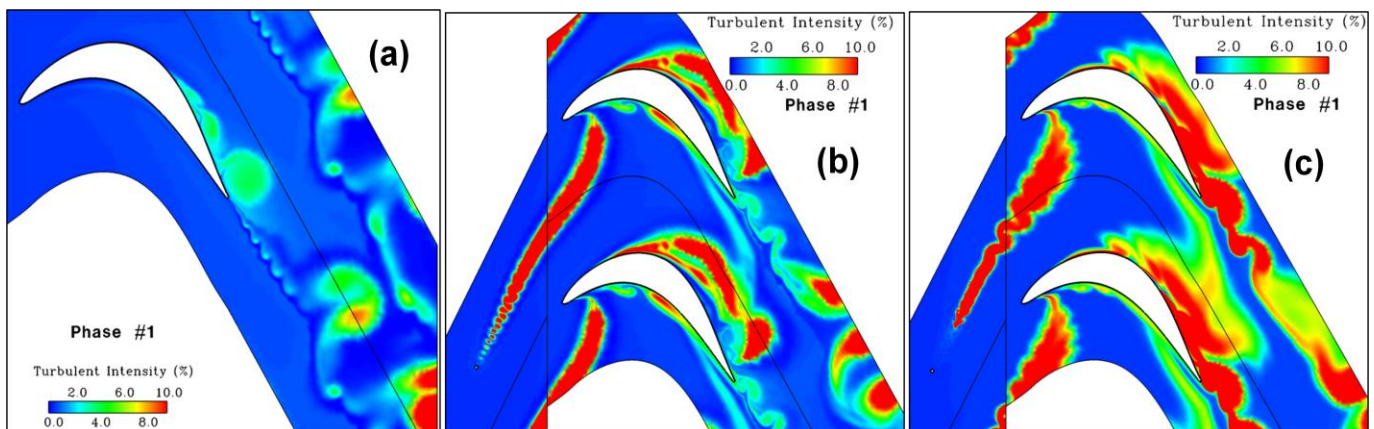


Figure 12. Comparison of the freestream turbulence intensity for the (a) L1A blade baseline case at Re = 31,000 and the addition of upstream wakes at Re = 25,000 using (b) the $k-k_L-\omega$ model and (c) the $k-\omega(SST)$ model

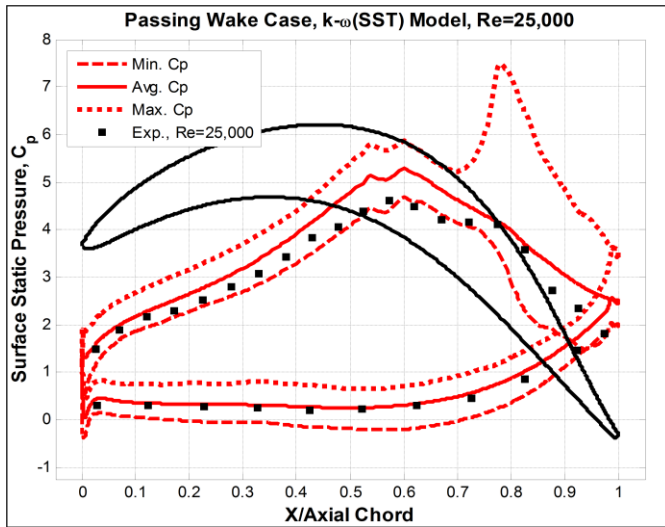


Figure 13. Comparison of the predicted surface static pressure coefficient with experiments for the L1A blade with upstream wakes using the $k-\omega(SST)$ model including unsteady C_p envelope

similar behavior. The wake was strained through the blade passage and impinged upon the blade surface, just upstream of the separation bubble. The dashed line in Fig. 14(a) indicated where the negative jet gets split into two streams; one pointing downstream accelerating the flow and the other point upstream retarding the flow. This behavior was mentioned in several studies [12,36-39]. In Phase #1 (Fig. 14(c)-(d)), both the CFD and PIV results showed good agreement of the perturbation vector field characteristics. As the wake progressed downstream it convected overtop the separation region, and lead to a reduction in the size of the separation region in shown Fig. 9 and Fig. 10(a).

CONCLUSIONS

The flow field of the L1A blade airfoil subjected to traversing upstream wakes was experimentally and computationally investigated at an inlet Reynolds number of 25,000. The L1A blade profile represented a high-lift aft-loaded low pressure turbine blade design that was prone to flow separation at Reynolds numbers below 40,000 and ideal for use in flow separation control studies. This study used upstream wakes that were generated by a circular cylinder traversing in the pitchwise direction. In this study, upstream traversing wakes was used to simulate the periodic flow field associated with rotor/vane flow interactions encountered in a multistage LP turbine geometry, where wakes shed from an upstream vane propagate and impinge on a downstream rotor. It is important that the upstream wake effect be used for the development of highly loaded LP turbine blade airfoil with improved low Reynolds performance. Velocity field measurements using two-dimensional planer Particle Image Velocimetry and CFD simulations were used to investigate the L1A blade flow field behavior in periodic unsteady conditions. The CFD using the Walters and Leylek [13] $k-k_L-\omega$ transitional flow model and Menter's [24] $k-\omega(SST)$ model predictions were compared to experimental cascade results to determine which RANS CFD model could predict the unsteady L1A blade flow field at low inlet Reynolds number.

Investigations of the wake generator characteristics were completed to characterize the wake that impinged on the L1A blade airfoil. Both the $k-k_L-\omega$ and $k-\omega(SST)$ models predicted the flow to be laminar with a separation location in agreement with classical theory that produced a discrete vortex shedding pattern. The CFD predictions of the wake showed a larger peak velocity deficit than the experimental hotwire measurements which could be attributed to imperfections in the wake generator shape and the rod vibrations while traversing through the wind tunnel resulting in more turbulent wake in the experimental setup. Comparisons with hotwire measurements in the blade passage showed both turbulence models predicted the velocity variation of the

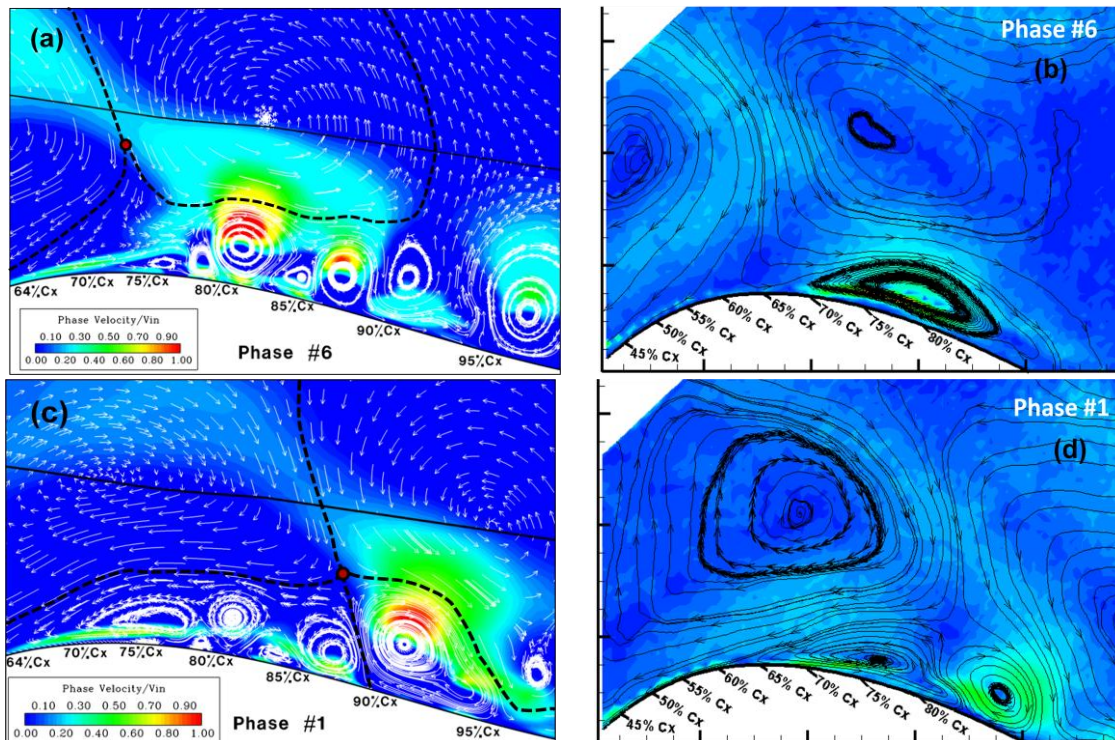


Figure 14. Comparisons of the perturbation velocity magnitude contours with superimposed streamlines for the (a)-(c) CFD prediction using $k-k_L-\omega$ model and (b)-(d) PIV measurements for Phase #1 & #6

wake similar to experimental results and provided adequate prediction of wake generator flow characteristics.

The traversing wakes had a significant effect on the flow separation and the vortex shedding. The suction surface shear layer produced unsteady vortices that were significantly smaller than the L1A blade without upstream wakes and caused the separation region to reduce. Differences were found in the behavior of the vortices produced with the $k-\omega(SST)$ model prediction producing larger vortices that dissipated across the aft-portion of the blade whereas the $k-k_L-\omega$ model the vortices remained relatively small and coherent as it traversed into the wake region. A similar flow structure was reported by Sarkar [12] using the higher fidelity LES CFD method. This was attributed to boundary layer being mostly laminar in the $k-k_L-\omega$ model predictions whereas the $k-\omega(SST)$ model the boundary layer was found to be more turbulent and with a higher amount of dissipation.

The best agreement with the PIV measurements was achieved using the $k-k_L-\omega$ model. The behavior of the velocity flow field due to the separation region and the vortex formation was adequately predicted for each wake phasing event when compared with the PIV measurements. Investigations in the perturbation velocity field found the same behavior mentioned in several other studies [12,36-39] where the wake acted as a negative jet. This negative jet causes the fluid in an individual wake segments to convect toward, and impinge on the suction surface. Thus, downstream of wake center the negative jet accelerated the flow, while upstream of the wake center, the negative jet decelerated the flow [39]. The Walters and Leylek [13] $k-k_L-\omega$ model provided the most effective prediction of the upstream wake generator effect on the L1A blade airfoil pressure loading where the addition of upstream wake caused an increase the blade loading and caused the separation location to move further downstream.

This study has contributed a successful application PIV measurements and CFD using the Walters and Leylek [13] $k-k_L-\omega$ transitional flow model to investigate low Reynolds number aerodynamic flow effects in recently developed highly loaded LP turbine blade airfoil geometry. The $k-k_L-\omega$ model was characterized and an effective model for improved prediction of unsteady wake effects associated with LP turbine flows. Also, CFD methods using RANS models such as Walters and Leylek [13] model and the more advanced Menter's [15] correlation-based transition model could provide the same improve prediction of the separation and transitional flow characteristics at a reduced computational cost than the higher fidelity LES and DNS methods. This supports that the $k-k_L-\omega$ flow model can provide the same prediction capability for the more complicated unsteady flow fields encountered in a multistage LP turbine blade geometry.

ACKNOWLEDGMENTS

The work presented was sponsored by the Air Force Research Laboratory, Propulsion Directorate Turbine Engine Division. Computing resources were provided by the U.S. Department of Defense Major Shared Resource Center, High Performance Computing facility at Wright Patterson AFB, OH. The L1A LP turbine blade airfoil geometry was provided by J. Clark from the Turbine Engine Division, AFRL. Also, the authors thank S. Gorrell from Mechanical Engineering Department at Brigham Young University for use of the high-priority computational hours on the super-computing systems. The mentorship of D. Rabe and M. Wolff from the Turbine Engine Division, AFRL, was key to the successful completion of this research.

NOMENCLATURE

C_p	=	pressure coefficient
C_x	=	axial chord
f_{shed}	=	vortex shedding frequency
f_{norm}	=	normalized vortex shedding frequency
f_{wake}	=	wake-passing frequency

k	=	kinetic energy
\hat{k}	=	unit vector in the z-direction
l_m	=	average turbulent length scale
P	=	pressure; production term
q	=	dynamic pressure
Re	=	Reynolds number based on inlet velocity and axial chord
s	=	blade pitch
t	=	time
LP	=	low pressure
$LSWT$	=	low speed wind tunnel
Tu	=	freestream turbulence intensity
u	=	velocity magnitude
\bar{W}	=	relative velocity vector
y^+	=	nondimensional wall distance
Z_w	=	Zweifel blade force coefficient
α	=	flow angle
μ	=	molecular viscosity
ν	=	kinematic viscosity
ρ	=	density
Ω_z	=	z-vorticity
ω	=	specific dissipation rate
Subscripts		
0	=	total
in	=	inlet
int	=	integrated
L	=	laminar
out	=	outlet

REFERENCES

- [1] Volino, R. J., and Hultgren, L. S., "Measurements in Separated and Transitional Boundary Layers Under Low-Pressure Turbine Airfoil Conditions," ASME J. Turbomachinery, Vol. 123, pp. 189-197, 2001.
- [2] Haselbach, F., Schiffer, H. P., Horsman, M., Dressen, S., Harvey, N., and Read, S., "The Application of Ultra High Lift Blading in the BR715 LP Turbine," ASME J. Turbomachinery, Vol. 124, pp. 45-51, 2002.
- [3] Curtis, E. M., Hodson, H. P., Banieghbal, M. R., Denton, J. D., and Howell, R. J., "Development of Blade Profiles for Low-Pressure Turbine Applications," ASME J. Turbomachinery, Vol. 119, pp. 531-538, 1997.
- [4] Schobeiri, M. T., Öztürk, B., and Ashpis, D. E., "Effect of Reynolds Number and Periodic Unsteady Wake Flow Condition on Boundary Layer Development, Separation, and Intermittency Behavior Along the Suction Surface of a Low Pressure Turbine Blade," ASME J. Turbomachinery, Vol. 129, pp. 92-107, 2007.
- [5] Schulte, V., and Hodson, H. P., "Unsteady Wake-Induced Boundary Layer Transition in High Lift LP Turbines," ASME J. Turbomachinery, Vol. 120, pp. 28-35, 1998.
- [6] Zhang, X. F., and Hodson, H. P., "Combined Effects of Surface Trips and Unsteady Wakes on the Boundary Layer Development of an Ultra-High-Lift LP Turbine Blade," ASME J. Turbomachinery, Vol. 127, pp. 479-488, 2005.
- [7] Pluim, J., Memory, C., Bons, J., and Chen, J. P., "Designing a High Fidelity Wake Simulator for Research using Linear Cascades," ASME Paper No. GT2009-59276, 2009.
- [8] Howell, R. J., Ramesh, O.N., Hodson, H.P., Harwey, N. W., and Schulte, V., "High Lift and Aft-Loaded Profiles for Low-Pressure Turbines," ASME, J. of Turbomachinery, Vol. 123, pp. 181-188, 2001.
- [9] Hodson, H. P., "Boundary Layer and Loss Measurements on the Rotor of an Axial Flow Turbine," ASME Journal of

- Engineering for Gas Turbines and Power, Vol. 106, No. 2, 1984.
- [10] McQuilling, M., Ph.D. Dissertation, "Design and Validation of a High-Lift Low Pressure Turbine Blade", Department of Mechanical and Materials Engineering, Wright State University, 2007.
 - [11] Wissink, J.G., "DNS of Separating, Low Reynolds Number Flow in a Turbine Cascade with Incoming Wakes," International J. Heat and Fluid Flow, Vol. 24, pp. 626-635, 2003.
 - [12] Sarkar, S., "Identification of Flow Structures on a LP Turbine Blade Due to Periodic Passing Wakes," ASME J. Fluid Engineering, Vol. 130, pp. 1-10, 2008.
 - [13] Walters, D.K., and Leylek, J.H., "A New Model for boundary Layer Transition Using a Single Point RANS Approach," Journal of Turbomachinery, Vol. 126, pp. 193-202, 2004.
 - [14] Suzen, Y.B., Huang, P.G., Volino, R.J., Corke, T.C., Thomas, F.O., Huang, J., Lake, J.P., and King, P.I., "A Comprehensive CFD Study of Transitional Flows in Low-Pressure Turbines Under a Wide Range of Operating Conditions," AIAA Paper No. 2003-3591.
 - [15] Menter, F.R., Langtry, R.B., Likki, S.R., Suzen, Y.B., Huang, P.G., and Volker, S., "A Correlation-Based Transition Model Using Local Variables- Part I: Model Formulation," Journal of Turbomachinery, Vol. 128, pp. 413 - 422, 2006.
 - [16] Praisner, T.J., and Clark, J.P., "Predicting Transition in Turbomachinery, Part I - A Review and New Model Development," ASME Paper No. GT-2004-54108.
 - [17] Langtry, R.B., Menter, F.R., Likki, S.R., Suzen, Y.B., Huang, P.G., and Volker, S., "A Correlation-Based Transition Model Using Local Variables- Part II: Test Cases and Industrial Applications," Journal of Turbomachinery, Vol. 128, pp. 423 - 434, 2006.
 - [18] Praisner, T.J., Grover, E.A., Rice, M.J., and Clark, J.P., "Predicting Transition in Turbomachinery, Part II - Model Validation and Benchmarking," Journal of Turbomachinery, Vol. 129, pp 14 - 22, 2007.
 - [19] Walters, D.K., and Leylek, J.H., "Computational Fluid Dynamics Study of Wake-Induced Transition on a Compressor-Like Flat Plate," Journal of Turbomachinery, Vol. 127, pp. 52-63, 2005.
 - [20] Sanders, D.D., O'Brien, W.F., Sondergaard, R., Polanka, M.D., and Rabe, D.C., "Predicting Separation and Transitional Flow in Turbine Blades at Low Reynolds Numbers," ASME Paper No. GT-2008-50283.
 - [21] Sanders, D.D., "CFD Modeling of Separation and Transitional Flow in Low Pressure Turbine Blades at Low Reynolds Numbers," Ph.D. Dissertation, Mechanical Engineering Dept., Virginia Tech, 2009.
 - [22] Sanders, D.D., O'Brien, W.F., Sondergaard, R., Polanka, M.D., and Rabe, D.C., "A Mixing Plane Model Investigation of Separation and Transitional Flow at Low Reynolds Numbers in a Multistage Low Pressure Turbine," AIAA Paper No. 2009-1467.
 - [23] Sanders, D.D., O'Brien, W.F., Sondergaard, R., Polanka, M.D., and Rabe, D.C., "Turbulence Model Comparisons for Mixing Plane Simulations of a Multistage Low Pressure Turbine at Low Reynolds Numbers," AIAA Paper No. 2009-4928.
 - [24] Menter, F. R., "Two-Equation Eddy-Viscosity Turbulence Models for Engineering Applications," AIAA Journal, Vol. 32, No. 8, pp. 1598-1605, 1994.
 - [25] Sondergaard, R., Rivir, R., Bons, J., "Control of Low-Pressure Turbine Separation Using Vortex Generator Jets," Journal of Propulsion and Power, Vol 18, No. 4, pp. 889-895, 2002.
 - [26] Rivir, R., Sondergaard, R., Bons, J., Yurchenko, N., "Control of Separation in Turbine Boundary Layers," AIAA 2004-2201.
 - [27] McQuilling, M., Ph.D. Dissertation, "Design and Validation of a High-Lift Low Pressure Turbine Blade," Department of Mechanical and Materials Engineering, Wright State University, 2007.
 - [28] Clark, J. and Koch, P. "Benchmark Turbines for the Guidance of Design System Improvement," Turbine Engine Technology Symposium, Dayton, OH, Sept. 14, 2006.
 - [29] Volino, R. J., "Separated Flow Measurements on a Highly Loaded Low-Pressure Turbine Airfoil," ASME J. Turbomachinery, Vol. 132, pp. 1-10, 2010.
 - [30] Marks, C., Sondergaard, R., Estevadeordal, J., Wolff, M., "PIV Investigation of a Highly-Loaded LPT Blade Using a Curved Laser Sheet," AIAA Paper No. 2009-301.
 - [31] Nessler, C., Marks, C., Sondergaard, R., Wolff, M., "An Investigation of Losses on a Highly Loaded Low Pressure Turbine Blade with Unsteady Wakes," AIAA Paper No. 2009-302.
 - [32] Nessler, C., Marks, C., Sondergaard, R., and Wolff, M., "PIV Investigation of Periodic Unsteady Wakes over a Highly Loaded LPT Blade," AIAA Paper No. 2009-5107
 - [33] ANSYS Fluent® User's Manual Version 12.0.16, 2009.
 - [34] Schlichting, H., 1979, Boundary Layer Theory, 7th ed., McGraw-Hill, New York.
 - [35] Stieger, R. D., Hollis, D., Hodson, H. P., 2004, "Unsteady Surface Pressures Due to Wake-Induced Transition in a Laminar Separation Bubble on a Low-Pressure Cascade," ASME J. Turbomachinery, Vol. 126, pp. 544-550.
 - [36] Stieger, R. D., and Hodson, H. P., "The Unsteady Development of a Turbulent Wake Through a Downstream Low-Pressure Turbine Blade Passage," ASME J. Turbomachinery, Vol. 127, pp. 388-394, 2005.
 - [37] Stieger, R. D., and Hodson, H. P., "The Transition Mechanism of Highly Loaded Low-Pressure Turbine Blades," ASME J. Turbomachinery, Vol. 126, pp. 536-543, 2004.
 - [38] Uzol, O., Zhang, X.F., Cranstone, A., and Hodson, H., "Investigation of Unsteady Wake-Separated Boundary Layer Interaction Using Particle-Image-Velocimetry," ASME Paper GT2007-28099, 2007.
 - [39] Hodson, H.P. and Howell, R.J., "Bladerow Interaction, Transition, and High-Lift Aerofoil in Low-Pressure Turbines," Annual Review of Fluid Mechanics. Vol. 37, pp. 71-98, 2005.
 - [40] Meyer, R. X., "The Effect of Wakes on the Transient Pressure and Velocity Distributions in Turbomachines," Transactions of the ASME, p.1544, 1958.

Curved laser-sheet for conformal surface flow diagnostics

Jordi Estevadeordal · Christopher Marks ·
Rolf Sondergaard · Mitch Wolff

Received: 12 January 2010 / Revised: 30 July 2010 / Accepted: 14 August 2010 / Published online: 29 August 2010
© US Government 2010

Abstract Three-dimensional surface illumination using curved laser-sheet techniques is introduced for optical flow measurements in conformal curved surfaces. The illumination method is applicable to many different optical-based flow measurement techniques, with this paper focusing on application to flow visualization and particle image velocimetry. A brief discussion and example of curved laser-sheet generation is given followed by an example of the technique applied to PIV of low Reynolds number transitional flow around a low-pressure turbine blade.

1 Introduction

A technique has been developed to obtain illumination in planes that are conformable to curved surfaces in three-dimensional (3D) spaces. The method can be applied to optical flow measurement techniques such as particle

image velocimetry (PIV). Its potential is, however, for applications to other flow or combustion diagnostics currently using planar-sheet illumination such as planar laser-induced fluorescence (PLIF), which could benefit from curved surfaces measurements. This investigation focuses on a demonstration for PIV, which is currently one of the strongest diagnostic tools for testing complex flow fields due to its capabilities of providing instantaneous flow-field data in two-dimensional (2D) planes (Raffel et al. 2007). Experimentally obtained 2D velocity flow fields are useful for both qualitative and quantitative understanding of complex flows. Data can be obtained quickly and in a large spatial area providing experimental data that can be directly compared to CFD results (Estevadeordal et al. 2008; Reynolds et al. 2010). Two-dimensional PIV is most common and the simplest to setup, but it provides velocity components in only two directions. In an attempt to better understand the three-dimensional (3D) nature of complex flows and obtain the third velocity component, a variety of techniques have been devised (Raffel et al. 2007). Examples include stereoscopic PIV, volumetric PIV, holographic PIV, and dual-plane PIV. Most of the above-mentioned techniques require specialized calibration or image correlation methods beyond those typically used for 2D single-plane PIV.

The present conformal surface technique is applicable to 3D surfaces. The general technique (Estevadeordal et al. 2008) was introduced for studying internal aerodynamics flows where axisymmetric or circumferential plane diagnostics would benefit from the conformal surface technique. However, since 3D spatial laser shapes could be readily visualized seeding flows with particles, the technique was not limited to simple surfaces and it was foreseen that it could be capable of tracking complex 3D surfaces such as complex blade and wing shapes; it was

J. Estevadeordal
ISSI, Dayton, OH, USA

Present Address:
J. Estevadeordal (✉)
GE Global Research, One Research Circle, Niskayuna,
NY 12309, USA
e-mail: Jordi.Estevadeordal@ge.com

C. Marks · R. Sondergaard · M. Wolff
US Air Force Research Laboratory, Propulsion Directorate,
1950 Fifth Street, WPAFB, Greene, Montgomery,
OH 45433, USA
e-mail: Christopher.Marks@wpafb.af.mil

R. Sondergaard
e-mail: Rolf.Sondergaard@wpafb.af.mil

M. Wolff
e-mail: James.Wolff2@wpafb.af.mil

also suggested that moving 3D surfaces such as those of unmanned air vehicles (UAV) wings could be tracked in time. Motion of the optical components that form the curved laser-sheet produces changes in the curvature shape and can change the illuminated 3D space and also change it in time. A more complex camera system including customized optics, several views, and optional high-speed capabilities would be needed for imaging.

In this investigation, a simple demonstration example of the use of a curved laser-sheet for flow diagnostics around a curved wall is presented. The principle is demonstrated by flow visualization and PIV around an airfoil to capture flow details around and near the curved wall and curved flow streamsurfaces. The demonstration of the technique is applied to a 2D airfoil having curvature in only one dimension, and the experimental setup and post processing are comparable to that of 2D PIV. The curved laser-sheets allow high fidelity measurement of flow velocity in areas and viewing planes that had previously been difficult. The present demonstration of the technique employs standard optical components such as a combination of cylindrical lenses or curved mirrors. Customized optics designs would allow using less optical elements and could deliver more complex curved laser shapes.

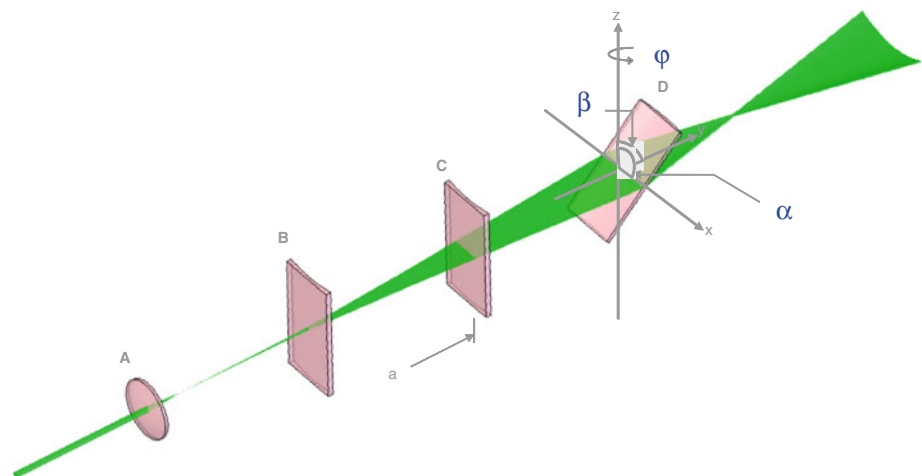
2 Curved laser-sheet generation

Setup of the illumination system differs from traditional PIV in that it requires generation of a laser-sheet that is curved to follow or conform to the wall curvature or flow streamlines along a curved surface. This can be accomplished by using a modified laser-sheet-forming lens system (the current approach) or by designing an optical lens or mirror system to form a given shape. The laser-sheet curvature effect is similar to that of a flat laser-sheet

intersecting not normally onto optical windows with curvature. If an application requires a simple conical-shaped laser-sheet, a series of sheet-forming lenses typical of those used to generate a flat laser-sheet can be used with the addition of a cylindrical lens (lens D in Fig. 1) rotated at various angles in the optical path. The cylindrical lens inclinations, distances, and physical properties (such as thickness and focal length) determine the shape and thickness of the curved sheet. Tilting the lens by an angle β in the x-axis will generate a curve in the sheet related to the geometry of the cylindrical lens.

Figure 2 shows a curved laser-sheet generated in this manner with a red diode laser for alignment purposes. It is also shown by ray-tracing modeling (Fig. 2a, c) and demonstrated with a two cylindrical lens setup (one rotated). Figure 2a, b show a curved sheet created by tilting the last cylindrical lens by 45 degrees in the x-direction. Notice that curve in Fig. 2a is parabolic so that the rate of curvature is not constant along the entire curve. By rotating the lens in the z-axis as shown in Fig. 2c, d, the area illuminated is shifted to the right to an area with high curvature at the left portion of the sheet and less curvature on the right. These images, if flipped and copied vertically, can generate a closer shape all around an airfoil, around a cylinder, and other surface shapes often encountered in fluid dynamics. A single customized optical element could also be designed to deliver curved-sheet shapes of constant or variable thickness. Since these curved laser-sheets allow tracking of curved shapes in space, it is plausible that they can be used for illumination of flow regions such as boundary layer or wall flows in conformal surfaces of airfoils, blades, and circumferential planes in turbomachinery (Estevadeordal et al. 2008). In addition, since moving the optical elements can produce changes in the laser curvature, the motion of surfaces (e.g., wing motions in flying insects or UAV) could also be tracked in time.

Fig. 1 An example of curved laser-sheet generation by adding a rotated, off-the-shelf convex cylindrical lens (lens D) to standard sheet-forming optical system



In this introductory application example, the curvature of the 3D surface is only in one dimension and not very severe, and the object plane can be readily projected into the image plane and the magnification variations readily established (Fig. 3). An example of 2D axisymmetric unwrapping transformation can be found in Esteveadeordal

and Kleis (1995). The optical setup was also designed so that working distance (WD), field-of-view (FOV), and depth-of-field (DOF) yielded the object plane in focus. Stereo-PIV-like techniques can be used to bring the plane in focus if necessary (Fig. 4a). Complex 3D shapes would require more complex unwrapping image registration

Fig. 2 Example of a two lens curved laser-sheet modeled in a ray-tracing program

(a and c) and demonstrated with a red diode laser (b and d). The second lens has orientation:

a and b $\varphi = 0^\circ$, $\beta = 45^\circ$;

c and d $\varphi = 45^\circ$, $\beta = 45^\circ$

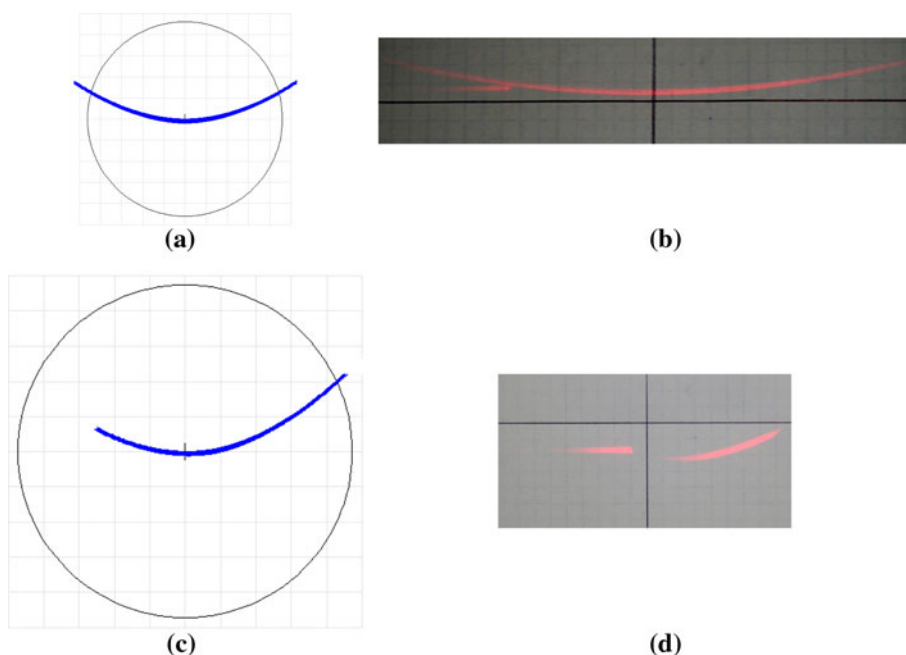


Fig. 3 Examples of magnification projection of a streamwise curved surface (a) and spanwise grid image variation of the 2D curve (b)

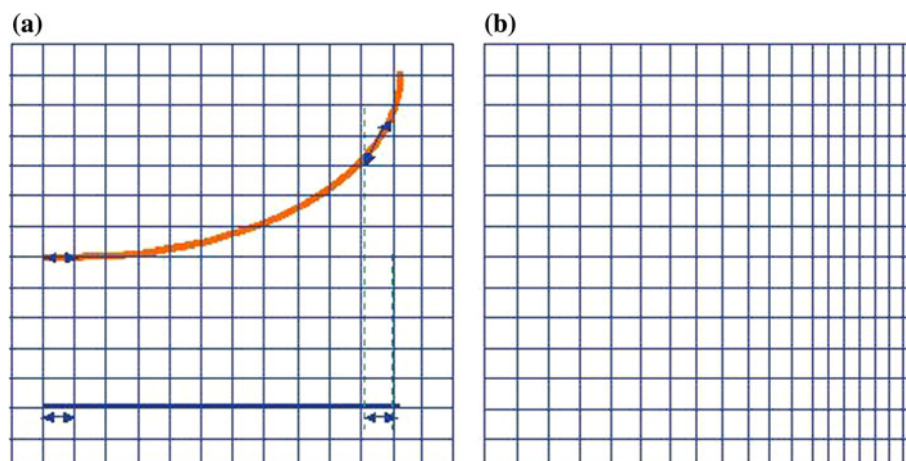
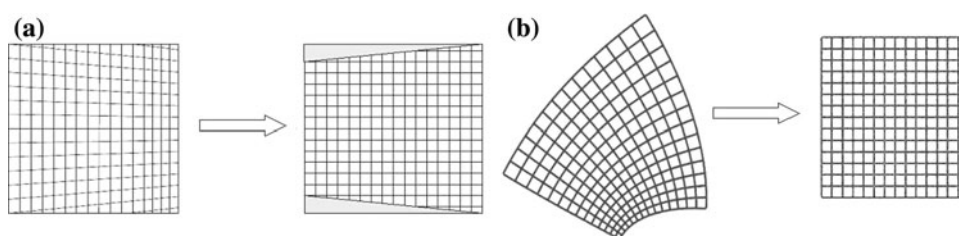


Fig. 4 Schematic of planar stereoscopic unwrapping (Raffel et al. 2007) (a) and conformal mapping of a 3D curved surface (b)



techniques (Fig. 4b) such as the photogrammetric approaches used in applications of pressure- and temperature-sensitive paint diagnostics on 3D surfaces (Liu and Sullivan 2004). In the current experiment, a grid pasted on the airfoil such as that shown in Fig. 3b sufficed to calculate the magnification on the FOV.

Although the benefits of the technique can be readily appreciated in the qualitative flow visualization form, the real usefulness resides in its potential for quantitative measurements, such as velocimetry. In the present example, velocimetry is based on using PIV, and the technique accuracy can be approached in an equivalent manner to PIV techniques that use a flat planar sheet with the exception of additional uncertainty due to magnification factor variation in the FOV, a typical situation encountered in stereo-PIV and off-axis PIV. Magnification factor then relates particle displacement in the image plane to displacement in the curved plane and must be accurately accounted for when calculating velocity from the correlated displacement field. In general, a conformal mapping (Fig. 4b) would be needed. In this investigation, the curvature is only in one dimension, and magnification correction can be related more straightforward. When needed, advanced 3D image registration algorithms and accuracy studies should be performed; many of these algorithms can be found, for example, in 3D surface diagnostic studies and applications such as pressure sensitive paints (Liu and Sullivan 2004). Many of the algorithms used in these techniques include very accurate and robust correlation-based techniques. Correlation techniques are also the main calculation tool in PIV, making the data very accurate. Examples of this robustness applied to out-of-focus, off-axis PIV, and streaky transonic particle shadow

velocimetry (PSV) can be found in the literature (Langford et al. 2005; Estevadeordal and Goss 2005).

A schematic of the optical arrangement in the current application example is shown in Fig. 5. In the setup shown Δx is the corresponding displacement in pixels in the image plane and Δs is the displacement in the curved plane illuminated by the laser. Velocity \hat{S} in the curved plane is calculated by:

$$\hat{S} = \frac{\Delta x}{\Delta t \cdot M}$$

where Δx is the displacement in the image plane, and Δt is the time between the two images (cross correlation PIV is implied). M is the magnification factor which is a function of x and given by:

$$M(x) = \frac{\Delta x}{\Delta s}$$

where Δs is incremental movement in the laser-sheet plane. The units of M are chosen to relate pixel units to physical units (e.g., mm).

The relationship between \hat{S} and velocity u and v (standard coordinates in object normal direction) is:

$$|V| = \sqrt{u^2 + v^2} = \hat{S}$$

assuming two dimensional flow.

For a general distorted 3D shape, the camera optics path could include optical elements that compensate for the otherwise out-of-focus image plane at the expense of magnification distortions; this is similar to an extension of the Scheimpflug arrangement used in stereo PIV or when viewing object planes at an angle (Raffel et al. 2007). The introductory example presented here does not use arrangements such as the Scheimpflug arrangement of stereo or off-angle views mostly because the plane curvature is not large and it is in focus (large enough depth of field).

Another concern of the technique is related to the effect of out-of-plane motion and its off-normal view. In one aspect, the curved laser-sheet minimizes the out-of-plane motion precisely because it is designed to follow the streamsurfaces of the flow. This is advantageous scenario, especially when compared to laser-sheet arrangements that have laser-sheet normal to the main flow, as some stereo-PIV use. Nonetheless, turbulence, for example, generates 3D motions and out-of-plane motion happens. As with PIV designs, the combination of laser-sheet thickness and the time between the two frames should be such that particles do not move out of the laser-sheet. Still, extreme scenarios like that depicted in the laser-sheet of Fig. 6 can occur where the off-normal view can severely distort the image particle positions. Examples of possible arrangements allowing correction of the curvature are suggested in the schematics of Fig. 6. Indeed, it can be shown that hidden

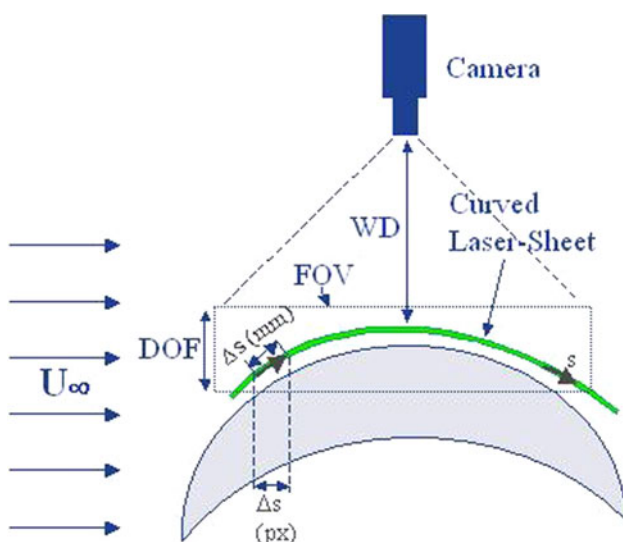


Fig. 5 Schematic of current application example optical arrangement

Fig. 6 Some optical correction schemes for extreme views: multi-camera allows capture various views (a), Scheimpflug arrangement corrects distortion (b), mirror arrangement allows off-angle views (c), and customized optical element can correct the distorted view (d)

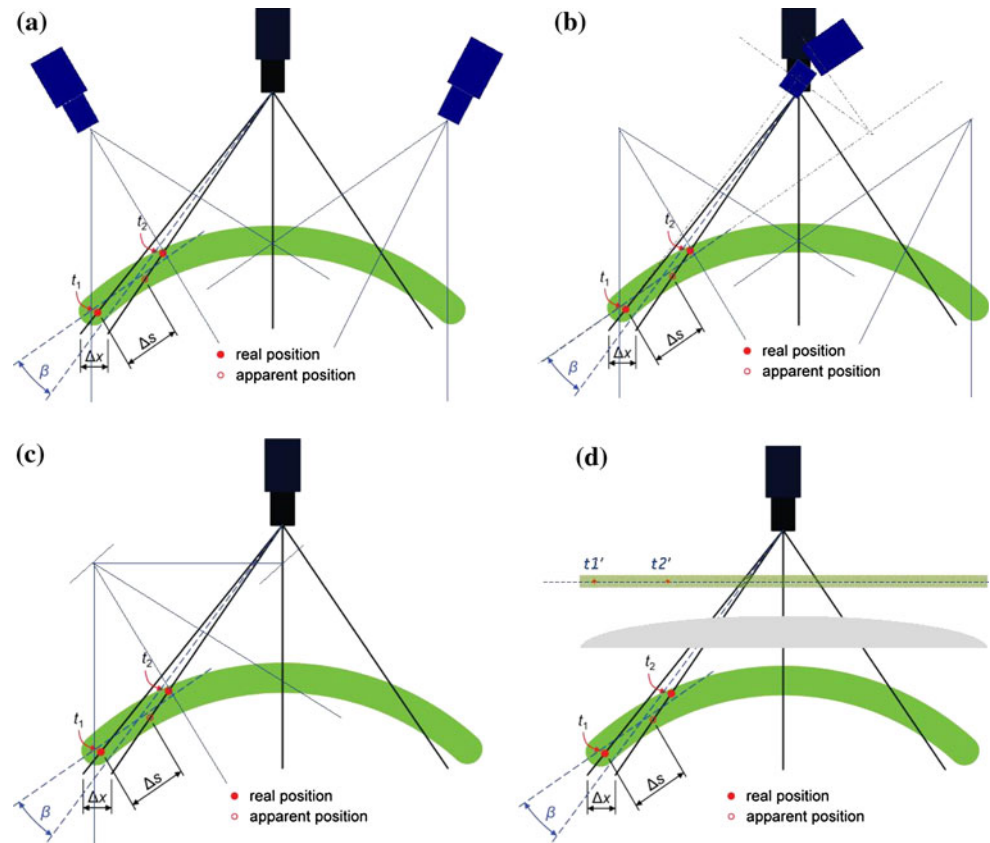
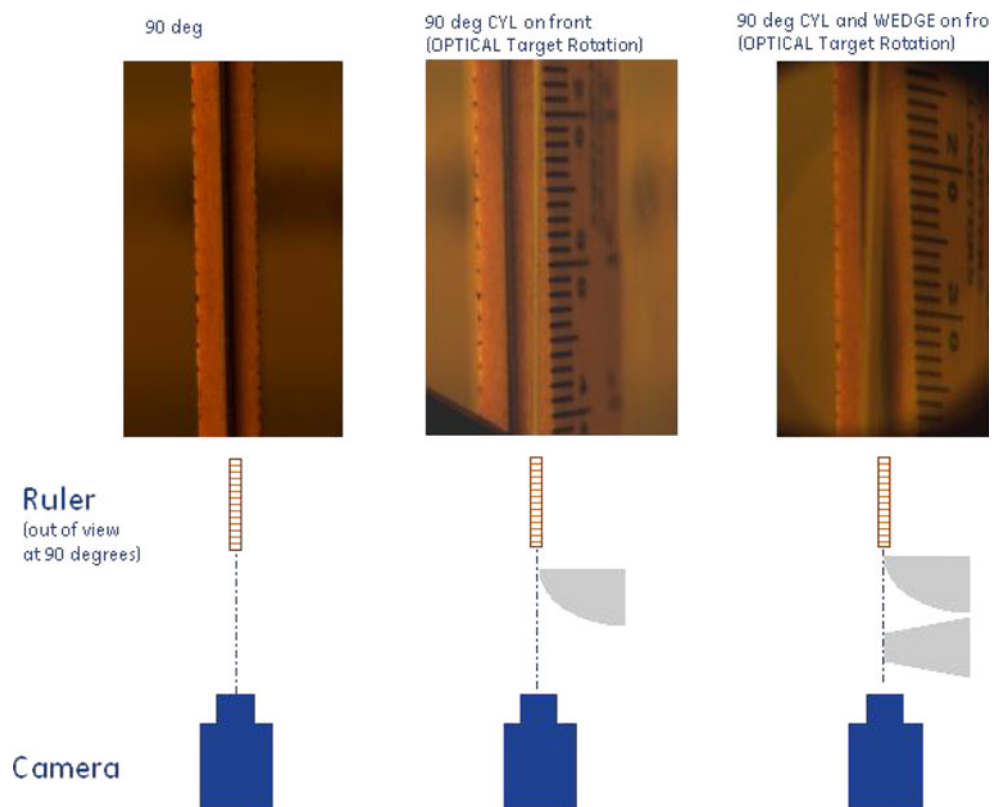


Fig. 7 Optical unwrapping of images from off-angle targets using simple optic elements (*cylindrical and wedge lenses*); a customized optical element could bring highly off-axis object planes to focused image planes



views due to severe off-normal angles can be readily corrected as shown with simple optics in Fig. 7, where a target ruler at 90° can be imaged by combination of cylindrical and wedge lenses; this suggests that complex customized lenses can do the photogrammetric correction avoiding or minimizing software corrections.

The technique as described above and demonstrated in the next section can be used for measurements in curved planes aligned with conical surfaces or streamsurfaces. Commercial optical programs can be used to aid in the inverse design of the sheet-forming system and will certainly make the experimental setup easier in practice. A ray trace-based code to design optical elements that will accurately match a given curved shape is currently being developed by the authors for use in their experiments.

3 Application of curved-laser technique to 2D PIV of low-pressure turbine blade flows

Often the focus of studies on transitional flow around low-pressure turbine (LPT) blades is on the flow behavior in the viscous region near the wall. The walls are curved in shape and attached laminar, transitional, and turbulent boundary layer streamlines primarily follow the shape of the curved wall. Curved walls make it difficult to use traditional PIV in the spanwise viewing direction near the wall. Several researchers (Burgmann et al. 2006; Zhang et al. 2008) have successfully applied 2D planar PIV in the spanwise direction plane parallel to the suction side of an airfoil or flat plate with adverse pressure gradient (Lang et al. 2004), by taking advantage of the low curvature of the blade in the region of interest. Burgmann et al. 2006 obtained spanwise scanning PIV near the wall and through a separation bubble on the suction side of a SD7003 airfoil at Reynolds numbers of 2.0×10^4 – 6.0×10^4 . The area of interest on the suction side of LPT blades, which have large turning angles, is often near the point of highest curvature that makes imaging in the spanwise direction using a planar sheet difficult. The conformal surface PIV technique using a curved laser-sheet allows spanwise imaging very near the surface of a highly loaded LPT blade.

As an example of the application of this technique, a laser-sheet was curved parallel to the wall profile at the aft end of the suction side of a LPT blade in a 2D linear cascade at low Reynolds number. The L1A blade profile can be found in Marks et al. (2009) and Bons et al. (2008) and full experimental details of the cascade in Marks et al. (2009). A schematic of the experimental arrangement is shown in Fig. 8.

PIV data was acquired in the blade normal direction using a flat laser-sheet and in the spanwise viewing direction by a curved laser-sheet. The laser was a New Wave Solo 120XT, its beam was split into two paths, and

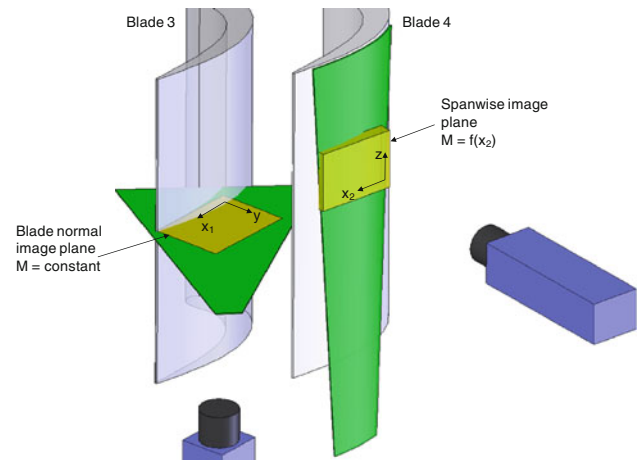


Fig. 8 Curved laser technique applied to PIV of flow over the suction surface of a linear cascade of LP turbine blades

double-exposure images were recorded with PCO 1600 cameras. Off-the-shelf optical elements consisting of a series of spherical and cylindrical lenses were arranged to generate a curved laser-sheet that closely matched the suction surface blade profile from 60 to 90% axial chord in the field of view. The spanwise viewing camera lens was a 105 mm set at $f\#2.8$ and located ~ 100 cm away from blade four (middle of the cascade). The optical path passed through two flat 1.25-cm-thick Lexan sheets from the wind tunnel outer wall and the cascade tailboard. The FOV was 124×93 mm. The curved laser-sheet was brought into focus in the camera by employing a large F-number (small aperture), and a grid on the blade profile was used for magnification calibration across the field of view (FOV). As discussed earlier, an additional source of uncertainty is introduced by magnification factor variation across the

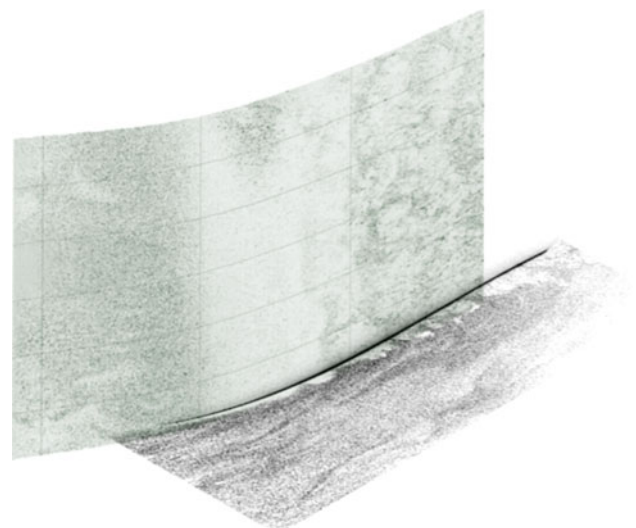
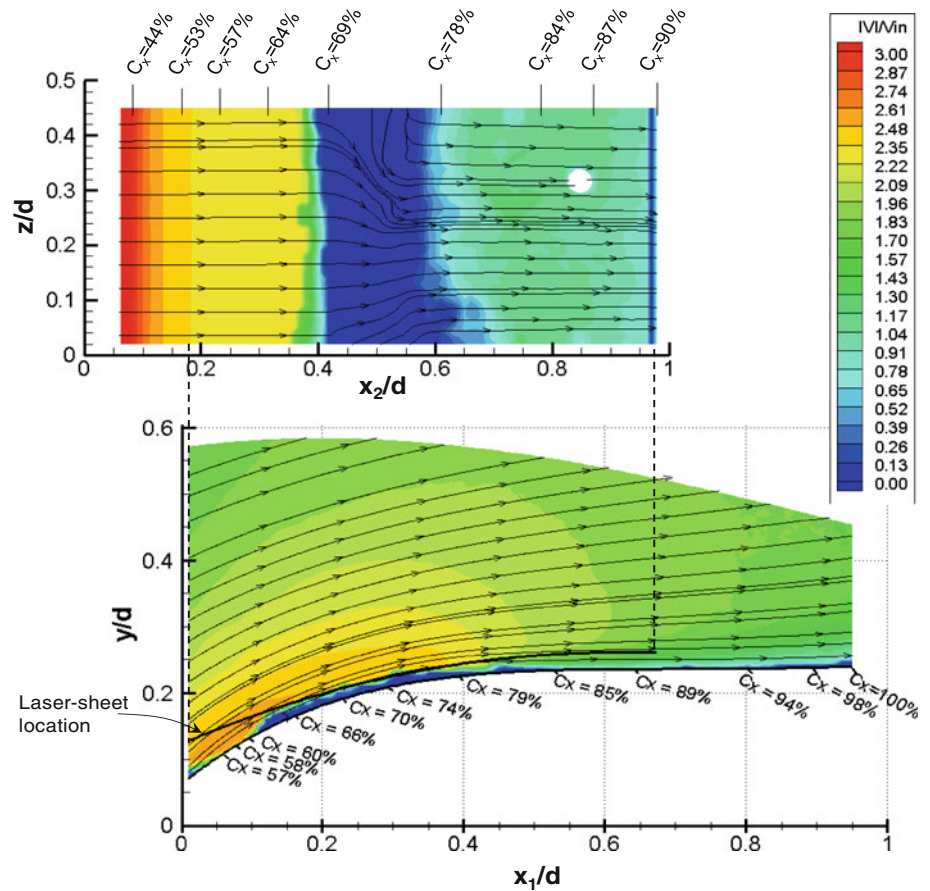


Fig. 9 Flow visualization in the blade normal plane and spanwise image plane combined into one image. The curved laser-sheet following the blade shape is shown with some grid lines for reference

Fig. 10 Averaged blade normal plane PIV flow field (*bottom*) and corresponding spanwise plot (*top*) at $Re = 6 \times 10^4$, $Tu = 4\%$



FOV, which must be accurately accounted for when calculating velocity from the correlated displacement field.

Figure 9 shows a flow visualization image in two perpendicular planes, the blade normal and spanwise directions. Samples of averaged PIV velocity fields calculated using parallel-PIV (PPIV) software (McCray et al. 2005) taken in the spanwise direction using the curved laser-sheet, and in the blade normal direction using a flat laser-sheet, are shown in Fig. 10 for a Reynolds number of 6.0×10^4 . The spanwise velocity plot is positioned above the blade normal plot with the blade axial positions in each view aligned in the vertical direction. Approximately 125 image pairs were used to calculate the average velocity fields for the blade normal and spanwise viewing directions. Under such low Reynolds number conditions, a closed reattaching separation bubble is present, and the curved laser-sheet passed through the top portion of the bubble. The curved laser-sheet location is shown as a black line in the bottom plot of Fig. 10. The laser location and thickness (1 mm) were identified by fitting photo-sensitive paper normal to the blade surface and using the laser to burn a line onto the paper.

An instantaneous flow visualization image taken in the spanwise direction is shown in Fig. 11 as well as corresponding unfiltered velocity vectors. The instantaneous

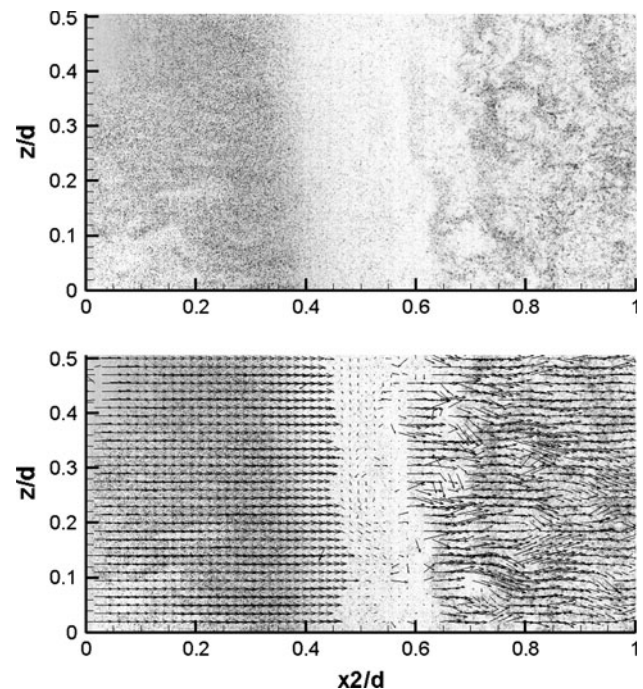


Fig. 11 Instantaneous flow visualization (*top*) and velocity vectors (*bottom*) above the suction surface of a low-pressure turbine blade in the spanwise viewing direction acquired using a curved laser-sheet at $Re = 6.0 \times 10^4$, $Tu = 4\%$ (image colors are inverted)

image reveals uniform laminar flow, then near zero velocity in the separation bubble, and followed by areas of unsteady, chaotic, and turbulent flow. The averages shown in Fig. 10 and the instantaneous image and vector field shown in Fig. 11 demonstrate the potential of this technique.

4 Conclusion

Images taken in the spanwise viewing direction around the suction side of a LPT blade at low Reynolds number are examples of flow visualization and PIV data obtained using the new curved laser-sheet technique conformable to curved surfaces. Off-the-shelf optical components were used to generate the curved laser-sheet in this work, but custom optical elements could be used to create curved sheets that match streamsurfaces or body surfaces for conformal surface flow diagnostics. This technique has been demonstrated using common 2D PIV methods but could be applied to a variety of optical flow measurement methods and is capable of providing views that have previously been unobtainable.

Acknowledgments This work was performed under sponsorship from the Air Force Office of Scientific Research, Thomas Beutner Contract Monitor. The authors would like to thank John Clark, designer of the LPT blade studied in this work, for his support and guidance. Chase Nessler is acknowledged for many productive discussions of the topic.

References

- Bons J, Pluim J, Gompertz K, Bloxham M, Clark J (2008) The application of flow control to an aft-loaded low pressure turbine cascade with unsteady wakes. ASME GT2008-50864
- Burgmann S, Brucker C, Schroder W (2006) Scanning PIV measurements of a laminar separation bubble. *Exp Fluids* 41:319–326
- Estevadeordal J, Goss L (2005) An investigation of particle-shadow velocimetry (PSV) for transonic-flow applications, AIAA 2005-5009, 35th AIAA Fluid Dynamics Conference and Exhibit 6–9 June 2005, Toronto, Canada
- Estevadeordal J, Kleis SJ (1995) Gradient-zone erosion by extraction in solar ponds. *J Sol Energy Eng* 117(2):144
- Estevadeordal J, Gorrell S, Puterbaugh S (2008) PIV Measurements of blade-row interactions in a transonic compressor for various operating conditions. AIAA 2008-4700
- Lang M, Rist U, Wagner S (2004) Investigations on controlled transition development in a laminar separation bubble by means of LDA and PIV. *Exp Fluids* 36:43–52
- Langford M, Minton C, Ng W, Estevadeordal J, and Burdisso R (2005) Fan flow control for noise reduction part 2: investigation of wake-filling techniques, AIAA-2005-3026, AIAA/CEAS Aeroacoustics Conference, 2005 May, Monterey
- Liu T, Sullivan JP (2004) Pressure and temperature sensitive paints. Springer, NY
- Marks C, Sondergaard R, Wolff M, Estevadeordal J (2009) PIV Investigation of a highly loaded lpt blade using a curved laser-sheet. AIAA 2009-0302
- McCray TW, Estevadeordal J, Puterbaugh SL (2005) Parallel computing for linux clusters—application to particle image velocimetry. AIAA 2005-1385
- Raffel M, Willert C, Wereley S, Kompenhans J (2007) Particle image velocimetry: a practical guide. Springer, New York
- Reynolds S, Gorrell S, Estevadeordal J (2010) PIV analysis on the effect of stator loading on transonic blade-row interactions. GT2010-22576, IGTI Turbo Expo, July 2010, Glasgow, Scotland
- Zhang W, Hain R, Kahler C (2008) Scanning PIV investigation of the laminar separation bubble on a SD7003 airfoil. *Exp Fluids* 45:725–743

APPENDIX G

CFD Modeling of Separation and Transitional Flow in Low Pressure Turbine Blades at Low Reynolds Numbers

Darius Demetri Sanders

A dissertation submitted to the faculty of the Virginia Polytechnic
Institute and State University in partial fulfillment of the requirements
for the degree of

Doctor of Philosophy

In

Mechanical Engineering

Walter F. O'Brien, Chair
Clinton L. Dancey
Marc D. Polanka
Douglas C. Rabe
Rolf Sondergaard
Danesh Tafti

September 28, 2009

Blacksburg, VA

Keywords: Low Pressure Turbines, Low Reynolds Number, CFD, Turbulence Modeling,
Unsteady Aerodynamics

CFD Modeling of Separation and Transitional Flow in Low Pressure Turbine Blades at Low Reynolds Numbers

By

Darius Demetri Sanders
Dr. Walter F. O'Brien, Chair
Mechanical Engineering
(ABSTRACT)

There is increasing interest in design methods and performance prediction for turbine engines operating at low Reynolds numbers. In this regime, boundary layer separation may be more likely to occur in the turbine flow passages. For accurate CFD predictions of the flow, correct modeling of laminar-turbulent boundary layer transition is essential to capture the details of the flow. To investigate possible improvements in model fidelity, both two-dimensional and three-dimensional CFD models were created for the flow over several low pressure turbine blade designs. A new three-equation eddy-viscosity type turbulent transitional flow model originally developed by Walters and Leylek was employed for the current RANS CFD calculations. Flows over three low pressure turbine blade airfoils with different aerodynamic characteristics were simulated over a Reynolds number range of 15,000-100,000, and predictions were compared to experiments. The turbulent transitional flow model sensitivity to inlet turbulent flow parameters showed a dependence on free-stream turbulence intensity and turbulent length scale. Using the total pressure loss coefficient as a measurement of aerodynamic performance, the Walters and Leylek transitional flow model produced adequate prediction of the Reynolds number performance in the Lightly Loaded blade. Furthermore, the correct qualitative flow response to separated shear layers was observed for the Highly Loaded blade. The vortex shedding produced by the separated flow was largely two-dimensional with small spanwise variations in the separation region. The blade loading and separation location was sufficiently predicted for the Aft-Loaded L1A blade flowfield. Investigations of the unsteady flowfield of the Aft-Loaded L1A blade showed the shear layer produced a large separation region on the suction surface. This separation region was located more downstream and significantly reduced in size when impinged upon by the upstream wakes, thus improving the aerodynamic performance consistent with experiments. For all cases investigated, the Walters and Leylek transitional flow model was judged to be sufficient for understanding the separation and transition characteristics, and superior to other widely-used turbulence models in accuracy of describing the details of the transitional and separated flow. This research characterized and assessed a new model for low Reynolds number turbine aerodynamic flow prediction and design improvement.

Acknowledgements

First and foremost, the author would like to thank my family and close friends for all their support, patience, and encouragement in pursuit of this degree. The author would like to thank Dr. Walter O'Brien, Dr. Douglas Rabe, Dr. Marc Polanka, Dr. Rolf Sondergaard, Dr. Clinton Dancey and Dr. Danesh Tafti for serving on my PhD committee. The work presented was sponsored by the Air Force Research Laboratory, Propulsion Directorate, Turbine Engine Division. Computing resources were provided by the AFRL, Department of Defense Super-Computing Resource Center, High Performance Computing facility at Wright Patterson AFB, OH. The author is grateful to Dr. Hugh Thornburg from AFRL DSRC and Frank Kelec from ANSYS®, who are acknowledged for assistance with mesh generation, CFD simulation set-up, and helpful discussions. Also, Dr. Donald P. Rizzetta from Air Vehicles Directorate, AFRL and Dr. Chunill Hah from NASA Glenn Research Center are acknowledged for their helpful advice. Also, the author is thankful to Dr. Steve Gorrell for the use of high priority CHALLENGER CPU hours in order to complete CFD simulations in a timely manner.

Table of Contents

Acknowledgements.....	iii
Table of Contents.....	iv
List of Figures.....	viii
List of Tables.....	xiv
Nomenclature.....	xv
1. Introduction.....	1
1.1 Research Program Goals.....	3
1.2 Low Pressure Turbine Aerodynamic Flow Effects.....	4
1.2.1 Laminar Flow Boundary Layers.....	6
1.2.2 Transitional Flow Boundary Layers.....	12
1.2.3 Turbulent Flow Characteristics.....	16
1.2.4 Turbulent Flow Boundary Layers.....	22
1.3 CFD Methods of Predicting Low Reynolds Number Effects in LPT Blades.....	24
1.3.1 Direct Numerical Simulation CFD Method.....	25
1.3.2. Large Eddy Simulation CFD Method.....	27
1.3.3. Reynolds Averaged Navier-Stokes (RANS) CFD Method.....	29
1.4 Transition Modeling.....	30
1.4.1. e^N Method.....	30
1.4.2. Dorney et al. Model.....	32
1.4.3. Suzen et al. Model.....	33
1.4.4. Prasnier and Clark Model.....	34
1.4.5. The Menter et al. γ - Re_θ Model.....	35
1.4.6. The Moore and Moore MARV Reynolds Stress Model.....	37
1.4.7. Walters and Leylek $k-k_L$ - ω Model.....	38
2. Description of Experimental Cascade Configurations Utilized in the Investigation.....	41
2.1 Linear Cascade Geometry.....	41
2.2 The AFRL Low Speed Wind Tunnel.....	42
2.2.1 Design of Moving Bar Wake Generator.....	43
2.3 Measurement Techniques.....	45
2.3.1 Surface Static Pressure Measurements.....	45
2.3.2 Wake Loss Measurements.....	45
2.3.3 Particle Image Velocimetry.....	46
D. Sanders.....	iv

2.4 Description of LPT Blade Airfoil Geometries.....	48
2.4.1 The “Lightly Loaded” LPT Blade Airfoil.....	49
2.4.2 The “Highly Loaded” LPT Blade Airfoil	51
2.4.3 The “Aft-Loaded L1A” LPT Blade Airfoil	55
3. Computational Model Methodology.....	61
3.1 Computational Grid Design Method.....	61
3.1.1 Grid Technique for the 2D Cascade CFD Models.....	63
3.1.2 Aft-Loaded L1A Blade with Upstream Wake Generators.....	67
3.1.3 Grid Technique for the 3D Cascade CFD Models.....	69
3.2 CFD Numerical Scheme	70
3.3 The Choice of Turbulence Model	71
3.3.1 Comparisons of the RANS Turbulence Models	73
3.4 CFD Boundary Conditions	78
3.5 Computational Resources	79
3.6 CFD Post Processing and Analysis.....	80
4. The Lightly Loaded Blade CFD Results.....	82
4.1 Performance Prediction at Different Inlet Reynolds Numbers	82
4.2 Effect of Inlet Turbulence Parameters on Transition and Performance Predictions	87
4.2.1 Inlet Turbulent Length Scale Study	88
4.2.2 Inlet Turbulence intensity Study	92
4.3 Summary of Results.....	98
5. The Highly Loaded Blade CFD Results	99
5.1 Two-Dimensional CFD Comparisons with Experimental Results	99
5.1.1 Surface Static Pressure Coefficient.....	100
5.1.2 Boundary Layer Velocity Profiles	102
5.1.3 Unsteady Features of the Flowfield	105
5.1.4 Total Pressure Loss Coefficient Predictions	112
5.2 Three-Dimensional CFD Comparisons with Experimental Results	115
5.2.1 Surface Static Pressure Coefficient.....	115
5.2.2 Mean Velocity Boundary Layer Profiles	116
5.2.3 Unsteady Features of the Flowfield	117
5.2.4 Total Pressure Loss Coefficient Predictions	121
5.3 Summary of Results	122
6. The Aft-Loaded L1A Blade CFD Results	124

6.1 CFD Predictions at Low Inlet Turbulence intensity	124
6.1.1 Surface Static Pressure Coefficient.....	125
6.1.2 Velocity Contours and Boundary Layer Profiles	127
6.1.3 Unsteady Features of the Flowfield	130
6.1.4 Total Pressure Loss Coefficient Predictions	135
6.2 CFD Predictions at High Inlet Turbulence intensity	137
6.2.1 Surface Static Pressure Coefficient.....	137
6.2.2 Mean and RMS Velocity Contours.....	139
6.2.3 Boundary Layer Velocity Profiles	144
6.2.4 Total Pressure Loss Coefficient Predictions	146
6.3 Summary of Results	148
7. Aft-Loaded L1A Blade with Upstream Wake Generators.....	151
7.1 CFD Predictions for the Wake Generator	152
7.1.1 Surface Static Pressure Coefficient.....	152
7.1.2 Unsteady Features of the Flowfield	153
7.1.3 Downstream Wake Characteristics	155
7.2 CFD Predictions for the Aft-Loaded L1A Blade	159
7.2.1 Unsteady Features of the Flowfield	159
7.2.2 Comparison of Phase Velocity Contours with Experimental PIV Results	166
7.2.3 Mean Flow Comparisons of the Surface Static Pressure and Boundary Layer Profiles	172
7.2.4 Total Pressure Loss Coefficient Predictions	177
7.3 Summary of Results	178
8. Summary and Conclusions	181
8.1 Future Work	187
References	190
Appendix I. Comparisons of the Fluent Formulations of Walters and Leylek's Transitional Flow Model.....	193
A.1 Fluent Formulations of the $k-k_L-\omega$ Model	194
A.1.1 Fluent 6.3 $k-k_L-\omega$ Model	194
A.1.2 Fluent 12.0 $k-k_L-\omega$ Model	195
A.2 CFD Predictions at Low Inlet Turbulence intensity	196
A.2.1 Mean Surface Static Pressure Coefficient.....	197
A.2.2 Velocity Contours and Boundary Layer Profiles	198
A.2.3 Unsteady Features of the Flowfield	200

A.2.4 Total Pressure Loss Coefficient	202
A.3CFD Predictions at High Inlet Turbulence intensity.....	204
A.3.1 Mean Surface Static Pressure Coefficient.....	204
A.3.2 Velocity Contours and Boundary Layer Profiles.....	205
A.3.3 Total Pressure Loss Coefficient	207

List of Figures

Figure 1.1. Illustration of passing wake behavior across a rotor blade row [5]	5
Figure 1.2. Endwall flow within a turbine blade passage [6].....	6
Figure 1.3. Diagram of typical boundary profile (a) and description of displacement thickness (b) [7]	7
Figure 1.4. Diagram of laminar and turbulent boundary layer flow over a flat plate [7].....	8
Figure 1.5. Inviscid flow past a cylinder (a) pressure distribution (b) and freestream velocity (c) on the cylinder surface [7]	9
Figure 1.6. The effect of pressure gradients on boundary layer profiles [8].....	11
Figure 1.7. The neutral stability curve [10]	14
Figure 1.8. Diagram of the Types of Boundary Layer Turbulent Transition [3]	16
Figure 1.9. Energy spectrum for a turbulent low in log-log scales [11]	21
Figure 2.1. Diagram of a typical rectilinear cascade geometry [32]	42
Figure 2.2. (a) AFRL Low Speed Wind Tunnel Facility[35] and (b) view of the test section [36].....	43
Figure 2.3. (a) Track configuration and (b) mechanical design CAD model of moving wake generator track [37]	44
Figure 2.4. Schematic of PIV setup of laser and camera[35].....	47
Figure 2.5. Inviscid static pressure coefficient distributions and blade profiles for the (a) Lightly Loaded, (b) Highly Loaded, and (c) Aft-Loaded L1A blade airfoils at $Re = 50,000$	49
Figure 2.6. (a) Wake total pressure loss coefficient profiles (b) and integrated loss coefficient with error bars at $Re = 10,000-100,000$ for the Lightly Loaded blade airfoil	51
Figure 2.7. Experimental measurements of the static pressure coefficient for the Highly Loaded blade airfoil taken by Bons <i>et al.</i> [38]	52
Figure 2.8. Mean boundary layer velocity profiles extracted from PIV measurements of Woods <i>et al.</i> [39] for the Highly Loaded blade	53
Figure 2.9. Wake total pressure loss coefficient measurements of Garmoe [36] and Casey <i>et al.</i> [40] for the Highly Loaded blade	54
Figure 2.10. Integrated wake total pressure loss coefficient measurements of Marks <i>et al.</i> [40] for the Aft-Loaded L1A blade at high and low turbulent intensities	56
Figure 2.11. Measurements of the Surface static pressure coefficient of Marks <i>et al.</i> [40] for the Aft-Loaded L1A blade at high and low turbulent intensities	57
Figure 2.12. Mean velocity contours obtained from PIV measurements and instantaneous flow visualizations of Marks <i>et al.</i> [40] for the Aft-Loaded L1A blade at $Tu = 0.5\%$	58
Figure 2.13. Mean velocity contours obtained from PIV measurements and instantaneous flow visualizations of Marks <i>et al.</i> [40] for the Aft-Loaded L1A blade at $Tu = 3.4\%$	60
Figure 3.1. Two dimensional hybrid O-H grid of the (a) Lightly Loaded, (b) Highly Loaded, and (c) Aft-Loaded L1A LPT blade airfoils	64
Figure 3.2. Comparison of the total pressure loss coefficient for the Lightly Loaded blade airfoil at different grids spatial resolutions	65

Figure 3.3. (a) Grid of the Highly Loaded blade with the extended outlet and (b) loss coefficient comparison of the baseline grid to the extended outlet grid	66
Figure 3.4. Two dimensional hybrid O-H grid of the Aft-Loaded L1A blade with upstream wake generators.....	67
Figure 3.5. Three-dimensional hybrid O-H grid of the Highly Loaded LPT blade airfoils.....	69
Figure 3.6. Turbulence model comparison of the suction surface turbulent kinetic energy at $Re = 100,000$, $Tu = 1\%$, $l_m = 10.4\text{mm}$ for the Lightly Loaded blade airfoil.....	74
Figure 3.7. Comparison of the boundary layer integral parameters of all three turbulence models at $Re = 100,000$ for the Lightly Loaded blade airfoil.....	74
Figure 3.8. Comparison of total pressure loss coefficient for turbulence models at $Re = 100,000$, $Tu = 1\%$ for the Lightly Loaded blade airfoil	77
Figure 3.9. AFRL Major Shared Resource Center HP XC Opteron (top left), SGI Altix 3700 (top right), and SGI Altix 4700 (bottom center) Super-Computers	80
Figure 4.1. Velocity magnitude contour plots of the Lightly Loaded blade airfoil simulated at a range of inlet Reynolds numbers.....	84
Figure 4.2. Comparison of the CFD and experimental [36] integrated wake loss coefficient at a range of inlet Reynolds numbers for the Lightly Loaded blade airfoil	84
Figure 4.3. Comparison of the CFD and Experimental [36] Maximum Loss Coefficient at a Range of Inlet Reynolds Numbers for the Lightly Loaded Blade Airfoil	87
Figure 4.4. Maximum wake loss coefficient verses inlet turbulent length scale for the Lightly Loaded blade.....	90
Figure 4.5. Wake region total pressure contours for the Lightly Loaded Blade at (a) $l_m = 8\text{mm}$, (b) $l_m = 14\text{mm}$, and (c) $l_m = 20\text{mm}$	91
Figure 4.5. Integrated wake loss coefficient verses inlet turbulent length scale for the Lightly Loaded blade.....	92
Figure 4.6. Comparison of the suction surface turbulent kinetic energy at different inlet turbulent intensities for the Lightly Loaded blade at $Re = 50,000$, $l_m = 5\text{mm}$	93
Figure 4.7. Comparison of (a) boundary layer velocity profiles and (b) integral parameters at different inlet freestream turbulent intensities at $Re = 50,000$, $l_m = 50\text{mm}$ for the Lightly Loaded blade airfoil.....	95
Figure 4.8. (a) Inlet turbulence intensity effect on the wake total pressure loss coefficient and instantaneous wake total pressure contours at (b) $Tu = 0.5\%$ and (c) $Tu = 0.724\%$, $Re = 50,000$ for the Lightly Loaded blade airfoil	97
Figure 5.1. Comparison of surface static pressure coefficient with 3D LES [45] simulations and experimental results [38] at inlet Reynolds numbers of a) 100,000 and b) 50,000 for the Highly Loaded blade airfoil	101
Figure 5.2. Comparison of surface static pressure coefficient with 3D LES [45] simulations and experimental results [38] at inlet Reynolds numbers of 25,000 for the Highly Loaded blade airfoil.....	102
Figure 5.3. Comparison of the boundary layer velocity profiles at inlet Reynolds numbers of a) 100,000 and b) 50,000 with the experimental results [39] for the Highly Loaded blade airfoil.....	104
Figure 5.4. Comparison of the mean boundary layer velocity profiles at 25,000 with the experimental results [39] for the Highly Loaded blade airfoil.....	105

Figure 5.5. Instantaneous vorticity contour plot at $Re = 100,000$ for the Highly Loaded blade airfoil ...	106
Figure 5.6. Instantaneous vorticity contours at $Re = 50,000$ for the Highly Loaded blade airfoil at $l_m = 50\text{mm}$ (a&b) and $l_m = 5\text{mm}$ (c&d)	107
Figure 5.7. Time signal, FFT calculation of the drag coefficient, instantaneous vorticity contours at $Re = 50,000$ for the Highly Loaded blade airfoil at $l_m = 5\text{mm}$ (a) & (c) and $l_m = 50\text{mm}$ (b) & (d)	109
Figure 5.8. Instantaneous Vorticity Contours at $Re = 25,000$ for the Highly Loaded Blade Airfoil at $l_m = 50\text{mm}$ (a&b) and $l_m = 5\text{mm}$ (c&d)	110
Figure 5.9. Time signal, FFT calculation of the drag coefficient, instantaneous vorticity contours at $Re = 25,000$ for the Highly Loaded blade airfoil at $l_m = 5\text{mm}$ (a) & (c) and $l_m = 50\text{mm}$ (b) & (d)	111
Figure 5.10. Comparison of total pressure loss coefficient with experimental [36,40] results at inlet Reynolds numbers of (a) 100,000, (b) 50,000, and (c) 25,000 for the Highly Loaded blade airfoil	114
Figure 5.11. Dimensional comparison of surface static pressure coefficient with 3D LES [45] simulations and experimental results [38] at inlet Reynolds numbers of 25,000 for the Highly Loaded blade airfoil	116
Figure 5.12. Two and three-dimensional comparisons of the mean boundary layer velocity profiles at 25,000 with the experimental results [39] for the Highly Loaded blade airfoil	117
Figure 5.13. Comparison of the instantaneous vorticity contours at $Re = 25,000$, $Tu = 0.5\%$ for the (a)-(b) 2-D and (c)-(d) 3-D simulations of the Highly Loaded blade airfoil	118
Figure 5.14. Iso-surfaces of instantaneous vorticity for the 3-D simulation of the Highly Loaded blade airfoil at $Re = 25,000$, $Tu = 0.5\%$	119
Figure 5.15. Comparisons of instantaneous spanwise vorticity for 2-D and 3-D LES simulation by Visbal [47]	120
Figure 5.16. 2-D and 3-D comparison of total pressure loss coefficient with experimental [36,40] results at $Re = 25,000$ for the Highly Loaded blade airfoil	122
Figure 6.1. Comparison of surface static pressure coefficient with Clark <i>et al.</i> [25] simulations and experimental results [35] at inlet Reynolds numbers of a) 50,000 and b) 31,000, $Tu = 0.5\%$ for the Aft-Loaded L1A blade airfoil	126
Figure 6.2. Mean velocity contours plots of the (a) PIV results at $Re=60,000$, (b) the CFD results at $Re = 50,000$, (c) PIV results at $Re = 25,000$, and (d) CFD results at $Re = 31,000$ for the Aft-Loaded L1A blade airfoil	127
Figure 6.3. Comparison of the mean boundary layer profiles of axial velocity with experimental ($Re=60,000$) results [35] at inlet $Re = 50,000$ for the Aft-Loaded L1A blade airfoil	128
Figure 6.4. Comparison of the mean boundary layer profiles of axial velocity with experimental ($Re = 25,000$) results [35] at inlet $Re = 31,000$ for the Aft-Loaded L1A blade airfoil	130
Figure 6.5. Instantaneous flow visualizations of Marks <i>et al.</i> [35] at (a) $Re = 60,000$ and (b) 25,000, $Tu = 0.5\%$ for the Aft-Loaded L1A blade airfoil. Image view taken 52.5% axial chord location to the trailing edge	131
Figure 6.6. Instantaneous vorticity contours at $Re = 50,000$, $Tu = 0.5\%$, $l_m = 50\text{mm}$ for the Aft-Loaded L1A blade airfoil	132
Figure 6.7. Instantaneous vorticity contours at $Re = 31,000$, $Tu = 0.5\%$, $l_m = 50\text{mm}$ for the Aft-Loaded L1A blade airfoil	133
Figure 6.8. Time signal, FFT calculation of the drag coefficient, instantaneous vorticity contours at (a)-(c) $Re = 50,000$ and (b)-(d) $Re = 31,000$, $Tu = 0.5\%$, and $l_m = 50\text{ mm}$	135

Figure 6.9. Comparison of total pressure loss coefficient with experimental [35] result at inlet Reynolds numbers of (a) 50,000 and (b) 31,000 for the Aft-Loaded L1A blade airfoil	136
Figure 6.10. Comparison of surface static pressure coefficient with Clark <i>et al.</i> [25] simulations and experimental results [35] at inlet Reynolds numbers of a) 50,000 and b) 25,000, $Tu = 3.4\%$ for the Aft-Loaded L1A blade airfoil.....	139
Figure 6.11. Mean velocity contour comparisons of $k-k_L-\omega$ model at (a) $l_m = 4mm$, (b) $l_m=40mm$, (c) $k-\omega(SST)$ model at $l_m =40mm$, and (d) PIV result of Marks <i>et al.</i> [35] at $Re=50,000$, $Tu=3.4\%$ for the Aft-Loaded L1A blade airfoil.....	141
Figure 6.12. RMS velocity contour comparisons of $k-k_L-\omega$ model at (a) $l_m = 4mm$, (b) $l_m=40mm$, (c) PIV result, and (d) flow visualizations of Marks <i>et al.</i> [35] at $Re=50,000$, $Tu=3.4\%$ for the Aft-Loaded L1A blade airfoil	141
Figure 6.13. Mean velocity contour comparisons of $k-k_L-\omega$ model at (a) $l_m = 4mm$, (b) $l_m=40mm$, (c) $k-\omega(SST)$ model at $l_m =40mm$, and (d) PIV result of Marks <i>et al.</i> [35] at $Re=25,000$, $Tu=3.4\%$ for the Aft-Loaded L1A blade airfoil.....	143
Figure 6.14. RMS velocity contour comparisons of $k-k_L-\omega$ model at (a) $l_m = 4mm$, (b) $l_m=40mm$, (c) PIV and (d) flow visualizations of Marks <i>et al.</i> [35] at $Re=25,000$, $Tu=3.4\%$ for the Aft-Loaded L1A blade airfoil.....	143
Figure 6.15. Comparison of the mean boundary layer profiles of axial velocity with experimental results [35] at inlet $Re = 50,000$ for the Aft-Loaded L1A blade airfoil at $Tu = 3.4\%$	145
Figure 6.16. Comparison of the mean boundary layer profiles of axial velocity with experimental results [35] at inlet $Re = 25,000$ for the Aft-Loaded L1A blade airfoil at $Tu = 3.4\%$	146
Figure 6.17. Comparison of total pressure loss coefficient with experimental [35] result at inlet Reynolds numbers of (a) 50,000 and (b) 25,000 for the Aft-Loaded L1A blade airfoil at $Tu = 3.4\%$	148
Figure 7.1. The mean surface static pressure coefficient at $Re_D = 794$ at (a) $Tu = 0.5\%$, $l_m = 50mm$ and (b) $Tu = 3.4\%$, $l_m = 40mm$ for the wake generator	153
Figure 7.2. Instantaneous Z-vorticity contours at $Re_D = 794$ at (a) $Tu = 0.5\%$, $l_m = 50mm$ and (b) $Tu = 3.4\%$, $l_m = 40mm$ for the wake generator	155
Figure 7.3. Comparison of the time-signal of the wake generator velocity for CFD at $Tu = 0.5\%$ and 3.4% with experimental [37] single point hot-film velocity measurements at $Tu = 0.5\%$ for $Re = 25,000$	157
Figure 7.4. Comparison of the velocity (a) Probe #1 and (b) #2 blade passage locations with the experimental [48] single point hot-film velocity measurements at $Re = 25,000$, $Tu = 3.4\%$	158
Figure 7.5. Diagram of the different wake generator locations for each of the six phases [37]	160
Figure 7.6. (a) CFD and (b) experimental time location for each phase with respect to the Probe #2 time signal of the freestream velocity [48]	160
Figure 7.7. Instantaneous z-vorticity contour plots for each of the six phases at $Re =25,000$, $Tu = 0.5\%$, $l_m = 50mm$	163
Figure 7.8. Instantaneous z-vorticity contour plots for each of the six phases at $Re =25,000$, $Tu = 3.4\%$, $l_m = 40mm$	164
Figure 7.9. Comparisons of the instantaneous z-vorticity contours of the separation region at Phase #1, #3, and #6 for baseline $Re = 31,000$ and $Re = 25,000$ with wakes, at $Tu = 0.5\%$, $l_m = 50mm$	165

Figure 7.10. Time signal and FFT calculation of the drag coefficient for the Aft-Loaded L1A blade airfoil with upstream wake generators at $Re = 25,000$ (a) $Tu = 0.5\%$, $l_m = 50\text{mm}$ and (b) $Tu = 3.4\%$, $l_m = 40\text{mm}$	166
Figure 7.11. Comparison of the velocity magnitude contour plots in the blade passage for the CFD and experimental [37] PIV results at $Re = 25,000$, $Tu = 3.4\%$, $l_m = 40\text{mm}$ for Phase #1 & #2	168
Figure 7.12. Comparison of the velocity magnitude contour plots in the blade passage for the CFD and experimental [37] PIV results at $Re = 25,000$, $Tu = 3.4\%$, $l_m = 40\text{mm}$ for Phase #3 & #4	168
Figure 7.13. Comparison of the velocity magnitude contour plots in the blade passage for the CFD and experimental [37] PIV results at $Re = 25,000$, $Tu = 3.4\%$, $l_m = 40\text{mm}$ for Phase #5 & #6	169
Figure 7.14. Comparison of the instantaneous boundary layer profiles of axial velocity the Aft-Loaded L1A blade with upstream wake generators to the experimental PIV results for Phase #1 at $Tu = 3.4\%$, $l_m = 40\text{mm}$	170
Figure 7.15. Comparison of the instantaneous boundary layer profiles of axial velocity the Aft-Loaded L1A blade with upstream wake generators to the experimental PIV results for Phase #3 at $Tu = 3.4\%$, $l_m = 40\text{mm}$	171
Figure 7.16. Comparison of the instantaneous boundary layer profiles of axial velocity the Aft-Loaded L1A blade with upstream wake generators to the experimental PIV results for Phase #6 at $Tu = 3.4\%$, $l_m = 40\text{mm}$	172
Figure 7.17. Comparison of surface static pressure coefficient of the Aft-Loaded L1A blade with upstream wake generators to the baseline CFD simulation at $Re = 25,000$ (b) $Tu = 0.5\%$ and (b) $Tu = 3.4\%$	173
Figure 7.18. Comparisons of the instantaneous turbulence intensity at Phase #1, #3, and #6 for $Re = 25,000$ with wakes, at $Tu = 0.5\%$, $l_m = 50\text{mm}$ and $Tu = 3.4\%$, $l_m = 40\text{mm}$	174
Figure 7.19. Comparison of the mean boundary layer profiles of axial velocity the Aft-Loaded L1A blade with upstream wake generators to the baseline CFD simulation at $Re = 25,000$, $Tu = 0.5\%$	176
Figure 7.20. Comparison of the mean boundary layer profiles of axial velocity the Aft-Loaded L1A blade with upstream wake generators to the baseline CFD simulation at $Re = 25,000$, $Tu = 3.4\%$	176
Figure 7.21. Comparison of total pressure loss coefficient with experimental [37,49] for the baseline and addition of wakes (a) $Tu = 0.5\%$ and (b) $Tu = 3.4\%$ at $Re = 25,000$ for the Aft-Loaded L1A blade airfoil	178
Figure A.1. The $k-k_L-\omega$ model formulation comparison of surface static pressure coefficient with Clark <i>et al.</i> [25] CFD simulations and experimental results [35] at $Re = 50,000$, $Tu = 0.5\%$ for the Aft-Loaded L1A blade airfoil	198
Figure A.2. Mean velocity contours plots of the (a) Fluent 12.0, and (b) Fluent 6.3 formulation of the $k-k_L-\omega$ model at $Re = 50,000$, and (c) PIV results [35] at $Re = 60,000$, $Tu = 0.5\%$ for the Aft-Loaded L1A blade airfoil	199
Figure A.3. The $k-k_L-\omega$ model formulation comparison of the mean axial velocity boundary layer profiles with experimental ($Re=60,000$) results [35] at inlet $Re = 50,000$, $Tu = 0.5\%$ for the Aft-Loaded L1A blade airfoil	200
Figure A.4. Instantaneous vorticity contours at $Re = 50,000$, $Tu = 0.5\%$ for (a)-(c) Fluent 12.0 and (d)-(f) Fluent 6.3 of the $k-k_L-\omega$ model for the Aft-Loaded L1A blade airfoil	201
Figure A.5. Time signal and FFT calculation of the drag coefficient for the Aft-Loaded L1A blade airfoil using the (a) Fluent 12.0 and (b) Fluent 6.3 formulation of the $k-k_L-\omega$ model.....	202

Figure A.6. The $k-k_L-\omega$ model formulation comparison of total pressure loss coefficient with experimental [35] result at inlet $Re = 50,000$, $Tu = 0.5\%$ for the Aft-Loaded L1A blade airfoil.....	203
Figure A.7. The $k-k_L-\omega$ model formulation comparison of surface static pressure coefficient with Clark <i>et al.</i> [25] CFD simulations and experimental results [35] at $Re = 50,000$, $Tu = 3.4\%$ for the Aft-Loaded L1A blade airfoil.....	205
Figure A.8. Mean velocity contours plots of the (a) Fluent 12.0, (b) Fluent 6.3 formulation of the $k-k_L-\omega$ model and (c) PIV [35] results at $Re = 50,000$, $Tu = 3.4\%$ for the Aft-Loaded L1A blade airfoil.....	206
Figure A.9. The $k-k_L-\omega$ model formulation comparison of the mean axial velocity boundary layer profiles with experimental results [35] at inlet $Re = 50,000$, $Tu = 3.4\%$ for the Aft-Loaded L1A blade airfoil ...	207
Figure A.10. The $k-k_L-\omega$ model formulation comparison of total pressure loss coefficient with experimental [35] result at inlet $Re = 50,000$, $Tu = 3.4\%$, for the Aft-Loaded L1A blade airfoil.....	208

List of Tables

Table 3.1. Grid Dimensions of each Cascade CFD Model	64
Table 3.2. Turbulence model comparison of the integrated total pressure loss coefficient with the experimental [36, 40] results for the Lightly Loaded blade airfoil	77
Table 3.3. CFD mathematical rake measurement locations created in Fluent CFD software	81
Table 4.1. Summary of inlet turbulence parameters on transition/separation location and maximum loss coefficient for the Lightly Loaded Blade	88
Table 5.1. Summary of the separation location and Strouhal number for the Highly Loaded blade airfoil	111
Table 5.2. Integrated total pressure loss coefficient comparison with the experimental [36, 40] results for the Highly Loaded blade airfoil	114
Table 5.3. Dimensional comparison of the integrated total pressure loss coefficient with the experimental [36, 40] results for the Highly Loaded blade airfoil.....	122
Table 6.1. Summary of the separation location and Strouhal number for the Aft-Loaded L1A blade at $Tu = 0.5\%$	135
Table 6.2. Maximum and integrated total pressure loss coefficient comparison with the experimental [35] results for the Aft-Loaded L1A blade airfoil	137
Table 6.3. Maximum and integrated total pressure loss coefficient comparison with the experimental [35] results for the Aft-Loaded L1A blade airfoil at $Tu = 3.4\%$	148
Table 7.1. Summary of the separation location, Strouhal number, and wake properties for the wake generator	158
Table 7.2. Summary of the separation location and Strouhal number for the Aft-Loaded L1A blade airfoil with upstream wake generators.....	166
Table 7.3. Maximum and integrated total pressure loss coefficient comparison with the experimental [35,37] results for the Aft-Loaded L1A blade with and without upstream wake generators.....	178
Table 8.1. Summary of the prediction capability achieved using Walters and Leylek [2] $k-k_L-\omega$ model for the prediction of low Reynolds number effects	187
Table A.1. Fluent 6.3 $k-k_L-\omega$ model constants	195
Table A.2. Fluent 12.0 $k-k_L-\omega$ model constants	196
Table A.3. Maximum and integrated total pressure loss coefficient comparison with the experimental [35] results at $Re = 50,000$, $Tu = 0.5\%$ for the Aft-Loaded L1A blade airfoil	203
Table A.4. Maximum and integrated total pressure loss coefficient comparison with the experimental [35] results at $Re = 50,000$, $Tu = 3.4\%$ for the Aft-Loaded L1A blade airfoil	208

Nomenclature

A	=	amplitude
b	=	wake width
c	=	phase speed
c_f	=	friction coefficient
C_P	=	pressure coefficient
C_x	=	axial chord
d	=	wall distance
D	=	cylinder diameter, kinetic energy near-wall dissipation
$E(\kappa)$	=	energy spectrum density
f_{shed}	=	vortex shedding frequency
f_{resol}	=	frequency resolution
F	=	nondimensional frequency
H	=	shape factor
k	=	turbulent kinetic energy
\hat{k}	=	unit vector in the z-direction
K_t	=	acceleration parameter
l_m	=	integral turbulent length scale
N	=	amplification factor, wave number
N_{avg}	=	averaging interval
n	=	distance normal from the wall
P	=	pressure; production term
q	=	dynamic pressure
q'	=	instability quantity
R	=	bypass transition production term
\Re_τ	=	autocorrelation function
R_{NAT}	=	natural transition production term
Re	=	Reynolds number
Re_θ	=	Reynolds number based on momentum thickness
s	=	pitch

D. Sanders

XV

St	=	Strouhal number
T	=	time interval
t	=	time
t_{step}	=	time-step
$TPLC$	=	total pressure loss coefficient
$TLPC_{int}$	=	integrated total pressure loss coefficient
Tu	=	freestream turbulence intensity
u	=	freestream velocity magnitude
u^+	=	law of the wall
\bar{u}	=	mean velocity
u'	=	streamwise fluctuation
\hat{u}	=	nondimensional Reynolds stress
u^+	=	nondimensional velocity
u_p	=	peak velocity deficit
u_{turb}	=	friction velocity
ν	=	Kolmogorov velocity scale
\vec{W}	=	relative velocity vector
w	=	relative velocity
x	=	directional component
y^+	=	nondimensional wall distance
Z_w	=	Zwiefel blade force coefficient
α	=	wave number, spatial growth rate, absolute flow angle
α_T	=	turbulent diffusivity
β	=	wave number, relative flow angle
γ	=	intermittency function
δ	=	boundary layer thickness
δ^*	=	boundary layer displacement thickness
δ_{ij}	=	Kronecker delta
ε	=	dissipation per unit mass
Θ	=	boundary layer momentum thickness
θ	=	angle
θ_{sep}	=	momentum thickness at separation

D. Sanders

xvi

κ	=	turbulent scales
λ	=	dimensionless momentum thickness
λ_{eff}	=	effective length scale
λ_T	=	Taylor microscale
η	=	Kolmogorov length scale
ϕ	=	complex disturbance stream function
μ	=	molecular viscosity
μ_t	=	turbulent viscosity
ν	=	kinematic viscosity
ρ	=	density
τ	=	Kolmogorov time scale
τ_{ij}	=	Reynolds stress tensor
τ_w	=	wall shear stress
ω	=	angular frequency, specific dissipation rate
Ω	=	vorticity

Subscripts

0	=	total
c	=	cylinder
i,j	=	indices
in	=	inlet
L	=	laminar
out	=	outlet
tur	=	turbulent

1. Introduction

The range and endurance of turbine-powered aircraft cruising at high altitude is limited by multiple factors, including the operational efficiency of the low pressure turbine (LPT). As aircraft elevation is increased, the operational Reynolds number decreases due to the change in density. The Reynolds number for turbomachinery is defined by the equation

$$\text{Re} = \frac{\rho U C_x}{\mu} \quad (1.1)$$

where C_x is the axial chord length and U is the inlet velocity. It is important to improve the low Reynolds number performance to achieve increased efficiency, reduced fuel consumption, increased range, and longer loiter at high altitudes.

Low Reynolds numbers promote the presence of laminar and transitional flow boundary layers on the suction surface of the LPT blades. Also, the desire to use high-lift LPT blade airfoil designs in order to decrease the total blade count thus, reducing weight and cost of turbomachinery designs. These high-lift LPT blade airfoil designs promotes the increase in the region of adverse pressure gradients located on the aft portion of the blade may cause the laminar flow boundary layer to separate from the surface. Also, the region of the boundary layer that undergoes laminar-turbulent boundary layer transition may increase. Current LPT blades suffer a dramatic increase in losses with decreasing Reynolds number, and this is usually due to the effects of separation [1]. Loss in efficiency due to the aerodynamic losses from boundary layer separation results in a loss in engine efficiency, which reduces the aircraft range and maximum altitude.

Chapter 1. Introduction

As a result, there is a need for improved prediction methods for separation and transitional flow using Computational Fluid Dynamics (CFD) for turbomachinery designs. With recent advances in numerical techniques and increased computational resources, CFD is being widely applied to further advance turbomachinery designs. Accurate prediction of aerodynamic losses due to separation and laminar-to-turbulent transitional flow is required for CFD to continue to play an integral role in the design process particularly for optimization. More advanced numerical methods are needed in order to properly resolve the complicated flow physics associated with low Reynolds number flows. The characterization of CFD models using experimental measurements is necessary for further advancement for both numerical methods and physical models. These CFD models can be used to gain more insight to the flow features that are difficult to measure. Yet, these numerical model cannot be so complex that they require excessive amounts of computing power and lengthy simulation times when applied to complicated geometries such as three-dimensional multistage rotating turbomachinery designs. The ideal CFD method is a balance between increased fidelity for accurate modeling of complicated flow physics associated with low Reynolds number effects, increased accuracy over a wide range Reynolds numbers, and yet effective enough to be applied to complex geometries without being too computationally expensive.

The recent development of an improved transition and turbulence model by Walters and Leylek [2] appears to offer the possibility of improved accuracy for low Reynolds number LPT flow predictions using the Reynolds-Averaged Navier-Stokes (RANS) CFD method. It is the purpose of this dissertation to test and evaluate CFD models incorporating the Walters and Leylek [2] model against a number of available benchmark experiments, and to compare experiments results with other widely used turbulence models. The emphasis in this study is on

Chapter 1. Introduction

low Reynolds number turbine flows, but it is hoped that the results will be of general use in expanding the validated knowledge base for prediction of transitional flows in turbomachinery.

1.1 Research Program Goals

The goals associated with this research program are as follows:

1. Provide a baseline methodology using LPT cascade models to investigate low Reynolds number aerodynamic effects
 - (a) Understand the impact of applying RANS turbulence models to the prediction of separation and transitional flow
 - (b) Evaluate the prediction capability of RANS turbulence models within the Ansys[®] Fluent CFD software
 - (i) Choose the best RANS turbulence model based on the criteria of modeling the correct aerodynamic flow physics and the successful prediction of the aerodynamic losses at low Reynolds numbers
 - (c) Understand the influence of the inlet turbulent boundary conditions on the prediction capability using the chosen turbulence model
2. Apply the developed methodology to LPT blade airfoils with different pressure loading characteristics
 - (a) Show the ability to predict laminar flow separation and laminar-to-turbulent transitional flow
 - (b) Predict the resulting total pressure loss from these aerodynamic flow effects
 - (c) Characterize predictions for each blade airfoil using experimental cascade database
3. Demonstrate the ability of the new methodology to predict unsteady flowfield of an advanced cascade model with upstream wake generators

Chapter 1. Introduction

The ability to predict the performance of LPT blades subjected to high altitude conditions is important to turbine engine designers. This research will apply a new methodology based on an existing prediction method that can effectively predict aerodynamic flows of LPT blade airfoils at high altitude conditions. This study will investigate the low Reynolds numbers flow effects associated with high altitude conditions on LPT cascade geometries. For accurate CFD predictions, correct modeling of laminar-turbulent boundary layer transition and flow separation is essential to capture the details of the flow. It will be determined if the new methodology is capable of providing the improved prediction of low Reynolds number effects for more complex geometries expected for future advanced multistage LPT's for turbine engines. This research will contribute a characterized model for low Reynolds number turbine performance prediction and design improvement.

1.2 Low Pressure Turbine Aerodynamic Flow Effects

The flows found within low pressure turbines are highly unsteady. Each blade row generates flow non-uniformities due to viscous and potential effects that propagate to the adjacent blade rows. Potential effects originate from unsteady variations in the pressure field that propagate both upstream and downstream. There are three types of viscous effects that can occur within the blade passages. The boundary layer along the surface of the airfoils begins as laminar at the leading edge and transition to turbulence can be initiated depending on the main flow conditions, and flow separation can occur due to low Reynolds inlet conditions.

Wakes are created due to the difference in the velocity in the viscous layers emerging from the pressure and suction surfaces at the blade trailing edge. A reduction in the total pressure occurs due to the wake region and increases the aerodynamic losses within the blade row. Boundary layer transition is affected by these passing wakes. As these wakes travel

Chapter 1. Introduction

downstream, the region on the blade affected by the wake quickly shifts from transitional flow to turbulent flow and then returns to transitional flow after the wake has passed [3]. Figure 1.2 shows the global effect of the stator wake as it is distorted by the downstream rotor and mitigated across the blade passage. Because of the velocity deficit in the wake, the inlet flow angle to the rotor is changed. The wake is sheared and stretched into a V-shaped segment due to the different velocity field existing within the blade passage. The pressure forces are observed to be driving the low momentum fluid within the wake from the pressure side toward the suction side [4].

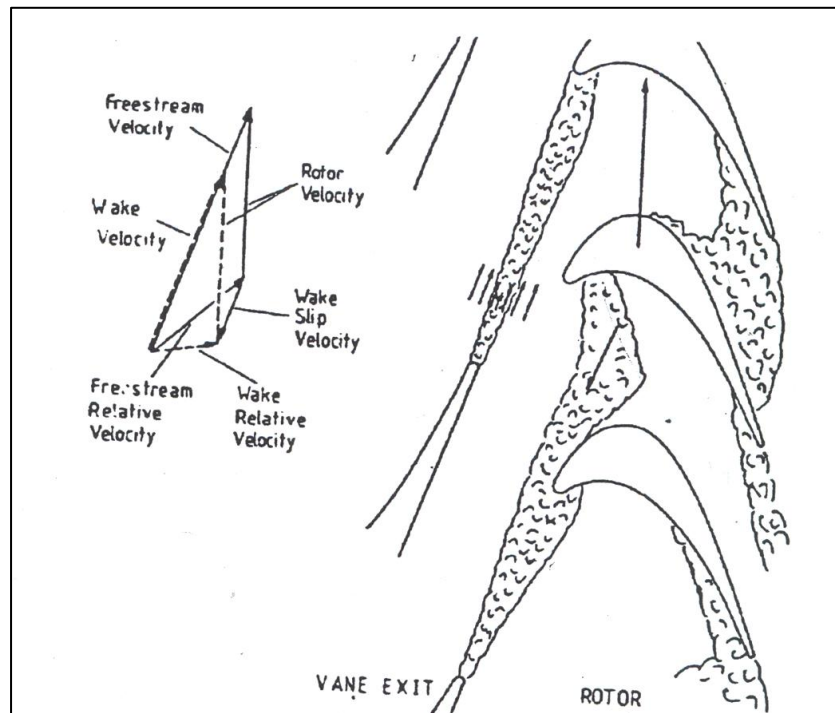


Figure 1.1. Illustration of passing wake behavior across a rotor blade row [5]

Within the passage, boundary layers on the end-walls caused by the incoming flow produces vortical structures called secondary flows. They are generated within the vicinity where the blade leading edge and the end-wall meet. Figure 1.2 shows the two types of vortical structures, a passage vortex formed from the pressure side and counter vortex formed on the suction surface. Both these vortices can interact and become more complex. The resulting total

Chapter 1. Introduction

pressure loss from these secondary flows can be another source of aerodynamic loss and cause a reduction in stage efficiency.

As discussed previously, low pressure turbine flows at low inlet Reynolds numbers are dominated by the increase of the laminar-to-turbulent transition region and laminar flow separation within the boundary layer. The flow physics involved with these effects are very complex. A complete understanding of the flow physics involved in low Reynolds number effects is necessary in order to formulate accurate numerical models. To establish the basis for the findings reported in this dissertation, the following sections present fundamental topics involving laminar flow separation, laminar-to-turbulent transition, and turbulent flows.

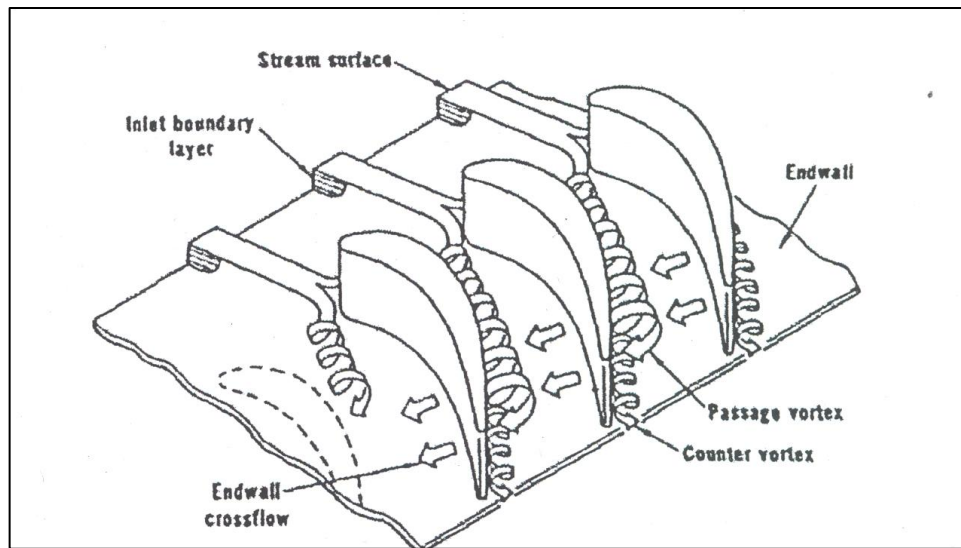


Figure 1.2. Endwall flow within a turbine blade passage [6]

1.2.1 Laminar Flow Boundary Layers

The following summary of classical flow concepts associated with laminar, transitional, turbulent and separating boundary layers is provided for completeness, and to support the discussions of results presented from the CFD modeling. The reader familiar with these

Chapter 1. Introduction

concepts may wish to move directly to Section 1.3, CFD Methods of Predicting Low Reynolds Number Effects in LPT Blades

When fluid flow moves over an object at a velocity U , the presence of viscosity causes the fluid to adhere to the surface of the body. Fluid velocity on the surface is zero following the accepted assumptions of a “no-slip” boundary. The fluid forms a boundary layer on the body surface where viscous effects are significant. The viscous effects within the boundary layer cause a velocity gradient and the velocity profile of the fluid particles found in the boundary layer begins to distort. The fluid velocity increases with distance from the surface of the body. The boundary layer has a finite thickness, defined as the distance from the body surface at which the fluid velocity is approximately 99% of the freestream velocity. Figure 1.3(a) shows a typical boundary layer profile having a thickness δ .

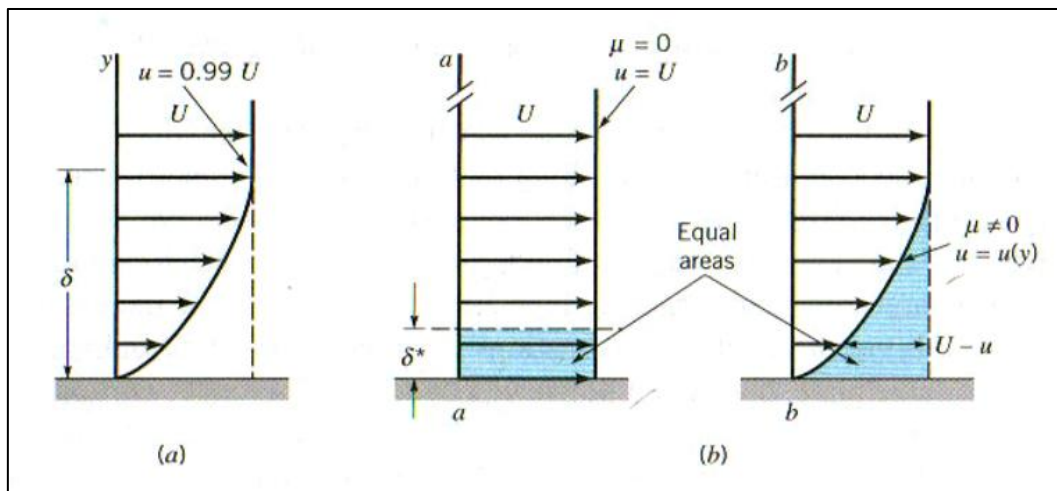


Figure 1.3. Diagram of typical boundary profile (a) and description of displacement thickness (b) [7]

The structure of the boundary layer within the viscous region is mainly dependent on the Reynolds number. The Reynolds number is defined as the ratio of inertia forces to viscous forces. If the Reynolds number is large enough, viscous effects are only important in the

Chapter 1. Introduction

boundary layer. Outside the boundary layer, the gradients are relatively small and the flow behaves as if it were inviscid. The simplest case is the development of the boundary layer on a flat plate as shown in Figure 1.4. The Reynolds number based on distance x on the plate is defined as

$$\text{Re}_x = \frac{\rho U x}{\mu} \quad (1.2)$$

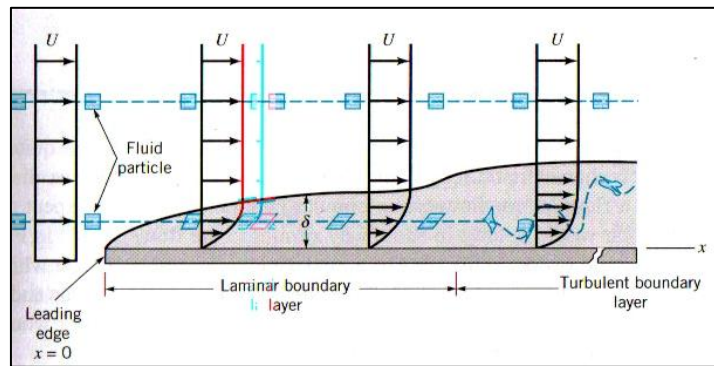


Figure 1.4. Diagram of laminar and turbulent boundary layer flow over a flat plate [7]

At the leading edge, the plate is assumed to have a negligible effect on the fluid flow ahead of it. A laminar flow boundary layer forms starting at the plate leading edge.. Laminar flow is defined as the type of flow in which fluid particles move along a well defined path or streamline. These streamlines are well defined and the fluid particles move in adjacent layers gliding smoothly over each other. The shear stress, τ_w , in a laminar fluid is defined as

$$\tau_w = \mu \frac{\partial U}{\partial n} \quad (1.3)$$

where μ is the laminar coefficient for viscosity which depends on the composition of the fluid and n is the direction normal to the direction of the shear stress. The relation is defined as *Stokes' law* and fluids that obey this law are defined as *Newtonian*.

Chapter 1. Introduction

In general for a flow past objects other than a flat plate the pressure gradient within the freestream is not uniform. The pressure gradient will vary depending on the shape of the body. The component of the pressure gradient in the streamwise direction is variable, although normal to the flow the pressure gradient is assumed negligibly small. The characteristics of the flow are highly dependent on the pressure gradient effects found within the boundary layer.

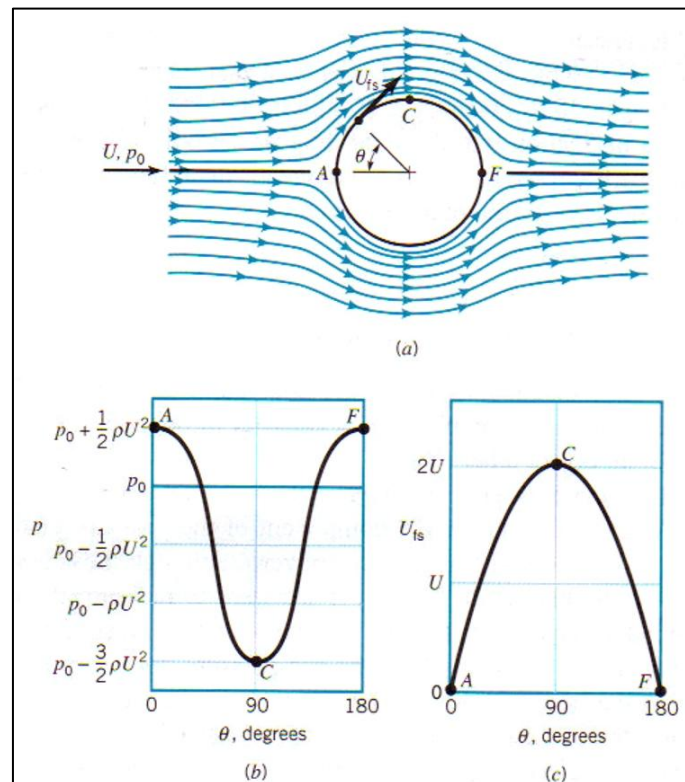


Figure 1.5. Inviscid flow past a cylinder (a) pressure distribution (b) and freestream velocity (c) on the cylinder surface [7]

For example, for a flow at inlet velocity U and static pressure P past a circular cylinder of diameter D , if the flow were inviscid, the Reynolds number would be infinite. The streamlines would be symmetrical as shown in Figure 1.5(a). The velocity and static pressure variation would be as shown in Figure 1.5(b) and Figure 1.5(c) and described with the following equations based on the potential flow method

Chapter 1. Introduction

$$P_c = P + \frac{1}{2}\rho U^2(1 - 4\sin^2 \theta) \quad (1.4)$$

$$U_c = 2U \sin(\theta) \quad (1.5)$$

The pressure is a maximum at the stagnation point at front and back of the cylinder. The maximum freestream velocity, U_c , would be at the top and bottom of the cylinder. Figure 1.5 shows from $\theta = 0$ to $\theta = 90^\circ$ the pressure decreases in the direction of the flow along front half of the cylinder and is called favorable pressure gradient. At the rear half of the cylinder, the pressure increases in the direction of the flow, producing an adverse pressure gradient. There is exchange between kinetic and potential energy, but there are no energy losses.

Considering viscous effects, the fluid within the boundary layer experiences a loss in energy as it flows along the cylinder surface. This loss of energy means the fluid particle does not have enough energy to travel from the front to the rear of cylinder as the inviscid case. The fluids flows against the adverse pressure gradient as far as it can until the boundary layer separates from the cylinder surface. At the separation point, the velocity gradient and shear stress, τ , at the wall are zero. From applying the momentum equation at the wall, where $u = v = 0$:

$$\left. \frac{\partial \tau}{\partial y} \right|_{wall} = \mu \left. \frac{\partial^2 u}{\partial y^2} \right|_{wall} = -\rho U \frac{dU}{dx} = \frac{dP}{dx} \quad (1.6)$$

$$\left. \frac{\partial^2 u}{\partial y^2} \right| = \frac{1}{\mu} \frac{dP}{dx} \quad (1.7)$$

the second derivative of the velocity is positive at the wall in an adverse gradient and yet must be negative at the outer boundary layer ($y = \delta$) to merge with the mainstream flow, $U(x)$. The second derivative must pass, a point of inflection (PI) for any boundary layer undergoing an adverse pressure gradient. Figure 1.6 shows the effect of pressure gradients on the boundary layer

D. Sanders 10

Chapter 1. Introduction

profile. In the favorable pressure gradient (Fig 1.6(a)), the boundary layer velocity profile is smooth with no point of inflection, so there cannot be any separation. Laminar profiles of this type will be resistant to transition to turbulence. In a zero pressure gradient flow (Fig 1.6(b)), the point of inflection is at the wall with no separation and the flow will eventually transition to turbulent. As the strength of the adverse pressure gradient increases (Fig 1.6(c)), the point of inflection will be located within the boundary layer and it will increase its distance from the wall. Figure 1.6(d) shows the critical situation where shear stress is exactly zero ($\tau_w = 0$), and is defined as the separation point. A increase in the adverse pressure gradient will cause backflow as in Figure 1.6(e).

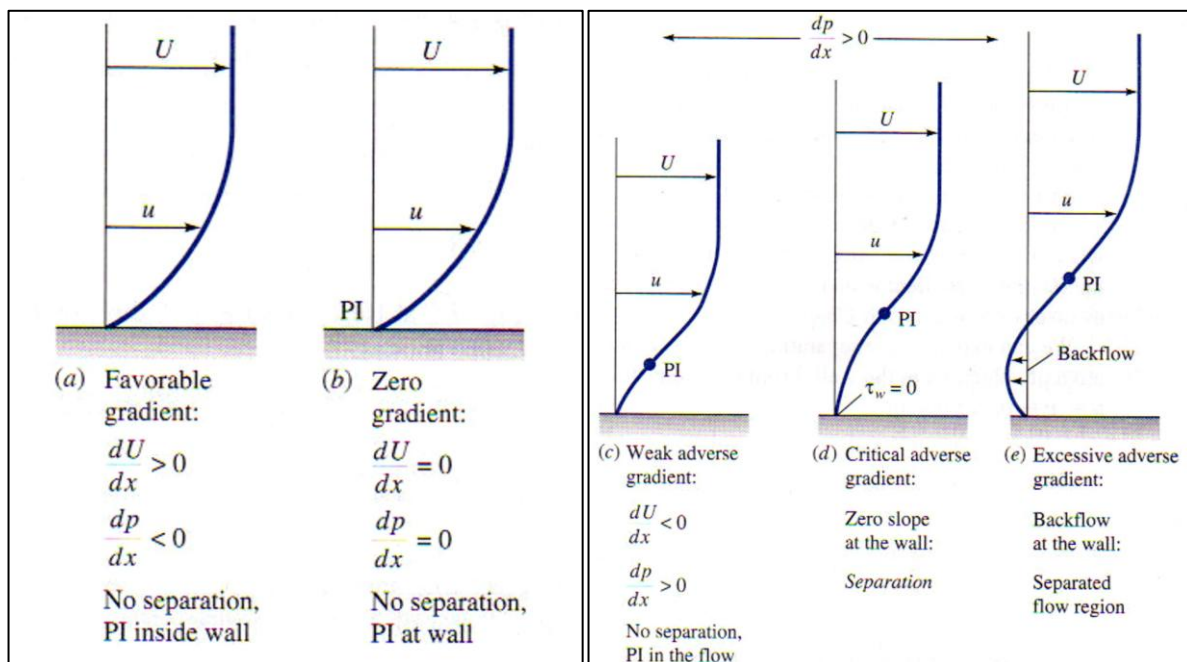


Figure 1.6. The effect of pressure gradients on boundary layer profiles [8]

One widely used numerical method for the estimation of growth of laminar flow boundary layers subjected to pressure gradients is Thwaites integral momentum method. It starts by taking the two-dimensional boundary layer integral relation for variable $U(x)$ given as

Chapter 1. Introduction

$$\frac{\tau_w}{\rho U^2} = \frac{1}{2} c_f = \frac{d\Theta}{dx} + (2 + H) \frac{\Theta}{U} \frac{dU}{dx} \quad (1.8)$$

where $H(x) = \delta^*(x)/\Theta(x)$ is the ratio of displacement thickness to momentum thickness, of the shape factor. The shape factor is a good indicator of the pressure gradient, the higher the $H(x)$ the stronger the adverse pressure gradient, and laminar flow separation occurs approximately at $H \approx 3.5$. Thwaites determined that the Eq. (1.10) can be correlated by using the dimensionless momentum-thickness variable, λ , and is defined as

$$\lambda = \frac{\Theta^2}{\nu} \frac{dU}{dx} \quad (1.9)$$

Thwaites was able to integrate Eq. (1.10) in closed form with the result

$$\Theta^2 = \Theta_0^2 \left(\frac{U_0}{U} \right)^6 + \frac{0.45\nu}{U^6} \int_0^x U^5 dx \quad (1.10)$$

where Θ_0 is the momentum thickness at $x = 0$. Separation was found to occur at $\lambda = -0.09$. The non-dimensional shear stress, $S = \tau_w \Theta / (\mu U)$, was also correlated with λ as follows

$$S(\lambda) = \frac{\tau_w \Theta}{\mu U} \approx (\lambda + 0.09)^{0.62} \quad (1.11)$$

Thwaites method is mainly used to make qualitative assessment of the boundary layer behavior. The range of accuracy is generally less than 10% for favorable pressure gradients, but about 20-30% in strong adverse pressure gradients [9].

1.2.2 Transitional Flow Boundary Layers

The flat plate example in Figure 1.4 shows a region where instabilities within the laminar flow boundary layer grow and become turbulent. The understanding of the origins of turbulent

Chapter 1. Introduction

flow and transition from laminar to turbulent flow are one of the most important unsolved problems in the field fluid mechanics.

Transition occurs in the boundary layer for external flows due to the disturbances in the freestream, such as vorticity or acoustic effects, which enter the boundary layer as steady and/or unsteady fluctuations of the basic state. This process is known as *receptivity* and it provides the initial conditions of amplitude, frequency, and phase for the breakdown of laminar flow. Receptivity may be initially too small to measure and is observed only after the onset of the instability [10]. A variety of different types of instabilities can occur either independently or coupled, and the type instability depends on the Reynolds number, wall curvature, roughness, and initial conditions.

Linear stability theory is used to describe initial growth of these disturbances. For example for flow over a flat plate, the basic state is assumed to be parallel flow where $u = u(y)$. Two-dimensional instabilities are superimposed on the Navier-Stokes equations (Eq. 1.37) which are linearized assuming a normal mode of the instability stated as

$$q'(x, y, t) = q(y) \exp i(\alpha x - \omega t) + C.C. \quad (1.12)$$

where C.C. is the complex conjugate, and q' represents the instability quantity such as pressure or a velocity component. The Orr-Sommerfeld equation describes the spatially varying instabilities as

$$(D^2 - \alpha^2)^2 \phi - iR \left[\left(\alpha \frac{u}{U_\infty} - \omega \right) (D^2 - \alpha^2) \phi - \left(\alpha D^2 \frac{u}{U_\infty} \right) \phi \right] = 0 \quad (1.13)$$

$$\alpha = \alpha_r + i\alpha_i \quad (1.14)$$

Chapter 1. Introduction

where $D = d/dy$, ϕ is the complex disturbance stream function, ω is the angular frequency, $-\alpha_i$ is the spatial growth rate, and $c = \omega/\alpha_r$ is the phase speed. The eigenvalues for Eq. (1.15) are found by looking at $\alpha = \alpha(Re, F)$, where F is the nondimensional frequency defined as

$$F = \frac{2\pi f\nu}{U_\infty^2} \quad (1.15)$$

The collection of points which $\alpha_i(Re, F) = 0$ is called the neutral stability curve shown in Figure 1.7. For a given frequency in the boundary layer, there can be two values of the Reynolds number. In the region between the two Reynolds numbers the flow is unstable. Transition depends on the measure of growth between the higher and lower Reynolds numbers. The Reynolds number defined where the flow is stable for all frequencies is called the minimum critical Reynolds number, Re_{crit} .

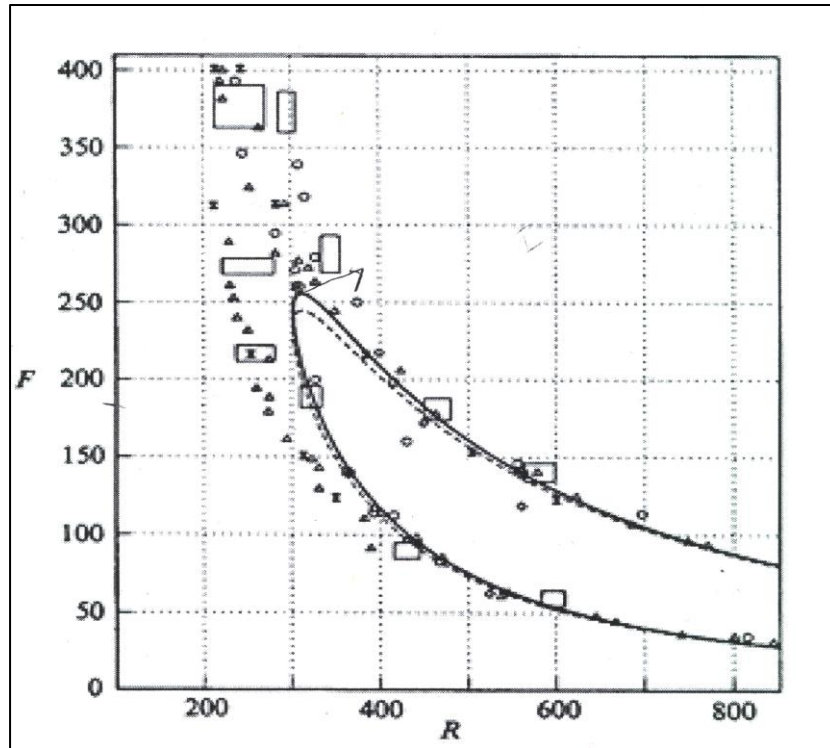


Figure 1.7. The neutral stability curve [10]

Chapter 1. Introduction

In the boundary layer of a flat plate, Reynolds number varies along the plate and a disturbance at a given frequency, F , is called a Tollmien-Schlichting (T-S) wave. At certain conditions this wave is amplified and three-dimensional nonlinear interactions occur, referred to as secondary instabilities. These disturbances grow rapidly and turbulent spots eventually form where the boundary layer alternates between laminar and turbulent flow states. The formation of turbulent spots occurs at different locations and the spots merge to form fully developed turbulence. This entire process from laminar flow to transition to turbulence through the generation of T-S waves is classified as “natural” transition.

In some instances, boundary layer transition occurs in flows that are laminar and stable and do not follow the natural path of transition. This is known as “bypass” transition, where the formulation and amplification of T-S waves are bypassed due to the presence of forced disturbances of sufficient amplitude. This disturbance can be caused by either higher freestream turbulence or surface roughness. The formation of turbulence spots is the first indication of transition. This process reduces the distance of unstable laminar flow significantly and promotes earlier transition. Under certain conditions, the laminar boundary layer may separate from the surface of the body. Rapid transition occurs within the separated shear layer, providing that the Reynolds number is not too low or the adverse pressure gradient too large. The turbulent layer will reattach to the surface and form a closed region of the flow called a separation bubble. The region beneath the separated shear layer has very low shear stress and approximately constant static pressure. Figure 1.9 illustrates the three processes by which transition to turbulence is known to occur.

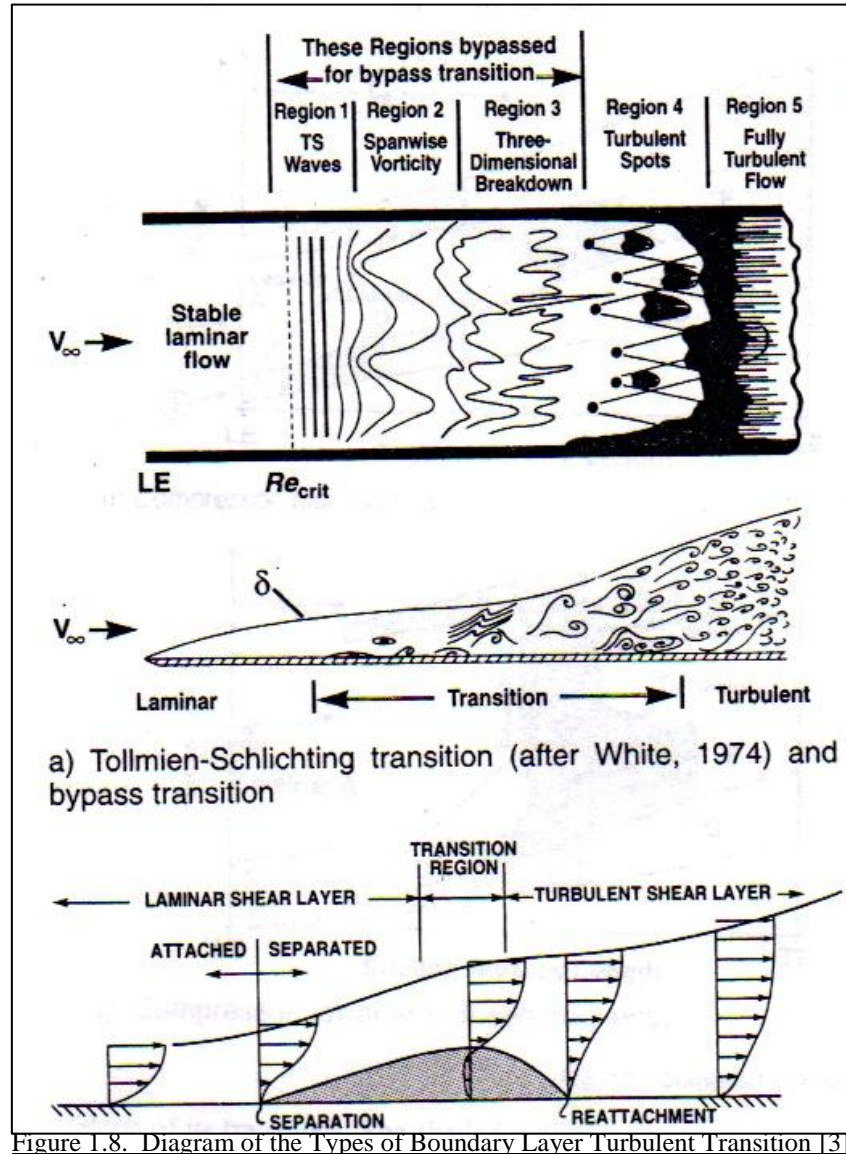


Figure 1.8. Diagram of the Types of Boundary Layer Turbulent Transition [3]

1.2.3 Turbulent Flow Characteristics

As the Reynolds number increases the fluid inertia overcomes the viscous stresses, and the laminar motion becomes unstable. The fluid goes through transitional flow regions as described previously. The pressure and velocity fluctuations become very rapid and the fluid motion becomes inherently three-dimensional and unsteady, which is described as turbulence. The flow in turbulence is a mixture of intertwined eddies or swirls of different sizes. There is a large amount of mixing involved with these finite-sized eddies compared to laminar flow. The

D. Sanders

Chapter 1. Introduction

three-dimensional eddy structure greatly promotes mixing within the fluid while the mixing is confined to the molecular scale for laminar flow. Fluctuating eddies within the turbulence exists over a large number of wavelengths due to the physical process of vortex stretching. The turbulence gains energy if the vortex elements are primarily oriented in a direction such that they can be stretched by the velocity gradients. This stretching of the vortex elements maintains the fluctuating vorticity and keeps the flow three-dimensional.

Flow properties in turbulence can be described in terms of their mean properties and the fluctuating components. For example, instantaneous velocity in the x-direction, $u = u(x, y, z, t)$, and the time mean is described as

$$\bar{u} = \frac{1}{T} \int_{t_0}^{t_0+T} u(x, y, z, t) dt \quad (1.16)$$

where T is the time interval, which is longer than the period of fluctuations but shorter than unsteadiness of the average velocity. The fluctuating part of velocity is, u' , is related to the mean velocity value by

$$u = \bar{u} + u' \quad (1.17)$$

The fluctuations are equally distributed on either side of the average so the square of the fluctuation quantity, $(u')^2$. The fluctuations within turbulent flow can occur temporally or spatially. Typically, turbulent flows are described as stationary and homogenous if the mean flow does not vary over time and is spatially uniform in all directions. The Reynolds stress components $\overline{u'^2}$, $\overline{v'^2}$, and $\overline{w'^2}$ or the root-mean squared fluctuations are a measurement of the intensity of the turbulent fluctuations. The Reynolds stress is typically normalized relative to the mean flow velocity using the equation

Chapter 1. Introduction

$$\hat{u} = \frac{\sqrt{\overline{(u')^2}}}{\bar{u}} \quad \hat{v} = \frac{\sqrt{\overline{(v')^2}}}{\bar{v}} \quad \hat{w} = \frac{\sqrt{\overline{(w')^2}}}{\bar{w}} \quad (1.18)$$

these definitions are known as the relative turbulent intensities. When these relative intensities are approximately equal, the turbulence is referred as isotropic.

Another important turbulence parameter is the period of fluctuations or time scale. This is determined by investigating the relative size of the turbulent eddies. The largest eddies carry most of the energy and enhance the transfer of mass, momentum, and energy. The range of eddies overlap in space, as larger eddies carry smaller eddies. Turbulence incorporates an energy cascade process where kinetic energy is transferred from larger eddies to smaller eddies. The smallest eddies dissipate the kinetic energy through viscous shear into heat.

Kolmogorov's universal equilibrium theory states that the smaller eddies should be in a state where the rate of receiving energy from the larger eddies is equal to the rate which the smallest eddies dissipate the energy to heat. The type of energy being transferred is the called turbulent kinetic energy, k (energy per unit mass) through the cascade process. The Reynolds stress and the turbulence intensity (measured in percent) are related to the turbulent kinetic energy using the equations

$$k = \frac{1}{2} (\overline{u'^2} + \overline{v'^2} + \overline{w'^2}) \quad (1.19)$$

$$Tu = 100 \frac{\sqrt{\overline{(u')^2}}}{\bar{u}} = 100 \sqrt{\frac{2}{3} \frac{k}{\bar{u}^2}} \quad (1.20)$$

Chapter 1. Introduction

The motion at the smallest scales should depend upon the rate at which the larger eddies supply the energy, $\varepsilon = -dk/dt$, and the kinematic viscosity, ν . The Kolmogorov scales of length (η), time (τ), and velocity (v) scales are depended on the dissipation rate, ε , and given as

$$\eta = (\nu^3/\varepsilon)^{1/4} \quad \tau = (\nu/\varepsilon)^{1/2} \quad v = (\nu\varepsilon)^{1/4} \quad (1.21)$$

Like light, turbulent eddies have a range of energies at different wave numbers (κ) or wavelengths ($\lambda = 2\pi/\kappa$). Using the Fourier transform, the turbulent kinetic energy can be described as

$$k = \int_0^\infty E(\kappa) d\kappa \quad (1.22)$$

where $E(\kappa)$ is the energy spectrum density. The spectral representation of turbulence for the large energy-containing eddies is defined as the integral length scale (l_m). The integral length scale is computed by taking the autocorrelation of the measurement of the velocity fluctuations using the equation

$$\mathfrak{R}_\tau = \frac{\overline{u(t)u(t+\tau)}}{\overline{u^2(t)}} \quad (1.23)$$

This autocorrelation function is integrated from the origin to the first zero crossing resulting in an integral time scale. The integral length scale is obtained by multiplying the integral time scale by the freestream velocity using Taylor's frozen turbulence assumption [11]. The Taylor microscale, λ_T , is derived from using the slope and curvature of autocorrelation function, f , at the origin with the equation

$$\lambda_T = \sqrt{\frac{-2}{(\partial^2 f / \partial x^2)_{x=0}}} \quad (1.24)$$

Chapter 1. Introduction

When the turbulence is homogenous and isotropic, the analysis of Taylor shows that the turbulent kinetic energy (k) and dissipation rate (ε) is related to the Taylor microscale with the equation

$$\varepsilon = -\frac{dk}{dt} = \frac{10vk}{\lambda_T^2} \quad (1.25)$$

Using this relationship and Eq. (1.23), the Kolmogorov length scale (η) can be put in terms of the Taylor microscale (λ_T) as

$$\eta = \frac{(\lambda_T \nu)^{1/2}}{(10k)^{1/4}} \quad (1.26)$$

Experimental measurements [11] indicate that

$$\varepsilon \approx 0.09 \frac{k^{3/2}}{l_m} \quad (1.27)$$

Using this correlation, the definition of the Kolmogorov length scale (Eq. 1.23), and combining Eq. (1.27) and Eq. (1.29) yields

$$\frac{\lambda_T}{\eta} \approx 7 \left(\frac{l_m}{\eta} \right)^{1/3} \quad (1.28)$$

Typically the Taylor microscale is estimated to be at least 70 times the Kolmogorov length scale. It involves a quantity characteristic of small, dissipating eddies as well as large, energy-containing eddies. It typically cannot be used to characterize either the large or small eddies. Kolmogorov hypothesized that for a very large Reynolds number there is a range of eddy sizes between the largest and smallest scale for which the cascade process is independent of the

Chapter 1. Introduction

statistics of the energy- containing eddies and the effects of viscosity. He concluded that $E(\kappa)$ depends upon κ and ε only and described with the equation

$$E(\kappa) = C_\kappa \varepsilon^{2/3} \kappa^{-5/3}, \quad \frac{1}{l_m} \ll \kappa \ll \frac{1}{\eta} \quad (1.29)$$

where C_κ is the Kolmogorov constant. Figure 1.10 shows the typical energy spectrum for turbulent flow. The Taylor microscale of turbulence is found within the inertial sub-range of the energy spectrum.

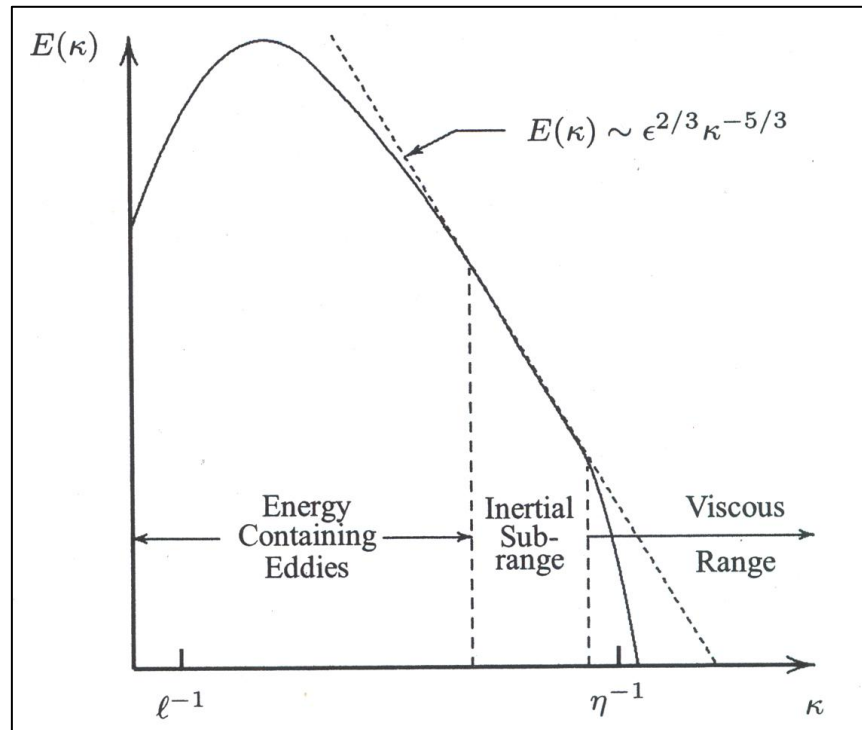


Figure 1.9. Energy spectrum for a turbulent flow in log-log scales [11]

These ranges of length scales are randomly transported within the flow resulting in a relatively large shearing force. The shear stress in turbulent flow is described with the following equation

$$\tau = \tau_{lam} + \tau_{turb} = \mu \frac{d\bar{u}}{dy} - \rho \overline{u'v'} \quad (1.30)$$

Chapter 1. Introduction

When the flow is laminar, $\overline{u'v'} = 0$. The turbulent shear stress ($-\rho\overline{u'v'}$) is positive hence the stress is greater in laminar flow than turbulent flow. The process of the transfer of momentum and other quantities in turbulence is sufficiently similar mathematically to the molecular process to suggest that an eddy or turbulent viscosity can be defined where:

$$\tau_{turb} = \mu_{turb} \frac{d\bar{u}}{dy} \quad (1.31)$$

The eddy viscosity is a function of the fluid properties and flow conditions and is not easily determined. The sum of the eddy viscosity and fluid viscosity, called the effective viscosity, is sometimes 400 times larger than the fluid viscosity. The reason for the difference is the characteristic length for turbulent flow is the size of the eddies rather than the mean free path of molecules as in laminar flow. The strong diffusiveness helps turbulent flow withstand much stronger adverse pressure gradients than laminar flow without separating.

1.2.4 Turbulent Flow Boundary Layers

The turbulent boundary layer can be treated as a composite layer consisting of an inner and outer region. The inner region of the turbulent boundary layer is much smaller than the outer region. The mean velocity distribution in the inner region is determined by the wall shear stress, density, viscosity, and distance from the wall by an expression known as the law of the wall.

$$u^+ = \frac{u}{u_{turb}} = \phi_1(y^+) \quad (1.32)$$

where $u_{turb} = (\tau_w/\rho)^{1/2}$ is the friction velocity. The parameter y^+ is the Reynolds number based on turbulent length scale ($y^+ = yu_{turb}/\nu$). The inner region can be divided into three layers identified as the viscous sublayer, the transitional region, and the fully turbulent region. In the

Chapter 1. Introduction

viscous sublayer, stress is mainly viscous since the turbulent fluctuations become zero at the wall. This region is non-uniform in time and distance along the wall. The effect of viscosity decreases as distance from the wall is increased. Ultimately, the region is reached where the flow is completely turbulent. The transition region, viscous and turbulent stresses are of similar magnitude. The size of the viscous and transition region is quite small compared to the overall turbulent region.

The outer region encompasses 80-90% of the boundary layer thickness. According to experiments [12], the mean velocity distribution in the outer region can be described by the following expression called the velocity deficit law.

$$\frac{(u_e - u)}{u_{turb}} = f\left(\frac{y}{\delta}\right) \quad (1.33)$$

This is not valid close to the wall and depends on the Reynolds number $(\delta u_{turb}/\nu)$ and ratio y/δ . As $y \rightarrow \delta$ the function goes to zero. Although the behavior of turbulent flow in the inner and outer regions is quite different, the regions are coupled by the shear stress-profile and the general diffusivity of turbulence.

The phenomena of laminar and turbulent flow, transition, separation and reattachment are evident in the flows modeled in this investigation, and the related flow theory provides the basis for the interpretation of the CFD predictions. Thus, the above review of fundamental boundary layer, transition and turbulence concepts has been provided as an introduction to the CFD modeling results to be described.

1.3 CFD Methods of Predicting Low Reynolds Number Effects in LPT Blades

The development of high speed digital computers has had a large impact on the way fluid mechanics and heat transfer is applied to design problems in modern engineering practice. Computational Fluid Dynamics (CFD) has been a well known methodology for solving complex problems of fluid mechanics and heat transfer. In CFD, the Navier-Stokes partial differential equations for fluid flow are solved numerically using finite difference methods. The beginning of modern numerical analysis is sometimes attributed to a famous paper by Courant, Friedrichs, and Lewy in 1928. The acronym CFL, frequently used in the CFD literature stands for the last names of these authors. In the paper, uniqueness and existence questions were addressed for the numerical solutions of partial differential equations [13].

Numerical modeling of turbulent flows using CFD has been a challenge due to the inherent randomness, three-dimensionally, and time dependence associated with turbulent flows. An enormous amount of information is required to completely describe a turbulent flow problem. The largest turbulent eddies can in some cases be as large as the width of the flow and are directly affected by the boundary geometry. There is a large range of time scales and length scales that need to be resolved.

There are three primary types of CFD methods used for modeling of turbulent flows. These methods are direct numerical simulations, large eddy simulations, and Reynolds-Averaged Navier-Stokes equations. The suitability of a particular method for a particular flow problem depends on several factors including computational cost, ease of use, range of applicability, and accuracy. It is the decision of the user based on these factors to judge whether a particular method would be suitable for the turbulent flow problem of interest. For this particular study, there is special interest in the accurate prediction of aerodynamic losses of boundary layers

Chapter 1. Introduction

undergoing turbulent transition and separation in turbomachinery geometries. The next sections will discuss the CFD methods of direct numerical simulations (DNS), large eddy simulations (LES), and Reynolds-Averaged Navier-Stokes (RANS) in greater detail including the advantages and disadvantages of each method. Also, a literature review of several studies will be presented where DNS, LES, and RANS CFD methods have been applied to LPT flows for the prediction of separated and transitional flow and compared to experimental cascade results.

1.3.1 Direct Numerical Simulation CFD Method

Advances in computing and storage capacity of high performance computing systems have made possible computations using direct numerical simulations. DNS uses the finite difference form of the three-dimensional incompressible Navier-Stokes and continuity equations stated below.

Continuity

$$\frac{\partial \rho}{\partial t} + \frac{\partial}{\partial x}(\rho u) + \frac{\partial}{\partial y}(\rho v) + \frac{\partial}{\partial z}(\rho w) = 0 \quad (1.34)$$

Navier-Stokes

$$\begin{aligned} \rho \frac{Du}{Dt} &= \rho f_x - \frac{\partial p}{\partial x} + \frac{\partial}{\partial x} \left[\frac{2}{3} \mu \left(2 \frac{\partial u}{\partial x} - \frac{\partial v}{\partial y} - \frac{\partial w}{\partial z} \right) \right] + \frac{\partial}{\partial y} \left[\mu \left(\frac{\partial u}{\partial y} + \frac{\partial v}{\partial x} \right) \right] + \frac{\partial}{\partial z} \left[\mu \left(\frac{\partial w}{\partial x} + \frac{\partial u}{\partial z} \right) \right] \\ \rho \frac{Dv}{Dt} &= \rho f_y - \frac{\partial p}{\partial y} + \frac{\partial}{\partial x} \left[\mu \left(\frac{\partial v}{\partial x} + \frac{\partial u}{\partial y} \right) \right] + \frac{\partial}{\partial y} \left[\frac{2}{3} \mu \left(2 \frac{\partial v}{\partial y} - \frac{\partial u}{\partial x} - \frac{\partial w}{\partial z} \right) \right] + \frac{\partial}{\partial z} \left[\mu \left(\frac{\partial v}{\partial z} + \frac{\partial w}{\partial y} \right) \right] \\ \rho \frac{Dw}{Dt} &= \rho f_z - \frac{\partial p}{\partial z} + \frac{\partial}{\partial x} \left[\mu \left(\frac{\partial w}{\partial x} + \frac{\partial u}{\partial z} \right) \right] + \frac{\partial}{\partial y} \left[\mu \left(\frac{\partial v}{\partial z} + \frac{\partial w}{\partial y} \right) \right] + \frac{\partial}{\partial z} \left[\frac{2}{3} \mu \left(2 \frac{\partial w}{\partial z} - \frac{\partial u}{\partial x} - \frac{\partial v}{\partial y} \right) \right] \end{aligned} \quad (1.35)$$

No turbulence modeling is required as in other numerical schemes, as DNS can directly resolve the whole spectrum of turbulent eddy scales. The value of DNS is obvious in that it can be used to understand the turbulent structures and processes for a given flow problem. It can also be viewed as an additional source of experimental data. It allows for detailed analysis of the

Chapter 1. Introduction

complex flow physics involved when separation and transition exist, which cannot be measured using current experimental methods. These results can be obtained only if the DNS simulation has high numerical accuracy and correct boundary and initial conditions. However, the computational cost required for DNS computations is proportional to Re_t^3 , where $Re_t = k^{1/2} l_m / \nu$, known as the turbulent Reynolds number. The number of grid points has to be high enough to be able to resolve the smallest eddy. Similarly, the time-step in the computation should be the same order as the Kolmogorov time scale, τ (Eq. (1.23)). Therefore DNS is rarely employed for simulations involving three-dimensional rotating turbomachinery due to the high computational cost even at low Reynolds numbers.

Several studies have been done where computations based on DNS were successfully applied to low Reynolds number flows [14-27] in stationary LPT cascade geometries. Enomoto *et al.* [14] applied DNS to the Pack-B turbine blade airfoil at a Reynolds number of 43,000 and compared the results to the experimental measurements of Lake [18]. The blade loading and total pressure loss coefficient showed a reasonable comparison with experimental results. It was demonstrated that the flowfield is dominated by relatively large eddies near the blade surface and that DNS can be used to simulate low Reynolds number flowfields relatively well. Singh *et al.* [15] simulated flow with Reynolds numbers of 10,000 and 25,000 on the Pack-B blade airfoil using two different boundary conditions, a static inflow boundary condition with extrapolated outflow, and dynamic inflow boundary condition which accounted for the upstream influence in subsonic flow. Results using the static inflow boundary condition showed that the laminar boundary layer on the suction surface becomes separated and forms two-dimensional clockwise vortices, which then become three-dimensional as they convect downstream to the trailing edge due to spanwise instabilities. The location of the onset of separation compared well to

Chapter 1. Introduction

experimental measurements. They observed different behavior at the Reynolds number of 25,000 using the dynamic inflow boundary conditions, where separation was found to be smaller when compared to the results from static boundary condition specification [15].

DNS simulations were advanced further by Rizzetta and Visbal [16,17] by modeling active flow control using vortex generating jets and plasma-based flow control to reduce separation and total pressure loss. It was reported that pulsed vortex generating jets helped to maintain the boundary layer attached for an additional distance of 19-21% along the blade with a 53-56% decrease in total pressure loss [16]. Plasma based flow control using dielectric barrier discharge actuators were simulated at an inlet Reynolds number of 25,000 [17]. Counter-flow plasma injection was found to provide the most effective control, producing vortices that enhanced mixing and brought higher momentum fluid to the boundary layer causing the flow to remain attached to the blade suction surface all the way to the trailing edge.

1.3.2. Large Eddy Simulation CFD Method

An alternative to the DNS method is large eddy simulation (LES). It enables the use of coarser meshes and larger time-steps with less computational cost than required by DNS. The governing equations in LES are obtained by filtering the unsteady Navier-Stokes equations using Fourier, Gaussian, or other filters. The filtering process separates the eddies whose scales are smaller than the grid spacing from the resolvable scaled eddies. The subgrid scale eddies are modeled because they are nearly isotropic and have universal characteristics. Some of the types of subgrid-scale models (SGS) are the Smagorinsky SGS model and Dynamic SGS model. Because the large scale eddy unsteady motions are resolved explicitly, LES can be more accurate than most RANS solvers, especially for flows over bluff bodies with unsteady separation and vortex shedding. The dynamics of these large scale eddy motions are computationally expensive

Chapter 1. Introduction

to model. Since the small scale eddy motions are described using simple models, LES has less computational expense than DNS. Nearly all the computation effort in DNS is used in resolving the smallest eddy dissipation. For boundary layer flows with isotropic turbulence, LES typically provides enough frequency modes to resolve 80% of the eddy energy spectrum even at high Reynolds numbers [12]. The grid resolution requirements are still high for boundary layer flows because the size of the near wall eddies within the boundary layer are relatively small. The boundary layer grid resolution increases with $Re_t^{1.8}$. Thus LES has been successfully applied to boundary layer flows at low and moderate Reynolds numbers. At high Reynolds numbers, LES is currently computationally expensive for flows involving aircraft wings and complex geometries such as rotating turbomachinery but it can be used to help improve engineering models of turbulence.

LES has emerged as a viable means for the investigation of transitional and separated flow associated with low Reynolds numbers in low pressure turbine cascade geometries [19-21]. Mittal *et al.* [19] simulated a cascade configuration at Reynolds numbers of 10,000 and 25,000 and found that the dynamics of the separation phenomenon on the suction surface are dominated by Karman vortex shedding and cannot occur without vortices shed from the pressure side. Accurate representation of the pressure side boundary layer is required to capture the separation dynamics on the suction side. Revady *et al.* [20] demonstrated the ability to successfully predict transition and identified a coupling between the separation bubble and the vortex shedding generated by the trailing edge. The effect of passing wakes on LPT blade airfoil surfaces was investigated using LES by Sarkar and Voke [21]. They observed that vortices form over the rear half on the suction surface by the rollup of the shear layer as wakes pass over the separation

Chapter 1. Introduction

region. Large pressure fluctuations were measured on the suction surface due to the wake passing and showed good agreement with experimental results and a similar DNS simulation.

1.3.3. Reynolds Averaged Navier-Stokes (RANS) CFD Method

The most widely adopted CFD method used for practical engineering applications is the Reynolds Averaged Navier-Stokes (RANS) equations. All flow quantities are expressed as the sum of mean and fluctuating parts, where the whole range of turbulent scales is being modeled. Reynolds averaging assumes a variety of forms involving either an integral or summation. Time averaging is the most appropriate forms of Reynolds averaging because most engineering problems involve inhomogeneous turbulence. The RANS equations are developed from the time-averaging of the Navier-Stokes equations and are given as

$$\rho \frac{\partial U_i}{\partial t} + \rho U_j \frac{\partial U_i}{\partial x_j} = -\frac{\partial P}{\partial x_i} + \frac{\partial}{\partial x_j} (2\mu S_{ij} - \rho u'_i u'_j) \quad S_{ij} = \frac{1}{2} \left(\frac{\partial U_i}{\partial x_j} + \frac{\partial U_j}{\partial x_i} \right) \quad (1.36)$$

where S_{ij} is the mean-strain rate tensor. Also note the appearance of the term $\overline{u'_i u'_j}$ in the RANS equation. The RANS equations are solved for the mean fluid properties. In order to compute the velocity field for turbulent flow, the term $\overline{u'_i u'_j}$ must be defined. This term is the Reynolds stress tensor and is defined as

$$\tau_{ij} = -\rho \overline{u'_i u'_j} \quad (1.37)$$

The Reynolds stress is a symmetric tensor where $\tau_{ij} = \tau_{ji}$. For general three-dimensional flows, the four unknowns of pressure and the three components of the velocity need to be solved along with the six Reynolds stresses as a result of the Reynolds averaging. The pressure and velocity components can be resolved from the Reynolds averaged continuity and RANS equations. An expression for the Reynolds stress is required to obtain a closed form solution. A turbulence

Chapter 1. Introduction

model or directly modeled Reynolds stress transport equation is used to obtain a closed form solution to the RANS equations.

Both the algebraic and transport equation turbulence models are used to bring closure to RANS equations. Algebraic models are based on the Boussinesq eddy-viscosity approximation which states that the Reynolds stress relates to the eddy viscosity, μ_t , with the equation

$$-\overline{\rho u'_i u'_j} = 2\mu_t S_{ij} - \frac{2}{3}\mu_t \frac{\partial U_k}{\partial x_k} \delta_{ij} - \frac{2}{3}\rho k \delta_{ij} \quad (1.38)$$

Algebraic turbulence models are the simplest turbulence models for determining the eddy viscosity. Transport equation models solve for the quantities of the turbulent kinetic energy and dissipation rate of the energy-containing eddies. There many types of turbulence models used to solve engineering flows and each model has its advantages and limitations. All the different types of conventional turbulence models are presented in text such as Wilcox [11]. The particular interest of this study is the type of RANS turbulence models that have been applied to prediction of transitional and separated flows associated with low Reynolds number effects with success.

1.4 Transition Modeling

1.4.1. e^N Method

The e^N method, based on linear stability theory, is one of the most popular methods available for transition prediction. It can be used with either the local stability approach or the non-local linear Parabolized Stability Equations (PSE) approach. The local approach implies that the stability of the flow at a particular location is determined by the local conditions at that

Chapter 1. Introduction

location and independent of all others and assumes the mean flow is locally parallel. The instabilities are described with the equation

$$q'(x, y, z, t) = q(y) \exp(-\alpha_i x) \exp[i(\alpha_r x + \beta z - \omega t)] \quad (1.39)$$

where z is the spanwise direction, α and β are complex representations of the wave number components in the x and z directions, and ω is the frequency. The non-local linear PSE approach states that the mean flow and amplitude functions is dependent on both x and y , and α depends on x , so that the instabilities are described as

$$q'(x, y, z, t) = q(x, y) \exp \left[i \left(\int_{x_0}^x \alpha(X) dX + \beta z - \omega t \right) \right] \quad (1.40)$$

The stability of the flow at a given location depends the upstream history of the disturbances. The surface of curvature of the body is taken to account by the linear PSE approach because these effects are of the same order of magnitude as the non-parallel effects [10]. Also, the streamwise pressure gradient is automatically taken into account through the shape of the mean velocity profile.

There are three steps in the application of the e^N method. The first involves computing the laminar flow velocity and temperature profiles at different streamwise locations for a given flowfield. Secondly, the amplification rates of the most unstable waves are calculated for each profile. These amplification rates are used to calculate the transition location in the third step. The value for the “ N ” factor is determined by looking at the amplification rate of the spatial varying wave defined as

$$\ln(A/A_0) = - \int_{x_0}^x \alpha_i dx \quad (1.41)$$

Chapter 1. Introduction

where A is the wave amplitude at any location and A_0 is the wave amplitude where that wave becomes unstable at x_0 . The “ N ” factor is calculated as

$$N = \underset{f}{Max}[\ln(A/A_0)] \quad (1.42)$$

where the total amplification rate has been determined for a series of instabilities (f_1, f_2, f_3, \dots). The e^N method assumes transition to occur for a predefined value of N factor defined as N_T . This means that the breakdown to turbulence is observed when the most amplified wave has been amplified by a critical ratio, $\exp(N_T)$. The one disadvantage is the value of the N factor is not universal for transition and needs to be validated based on experimental data.

1.4.2. Dorney *et al.* Model

Dorney *et al.* [22] modified both the Baldwin-Lomax and standard $k-\varepsilon$ model to include numerical models for the prediction of separated and transitional flows. A natural transition model called the Abu-Ghannam and Shaw (AGS) model which determines the start of transition based on the momentum thickness is given as

$$Re_\Theta = 163 + \exp\left[F(\lambda_\Theta) - \frac{F(\lambda_\Theta)}{6.91} Tu\right] \quad (1.43)$$

The relationship of $F(\lambda_\Theta)$ is given in Ref. [22] with more details. This model is considered to be valid up to turbulent intensities of $Tu = 10\%$. The end of the transition region is calculated as

$$Re_L = 31.8(Re_\Theta)^{1.6} \quad (1.44)$$

An intermittency function γ was used in the region between the start and end of transition and is calculated as

$$\gamma = 1 - \exp(-4.64\zeta^2) \quad (1.45)$$

Chapter 1. Introduction

This function represents the fraction of the total time that the flow is turbulent. It is equal to zero in laminar flow and unity in fully turbulent flow. The intermittency is multiplied by the turbulent viscosity in the turbulence model. The separated flow region was modeled with the correlation

$$\text{Re}_\Theta = 25000 \log_{10}(1/\tanh(0.173205\tau)) \quad (1.46)$$

The Dorney *et al.* [22] model was applied at three inlet Reynolds numbers of 43,000, 86,000, and 172,000 for the Pack-B blade airfoil. The predicted total pressure losses using both of the modified turbulent flow models were greater than the experimental values at all three Reynolds numbers due to the difference in the separation and reattachment locations and the size of the separation region.

1.4.3. Suzen *et al.* Model

A study by Suzen *et al.* [23] used the turbulent viscosity expression from Menter's k - ω (SST) model as $\mu_t^* = \gamma\mu_t$. A transport equation was used to solve for the intermittency function, γ , given as

$$\begin{aligned} \frac{\partial \rho \gamma}{\partial t} + \frac{\partial \rho u_j \gamma}{\partial x_j} = (1 - \gamma) & \left[(1 - F) 2 C_0 \rho \sqrt{u_k u_k} f(s) f'(s) + F \left(\frac{C_1 \gamma}{k} \tau_{ij} \frac{\partial u_i}{\partial x_j} - C_2 \gamma \rho \frac{k^{3/2}}{\varepsilon} \frac{u_i}{(u_k u_k)^{1/2}} \frac{\partial u_i}{\partial x_j} \frac{\partial \gamma}{\partial x_j} \right) \right] \\ & + C_3 \rho \frac{k^2}{\varepsilon} \frac{\partial \gamma}{\partial x_j} \frac{\partial \gamma}{\partial x_j} + \frac{\partial}{\partial x_j} \left(((1 - \gamma) \gamma \sigma_\gamma \mu + (1 - \gamma) \gamma \sigma_\gamma \mu_t) \frac{\partial \gamma}{\partial x_j} \right) \end{aligned} \quad (1.47)$$

The constants and auxiliary relations were given in more detail in Ref. [23]. The intermittency transport equation was used to obtain the distribution of intermittency in the transitional flow region, while the onset of transition was determined by correlations. The onset of attached transitional boundary layer flow was determined with a correlation for Reynolds number based on momentum thickness, given as

D. Sanders

33

Chapter 1. Introduction

$$\text{Re}_{\ominus} = (120 + 150Tu^{-2/3}) \coth[4(0.3 - K_t \times 10^5)] \quad (1.48)$$

where K_t is called the acceleration parameter. In order to determine the onset of separated flow transition, the Reynolds number, Re_{st} , is expressed in terms of the turbulence intensity (Tu) and momentum thickness Reynolds number of the separation point, Re_{\ominus} using the correlation as

$$\text{Re}_{st} = 874 \text{Re}_{\ominus}^{0.71} \exp[-0.4Tu] \quad (1.49)$$

The Suzen *et al.* [23] model was applied to two different cascade grid topologies. Results compared well with three different experiments with differences in separation and reattachment locations.

1.4.4. Prasnier and Clark Model

Another approach by Prasnier and Clark [24] used correlations developed from an experimental database for attached flow transition, laminar separation with turbulent attachment, and separated-flow transition. The experimental database consisted of 57 cases of seven different turbomachinery-specific airfoils at various boundary conditions. Laminar flow simulations were performed for experimental cascade configurations at the appropriate in boundary conditions. The pre-transitional boundary layer was modeled using a “quasi-laminar” formulation of the Wilcox $k-\omega$ model in the laminar region of the boundary layer. In this formulation, the production of k and ω were kept at a minimum to allow for the convection and diffusion of freestream turbulence into a quasi-laminar boundary layer.

A momentum thickness Reynolds number correlation based on the experimental database was given as

Chapter 1. Introduction

$$\text{Re}_\Theta = A \left(Tu \frac{\Theta}{l_m} \right)^B \quad (1.50)$$

It was used to determine the onset of attached transitional flow, where A and B were constants equal to 8.52 and 0.956, respectively. The onset of separated-flow transition was modeled using

$$\frac{L_{sep}}{S_{sep}} = C \text{Re}_{\Theta-sep}^D \quad (1.51)$$

where C and D were constants equal to 173.0 and -1.227, respectively, L_{sep} was the distance between separation and transition onset, and S_{sep} was the surface distance from the stagnation point to the separation location. If the separated-flow transition was predicted to occur downstream of the trailing edge, the simulation was run as fully laminar. Once transition occurred, the Wilcox $k-\omega$ model was used to model the fully turbulent flow. The Prasnier and Clark [25] model showed significant improvement over a conventional fully turbulent flow model in the predicted accuracy of the total pressure loss for both linear cascades and multistage LPT rigs.

1.4.5. The Menter *et al.* $\gamma\text{-Re}_\Theta$ Model

Menter *et al.* [26] has developed a new transitional flow model called the $\gamma\text{-Re}_\Theta$ model. Instead of using the momentum thickness Reynolds number to trigger the onset of transition, the $\gamma\text{-Re}_\Theta$ model was based on the vorticity Reynolds number, Re_v , given as

$$\text{Re}_v = \frac{\rho y^2}{\mu} \frac{\partial u}{\partial y} = \frac{\rho y^2}{\mu} \Omega \quad (1.52)$$

Chapter 1. Introduction

where y is the distance from the wall, and Ω is the vorticity. The maximum value of Re_v was dependent on the momentum thickness Reynolds number. A transport equation for the intermittency was used to trigger the transition process and defined as

$$\frac{\partial \rho \gamma}{\partial t} + \frac{\partial \rho u_j \gamma}{\partial x_j} = P_{\gamma 1} - E_{\gamma 1} + P_{\gamma 2} - E_{\gamma 2} + \frac{\partial}{\partial x_j} \left[\left(\mu + \frac{\mu_t}{\sigma_f} \right) \frac{\partial \gamma}{\partial x_j} \right] \quad (1.53)$$

Also, a transport equation for the momentum thickness Reynolds number at the transition onset, $Re_{\Theta t}$ was used and given as

$$\frac{\partial Re_{\Theta t}}{\partial t} + \frac{\partial \rho u_j Re_{\Theta t}}{\partial x_j} = P_{\Theta t} + \frac{\partial}{\partial x_j} \left[\sigma_{\Theta t} (\mu + \mu_t) \frac{\partial Re_{\Theta t}}{\partial x_j} \right] \quad (1.54)$$

The intermittency transport equation included two terms that controlled the production of intermittency. These terms were the F_{length} and $Re_{\Theta c}$, which were determined by proprietary empirical correlations. $Re_{\Theta c}$ was defined as the momentum thickness Reynolds number at the point where the intermittency started to increase in the boundary layer and F_{length} controlled the length of the transition zone. The $Re_{\Theta t}$ transport equation outside the boundary layer was forced to follow an experimental empirical correlation. This was then diffused by the boundary layer by a standard diffusion term. When the boundary layer became separated, the transition model was modified so that the intermittency could exceed unity when the boundary layer separated. This modification was given as

$$\gamma_{sep} = \min \left\{ 8 \max \left[\left(\frac{Re_v}{2.193 Re_{\Theta c}} \right) - 1, 0 \right] \exp - \left(\frac{R_T}{15} \right)^4, 5 \right\} F_{\Theta t} \quad (1.55)$$

where $F_{\Theta t}$ is a blending function within the auxiliary relationship from Eq. (1.54) and is confined the modification to boundary layer flows. Eq. (1.55) allowed for the control of the

D. Sanders 36

Chapter 1. Introduction

separation bubble resulting in a larger production of turbulent kinetic energy, which corrected the prediction of reattachment [26]. The $\gamma-Re_\theta$ model transport equation was coupled with the Menter's $k-\omega(SST)$ model where the production and destruction terms were modified using intermittency. The $\gamma-Re_\theta$ model has been applied to several 2D and 3D geometries by Langtry *et al.* [27] including the Pack-B cascade, a 3D GE low-pressure turbine vane, and the T106 blade undergoing passing wakes. All simulations agreed well with experiments for all test cases at a wide range of Reynolds numbers and freestream turbulent intensities.

1.4.6. The Moore and Moore MARV Reynolds Stress Model

Moore and Moore [28] developed a Reynolds stress model for application of separated and transitional flows called the MARV Reynolds Stress Model. Traditional Reynolds stress models solved differential equations for the Reynolds stress, $\overline{u'_i u'_j}$, and the dissipation rate, ε . The MARV model specified equations for $q = \sqrt{k}$, $\omega = \varepsilon/k$, and five independent turbulent anisotropies, defined as

$$b_{ij} = \frac{\overline{u_i u_j}}{2k} - \frac{1}{3} \delta_{ij} \quad (1.56)$$

Also, the MARV model used a non-isotropic viscosity based on DNS calculations. It correctly models the behavior of the strain rate and shear stress within the boundary layer. This behavior was described as the larger velocity fluctuations in the outer portion of the boundary layer pointing toward the wall and becoming more parallel to the mean velocity vectors as the wall is approached, similar to DNS predictions. This behavior was not seen in turbulence models that used the Boussinesq approximation, where the direction of velocity fluctuations were always aligned 45° to the mean velocity vectors. The MARV Reynolds Stress model of Moore and

Chapter 1. Introduction

Moore [28] was applied to a UTRC/Pratt & Whitney cascade design of the JT9D. Reasonable agreement was achieved with experimental results for the location of increased heat transfer on the suction surface due to transition. Also, the trends in the prediction of performance were consistent with the experimental results.

1.4.7. Walters and Leylek k - k_L - ω Model

Walters and Leylek [2] developed a three-equation eddy-viscosity type model named the k - k_L - ω model. This model contained transport equations for the turbulent kinetic energy (k_T), laminar kinetic energy (k_L), and the specific dissipation rate (ω) which were given as

$$\frac{Dk_T}{Dt} = P_{k_T} + R + R_{NAT} - \omega k_T - D_T + \frac{\partial}{\partial x_j} \left[\left(\nu + \frac{\alpha_T}{\sigma_k} \right) \frac{\partial k_T}{\partial x_j} \right] \quad (1.57)$$

$$\frac{Dk_L}{Dt} = P_{k_L} - R - R_{NAT} - D_L + \frac{\partial}{\partial x_j} \left[\nu \frac{\partial k_L}{\partial x_j} \right] \quad (1.58)$$

$$\frac{D\omega}{Dt} = P_\omega + C_{\omega R} \frac{\omega}{k_T} (R + R_{NAT}) - C_{\omega 2} \omega^2 - C_{\omega 3} f_\omega \alpha_T \left(\frac{\lambda_{eff}}{\lambda_T} \right)^{4/3} \frac{\sqrt{k_T}}{d^3} + \frac{\partial}{\partial x_j} \left[\left(\nu + \frac{\alpha_T}{\sigma_\omega} \right) \frac{\partial \omega}{\partial x_j} \right] \quad (1.59)$$

The influence of the laminar and turbulent kinetic energy on the Reynolds stress term was included through the prescription of the total eddy viscosity as given in Eq. (1.60).

$$-\overline{u'_i u'_j} = \nu_{TOT} \left(\frac{\partial u_i}{\partial x_j} + \frac{\partial u_j}{\partial x_i} \right) - \frac{2}{3} k_{TOT} \delta_{ij} \quad (1.60)$$

The laminar kinetic energy was used to describe the low frequency, high amplitude fluctuations that originated from the pre-transitional boundary layer. These fluctuations primarily occurred at one scale and almost all energy was contained in a single streamwise component. The production of laminar kinetic energy was assumed to occur due to a “splat

Chapter 1. Introduction

mechanism”. This “splat mechanism” redirected the normal fluctuations of the freestream turbulence into a streamwise component while creating local pressure gradients in the boundary layer, increasing the low frequency fluctuations. These fluctuations grow to the development of turbulent spots and then to full turbulence. A local transition parameter that depended on the turbulent energy, effective length scale, and fluid viscosity determined when this occurred. Once this parameter reached a threshold value, a transfer of energy began from streamwise fluctuations (k_L) to turbulent fluctuations (k_T). In the near-wall region, the turbulent kinetic energy was split into small-scale and large-scale energy. The small-scale energy contributed to the turbulent production, and the large-scale energy contributed to the laminar kinetic energy.

Both natural, mixed, and bypass transition were resolved in the Walters and Leylek [2] model. The production terms in this model controlled the transfer from streamwise fluctuations to full turbulence which depended on the laminar kinetic energy and the local mean velocity in order to include natural and mixed transition. For the onset of transition, a parameter was calculated from the turbulent kinetic energy, kinematic viscosity, and the wall distance. When this parameter exceeded a certain threshold, transition was assumed to start. The onset of transition was associated with the reduction of laminar kinetic energy and the increase in the turbulent kinetic energy. A full description of all model constants and auxiliary equations was presented by Walters and Leylek [2].

The Walters and Leylek [2] model has been applied to the cases of a zero-pressure-gradient flat plate at various freestream turbulent intensities [2] and a circular cylinder at subcritical, critical, and supercritical Reynolds numbers [29] with good results. Also, the capability of the new model to predict transitional flow behavior has been demonstrated on a

Chapter 1. Introduction

highly loaded turbine blade airfoil with and without film cooling [30] and a flat plate with pressure distribution similar to an axial compressor undergoing passing wakes [31].

In the foregoing material, fundamental boundary layer theory and examples of CFD models applied to turbomachinery have been reviewed. This supports the dissertation goal to examine representative turbulence models and RANS solvers for LPT flow modeling and, if possible, to offer a new, characterized model for the applicability of low Reynolds numbers flow predictions.

2. Description of Experimental Cascade Configurations Utilized in the Investigation

Linear cascades have long been important in the testing of axial flow turbines and compressors. A cascade is a stationary array of blades constructed for the measurement of aerodynamic effects around the blades. Flowfield conditions are varied independently of each other in order to yield performance and efficiency data, relate flow turning angles to the blade geometry, or give qualitative clues about conditions for separation. Cascade testing has brought about the development of correlations that have been used for many current day design procedures [32]. In the present study, experimental cascade results provided reliable data of the aerodynamic properties to validate the CFD predictions.

2.1 Linear Cascade Geometry

The cascade geometry shown in Figure 2.1 is typical of compressor/turbine blade cascade test setups. The spacing (s) or pitch is defined as the distance in the tangential direction between corresponding points on adjacent blades. The chord (c) is equal to the linear distance between the front or leading edge and the rear or trailing edge of the blade. The camber line is the mean line of the blade profile. It extends from the leading edge to the trailing edge, midway between the pressure and suction surface. The stagger angle (ξ) is the angle between the chord line and axial turbine direction. The inlet and outlet flow angles are defined as the angle between the fluid flow direction and machine axial direction at the blade inlet and outlet, respectively. The inlet and exit velocities can be broken down into their axial (x) and tangential (y) components to form typical velocity triangles (Fig. 2.1). The solidity or the ratio of c/s is another important

Chapter 2. Description of Experimental Cascade Configurations Utilized in the Investigation

parameter for cascade aerodynamics. The higher this ratio, the more closely packed are the blades.

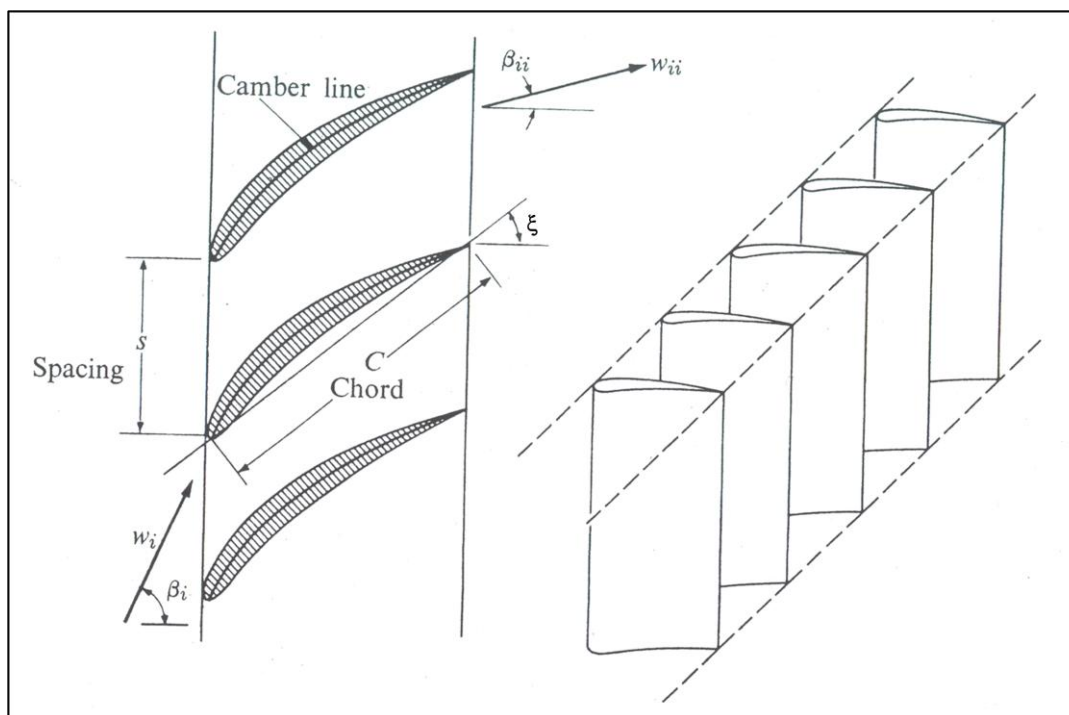


Figure 2.1. Diagram of a typical rectilinear cascade geometry [32]

2.2 The AFRL Low Speed Wind Tunnel

The experimental investigations used for comparisons with the CFD results were conducted in the Air Force Research Lab (AFRL) Low Speed Wind Tunnel (LSWT) at Wright Patterson Air Force Base [18,34-40]. The wind tunnel was a modified Aerolab Corporation open loop tunnel. A photo of facility and a schematic of the test section is shown in Figure 2.2. The inlet bell-mouth was 3.05m wide and 2.67m tall. The wind-tunnel test section is 1.22m wide and 0.85m tall at the inlet and houses the linear turbine case cascade. A 125-hp electric motor drives an axial flow fan which is capable of producing air speeds up to 80m/sec. A honeycomb flow straightener led to a convergent nozzle which reduced the flow area by 87%. Stryofoam inserts were placed in the flow straightener to help minimize corner vortices and to provide freestream

D. Sanders

42

Chapter 2. Description of Experimental Cascade Configurations Utilized in the Investigation

uniformity of better than 1% with a turbulence intensity of approximately 0.5%. An optional turbulence grid can be installed yielding freestream turbulence levels up to a maximum of approximately 4%. Turbulent length scales with these grids have been characterized by both Lake [18] and McQuilling [33].

The test section of the cascade wind tunnel (Fig. 2.2(b) had a central hinge pivot joint that allowed the inlet and outlet flow angles to be set for the referenced tests involving all airfoils studied in this research. Eight airfoils with an outboard pressure surface blade were bolted to acrylic endplates and placed in the test section. The blade axial chord was 0.18m with span of 0.88m to ensure two-dimensional flow over the midspan region of the blade. The cascade test section exhibited good uniformity and periodicity as confirmed by Lake [18].

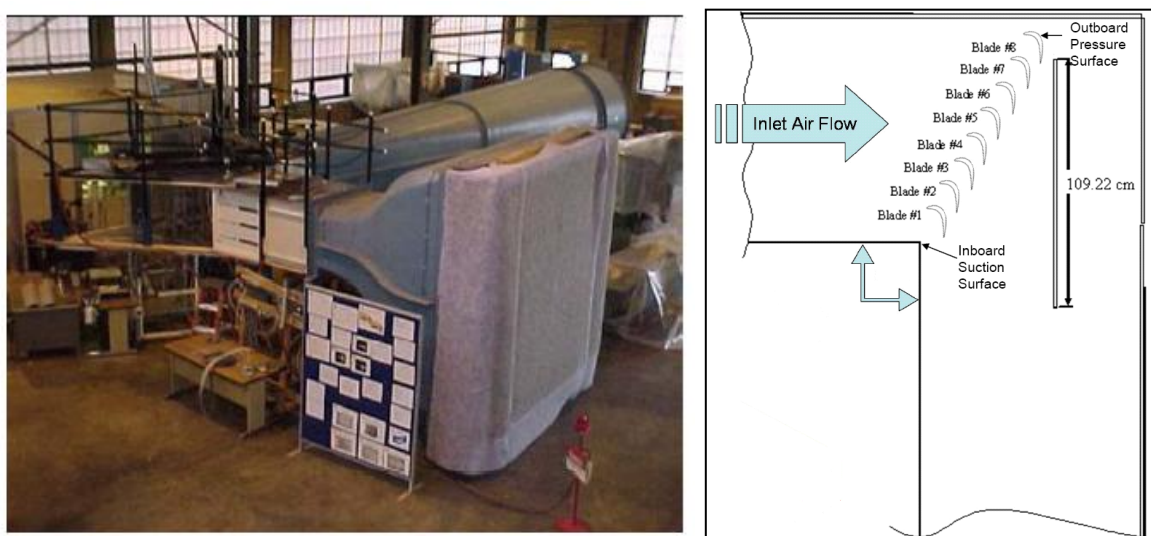


Figure 2.2. (a) AFRL Low Speed Wind Tunnel Facility[35] and (b) view of the test section [36]

2.2.1 Design of Moving Bar Wake Generator

A moving bar wake generator was designed by Nessler *et al.* [37] for the AFRL Low Speed Wind Tunnel in order to simulate the conditions in a low pressure turbine stage. The objective was to produce periodic unsteadiness in the flow impinging on the linear cascade to

Chapter 2. Description of Experimental Cascade Configurations Utilized in the Investigation

simulate the effect of upstream vane wake shedding [37]. The wake generator consisted of 0.318cm diameter unidirectional carbon fiber rods spaced 17.9cm apart which matched the trailing edge boundary layer and blade spacing of the Aft-Loaded L1A blade to be presented and discussed in further detail in Section 3.1.3. The rods were oriented vertically and fastened to a hollow pin chain which was directed through a series of sprockets and chain guides. A 3 horsepower variable frequency motor drove the chain system at speeds up to 5.0m/sec to match inlet flow velocities for Reynolds numbers below 50,000. A design optimization routine produced a track configuration with a length of 8.4m using 18 cylindrical rods equally spaced across a 3.04m span. The configuration maximized the number of primary wakes being measured while minimizing the cycle time before the first secondary wake passed through the cascade inlet. Figure 2.3 shows a track configuration and a CAD model of the wake generator.

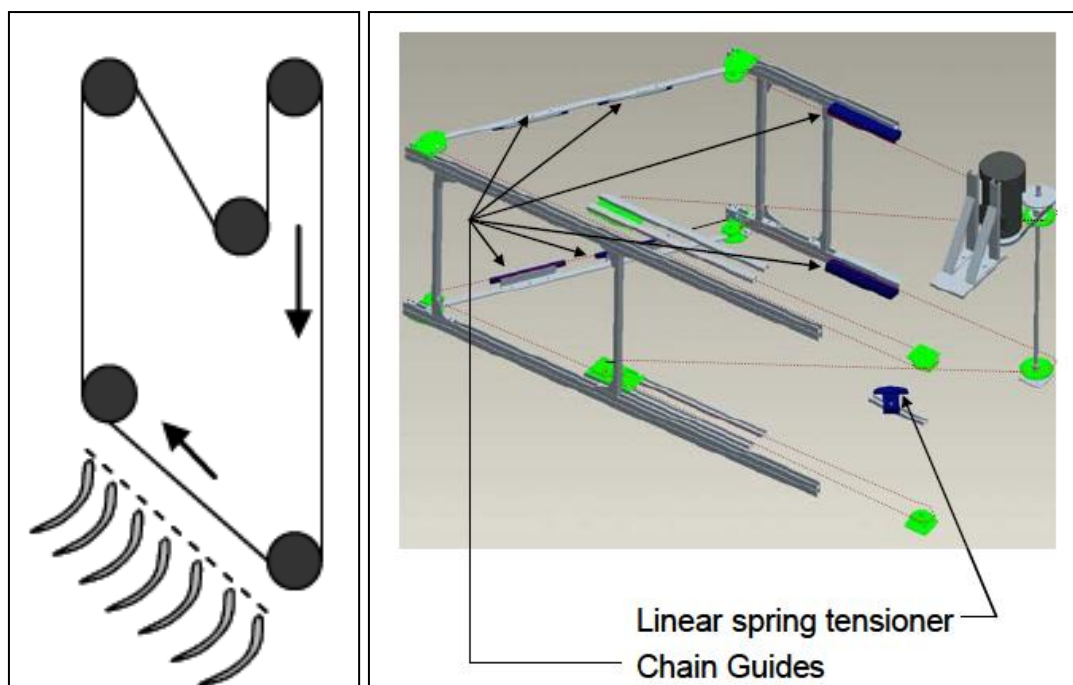


Figure 2.3. (a) Track configuration and (b) mechanical design CAD model of moving wake generator track [37]

Chapter 2. Description of Experimental Cascade Configurations Utilized in the Investigation

2.3 Measurement Techniques

Flow measurements from several different experimental studies in the AFRL LSWT were used for comparison with the CFD results. All experimental measurements were done on the middle blade to reduce side-wall effects from the cascade. Inlet Reynolds numbers were set based on inlet velocity measurements and the blade axial chord length. Surface static pressure, Particle Image Velocimetry, and wake loss measurements were made over a wide range of Reynolds numbers and freestream conditions. The next sections describe each measurement technique in greater detail.

2.3.1 Surface Static Pressure Measurements

Static pressure measurements were made using up to forty static pressure taps placed around the blade pressure and suction surface. A Druck pressure transducer with a measurement range of 0-2.0 in-H₂O was used for static pressure coefficient calculations. The static pressure coefficient (C_p) is calculated using Eq. (2.1),

$$C_p = \frac{(\overline{P_{0,i}} - P_s)}{\overline{q_i}} \quad (2.1)$$

where $\overline{P_{0,i}}$ is the average inlet total pressure, $\overline{q_i}$ is the average inlet dynamic pressure, and P_s is the static pressure on the surface of the blade. Measurements taken by Bons *et al.* [38] and Marks *et al.* [35] were used for static pressure coefficient comparisons with the CFD results.

2.3.2 Wake Loss Measurements

An upstream Pitot-static probe and a downstream total pressure Kiel probe were used to measure the static and total pressure upstream and the downstream blade wake total pressure. Each of the probes was mounted on a pitchwise traverse. A -0.2 to 0.8 in-H₂O Druck pressure

Chapter 2. Description of Experimental Cascade Configurations Utilized in the Investigation

transducer was used for the wake loss measurements. The local total pressure loss coefficient was calculated based on these measurements using Eq. (2.2) by taking the time-averaged difference between the inlet and outlet total pressure and dividing by the difference between the time-averaged inlet total and static pressure.

$$TPLC = \frac{(P_{0,inlet} - P_{0,outlet})}{(P_{0,inlet} - P_{inlet})} \quad (2.2)$$

The integrated total pressure loss coefficient was calculated for one pitch (s) using Simpson's rule based on the local total pressure loss coefficient with the equation

$$TPLC_{int} = \frac{1}{s} \int_{-s/2}^{s/2} \left(\frac{P_{0,inlet} - P_{0,outlet}}{P_{0,inlet} - P_{inlet}} \right) ds \quad (2.3)$$

Performance of the blade airfoils was evaluated based on the total pressure loss coefficient, which is an indirect measurement of the entropy generation. As entropy is generated, the total pressure at the outlet decreases due to the blade airfoil trailing edge wake and the loss coefficient increases. Inlet and outlet turbulence intensity measurements were made at the same locations using a single element hot film.

2.3.3 Particle Image Velocimetry

Particle Image Velocimetry (PIV) involves two main steps. First, a plane within the flowfield is created by illuminating seeding particles with a thin, laser-light sheet. The laser-light sheet was formed using a combination of optical lenses. The light scattered by seeding particles in the illumination plane was recorded using double-exposure photographs. In the second step, the ratio of the measured displacement between successive images of the same seed particles and the known change in time was used to calculate the local fluid velocity.

Chapter 2. Description of Experimental Cascade Configurations Utilized in the Investigation

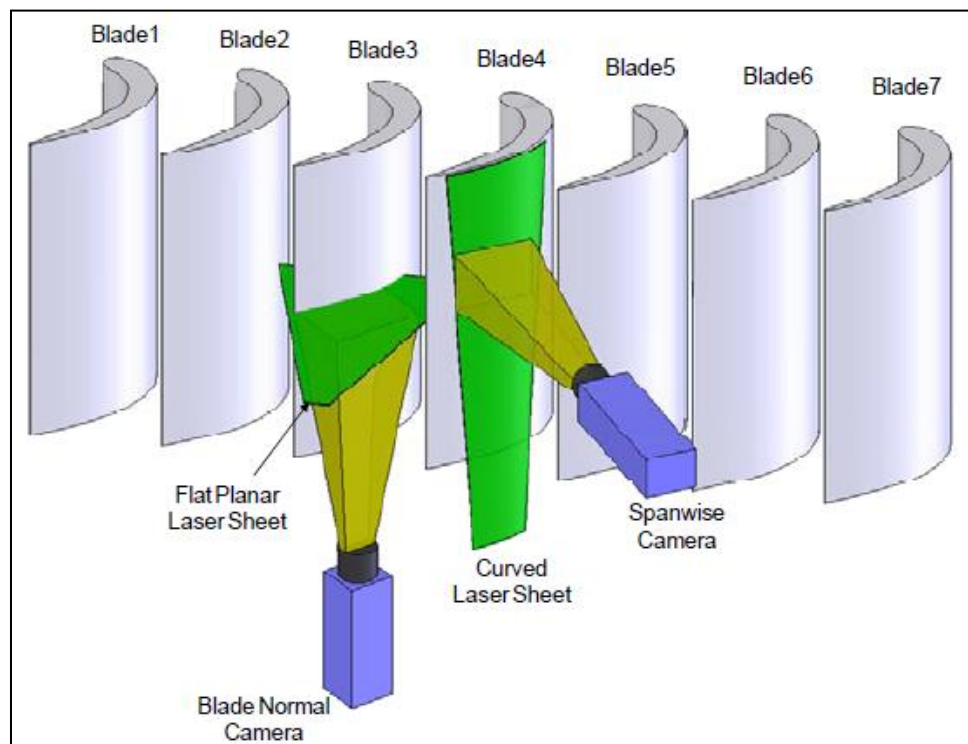


Figure 2.4. Schematic of PIV setup of laser and camera[35]

A PIV system was implemented in the Low Speed Wind Tunnel facility as shown in Figure 2.4. The lasers and cameras were mounted underneath and adjacent to the cascade. A dual-head, flashlamp-pumped Nd:YAG laser was used as the laser source, capable of dual 120mJ pulses at 15Hz repetition rate. Scattering from the seed particles was recorded on high resolution CCD digital camera sensors with a 1600x1200 pixel resolution at a maximum framerate of 30frames/sec. Two frames can be recorded sequentially with a time spacing of 100-200 μ sec depending on the flow velocity and magnification. Image pairs from the CCD cameras were recorded at a frequency of 10Hz. The camera lens provided a field of view of 119x158mm. The uncertainty PIV measurements was found to be associated with the velocity calculation that involves the displacement of pixels, the time intervals between exposures, and the magnification of the digital image relative to the object. It was found the uncertainty in the velocity to yield a maximum error of <2% in the freestream velocity and ~10% in the viscous region [35].

Chapter 2. Description of Experimental Cascade Configurations Utilized in the Investigation

The blade normal PIV images were primarily used for flowfield comparisons with the CFD results. Boundary layer velocity profiles were extracted normal to the blade surface from the PIV experiments of Marks *et al.* [35] and Woods *et al.* [39]. This PIV technique has successfully demonstrated the resolution necessary for examining flow features in complex flowfields [41].

2.4 Description of LPT Blade Airfoil Geometries

The three different LPT blade airfoils used in this study have different blade loading characteristics. The Zweifel blade force coefficient was used as the parameter to compare the blade loading for each LPT blade airfoil. The incompressible form of the Zweifel blade force coefficient, Z , is calculated with Eq. (2.4)

$$Z = 2 \frac{s}{C_x} \cos^2 \alpha_{out} (\tan \alpha_{in} - \tan \alpha_{out}) \quad (2.4)$$

where C_x is the axial chord, α_{in} and α_{out} is the inlet and outlet flow angles, respectively and s , is defined as the blade pitch. The Zweifel coefficient is a measure of the amount of work which can be extracted from a turbine blade and was originally developed to determine the number of blades and solidity needed for optimal turbine performance [33].

A study done by Curtis *et al.* [42] used LPT blade airfoils with a $Z_w \approx 1$ where the suction surface pressure distribution was changed using flaps and inserts over Reynolds number range of 70,000 - 400,000. They proposed that the two most significant factors that determine the suction surface velocity distribution are the degree of deceleration along the blade surface and the location of the velocity peak. The degree of deceleration was defined as the magnitude of the adverse pressure gradient along the suction surface of the LPT blade airfoil. The location of the velocity peak describes the loading characteristic of the LPT blade where the minimum pressure

D. Sanders

Chapter 2. Description of Experimental Cascade Configurations Utilized in the Investigation

is located on the airfoil. LPT blade designs were given the classification of front-loaded, mid-loaded, or aft-loaded depending on the location of the velocity peak on the blade suction surface.

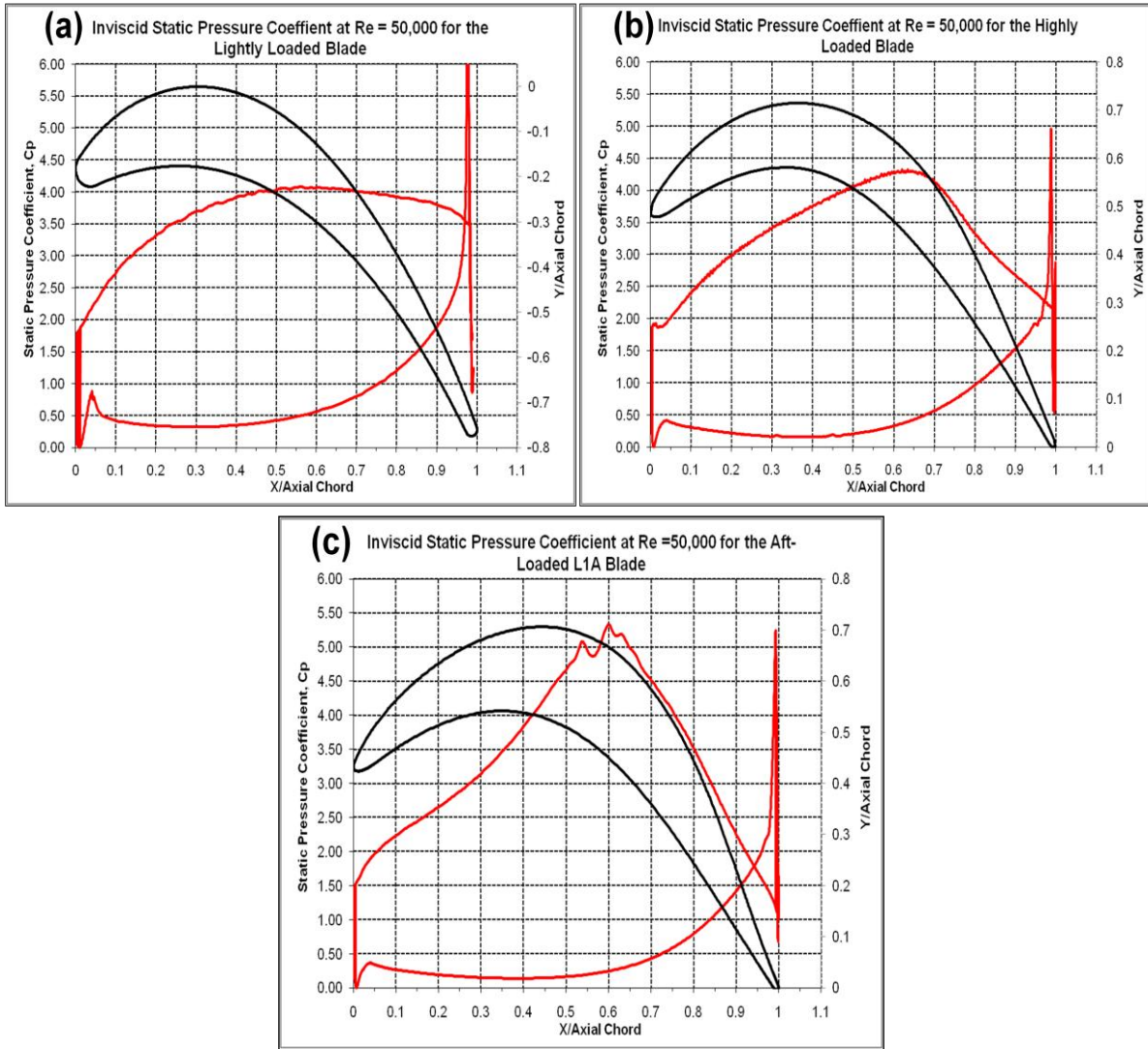


Figure 2.5. Inviscid static pressure coefficient distributions and blade profiles for the (a) Lightly Loaded, (b) Highly Loaded, and (c) Aft-Loaded L1A blade airfoils at $Re = 50,000$

2.4.1 The “Lightly Loaded” LPT Blade Airfoil

The LPT blade airfoil defined as “Lightly Loaded” with a $Z_w = 0.94$ was based on the midspan airfoil of a typical three-dimensional LPT rotor blade. The axial chord length, C_x , and axial solidity were 17.78cm and 1.20, respectively. The inlet and outlet flow angle for the Lightly Loaded blade airfoil were 30.75° and 60.94° , respectively. Figure 2.5(a) shows the blade

Chapter 2. Description of Experimental Cascade Configurations Utilized in the Investigation

profile for the Lightly Loaded blade airfoil and the inviscid distribution of the static pressure coefficient along the blade surface at $Re = 50,000$. The location of the peak velocity corresponded to the same location of the peak pressure coefficient. This peak was found at the 56.0% axial chord location, indicating that the Lightly Loaded blade is more of a mid-loaded blade design. The more upstream the peak velocity location, the more the blade will be intrinsically separation resistant when operated at low Reynolds numbers. Also, the slope of the pressure coefficient downstream of the peak pressure location is relatively flat indicating a very weak adverse pressure gradient. Flow separation is less likely to occur because there is little total pressure change from the peak velocity location to the trailing edge.

Experimental measurements of the flow over the Lightly Loaded blade were performed by Garmoe [36] in the LSWT. Wake total pressure loss measurements were collected at an inlet Reynolds number range of 10,000-100,000 and inlet turbulence intensity, $Tu = 1\%$. Figure 2.6 show the total pressure loss coefficient profiles along with the integrated total pressure loss coefficient. The integrated value of the loss coefficient was plotted as a function of the inlet Reynolds number including the experimental error bars calculated based on the Reynolds number variance. The trend in both plots indicated that as the Reynolds number decreased, the magnitude and width of the loss coefficient distribution increased. Also, boundary layer velocity profiles were taken at several locations normal to the blade suction surface and indicated very little evidence of separation on suction surface, not even at the lowest inlet Reynolds number. It was later discovered that the hot-film anemometers used in the study were incorrectly calibrated, so only the wake loss coefficient distributions were used for comparisons with the CFD results [36].

Chapter 2. Description of Experimental Cascade Configurations Utilized in the Investigation

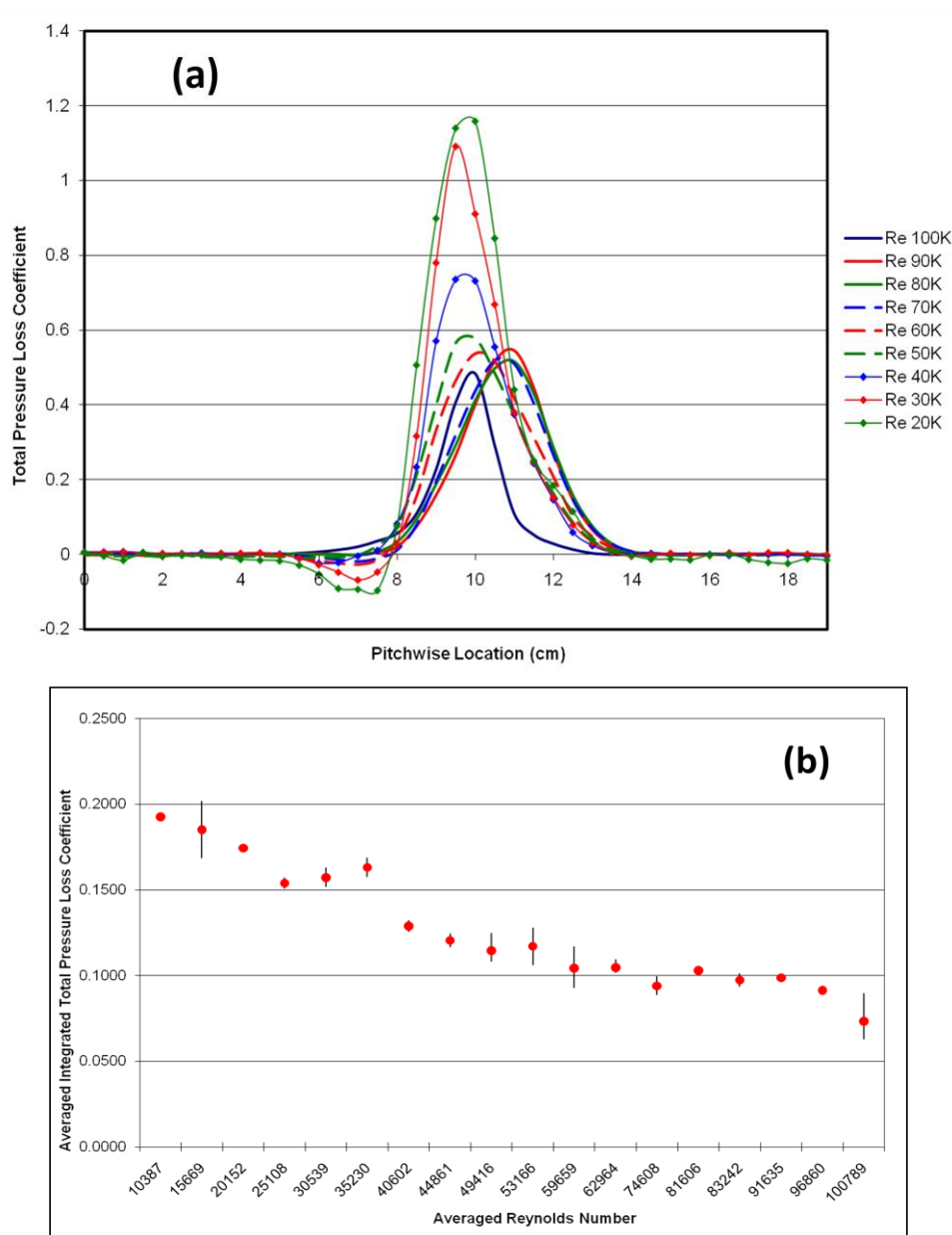


Figure 2.6. (a) Wake total pressure loss coefficient profiles (b) and integrated loss coefficient with error bars at $Re = 10,000-100,000$ for the Lightly Loaded blade airfoil

2.4.2 The “Highly Loaded” LPT Blade Airfoil

The second LPT blade geometry used was the Pack-B research LPT blade with a $Z = 1.07$ and defined as “Highly Loaded”. Pratt & Whitney introduced the Highly Loaded LPT design in order to provide a current higher lift design with an improved low Reynolds number efficiency [33]. The Highly Loaded blade is an incompressible Mach number scaled version of a *D. Sanders*

51

Chapter 2. Description of Experimental Cascade Configurations Utilized in the Investigation

conventional LPT geometry used in a commercial aircraft turbine engine. The axial chord length was 17.78cm with an axial solidity of 1.13. The inlet and outlet flow angle was 35° and 60° , respectively. Figure 2.5(b) indicates the peak velocity location was 62.1% of the axial chord for the Highly Loaded blade and was located more downstream compared to the Lightly Loaded blade. The Highly Loaded blade is therefore an aft-loaded blade design [34]. The slope of the pressure coefficient is downstream of the peak velocity location creating a strong adverse pressure gradient on the blade suction side. The strength of the adverse pressure gradient and lower solidity makes flow separation more likely to occur at low Reynolds numbers.

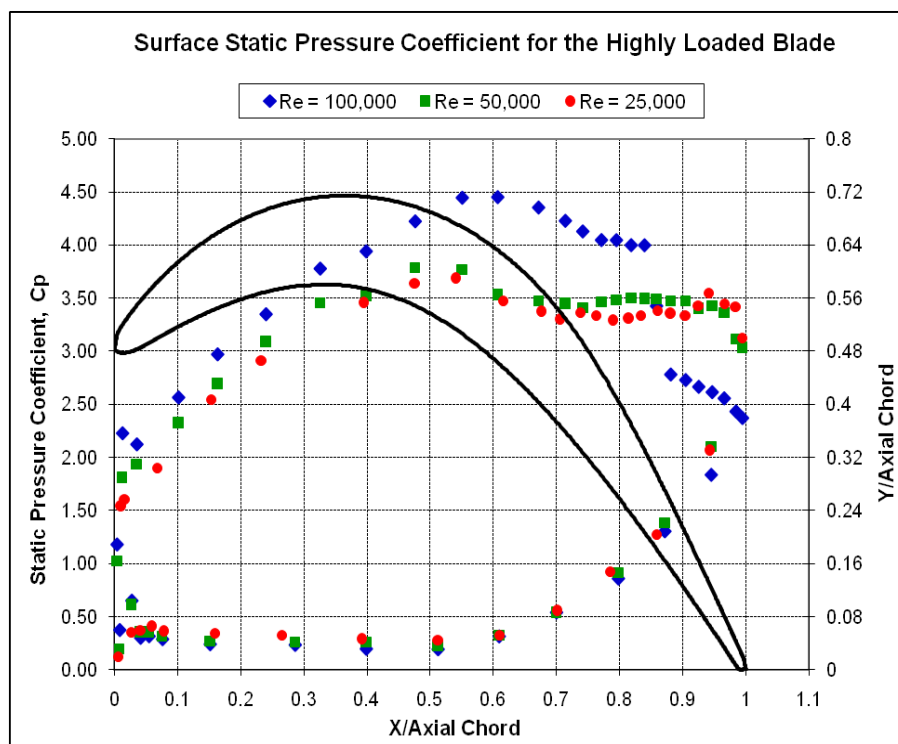


Figure 2.7. Experimental measurements of the static pressure coefficient for the Highly Loaded blade airfoil taken by Bons *et al.* [38]

The Highly Loaded blade has been extensively tested in the LSWT in several different experimental studies [36-40] mainly due to its aerodynamic characteristics at low Reynolds numbers. Those studies indicated the Highly Loaded blade tends to separate at Reynolds

Chapter 2. Description of Experimental Cascade Configurations Utilized in the Investigation

numbers of 100,000 and below. Figure 2.7 shows the static pressure coefficient measurements taken by Bons *et al.* [38] at $Re = 25,000$, 50,000, and 100,000. The formation of a plateau where the static pressure remained constant after the maximum C_p location was an indicator of boundary layer separation on the suction surface. At the $Re = 100,000$, this plateau began at the 75% axial chord and continued downstream to 88% axial chord. The decrease in C_p downstream of 88% axial chord indicated that the boundary layer reattached to the blade surface, forming a closed separation bubble on the suction surface. The distribution of the static pressure for $Re = 50,000$ and 25,000 show the same trend where the constant C_p plateau begins at approximately 60% axial chord and continues downstream of that location to the blade trailing edge which indicates a separation region at the rear of the blade.

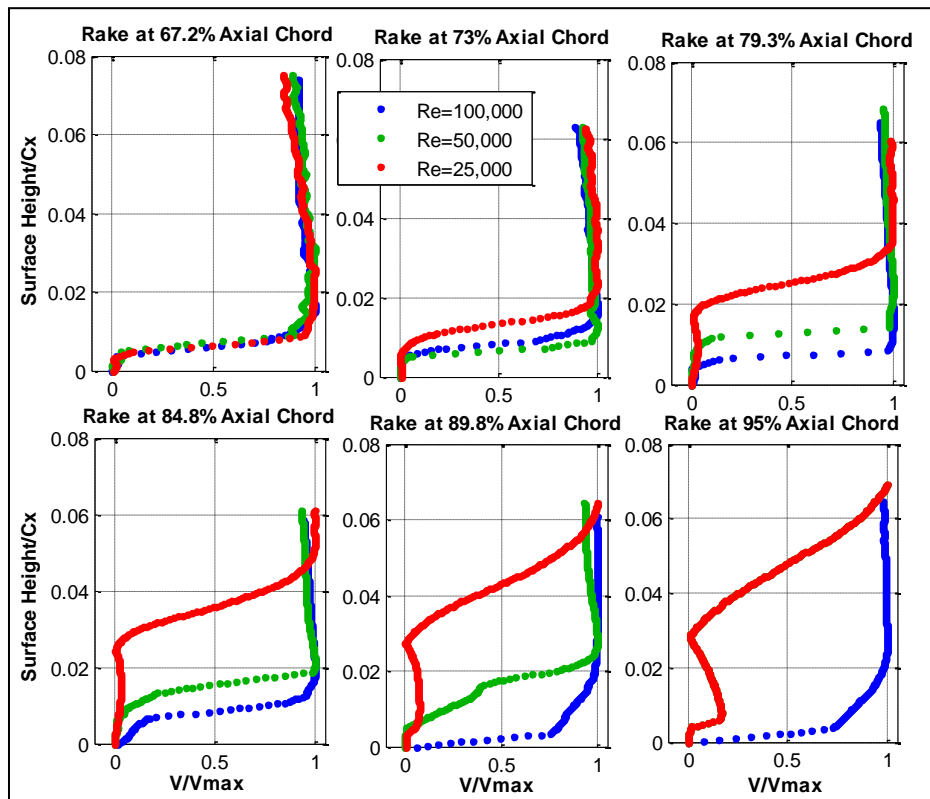


Figure 2.8. Mean boundary layer velocity profiles extracted from PIV measurements of Woods *et al.* [39] for the Highly Loaded blade

Chapter 2. Description of Experimental Cascade Configurations Utilized in the Investigation

Mean boundary layer velocity profiles were extracted from the PIV experiments taken by Woods *et al.* [39] shown in Figure 2.8 at all three Reynolds numbers and 0.6% freestream intensity. These profiles were extracted normal to the blade surface at 67.2%, 73%, 79.0%, 84.8%, 89.8%, and 95% axial chord locations. At the $Re = 100,000$, the boundary layer profiles reconfirmed the trend observed from the static pressure measurements that a closed separation bubble was present on the suction surface. This separation bubble was formed due to the high energy present in the freestream flow caused the shear layer re-energizing the boundary layer and reattaching the flow to the blade surface. This flow behavior is known as separation-induced turbulent-transition as described by Halsted *et al.* [3]. At the $Re = 50,000$, the boundary layer profiles indicated the separation region extended to the trailing edge because there was not enough energy present in freestream to cause boundary layer reattachment. The further decrease in the Reynolds for the $Re = 25,000$ case caused the separation region to increase compared to the higher Reynolds number cases.

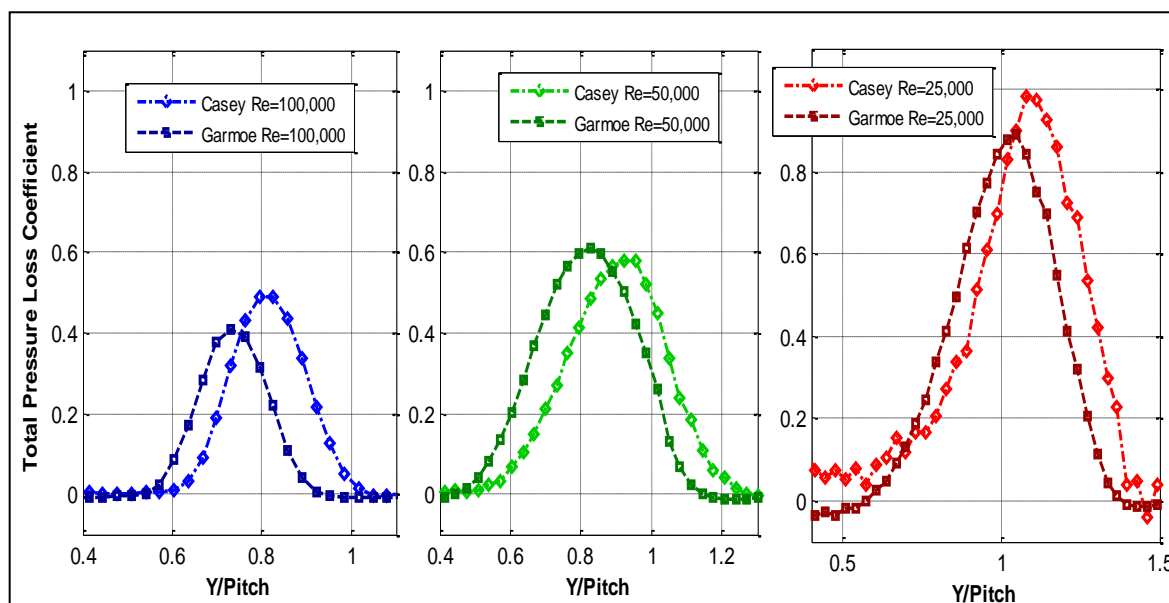


Figure 2.9. Wake total pressure loss coefficient measurements of Garmoe [36] and Casey *et al.* [40] for the Highly Loaded blade

Chapter 2. Description of Experimental Cascade Configurations Utilized in the Investigation

Figure 2.9 shows the wake total pressure loss coefficient profiles as measured by Garmoe [36] and Casey *et al.* [40] for all three inlet Reynolds numbers. The discrepancy in the measurement of the wake loss coefficient between the two experiments was due to the difference in the inlet turbulent boundary conditions. For the $Re = 100,000$ Garmoe [36] reported the inlet turbulence intensity as 0.735% compared with 0.437% for Casey *et al.* [40] measurements. As the Reynolds number decreased, the magnitude of the loss coefficient and the width of the region increased due to growth of the separation region. The $Re = 100,000$ case showed that even though a closed separation bubble was present, the total pressure loss was not significantly higher due to the attached turbulent boundary layer downstream of the separation bubble. An approximate 50% increase in the peak loss coefficient compared to $Re = 100,000$ was observed for the $Re = 50,000$ due to the increase in the amount of separated flow on the suction surface. The inlet turbulence intensity was 0.34% for the Casey *et al.* [40] measurements and 0.84% for Garmoe's [36] measurement at $Re = 50,000$. At $Re = 25,000$, a $Tu = 0.36\%$ was used in the Casey *et al.* [40] experiment while a $Tu = 0.89\%$ was used in the Garmoe [36] experiments. The amount of separated flow was the highest for the $Re = 25,000$ case, and as a result the peak loss coefficient was the highest and the width of the wake region was larger than for the higher inlet Reynolds number cases.

2.4.3 The "Aft-Loaded L1A" LPT Blade Airfoil

Clark and Koch [43] designed an aft-loaded LPT blade airfoil with $Z_w = 1.23$, a 15% increase in the blade loading compared to the Highly Loaded blade. The blade was designated as the "Aft-Loaded L1A" LPT blade airfoil. The axial chord length was 17.76cm with an axial solidity of 0.99. The inlet and outlet flow angle was 35° and 60° , respectively as set with the Highly Loaded blade. The peak velocity location at 60% axial chord location had a similar peak

Chapter 2. Description of Experimental Cascade Configurations Utilized in the Investigation

velocity location as the Highly Loaded blade (Figure 2.5(c)). Yet, the adverse pressure gradient was much stronger than was observed for the Highly Loaded blade, which was due to the decrease in the blade solidity. This indicated that the Aft-Loaded L1A blade will be more prone to flow separation on the suction surface than both Lightly Loaded and Highly Loaded blades.

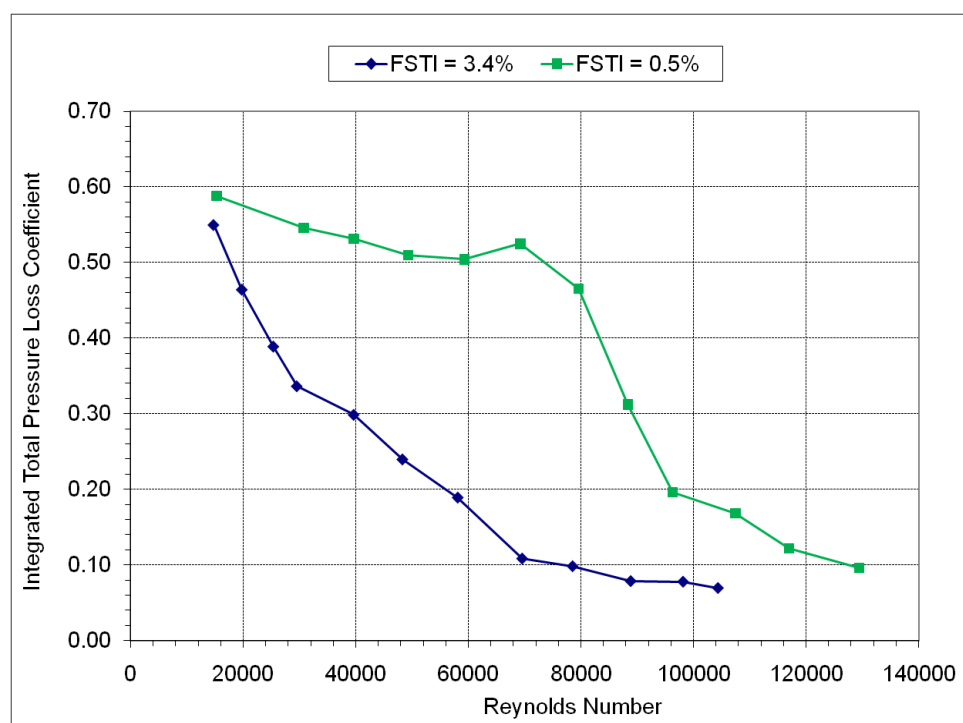


Figure 2.10. Integrated wake total pressure loss coefficient measurements of Marks *et al.* [40] for the Aft-Loaded L1A blade at high and low turbulent intensities

Marks *et al.* [35] experimentally investigated the aerodynamic characteristics of the Aft-Loaded L1A blade in the LSWT. The wake loss coefficient and the static pressure distribution along the blade surface were measured at both low and high freestream turbulent intensities. Also, flow visualizations were completed using PIV measurements in the blade normal direction at $Re = 15,000$ - $120,000$. Figure 2.10 shows the inlet Reynolds number effect on the integrated total pressure loss coefficient calculated using Eq. 2.3 at both turbulence intensity levels. The loss profile for $Tu = 0.5\%$ showed a gradual increase in the loss coefficient with decreasing Reynolds number down to $Re \approx 96,000$. This was followed by a more rapid rise at $Re \approx 60,000$ - $120,000$.

D. Sanders

56

Chapter 2. Description of Experimental Cascade Configurations Utilized in the Investigation

96,000, and then a more gradual increase as Reynolds number was decreased further. The $Re \approx 60,000$ -96,000 region was referred to as the loss knee and its behavior was attributed to flow separation without reattachment on the suction surface [44]. The loss profile at $Tu = 3.4\%$ has a gradual increase in the loss coefficient with decreasing Reynolds number compared to the loss knee of the $Tu = 0.5\%$ case. Also, the magnitude of the loss coefficient decreased compared to the $Tu = 0.5\%$ case, which was due to the elevated amount of freestream turbulence causing a reduction in flow separation and lower total pressure loss.

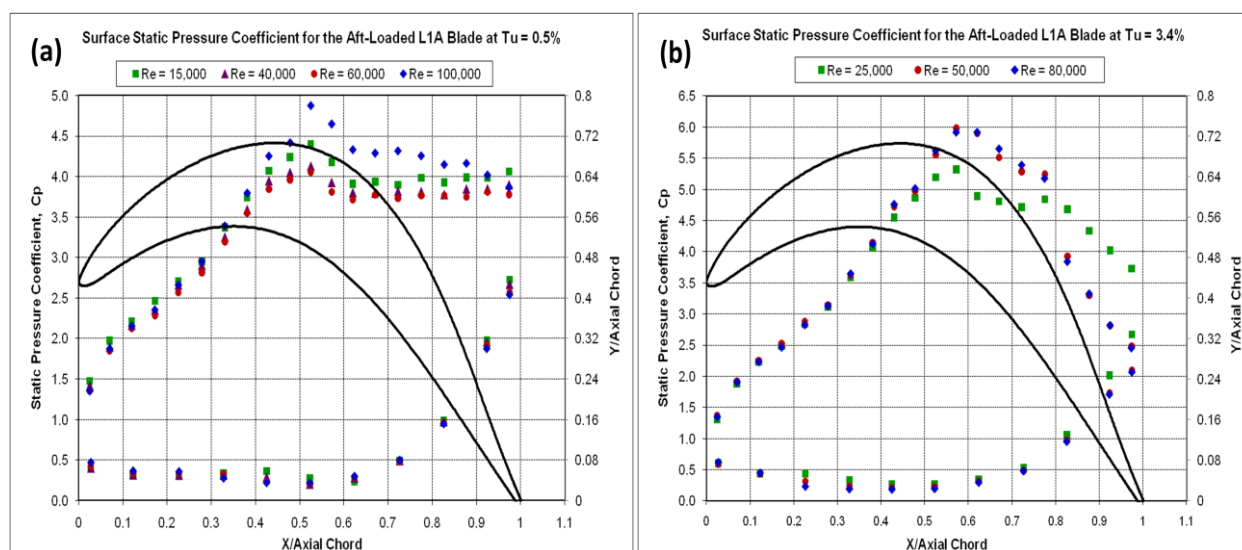


Figure 2.11. Measurements of the Surface static pressure coefficient of Marks *et al.* [40] for the Aft-Loaded L1A blade at high and low turbulent intensities

The surface static pressure coefficient is shown in Figure 2.11 for both low and high turbulent intensities. The C_p distribution at the $Tu = 0.5\%$ indicated a separated flow region on the suction surface continuing to the blade trailing edge for all Reynolds numbers shown. The separation location was approximately 57% axial chord for Reynolds number below 60,000 and 62% axial chord for the $Re = 99,000$ case. A closed separation bubble was observed for the $Tu = 3.4\%$ C_p measurements (Fig 2.11(b)) at $Re = 50,000$ and $80,000$ which began at approximately 62% axial chord and reattached between the 78% and 83% axial chord. The separated flow

Chapter 2. Description of Experimental Cascade Configurations Utilized in the Investigation

region starting at the 62% axial chord location extended all the way to the trailing edge for the $Re = 25,000$ case.

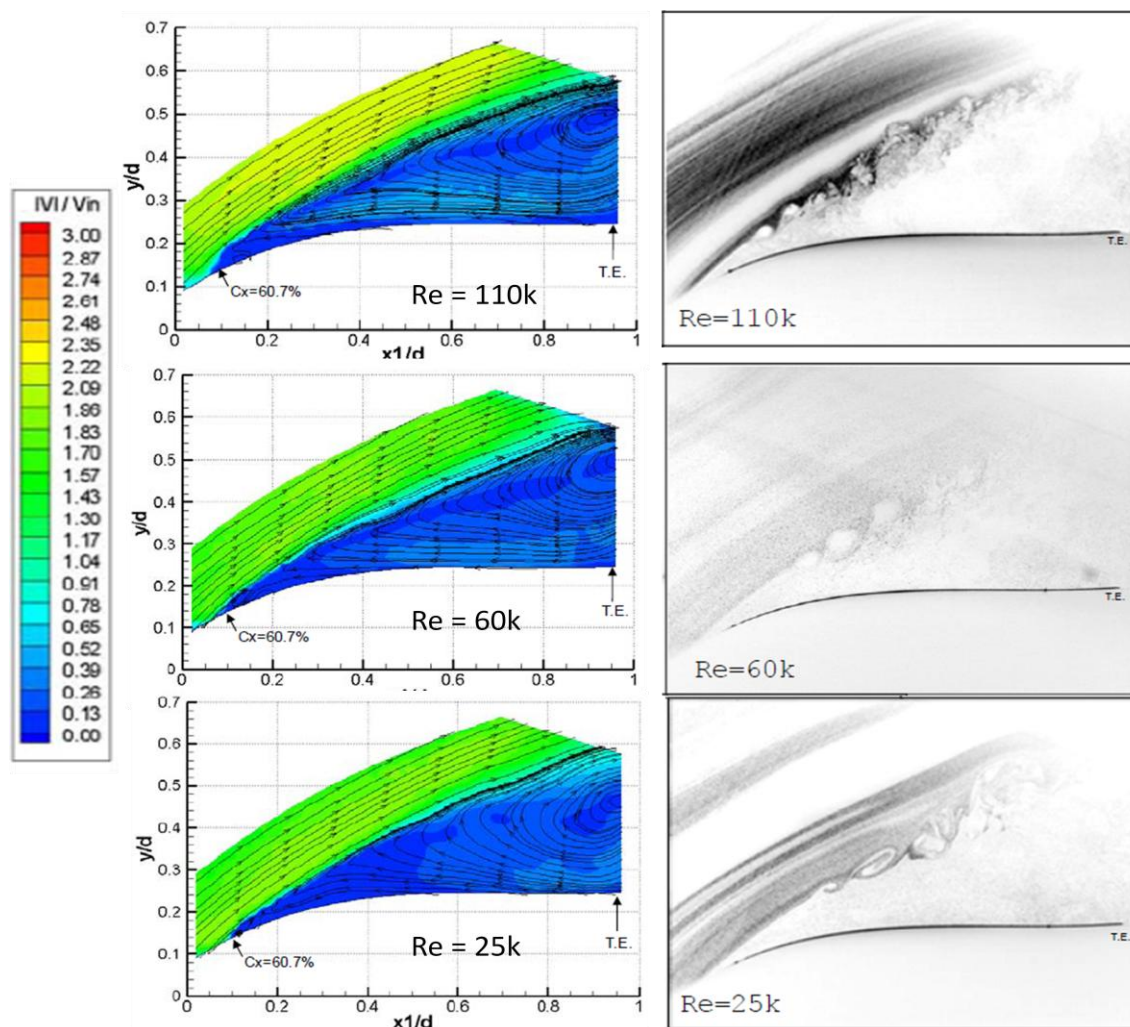


Figure 2.12. Mean velocity contours obtained from PIV measurements and instantaneous flow visualizations of Marks *et al.* [40] for the Aft-Loaded L1A blade at $Tu = 0.5\%$

The PIV measurements confirmed the trends observed from the behavior of the static pressure distribution. Figure 2.12 shows contour plots of the average velocity magnitude obtained using the PIV measurement technique including instantaneous flow visualizations at $Tu = 0.5\%$. At the lowest Reynolds number of 25,000, the flow visualizations show that the separated shear layer produced large vortices that traveled downstream. As the Reynolds

Chapter 2. Description of Experimental Cascade Configurations Utilized in the Investigation

number was increased to the $Re = 60,000$ and $110,000$ cases, these vortices reduced in size and transitioned to turbulent vortices. The average velocity contours for all Reynolds numbers did not show the unsteady vortices as a result of the flow averaging but, a recirculation region was present due to separated flow. In Figure 2.13, the instantaneous flow visualizations at $Tu = 3.4\%$ show that at $Re = 90,000$, the initially laminar flow boundary layer grew in thickness and transitioned to turbulence. The PIV average velocity contour plot showed a separation bubble present between approximately the 60% and 85% axial chord locations, which was consistent with the static pressure measurements. At the $Re = 50,000$, the separation bubble region increased in thickness and at the $Re = 90,000$ case, the boundary layer became attached to the blade surface and underwent turbulent transition. The flow remained separated without reattachment for the $Re = 25,000$ case, similar to the lower turbulence intensity result. The instantaneous flow visualizations showed vortices generated from the separated shear layer and recirculation region present in the PIV results.

In summary, the aerodynamic characteristics and performance at low Reynolds numbers were experimentally measured for each blade airfoil. CFD models were created based on the experimental configuration of the LSWT. The experimental results presented here will be used to validate the CFD predictions and provide more insight on the flow features produced at low Reynolds numbers.

Chapter 2. Description of Experimental Cascade Configurations Utilized in the Investigation

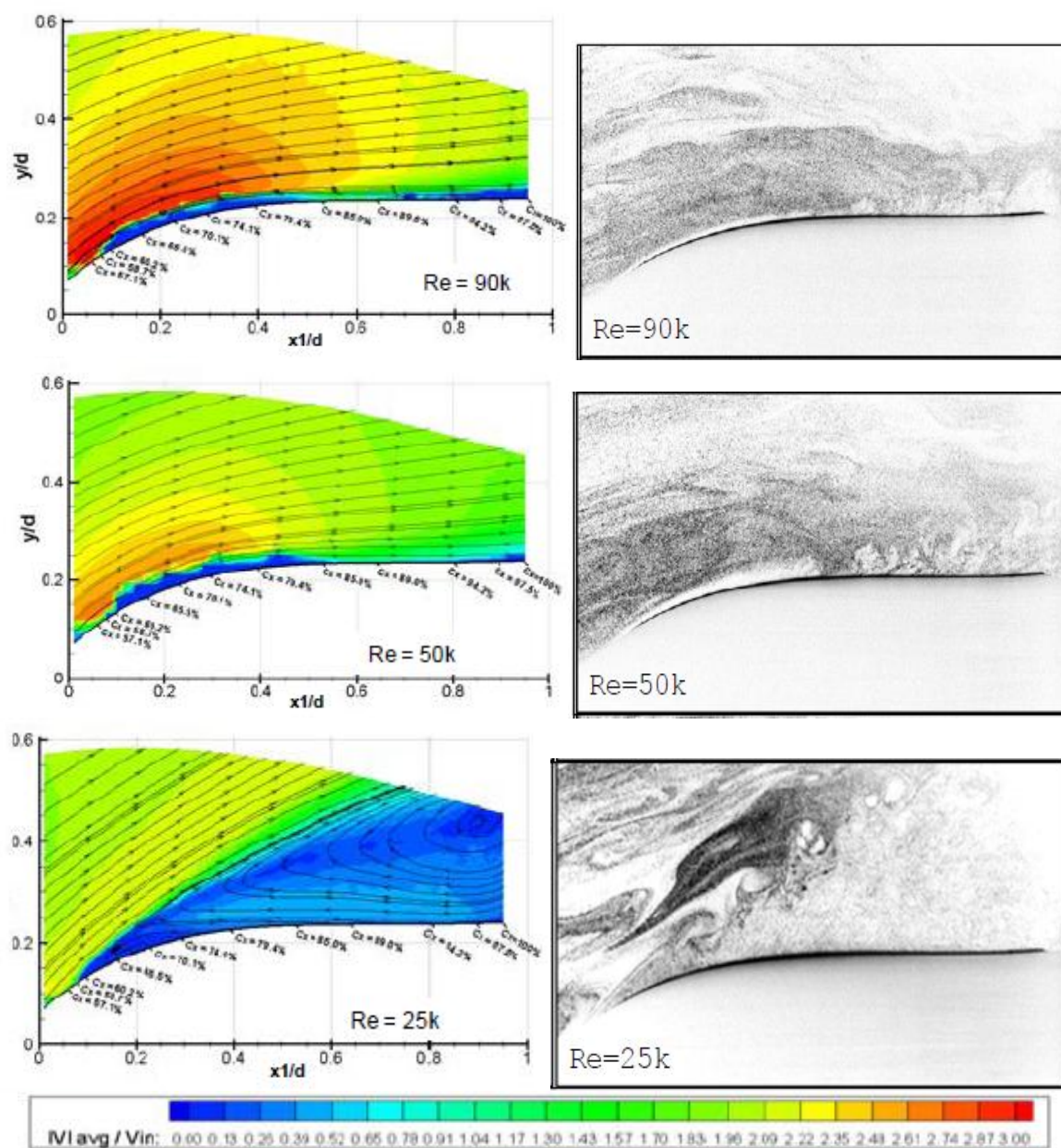


Figure 2.13. Mean velocity contours obtained from PIV measurements and instantaneous flow visualizations of Marks *et al.* [40] for the Aft-Loaded L1A blade at $Tu = 3.4\%$

CHAPTER THREE**3. Computational Model Methodology**

Numerical methods used for the current study included grid generation techniques, the CFD numerical scheme, the applied boundary conditions, discussion on the choice of turbulence models, CFD post-processing methods, and computational resources available for this study. The design of each LPT blade airfoil will be presented including a brief discussion of LPT blade design parameters. The design of the grid topology for LPT cascade geometries will be discussed including grid independence studies completed. The numerical schemes used within the CFD solver are presented along with appropriate boundary conditions. A brief summary of the current transitional flow model functionality is given including transport equations. Lastly, a description of the computational resources used to complete the CFD simulations including computing platforms available for large model simulations is provided.

3.1 Computational Grid Design Method

One key element in CFD for successful application to the modeling of fluid flow is the process of grid construction. Grids or meshes are made of discrete elements or volumes where the numerical form of the conservation laws are applied. Grid generation is an important part of completing successful CFD simulations. A well constructed grid greatly improves the quality of the CFD solution, and conversely, a poorly designed grid can lead to difficulty with the CFD simulation and poor numerical results. Grids that contain elements that are quadrilateral or hexahedral shaped cells are called structured grids. Unstructured grids contain only triangular, tetrahedral, pyramidal, and/or prismatic elements. A grid that contains both structured and unstructured grid elements is as defined as a hybrid grid.

Chapter 3. Computational Model Methodology

Structured grids have considerable advantage over other grid methods because they allow a high degree of control and high amount of skewness and stretching within a cell before the solution is drastically affected. Also, a higher degree of accuracy is achieved because the grid is often aligned with the flow. Structured grids typically require a lower amount of memory for a given mesh size and have faster convergence rate than unstructured grid solvers. The main drawback with structured grids is they require more construction time when dealing with complex geometries. Cells elements can become highly skewed and stretched in areas with high degree of curvature as are typically associated with turbine blade geometries. Most of the current grid generation software contains elliptical solvers that can be used to optimize grid smoothness and reduce the cell skewness on topologies containing a high degree of curvature.

Unstructured grids use an arbitrary collection of elements to fill the domain, typically with triangles for 2D grids and tetrahedrons for 3D grids. Automated algorithms within unstructured grids typically involve meshing the boundary and adding elements on the boundary surface or adding points in the interior and reconnecting the elements. The main advantage of using an unstructured grid is that the gridding method is highly automated and requires less construction time. They are capable of handling complicated geometries providing that the CAD geometry is of good quality. If the CAD model contains even minor errors, it can cause grid failures with the CFD solver. The triangle and tetrahedral cell elements are usually isotropic and do not stretch well. So, if refinement within a region such as a viscous layer is needed, the entire grid must be made finer in order to provide the required grid resolution. Unstructured flow solvers typical require more memory and have longer run times compared to structured flow solvers with a similar mesh size.

Chapter 3. Computational Model Methodology

Hybrid grids are designed to take advantage of positive aspects of both structured and unstructured grids. Typically hybrid grids use structured grids for the local regions, for instance within the boundary layer, and unstructured grids in the main flow domain. The hybrid grid method provide full control of the shape and distribution of the structured grid in local regions, while providing automated unstructured cell creation in the main flow region. Hybrid grids do require more user expertise than unstructured meshes for design of the grid topology. CFD flow solvers using hybrid grids require the same computing requirements as unstructured grids, but the overall cells size can be reduced when compared to a purely unstructured grid.

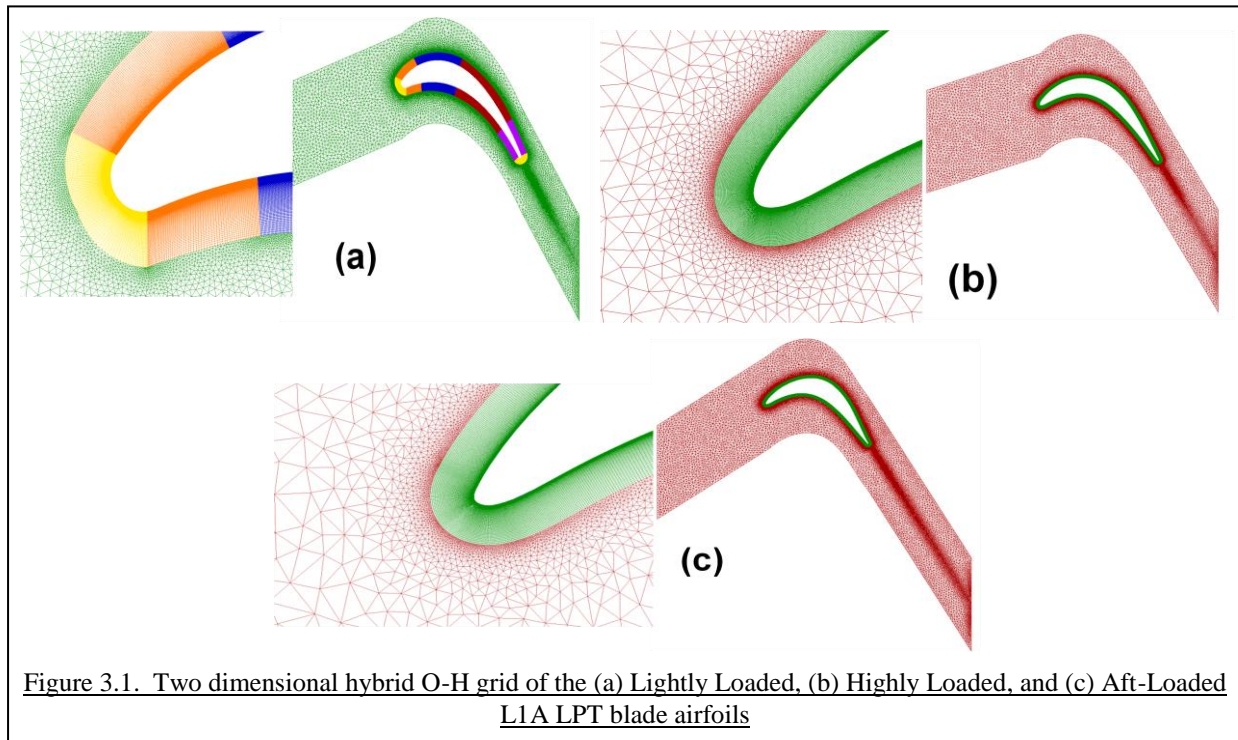
Both two-dimensional and three-dimensional hybrid grid topologies were used to construct the CFD models for this study. The topologies were designed to provide enough resolution to capture the viscous effects within the boundary layer and wake region. The grids were designed to be adequately fine, and to reduce the amount of computational time needed for the simulations. The grid geometries were based on the experimental cascade configuration of the AFRL Low Speed Wind Tunnel. The next sections describe the grid construction technique used for each LPT blade airfoil cascade CFD model. Also, the three-dimensional grid technique used for the Highly Loaded blade airfoil will be presented.

3.1.1 Grid Technique for the 2D Cascade CFD Models

The two-dimensional grid for the cross section of the each blade airfoil is shown in Figure 3.1. The inlet and outlet of the computational domain was placed one axial chord length upstream and one axial chord downstream of the blade leading and trailing edge, respectively, for the Lightly Loaded and Highly Loaded blades. The inlet domain was located 22.86 cm from leading edge of the Aft-Loaded L1A blade, while the outlet domain was placed two axial chords downstream in the streamwise direction of the blade trailing edge. The location of the inlet and

Chapter 3. Computational Model Methodology

outlet domains was placed far enough from the LPT blade to encompass the experimental loss coefficient measurement locations. The mid-passage flow around the blade airfoil was modeled with the passage length equal to the blade pitch. Periodic boundaries were applied to model an infinite cascade.



CFD Model	O-Grid Dimensions	H-Grid Dimensions	Cells	Aft-Loaded L1A Blade with Wake Generators			
				Domain	O-Grid Dimensions	H-Grid Dimensions	Total Cells
Lightly Loaded Blade	1749×110	33,209	221,081	Inflow Wake Generator Aft-Loaded L1A Blade		733	172,904
Highly Loaded Blade	1749×67	44,091	150,392				
Aft-Loaded L1A Blade	1099×71	16,399	108,011		249×46	20,266	
3D Highly Loaded Blade	1099×67×51	15,698×51	5,116,700		1099×71	23,018	

Table 3.1. Grid Dimensions of each Cascade CFD Model

The computational meshes used consisted of a hybrid O-H grid topology created with Gridgen[®] 15 mesh generation software (Figure 3.1). A structured O-grid was extruded normal to each blade surface in order to provide the resolution needed to resolve the boundary layer. The first cell wall distance was such that the y^+ was less than unity at every grid point around the

D. Sanders

Chapter 3. Computational Model Methodology

blade airfoil surface, satisfying the y^+ tolerance requirement for the transitional flow model. The average aspect ratio for each grid topology was 6.5:1, but was as high as 30:1 in cells close to the blade surface. An unstructured mesh was placed in the main flowpath consisting of triangles generated by a modified Delauney method. Triangular cell clustering was increased to provide enough resolution for the wake region generated by the trailing edge. Table 3.1 shows the grid dimensions for the structured O-grid and unstructured H-grid for each LPT blade airfoil.

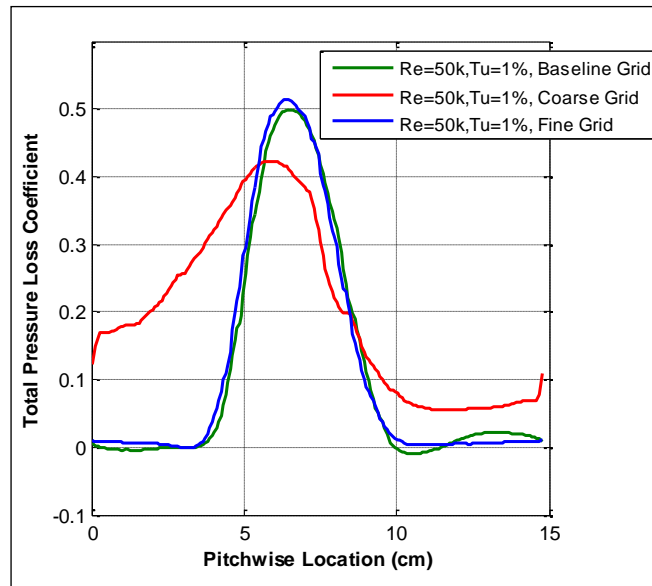


Figure 3.2. Comparison of the total pressure loss coefficient for the Lightly Loaded blade airfoil at different grids spatial resolutions

A grid independence study was completed using the Lightly Loaded blade mesh to determine if the selected meshing scheme provides enough spatial resolution to capture the features of the flowfield within the computational domain. Two additional grid topologies were created by increasing and decreasing the number of nodes on the blade surface and in the main flowfield by 50% while maintaining the same hybrid O-H grid topology. The coarse and fine grids contained 94,846 and 451,866 cells, respectively while the baseline grid contained 238,230 cells. All three grid topologies were used in a computation at an inlet Reynolds number of 50,000, with an inlet freestream turbulence intensity of 1%, and an average turbulent length scale

D. Sanders

Chapter 3. Computational Model Methodology

of 5 mm using a 2nd order spatial accurate steady flow pressure-based solver in Fluent 6.3[®]. The y^+ was less than unity around the blade surface and the turbulent transition point was the same for all three grid topologies. The wake total pressure loss coefficient in Figure 3.2 shows the effect of the wake distribution at the different grid spatial resolutions. The results from the coarse grid showed a distorted total pressure loss coefficient due to the low cell count in the wake region while the baseline and fine grid indicated a similar total pressure loss coefficient distribution. The fine grid has only 2% difference in prediction of the peak loss coefficient, while the coarse grid has 15% difference compared to the baseline grid. This indicated that the baseline grid provided enough spatial resolution to capture the effects of the flowfield in the boundary layer and within the wake. The additional grid points in the fine grid were not needed, thus making the overall grid size smaller and reducing the computational cost of running simulations. Based on these results, the resolution provided with the baseline meshing scheme was used for all three cascade CFD models.

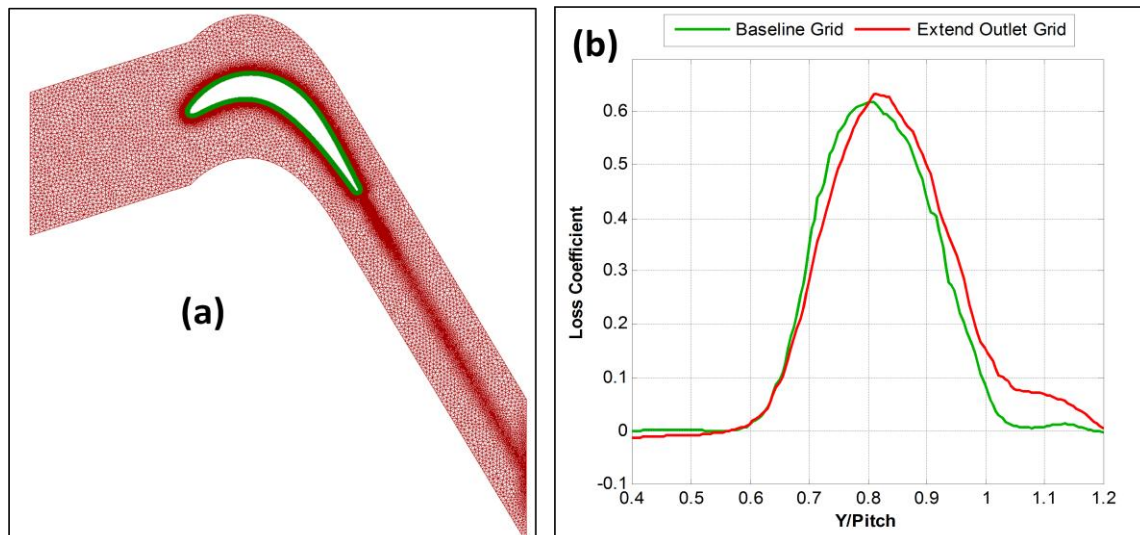
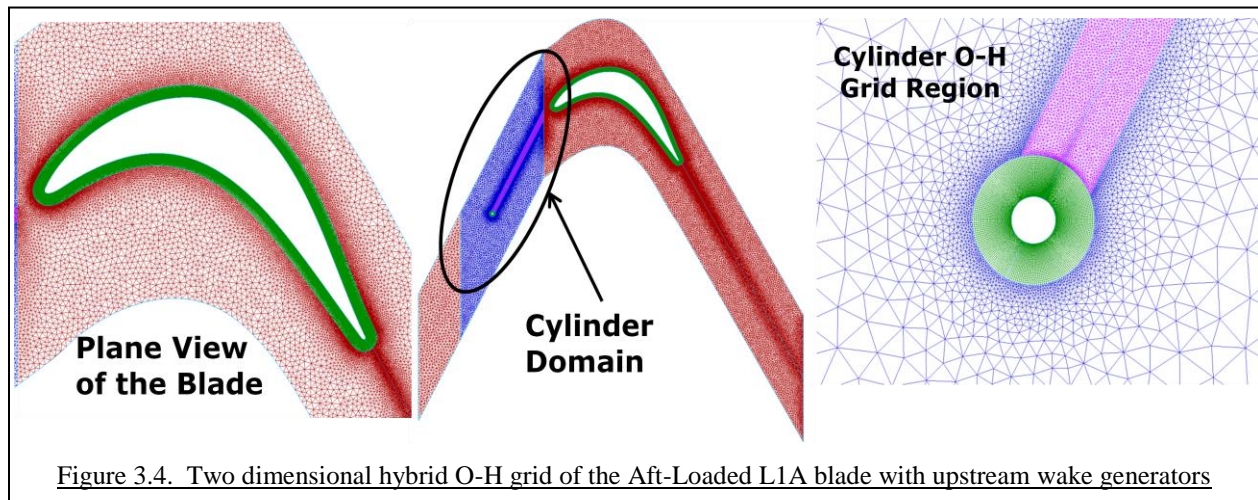


Figure 3.3. (a) Grid of the Highly Loaded blade with the extended outlet and (b) loss coefficient comparison of the baseline grid to the extended outlet grid

Chapter 3. Computational Model Methodology

The length of the outlet domain from the trailing edge was varied using the Highly Loaded blade grid to determine how far the outlet boundary needed to be placed from the simulated wake measurement location. A grid shown in Figure 3.3(a) was created that placed the outlet boundary two axial chord lengths in the streamwise direction from the blade trailing edge while, the baseline grid outlet boundary was one axial chord length from the blade trailing edge (Fig. 3.1(b)). Unsteady simulations were completed at a $Re = 50,000$ at an inlet freestream turbulence intensity of 0.6% and average turbulent length scale of 50 mm. The total pressure loss coefficient was measured across the pitch length using a 200 point simulated rake placed one axial chord length from the blade trailing edge. Figure 3.3(b) compares the loss coefficient obtained from the baseline grid to the extend outlet grid. There was a 3% difference in the prediction in the peak loss coefficient for the extended outlet grid compared to the baseline result. Based on these results, the baseline grid outlet boundary was judged to be the correct length from the blade trailing edge to provide adequate measurements of wake region at a reduced overall grid size.

3.1.2 Aft-Loaded L1A Blade with Upstream Wake Generators



Chapter 3. Computational Model Methodology

A CFD grid of the Aft-Loaded L1A blade with upstream wake generators was constructed based on the experimental setup of Nessler *et al.* [40]. The grid consisted of a modified hybrid O-H grid of the Aft-Loaded L1A blade as shown in Figure 3.4. The inlet to the L1A blade domain was reduced to 1.53cm in the axial direction from blade leading edge. Also, the number of cells within the unstructured H-grid was increased to resolve the unsteady viscous effects within this region. The outlet of the Aft-Loaded L1A blade domain was placed 2 axial chord lengths downstream of the trailing edge in the streamwise direction to encompass the experimental loss coefficient measurement location.

Another hybrid O-H grid for a circular cylinder with a diameter of 0.318cm was placed upstream of the L1A blade. The center of the cylinder was placed a distance of 8.88cm in the axial flow direction from the leading edge of the Aft-Loaded L1A blade. The cylinder was used to generate unsteady wakes similar to the actual wakes generated from an upstream LPT vane. The cylinder grid was translated in order to simulate the effect of a passing wake from the upstream vane. The translating motion of the circular cylinder was modeled using the sliding mesh technique within Fluent 12.0. Interface zones were set up at the inlet and outlet of the circular cylinder domain at the points where the domain was moved relative L1A blade domain. The inlet boundary was placed 22.86cm in the streamwise direction from the cylinder center. The shape of the cylinder domain was based on the inlet relative flow angle, $\beta = 62.54^\circ$, which corresponded to a flow coefficient ($\Phi = u_{axial}/u_{rod}$) of 0.817 and cylindrical rod speed, $u_{rod} = 2.298\text{m/sec}$ as set in the experimental [40] results. A structured O-grid was placed around the cylinder and the unstructured H-grid was placed in the flowpath and the cylinder wake region. The unstructured cell count and clustering was made fine enough to resolve the small vortical structures produced from the cylinder (Fig. 3.4).

Chapter 3. Computational Model Methodology

3.1.3 Grid Technique for the 3D Cascade CFD Models

Figure 3.5 shows the three-dimensional grid domain for the Highly Loaded blade. The baseline two-dimensional structured O-grid dimensions were (1099×67) and the unstructured H-grid contained 15,698 cells in the main flowpath. The O-grid dimensions were reduced compared to the two-dimensional grid topology in order to reduce the overall size of the grid and conserve computational resources. The grid was created by taking the original two-dimensional grid and performing a geometric extrusion to 20% of the axial chord length in the spanwise direction. The length of the spanwise extent of the Highly Loaded blade was based on the recommendations suggested by Rizzetta and Visbal [45]. The grid provided enough spanwise distance to resolve the effects of spanwise instabilities, while keeping the grid size reasonable for successful completion of unsteady computations. The final three-dimensional structured O-grid dimensions were $(1099 \times 67 \times 51)$ with the unstructured H-grid contained prism-shaped cells with the dimensions of $(33,209 \times 51)$. Prism-shaped cells were used instead of tetrahedral cells in order to reduce overall cell count while maintaining cell quality and to reduce the three-dimensional cells skewness. The total grid size was 5,116,700 cells.

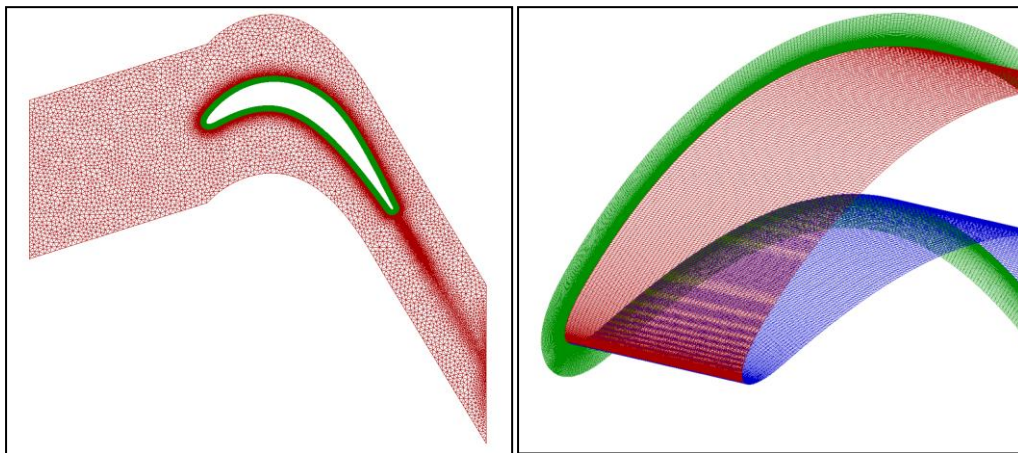


Figure 3.5. Three-dimensional hybrid O-H grid of the Highly Loaded LPT blade airfoils

3.2 CFD Numerical Scheme

CFD simulations were performed using ANSYS Fluent 6.3[®] which is based on a finite volume method. The domain was discretized onto a finite set of control volumes and the general conservation equations for mass and momentum were solved on this set of control volumes. The partial differential equations based on the RANS equations shown in Eq.(3.1) and Eq. (3.2) were discretized algebraically and solved for the mapping of the flowfield.

$$\frac{\partial \rho}{\partial t} + \frac{\partial}{\partial x_i}(\rho u_i) = 0 \quad (3.1)$$

$$\frac{\partial}{\partial t}(\rho u_i) + \frac{\partial}{\partial x_j}(\rho u_i u_j) = -\frac{\partial p}{\partial x_i} + \frac{\partial}{\partial x_j} \left[\mu \left(\frac{\partial u_i}{\partial x_j} + \frac{\partial u_j}{\partial x_i} - \frac{2}{3} \delta_{ij} \frac{\partial u_k}{\partial x_k} \right) \right] + \frac{\partial}{\partial x_j}(-\rho \overline{u'_i u'_j}) \quad (3.2)$$

All solution variables represent ensemble or time averaged values. The Reynolds stress term $-\rho \overline{u'_i u'_j}$ is resolved according to the chosen turbulence model in order to close the equation. The RANS equations were discretized using the pressure-based coupled algorithm which solved a coupled system of equations comprising the momentum equations and the pressure-based continuity equation.

Steady flow solutions were initialized based on the inlet boundary conditions and iteratively run with a first-order upwind scheme until the residual tolerance for continuity, linear momentum, and turbulence variables were below 10^{-4} . Then the second-order upwind discretization scheme was used until the minimum convergence tolerance for all flow parameters was below 10^{-5} . Also, the drag and lift coefficients were monitored to determine if the steady state solution was adequately converged. Unsteady flow cases were initialized with the first-order discretization steady flow solutions and run using a second-order upwind spatial discretization with a second-order implicit temporal solver. Time steps were chosen in order to

70

Chapter 3. Computational Model Methodology

obtain enough temporal resolution to allow the solution to converge locally within 20-30 iterations per time step.

The sliding mesh model was used in order to simulate the translating motion of the wake generators placed upstream of the Aft-Loaded L1A blade. The relative motions of stationary and rotating components were accounted for using the sliding mesh models. It is the most accurate method for simulating flows in multiple moving reference frames and yet the most computationally demanding. Unsteady interactions due to the potential flowfield, and convecting wakes needed to be accounted for, so a time-dependent solution procedure was required. Each cell zone was bounded by at least one “interface zone” where it met the opposing cell zone. The interface zones of adjacent cell zones are associated with each other to form a “grid interface”. The two cell zones will move relative to each other along the grid interface in discrete steps during the calculation. The flux at the interface was computed using the intersection between interface zones at each new time step. The resulting intersection produced one zone with fluid cells on both sides and one or more periodic zones. The number of faces in these intersection zones will vary as the interface zones moves relative to each other. Grid interfaces were set up at the inlet and outlet of the wake generator domain.

3.3 The Choice of Turbulence Model

The choice of the turbulence model was known to be critically important for success in predicting the turbine blade flowfields at low Reynolds numbers. Section 1.3.3 reviewed the feature of turbulence models that were candidates for selection for the present investigation. It was decided that the model that promised the best accuracy, and that could be readily applied without the need of code development for implementation would be used. All turbulence models already implemented within available CFD software were researched to determine which could

Chapter 3. Computational Model Methodology

best provide the prediction capability needed for this study. To close on the selection, a test case described in Section 3.3.1 below of the flow over the Lightly Loaded blade airfoil was simulated. Three turbulence models were evaluated; the Realizable $k-\varepsilon$ [46] model with enhanced wall treatment, Menter's $k-\omega(SST)$ turbulence model [46] using a low Reynolds number correction to the turbulent viscosity, and the Walters and Leylek [2] $k-k_L-\omega$ transitional flow model. The Realizable $k-\varepsilon$ model was tested because it was known to provide improved prediction of turbulent flows involving rotation, boundary layers under strong pressure gradients, separation, and recirculation [46]. The Realizable $k-\varepsilon$ model transport equations are calculated using Eq. (3.3) and (3.4)

$$\frac{\partial}{\partial t}(\rho k) + \frac{\partial}{\partial x_j}(\rho k u_j) = \frac{\partial}{\partial x_j} \left[\left(\mu + \frac{\mu_t}{\sigma_k} \right) \frac{\partial k}{\partial x_j} \right] + G_k + G_b - \rho \varepsilon - Y_M + S_k \quad (3.3)$$

$$\frac{\partial}{\partial t}(\rho \varepsilon) + \frac{\partial}{\partial x_j}(\rho \varepsilon u_j) = \frac{\partial}{\partial x_j} \left[\left(\mu + \frac{\mu_t}{\sigma_k} \right) \frac{\partial \varepsilon}{\partial x_j} \right] + \rho C_1 S_\varepsilon - \rho C_2 \frac{\varepsilon^2}{k + \sqrt{\nu \varepsilon}} + C_{1\varepsilon} \frac{\varepsilon}{k} C_{3\varepsilon} G_b + S_\varepsilon \quad (3.4)$$

The $k-\omega(SST)$ turbulence model was examined because it is known to be more accurate for adverse pressure gradient flows and has a low Reynolds number correction to the turbulent viscosity. This feature dampens the production of the turbulence and reduces the possibility of over-prediction of viscous effects for flows that may not be fully turbulent. The Realizable $k-\varepsilon$ model transport equations are calculated using Eq. (3.5) and (3.6)

$$\frac{\partial}{\partial t}(\rho k) + \frac{\partial}{\partial x_j}(\rho k u_j) = \frac{\partial}{\partial x_j} \left[\Gamma_k \frac{\partial k}{\partial x_j} \right] + \tilde{G}_k - Y_k + S_k \quad (3.5)$$

$$\frac{\partial}{\partial t}(\rho \omega) + \frac{\partial}{\partial x_j}(\rho \omega u_j) = \frac{\partial}{\partial x_j} \left[\Gamma_\omega \frac{\partial \omega}{\partial x_j} \right] + G_\omega - Y_\omega + D_\omega + S_\omega \quad (3.6)$$

Chapter 3. Computational Model Methodology

All auxiliary equations and constants are given in the ANSYS Fluent[®] User's Manual [46] for both the Realizable $k-\varepsilon$ and $k-\omega(SST)$ turbulence models. In the end, the model judged to have the most potential to provide the prediction capability needed was the Walters and Leylek [2] $k-k_L-\omega$ transitional flow model. This turbulence model was designed to model the laminar-to-turbulent transition process using three transport equations. The $k-k_L-\omega$ model was implemented in Ansys[®] Fluent 6.3.26 as a beta version.

3.3.1 Comparisons of the RANS Turbulence Models

The inlet Reynolds number was set to 100,000 using the Lightly Loaded blade airfoil with inlet turbulence intensity of 1% and inlet turbulent length scale of 10.4 mm. The transition to turbulence, the boundary layer integral parameters, and the wake total pressure loss coefficient were compared for all three turbulence models. Figure 3.6 shows the turbulent kinetic energy around the blade suction surface for the three RANS turbulence models. A sudden increase in the magnitude of the turbulent kinetic energy was used as an indicator of the turbulent transition point. The $k-\omega(SST)$ and the $k-k_L-\omega$ model both produced transition at 65% axial chord. The $k-\omega(SST)$ model generated much less turbulent kinetic energy after the transition point when compared to the $k-k_L-\omega$ model. It was discovered that the specific dissipation rate around the blade surface was higher for the $k-\omega(SST)$ model than for the $k-k_L-\omega$ model. So, the turbulent kinetic energy that was being generated in the boundary layer was being converted into viscous losses at a much higher rate than the $k-k_L-\omega$ model. The $k-\omega(SST)$ model was not designed to model the laminar-to-turbulent transitional flow process within its transport equations, making it less desirable for the purpose of completing the goals of this research program. In contrast, the $k-\varepsilon$ model became turbulent from the leading edge and exhibited no transition behavior, which is not the correct boundary layer behavior for these types of flows.

D. Sanders

73

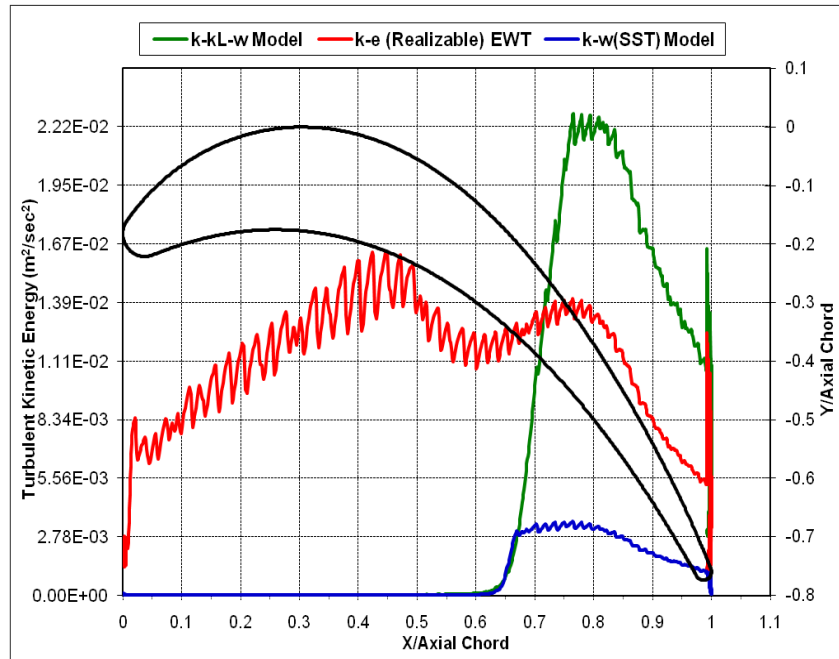


Figure 3.6. Turbulence model comparison of the suction surface turbulent kinetic energy at $Re = 100,000$, $Tu = 1\%$, $L_m = 10.4\text{mm}$ for the Lightly Loaded blade airfoil

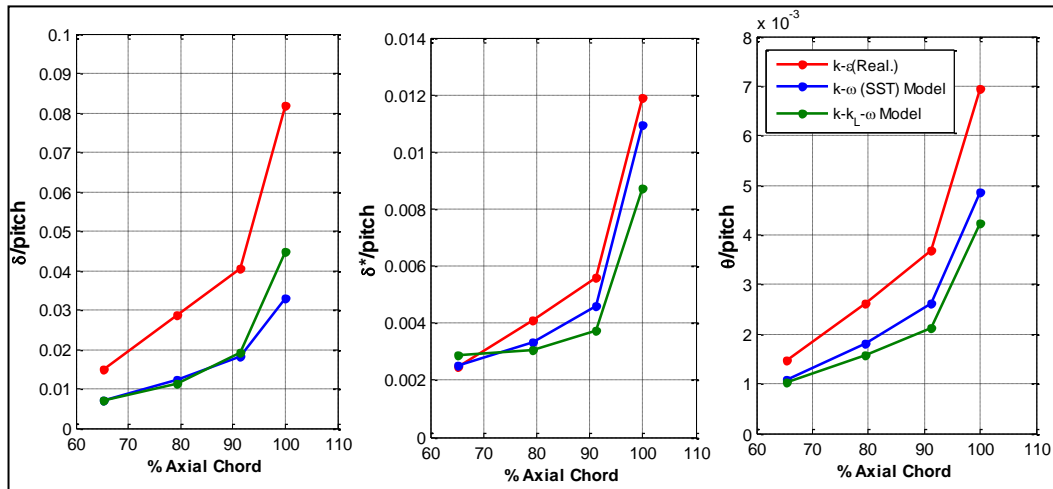


Figure 3.7. Comparison of the boundary layer integral parameters of all three turbulence models at $Re = 100,000$ for the Lightly Loaded blade airfoil

Boundary layer integral parameters were calculated from the velocity profiles at four axial chord locations of 65.3%, 79.4%, 91.3%, and 100% normal to the Lightly Loaded blade airfoil surface. Figure 3.7 compares the predicted boundary layer thickness, displacement thickness, and momentum thickness for all three turbulence models. The $k-\epsilon$ model result has the largest boundary layer thickness because the boundary layer was fully turbulent from the leading edge. *D. Sanders*

Chapter 3. Computational Model Methodology

edge. This resulted in a faster growth of the boundary layer thickness than for the boundary layers undergoing transition as with the $k-\omega(SST)$ and $k-k_L-\omega$ models. The momentum thickness plot showed that the $k-\varepsilon$ model yielded a higher momentum loss than both the $k-\omega(SST)$ and $k-k_L-\omega$ models, indicating a more turbulent boundary layer. The boundary layer thickness for the $k-\omega(SST)$ and $k-k_L-\omega$ models were in good agreement with each other until the 100% axial chord location, where the boundary layer of the $k-k_L-\omega$ model grew at a higher rate after transitioning to turbulence. The $k-\omega(SST)$ model exhibited a higher displacement and momentum thickness which indicated a larger mass deficit in the boundary layer with a slightly higher momentum loss as compared to the $k-k_L-\omega$ model. This was attributed to the large amount of specific dissipation produced in the boundary layer from the $k-\omega(SST)$ model. Even though the flow was transitional, the high specific dissipation rate produced more viscous losses in the boundary layer, which resulted in larger mass deficit and momentum loss than the $k-k_L-\omega$ model.

The total pressure loss coefficient plot shown in Figure 3.8 indicated that the $k-\varepsilon$ model produced the highest amount of total pressure loss because the flow was predicted as fully turbulent. The high momentum loss observed in the boundary layer created a larger total pressure loss in the wake region, which was over-predicted compared to the experimental results [36]. The most interesting result was for the case using the $k-\omega(SST)$ model. The total pressure loss was as high as the fully turbulent $k-\varepsilon$ model even though the boundary layer exhibited transitional flow behavior. The momentum loss was slightly higher in the boundary layer than with the $k-k_L-\omega$ model. This again can be attributed to the specific dissipation present in the wake for the $k-\omega(SST)$ model which was observed to be about 20 times larger than the level

Chapter 3. Computational Model Methodology

predicted with the $k-k_L-\omega$ model. Agreement with respect to the experimental results was calculated using Eq. (3.7)

$$\%agreement = \left[1 - \frac{(X_{CFD} - X_{exp})}{X_{exp}} \right] \times 100 \quad (3.7)$$

where X is the compared flowfield parameter. The total pressure loss prediction made with the $k-k_L-\omega$ model achieved 98% agreement with the experimental results [36] for the peak value of the loss coefficient while the $k-\varepsilon$ and $k-\omega(SST)$ models obtained 17% and 20% agreement, respectively. When compared to the integrated value of the loss coefficient, the $k-k_L-\omega$ model showed 99% agreement with the experimental results. The $k-\varepsilon$ and $k-\omega(SST)$ model produced a 56% and 96% agreement, respectively with the experimental result in the prediction of the integrated loss coefficient. Thus, the $k-k_L-\omega$ model achieved the best agreement with experimental results for the prediction of the amount of viscous losses produced and the magnitude of the total pressure loss in the wake region. So, this demonstrated that for the turbulence models evaluated, the $k-k_L-\omega$ transitional flow model has superior ability to predict transitional flow behavior associated with low Reynolds number flows than the $k-\varepsilon$ and $k-\omega(SST)$ turbulence models. The Walters and Leylek [2] $k-k_L-\omega$ transitional flow model was chosen as the turbulence model to be used in this study because it was shown to be an effective model for laminar-to-turbulent transitional flow and was considered more suitable for the successful completion of the research program goals.

Chapter 3. Computational Model Methodology

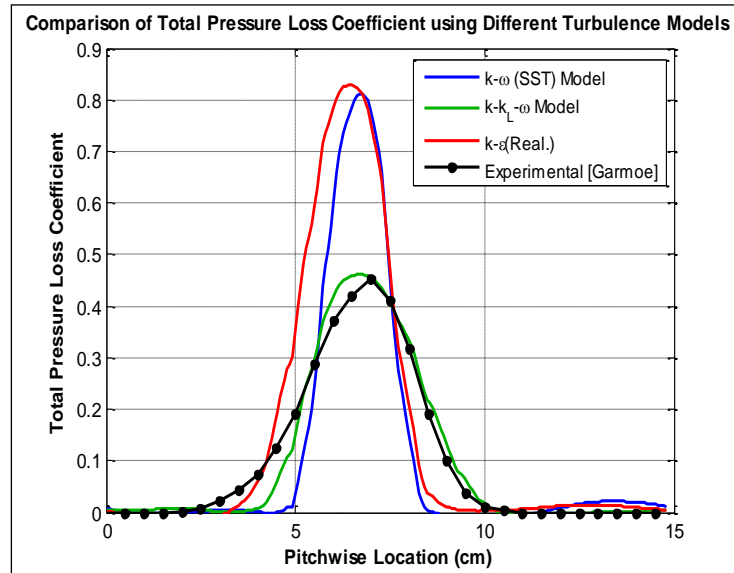


Figure 3.8. Comparison of total pressure loss coefficient for turbulence models at $Re = 100,000$, $Tu = 1\%$ for the Lightly Loaded blade airfoil

Turbulence Model	Integrated Total Pressure Loss Coefficient	
	CFD	Garmoe [36]
$k-k_L-\omega$	0.1033	0.1026
$k-\omega(SST)$	0.1066	
$k-\epsilon$	0.1473	

Table 3.2. Turbulence model comparison of the integrated total pressure loss coefficient with the experimental [36, 40] results for the Lightly Loaded blade airfoil

Recently, an updated version of the $k-k_L-\omega$ model has been fully integrated in the newest software release as Ansys[®] Fluent 12.0. CFD simulations of the Lightly Loaded and Highly Loaded blades were completed using the Fluent 6.3 version of the $k-k_L-\omega$ model while all simulation of the Aft-Loaded L1A blade were completed using the Fluent 12.0 version of the model. This version was used for the simulations using the Aft-Loaded L1A blade because only the Fluent 12.0 version of the model can be used in combination with the sliding mesh model, which was needed for the Aft-Loaded L1A blade simulations using the passing wake generators. Flowfield comparisons of the Aft-Loaded L1A blade were made using the 6.3 and 12.0 versions Fluent with the Walters and Leylek [2] $k-k_L-\omega$ model and are discussed in Appendix I. In

D. Sanders

Chapter 3. Computational Model Methodology

summary, the Fluent 12.0 version of the model showed similar results to the Fluent 6.3 version for unsteady prediction of the flowfield at low turbulent intensities, but it showed improved prediction of the blade loading and flowfield at higher turbulent intensities with respect to Fluent 6.3 version of model.

3.4 CFD Boundary Conditions

CFD boundary conditions were set to mirror the experimental cascade test conditions. The inlet boundary condition for the steady flow cases was specified as a total pressure inlet where static pressure was set according to an experimentally determined value of 98870 Pa. The inlet total pressure reflected the chosen Reynolds number based on the axial chord. Unsteady cases used a mass flow inlet boundary condition permitting the total pressure to be calculated from the interior solution which aided the local convergence per time step. The mass flow was calculated based on the normal component of the velocity and inlet domain length (kg/sec·m). Simulations were run for a Reynolds number range of 10,000-100,000. The axial and tangential components of the flow direction were set based on the design inlet flow angle for each blade. The inlet flowfield was uniformly distributed across the pitch length of the inlet boundary as measured by the experimental results. The experimental cascade blade airfoil geometries were scaled-up, causing the inlet Mach number to be less than 0.03 for a given inlet Reynolds number. Each blade airfoil in the CFD model had the same dimensions as the blade airfoil used in the LSWT. The flow was assumed to be incompressible in the CFD simulations because of the low Mach number. The inlet turbulence intensity and turbulent length scale were chosen based on user specification or experimental values, when available. The inlet laminar kinetic energy was set to $10^{-6} \text{ m}^2/\text{sec}^2$ in accordance with specifications of the turbulence model. No-slip conditions were assigned to the blade surface, and turbulence parameters used a zero-flux boundary

Chapter 3. Computational Model Methodology

condition. The initial static pressure boundary condition at the outlet was estimated using conservation of mass of the axial velocity, the ideal outlet flow angle, and the assumption that no total pressure loss occurred between the inlet and outlet planes following Eq. (3.8) and (3.9).

$$u_{out} = u_{in} \left[\frac{\cos(\alpha_{in})}{\cos(\alpha_{out})} \right] \quad (3.8)$$

$$P_{out} = P_0 - \frac{1}{2} \rho u_{out}^2 \quad (3.9)$$

This assumption of the outlet static pressure provided an initial guess for the pressure-based solver and was adjusted during the calculation to account for the actual total pressure loss. The target mass flow rate option was implemented at the pressure outlet for the steady flow solutions in order to adjust the pressure at the outlet to meet the mass flow rate. The target mass flow rate option was not used for the unsteady cases because the mass flow was set in the inlet boundary condition.

3.5 Computational Resources

The computational resources shown in Figure 3.9 for this work were provided by the U.S. Department of Defense, AFRL Distributed Computing Research Center, High Performance Computing facility at Wright-Patterson AFB, OH. Three different supercomputing systems were available for performing the CFD simulations. The HP XC Opteron high performance super-computer has 2048 AMD[®] Opteron 2.8GHz processors with 2 Gigabytes of memory per processor. The SGI Altix 3700 super-computer has 2048 Intel[®] Itanium 2, 1.6GHz processors with 1 Gigabyte of memory per processor. The largest super-computing system is the SGI Altix 4700 with 9216 core processors and 2 or 4 Gigabytes of memory per processor. There are two cores per 1.6GHz Intel[®] Itanium2 processor.

Chapter 3. Computational Model Methodology

The double-precision parallel version of Fluent 6.3[®] was run on a HP XC Opteron super-computer for two-dimensional cascade simulations. A total of 8-10 processors were used for the steady simulations and 16-32 processors for the transient two-dimensional cascade simulations. The three-dimensional cascade simulations were run on the SGI Altix 4700 using 80-104 processors.



Figure 3.9. AFRL Major Shared Resource Center HP XC Opteron (top left), SGI Altix 3700 (top right), and SGI Altix 4700 (bottom center) Super-Computers

3.6 CFD Post Processing and Analysis

Once the CFD simulations were completed, a number of different software tools were used to complete the analysis of the CFD results. Mathematical rakes were created in Fluent using the Rake Creation Tool for measurements of flow quantities. The locations of these rakes correspond to the same measurement locations as the experimental rakes. Table 3.2 shows the location of rakes, total length, and total number of points for each CFD model. Text files containing the CFD rake data were exported from Fluent to a Microsoft[®] Excel file for further

Chapter 3. Computational Model Methodology

analysis. Two-dimensional plots were made within Microsoft® Excel or using Mathworks® Matlab 2008.

Flow visualizations were completed using Intelligent Light® FieldView 12.0 CFD post-processing and visualization software. FieldView files (.fvuns & .fvuns.fvreg) were exported from Fluent after the completion of steady flow simulations or during calculations for unsteady simulations every 10-20 time-steps. Contour plots and animations were made to visualize steady and unsteady aerodynamic flow characteristics.

CFD Model	Rake Type	Total Pts.	Length	Location
Lightly Loaded Blade	Inlet	200	One pitch length	One C_x from leading edge (streamwise)
	Outlet Wake	200	One pitch length	One C_x from trailing edge (streamwise)
	Boundary Layer	300	30.0cm	65.3% C_x , 79.4% C_x , 91.3% C_x , 100% C_x (normal to blade surface)
Highly Loaded Blade	Inlet	200	One pitch length	One C_x from leading edge (streamwise)
	Outlet Wake	200	One pitch length	One C_x from trailing edge (streamwise)
	Boundary Layer	300	30.0cm	67.2% C_x , 73.0% C_x , 79.3% C_x , 84.8% C_x , 89.8% C_x , 95.0% C_x , (normal to blade surface)
Aft-Loaded L1A Blade	Inlet	200	One pitch length	22.86cm from leading edge (streamwise)
	Outlet Wake	200	One pitch length	25.4cm from trailing edge (streamwise)
	Boundary Layer	300	30.0cm	57.0% C_x , 58.8% C_x , 60.4% C_x , 65.5% C_x , 70.0% C_x , 74.1% C_x , 79.4% C_x , 85.0% C_x , 89.0% C_x , 94.2% C_x (normal to blade surface)
Aft-Loaded L1A Blade with Wake-Generators	Inlet	200	One pitch length	21.27cm from cylinder center (streamwise)
	Outlet Wake	200	One pitch length	17.46cm from trailing edge (streamwise)
	Boundary Layer	300	30.0cm	57.0% C_x , 58.8% C_x , 60.4% C_x , 65.5% C_x , 70.0% C_x , 74.1% C_x , 79.4% C_x , 85.0% C_x , 89.0% C_x , 94.2% C_x (normal to blade surface)
	Point Probe	1		Mid-pitch at the blade leading edge axial location

Table 3.3. CFD mathematical rake measurement locations created in Fluent CFD software

CHAPTER FOUR

4. The Lightly Loaded Blade CFD Results

The Lightly Loaded blade geometry was used for the initial baseline study because of its low blade loading level. As previously described, it was used to determine which RANS turbulence model within Fluent was the most capable for the prediction of low Reynolds number aerodynamic flow effects. To obtain the following results of this Section, the Walters and Leylek [2] $k-k_L-\omega$ model was applied to flows over a Reynolds number range of 15,000-100,000 using the Lightly Loaded blade airfoil. The simulation results were compared to available data from experimental studies to determine if total pressure loss was successfully predicted. Additionally, parametric studies of the $k-k_L-\omega$ model sensitivity to inlet freestream turbulence intensity and turbulent length scale were conducted to investigate how the inlet turbulence parameters affect boundary behavior and total pressure loss.

4.1 Performance Prediction at Different Inlet Reynolds Numbers

The Lightly Loaded blade airfoil flow was simulated at individual Reynolds numbers of 100,000, 75,000, 50,000, 40,000, and 15,000 to determine if the $k-k_L-\omega$ transitional flow model could adequately predict the varying Reynolds number performance. The inlet freestream turbulence intensity for the CFD simulations was set to the average inlet turbulence intensity measured in the experimental [36] results with the turbulent length scale, $l_m = 5mm$. The steady and time-mean velocity contour plots at each inlet Reynolds number are shown in Figure 4.1. The flow around the Lightly Loaded blade airfoil behaved similarly at Reynolds number from 100,000 to 50,000, where the flow was predicted as transitional and boundary layer was well attached to the blade surface producing a turbulent wake similar to Figure 4.3(c). The freestream

Chapter 4. The Lightly Loaded Blade CFD Results

length scales as modeled by the specific dissipation rate (ω) transport Eq. (1.59) were small enough to couple with the k - k_L - ω model and cause transition to turbulence in the boundary layer. When the Reynolds number decreased below 50,000, the flow around the suction side of the blade became laminar and began to separate, resulting in a von Kàrmàn vortex street in the wake region of the blade (Fig. 4.3(b)). The freestream length scales at these Reynolds number ranges were large enough to decouple with the k - k_L - ω model and contribute to the growth in the laminar kinetic energy [2] resulting in a laminar boundary layer and vortex shedding in the wake region.

At the inlet Reynolds number of 15,000, the steady flow simulation (Fig. 4.1(e)) predicted a very large separation region beginning at the 70% axial chord on the suction side of the blade. However, the unsteady simulation (Fig. 4.1(f)) predicted a separation beginning at approximately 90% axial chord with the presence of von Kàrmàn vortex shedding at a frequency of 75Hz in the wake region. A Strouhal number, $St = 0.0220$, was calculated based on the observed vortex shedding frequency, freestream velocity, and momentum thickness at separation with Eq. (4.1).

$$St = \frac{f_{shed}\theta_{sep}}{U_{\infty}} \quad (4.1)$$

The presence of the vortex shedding caused the boundary layer to remain attached for an additional 20% chord than for the steady flow solution. The separation region was reduced due to the unsteady generation of vortices from the trailing edge of the blade. The unsteady simulation provided a better prediction of the flowfield because unsteady effects from the separated shear layers on pressure and suction side were allowed form into discrete vortices. However, unsteady flow simulations require significantly larger computational resources

Chapter 4. The Lightly Loaded Blade CFD Results

compared to steady flow simulations because the solution must be converged spatially for every time-step and run until the solution is time-periodic.

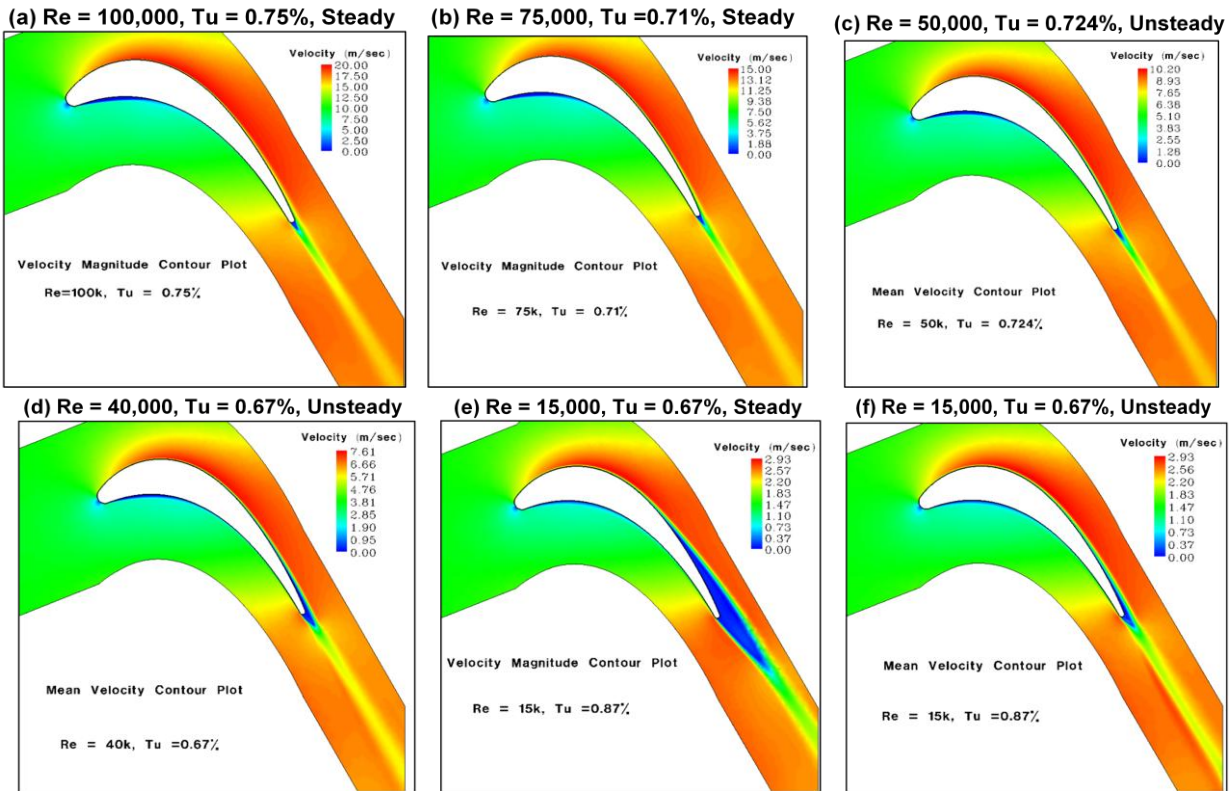


Figure 4.1. Velocity magnitude contour plots of the Lightly Loaded blade airfoil simulated at a range of inlet Reynolds numbers

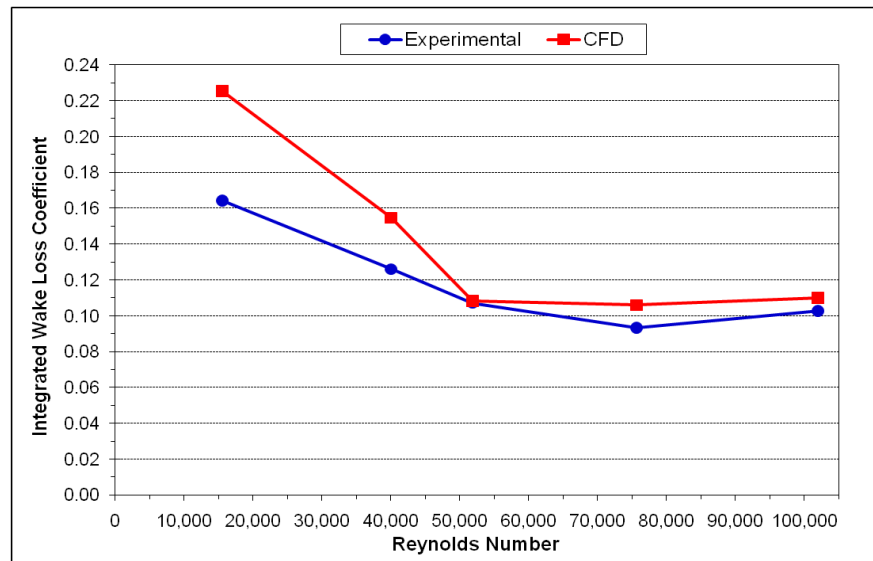


Figure 4.2. Comparison of the CFD and experimental [36] integrated wake loss coefficient at a range of inlet Reynolds numbers for the Lightly Loaded blade airfoil

Chapter 4. The Lightly Loaded Blade CFD Results

Aerodynamic performance was evaluated based on the total pressure loss coefficient, which was used as an indicator the viscous losses. The integrated loss coefficient was used as an indicator of the total amount of viscous losses generated in the wake region, and the peak loss coefficient was used as an indicator of the strength of the wake region and how the viscous losses were distributed within the wake region. The integrated and maximum value of the wake total pressure loss coefficient are plotted in Figures 4.2 and 4.3 versus the inlet Reynolds number for both the experimental and the CFD results to show the Reynolds number performance of the Lightly Loaded blade airfoil. Figure 4.2 shows the integrated wake loss coefficient was over-predicted by 23% and 37% for the Reynolds number of 40,000, and 15,000, respectively. This was attributed to the width of the wake region being larger in the CFD predictions than the experimental result [36]. The specific dissipation rate calculated from the $k-k_L-\omega$ model which was set based on the inlet turbulent length scale and its effect on integrated and peak loss coefficient was investigated in Section 4.2.1. The CFD predictions at the other Reynolds numbers showed better than 88% agreement with the experimental results [36]. Also, the gradual increase of the integrated loss coefficient with decreasing Reynolds number was predicted in the CFD results.

The CFD results showed better than 90% agreement with the experimental results [36] at inlet Reynolds numbers of 100,000, 75,000, and 40,000 for the prediction of the peak value of the loss coefficient as shown in Figure 4.3. Discrepancies existed between the experimental and CFD predictions at 50,000 and 15,000. The CFD results for the $Re = 50,000$, $Tu = 0.724\%$ case predicted that the flow does not transition until 85% axial chord, causing the total pressure loss coefficient to be 20% under-predicted with respect to the experimental result [36]. At a Reynolds number of 15,000, the unsteady case resulted in 83% agreement of the total pressure

Chapter 4. The Lightly Loaded Blade CFD Results

loss coefficient with the experimental result [36] due to the presence of vortex shedding, caused by an increased amount of losses present in the wake. Overall, the CFD simulations using the k - k_L - ω model demonstrated the ability to adequately predict the inlet Reynolds number aerodynamic loss trends for the Lightly Loaded blade airfoil. Based on comparisons of the integrated and peak loss coefficient, the k - k_L - ω model was able to effectively predict the amount of losses generated and their distribution within the wake region. Based on the prediction of aerodynamic losses and comparisons with other turbulence model presented in Section 3.3.1, the k - k_L - ω model showed the potential to provide improved prediction low Reynolds number flow effects. This provided confidence in its capability for providing the same type of results for more highly loaded turbine blade airfoil geometries such as the Highly Loaded and Aft-Loaded L1A blade to be presented Section 5 and 6, respectively.

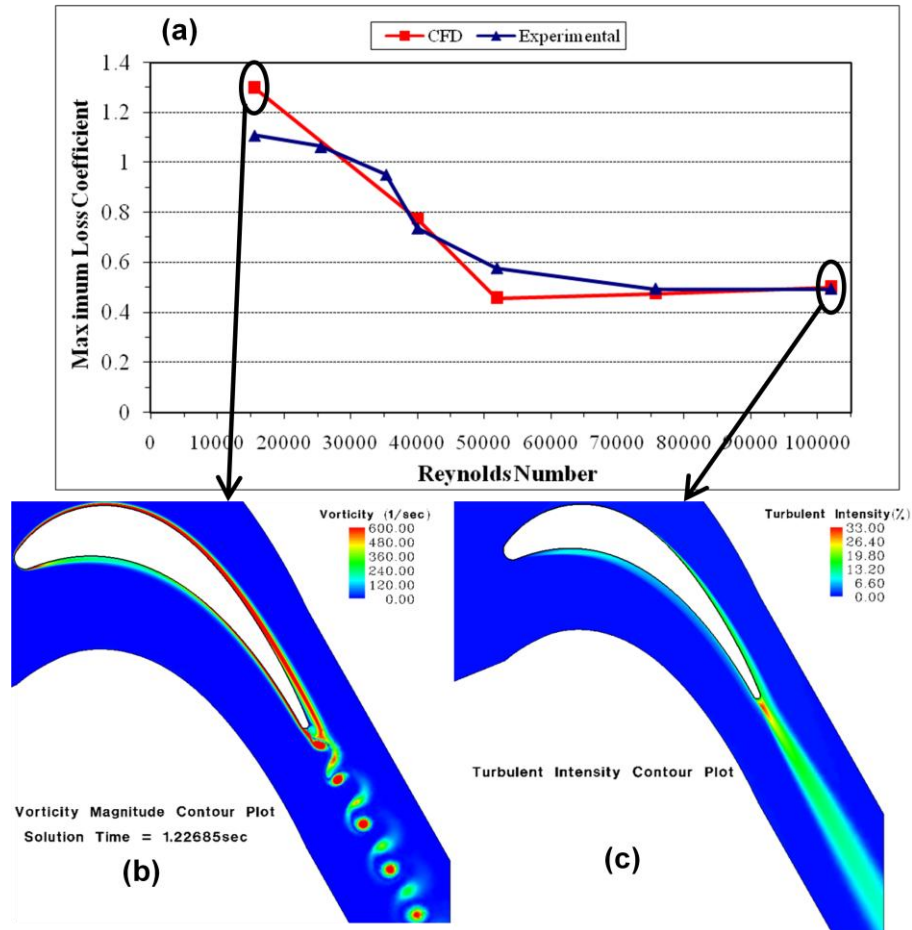


Figure 4.3. Comparison of the CFD and Experimental [36] Maximum Loss Coefficient at a Range of Inlet Reynolds Numbers for the Lightly Loaded Blade Airfoil

4.2 Effect of Inlet Turbulence Parameters on Transition and Performance Predictions

Since the $k-k_L-\omega$ transitional flow model was a newly formulated model, an understanding of how the inlet turbulence parameters affected the CFD predictions of aerodynamic effects at low Reynolds numbers was needed. Simulations were completed at $Re = 50,000$ using the Lightly Loaded blade airfoil where either the inlet turbulent length scale was held constant and the inlet turbulence intensity was varied, or inlet turbulence intensity was held constant and the inlet turbulent length scale was varied. The effect of these inlet turbulent boundary condition variations was investigated on the turbulent transition point, the behavior of the boundary layer, and the total pressure loss coefficient.

Chapter 4. The Lightly Loaded Blade CFD Results

(a) Inlet Length Scale Parametric Study Re = 50,000, Tu = 1%					(b) Inlet Turbulent Intensity Parametric Study Re = 50,000, $l_m = 5mm$				
$l_m (mm)$	X_{trans}/C_x		Max. TPLC	ITPLC	Tu (%)	X_{trans}/C_x	Max. TPLC	ITPLC	
2	0.831		0.471	0.1099	0.724	0.879	0.455	0.1076	
3.5	0.761		0.495	0.1136	0.75	0.862	0.457	0.1084	
4	0.753		0.498	0.1141	1	0.747	0.499	0.1144	
5	0.747		0.499	0.1144	1.5	0.615	0.546	0.1239	
6	0.749		0.497	0.1143					
8	0.778		0.523	0.1249					
14	0.823		1.052	0.1313					
$l_m (mm)$	X_{sep}/C_x	St	Max. TPLC	ITPLC	Tu (%)	X_{sep}/C_x	St	Max. TPLC	ITPLC
20	0.938	0.015	0.988	0.1527	0.5	0.931	0.014	0.718	0.1364
25	0.942	0.015	1.069	0.1630					
30	0.944	0.015	1.040	0.1814	Experimental Result [36]				
40	0.966	0.015	1.000	0.1733	Tu (%)		Max. TPLC	ITPLC	
50	0.947	0.015	1.015	0.1652	0.724		0.577	0.1083	

Table 4.1. Summary of inlet turbulence parameters on transition/separation location and maximum loss coefficient for the Lightly Loaded Blade

4.2.1 Inlet Turbulent Length Scale Study

An estimate of the inlet turbulent length scale range was needed for the boundary condition specification because measurements of the inlet turbulent length scale were unavailable for the Lightly Loaded blade airfoil cascade experiments. Typically, integral length scale measurements obtained from experiments were used to set the inlet turbulent length scale in Fluent CFD software. The sensitivity of the $k-k_L-\omega$ transitional flow model to the inlet turbulent length scales was investigated in order to determine the prediction accuracy tolerance to the inlet turbulent length scale. The inlet turbulent length scale (l_m) specification in Fluent CFD software was used to set the initial inlet specific dissipation rate (ω) in the $k-k_L-\omega$ model with the Eq. (5.2)

$$\omega = \frac{k^{1/2}}{C_\mu^{1/4} l_m} \quad (4.2)$$

Chapter 4. The Lightly Loaded Blade CFD Results

where the empirical constant $C_\mu = 0.09$ used was specified in the $k-k_L-\omega$ model. Then the specific dissipation rate was calculated within the flowfield according to the transport equation in Eq. (1.59). The specific dissipation controls the rate of transfer of turbulent kinetic energy to viscous losses. RANS turbulence models use the dissipation transport equation to model the energy cascade of turbulence where the turbulent kinetic energy is transferred from larger eddies to smaller eddies and the smallest eddies dissipate the kinetic energy into viscous heat. The difference with the $k-k_L-\omega$ model compared to conventional turbulence models is that it divides the eddy sizes according to a cutoff eddy size called the effective length scale. Length scales smaller than the effective length scale interacted with the mean flow as typical turbulence and larger scales contribute to the production mechanism for laminar kinetic energy [2].

The separation/transition to turbulence point on the blade suction side and the wake total pressure loss coefficient were used to study this effect. The inlet Reynolds number for these steady and unsteady flow simulations was set to 50,000 with an inlet turbulence intensity, $Tu = 1\%$. The turbulent length scale was varied over a range of $2 - 50\text{ mm}$ as shown in Table 4.1(a). Over a range of $l_m = 3.5 - 8\text{ mm}$, Table 4.1(a) shows that the location of the transition region does not vary significantly. For the $l_m = 2\text{ mm}$ case, the transition region moved further downstream to the 83% axial chord position indicating that as the length scale becomes very small, the transition region will move downstream. This is consistent with the fact that the magnitude of the disturbance that couples with the boundary layer will be reduced as the turbulent length scale decreases. The $l_m = 14\text{ mm}$ case, showed a similar turbulence transition point as the $l_m = 2\text{ mm}$ case. This indicated a nonlinear variation in the location of the turbulent transition point at the inlet turbulent length scale range of $l_m = 2 - 14\text{ mm}$. At a turbulent length scale of $l_m = 20\text{ mm}$ and above, the flow within the boundary layer remained laminar and separated. The turbulent length

Chapter 4. The Lightly Loaded Blade CFD Results

scale has grown large enough that the freestream eddies no longer couple to the boundary layer through the turbulence model, hence the boundary layer does not transition to turbulent.

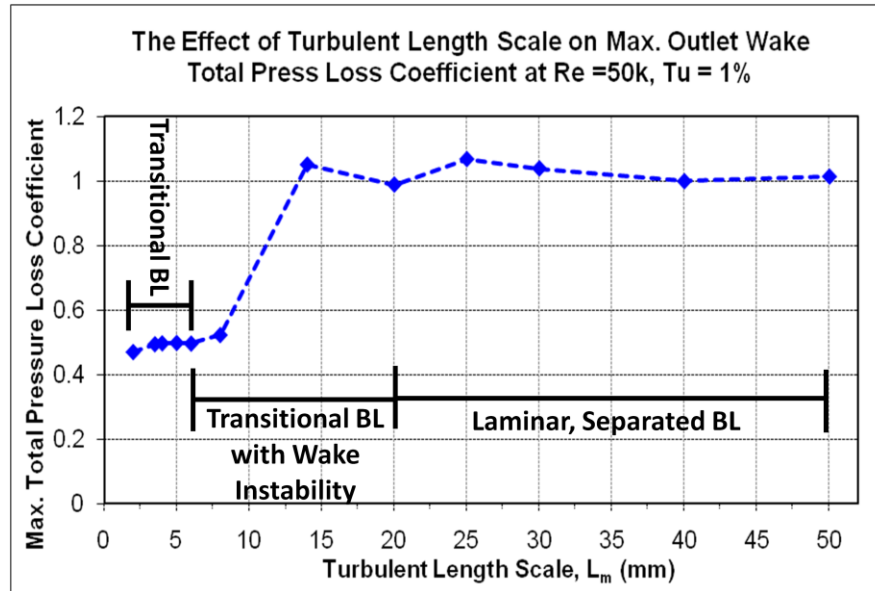


Figure 4.4. Maximum wake loss coefficient versus inlet turbulent length scale for the Lightly Loaded blade

The maximum value of the wake total pressure loss coefficient shown in Figure 4.4 also shows no significant variation for the $l_m = 3.5 - 6mm$ range. The lowest value of the maximum total pressure loss coefficient was calculated for the $l_m = 2mm$ case due to the transition region being located far downstream in comparison to the other cases. This resulted in a lower momentum loss in the boundary layer. The $l_m = 8mm$ and $14mm$ cases showed an increase in the loss coefficient even though the boundary layer was transitional. This increase was due to a wake instability present in the flowfield. It caused the vortex shedding similar to the separated flow cases at the higher inlet turbulent length scales shown in the contour plots in Figure 4.5. For the $l_m = 8mm$ case (Fig. 4.5(a)) the wake instability was weak, causing the initial trailing edge vortex shedding to dissipate. The wake instability was the strongest for the $l_m = 14mm$ case (Fig. 4.5(b)) and caused a higher loss coefficient compared to the $l_m = 8mm$ case. The total pressure loss remained constant at turbulent length scales above $20mm$ because the separation

Chapter 4. The Lightly Loaded Blade CFD Results

within the laminar flow boundary layer caused vortex shedding within the wake region (Fig. 4.5(c)). The turbulent length scale must be within a range of $l_m = 2 - 6mm$ in order to couple with the boundary layer and affect turbulent transition. Also, a length scale range of $l_m = 8 - 14mm$ was found to cause transition in the boundary layer and produce eddies that were large enough to cause instabilities in the wake and produce vortex shedding.

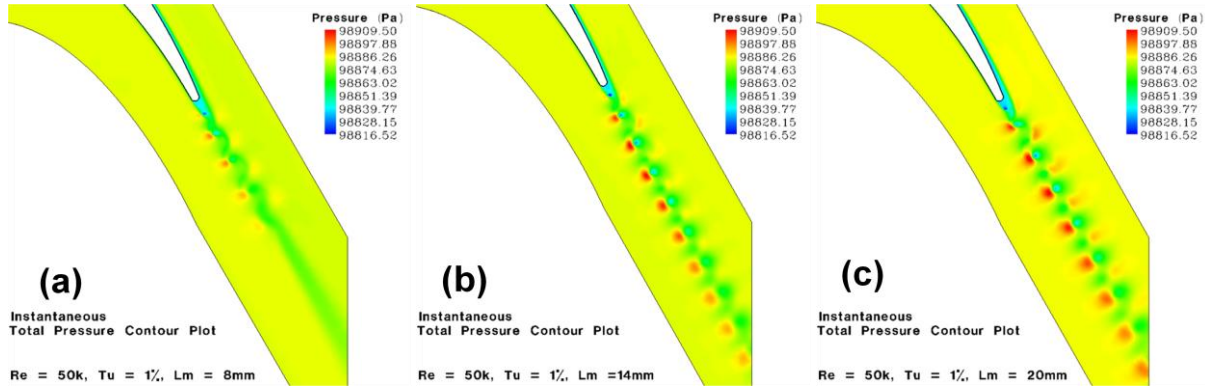


Figure 4.5. Wake region total pressure contours for the Lightly Loaded Blade at (a) $l_m = 8mm$, (b) $l_m = 14mm$, and (c) $l_m = 20mm$

Figure 4.5 shows the integrated total pressure loss coefficient that was calculated at each inlet turbulent length scale. The trends were similar to the maximum loss coefficient plot in Figure 4.4. The integrated loss coefficient remained essentially constant from $l_m = 2 - 6mm$ and it began to linearly increase from $l_m = 6 - 30mm$ due to an increase in the width of the wake region and the peak loss coefficient. At length scales above $l_m = 30mm$, the integrated loss coefficient decreased as the inlet turbulent length scale was increased, mainly due to the decrease in the wake region.

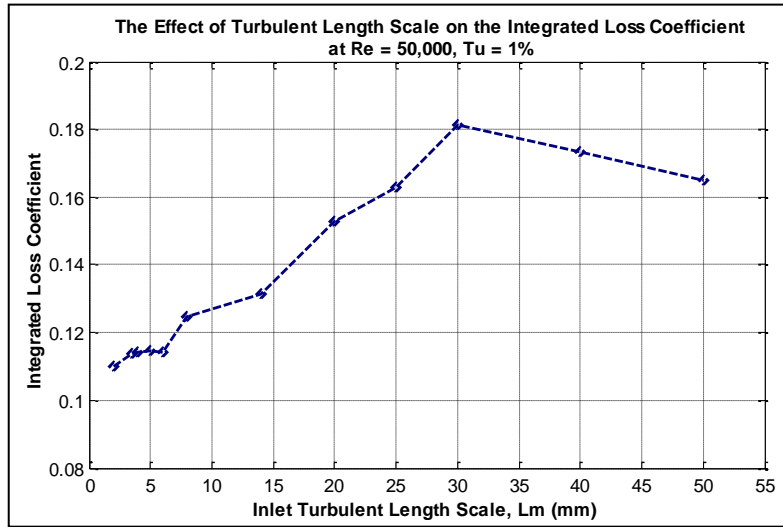


Figure 4.5. Integrated wake loss coefficient verses inlet turbulent length scale for the Lightly Loaded blade

4.2.2 Inlet Turbulence intensity Study

Sensitivity to the inlet turbulence intensity level on the turbulent transition location and the total pressure loss coefficient was investigated. The inlet turbulence intensity was used to set the initial value of the turbulent kinetic energy in the $k-k_L-\omega$ model using Eq. (5.3).

$$k = \frac{3}{2}(u_{inlet}Tu)^2 \quad (4.3)$$

The transport equation (Eq. (1.59)) was used to calculate the turbulent kinetic within the flowfield. Steady flow simulations at $Re = 50,000$ for the Lightly Loaded blade airfoil were also completed at inlet turbulent intensities of 0.75%, 1%, and 1.5%. Unsteady flow simulations were completed at inlet turbulent intensities of 0.5% and the experimentally [36] measured inlet turbulence intensity of 0.724%. There was a significant amount of unsteadiness present in the flowfield for the $Tu = 0.5\%$ case due to separation and vortex shedding whereas the $Tu = 0.724\%$ case was quasi-steady with no significant flow unsteadiness present in the flowfield. All these cases used a constant turbulent length scale of 5mm. Figure 4.6 and Table 4.1(b) shows the

Chapter 4. The Lightly Loaded Blade CFD Results

effect of varying the inlet turbulence intensity on transition. The location of turbulent transition on the suction side moved downstream as inlet freestream turbulence intensity was decreased, while the transition on the pressure side remained unchanged. The low-frequency high amplitude fluctuations in the pre-transitional boundary layer took longer to develop because the freestream turbulence was reduced, causing transition on the suction surface to be further delayed. In the 0.5% inlet turbulence intensity case, the boundary layer did not transition along the blade surface and flow remained laminar. The presence of laminar flow caused vortex shedding at a frequency of 325Hz with a $St = 0.014$, and explained the origin of the increase in the turbulent kinetic energy at the trailing edge.

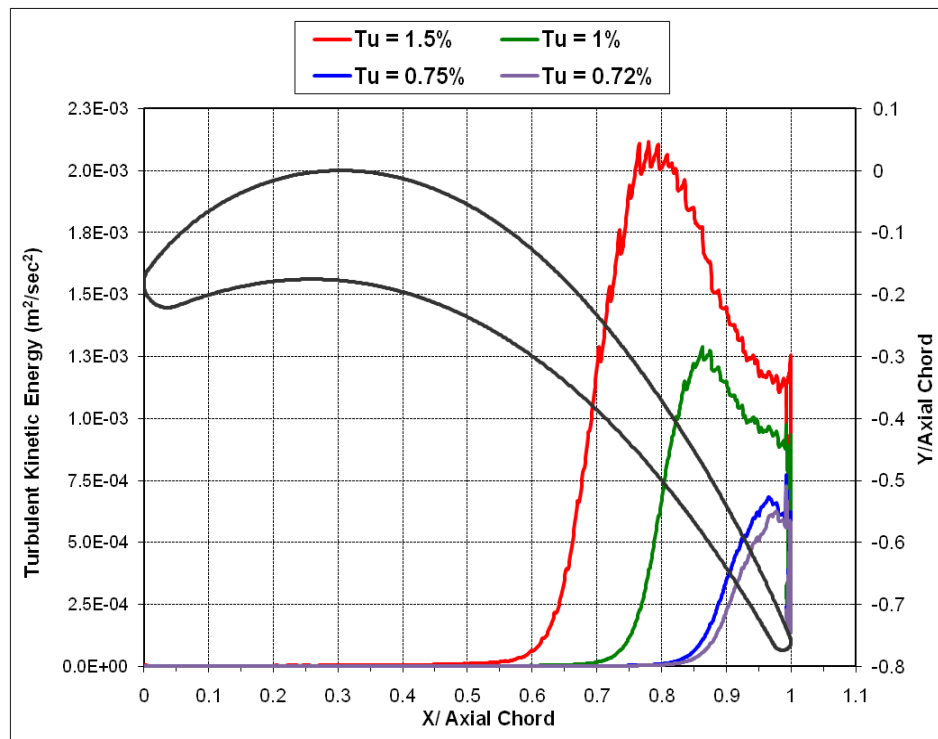


Figure 4.6. Comparison of the suction surface turbulent kinetic energy at different inlet turbulent intensities for the Lightly Loaded blade at $Re = 50,000$, $l_m = 5mm$

Boundary layer velocity profiles were then obtained at four axial locations of 65.3%, 79.4%, 91.3%, and 100% normal to the Lightly Loaded blade surface. The profiles shown in

Chapter 4. The Lightly Loaded Blade CFD Results

Figure 4.7(a) revealed that the flow remained attached for all four measured locations except for the $Tu = 0.5\%$ case. The flow separated at the 100% axial chord location due to the initial creation of vortices from the shear layer on suction side. The boundary layer thickness, displacement, and momentum thickness shown in Figure 4.7(b) were calculated from the velocity profiles. The largest boundary layer thickness was found in the $Tu = 1.5\%$ case because the boundary layer transitioned to turbulent farthest upstream of all the cases and underwent more of the exponential growth associated with turbulent boundary layers. It also contained the highest momentum thickness because of the larger amount of turbulence present in the mean flow. At the 65.3% axial chord location, the boundary layer thickness was approximately the same for all cases. The smallest boundary thickness was found for the $Tu = 0.75\%$ and $Tu = 0.724\%$ cases, because the transition locations are more downstream than the $Tu = 1\%$ and $Tu = 1.5\%$ cases. The displacement thickness at the four axial chord locations increased as the inlet turbulence intensity decreased. The largest displacement thickness was found in the $Tu = 0.5\%$ case because the flow around the suction side of the blade was laminar and separated at the 100% axial chord location.

Chapter 4. The Lightly Loaded Blade CFD Results

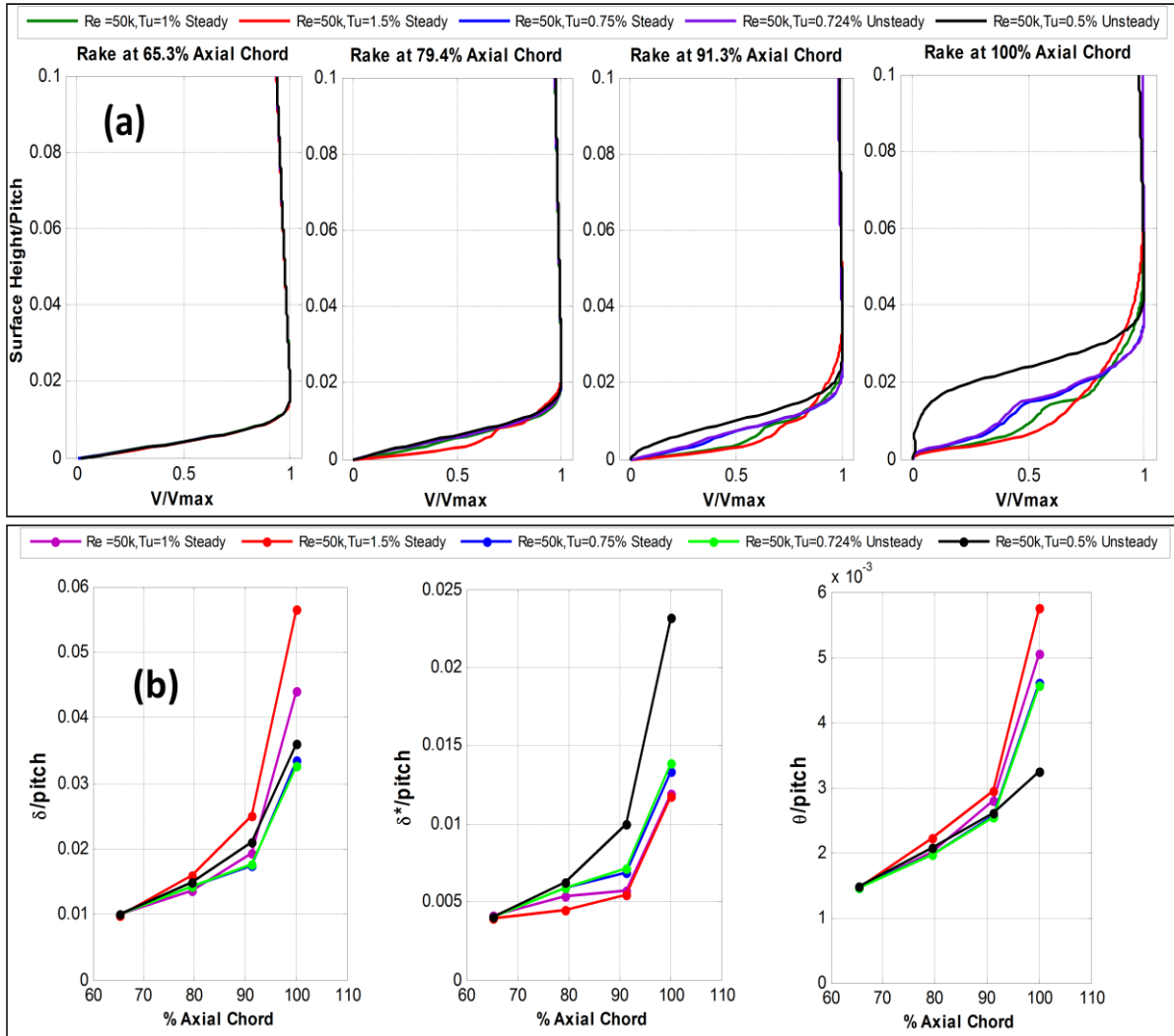


Figure 4.7. Comparison of (a) boundary layer velocity profiles and (b) integral parameters at different inlet freestream turbulent intensities at $Re = 50,000$, $L_m = 50mm$ for the Lightly Loaded blade airfoil

The behavior of the boundary layer at the various inlet turbulent intensities was reflected in the calculation of the total pressure loss coefficient. In Table 4.1 and Figure 4.8(a), the total pressure loss coefficient for the several freestream inlet turbulent intensities were compared to the $Tu = 0.724\%$ experimental result and showed the best agreement with the $Tu = 1.5\%$ case. The $Tu = 0.5\%$ and $Tu = 1.5\%$ cases show that large values of the total pressure losses can be produced by two different types of flow behaviors. High values of turbulence intensity caused turbulent transition further upstream of the blade resulting in higher momentum loss in the boundary layer. This high momentum flow leads to a higher total pressure loss. In contrast, at *D. Sanders*

Chapter 4. The Lightly Loaded Blade CFD Results

low turbulence intensity the flow remains laminar and separated, thus causing a von Kàrmàn vortex street (Fig 4.8(b)). The vortices shed from the trailing edge increased the total pressure loss in the wake. The $Tu = 0.724\%$ CFD result predicted the flow to transition furthest downstream of all the cases. The total pressure loss coefficient was under-predicted because the momentum loss within the boundary layer was the lowest of all the cases where the flow transitioned. Figure 4.8(c) shows the wake was narrow with relatively low total pressure loss. The experimental [36] loss coefficient result indicated that the flow was more laminar than predicted with the CFD. So, if the inlet turbulence intensity was set in the CFD result between $Tu = 0.5\%$ and $Tu = 0.724\%$ such that the flow did not transition but remained laminar, better agreement might be achieved with the experimental results.

Chapter 4. The Lightly Loaded Blade CFD Results

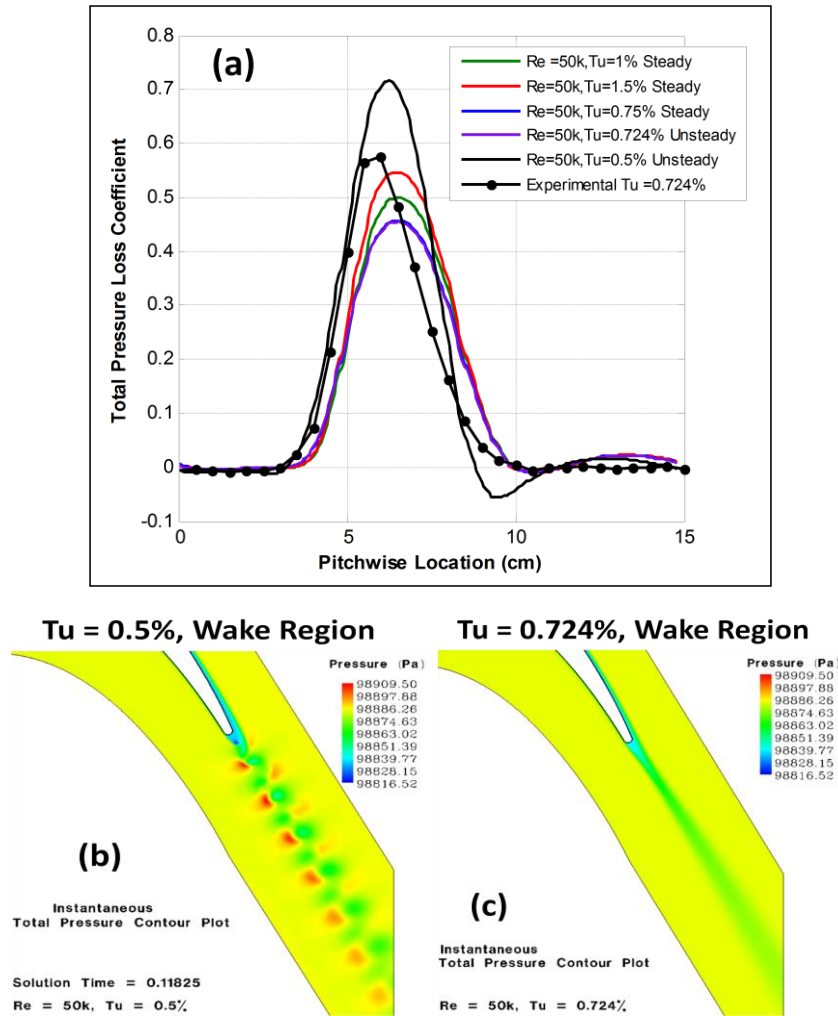


Figure 4.8. (a) Inlet turbulence intensity effect on the wake total pressure loss coefficient and instantaneous wake total pressure contours at (b) $Tu = 0.5\%$ and (c) $Tu = 0.724\%$, $Re = 50,000$ for the Lightly Loaded blade airfoil

Table 4.1 summarizes the results of the predicted turbulent transition point and the peak and integrated value of the loss coefficient as inlet turbulent length scale and turbulence intensity was varied. The $k-k_L-\omega$ transitional flow model does show that the inlet turbulence intensity has a first order effect on transition and prediction of the total pressure loss coefficient. Clearly, setting the correct inlet turbulence intensity was crucial to being able to predict performance at low Reynolds numbers when using current transitional flow model. The CFD simulation demonstrated that high total pressure loss can originate from high freestream turbulence or laminar flow with the presence of vortex shedding. The inlet turbulent length scale had a second

D. Sanders

Chapter 4. The Lightly Loaded Blade CFD Results

order effect on transition and total pressure loss coefficient and needs to be in the correct range in order to penetrate the boundary layer to affect transition and allow for successful performance prediction.

4.3 Summary of Results

A new three-equation eddy-viscosity type turbulent transitional flow model developed by Walters and Leylek [2] was tested to predict the performance a CFD model of LPT cascade configuration. A Lightly Loaded blade airfoil was simulated for inlet Reynolds numbers from 15,000 to 100,000. Walters and Leylek's [2] $k-k_L-\omega$ transitional flow model showed the ability to predict the transitional flow behavior associated with low Reynolds number flows for the Lightly Loaded blade airfoil. The $k-k_L-\omega$ transitional flow model provided a more accurate method for performance predictions compared to conventional RANS turbulence models. Sensitivity of the inlet turbulence boundary conditions to the turbulent length scale and freestream inlet turbulence intensity was investigated to determine the effect on prediction of the total pressure loss coefficient. The turbulent transition point and total pressure loss coefficient showed strong sensitivity to changes in the inlet freestream turbulence intensity, and second order sensitivity effect to the inlet turbulent length scale. Good agreement was obtained for the effect of Reynolds number sensitivity with the experimental results. The ability to adequately predict the Reynolds number effect was demonstrated for the Lightly Loaded blade airfoil.

5. The Highly Loaded Blade CFD Results

Walters and Leylek's [2] $k-k_L-\omega$ transitional flow model was applied to the Highly Loaded blade airfoil to determine if it could effectively predict the low Reynolds number aerodynamic flow effects associated with this geometry. Experimental studies [36,38-40] reported that the flowfield was largely separated when the Highly Loaded blade airfoil was subjected to low inlet Reynolds numbers due the increased loading level and strong suction surface adverse pressure gradient. Two-dimensional simulations were compared to experimental cascade results and investigations of the unsteady flowfield were made at various inlet Reynolds numbers. The inlet turbulent length scale was varied to investigate its effect on the unsteady flowfield and the loss coefficient predictions. Additionally, a three-dimensional cascade model was developed and run to study the effect of the spanwise dimension on the CFD predictions for the Highly Loaded blade airfoil.

5.1 Two-Dimensional CFD Comparisons with Experimental Results

The two-dimensional cascade model of the Highly Loaded blade airfoil (Fig. 3.5(b)) was simulated at an inlet Reynolds number of 25,000, 50,000, and 100,000. Unsteady simulations were run with an inlet $Tu = 0.6\%$ for all inlet Reynolds numbers. The inlet turbulent length scale was set for $Re = 50,000$ and $25,000$ at $l_m = 5mm$ and $50mm$ to investigate the impact of the length scale on the CFD predictions using the $k-k_L-\omega$ model. The $Re = 100,000$ case, the inlet turbulent length scale was set as $l_m = 50mm$. The next sections present the comparisons of the static pressure coefficient, boundary layer profiles, and total pressure loss coefficient with the

Chapter 5. The Highly Loaded Blade CFD Results

experimental measurements taken at the AFRL Low Speed Wind Tunnel. Also, the unsteady features of the flowfield predicted with the $k-k_L-\omega$ model were discussed.

5.1.1 Surface Static Pressure Coefficient

In Figure 5.1, the mean static pressure coefficient distributions on the blade airfoil suction and pressure side were compared to the measurements of Bons *et al.* [38] and the three-dimensional LES results of Rizzetta and Visbal [45]. The present CFD result predicted a higher static pressure on the suction side of the blade for the $Re = 100,000$ case (Fig 5.1(a)), but it did predict the flow separation and reattachment and followed the same trend as the experimental [38] results. The flow separated at 70% axial chord location and then underwent turbulent reattachment at approximately the 93% axial chord location. The uncertainty separation location was 0.1% axial chord in the CFD whereas experimental results were 3% axial chord. The experiment showed that separation began more downstream at 75% axial chord and there was reattachment at 88% axial chord. On the pressure side of the blade, the predicted values were in excellent agreement with the experimental values.

At 50,000, the current CFD results showed similar blade loading characteristics as the LES simulation up to the 80% axial chord location (Fig. 5.1(b)). There was a large amount of unsteadiness present on the suction and pressure sides due to the production of vortices from the separated shear layers. The pressure coefficient trend downstream of the 80% axial chord location was due to the motion of suction side vortices. The $k-k_L-\omega$ model predicted the suction side vortex in a time-averaged perspective to be fixed in space. As a result, the pressure coefficient has a sharp increase and then decreases further downstream. The decrease in the inlet turbulent length scale from $l_m = 50mm$ to $l_m = 5mm$ caused the localized increase of the pressure coefficient to extend further downstream. The experimental result [38] for the $Re = 50,000$ cases

Chapter 5. The Highly Loaded Blade CFD Results

showed that the flow at 60% axial chord remained separated all the way to the trailing edge of the blade. The discrepancy in the CFD and experimental results could be attributed to possible differences in inlet turbulent boundary conditions.

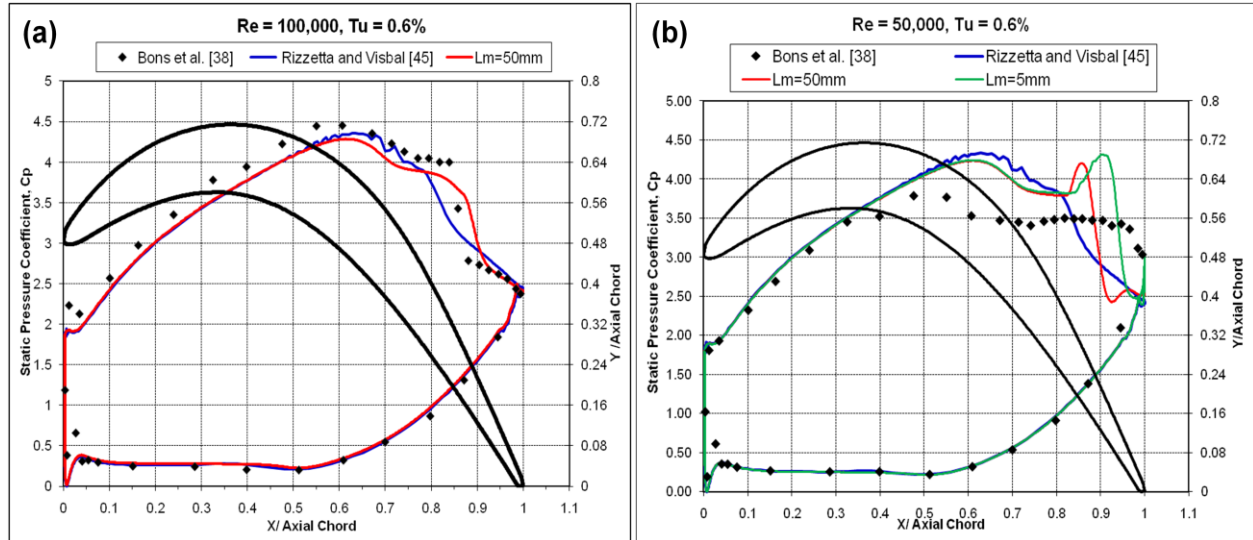


Figure 5.1. Comparison of surface static pressure coefficient with 3D LES [45] simulations and experimental results [38] at inlet Reynolds numbers of a) 100,000 and b) 50,000 for the Highly Loaded blade airfoil

The pressure coefficient on the suction side was predicted to be higher than the experimental result [38] for the $Re = 25,000$ case as shown in Figure 5.2. The location where the separation first began was the 60% axial chord location for both the experimental result and the current CFD prediction. The CFD was able to adequately reproduce the static pressure distribution on the pressure side of the blade. There was a large unsteadiness present in the $Re = 25,000$, $l_m = 50mm$ case due to vortex shedding from the separation bubble as the $Re = 50,000$ case, which caused a small increase in the pressure coefficient beginning at 95% axial chord. When the inlet length scale was decreased to $5mm$, the increase in the pressure coefficient began at the 85% axial chord location. The unsteady vortex shedding caused a larger localized increase in the pressure coefficient as observed in the $Re = 50,000$ CFD results.

Chapter 5. The Highly Loaded Blade CFD Results

The LES results from Rizzetta and Visbal [45] predicted separation and turbulent reattachment for all simulated inlet Reynolds numbers. At $Re = 100,000$, the separated and turbulent reattachment region was smaller and located more upstream of the blade than found in the Bons *et al.* [38] experimental result. The separation and reattachment region increased as inlet Reynolds number decreased from 100,000 to 25,000. In summary, this shows that the $k-k_L-\omega$ transitional flow model was very suitable for the prediction of the qualitative flow response of the Highly Loaded blade airfoil to separated shear layers in low Reynolds number turbine flows. It demonstrated the improved prediction of the static pressure distribution and the unsteady effects of the separation and reattachment behavior.

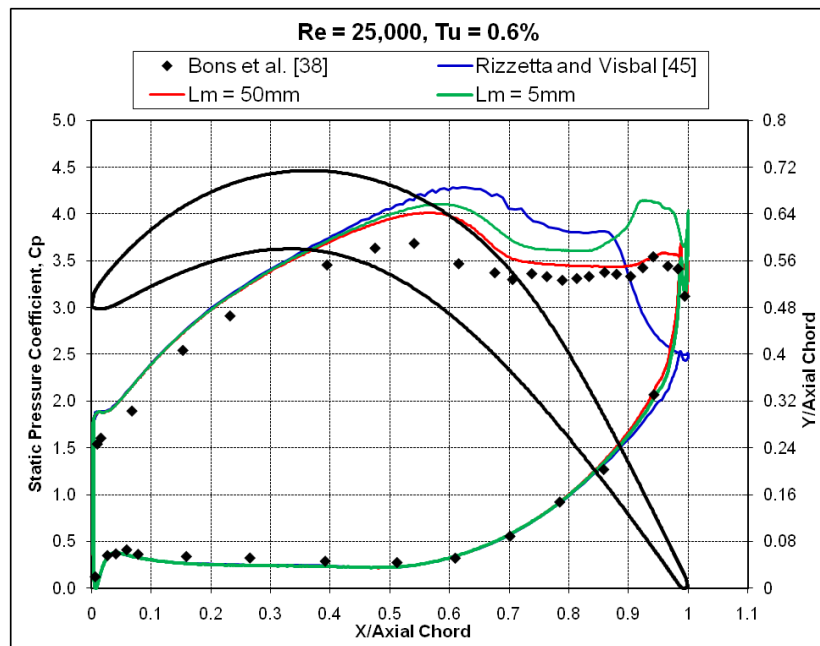


Figure 5.2. Comparison of surface static pressure coefficient with 3D LES [45] simulations and experimental results [38] at inlet Reynolds numbers of 25,000 for the Highly Loaded blade airfoil

5.1.2 Boundary Layer Velocity Profiles

Time-averaged values of the boundary layer velocity profiles obtained at six axial chord locations of 67.2%, 73.0%, 79.3%, 84.8%, 89.8%, and 95.0% normal to the blade surface are shown in Figure 5.3 and Figure 5.4, with boundary layer velocity measurements from the PIV *D. Sanders*

Chapter 5. The Highly Loaded Blade CFD Results

experiments of Woods *et al.* [39] extracted at the same locations. The high Reynolds number at $Re = 100,000$ caused the separated shear layer to re-energize and undergo transition to turbulence, causing the flow to reattach to the blade surface. The CFD predicted the flow to be reattached before the 95% axial chord location, while the experiments showed turbulent flow reattachment to occur upstream at approximately the 90% axial chord location. For the $Re = 50,000$ case, (Fig. 5.3(b)) the velocity profile at the 73% axial chord location in the CFD prediction was in good agreement with the experimental results [39] at both inlet turbulent length scales. The size of the separation region was slightly over-predicted for the CFD results at the 84.8% axial chord location with the $l_m = 5mm$ case having a larger separation region. Both inlet length scale results showed the presence of a recirculation region at 84.8% axial chord location while the experimental results showed the flow remained separated. At the 95% axial chord location, the boundary layer reattached to the blade surface for the $l_m = 50mm$ case, where the $l_m = 5mm$ case flow remained separated. The experimental result showed a recirculation region had formed at the 95% axial chord location.

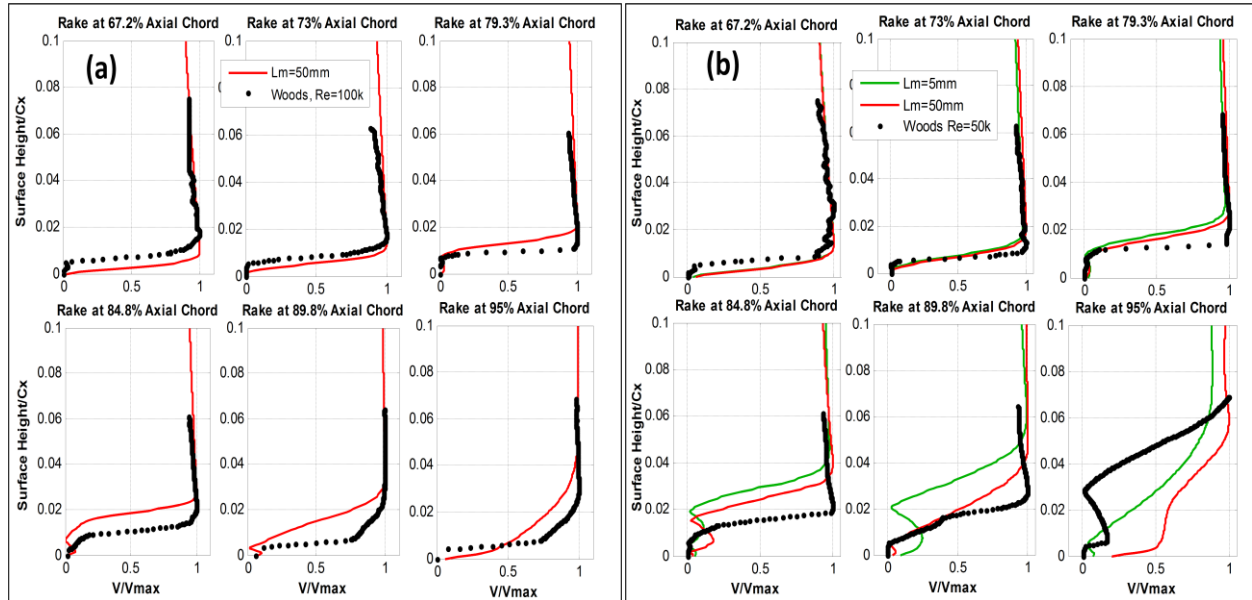


Figure 5.3. Comparison of the boundary layer velocity profiles at inlet Reynolds numbers of a) 100,000 and b) 50,000 with the experimental results [39] for the Highly Loaded blade airfoil

Figure 5.4 shows the $Re = 25,000$ case where the shape of velocity profiles were in good agreement with experimental results [39] at the 73% axial chord location for both inlet turbulent length scales. Downstream of those locations, the CFD predicted a larger separation region than the experimental results [39]. The time-averaged behavior of the recirculation region caused by the separation bubble was shown to be similar for both the CFD and experimental results. Figure 5.4 shows that the separated flow region decreased when the inlet turbulent length scale was decreased to 5mm. The opposite trend was observed for the $Re = 50,000$ when the inlet turbulent length scale was decreased to 5mm. The CFD results did follow the same trend as the experimental results [39] in that the separation grew as the Reynolds number was decreased. There were differences in the boundary layer behavior of the separation region compared to the experimental results [39]. The effect of neglecting the spanwise dimension was found not to be the reason for the discrepancy, which will be discussed in Section 5.2. The $k-k_L-\omega$ transitional flow model demonstrated that it can show a qualitative response to separated boundary layers.

Chapter 5. The Highly Loaded Blade CFD Results

There were differences using the $k-k_L-\omega$ transitional model in the prediction of the size of the separation region for all Reynolds number cases. It is noted that the $k-k_L-\omega$ flow model was not specifically designed to model boundary layer transition in separated shear layers [30]. It was intended to model attached transitional flows.

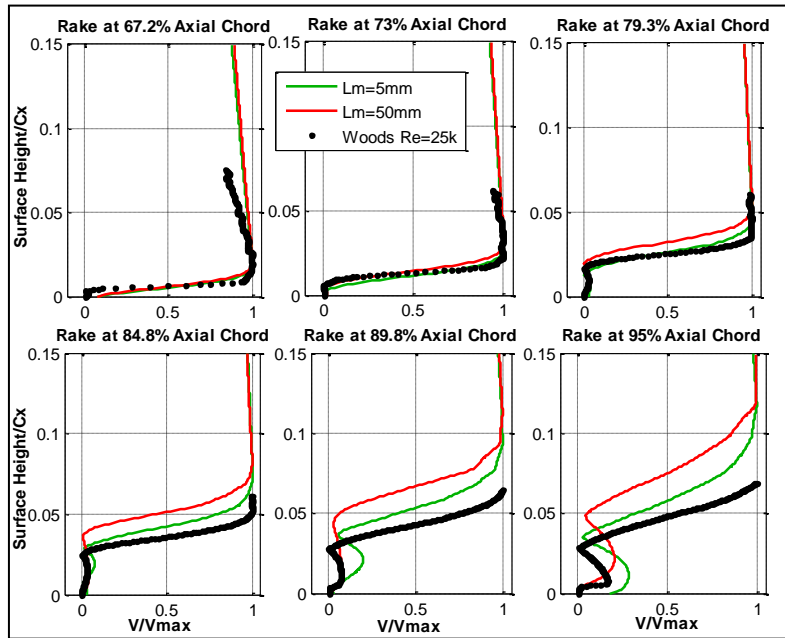


Figure 5.4. Comparison of the mean boundary layer velocity profiles at 25,000 with the experimental results [39] for the Highly Loaded blade airfoil

5.1.3 Unsteady Features of the Flowfield

The features of the unsteady flowfield were investigated to gain insight on the behavior of the unsteady flow separation and vortex generation. Instantaneous “snapshots” of the predicted flowfield were taken for all three Reynolds number simulations. For the $Re = 100,000$ case, a total of 44,700 time-steps or 0.223sec were utilized for averaging of mean-flow quantities with a flow time-step of $5\mu\text{sec}$. The flow-time, which is described as the time interval it takes for the simulated fluid flow to travel from the inlet to the exit CFD domain, was 0.0654sec. The mean-flow averaging time-interval was calculated with Eq. (5.1)

Chapter 5. The Highly Loaded Blade CFD Results

$$\text{flow - time interval} = \frac{\text{mean - flow averaging time interval}}{\text{flow - time}} \quad (5.1)$$

was 3.41 flow-time intervals. Upon investigation of the unsteady flow features, separation and reattachment were seen to occur at every time step as representatively indicated in Figure 5.5. The separated shear layer on the suction side produces two clockwise vortical structures that move downstream. These vortical structures break down and reduce in magnitude when the separated boundary layer becomes reattached to the blade surface.

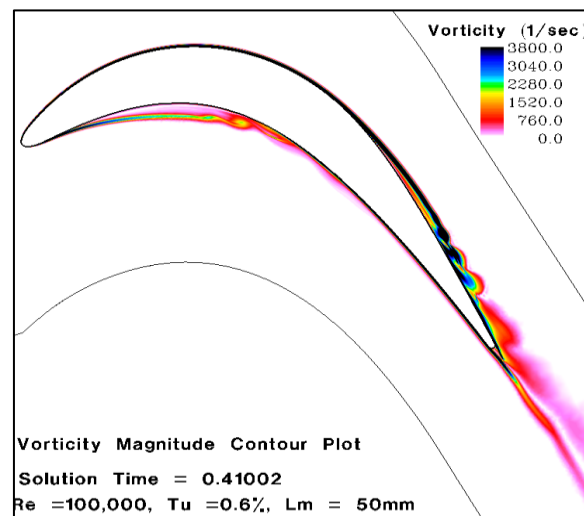


Figure 5.5. Instantaneous vorticity contour plot at $Re = 100,000$ for the Highly Loaded blade airfoil

The inlet turbulent length scale had a significant effect on the flow unsteadiness for the $Re = 50,000$ simulations. For the $l_m = 50mm$ case, a total of 70,000 time-steps or 0.07074sec were utilized for averaging of mean-flow quantities with a flow time-step of $1\mu\text{sec}$. The total flow-time was 0.131sec and mean flow-averaging was 0.54 flow-time intervals as calculated with Eq. (5.1). As in the $Re = 100,000$ case, the separated shear layer produced vortices on the blade suction side, but they were larger in size. Once the suction side vortex formed, it traveled downstream and rolled off the blade surface and into the freestream as shown in Figure 5.6(a)-(b). The boundary layer became reattached once the suction side vortex moved into the

Chapter 5. The Highly Loaded Blade CFD Results

freestream giving the boundary layer velocity profiles in Figure 5.3 its unique shape. For the $l_m = 5mm$ case, a total of 64,100 time-steps 0.1284sec or were used for averaging of mean-flow quantities with a flow time-step of $2\mu\text{sec}$ with 0.98 flow-time intervals. The suction side vortices created from the separated shear layer were larger compared to the $l_m = 50mm$ case and this was verified from the velocity profiles in Figure 5.3(b). Also there were smaller vortices created within the shear layer as shown in Figure 5.6(c)-(d). The suction side vortex exhibited the same behavior of forming and rolling off the blade surface as in the $l_m = 50mm$ case, but occurred slightly more downstream and closer to the blade trailing edge.

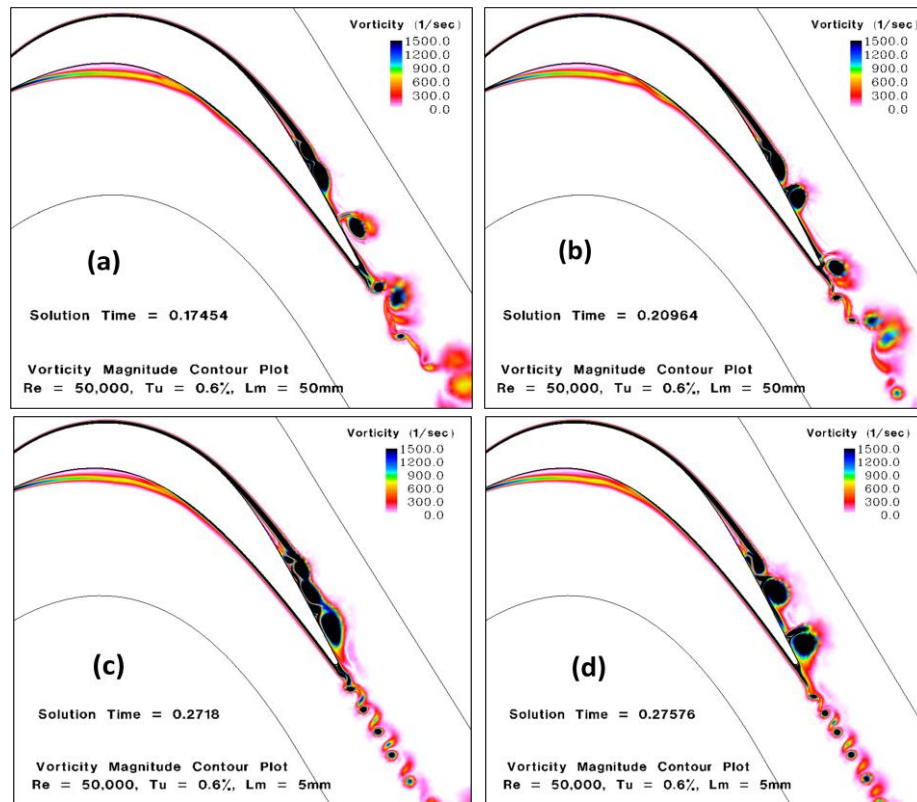


Figure 5.6. Instantaneous vorticity contours at $Re = 50,000$ for the Highly Loaded blade airfoil at $L_m = 50mm$ (a&b) and $L_m = 5mm$ (c&d)

The time signal of the drag coefficient was calculated by summing the dot product of the pressure and viscous forces with the force vector along the blade surface boundary as shown in Figure 5.7. A Fast-Fourier Transform (FFT) was performed to examine the frequency content

D. Sanders

Chapter 5. The Highly Loaded Blade CFD Results

present in the time signal of the drag coefficient. The frequency resolution (f_{resol}) was based on the time-step (t_{step}) and the averaging interval (N_{avg}) and calculated based on the equation

$$f_{resol} = \frac{1}{t_{step}(N_{avg})} \quad (5.2)$$

The frequency resolution was 8Hz and 14Hz for the $l_m = 5mm$ and $l_m = 50mm$ cases, respectively. The dominant frequencies present in the FFT calculation originated from the vortex generation on the pressure and the suction side caused by the separated shear layers. Also, Figure 5.7(c)-(d) and Figure 5.9(c)-(d) shows the shedding frequency for each vortical structure for the $Re = 50,000$ and $25,000$ cases, respectively. Table 5.1 shows the comparison of the separation location, shedding frequencies, and Strouhal number based on Eq. (4.1) for both inlet turbulent length scales. The shedding frequency and Strouhal number was higher for the $l_m=50mm$ case due to the lower specific dissipation rate while the separation point was approximately the same for both inlet turbulent length scales.

Chapter 5. The Highly Loaded Blade CFD Results

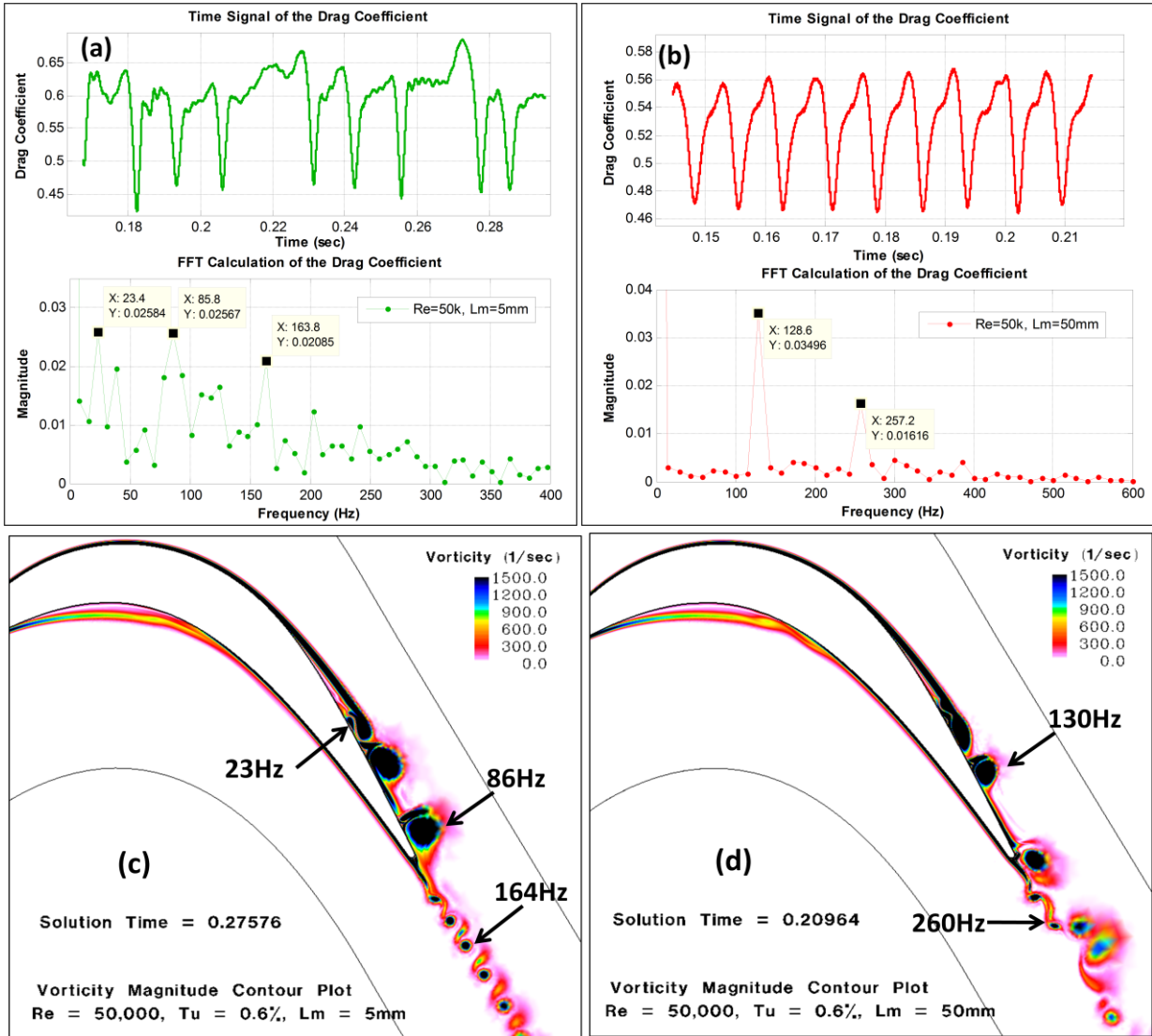


Figure 5.7. Time signal, FFT calculation of the drag coefficient, instantaneous vorticity contours at $Re = 50,000$ for the Highly Loaded blade airfoil at $L_m = 5mm$ (a) & (c) and $L_m = 50mm$ (b) & (d)

In Figure 5.8(a)-(b), the unsteady nature of the $Re = 25,000, l_m = 50mm$ case is shown. The flow time-step was $10\mu sec$ and 43,000 time-steps or 0.4297sec was completed for mean flow averaging. The total flow-time was 0.262sec and mean flow-averaging was 1.64 flow-time intervals. The separated shear layer on the suction side produced a clockwise vortex, while the pressure side shear layer produced a counterclockwise vortex that moved from the trailing edge to the wake region. The decrease in length scale to $5mm$ caused the opposite effect as the $Re = 50,000$ case where the separation region decreased when the turbulent length scale decreased as

D. Sanders

Chapter 5. The Highly Loaded Blade CFD Results

shown in Figure 5.8(c)-(d). Also, the vortex shedding frequencies on pressure and suction side remained unchanged unlike the $Re = 50,000$ case (Fig. 5.9). This could be due to the separation region in the $Re = 25,000$ cases being significantly larger than the $Re = 50,000$ cases. The suction side vortex was formed above the blade surface and became insensitive to changes in the inlet turbulent length scale. The same trend was found for the inlet $Re = 25,000$ and $50,000$ cases in which decreasing the turbulent length scale caused the separation location to occur slightly more downstream as indicated in Table 5.1.

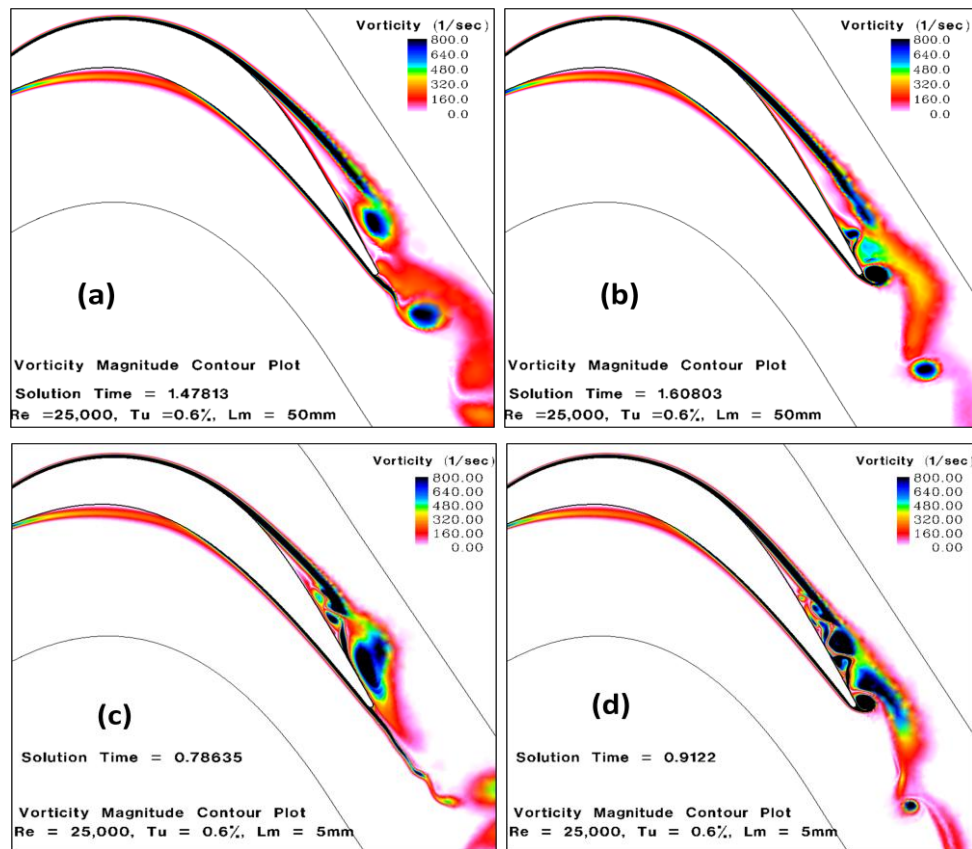


Figure 5.8. Instantaneous Vorticity Contours at $Re = 25,000$ for the Highly Loaded Blade Airfoil at $L_m = 50mm$ (a&b) and $L_m = 5mm$ (c&d)

Chapter 5. The Highly Loaded Blade CFD Results

Re	$l_m(mm)$	X_{sep}/C_x	Pressure Side		Suction Side			
			f_{shed}	St	f_{shed}	St	f_{shed}	St
25,000	5	0.709	45	0.0045	10	0.0010	20	0.0020
25,000	50	0.722	45	0.0045	12	0.0012	20	0.0020
50,000	5	0.717	164	0.0050	23	0.00070	86	0.0026
50,000	50	0.726	260	0.0082	130	0.0041	-	-
100,000	50	0.713	-	-	-	-	-	-

Table 5.1. Summary of the separation location and Strouhal number for the Highly Loaded blade airfoil

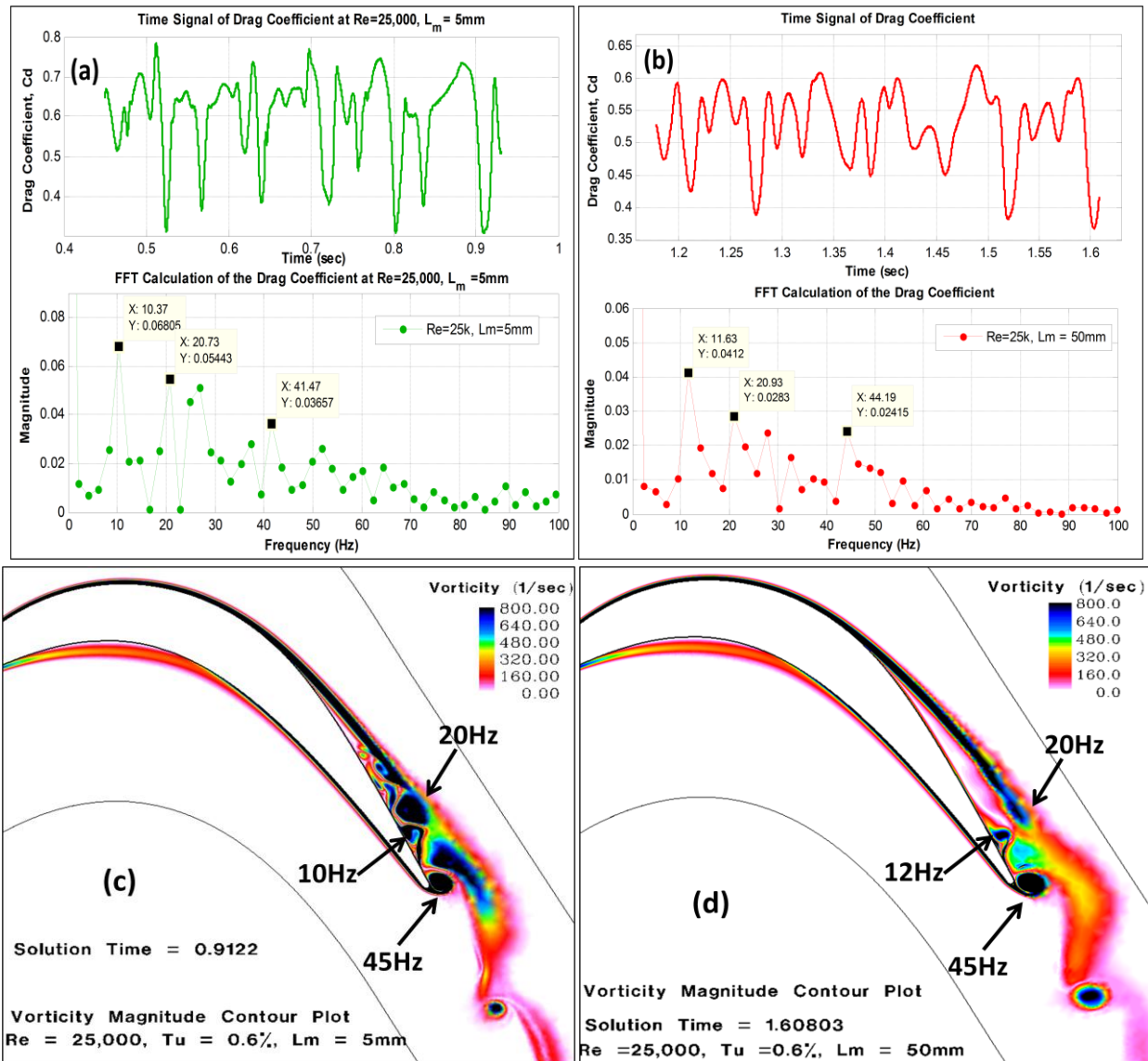


Figure 5.9. Time signal, FFT calculation of the drag coefficient, instantaneous vorticity contours at $Re = 25,000$ for the Highly Loaded blade airfoil at $l_m = 5mm$ (a) & (c) and $l_m = 50mm$ (b) & (d)

Chapter 5. The Highly Loaded Blade CFD Results

5.1.4 Total Pressure Loss Coefficient Predictions

The total pressure loss coefficient predictions using the $k-k_L-\omega$ transitional model for all three Reynolds number simulations are shown in Figure 5.10. The CFD results are compared to experimental wake measurements taken by Garmoe [36] and Casey [40] for a total of two pitch lengths. The major difference in the experimental measurements at $Re = 100,000$ (Fig. 5.10(a)) was in the average inlet turbulence intensity, which was reported as 0.785% for the Garmoe [36] measurements and 0.437% for the Casey [40] measurements. For the $Re = 100,000$ case, the CFD results under-predicted the loss coefficient, with 88% and 60% percent agreement with the Garmoe [36] and Casey [40] measurements, respectively. It was expected that the CFD prediction would lie between the two experimental results since the computational inlet turbulence intensity was 0.6%. The reason for the under-prediction was due to the turbulent boundary layer reattachment point being located further downstream on the blade than the experimental measurements, resulting in a lower predicted momentum loss than experimentally measured. Table 5.2 showed a 62% and 72% agreement in the integrated loss coefficient comparisons with Garmoe [36] and Casey [40] experimental results, respectively due to differences in the width of wake region and the maximum value of the loss coefficient.

The total pressure loss coefficient prediction at $Re = 50,000$ (Fig. 5.10(b)) was found to have good agreement with respect to both Casey's [40] measurement made at an inlet Reynolds number of 45,000 and inlet turbulence intensity of 0.34%, and Garmoe's [36] measurement at $Re = 50,000$ with a turbulence intensity of 0.84%. Changing the inlet turbulent length scale was observed to have no effect on the peak loss coefficient predictions. Both CFD results were with 93% agreement with experimental results [36, 40] on the peak value of the loss coefficient. A length scale effect was observed in the integrated loss coefficient with the $l_m = 5\text{mm}$ case having

Chapter 5. The Highly Loaded Blade CFD Results

the largest value. The higher dissipation rate caused the wake width to increase across the pitch length thus increasing the integrated loss coefficient. Comparison with the experimental results indicated a 60% and 68% agreement for the $l_m = 50\text{mm}$ and $l_m = 5\text{mm}$ cases, respectively which was attributed to the width of the wake region being larger in the experimental results.

For the $Re = 25,000$ cases, (Fig. 5.10(c)) the size of the separation region was over-predicted by the CFD, yet the total pressure loss predictions were lower than both experimental results. The decrease in the inlet turbulent length scale caused the wake region to spread and further decrease the maximum value to the loss coefficient. A similar trend was observed in the $Re = 50,000$ case. The increase in specific dissipation rate, which resulted from lowering inlet turbulent length scale, increased the width of the wake instead of transferring the turbulent flow being generated from the boundary layer to viscous losses at a higher rate which should have caused an increase in the loss coefficient predictions. Better agreement with the experimental results of integrated loss coefficient was achieved with an 84% and 79% agreement with Garmoe [36] and Casey [40], respectively. Also, the CFD prediction of the integrated loss coefficient was independent of changes in inlet turbulent length scale which indicated the amount of viscous losses generated in the wake region was similar in both CFD cases. This confirmed the previous observation that a higher inlet length scale caused only the width of wake region to increase and did not affect the peak value of the loss coefficient.

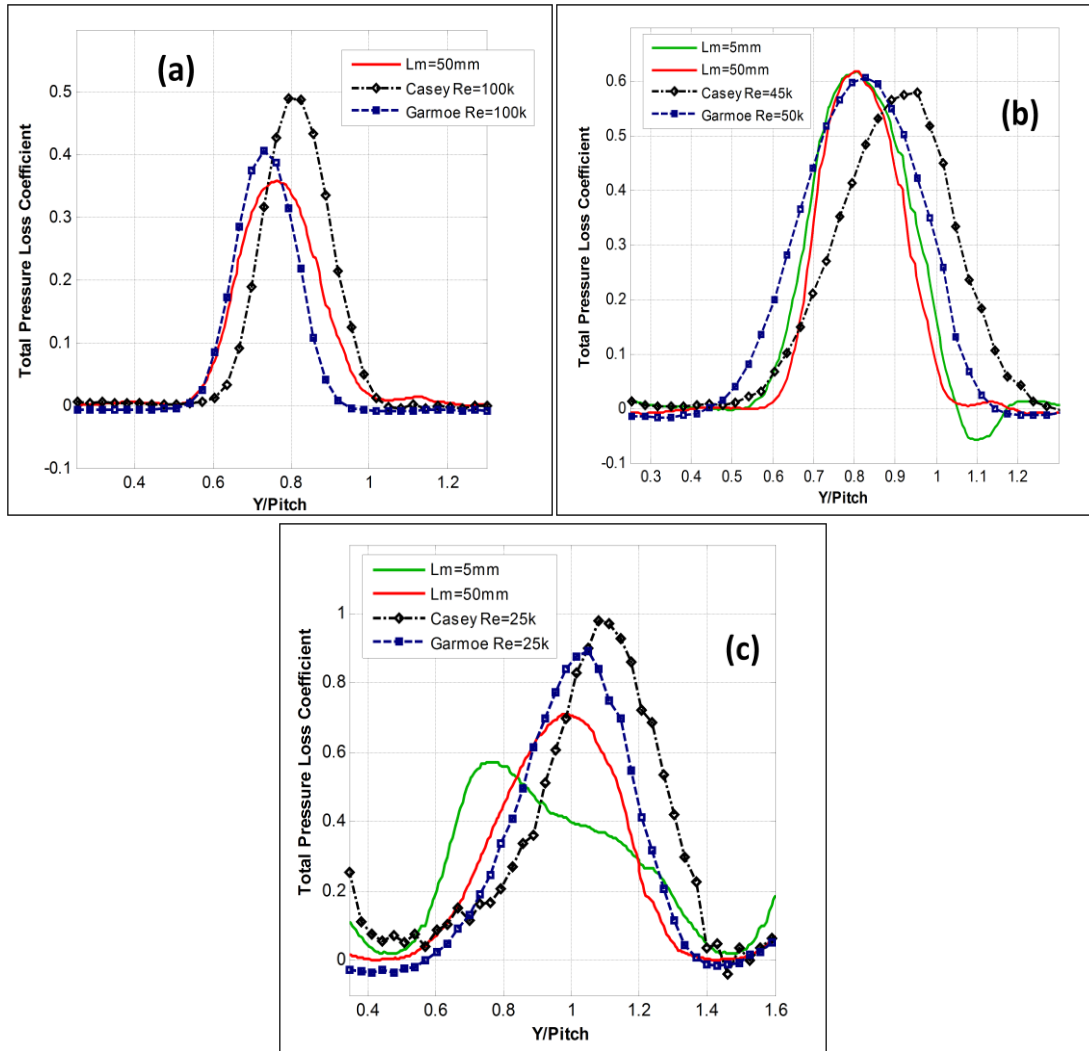


Figure 5.10. Comparison of total pressure loss coefficient with experimental [36,40] results at inlet Reynolds numbers of (a) 100,000, (b) 50,000, and (c) 25,000 for the Highly Loaded blade airfoil

Re	$l_m(mm)$	Integrated Total Pressure Loss Coefficient		
		CFD	Garmoe [36]	Casey [40]
25,000	5	0.3045	0.3562	0.3808
	50	0.3018		
50,000	5	0.1708	0.2472	0.2494
	50	0.1490		
100,000	50	0.0896	0.06535	0.1242

Table 5.2. Integrated total pressure loss coefficient comparison with the experimental [36, 40] results for the Highly Loaded blade airfoil

5.2 Three-Dimensional CFD Comparisons with Experimental Results

An unsteady simulation was completed using the three-dimensional cascade CFD model of the Highly Loaded blade airfoil presented in Section 4.3.1 at inlet Reynolds number of 25,000. The main goal was to determine the effect of the added spanwise dimension on the flowfield predictions using the $k-k_L-\omega$ model. The inlet turbulence intensity was set to $Tu = 0.6\%$ with an inlet turbulent length scale at $l_m = 50\text{mm}$. The flowfield of the three-dimensional simulation was compared to the two-dimensional CFD results completed at same inlet conditions and experimental results. Spanwise-averaged surface static pressure coefficient, boundary layer velocity profiles, and the wake total pressure loss coefficient were used for comparisons. Also, the unsteady features of separation and vortex shedding were investigated qualitatively.

5.2.1 Surface Static Pressure Coefficient

Figure 5.11 compares the blade surface static pressure coefficient of both the two and three-dimensional simulations using the $k-k_L-\omega$ model to the measurements of Bons *et al.* [38] and three-dimensional LES results of Rizzetta and Visbal [45]. A similar distribution of the suction side blade loading was observed for both the two and three-dimensional results to the 90% axial chord location. Downstream of that location, the three-dimensional results showed a larger increase in the local pressure peak due to the motion of shed vortices compared to the two-dimensional result. The mean-flow averaging time interval in the three-dimensional prediction was 14.6 times smaller compared to the two-dimensional prediction. This caused an increase in the effect that the intermittent vortex shedding had on the static pressure distribution. The LES results from Rizzetta and Visbal [45] predicted separation and turbulent reattachment for $Re = 25,000$ while the experimental [38] results show separation to the trailing edge. This indicated the addition of the spanwise dimension did not have significant effect on the blade loading and

the two-dimensional result provided adequate prediction of the surface static pressure coefficient for the Highly Loaded blade airfoil.

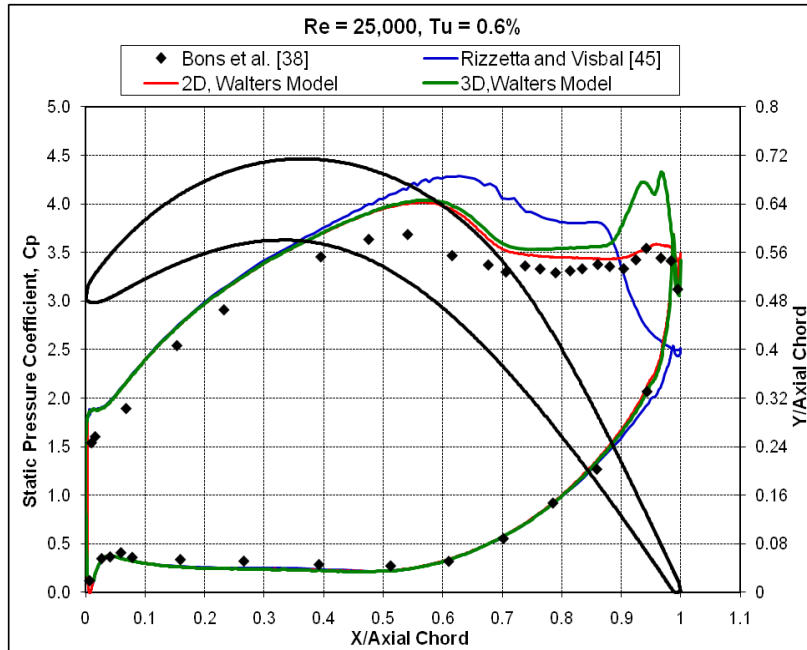


Figure 5.11. Dimensional comparison of surface static pressure coefficient with 3D LES [45] simulations and experimental results [38] at inlet Reynolds numbers of 25,000 for the Highly Loaded blade airfoil

5.2.2 Mean Velocity Boundary Layer Profiles

The spanwise-averaged boundary layer profiles of the mean velocity obtained from the three-dimensional simulation were compared to the two-dimensional $k-k_L-\omega$ model prediction and experimental [39] results at the same axial chord locations. Figure 5.12 shows the three-dimensional predictions were in good agreement with the experimental results to the 79.3% axial chord location. Downstream of those locations, the three-dimensional result predicted a slightly smaller separation region compared the two-dimensional results, but showed a larger separation region than the experimental results [39]. The shape of boundary layer profiles starting at the 84.8% axial chord location in the three-dimensional prediction was due to the spanwise averaging. The suction surface separation point was located at 71.2% axial chord location

similar to the 72.2% separation location in the two-dimensional simulation. The added spanwise dimension did produce a slightly smaller separation region as reported in Rizzetta *et al.* [45] thus provided somewhat better agreement with the experimental result.

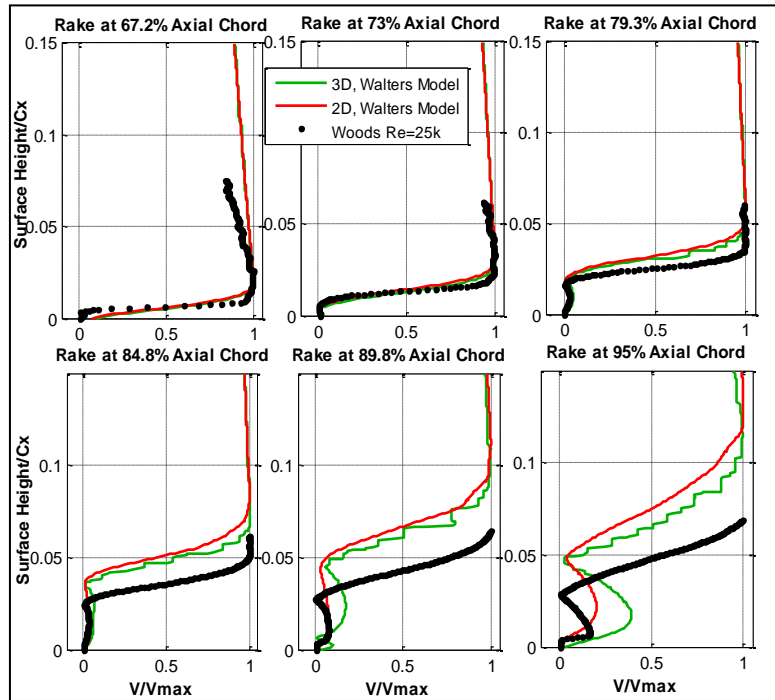


Figure 5.12. Two and three-dimensional comparisons of the mean boundary layer velocity profiles at 25,000 with the experimental results [39] for the Highly Loaded blade airfoil

5.2.3 Unsteady Features of the Flowfield

The features of the unsteady flowfield have been investigated for the three-dimensional simulation of the Highly Loaded blade in order to compare with the unsteady flowfield predictions from the two-dimensional results. Instantaneous contours of the vorticity magnitude at mid-span location (0.01778m) were compared to the two-dimensional result as shown in Figure 5.13. A total of 5898 time-steps (0.113 flow-time intervals or 0.02949sec) were utilized for averaging of mean-flow quantities with a flow time-step of $5\mu\text{sec}$ which was significantly smaller time interval compared to the two-dimensional simulation. Unsteady averaging of the flowfield for a large number of time-steps using the three-dimensional Highly Loaded blade

D. Sanders

Chapter 5. The Highly Loaded Blade CFD Results

CFD model could not be made because of the large amount of processors and long simulation times required. The current flow-averaging interval was considered adequate to show the three-dimensional unsteady effects due to vortex shedding. Figure 5.13 shows that similar unsteady effects were seen in both the two and three-dimensional results. The separated shear layer produced a large clockwise vortex (Fig 5.13(a) &(c)) and a smaller counter-clockwise vortex seen in the two and three-dimensional result in Figure 5.13(b) and 5.13(c), respectively. Also, a counter-clockwise vortex was produced from the pressure side at the blade trailing edge (Fig 5.13(b) &(d)).

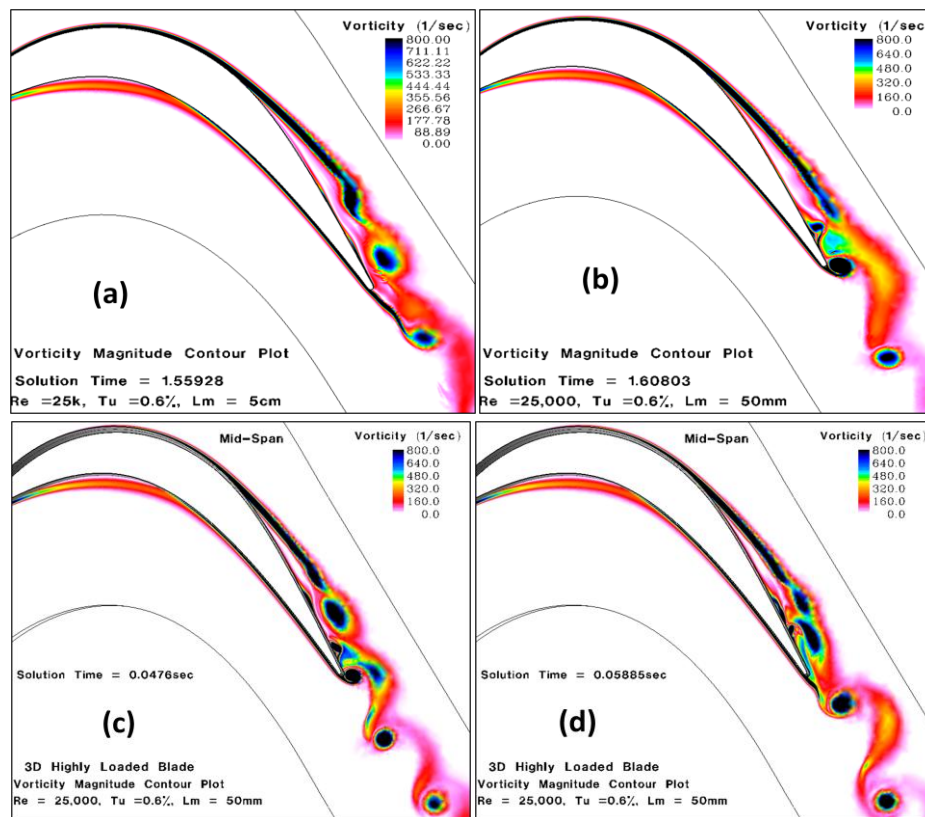


Figure 5.13. Comparison of the instantaneous vorticity contours at $Re = 25,000$, $Tu = 0.5\%$ for the (a)-(b) 2-D and (c)-(d) 3-D simulations of the Highly Loaded blade airfoil

Iso-surfaces of the vorticity were made to show the three-dimensional structure of the vortices shed from the separated shear layers. Figure 5.14 shows iso-surfaces of constant

Chapter 5. The Highly Loaded Blade CFD Results

vorticity of 800, 600, 400, and 150 sec^{-1} in the separated flow region. The vortices shed from the pressure and suction surfaces were largely two-dimensional in shape as shown in Figure 5.14(a)-(c). Also, there were small three-dimensional vortical structures present in the separation and wake region (Fig 5.14(d)) that broke-up in the spanwise direction. The vortical flow structure was largely laminar and the two-dimensional simulation was effective in predicting the shape of the unsteady vortices at the $\text{Re} = 25,000$ for the Highly Loaded blade.

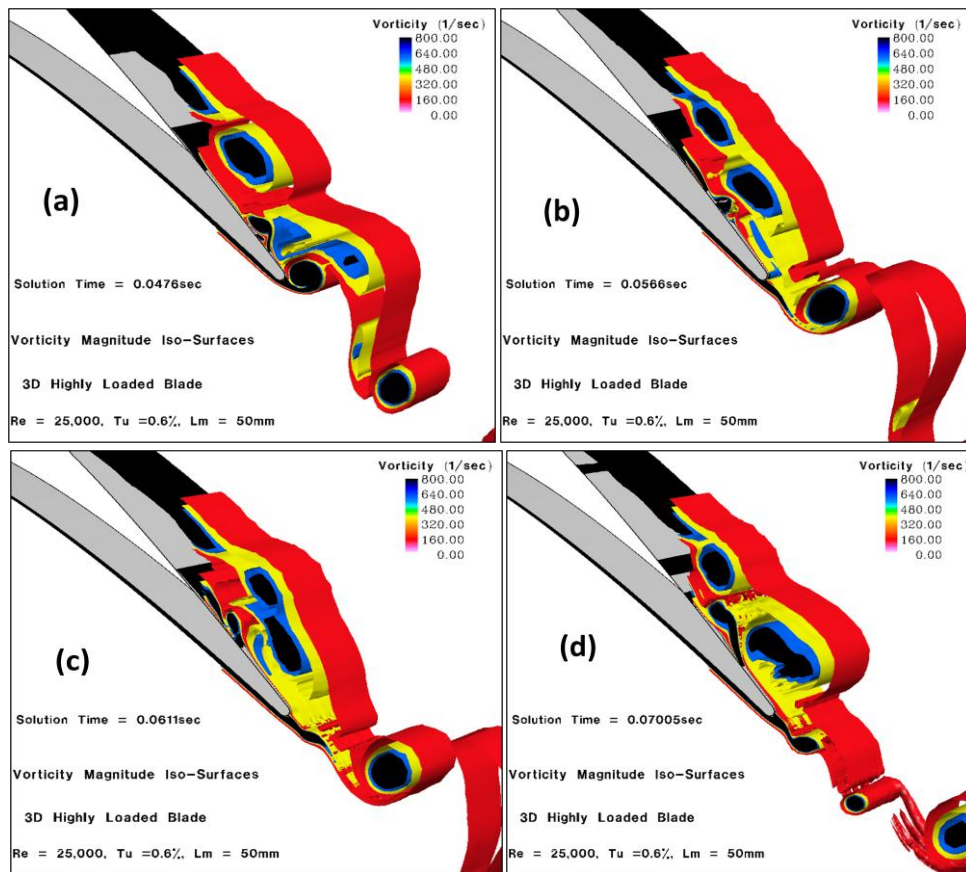


Figure 5.14. Iso-surfaces of instantaneous vorticity for the 3-D simulation of the Highly Loaded blade airfoil at $\text{Re} = 25,000$, $Tu = 0.5\%$

Similar results were obtained in a LES study by Visbal [47] on an oscillating SD7003 airfoil at low inlet Reynolds numbers. Figure 5.15 shows the comparison of the instantaneous spanwise vorticity for two and three-dimensional simulations at Reynolds numbers of 10,000 and

Chapter 5. The Highly Loaded Blade CFD Results

40,000. At $Re = 10,000$, the two and three-dimensional results were in good agreement with each other over a significant portion of the airfoil as shown in 5.15(a)-(b). The vortices were mostly two-dimensional in shape with some three-dimensional effects due to spanwise breakdown from transitional flow effects [47] (Fig. 5.15(b)). At $Re = 40,000$, significant differences were observed between two and three-dimensional results (Fig. 5.15(c)-(d)). The coherent vortices observed from the two-dimensional simulations breakdown in the spanwise direction into small-scale structures. The higher Reynolds number caused the increase in the spanwise breakdown in vortices due transitional flow effects.

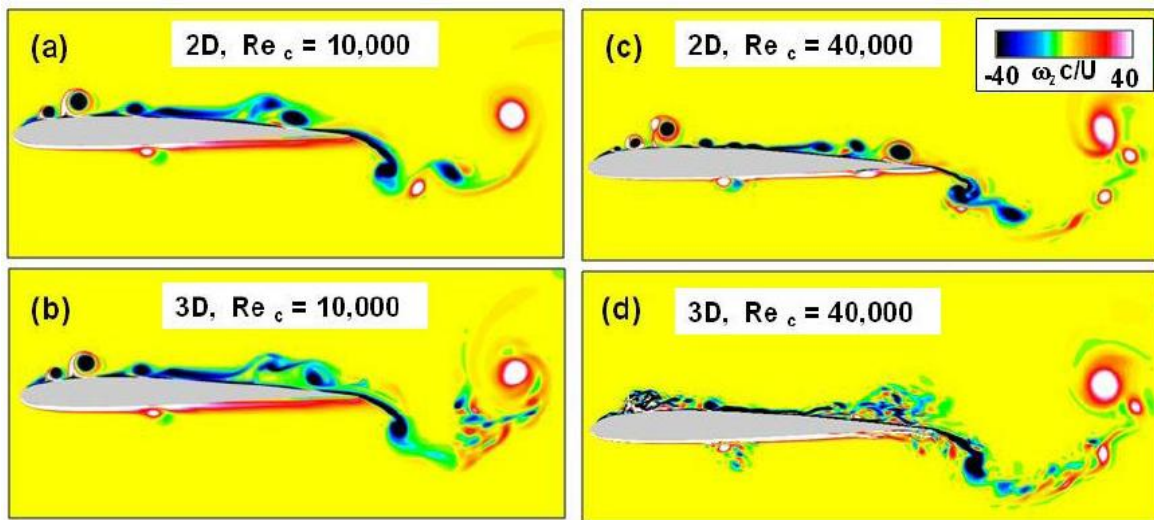


Figure 5.15. Comparisons of instantaneous spanwise vorticity for 2-D and 3-D LES simulation by Visbal [47]

The three-dimensional Highly Loaded blade CFD model was run at $Re = 25,000$, the midpoint between the Reynolds numbers simulated in the Visbal [47] LES results. As seen in Fig 5.15(c)-(d), vortical structures broke down in the spanwise direction. So, a larger amount of spanwise instabilities were expected to be present than shown at $Re = 10,000$ condition run by Visbal [47]. However, the Walters and Leylek [2] $k-k_L-\omega$ model is based on the RANS CFD method and modeled transitional flow due to only streamwise instabilities. Thus, the present

Chapter 5. The Highly Loaded Blade CFD Results

three-dimensional Highly Loaded blade CFD model will not be able to capture spanwise instabilities due to transitional flow. Based on this fact, the trends observed in comparing the two and three-dimensional simulations at $Re = 25,000$ for the Highly Loaded blade airfoil with the present model will be expected to be similar for simulations at higher inlet Reynolds numbers.

5.2.4 Total Pressure Loss Coefficient Predictions

The wake total pressure loss coefficient distribution and the integrated value are shown in Figure 5.16 and Table 5.3, respectively. The three-dimensional simulation indicated a 41% over-prediction in the peak loss coefficient with 87% agreement in the integrated loss coefficient compared to Casey's [40] experimental result. The two-dimensional predictions showed better comparison to Garmoe's [36] experimental result with a 29% under-prediction in the peak loss coefficient and 84% agreement with the integrated loss coefficient. The over-prediction and distribution in the loss coefficient was significantly different in the three-dimensional simulation due to the mean-flow-averaging time interval which was 14.6 times smaller than for the two-dimensional simulation. A longer mean-flow-averaging time interval would have resulted in a decrease in the effect that the intermittent vortex shedding had on the total pressure loss in the wake region. So, if the averaging interval of the three-dimensional simulation were increased, the loss coefficient would be reduced significantly. Good agreement was achieved in the prediction of the integrated loss coefficient indicating the amount of viscous loss generated from the vortex shedding was predicted sufficiently.

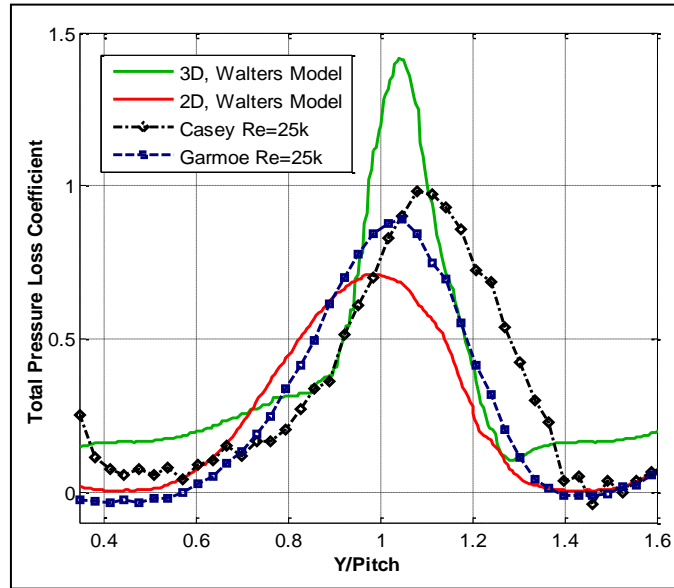


Figure 5.16. 2-D and 3-D comparison of total pressure loss coefficient with experimental [36,40] results at $Re = 25,000$ for the Highly Loaded blade airfoil

Re	CFD Model	Tu (%)	$l_m(mm)$	Integrated Total Pressure Loss Coefficient		
				CFD	Garmoe [36]	Casey [40]
25,000	2D	0.5	50	0.3018	0.3562	0.3808
	3D	0.5	50	0.4279		

Table 5.3. Dimensional comparison of the integrated total pressure loss coefficient with the experimental [36, 40] results for the Highly Loaded blade airfoil

5.3 Summary of Results

Flows over the Highly Loaded blade airfoil were simulated at inlet Reynolds numbers of 100,000, 50,000, and 25,000. The unsteady features of separation and vortex generation of the flowfield were qualitatively investigated. Boundary layer velocity profiles, surface static pressure distributions, and the wake total pressure loss coefficient were compared to the available experimental data. The CFD simulations showed good agreement with the experimental results in prediction of separation and reattachment. The $k-k_L-\omega$ transitional flow model showed a better qualitative response to separated shear layers as seen in the experimental measurements, but quantitative inaccuracies in the size of the separation region were observed.

Chapter 5. The Highly Loaded Blade CFD Results

Compared to the Lightly Loaded blade airfoil, the flowfield for the Highly Loaded blade airfoil was very complex involving unsteady separated shear layers. The separated flow is known to produce three-dimensional vortical structures, so a three-dimensional CFD model of the Highly Loaded blade was simulated at $Re = 25,000$ and compared to the two-dimensional CFD predictions. The addition of the spanwise dimension did not have significant effect on the blade loading and the surface static pressure coefficient distribution was similar to the two-dimensional result. The two and three-dimensional results were in good agreement with each other on the prediction of the separation region, but the three-dimensional result predicted a slightly smaller separation region. This produced closer agreement with the experimental [39] results but, the separation region was still over-predicted compared to the experiments. Investigations on the three-dimensional shape of the unsteady vortices showed the vortices shed were very coherent and largely two-dimensional in shape similar to the LES results by Visbal [47]. The $k-k_L-\omega$ model did not take into account transitional flow due to spanwise instabilities, so it does not capture the same effects like the more superior LES CFD method. The peak value of the loss coefficient was over-predicted compared to the experimental result because of the short averaging interval for the mean flow predictions. The three-dimensional result showed good agreement with the experimental result in the prediction of the amount of viscous loss generated within the wake region. This study provided an evaluation on how well the $k-k_L-\omega$ model captures the separation and unsteady characteristics observed in the Highly Loaded blade airfoil.

CHAPTER SIX

6. The Aft-Loaded L1A Blade CFD Results

The last blade geometry used for the investigation of Walters and Leylek's [2] $k-k_L-\omega$ transitional flow model was the Aft-Loaded L1A blade airfoil. The low Reynolds number aerodynamic effects of the Aft-Loaded L1A blade were the most challenging to predict because of very high loading level and strong adverse pressure gradient present on the aft portion of the suction surface. Two-dimensional flow simulations were completed at both high and low inlet turbulence levels and compared to experimental results of Marks *et al.* [35] and CFD results of Clark *et al.* [25]. Investigations of the unsteady flowfield were made at low and high inlet turbulent intensities. The inlet turbulent length scale was varied at the high inlet turbulence intensity to investigate its effect on the total pressure loss predictions. This study will serve as a baseline study for the flowfield comparisons with simulations completed using the Aft-Loaded L1A blade with upstream wake-generators CFD model.

6.1 CFD Predictions at Low Inlet Turbulence intensity

The performance of the two-dimensional cascade CFD model of Aft-Loaded L1A blade airfoil (Fig. 3.5(c)) was simulated at an inlet Reynolds number of 31,000 and 50,000. Unsteady simulations were run with an inlet freestream turbulence intensity of 0.5% for all inlet Reynolds numbers. The inlet turbulent length scale was set as $l_m = 50mm$ which was based on simulations of the Highly Loaded blade since updated length scale measurements were not available for the LSWT at low inlet turbulent intensities. The next sections present the comparisons of the static pressure coefficient, boundary layer profiles, and total pressure loss coefficient with the experimental measurements taken by Marks *et al.* [35] in the LSWT. Also comparisons were

D. Sanders 124

Chapter 6. The Aft-Loaded L1A Blade CFD Results

made with CFD result of Clark *et al.* [25] which used the Praisner and Clark [24] correlation based transitional flow model.

6.1.1 Surface Static Pressure Coefficient

In Figure 6.1, the mean static pressure coefficient distributions were compared to the measurements of Mark *et al.* [35] and the CFD results of Clark [25]. At the $Re = 50,000$ (Fig 6.1(a)), the $k-k_L-\omega$ model results showed good agreement with Clark's CFD result to the 55% suction surface axial location. The present CFD results predicted a lower peak pressure than Clark's CFD result but both predictions over-predicted the peak pressure compared to the experimental results. Downstream of the peak static pressure location, the $k-k_L-\omega$ model result predicted that the flow would separate at the 62.8% axial chord location. There was a large amount of unsteadiness present on the suction surface due to the vortical production from the separated shear layer. The local peak pressure coefficient at 82% axial chord location was due to the motion of the vortices as they lifted off the blade surface and traveled downstream to the wake region. The Clark CFD results predicted the separation point at approximately 68% axial chord which was more downstream than observed in both experimental and $k-k_L-\omega$ model results. The static pressure distribution downstream of the separation point of the Clark CFD results predicted flow separation and reattachment which indicated a closed separation bubble present on the suction surface. The experimental measurements were taken at inlet $Re = 60,000$, but all measurement at $Tu = 0.5\%$ indicated a separated non-reattaching boundary layer. The separation location was between 57% and 62% axial chord, which was in good agreement with the $k-k_L-\omega$ model results.

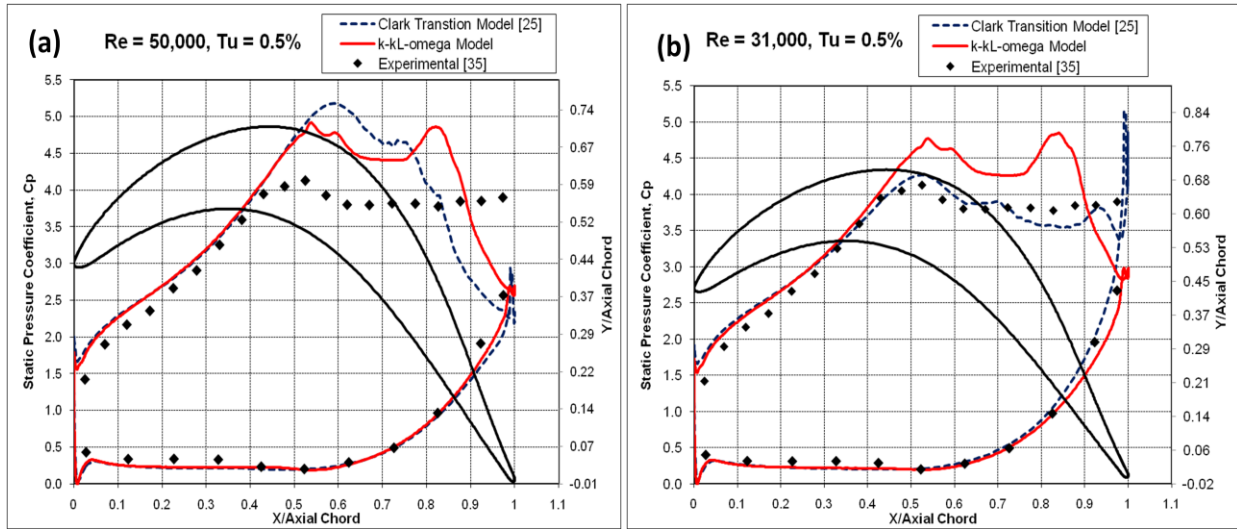


Figure 6.1. Comparison of surface static pressure coefficient with Clark *et al.* [25] simulations and experimental results [35] at inlet Reynolds numbers of a) 50,000 and b) 31,000, $Tu = 0.5\%$ for the Aft-Loaded L1A blade airfoil

A similar distribution of the static pressure coefficient was predicted with the $k-k_L-\omega$ model at $Re = 31,000$ as shown in Figure 6.1(b). The boundary layer separation location at 62.8% axial chord location was in good agreement with experimental ($Re = 40,000$) and Clark's CFD results of approximately 62% axial chord. The local pressure peak at the 82% axial chord location was due to the unsteady vortex shedding on the suction surface as observed in the $Re = 50,000$ case. Clark's CFD results showed the same local pressure peak located at the 95% axial chord, which was more downstream than the $k-k_L-\omega$ model result. The experimental results taken at inlet $Re = 40,000$ showed separated flow to the trailing edge. Yet, there was no evidence of the local pressure peaks within the separated flow region. This could be due to frequency response limitations or the time-averaging of the pressure transducers used in the experimental measurements. In summary, the $k-k_L-\omega$ transitional flow model was adequate in the prediction of the blade loading at low inlet turbulent intensities. Good agreement was achieved with the experimental result in the prediction of the separation location. The $k-k_L-\omega$

Chapter 6. The Aft-Loaded L1A Blade CFD Results

model demonstrated the ability to predict the static pressure distribution and the qualitative flow response to the separated shear layers observed in the Aft-Loaded L1A blade airfoil.

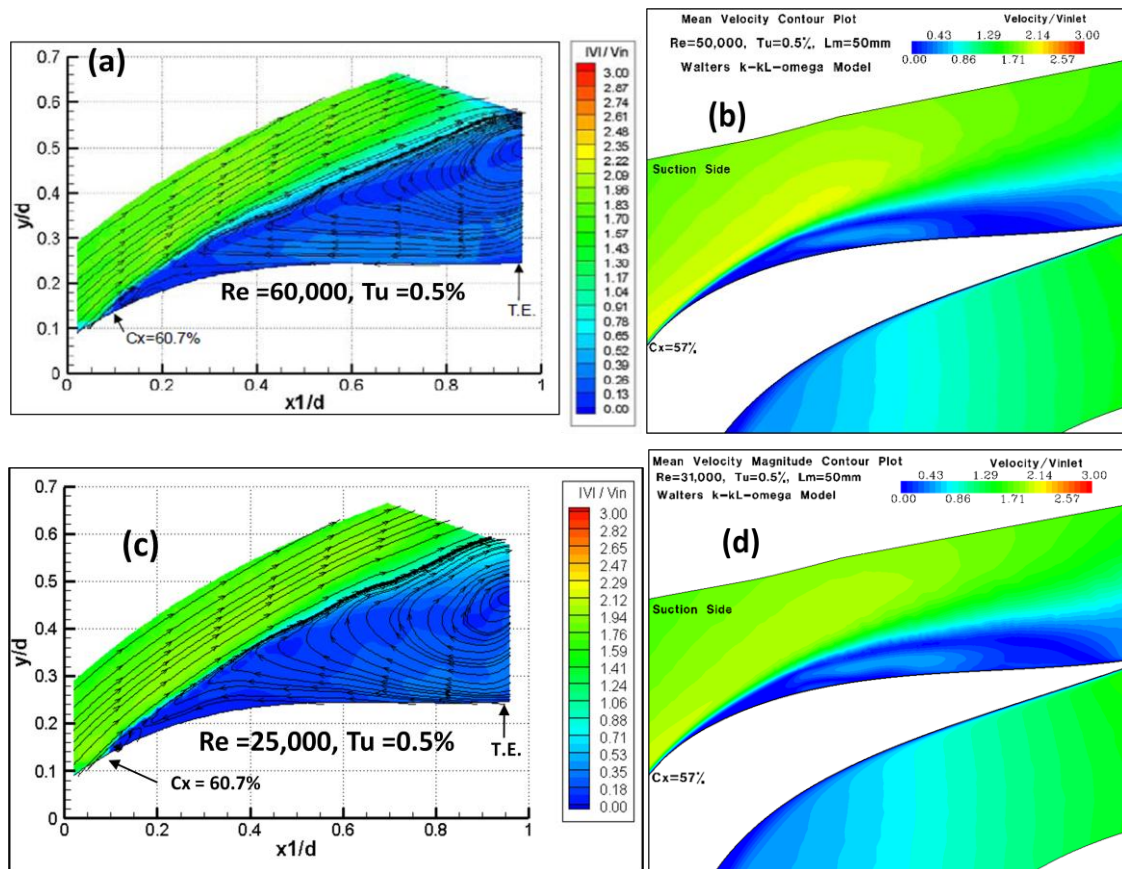


Figure 6.2. Mean velocity contours plots of the (a) PIV results at $Re=60,000$, (b) the CFD results at $Re = 50,000$, (c) PIV results at $Re = 25,000$, and (d) CFD results at $Re = 31,000$ for the Aft-Loaded L1A blade airfoil

6.1.2 Velocity Contours and Boundary Layer Profiles

Mean velocity magnitude contour plots from the CFD were compared to the PIV contour plots taken by Marks *et al.* [35] in Figure 6.2. The PIV results for the $Re = 50,000$ (Fig 6.2(a)) showed the flowfield on the suction surface of the blade starting at approximately the 50.0% to the 94% axial chord location, while the $Re = 25,000$ result showed from 57.0% to the 100% axial chord location. The CFD results were oriented in a similar manner to aid the comparisons. Both the CFD and experimental results indicated a significant amount of separated flow present on the

Chapter 6. The Aft-Loaded L1A Blade CFD Results

suction surface with the experimental result having a larger region of separated flow. The experimental separation region was also larger than the CFD for the $Re = 25,000$ shown in Figure 6.2(c)-(d). The behavior of the streamlines showed a recirculation region in the separated flow area at both inlet Reynolds numbers (Fig 6.2(a)&(c)).

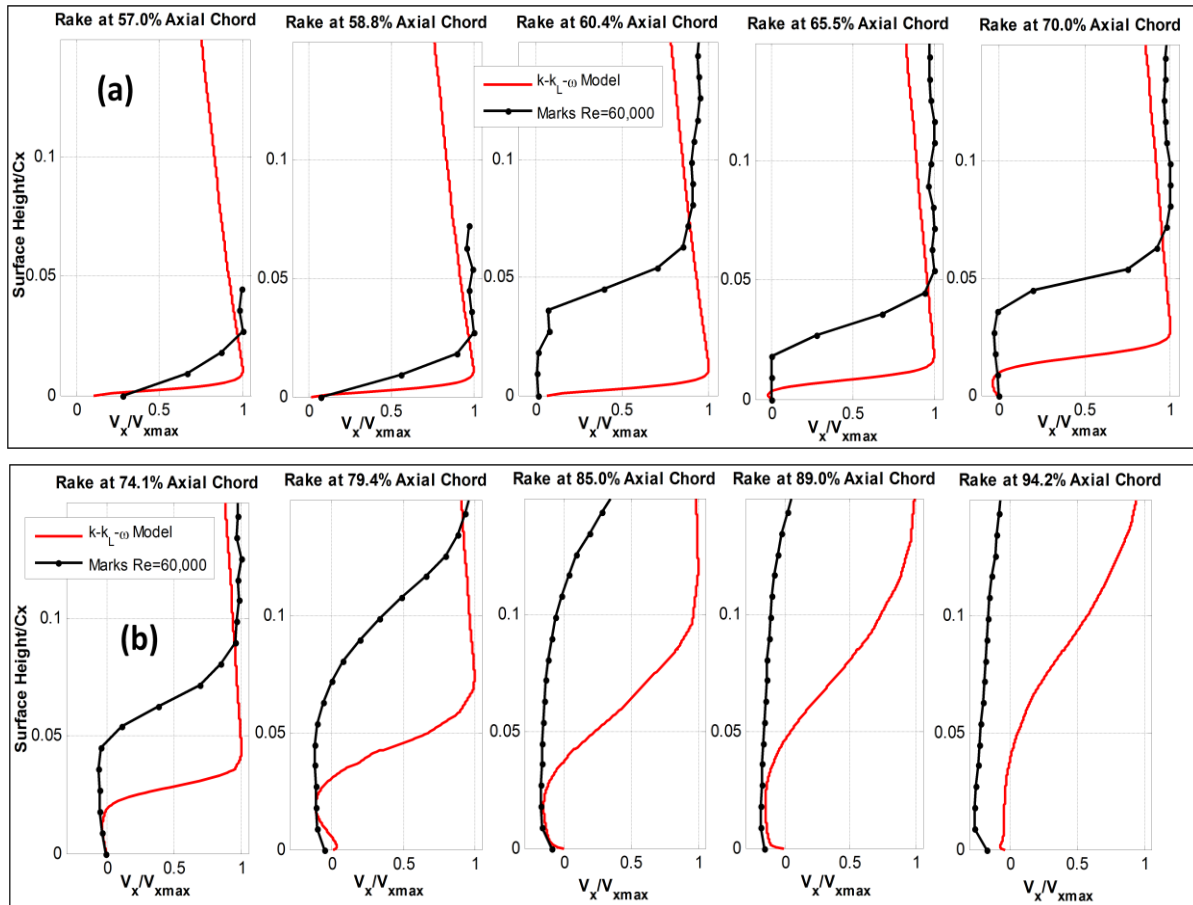


Figure 6.3. Comparison of the mean boundary layer profiles of axial velocity with experimental ($Re=60,000$) results [35] at inlet $Re = 50,000$ for the Aft-Loaded L1A blade airfoil

Time-averaged values of the boundary layer velocity profiles obtained at ten axial chord locations of 57%, 58.8%, 60.4%, 65.5%, 70%, 74.1%, 79.4%, 85%, 89.0%, and 94.2% normal to the blade surface from both the CFD and experimental PIV results. The axial component of the velocity was used in order to compare the amount of reversed flow present in the separation region. The separation point for the $Re = 50,000$ case was predicted to occur at the 62.8% axial

Chapter 6. The Aft-Loaded L1A Blade CFD Results

chord location, which was in 96% agreement with the experimental result at $Re = 60,000$. Figure 6.3(a) indicated the separation point at 58.8% and 60.4% axial chord location for the experimental results. The CFD under-predicted the separation region compared to the experimental results starting at the 60.4% axial chord location and continued for every downstream location (Fig. 6.3(a)-(b)). In Figure 6.4(a), the experimental result indicated the boundary layer separation point was located between the 58.8% and 60.4% axial chord location which was more upstream than the static pressure distribution indicated. The CFD predicted the separation point more downstream at the 64.4% axial chord location which is in 93% agreement with the experimental results. Similar trends were observed for the $Re = 50,000$ where the separation region was significantly under-predicted compared to experimental results (Fig 6.4(a)-(b)).

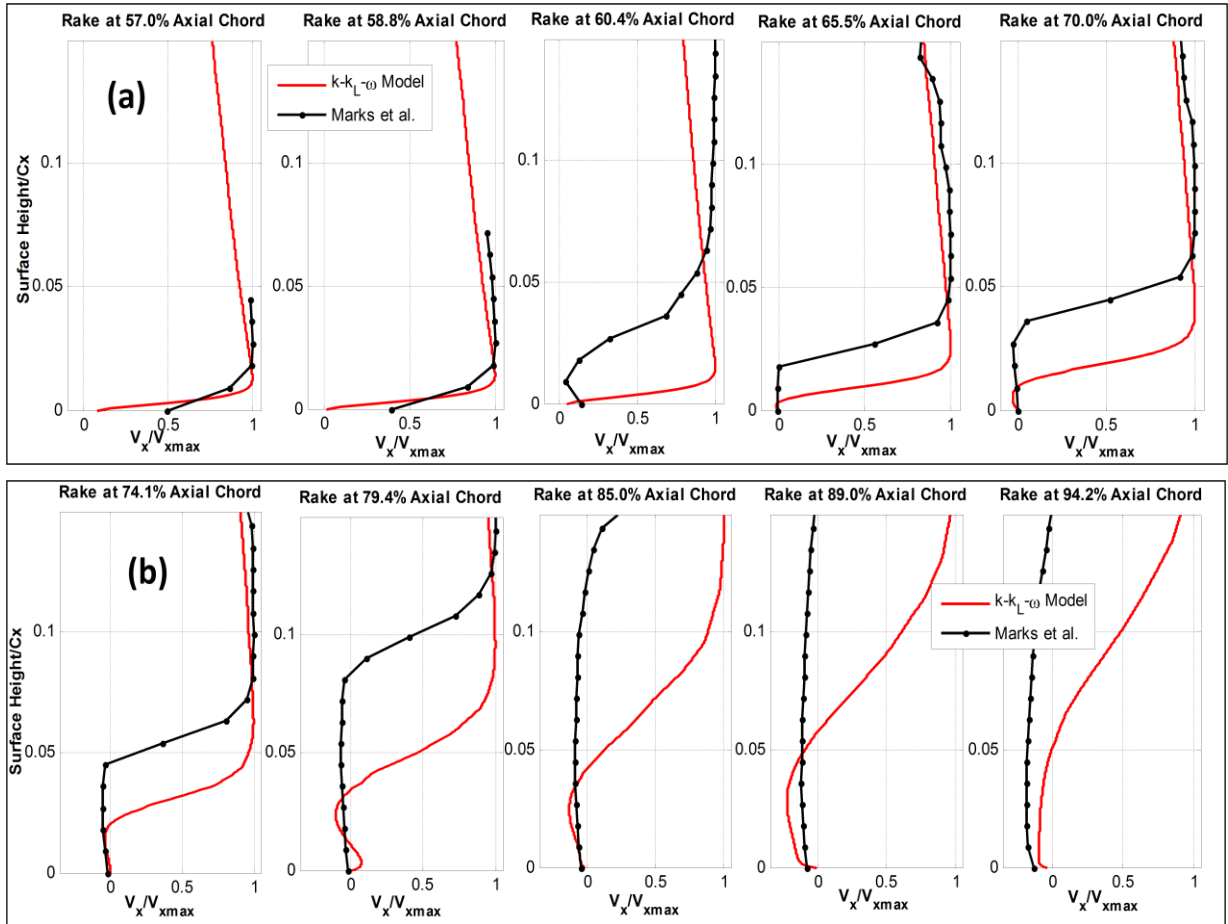


Figure 6.4. Comparison of the mean boundary layer profiles of axial velocity with experimental ($Re = 25,000$) results [35] at inlet $Re = 31,000$ for the Aft-Loaded L1A blade airfoil

6.1.3 Unsteady Features of the Flowfield

The unsteady features of the flowfield were investigated to understand the behavior of the flow separation and vortex generation. Instantaneous contour plots of vorticity were used to visualize the features of the flowfield. The flowfield was periodically repeated for two pitch lengths to aid the visualization of vortex shedding in the wake region. For the $Re = 50,000$ case, a total of 221,549 time-step or 0.425sec were used for averaging of mean flow quantities with a flow time step of $2 \mu\text{sec}$. The total flow-time was 0.181sec and mean flow-averaging was 2.35 of the flow-time interval calculated with Eq. (4.1). In Figure 6.6(a)-(b), the separated shear layer on blade suction surface consistently produced a clockwise vortex, while smaller counter-

Chapter 6. The Aft-Loaded L1A Blade CFD Results

clockwise vortices were present beneath the separated shear layer vortex. As the separated shear layer vortex traveled downstream, it disrupted the smaller vortices originally located beneath it and continued to move downstream into the wake region as shown in Figure 6.6(c)-(d). Once this vortex reached the wake region it began to dissipate rapidly across the pitch. Also, the pressure surface shear layer from the trailing edge produced small counter-clockwise vortices that moved downstream in the wake region (Fig 6.6(a)). The structure of the shear layer vortex was similar to the experimental flow visualization completed by Marks *et al.* [35] at $Re = 60,000$ shown in Figure 6.5(a). The suction side vortices in CFD predictions stayed near the blade surface whereas the experiment indicated the vortices moved into the freestream.

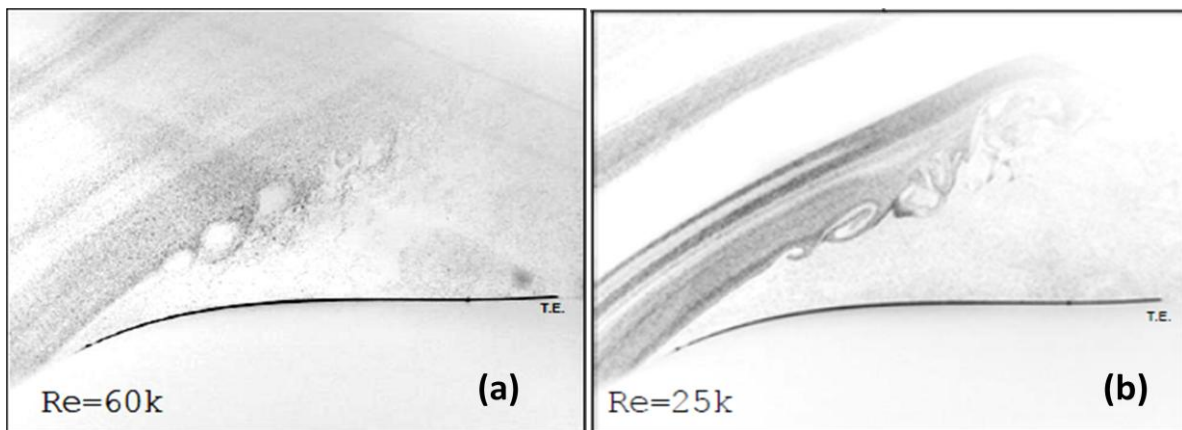


Figure 6.5. Instantaneous flow visualizations of Marks *et al.* [35] at (a) $Re = 60,000$ and (b) $25,000$, $Tu = 0.5\%$ for the Aft-Loaded L1A blade airfoil. Image view taken 52.5% axial chord location to the trailing edge.

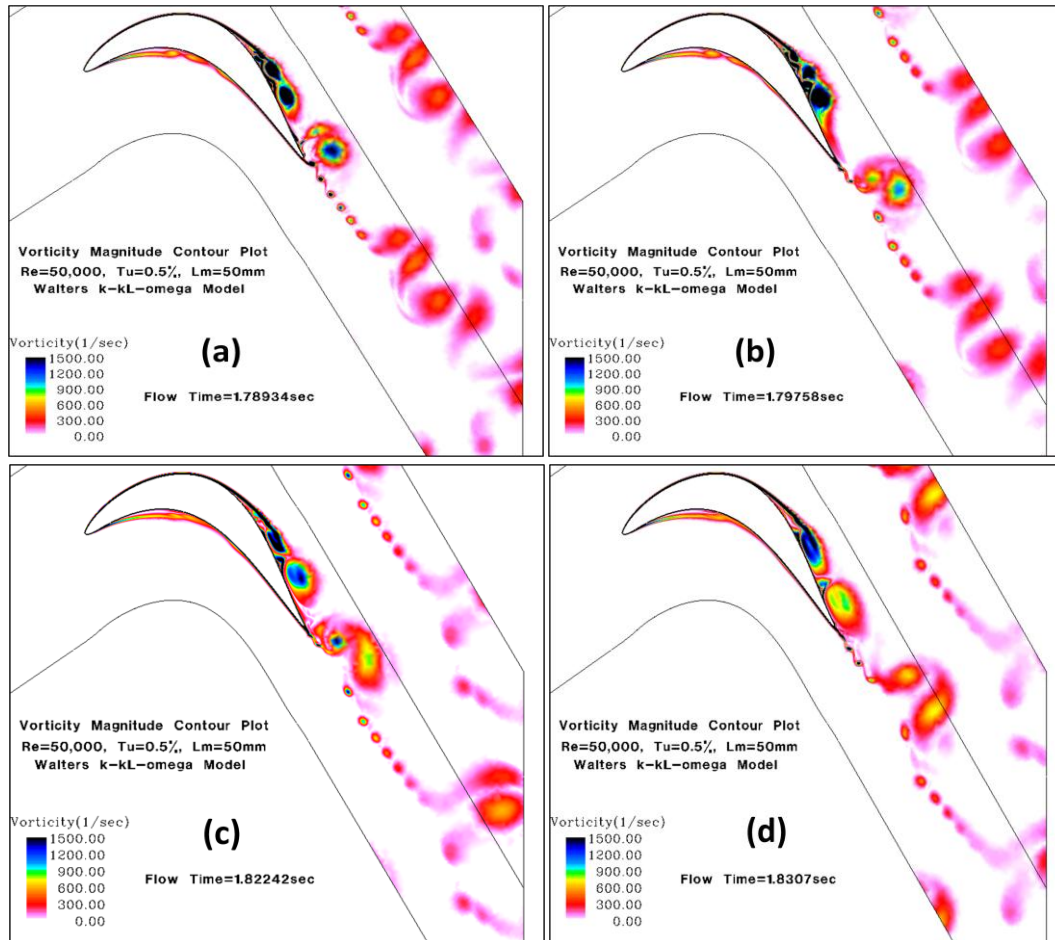


Figure 6.6. Instantaneous vorticity contours at $Re = 50,000$, $Tu = 0.5\%$, $L_m = 50\text{mm}$ for the Aft-Loaded L1A blade airfoil

In Figure 6.7(a)-(d), the flowfield unsteadiness of the $Re = 31,000$ case is shown. The flow time-step was $10\mu\text{sec}$ with 99,245 time-steps or 0.990sec being used for mean-flow averaging. The total flow-time was 0.292sec and mean flow-averaging was 3.39 of the flow-time interval. The suction side separated shear layer produced a clockwise vortex that was similar in size as the $Re = 50,000$ case. Also, the structure of the separated shear layer vortex was comparable to the experimental flow visualizations at $Re = 25,000$ in Figure 6.5(b). As in the $Re = 50,000$ case, there was a thin shear layer located directly beneath the separated shear layer vortex as it lifted off the blade surface. This thin shear layer separated from the blade surface and produced small counterclockwise vortices that interacted with the separated shear

D. Sanders

Chapter 6. The Aft-Loaded L1A Blade CFD Results

layer vortex and traveled downstream to the wake region. The trailing edge shear layer produced a small counterclockwise vortex that would periodically increase in size, roll up on the suction side near the trailing edge, and interact with the separated shear layer vortex. These vortices began to dissipate across the pitch length as they reached the wake region.

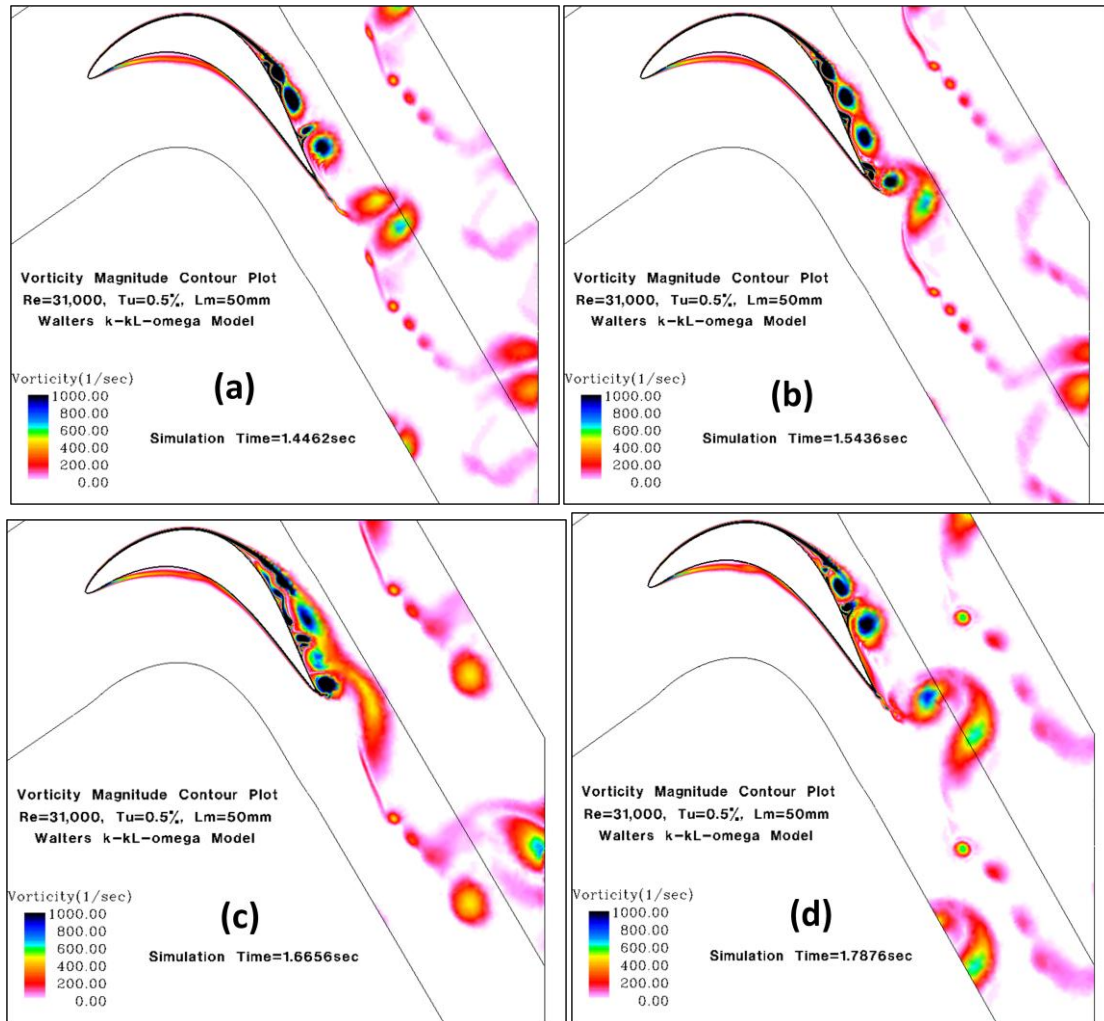


Figure 6.7. Instantaneous vorticity contours at $Re = 31,000$, $Tu = 0.5\%$, $L_m = 50mm$ for the Aft-Loaded L1A blade airfoil

The time signal and the FFT of the drag coefficient were calculated for the Aft-Loaded L1A blade for both Reynolds numbers at low turbulence intensity. The frequency resolution was 2Hz and 1Hz for the $Re = 50,000$ and $Re = 31,000$ cases, respectively. In Figure 6.8(a), there

Chapter 6. The Aft-Loaded L1A Blade CFD Results

were several dominant and harmonic frequencies calculated using the FFT for the $Re = 50,000$ case. An animation of the last 41,400 time-steps was made to help determine the shedding frequency for the main vortices present in the flowfield. The shedding events were counted individually, divided by the animation time interval of 0.0828sec to estimate the shedding frequency, and compared to frequencies calculated from the FFT. Also, Figure 6.8(c)-(d) and shows the shedding frequency for each vortical structure for the $Re = 50,000$ and 31,000 cases, respectively. It was determined that the separated shear layer vortex was being shed at frequency of 108Hz, while the smaller suction side vortices were shed at approximately 33Hz and 75Hz. Also, the vortex created by the pressure side separation region was shedding at a frequency of 48Hz. The trailing edge vortices had little impact on the blade drag coefficient because the vortex shedding did not occur until the shear layer reached the wake region (Fig 6.8(c)). A vortex shedding frequency of 350Hz was estimated for the smaller trailing edge vortex. At $Re = 31,000$ (Fig 6.8(b)) the shedding frequencies were estimated from the animation time interval of the last 0.3941sec mean flow-averaging. It was determined the separated shear layer vortex was being shed at a frequency of 51Hz, while the smaller suction side vortices were shed at approximately 18Hz and 32Hz. The large trailing edge vortex would periodically roll-up on the suction surface at a frequency of 22Hz while the smaller trailing edge vortices were shedding in the wake region at 102Hz (Fig 6.8(d)). Table 6.1 shows the separation location, shedding frequencies, and corresponding Strouhal numbers calculated from Eq. 4.1.

Chapter 6. The Aft-Loaded L1A Blade CFD Results

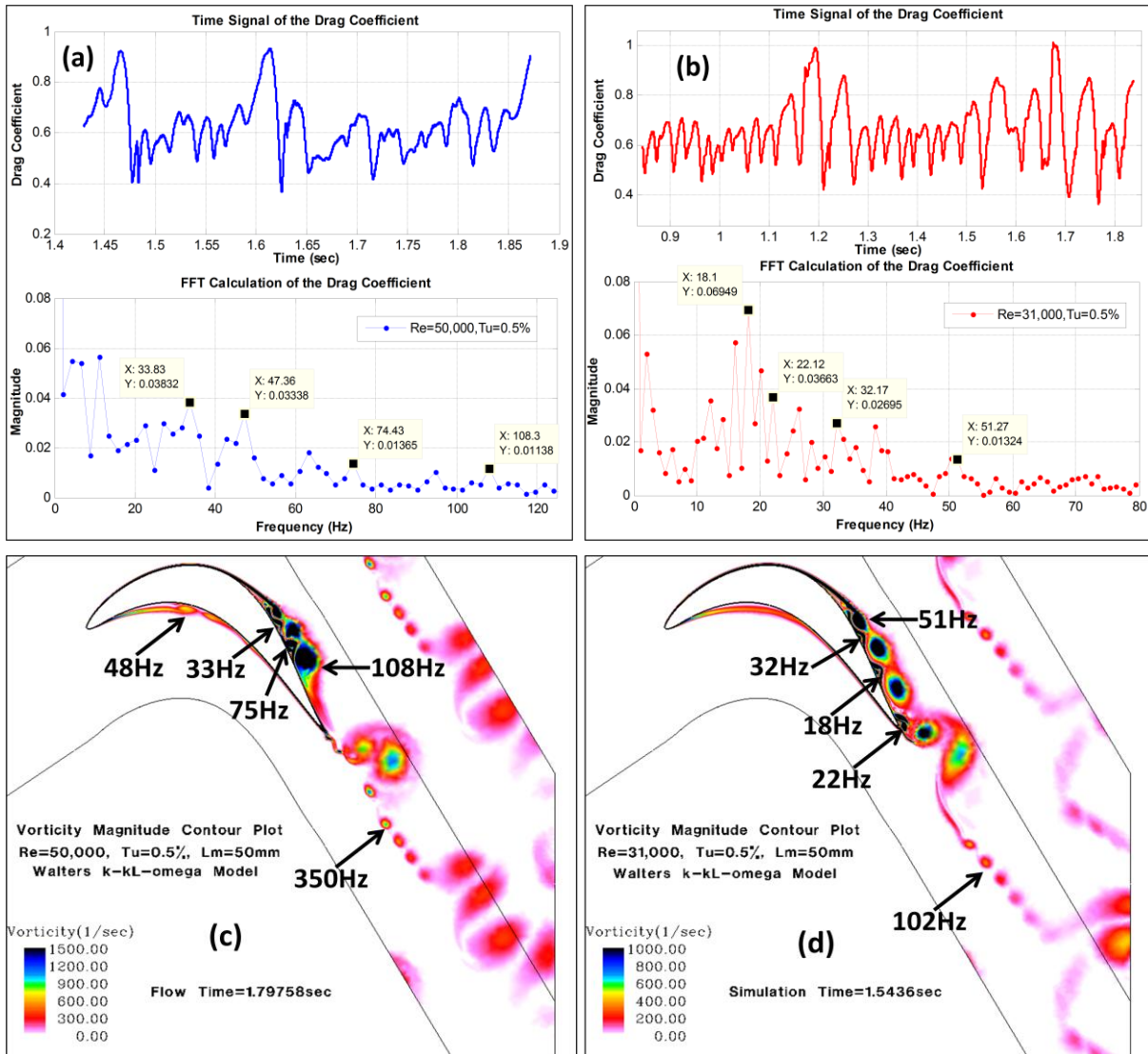


Figure 6.8. Time signal, FFT calculation of the drag coefficient, instantaneous vorticity contours at (a)-(c) $Re = 50,000$ and (b)-(d) $Re = 31,000$, $Tu = 0.5\%$, and $l_m = 50$ mm

Re	$l_m(mm)$	X_{sep}/C_x	Pressure Side		Suction Side						Trailing Edge	
			f_{shed}	St	f_{shed}	St	f_{shed}	St	f_{shed}	St	f_{shed}	St
50,000	50	0.628	48Hz	0.0010	108Hz	0.0010	75Hz	0.0016	33Hz	0.00071	350Hz	0.0076
31,000	50	0.633	32Hz	0.0016	51Hz	0.0025	18Hz	0.00087	32Hz	0.0015	102Hz	0.0049

Table 6.1. Summary of the separation location and Strouhal number for the Aft-Loaded L1A blade at $Tu = 0.5\%$

6.1.4 Total Pressure Loss Coefficient Predictions

The total pressure loss coefficient obtained from the CFD was compared to the experimental results of Marks *et al.* [35] as shown in Figure 6.9. The CFD using the Walters and D. Sanders

Chapter 6. The Aft-Loaded L1A Blade CFD Results

Leylek [2] $k-k_L-\omega$ transitional model significantly under-predicted the maximum value of the loss coefficient compared to the experimental results for both inlet Reynolds numbers. Also, the width of the wake region was over-predicted due to the unsteady vortices being spread across the wake region. The high numerical specific dissipation rate calculated from the $k-k_L-\omega$ model caused the total pressure loss from vortices created from the separated shear layers to be under-predicted and over-predict the width of the wake region. Table 6.1 shows that better agreement was achieved when comparing the integrated loss coefficient with 81% and 97% agreement for $Re = 50,000$ and $Re = 31,000$ to the experimental results, respectively. This indicated that the $k-k_L-\omega$ model predicted an adequate amount of viscous losses but the distribution of the viscous losses across the wake region was not well predicted. This could be due to the limitation of the $k-k_L-\omega$ model to dampen the production of any small scale turbulent structures. The dynamic behavior of the small scale turbulence is not present to attribute to viscous losses. The large coherent vortices produced from the separated shear layer dissipate more across the wake region.

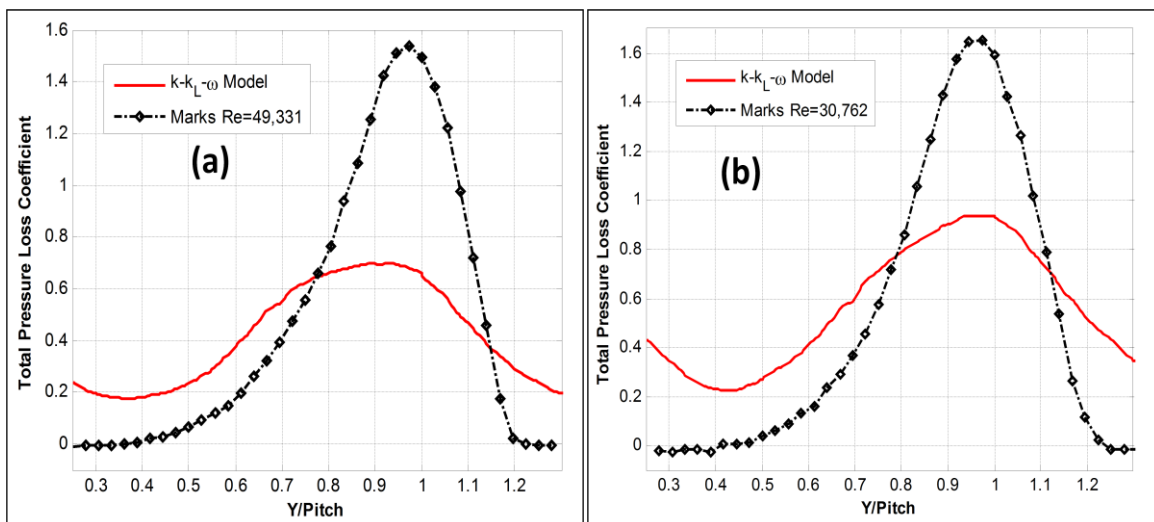


Figure 6.9. Comparison of total pressure loss coefficient with experimental [35] result at inlet Reynolds numbers of (a) 50,000 and (b) 31,000 for the Aft-Loaded L1A blade airfoil

Re	$l_m(mm)$	Integrated Loss Coefficient		Maximum Loss Coefficient	
		CFD	Marks <i>et al.</i> [35]	CFD	Marks <i>et al.</i> [35]
50,000	50	0.4131	0.5099	0.7001	1.5974
31,000	50	0.5715	0.5526	0.9391	1.6549

Table 6.2. Maximum and integrated total pressure loss coefficient comparison with the experimental [35] results for the Aft-Loaded L1A blade airfoil

6.2 CFD Predictions at High Inlet Turbulence intensity

Simulations were completed with the Aft-Loaded L1A blade at higher inlet turbulent intensities to determine if prediction capability using the $k-k_L-\omega$ model would improve at similar inlet Reynolds numbers. The inlet turbulence intensity was set to 3.4% corresponding to experiments completed with the turbulence grid placed at the inlet of the LSWT. Unsteady simulations were completed at $Re = 50,000$ and $25,000$ and compared to experiments taken by Marks *et al.* [35], CFD simulations completed with Menter's $k-\omega(SST)$ turbulence model and the Clark *et al.* [24] transition model. The inlet turbulent length scale was measured as $l_m = 40mm$ by McQuilling [34] at $Tu = 3.4\%$ for the LWST. Simulations were also completed at $l_m = 4mm$, $Tu = 3.4\%$ to investigate the impact of the length scale on the CFD predictions at high inlet turbulent intensities. Comparisons were made using the surface static pressure coefficient, mean and RMS velocity contours, and total pressure loss coefficient.

6.2.1 Surface Static Pressure Coefficient

In Figure 6.10, the mean static pressure coefficient distributions were compared to the measurements of Marks *et al.* [35] and CFD results of Clark [25]. Also, CFD simulations completed with the $k-k_L-\omega$ model at $l_m = 4mm$ & $40mm$ and $k-\omega(SST)$ model at $l_m = 40mm$ were included in Figure 6.10(a)-(b). At $Re = 50,000$, the $k-k_L-\omega$ model at both inlet turbulent length scales predicted a similar pressure distribution due to flow separation and turbulent reattachment

Chapter 6. The Aft-Loaded L1A Blade CFD Results

which were comparable to Clark's CFD results. The turbulent reattachment point from the Clark's CFD results indicated that reattachment location was slightly upstream than the $k-k_L-\omega$ model results. The experimental result had higher suction surface peak velocity than all the CFD simulations which indicated the experimental results had a higher loading level. However, the shape of the pressure distribution due to the reattaching separation bubble in the experimental results was similar to the CFD results using the $k-k_L-\omega$ and Clark and Praisner [24] transitional flow models. The CFD prediction using Menter's $k-\omega(SST)$ turbulence model did not show an indication of a closed separation bubble on the blade suction surface. The pressure distribution showed an indication of a separation region starting at the 80% axial chord location.

When the Reynolds number was decreased to 25,000, the length of the separation region on the suction surface increased for all results (Fig 6.10(b)). Both the $k-\omega(SST)$ turbulence model and Clark's CFD results predicted a separated flow region to the trailing edge and showed a constant pressure starting at the 60% axial chord location which was not measured in the experimental results. The experiment as in $Re = 50,000$ case had a higher loading level than CFD results but the $k-k_L-\omega$ model produced the best agreement with experimental results on the static pressure behavior of the separation region. Also, the prediction of the static pressure distribution was independent of inlet turbulent length scale using the $k-k_L-\omega$ model.

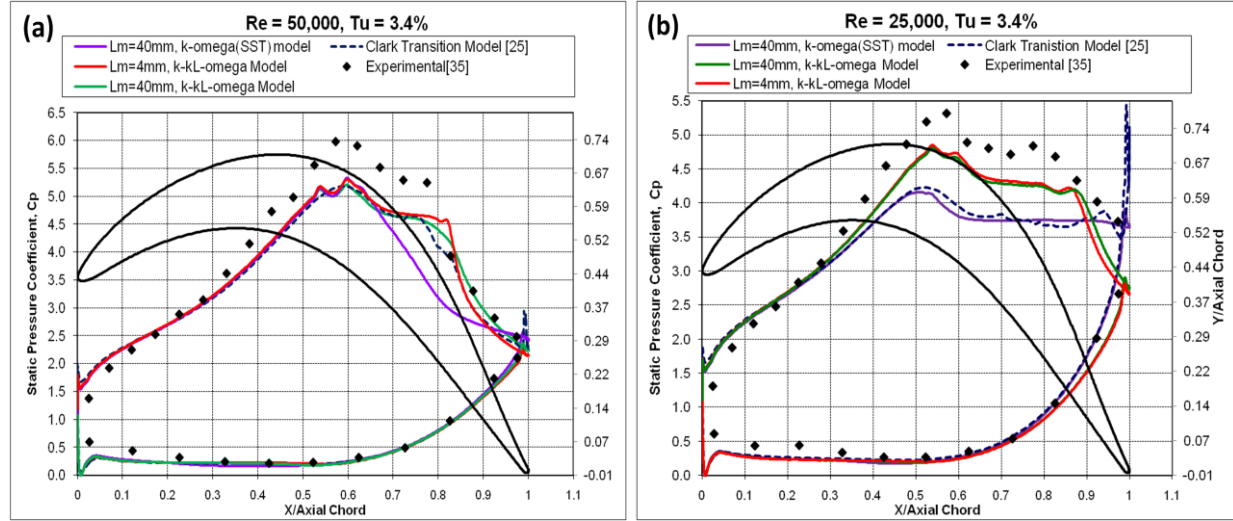


Figure 6.10. Comparison of surface static pressure coefficient with Clark *et al.* [25] simulations and experimental results [35] at inlet Reynolds numbers of a) 50,000 and b) 25,000, $Tu = 3.4\%$ for the Aft-Loaded L1A blade airfoil

6.2.2 Mean and RMS Velocity Contours

A CFD comparison of the mean and RMS velocity contours was made with the experimental PIV measurements taken by Marks *et al.* [35] at high turbulent intensities. The RMS contours have been modified to include the unsteadiness due to turbulence because a significant portion of the flow unsteadiness goes into the production of turbulence using the $k-k_L-\omega$ model. The RMS velocity was calculated using Eq. (6.1).

$$u_{RMS} = u_{RMS(global)} + (Tu)u_{avg} \quad (6.1)$$

Isotropic turbulence was assumed in order to relate the turbulent intensity to the RMS velocity using Eq. (1.20). The flow unsteadiness from the separated shear layers contributed 10% of the total RMS velocity whereas 90% the flow unsteadiness went into the production of turbulence. The $k-k_L-\omega$ model is based on the RANS CFD method. The limitation with $k-k_L-\omega$ model was any small scale unsteadiness present in the flowfield went into the production of turbulence at the high inlet turbulent intensity predictions even if the simulation was run as unsteady.

Chapter 6. The Aft-Loaded L1A Blade CFD Results

For the $k-k_L-\omega$ model simulations, a total of 50,000 time-steps were used for averaging of mean flow quantities with a flow time step of $40\mu\text{sec}$, while all the steady flow simulations were completed with Menter's $k-\omega(SST)$ model at both Reynolds numbers. For the $\text{Re} = 50,000$ case in Figure 6.11, there was a difference in the prediction of the separation region in the $k-k_L-\omega$ model results. The lower dissipation present in the $l_m = 40\text{mm}$ case (Fig 6.11(b)) caused the separation region to increase on the blade surface compared to the $l_m = 4\text{mm}$ case in Fig 6.11(a). This same observation was made with the Lightly Loaded blade in Section 4.2.2, e.g., that the freestream eddies no longer couple to the boundary layer through the turbulence model causing the increase in the separation region. The $l_m = 4\text{mm}$ case closely resembled the experimental PIV result which indicated a closed separation region starting at approximately the 60% axial chord location. The fully turbulent flow simulation using the $k-\omega(SST)$ model predicted a larger separation region than the $k-k_L-\omega$ model at the same length inlet turbulent length scale, which was not observed in the experimental result.

The RMS velocity contour plots in Figure 6.12 show the flow unsteadiness produced from the separated shear layer in the $k-k_L-\omega$ model result was under-predicted compared to the experimental result (Fig 6.12(c)) particularly in the 57%-79.4% axial chord locations. Downstream of the 79.4% axial chord location, a similar amount of unsteadiness was observed in the $k-k_L-\omega$ model and experimental results. The increase in the inlet turbulent length caused the amount of unsteadiness in the separation region to slightly increase (Fig 6.12(b)) in the $k-k_L-\omega$ model results. The experimental flow visualizations in Fig. 6.12(d) show a closed separation region with turbulent structures immediately downstream. These structures were not present in the instantaneous flowfield predictions in the $k-k_L-\omega$ model results due to the limitation of model at high inlet turbulent intensities.

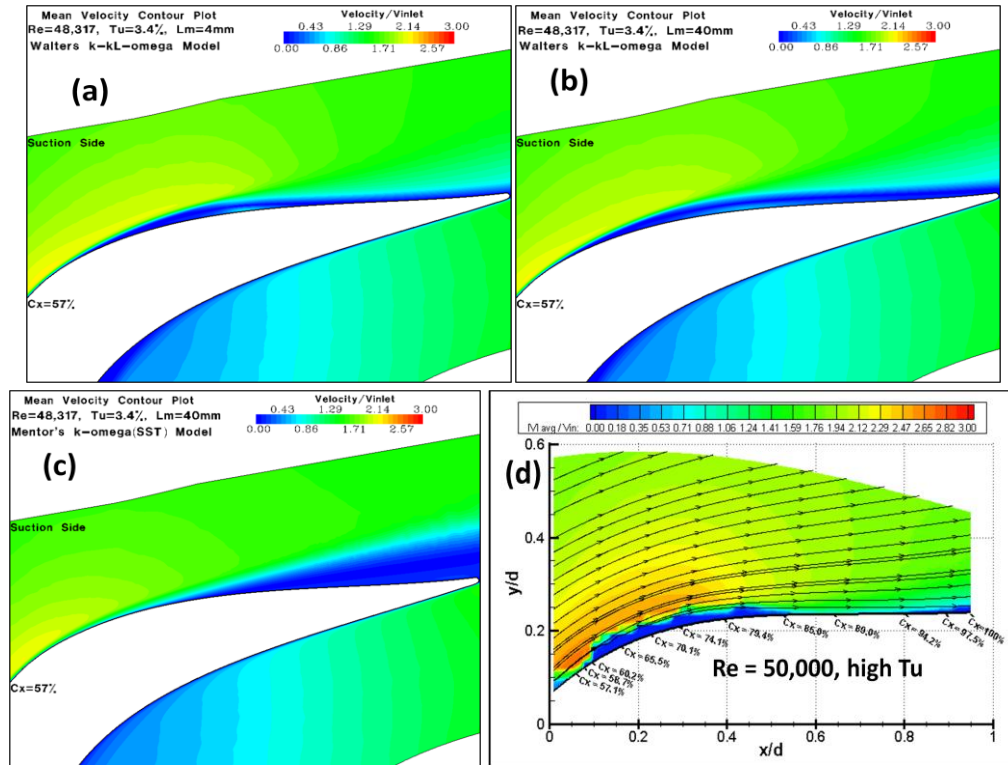


Figure 6.11. Mean velocity contour comparisons of $k-k_L-\omega$ model at (a) $L_m = 4mm$, (b) $L_m = 40mm$, (c) $k-\omega(SST)$ model at $L_m = 40mm$, and (d) PIV result of Marks *et al.* [35] at $Re=50,000$, $Tu=3.4\%$ for the Aft-Loaded L1A blade airfoil

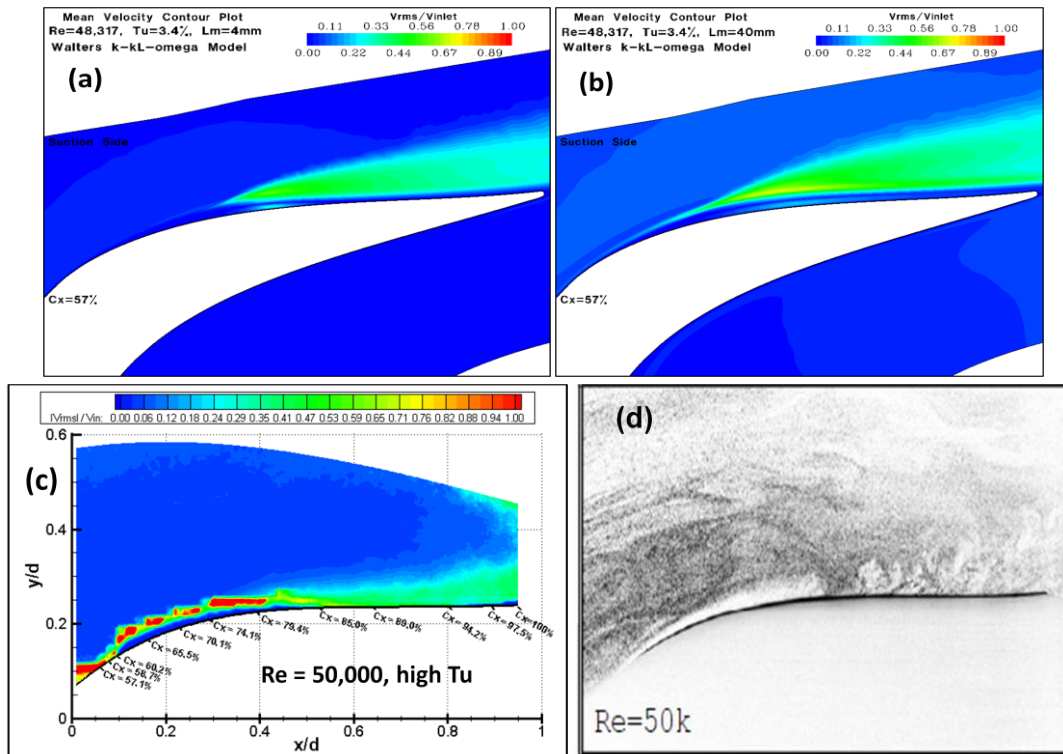


Figure 6.12. RMS velocity contour comparisons of $k-k_L-\omega$ model at (a) $L_m = 4mm$, (b) $L_m = 40mm$, (c) PIV result, and (d) flow visualizations of Marks *et al.* [35] at $Re=50,000$, $Tu=3.4\%$ for the Aft-Loaded L1A blade airfoil

Chapter 6. The Aft-Loaded L1A Blade CFD Results

At the $Re = 25,000$, both the $k-k_L-\omega$ model result at $l_m = 4mm$ and $40mm$ showed a similar prediction of the separation region as shown in Figure 6.13(a)-(b). Both simulations predicted a separation region to the trailing edge as the experimental result shown in Figure 6.13(d), yet the CFD result using the $k-k_L-\omega$ model predicted a smaller separation compared to experimental result. The fully turbulent flow simulation in Figure 6.13(c) using the $k-\omega(SST)$ model was found to be more comparable with the experimental result on the prediction on the size of the separation region. The RMS velocity contour plot comparison in Figure 6.14(a)-(b) for the $k-k_L-\omega$ model showed the RMS velocity produced from the separated shear layer was under-predicted compared to the experimental PIV results (Fig. 6.14(c)). This was due to the dampening of the effect the separated shear layer had on the flowfield unsteadiness similar to the $Re = 50,000$ case. According to the flow visualizations by Mark *et al.* [35] (Fig 6.14(d)), laminar flow eddies were generated from the separated shear layer and transitioned to turbulence further downstream of the separation point. The dampening of the global unsteady effects using the $k-k_L-\omega$ model at high inlet turbulence intensity was observed for both inlet Reynolds numbers. A significant portion of the flow unsteadiness went into the production of turbulence. As a result, there was not any vortex shedding observed in the wake region as seen at the lower inlet turbulent intensities.

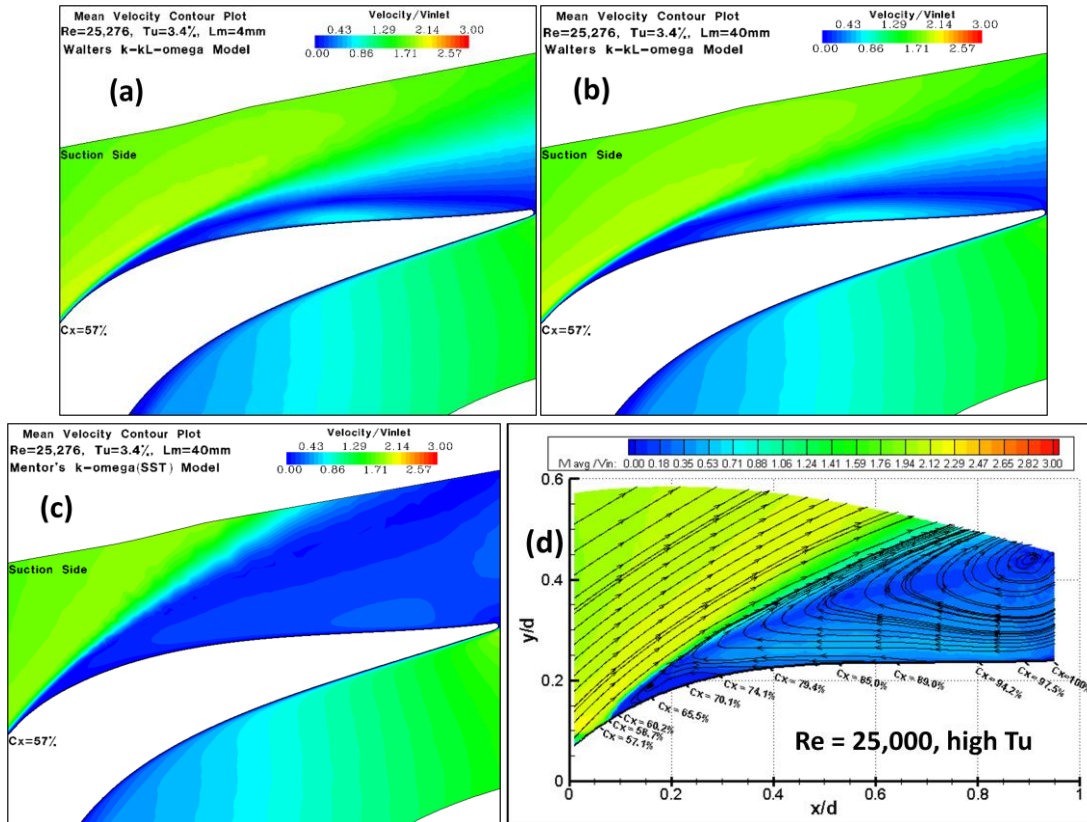


Figure 6.13. Mean velocity contour comparisons of $k-k_L-\omega$ model at (a) $L_m = 4mm$, (b) $L_m = 40mm$, (c) $k-\omega(SST)$ model at $L_m = 40mm$, and (d) PIV result of Marks *et al.* [35] at $Re=25,000$, $Tu=3.4\%$ for the Aft-Loaded L1A blade airfoil

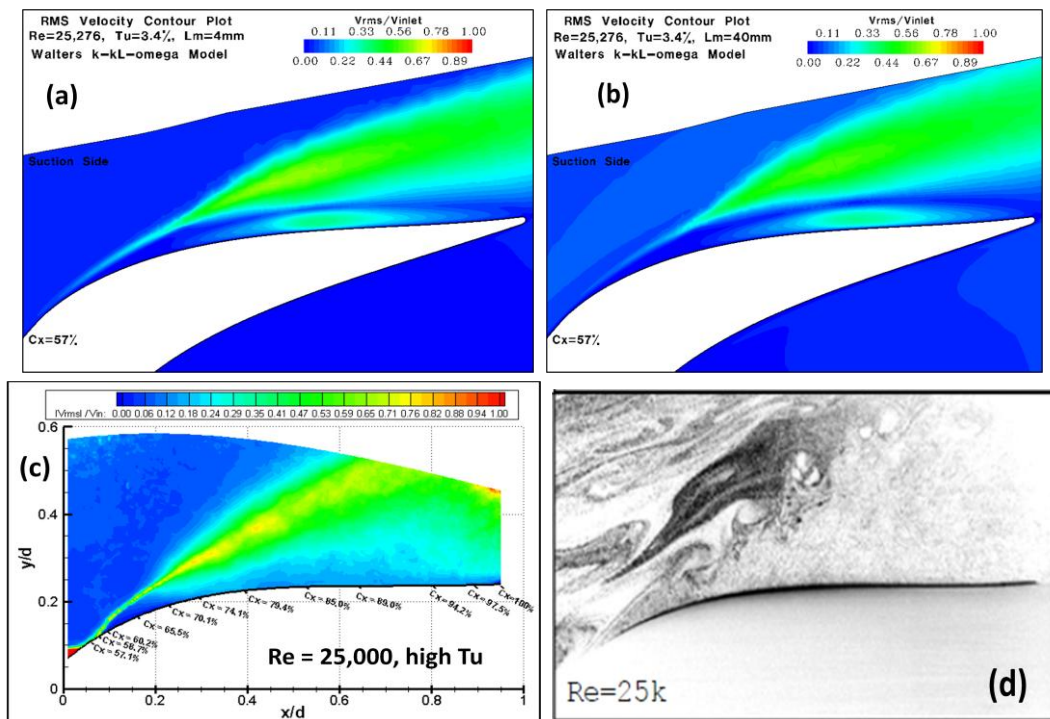


Figure 6.14. RMS velocity contour comparisons of $k-k_L-\omega$ model at (a) $L_m = 4mm$, (b) $L_m = 40mm$, (c) PIV and (d) flow visualizations of Marks *et al.* [35] at $Re=25,000$, $Tu=3.4\%$ for the Aft-Loaded L1A blade airfoil

6.2.3 Boundary Layer Velocity Profiles

The time-averaged axial velocity profiles were obtained at ten axial chord locations for $Re = 50,000$ and $25,000$ at $Tu = 3.4\%$ as shown in Figure 6.15 and Figure 6.16, respectively. For $Re = 50,000$, all three CFD results were in good agreement with each other on the prediction of the thickness of the boundary layer up to the 60.4% axial chord location. Yet, all the CFD under-predicted the boundary layer thickness compared to the experimental results starting at the 57% and up to the 74.1% axial chord location. The separation point was reported to be near $\approx 62\%$ axial chord location and the flow reattached between the 79.4 and 85% axial chord for experimental result. The $k-\omega(SST)$ model case predicted the separation point at 79.2% axial chord location and the boundary layer remained separated to the trailing edge. In the $k-k_L-\omega$ model results, the separation point was more downstream compared to the experimental results at the 65.9% and 65.1% axial chord location for the $l_m = 4mm$ and $l_m = 40mm$ cases, respectively. The increase in length scale caused a larger separation region with more reversed flow compared to the $l_m = 4mm$ case. Also, reversed flow was present to the trailing edge for the $l_m = 40mm$ case whereas, the $l_m = 4mm$ case showed the boundary layer being reattached at the 89% axial chord location.

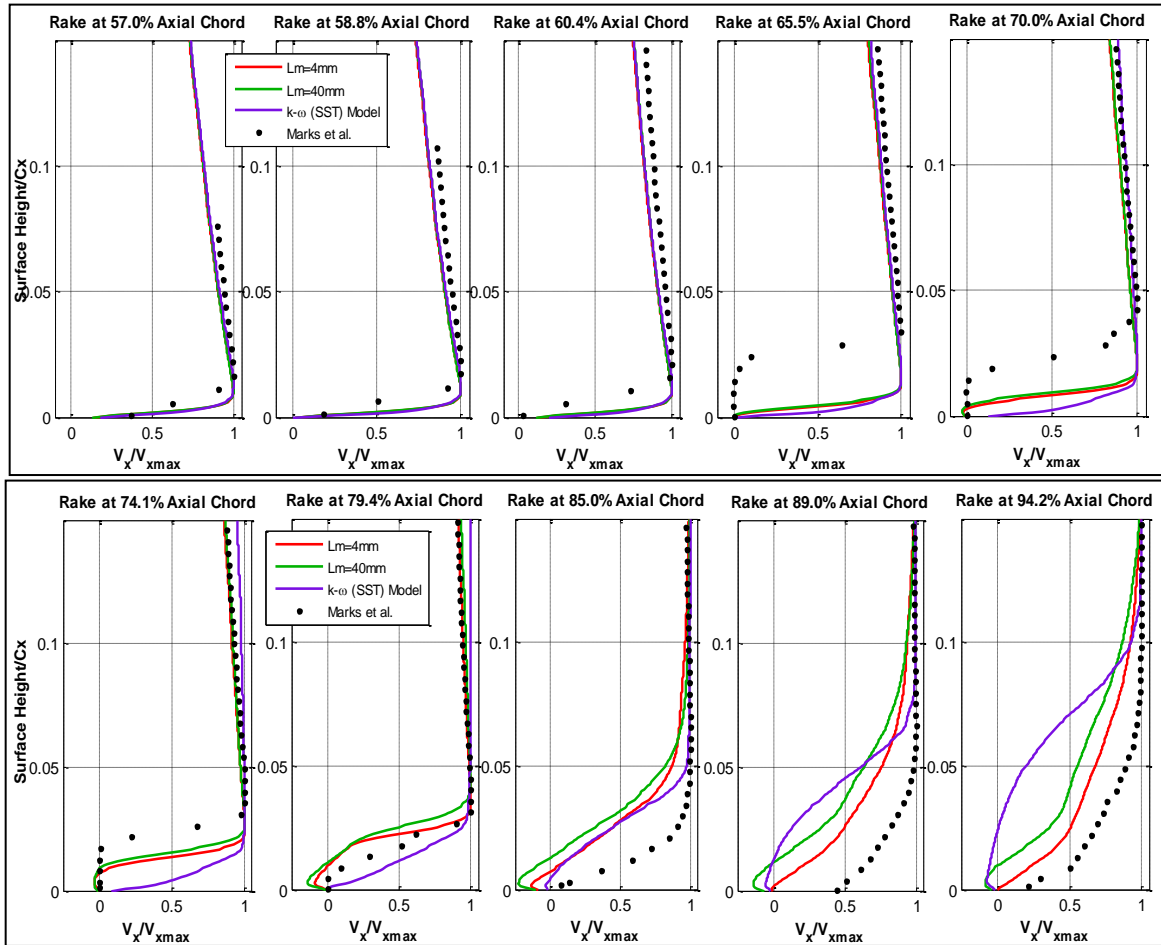


Figure 6.15. Comparison of the mean boundary layer profiles of axial velocity with experimental results [35] at inlet $Re = 50,000$ for the Aft-Loaded L1A blade airfoil at $Tu = 3.4\%$

The prediction of the separation point at 63% axial chord was independent of the inlet length scale variation for the $k-k_L-\omega$ model at $Re = 25,000$. The $l_m = 40mm$ case predicted a slightly larger separation region approaching the trailing edge as shown at the 94.2% axial chord location. Yet, both of the $k-k_L-\omega$ model predictions under-predicted the separation region compared to the experimental results starting at the 60.4% axial chord location. The best agreement was achieved with the experimental results with the $k-\omega(SST)$ model prediction with the separation point at 63.2% axial chord location. The size of the separation region and the amount of reversed flow was good agreement with experimental results to the 89% axial chord location where the $k-\omega(SST)$ model over-predicted the amount of reversed flow.

D. Sanders

145

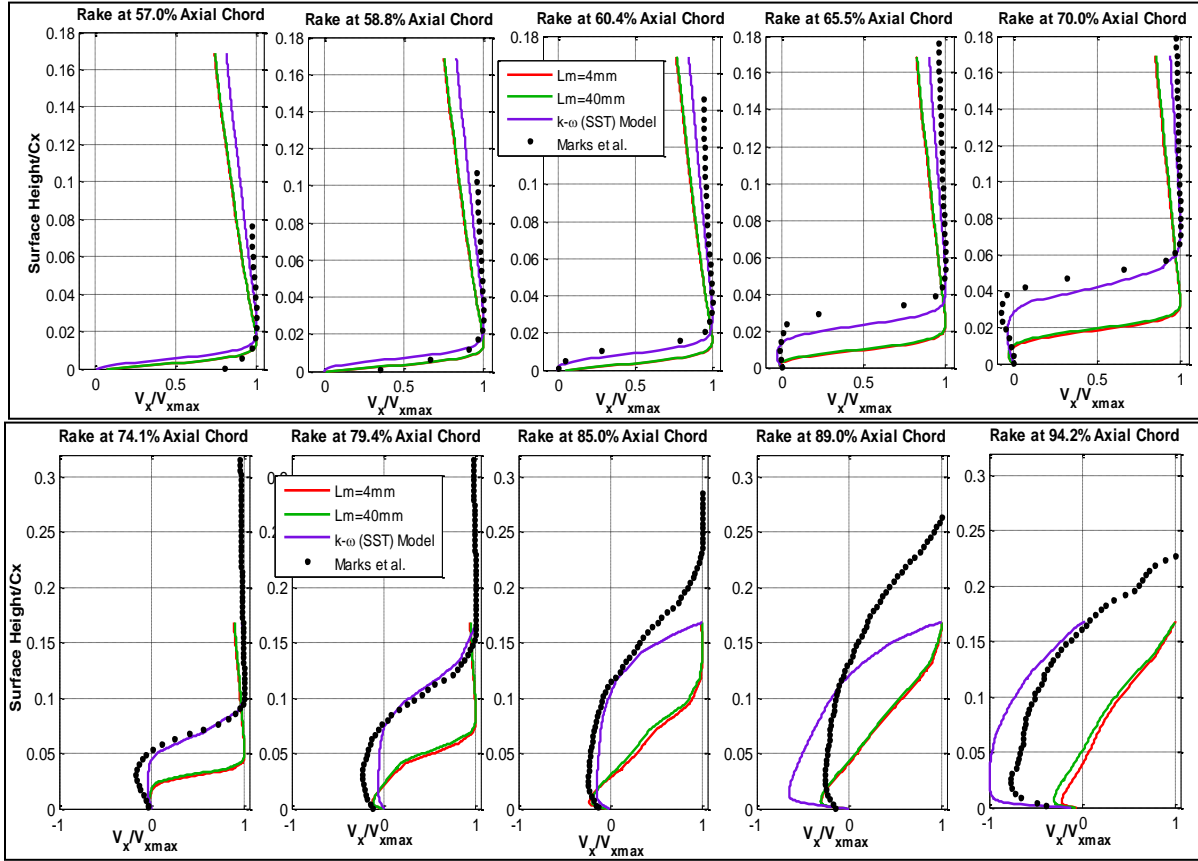


Figure 6.16. Comparison of the mean boundary layer profiles of axial velocity with experimental results [35] at inlet $Re = 25,000$ for the Aft-Loaded L1A blade airfoil at $Tu = 3.4\%$

6.2.4 Total Pressure Loss Coefficient Predictions

The wake loss coefficient obtained from the CFD predictions at inlet high turbulence intensity was compared to experimental results in Figure 6.17. For the $Re = 50,000$ case, both of the $k-k_L-\omega$ model results under-predicted the loss coefficient compared to the experimental results with 60% and 65% agreement in the peak loss coefficient for the $l_m = 4mm$ and $l_m = 40mm$ cases, respectively. The reason for this was due to the under-prediction of the separation region and the absence of the unsteady vortex shedding observed in the experimental results. Better agreement was achieved when comparing the integrated wake loss coefficient with 83% agreement with the experimental results for the $l_m = 40mm$ case. This indicated the amount of viscous losses produced by the $k-k_L-\omega$ model, $l_m = 40mm$ case was similar to the experimental

Chapter 6. The Aft-Loaded L1A Blade CFD Results

results but the viscous losses were dissipated across the wake more causing a reduction in the peak loss coefficient. The increase in the inlet turbulent length scale caused a 9% increase in the peak loss coefficient and 33% increase in the integrated wake loss coefficient due to the larger separation region present on the blade suction surface and lower dissipation present in the wake region. The $k-\omega(SST)$ model produced an 89% and 72% agreement in the peak and integrated loss coefficient with the experimental results, respectively. Yet, the behavior of the blade loading and separation on suction side did not qualitatively agree with the experimental results.

The same trend was observed for the $Re = 25,000$ where the $k-k_L-\omega$ model results under-predicted the loss coefficient, with 70% and 66% agreement in the peak value of the loss coefficient for the $l_m = 4mm$ and $l_m = 40mm$ cases, respectively compared to the experimental result. Better comparisons were made with the integrated wake loss coefficient. The $k-k_L-\omega$ model results produced 92% and 87% agreement with the experimental results. For the $Re = 50,000$ case, the $k-k_L-\omega$ model predicted the amount of viscous losses but the distribution across the wake region was different. Also, the absence of vortex shedding caused the $k-k_L-\omega$ model to under-predict the peak loss coefficient. Figure 6.17(b) shows that the $k-\omega(SST)$ model grossly over-predicted the peak loss coefficient by 112% mainly due to the over-prediction of the extent of the separation region in the wake region.

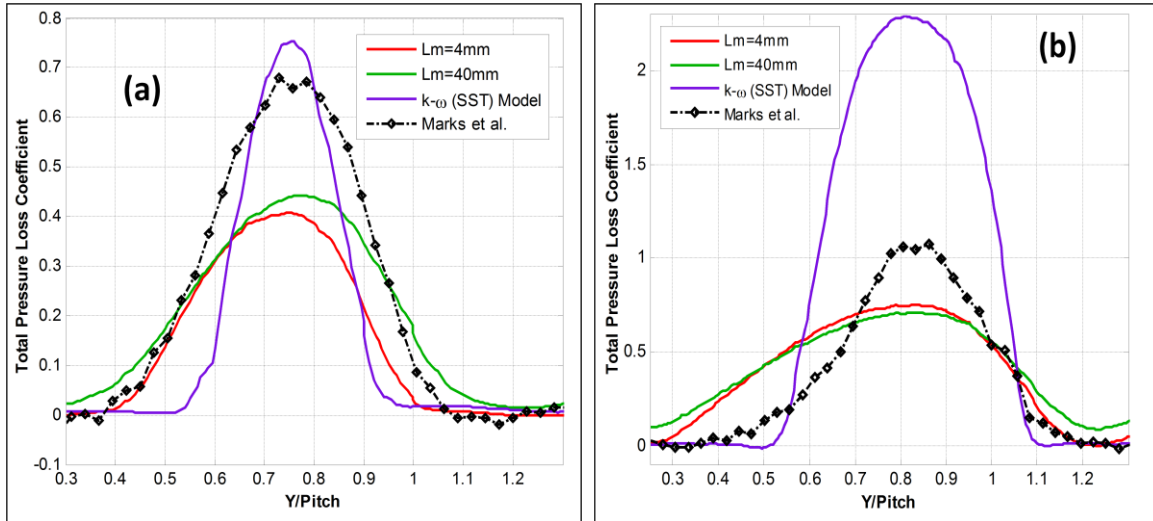


Figure 6.17. Comparison of total pressure loss coefficient with experimental [35] result at inlet Reynolds numbers of (a) 50,000 and (b) 25,000 for the Aft-Loaded L1A blade airfoil at $Tu = 3.4\%$

Re	$l_m(mm)$	CFD Model	Integrated Loss Coefficient		Maximum Loss Coefficient	
			CFD	Marks <i>et al.</i> [35]	CFD	Marks <i>et al.</i> [35]
50,000	4	$k-k_L-\omega$	0.1502	0.2397	0.4083	0.6791
	40	$k-k_L-\omega$	0.2000		0.4432	
	40	$k-\omega(SST)$	0.1714		0.7549	
25,000	4	$k-k_L-\omega$	0.4208	0.3893	0.7494	1.0774
	40	$k-k_L-\omega$	0.4383		0.7119	
	40	$k-\omega(SST)$	0.8471		2.2932	

Table 6.3. Maximum and integrated total pressure loss coefficient comparison with the experimental [35] results for the Aft-Loaded L1A blade airfoil at $Tu = 3.4\%$

6.3 Summary of Results

The flowfield of the Aft-Loaded L1A blade airfoil was simulated at inlet Reynolds numbers of 50,000 and 25,000. The flowfield was very complex due to the very high loading level and strong suction surface adverse pressure gradient. The surface static pressure distribution, boundary layer profiles, and the wake total pressure loss coefficient were compared to available experimental and CFD data. Also, the unsteady features of separation were qualitatively investigated at high and low inlet turbulent intensities. Good agreement was

Chapter 6. The Aft-Loaded L1A Blade CFD Results

achieved with the experimental results on the prediction of the separation location and the blade loading at low turbulent intensities. The $k-k_L-\omega$ model demonstrated the ability to predict the qualitative flow response to the unsteady vortex shedding due to the separated shear layers as observed in the experimental flow visualizations. Yet, the CFD results at both Reynolds numbers under-predicted the size of the separation region which resulted in the under-prediction of the peak value of the loss coefficient. Better comparisons were achieved in the prediction of the integrated loss coefficient with 80% or better agreement with the experimental results. This indicated that the amount viscous losses produced was comparable to the experimental results, but, the higher dissipation caused those losses to be distributed more across the wake.

Similar trends were observed for simulations at the higher inlet turbulent intensities. The qualitative effects of the blade loading were adequately predicted, but, the size of the separation region was under-predicted with the $k-k_L-\omega$ model. Also, the unsteady vortex generation from the separated shear layers was not present in the CFD results using the $k-k_L-\omega$ model. The absence of the unsteady effects from vortex shedding caused the under-prediction of the maximum value of wake loss coefficient. Increasing the inlet turbulent length scales from $l_m = 4 \text{ mm}$ to $l_m = 40 \text{ mm}$ caused an increase in the size of separation region due to the lower dissipation present in the flowfield with a similar static pressure distribution. As in the low turbulence intensity cases, better agreement was achieved with the integrated wake loss coefficient. The fully turbulent $k-\omega(SST)$ model was simulated at the same inlet Reynolds number to determine if it would provide a better prediction than the $k-k_L-\omega$ model at higher turbulent intensities. Better agreement with the experimental result was achieved at $Re = 50,000$ in comparing the peak loss coefficient but, the qualitative flow effects of the blade loading and the separation location did not agree well with experimental results. At $Re = 25,000$, good

Chapter 6. The Aft-Loaded L1A Blade CFD Results

agreement was achieved on the size of the separation region yet, the loss coefficient was grossly over-predicted using the $k-\omega(SST)$ model. Overall, the Walters and Leylek's [2] $k-k_L-\omega$ transitional model flow was achieved better prediction of the low Reynolds number aerodynamic flow effects than the conventional $k-\omega(SST)$ turbulence model for the Aft-Loaded L1A blade airfoil at higher turbulent intensities.

CHAPTER SEVEN

7. Aft-Loaded L1A Blade with Upstream Wake Generators

The CFD model of the Aft-Loaded L1A blade with upstream wake generators presented in Section 3.1.2 was run at $Re = 25,000$ at high and low inlet turbulent intensities. The inlet turbulent boundary conditions for the low turbulence intensity case were set to $Tu = 0.5\%$ with an inlet turbulent length scale, $l_m = 50mm$, whereas the high turbulence intensity case was simulated at $Tu = 3.4\%$ and $l_m = 40mm$. These inlet turbulent boundary conditions corresponded to the baseline CFD simulations completed without upstream wakes. In the cascaded experiment on the L1A blade, circular cylinders were used to generate an upstream translating wake impinging on the downstream blade. The purpose of this study was to simulate the periodic disturbances associated with rotor/vane flow interactions encountered in a multistage LPT geometry, where wakes shed from an upstream vane propagate and impinge on the downstream rotor blade.

Unsteady simulations were completed for both the high and low turbulence intensity cases based on the experimental results of Nessler *et al.* [37,48] taken in the AFRL LSWT. This included matching the flow coefficient ($\Phi = u_{axial}/u_{rod}$) of 0.817 and cylindrical rod speed, $u_{rod} = 2.298m/sec$. The low turbulence intensity case utilized a total of 112,799 time-steps or 0.2256sec for averaging of mean-flow quantities with the flow time-step of $2\mu sec$. The total flow-time interval through the CFD domain was 0.436sec and the mean-flow averaging interval represented 0.516 flow-time intervals. The high turbulence intensity cases used 112,199 time-steps or 0.2244sec for mean flow-averaging and this interval represented 0.514 flow-time

Chapter 7. The Aft-Loaded L1A Blade with Upstream Wake Generators

intervals. The flowfield of the upstream wake configuration of the Aft-Loaded L1A blade airfoil was compared with the CFD predictions and experiments of the baseline Aft-Loaded L1A blade cases.

7.1 CFD Predictions for the Wake Generator

The flowfield of the upstream wake generators was investigated in order to characterize the wake produced by the circular cylinder that impinged upon the downstream Aft-Loaded L1A blade airfoil. The inlet Reynolds number based on diameter of the cylinder and the relative velocity was 794. Flowfield comparisons were made against reported theory, since the flowfield around a circular cylinder has been presented in many fluid dynamics texts [7-9]. The cylinder surface static pressure, vortex shedding behavior, and wake properties were calculated for at high and low inlet turbulent intensities and the results are discussed in the next sections.

7.1.1 Surface Static Pressure Coefficient

Figure 7.1 shows the wake generator mean surface static pressure coefficient for both high and low turbulent intensities as calculated with Eq. (7.1)

$$C_p = \frac{(P_{surface} - P_{in})}{\frac{1}{2} \rho w_{in}^2} \quad (7.1)$$

where the w_{in} is the inlet relative velocity. The static pressure coefficient was plotted as a function of angular surface location (θ) from the stagnation point. The CFD-predicted static pressure distribution was similar to that reported results in several fluid dynamic texts [7,8] where the boundary layer remained attached in the favorable pressure gradient for θ up to 75° , and separated from the wake generator surface once it reached the adverse pressure gradient

Chapter 7. The Aft-Loaded L1A Blade with Upstream Wake Generators

portion of the wake generator surface. The static pressure distribution was very similar for both the low and high turbulence intensity cases with a predicted separation location of 103.5° . This location corresponded to a laminar boundary flow separation point and was within 95% agreement of the 108.8° separation point for laminar flow around a circular cylinder calculated using the Blasius series [49]. Investigations indicated that the turbulent kinetic energy around the wake generator was an order of magnitude smaller than the freestream value and confirmed that the boundary layer was predicted as laminar.

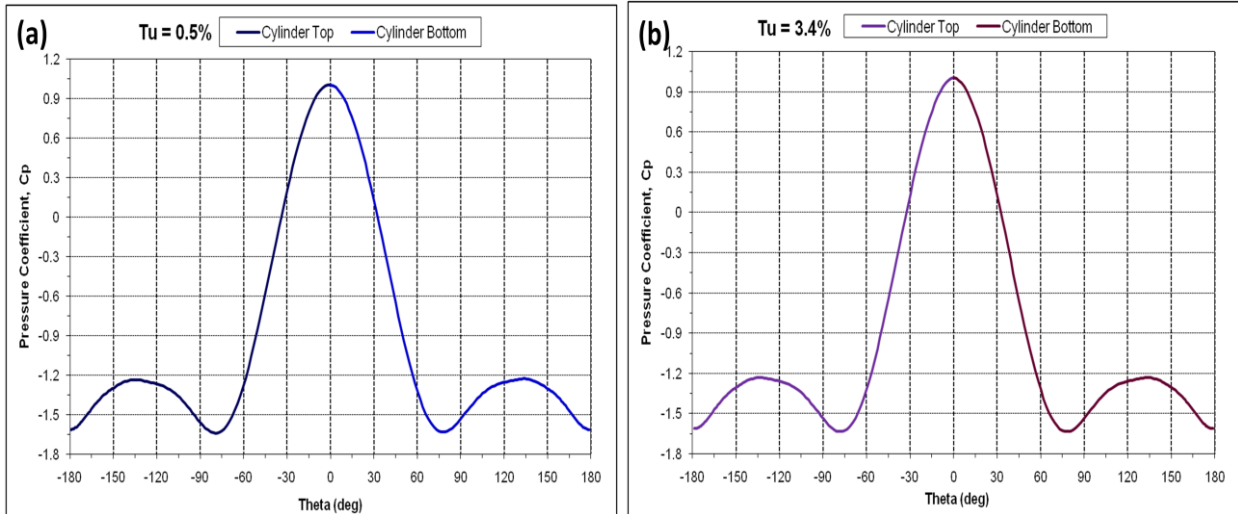


Figure 7.1. The mean surface static pressure coefficient at $Re_D = 794$ at (a) $Tu = 0.5\%$, $L_m = 50mm$ and (b) $Tu = 3.4\%$, $L_m = 40mm$ for the wake generator

7.1.2 Unsteady Features of the Flowfield

Contour plots of the vorticity in the spanwise or z-direction were made to show unsteady vortex generation of the upstream wake generator as shown in Figure 7.2. The z-vorticity (Ω_z) was calculated using Eq. (7.2)

$$\Omega_z = (\nabla \times \vec{W}) \cdot \hat{k} \quad (7.2)$$

Chapter 7. The Aft-Loaded L1A Blade with Upstream Wake Generators

where \hat{k} is the unit vector in the z-direction and \vec{W} is the relative velocity vector. Figure 7.2 shows the separated shear layer from the wake generator produced two large vortices. Both the low and high inlet turbulence intensity cases produced very similar vortex shedding behavior. The shear layer on the top surface of the wake generator produced a clockwise vortex as indicated by the positive z-vorticity whereas, the shear layer on the bottom portion of the wake generator produced a counter-clockwise vortex with negative z-vorticity. This shedding pattern is known as a von Karman vortex street [48]. The FFT calculation of the dynamic drag coefficient showed that the vortex shedding frequency was $296 \pm 4\text{Hz}$ for both the low and high turbulence intensity cases. The Strouhal number was calculated using Eq. (7.3)

$$St = \frac{fD}{u_{in}} \quad (7.3)$$

with the result $St = 0.23$ for the both the low and high turbulence intensity cases. Table 7.1 shows the vortex shedding frequency and Strouhal number based on characteristic length and momentum thickness at separation for both the upstream wake generator and the Aft-Loaded L1A blade.

Chapter 7. The Aft-Loaded L1A Blade with Upstream Wake Generators

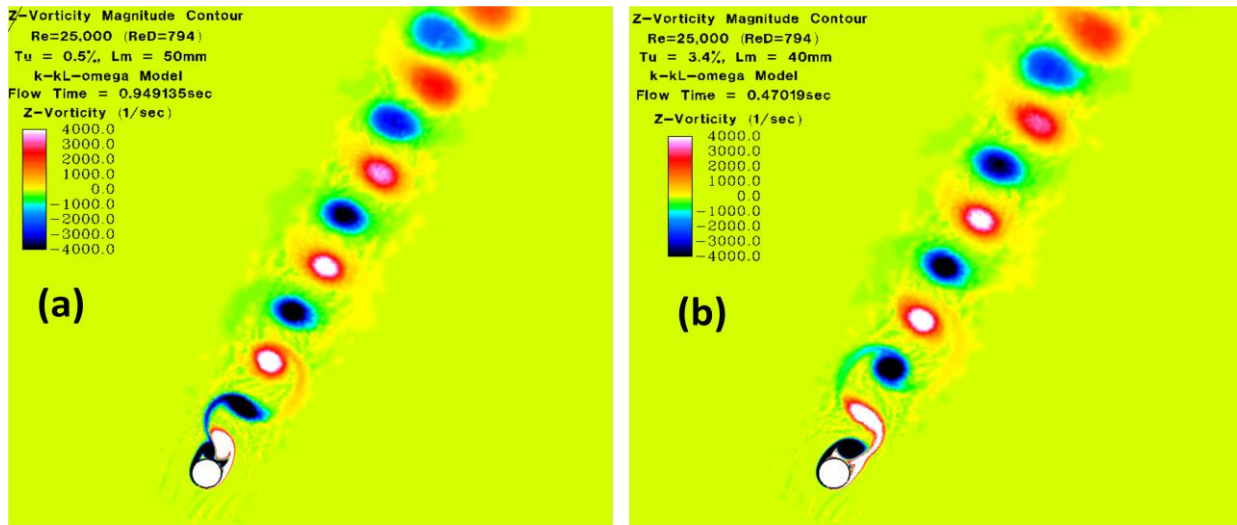


Figure 7.2. Instantaneous Z-vorticity contours at $Re_D = 794$ at (a) $Tu = 0.5\%$, $l_m = 50mm$ and (b) $Tu = 3.4\%$, $l_m = 40mm$ for the wake generator

7.1.3 Downstream Wake Characteristics

Several single point measurements of the velocity were made downstream of the wake generator. The first velocity probe was located one-half of the blade axial chord length (8.9cm) downstream from wake generator center and one-half of the blade pitch length (8.95cm) in the axial and pitchwise flow directions, respectively. Figure 7.3 shows the time-signal of this single point velocity probe measurement for the CFD and experimental results [37]. The experimental measurements were taken with a single element hot-film probe and represented a 100 blade passes ensemble time-averaged measurements of the velocity. The mean-flow averaging was completed for a total of 2.9 wake passes for both CFD results based on a wake passing frequency of 12.77Hz. The wake profiles were similar for the CFD results due to the laminar boundary layer present on the wake generator surface with the same separation location. The wake was quantified using wake width b , and the peak velocity deficit, u_p . The peak velocity deficit was calculated using Eq 7.4.

Chapter 7. The Aft-Loaded L1A Blade with Upstream Wake Generators

$$u_p = \frac{U - u_0}{U} \quad (7.4)$$

where U is the average velocity outside the wake region and u_0 is the minimum velocity within the wake region as given in Table 7.1. Both CFD result had a 122% higher peak velocity deficit and 35% smaller wake width compared to the experimental results. This could be attributed to the surface of the actual wake generator not being perfectly circular and smooth. The boundary layer of the real hardware may have been turbulent, thus reduced the wake peak velocity deficit in the experimental results. Currently, a simulation of the wake generator is being completed at the same inlet conditions as the low and high turbulence intensity cases using the fully turbulent form Wilcox [11] $k-\omega$ model. This will determine the difference between a wake produced from a turbulent boundary layer compared to a laminar boundary layer around the wake generator. If there is a significant difference between the results, future work will explore methods of tripping the boundary layer around the wake generator to become turbulent using the Walters and Leylek [2] $k-k_L-\omega$ model.

Chapter 7. The Aft-Loaded L1A Blade with Upstream Wake Generators

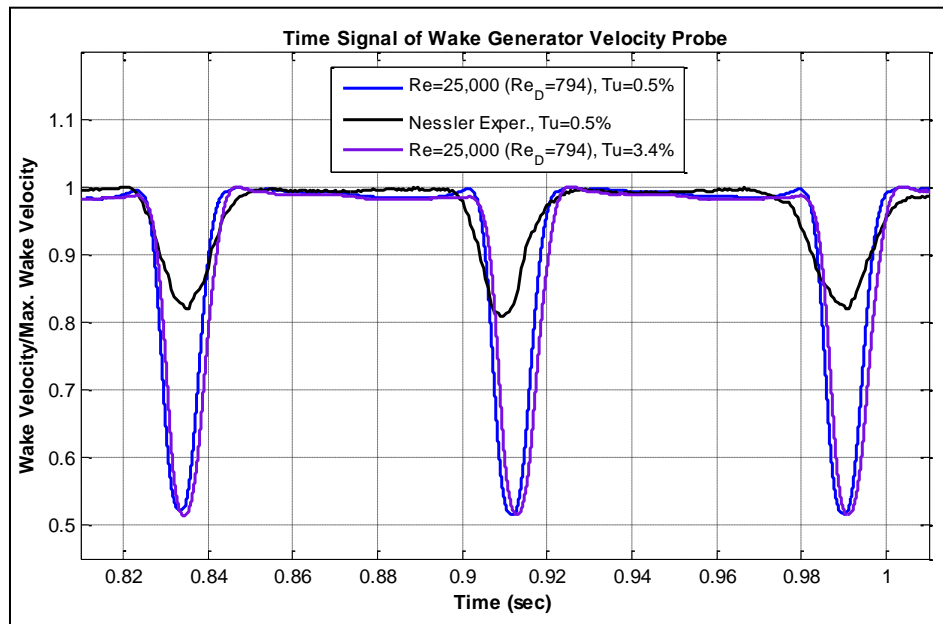


Figure 7.3. Comparison of the time-signal of the wake generator velocity for CFD at $Tu = 0.5\%$ and 3.4% with experimental [37] single point hot-film velocity measurements at $Tu = 0.5\%$ for $Re = 25,000$

For the high inlet turbulence intensity condition, single point velocity measurements of the wake were made at two different locations within the blade passage. Velocity Probe #1 was placed at the 66.25% axial chord position, 3.71 cm above and normal to the blade surface whereas, Velocity Probe #2 was placed at the 80.63% axial chord position, 2.87 cm above and normal to the blade surface. Figure 7.4 shows a comparison at $Tu = 3.4\%$ between the CFD and experimental results of the time signal of the blade passage velocity at the Probe #1 and #2 locations. The CFD predictions showed a higher amplitude change of velocity compared to the experimental results for both probe locations. This was due to a higher peak velocity deficit produced by the upstream wake generator in the CFD predictions. Also, the time variation of Probe #1 was significantly different in CFD predictions for the time interval of $0.76 < t < 0.81$ sec range (Fig. 7.4(a)) when compared to the experimental results. This was attributed to the CFD only having 3 wake passes to average over instead of the 100 wake passes for flow-averaging in the experimental results causing the local peaks in this range to be significantly reduced. In

D. Sanders

Chapter 7. The Aft-Loaded L1A Blade with Upstream Wake Generators

Figure 7.4(b), the flow-averaging effect was reduced because of the higher amplitude change of the velocity at the Probe #2 location in the experimental result. The periodic pattern of the velocity variation for Probe #2 in the CFD predictions was slightly different compared to experimental result with a much larger amplitude change of the velocity.

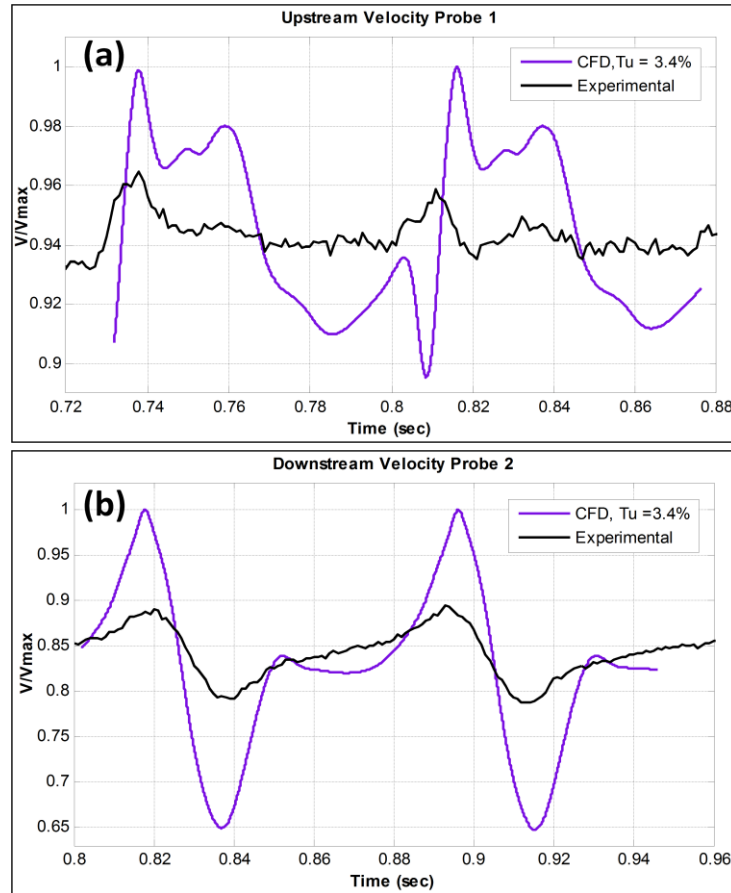


Figure 7.4. Comparison of the velocity (a) Probe #1 and (b) #2 blade passage locations with the experimental [48] single point hot-film velocity measurements at $Re = 25,000$, $Tu = 3.4\%$

	Re	Tu	$l_m(mm)$	Re_D	θ_{sep}	f_{shed}	St (Eq. 5.1)	St (Eq. 7.3)	$b(m)$	U_p
CFD	25,000	0.5%	50	794	103.5°	296Hz	1.65×10^{-3}	0.23	0.0684	0.476
	25,000	3.4%	40	794	103.5°	298Hz	1.65×10^{-3}	0.23	0.0637	0.477
Exp.	25,000	0.5%	-	761	-	-	-	-	0.0861	0.214

Table 7.1. Summary of the separation location, Strouhal number, and wake properties for the wake generator

Chapter 7. The Aft-Loaded L1A Blade with Upstream Wake Generators

7.2 CFD Predictions for the Aft-Loaded L1A Blade

The effect of the traversing upstream wakes was investigated on the flowfield of the Aft-Loaded L1A blade. The traversing wakes had a significant effect on the blade loading, behavior of the boundary layer, unsteady vortex shedding, and total pressure loss coefficient. These properties of the flowfield were explored at low and high turbulent intensities and compared to the baseline simulations of the Aft-Loaded L1A blade. Comparisons were also made with PIV images of the unsteady flowfield and total pressure loss coefficient measurements taken by Nessler *et al.* [37].

7.2.1 Unsteady Features of the Flowfield

The unsteady features of the flowfield were investigated to understand the behavior of the upstream wake on the separation and vortex shedding. The upstream wake traversing event was divided into six phases with the first phase beginning with the rod positioned directly in front of the blade leading edge and in line with the inlet flow direction. A diagram of the six different phases is shown in Figure 7.5. Also, the time location was determined for each phase with respect to the freestream velocity Probe #2 as shown in Figure 7.6 for both the CFD and experimental results. Each phase in the CFD was positioned at different locations with respect to the experimental results for the Probe #2 time signal because the CFD predictions had a larger wake deficit thus producing a time-signal of the velocity. The time location of Phase #1 was verified by making sure the location of the wake generator was in the correct relative position to the blade.

Chapter 7. The Aft-Loaded L1A Blade with Upstream Wake Generators

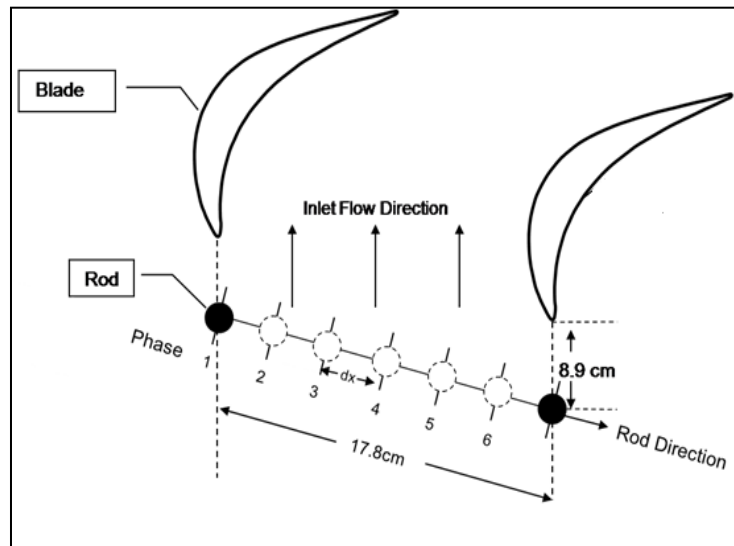


Figure 7.5. Diagram of the different wake generator locations for each of the six phases [37]

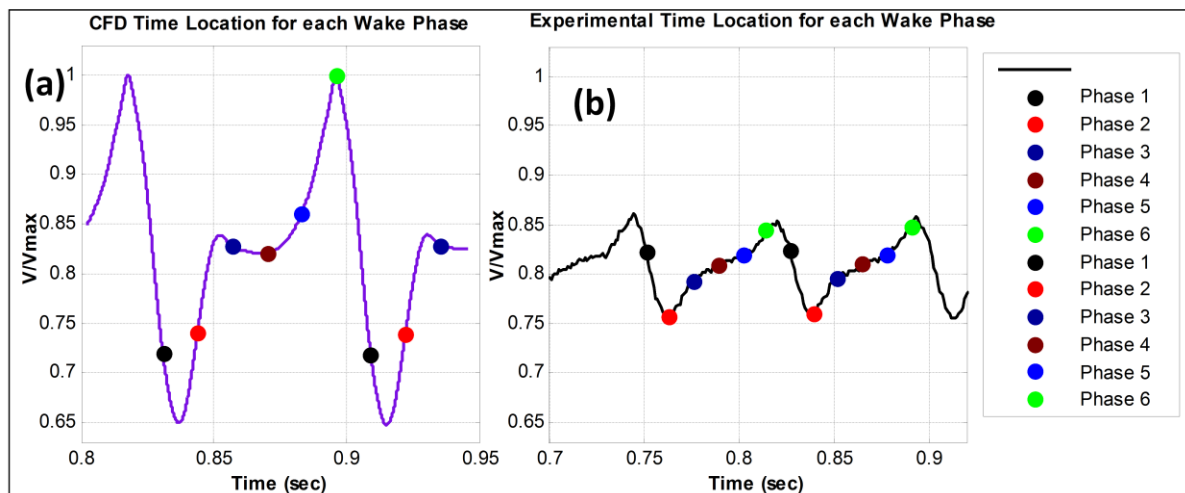


Figure 7.6. (a) CFD and (b) experimental time location for each phase with respect to the Probe #2 time signal of the freestream velocity [48]

Instantaneous contour plots of z -vorticity were used to visualize the features of the flowfield for each of the six phases. The flowfield was periodically repeated for three pitch lengths to aid the visualization of the traversing wake generator and the vortex shedding in the wake region of the downstream blade. The z -vorticity contours for each phase for the $Re = 25,000$, $Tu = 0.5\%$, $l_m = 50\text{mm}$ and the $Re = 25,000$, $Tu = 3.4\%$, $l_m = 40\text{mm}$ cases is shown in Figure 7.7 and 7.8, respectively. Both simulations showed identical unsteady behavior of the

D. Sanders

Chapter 7. The Aft-Loaded L1A Blade with Upstream Wake Generators

traversing wake and the vortex shedding caused by the blade surface separated shear layers. Phase #1 and #2 (Fig 7.7(a)-(b) and Fig 7.8(a)-(b)) shows the traversing wake affecting the boundary layer separation of the pressure side of the blade. The vortex created on the pressure side was clockwise in direction as indicated by positive z -vorticity. The freestream pressure field in the blade passage caused the traversing wake to form into the V-shape as shown in Figure 7.7(c)-(e) and Figure 7.8(c)-(e) for Phases #3-#5. The wake began to reach the aft portion of the blade and affected the vortices created by the separated shear layer in Phase #6 and #1.

Figure 7.9 presented a magnified view of the vortices produced by suction surface separated shear layer for the $Re = 31,000$, $Tu = 0.5\%$ baseline case compared to the $Re = 25,000$, $Tu = 0.5\%$ with the addition of wakes. The baseline case was divided into six phases corresponding to the same time interval as the $Re = 25,000$ case with the wakes. The vortices were significantly smaller compared to the baseline case for all six phases (Phase #1, #3, & #6 only shown in Fig. 7.9). The traversing wake caused an increased amount of turbulence present in the freestream and reduced the separation region compared to the baseline case. The separated shear layers produced clockwise vortices that were lifted off the blade surface by the traversing wake. The separated shear layer from the trailing edge produced a similar counter-clockwise vortex as in the baseline case.

The time signal and the FFT of the drag coefficient were calculated for the Aft-Loaded L1A blade with upstream wake generators for both low and high turbulence intensity cases. Within the frequency resolution, 4Hz based Eq. (5.1) for both low and high inlet turbulence intensity cases, the dominant and harmonic frequencies were similar. The suction side separated shear layer vortex was being shed at a frequency of 75Hz as shown in Figure 7.10. Also, evident

Chapter 7. The Aft-Loaded L1A Blade with Upstream Wake Generators

is the pressure side separation region was shedding at a frequency of 27Hz. The trailing edge counterclockwise vortex was shedding in the wake region at 36Hz as shown in Fig. 7.9(b). Table 7.2 shows the separation location, shedding frequencies, and corresponding Strouhal number calculated from Eq. (4.1).

Chapter 7. The Aft-Loaded L1A Blade with Upstream Wake Generators

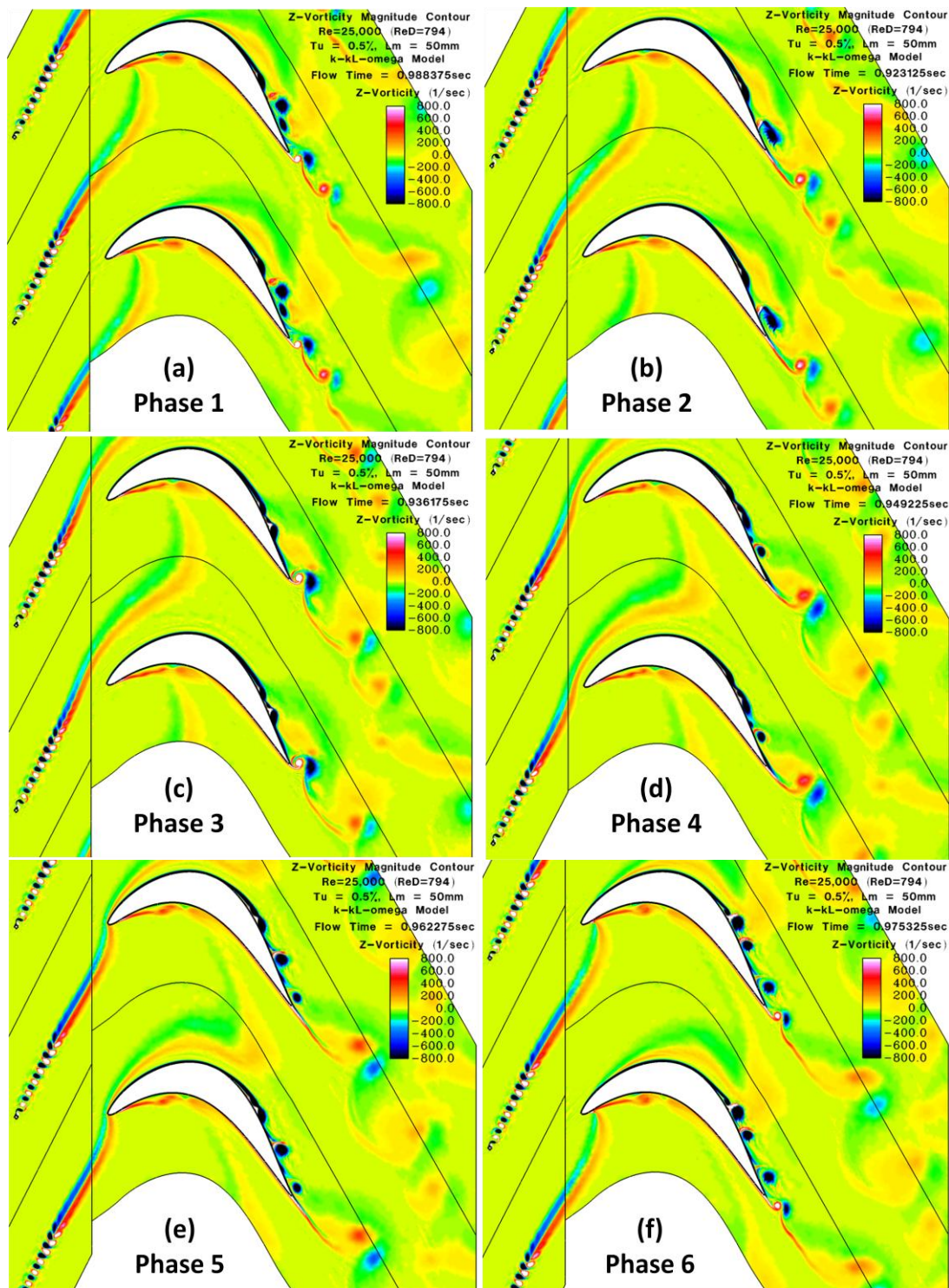


Figure 7.7. Instantaneous z-vorticity contour plots for each of the six phases at $Re=25,000$, $Tu=0.5\%$, $L_m=50mm$

Chapter 7. The Aft-Loaded L1A Blade with Upstream Wake Generators

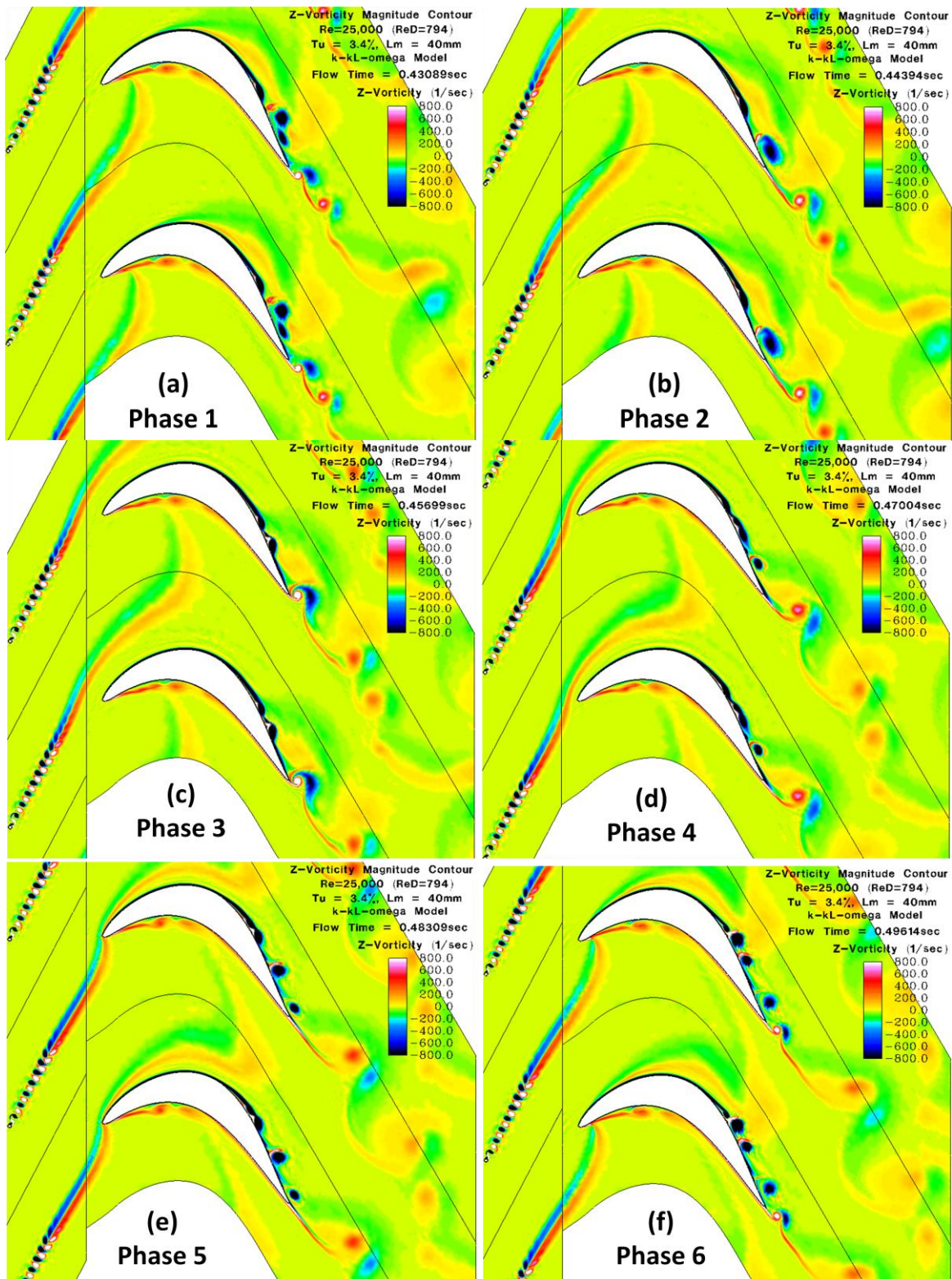


Figure 7.8. Instantaneous z-vorticity contour plots for each of the six phases at $Re = 25,000$, $Tu = 3.4\%$, $L_m = 40mm$

Chapter 7. The Aft-Loaded L1A Blade with Upstream Wake Generators

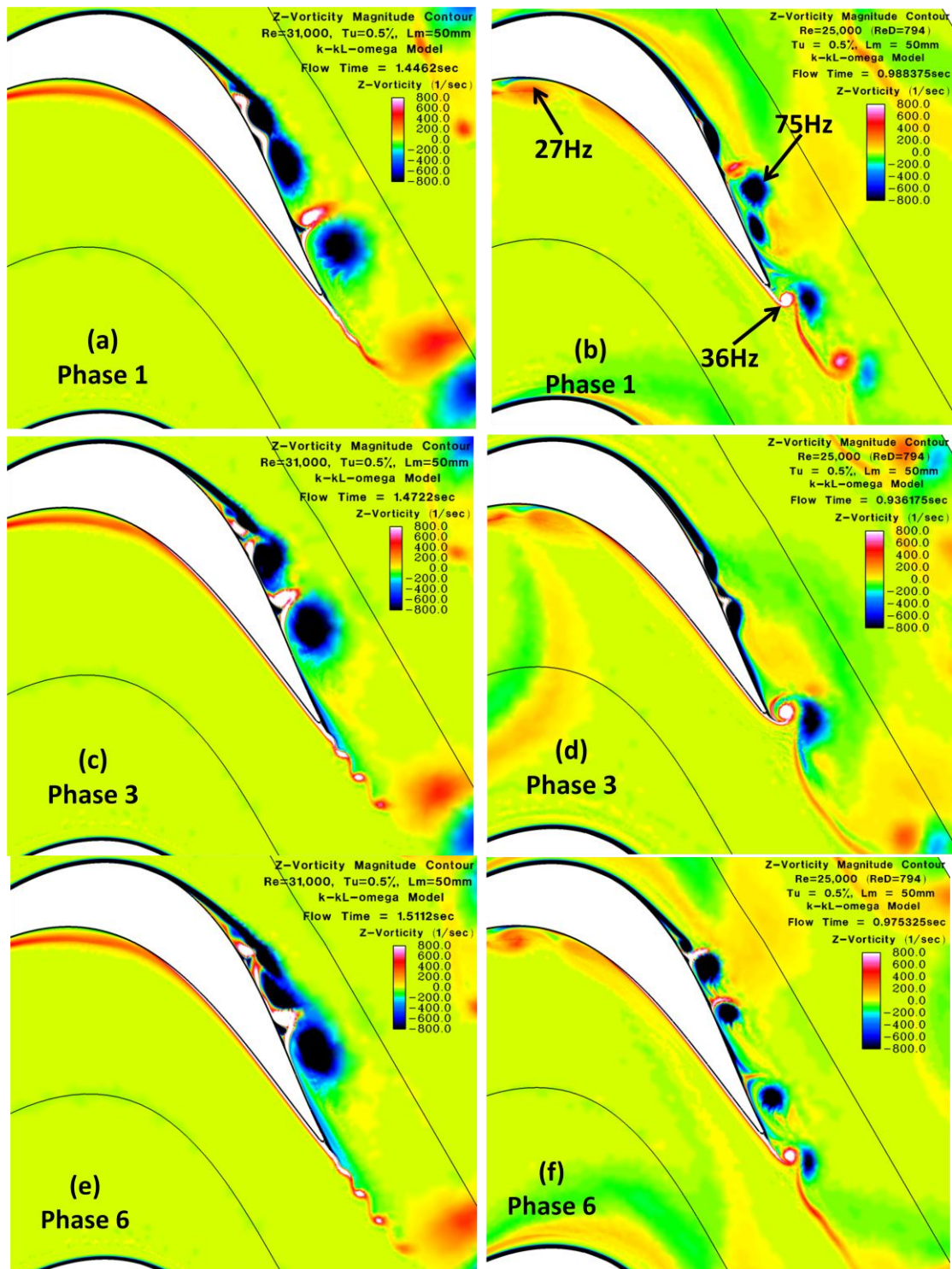


Figure 7.9. Comparisons of the instantaneous z-vorticity contours of the separation region at Phase #1, #3, and #6 for baseline $Re = 31,000$ and $Re = 25,000$ with wakes, at $Tu = 0.5\%$, $L_m = 50mm$

Chapter 7. The Aft-Loaded L1A Blade with Upstream Wake Generators

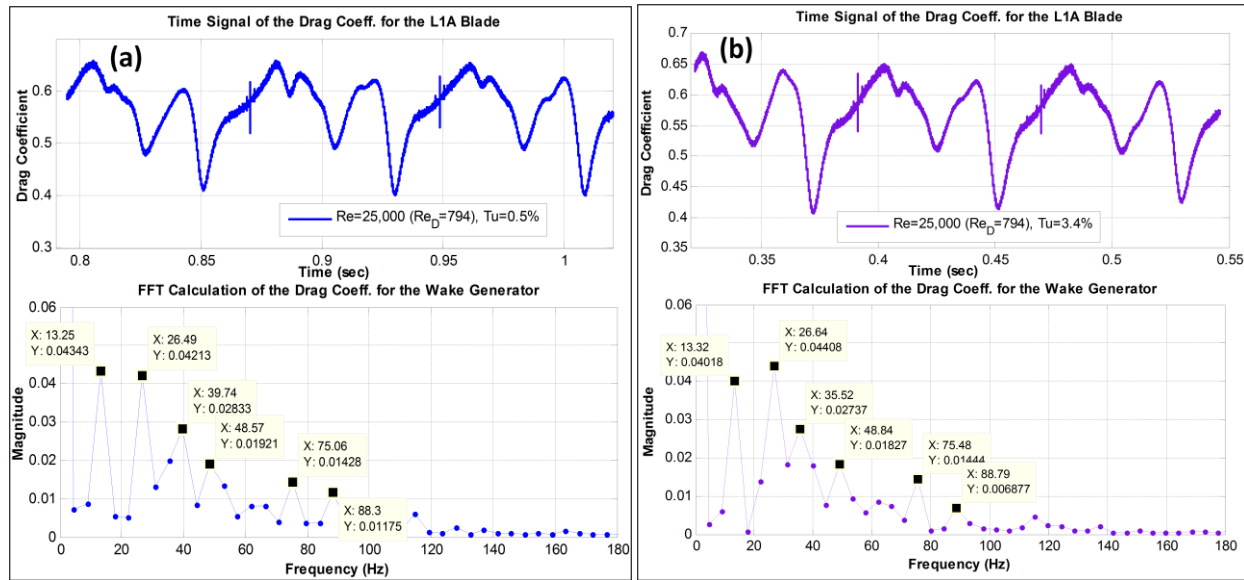


Figure 7.10. Time signal and FFT calculation of the drag coefficient for the Aft-Loaded L1A blade airfoil with upstream wake generators at Re = 25,000 (a) Tu = 0.5%, $l_m = 50\text{mm}$ and (b) Tu = 3.4%, $l_m = 40\text{mm}$

				Pressure Side			
Re	$l_m(\text{mm})$	Tu	X_{sep}/C_x	f_{shed}	St		
25,000, Passing Wake	50	0.5%	0.690	25Hz	1.92×10^{-3}		
31,000, Baseline	50	0.5%	0.633				
25,000, Passing Wake	40	3.4%	0.673	27Hz	1.83×10^{-3}		
Suction Side						Trailing Edge	
Re	f_{shed}	St	f_{shed}	St	f_{shed}	St	f_{shed}
25,000, Passing Wake	75Hz	5.76×10^{-3}	13Hz	1.00×10^{-3}	-	-	40Hz
31,000, Baseline	51Hz	2.46×10^{-3}	18Hz	8.69×10^{-4}	32Hz	1.55×10^{-3}	102Hz
25,000, Passing Wake	76Hz	5.15×10^{-3}	13Hz	8.81×10^{-4}	-	-	36Hz

Table 7.2. Summary of the separation location and Strouhal number for the Aft-Loaded L1A blade airfoil with upstream wake generators

7.2.2 Comparison of Phase Velocity Contours with Experimental PIV Results

Experimental PIV images were taken by Nessler *et al.* [37] of the blade passage for each of the six phases. Velocity magnitude contours were made based on the PIV images for the comparisons with CFD prediction at the high inlet turbulence intensity cases as shown in Figure 7.11 - 7.13. Figure 7.11(a) shows for Phase #1 the flow was attached with a separation region

Chapter 7. The Aft-Loaded L1A Blade with Upstream Wake Generators

present in the aft portion of the blade downstream of 90% axial chord location for both the CFD and experimental result. Also, the negative z-vorticity region shown in Figure 7.8(a) corresponded to the same region of high velocity whereas the positive z-vorticity regions corresponded to the low velocity regions and was found for all six phases. There was a larger high velocity region in the CFD prediction compared to the experimental result due to a much larger velocity deficit in the CFD predictions. In Phase #2 (Fig. 7.11(b)), the separation region moved more downstream near the blade trailing edge with attached flow across the visible length of the suction surface in the PIV results. The high velocity region returned along the blade surface with the location of the wake moving out of the view for the PIV and CFD results in Phase #3 as shown in Fig. 7.12(a). Similarly in Phase #2 and #3, the CFD prediction had a larger region high velocity region compared to experimental PIV result. The high velocity region moved more downstream, indicating that a new wake was entering the blade passage in Phase #4 (Fig 7.12(b)). For Phase #5 and #6, in Figure 7.13, the high velocity region continued to move downstream with a localized separation region approximately at the 89% axial chord region in Phase #5 and moving near the trailing edge in Phase #6. The high velocity region was in the CFD prediction similar in size as the PIV result for Phases #4 - #6 because the upstream wake was not present on the aft portion of the blade for these phases.

Chapter 7. The Aft-Loaded L1A Blade with Upstream Wake Generators

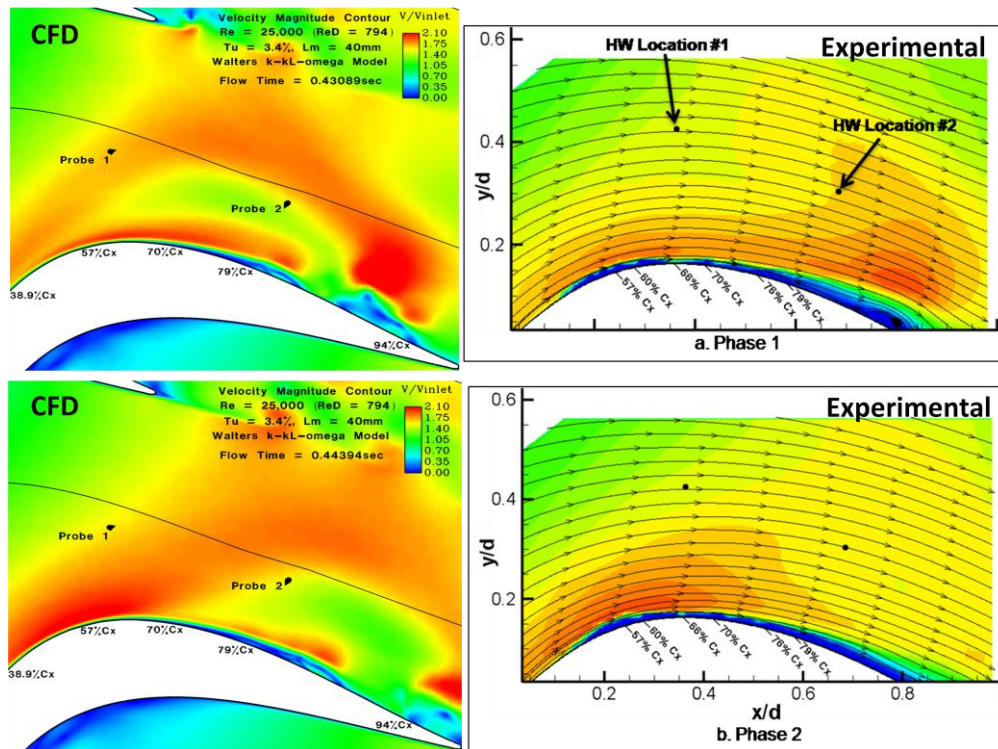


Figure 7.11. Comparison of the velocity magnitude contour plots in the blade passage for the CFD and experimental [37] PIV results at $Re = 25,000$, $Tu = 3.4\%$, $L_m = 40mm$ for Phase #1 & #2

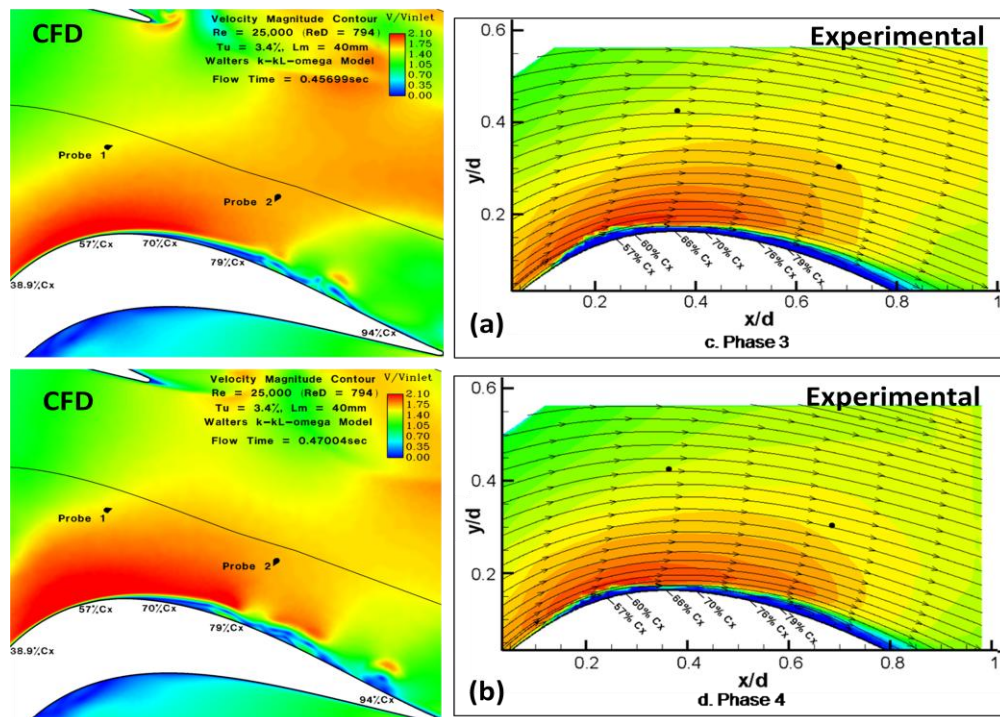


Figure 7.12. Comparison of the velocity magnitude contour plots in the blade passage for the CFD and experimental [37] PIV results at $Re = 25,000$, $Tu = 3.4\%$, $L_m = 40mm$ for Phase #3 & #4

Chapter 7. The Aft-Loaded L1A Blade with Upstream Wake Generators

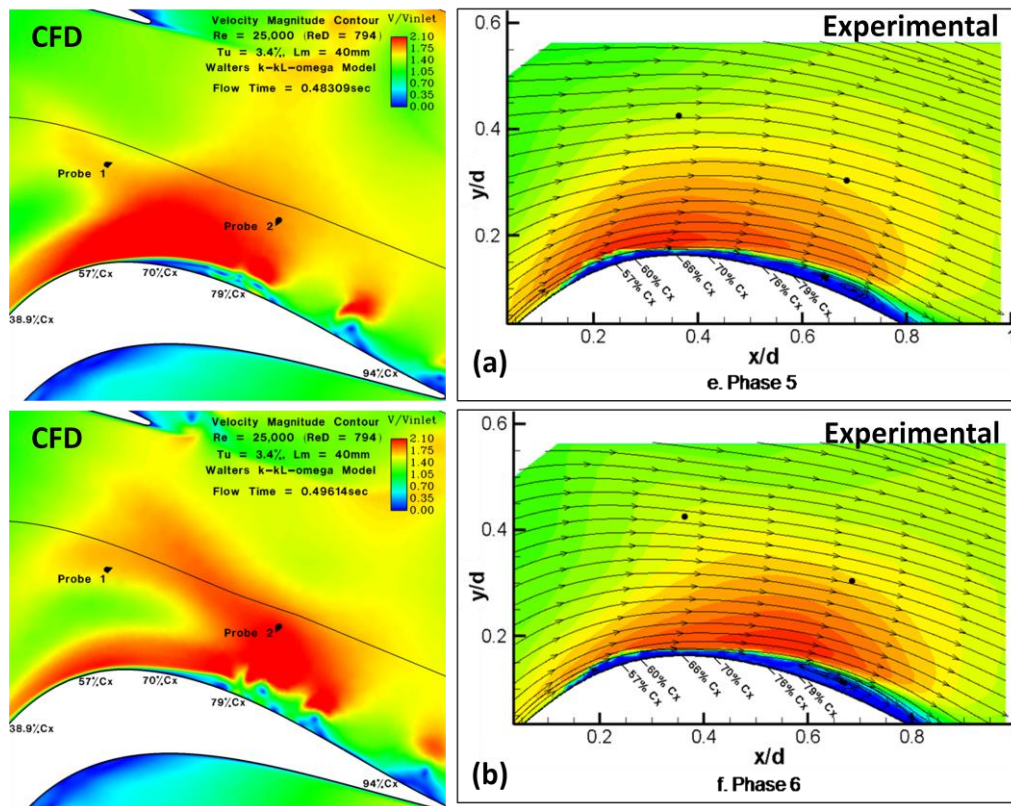


Figure 7.13. Comparison of the velocity magnitude contour plots in the blade passage for the CFD and experimental [37] PIV results at $Re = 25,000$, $Tu = 3.4\%$, $l_m = 40\text{mm}$ for Phase #5 & #6

Instantaneous boundary layer profiles of the axial velocity were obtained at six axial chord locations for Phase #1, #3, and #6 for CFD and experimental results for the $Re = 25,000$, $Tu = 3.4\%$, $l_m = 40\text{mm}$ case as shown in Figure 7.14 - 7.16. For the experimental results, the boundary layer profiles were extracted from PIV measurement of the flowfield for each phase. Phase #1 in Figure 7.14(a) showed the good agreement with the experimental results in the thickness of the boundary layer to the 70.0% axial chord location. Downstream of that location, the CFD result over-predicted the thickness of the boundary to the 85.0% axial chord location (Fig. 7.14(b)). This difference could be attributed to over-prediction of the size of the unsteady vortices produced from the suction surface separated shear layer. Also, the averaging of the instantaneous velocity field completed by the post-processing of the PIV images could have

Chapter 7. The Aft-Loaded L1A Blade with Upstream Wake Generators

reduced the boundary layer thickness in experimental results. Similar over-prediction of the boundary layer thickness in CFD prediction was observed in Phase #3 (Fig. 7.15(b)) starting at the 74.1% axial chord location. A significant amount of reversed flow was present in the CFD prediction starting at the 70.0% axial chord location for Phase #3 whereas, Phase #1 had the reversed flow beginning more downstream of that location. This indicated that the separation location moved more downstream in Phase #3 as compared to Phase #1. Figure 7.16 shows in Phase #6 that the boundary layer profiles showed a unique shape starting at the 79.4% axial chord location. This was due to the unsteady vortices lifting off the blade surface into the freestream and the boundary layer below reattaching to the blade surface. The amount of reversed flow present in the boundary layer has significantly reduced compared to Phase #1 and Phase #3.

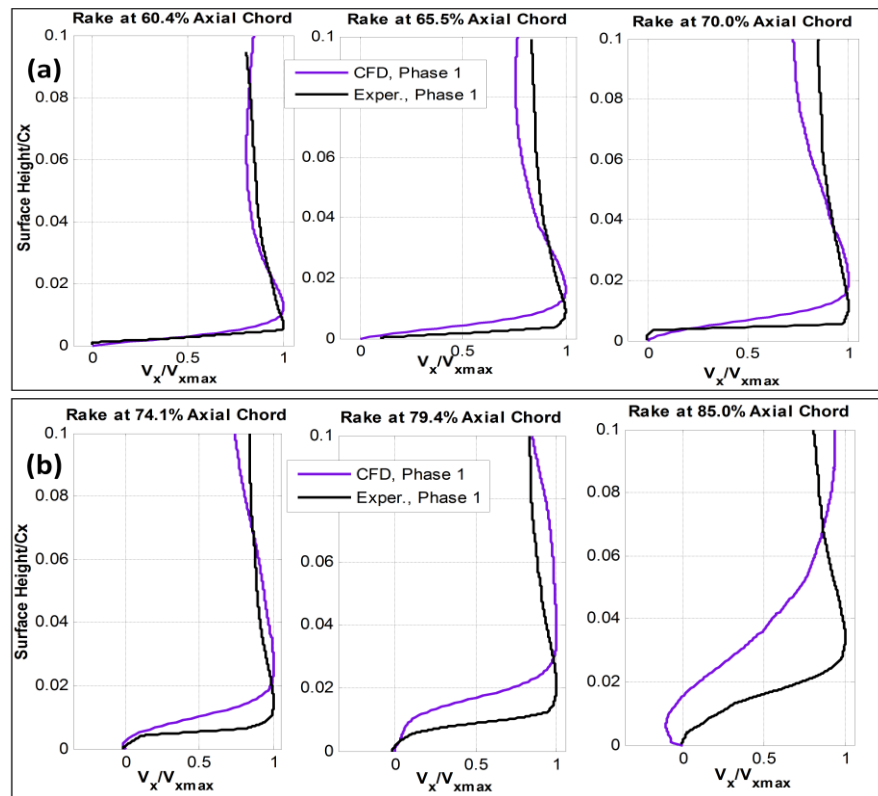


Figure 7.14. Comparison of the instantaneous boundary layer profiles of axial velocity the Aft-Loaded L1A

Chapter 7. The Aft-Loaded L1A Blade with Upstream Wake Generators

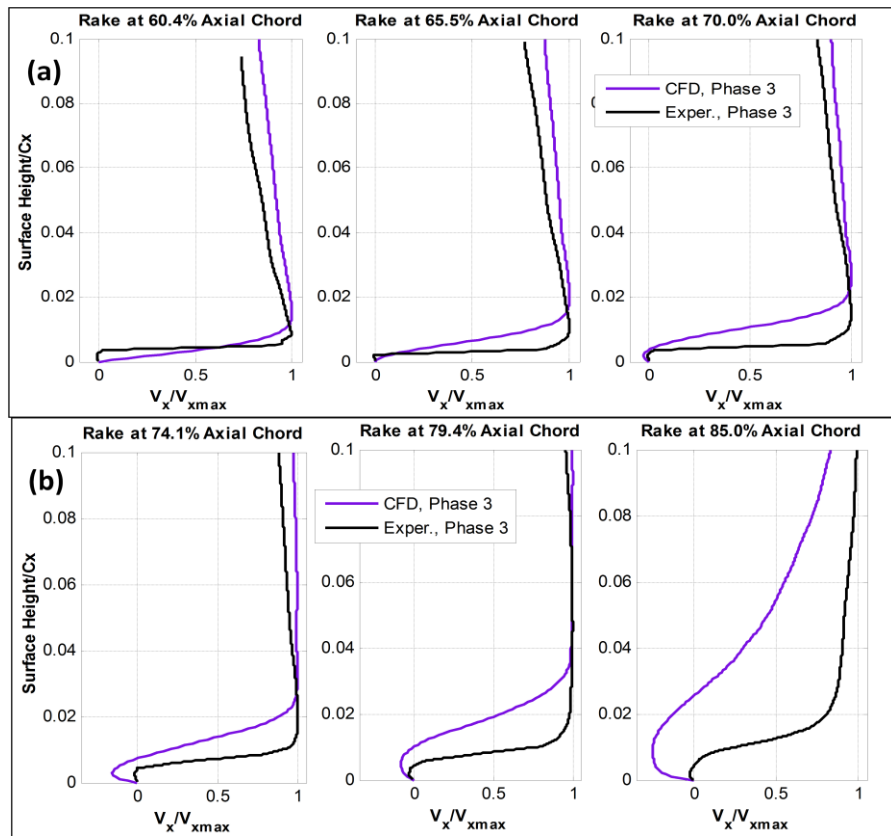


Figure 7.15. Comparison of the instantaneous boundary layer profiles of axial velocity the Aft-Loaded L1A blade with upstream wake generators to the experimental PIV results for Phase #3 at $Tu = 3.4\%$, $l_m = 40\text{mm}$

Chapter 7. The Aft-Loaded L1A Blade with Upstream Wake Generators

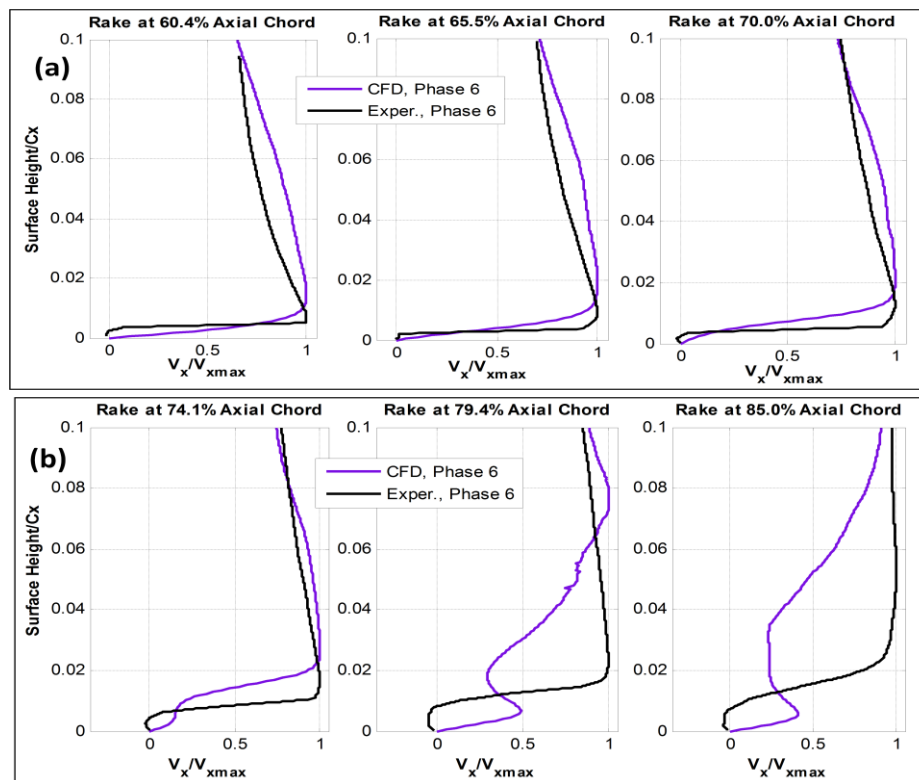


Figure 7.16. Comparison of the instantaneous boundary layer profiles of axial velocity the Aft-Loaded L1A blade with upstream wake generators to the experimental PIV results for Phase #6 at $Tu = 3.4\%$, $L_m = 40\text{mm}$

7.2.3 Mean Flow Comparisons of the Surface Static Pressure and Boundary Layer Profiles

In Figure 7.17, the mean static pressure coefficient distributions of the Aft-Loaded L1A blade airfoil were compared to baseline CFD cases at low and high inlet turbulent intensities. Figure 7.17(a) shows that the addition of the upstream wake caused an increase in the pressure peak compared to the baseline case, which resulted a higher blade loading for the $Tu = 0.5\%$ case. The separation point was located more downstream at the 69.9% axial chord location with the addition of the upstream wake, compared to the baseline separation point at 64.4% axial chord. The region of constant pressure downstream of the separation point due to the separation region was smaller in the passing wake case compared to the baseline case, which indicated a smaller separation region. The local peak pressure coefficient at 78% axial chord location was due to the motion of the vortices as they lifted off the blade surface and traveled downstream to

Chapter 7. The Aft-Loaded L1A Blade with Upstream Wake Generators

the wake region and this peak was smaller and located more upstream compared to the baseline case. This was due to the reduction in size of the vortices created by the separated shear with the addition of the upstream wake. Downstream of this local pressure peak, the static pressure distribution indicated a reattached boundary layer for both the baseline and the passing wake cases. The blade surface static pressure distribution for the high inlet turbulence intensity case in Figure 7.17(b) was similar to the low inlet turbulence intensity case, with similar trends, when compared with the baseline case. This reason for this trend is shown in Figure 7.18 in the turbulence intensity contours for Phase #1, #3, and #6 at both inlet turbulence intensity cases. The turbulence produced by the upstream wake increased to the freestream turbulence to a similar level for both cases and therefore the change in inlet turbulence intensity had no effect prediction of the flowfield with the addition of upstream wakes. Yet, the baseline case showed at higher inlet turbulence intensity a reduction of the separation region. The addition of the upstream wake caused an increase in the blade loading and a decrease in the separated flow present on the blade suction surface for both the low and high inlet turbulence intensity cases.

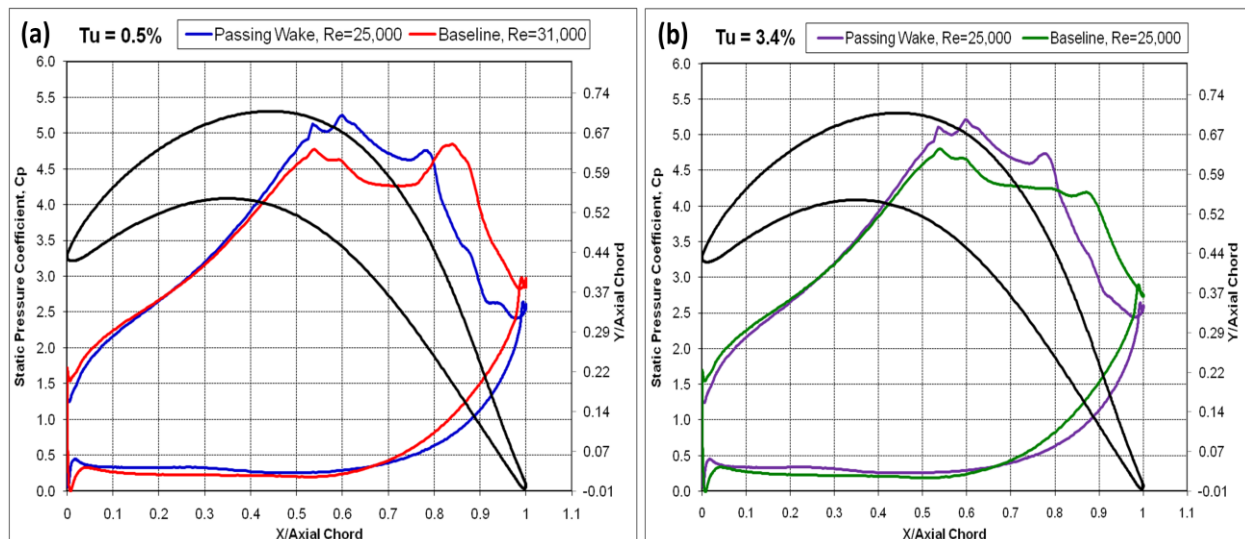


Figure 7.17. Comparison of surface static pressure coefficient of the Aft-Loaded L1A blade with upstream wake generators to the baseline CFD simulation at $Re = 25,000$ (a) $Tu = 0.5\%$ and (b) $Tu = 3.4\%$

Chapter 7. The Aft-Loaded L1A Blade with Upstream Wake Generators

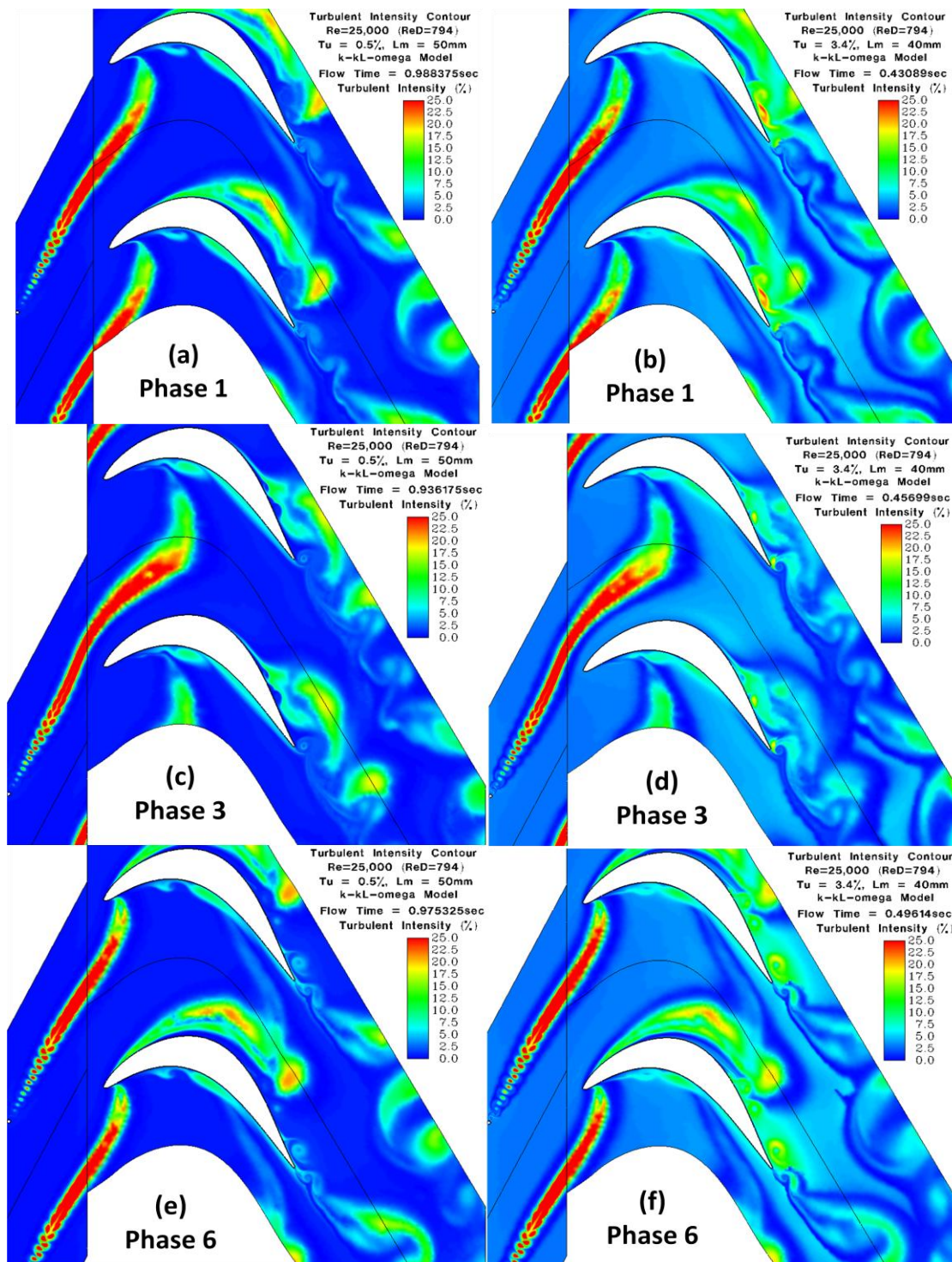


Figure 7.18. Comparisons of the instantaneous turbulence intensity at Phase #1, #3, and #6 for $Re = 25,000$ with wakes, at $Tu = 0.5\%$, $L_m = 50\text{mm}$ and $Tu = 3.4\%$, $L_m = 40\text{mm}$

Chapter 7. The Aft-Loaded L1A Blade with Upstream Wake Generators

Time-averaged values of the boundary layer velocity profiles were obtained at ten axial chord locations normal to the blade surface for both the upstream passing wake cases, at both low and high inlet turbulence intensity. The axial velocity was plotted in order to compare the amount of reversed flow present in the separation region. The result is shown in Figures 7.19 and 7.20. The separation point for the $Tu = 0.5\%$, $l_m = 50\text{mm}$ case (Fig 7.17(a)) was predicted to occur at the 69.0% axial chord location, which was more downstream than the baseline case separation point at the 64.4% axial chord location. The boundary layer profiles confirmed the trends observed in the surface static pressure coefficient comparisons. There was significantly less separated flow present with the addition of the passing upstream wake compared to the baseline case. Figure 7.19(b) shows the mean flow boundary layer reattached to the blade surface slightly downstream of the 89% axial chord location while the baseline case remained separated to the blade trailing edge. For the high turbulence intensity case, the separation point was located at the 63.3% and 67.3% axial chord position for the baseline case and with upstream passing wakes, respectively. For both the low and high turbulent intensities, the addition of the passing wake caused a significantly smaller separation region as compared to the baseline case as shown in Figure 7.20(a)-(b) for the high inlet turbulence intensity case.

Chapter 7. The Aft-Loaded L1A Blade with Upstream Wake Generators

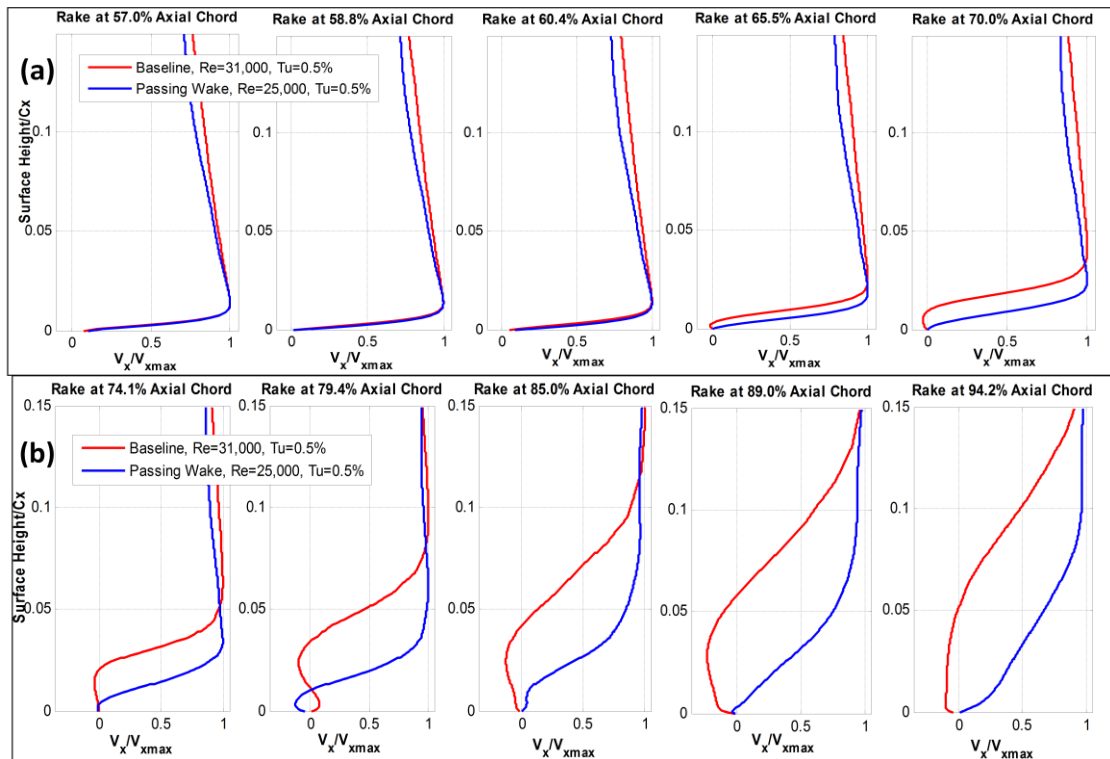


Figure 7.19. Comparison of the mean boundary layer profiles of axial velocity the Aft-Loaded L1A blade with upstream wake generators to the baseline CFD simulation at $Re = 25,000$, $Tu = 0.5\%$

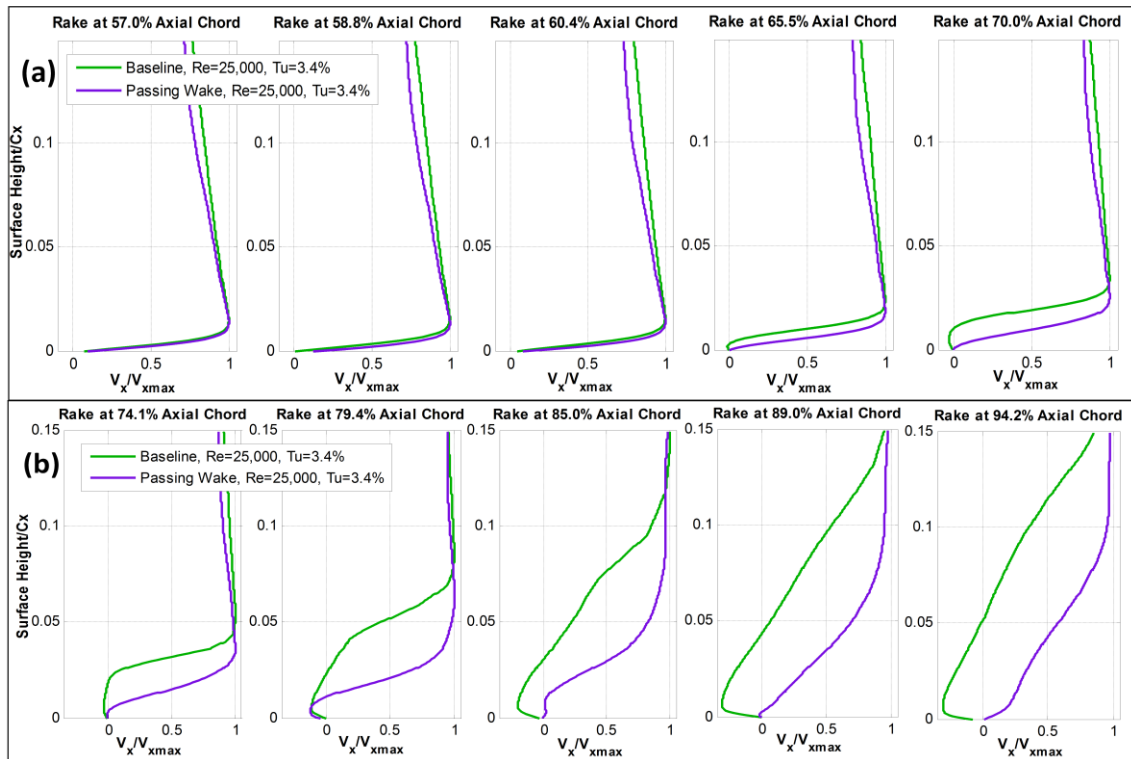


Figure 7.20. Comparison of the mean boundary layer profiles of axial velocity the Aft-Loaded L1A blade with upstream wake generators to the baseline CFD simulation at $Re = 25,000$, $Tu = 3.4\%$

Chapter 7. The Aft-Loaded L1A Blade with Upstream Wake Generators

7.2.4 Total Pressure Loss Coefficient Predictions

The wake total pressure loss coefficient distribution and the integrated value are shown in Figure 7.21 and Table 6.3, respectively. For $Tu = 0.5\%$ case, the addition of upstream wake caused a 17% and 36% decrease in the peak and integrated loss coefficient, respectively. The increased amount of turbulence produced from the wake re-energized the boundary layer and delayed the separation event. The low turbulence intensity case showed good agreement, 98%, with the experimental loss coefficient measurement and 87% agreement in the integrated loss coefficient. For the $Tu = 3.4\%$ case, the addition of the upstream wake caused a 3% increase in the peak loss coefficient and 15% decrease in the integrated loss coefficient, respectively. Good agreement with the experimental loss coefficient measurements was achieved, with 95% agreement in the peak loss coefficient and 98% agreement in the integrated value for the high turbulence intensity case. The peak loss coefficients in the baseline cases were significantly under-predicted compared to the experimental results as presented in Section 6.1.4 and 6.2.4. Better comparisons were made with the integrated wake loss coefficients, with 87% and 98% agreement with experimental results for the low and high turbulence intensity baseline cases, respectively.

Chapter 7. The Aft-Loaded L1A Blade with Upstream Wake Generators

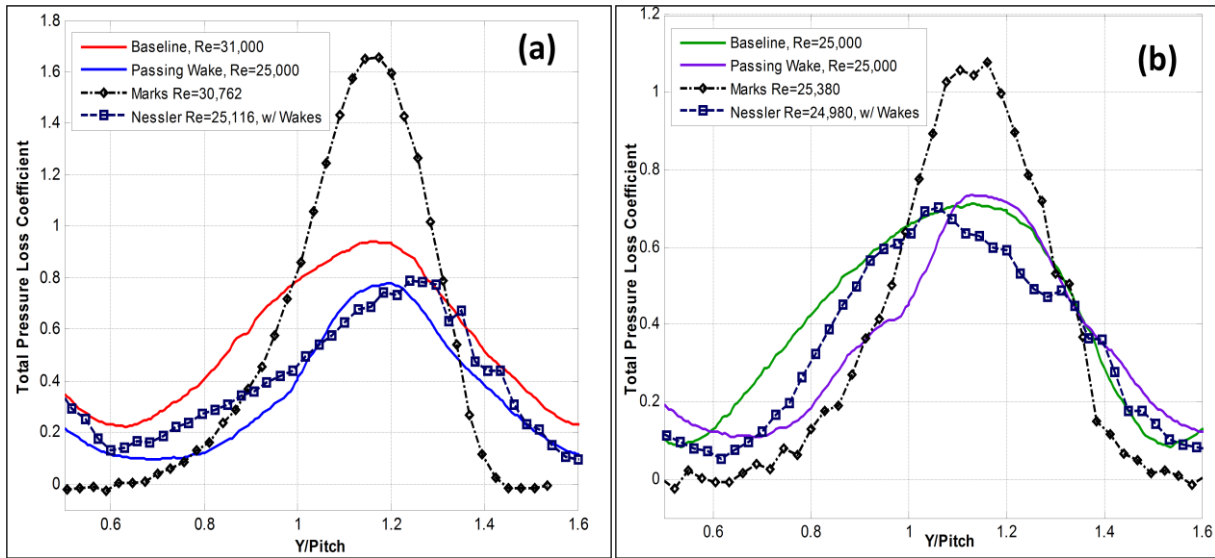


Figure 7.21. Comparison of total pressure loss coefficient with experimental [35,37] for the baseline and addition of wakes (a) $Tu = 0.5\%$ and (b) $Tu = 3.4\%$ at $Re = 25,000$ for the Aft-Loaded L1A blade airfoil

Re	Tu	$l_m(mm)$	Integrated Loss Coefficient		Maximum Loss Coefficient	
			CFD	Experimental	CFD	Experimental
25,000, Passing Wake	0.5%	50	0.3639	0.4187	0.7793	0.7912
31,000, Baseline	0.5%	50	0.5772	0.5526	0.9391	1.6549
25,000, Passing Wake	3.4%	40	0.3736	0.3804	0.7344	0.7013
25,000, Baseline	3.4%	40	0.4383	0.3893	0.7119	1.0774

Table 7.3. Maximum and integrated total pressure loss coefficient comparison with the experimental [35,37] results for the Aft-Loaded L1A blade with and without upstream wake generators

7.3 Summary of Results

The flowfield of the Aft-Loaded L1A blade airfoil subjected to traversing upstream wakes was simulated using the $k-k_L-\omega$ model at an inlet Reynolds number of 25,000. The upstream wakes were generated by a circular cylinder traversing in the pitchwise direction. This setup was used to simulate the periodic flowfield associated with rotor/vane flow interactions encountered in a multistage LPT geometry, where wakes shed from an upstream vane propagate

Chapter 7. The Aft-Loaded L1A Blade with Upstream Wake Generators

and impinge on a downstream rotor. CFD simulations were completed at low and high inlet turbulent intensities and compared to experimental cascade measurements taken by Nessler *et al.* [37,48], and the baseline CFD results.

The flowfield of the upstream wake generator was investigated in order to characterize the wake produced by the circular cylinder impinging upon the downstream Aft-Loaded L1A blade airfoil. The boundary layer on the wake generator surface was predicted as laminar at both the low and high inlet turbulent boundary conditions. The wake generator produced a von Karman vortex street in the wake region that dissipated as the wake reached blade flow passage. Comparisons were made with experimental results of single point velocity measurements placed in the blade passage. The wake produced in the CFD results had a higher velocity deficit as compared to the experimental results. The difference could be attributed to the surface of the experimental wake generator not being perfectly circular and smooth. This could have caused the boundary to become turbulent, reducing the wake peak velocity deficit in the experimental results. Future work will consist of completing simulations with the wake generator ran as a turbulent boundary layer in order achieved better agreement with the experimental wake deficit measurements.

Investigations of the flowfield of the Aft-Loaded L1A blade showed the traversing wakes had a significant effect on the blade loading, behavior of the boundary layer, unsteady vortex shedding, and total pressure loss coefficient. The addition of the wakes increased the blade loading and caused the separation location to be moved further downstream. The traversing wake could be thought of as negative jet flowing toward the origin of the wake superimposed on a uniform freestream [50]. This negative jet causes the fluid in an individual wake segments to

Chapter 7. The Aft-Loaded L1A Blade with Upstream Wake Generators

convect toward, and impinge on the suction surface. Thus, downstream of wake center the negative jet accelerated the flow, while upstream of the wake center, the negative jet decelerated the flow [51]. The suction surface shear layer produced unsteady vortices that were significantly smaller than the baseline CFD results and caused the separation region in the mean flow to reduce. Similar predictions of the flowfield were made at both the low and high inlet turbulence intensity. Also, the CFD result showed similar unsteady behavior as the experimental results. Good agreement was achieved in the prediction of the both the peak and integrated loss coefficient with over 85% agreement with the experimental measurements. The Walters and Leylek [2] $k-k_L-\omega$ transitional flow model successfully demonstrated the ability to predict the separated flowfield of Aft-Loaded L1A blade subjected to an unsteady traversing wake. This shows that the $k-k_L-\omega$ flow model can provide the same prediction capability for the more complicated unsteady flowfields found in a multistage LPT blade geometry.

CHAPTER EIGHT**8. Summary and Conclusions**

The flowfields found in low pressure turbine stages are known to be affected by separation and transitional flow effects associated with operational situations and design factors. Separation and transitional flow can occur when LPT blades are subjugated to low Reynolds number flow effects due to the change in density associated with high altitude operation. Also, there is design pressure to increase the blade airfoil loading level in order to reduce weight and cost of the turbomachinery. Both factors lead to an increased probability of separated and transitional flow in turbine blade passages. High altitude operation and high stage work are known to affect the aerodynamic performance of the low pressure turbine stages. Laminar and transitional flow boundary layers may develop on the blade surface as result of both these situations. The increase in the region of adverse pressure gradients on the aft portion of the blade may cause the laminar flow boundary layer to separate from the surface. Also, the region of the boundary layer that undergoes laminar-to-turbulent boundary layer transition may increase. There is a need for CFD to provide improved prediction of separated and transitional flow for turbomachinery designs, especially for turbines operating at high altitude. The best CFD method must provide a balance between increased fidelity for accurate modeling of the complicated flow physics associated with low Reynolds number effects, and be applicable to complex geometries without being too computationally expensive.

The current study sought to use a selected CFD method to predict both laminar separation and transitional flow effects in low pressure turbine blades at low inlet Reynolds numbers, and to report the accuracy that was achieved. This CFD method was to be based on a RANS turbulence

Chapter 8. Summary and Conclusions

model that was developed to predict aerodynamic flow effects at low Reynolds numbers. Use of the RANS CFD method was established as a requirement for this study because of its current wide adoption and computational efficiency with respect to LES and DNS CFD methods. This study also sought to find the best RANS turbulence model already implemented into existing CFD software, in other words, to establish the state of the art for practical CFD predictions of low Reynolds number turbine flows. Ansys[®] Fluent was chosen as the CFD software and wide adoption in the CFD community. Turbulence models available in Fluent were investigated to determine if they could provide the flow prediction capability to complete the goals of this study. The $k-k_L-\omega$ model developed by Walters and Leylek [2] to model the laminar-to-turbulent boundary layer transition process was chosen as the turbulence model to complete this study.

Fluent CFD with the Walters and Leylek [2] $k-k_L-\omega$ model was applied to flow predictions for three types of LPT blade airfoils for which cascade tests had been made in the AFRL Low Speed Wind Tunnel. The LPT blade airfoils were classified based on the blade loading characteristics defined using the Zweifel blade force coefficient, Z . Experimental flow measurements of the surface static pressure, boundary layer flow velocities using Particle Image Velocimetry, and wake losses were made in the cascade test over a wide range of Reynolds number and freestream conditions. The CFD models simulated the same flow conditions, and the predictions were compared to the corresponding experimental measurements for each LPT blade airfoil. Also, additional comparisons were made with predictions available from other CFD studies.

The Lightly Loaded LPT blade airfoil with $Z = 0.94$ representing a mid-loaded blade design was used initially to determine the best choice of RANS turbulence model to complete the objectives of this study. The inlet Reynolds number range of 10,000 – 100,000 was simulated

Chapter 8. Summary and Conclusions

using the Lightly Loaded blade CFD model. Based on flowfield comparisons with the $k-\omega(SST)$ and $k-\varepsilon$ models, the Walters and Leylek [2] $k-k_L-\omega$ model achieved the best agreement with experimental results for the prediction of the amount of viscous losses produced and the magnitude of the total pressure loss in the wake region. Good agreement was also obtained for the effect of Reynolds number sensitivity of the loss coefficient with the experimental results. Also, a parametric study on the effect of the inlet turbulent boundary conditions showed the inlet freestream turbulence intensity had a strong effect on the turbulent transition point and total pressure loss coefficient. A study on the effect of the inlet turbulent length scale showed a second order sensitivity effect to the turbulent transition location and the peak loss coefficient. The inlet turbulent length scale caused a 10% variation in the integrated loss coefficient due to the changes in the wake region. The boundary layer of the Lightly Loaded blade airfoil was mostly attached and transitional, and showed mild separation at the trailing edge at Reynolds numbers below 50,000 mainly due to its low blade loading level. The $k-k_L-\omega$ model successfully demonstrated that it could predict the low Reynolds number aerodynamic effects on the Lightly Loaded blade, and yielded confidence that it could provide same type of prediction capability for highly loaded LPT geometries.

The Walters and Leylek [2] $k-k_L-\omega$ model was applied to low Reynolds flow prediction for the Highly Loaded blade airfoil ($Z = 1.07$), an aft-loaded LPT blade design. Flowfield comparisons with experimental cascade data [36,38-40] showed good agreement in prediction of the separation and reattachment at inlet Reynolds numbers of 100,000, 50,000, and 25,000. The $k-k_L-\omega$ model showed a better qualitative response to the separated shear layers yet, the two-dimensional CFD predictions showed an over-prediction on the size of the separation region. So, a three-dimensional CFD model of the Highly Loaded blade was simulated to investigate the

Chapter 8. Summary and Conclusions

addition of the spanwise dimension on the flowfield predictions. The observed unsteady vortex shedding was largely two-dimensional with small spanwise variations in the separation region and produced a similar prediction of the flowfield as the two-dimensional predictions. It is noted that the Walters and Leylek [2] $k-k_L-\omega$ model was not specifically design to model boundary layer transition in separated shear layers [30] or due to spanwise instabilities [2]. Yet, overall, it provided effective prediction of the low Reynolds number aerodynamic effects of the Highly Loaded blade.

The most challenging LPT blade design used for the application of the Walters and Leylek [2] $k-k_L-\omega$ model was the Aft-Loaded LIA blade airfoil. This geometry with a $Z = 1.23$, was 15% more loaded and had a much stronger adverse pressure gradient present on the aft portion of the suction surface than the Highly Loaded blade airfoil. Simulations were completed at individual inlet Reynolds numbers of 25,000 and 50,000 at low and high inlet turbulent intensities. At low inlet turbulent intensities, good agreement was achieved with experimental results on prediction of the separation locations and the qualitative flow response to the unsteady vortex generation from the separated shear layers. Also, over 80% agreement with the experimental [35] results was achieved in the prediction of the amount of viscous losses present within the wake region, but the higher dissipation predicted with the $k-k_L-\omega$ model caused those losses to be distributed more across the wake.

At high inlet turbulent intensities, the loading of the Aft-Loaded L1A blade airfoil was predicted effectively with over 87% agreement with the experimental results [35] for the integrated loss coefficient predictions. Yet, the size of the separation region was under-predicted and the unsteady effects from the vortex shedding were not present compared to the experimental results. The absence of unsteady vortex shedding could be attributed the Reynolds averaging

Chapter 8. Summary and Conclusions

effect present within all RANS turbulence models where any unsteadiness produced from freestream turbulence will be significantly damped. Overall, the $k-k_L-\omega$ model did provide effective prediction of the aerodynamic flow effects for this very challenging LPT blade geometry, but some inaccuracies were observed at high inlet turbulent intensities. Yet, the $k-k_L-\omega$ model showed superior flowfield prediction capability compared to the fully turbulent $k-\omega(SST)$ model, similar to results obtained for the Lightly Loaded blade airfoil at the low inlet turbulent intensities.

The effect of a periodically passing upstream wake on the separation region of the Aft-Loaded L1A blade airfoil was studied using the $k-k_L-\omega$ model. A CFD model of the experimental cascade setup of Nessler *et al.* [37,48] was made to simulate the flowfield. The model and cascade test were designed to generate wake similar what are normally encountered in a multistage LPT geometry, where the wakes shed from one stage travel downstream and impinge on the successive stage. The flowfield of the wake generator was characterized, and the laminar boundary layer produced a von Karman vortex street in the wake region. Differences in the wake deficit were observed compared with the experimental results due the cylindrical wake generators used in cascade setup not being hydraulically smooth, and producing a turbulent boundary layer. Future work will investigate methods of tripping the boundary around the wake generator to turbulent in order to achieve closer agreement with experimental velocity deficit measurements. The addition of the wakes increased the Aft-Loaded L1A blade loading and caused the separation location to be moved further downstream compared to the baseline simulations. The separation region significantly reduced in size when it was impinged upon by the upstream wakes. The influence of the upstream wake caused lower total pressure loss and

Chapter 8. Summary and Conclusions

improved the aerodynamic performance. Overall good agreement was achieved with the experimental PIV and loss coefficient measurements taken by Nessler *et al.* [37,48].

The prediction capability of Walters and Lekylek [2] $k-k_L-\omega$ model was characterized in the prediction of separation and transitional flow in LPT blade airfoils. Greater than 80% agreement with experimental results was achieved on the prediction of several flowfield parameters. The $k-k_L-\omega$ model provided good agreement for attached transitional flows in the prediction of the transition location, peak and integrated loss coefficient. When the flow was separated, good agreement was observed in the prediction of the separation location and the integrated loss coefficient. Also, the $k-k_L-\omega$ model qualitatively predicted unsteady vortex shedding at low turbulent intensity and the pressure distribution due to the separated shear layers. Differences were observed with less than 80% agreement in the prediction of separation region and the peak loss coefficient. Also, the spanwise variation of the separation region, the unsteady vortex shedding at high turbulent intensities was not well predicted using the $k-k_L-\omega$ model. The $k-k_L-\omega$ model main limitation was the absence of the unsteady behavior of the small-scale turbulent structures. The prediction capability of the Walters and Leylek [2] $k-k_L-\omega$ model is summarized in Table 8.1.

This dissertation has presented a complete evaluation of the Walters and Leylek [2] $k-k_L-\omega$ model for the prediction of low Reynolds number flows in low pressure turbine blades. The $k-k_L-\omega$ model accuracy was judged to be sufficient for understanding the separation and transition characteristics in the cases studied. The Walters and Leylek [2] $k-k_L-\omega$ model provided a more accurate method for aerodynamic loss predictions compared to conventional, widely used RANS turbulence models at low inlet Reynolds numbers. Successful flowfield predictions were

Chapter 8. Summary and Conclusions

achieved with data from several low Reynolds number turbine flow applications. This research has contributed a characterized and assessed model for improved prediction of low Reynolds number turbine flows and design applications.

	Greater than 80% agreement	Less than 80% agreement
Attached Transitional Flow	Transition Location	
	Peak Loss Coefficient	
	Integrated Loss Coefficient	
Separated Flow	Separation Location	Peak Loss Coefficient
	Integrated Loss Coefficient	Separation Region
	Pressure Distribution	Spanwise Variation of the Separation Region
	Unsteady Vortex Shedding at Low Tu	Unsteady Vortex Shedding at High Tu
		Unsteady Behavior of the Small-Scale Turbulent Structures

Table 8.1. Summary of the prediction capability achieved using Walters and Leylek [2] $k-k_L-\omega$ model for the prediction of low Reynolds number effects

8.1 Future Work

Based on the results reported in this study, the Walters and Leylek [2] $k-k_L-\omega$ model was applied to a multistage LPT geometry based on the Lightly Loaded blade airfoil operating a low Reynolds numbers [52,53]. Steady flow simulations using the mixing plane numerical method were completed at both a nominal and high altitude operating conditions corresponding to an order of magnitude decrease in the inlet Reynolds number. This model provided a more detailed understanding of the aerodynamic loss mechanisms present in a multistage LPT operating at low Reynolds number. Experimental results are needed to fully validate the CFD predictions using

Chapter 8. Summary and Conclusions

the $k-k_L-\omega$ model technique for the multistage LPT geometry. Unsteady CFD simulations are also needed to compare with steady-state predictions using the mixing plane CFD technique.

Additional CFD work could include applying flow control techniques such as vortex generating jets and providing computational support for additional experimental work completed by Woods *et al.* [39] on the Highly Loaded blade airfoil. The CFD model would have to be three-dimensional in order to model the shape of the vortex-generating jet. It could also be used to simulate steady and pulsed jet operation. Additionally, CFD modeling using the $k-k_L-\omega$ model in plasma-based flow control could also be completed in support of future experiment that will be completed by Chris Marks at the AFRL LSWT. Since the electric field equations cannot be implemented into the Fluent CFD software, the effect of the plasma flow control can be modeled as an applied body force to the blade surface similar to Thompson [54] and could be used in both two and three-dimensional CFD models.

The Aft-Loaded L1A blade was the most challenging LPT blade airfoil geometry to predict low Reynolds number aerodynamic effects. Simulations could be completed using the more advanced LES CFD method to determine if it could provide better prediction capability compared to Walters and Leylek [2] $k-k_L-\omega$ model. This would be first time the LES CFD method would be applied to the Aft-Loaded L1A blade, and would give a unique contribution to low Reynolds number turbine prediction work.

Further improvements of the Walters and Leylek $k-k_L-\omega$ model can be explored in order enhance the prediction capability for transitional boundary layer flows. For instance, the $k-k_L-\omega$ model could be modified to account for transitional flow due to spanwise instabilities in three-dimensional CFD models. The laminar-to-turbulent transitional flow process is highly three-dimensional, and spanwise instabilities are known to cause initially laminar and coherent

D. Sanders

188

Chapter 8. Summary and Conclusions

vortices to breakdown into fine-scale turbulent structures [47]. Also, the $k-k_L-\omega$ model could be modified to account for transition due to separated flow by including correlations to model this effect such as those included in the Menter *et al.* [26] $\gamma-Re_\theta$ model and the Praisner and Clark [24] models. The flowfields in both the Highly Loaded and Aft-Loaded L1A blade airfoils were dominated by separated flow and closer agreement with the experiments could likely be achieved if this modification were implemented in the $k-k_L-\omega$ model.

References

- [1] Sharma, O., “Impact of Reynolds Number on LP Turbine Performance”. Minnowbrook II 1997 Workshop on Boundary Layer Transition in Turbomachines, NASA/CP-1998-206958, 1998.
- [2] Walters, D.K., and Leylek, J.H., “A New Model for boundary Layer Transition Using a Single Point RANS Approach”, *Journal of Turbomachinery*, Vol. 126, January 2004, pp 193–202.
- [3] Halstead, D.E., D.C. Wisler, T.H. Okiishi, G.J. Walker, H.P. Hodson and H.W. Shin, “Boundary Layer Development in Axial Compressors and Turbines Part 1 of 4: Composite Picture.” ASME Paper No. 95-GT-461, 1995.
- [4] Hodson H.P. and Dawes W.N., “On the Interpretation of Measured Profile Losses in Unsteady Wake-Turbine Blade Interaction Studies”, ASME Paper No. 96-GT-494, 1996.
- [5] Dietz, A.J. and Ainworth, R.W., “Unsteady Pressure Measurements on the Rotor of a Model Turbine Stage in a Transient Flow Facility”, ASME Paper No. 92-GT-156, 1992.
- [6] Langston, L.S., “Secondary Flows in Axial Turbines- A Review”, *Annals of the New York Academy of Sciences*, pp. 11-26, 2001.
- [7] Munson, B.R., Young, D.F., and Okiishi, T.H., “Fundamental of Fluid Mechanics”, 4th Edition, John Wiley & Sons, Inc., 2002.
- [8] White, F., “Fluid Mechanics”, 4th Edition, McGraw-Hill, 1999.
- [9] Schetz J.A., “Foundations of Boundary Layer Theory for Momentum, Heat, and Mass Transfer”, Prentice –Hall, Inc., 1984.
- [10] VKI Lectures Series, “Advances in Laminar-Turbulent Transition Modeling”, Wright State University, Dayton, OH, January 12-15, 2009.
- [11] Wilcox, D.C., “Turbulence Modeling for CFD”, DCW Industries, Inc., 2005.
- [12] Cebeci, T., “Analysis of Turbulent Flows”, 2nd Revised and Expanded Edition, Elsevier Publishing, 2004.
- [13] Tannehill, J.C., Anderson, D.A., and Pletcher, R.H., “Computational Fluid Mechanics and Heat Transfer”, 2nd Edition, Tayler & Francis, In., 1997.
- [14] Enomoto, S., Hah, C., and Loelbach, J., “Numerical Investigation of a Low Reynolds Number Flow Field in a Turbine Blade Row”, AIAA 2001-0524.
- [15] Singh, N., Ghia, K., and Ghia, U., “Simulation of Separated Flow inside a Low-Pressure Turbine Cascade”, AIAA 2005-1273.
- [16] Rizzetta, D.P., and Visbal M.R., “Numerical Investigation of Active Flow Control for a Transitional Highly-Loaded Low Pressure Turbine”, AIAA 2005-5020
- [17] Rizzetta, D.P., and Visbal M.R., “Numerical Investigation of Plasma-Based Flow Control for a Transitional Highly-Loaded Low Pressure Turbine”, AIAA 2007-938.
- [18] Lake, J.P., “Flow Separation Prevention on a Turbine Blade in Cascade at Low Reynolds Number” *PhD Dissertation*, Air Force Institute of Technology, AFIT/DS/ENY/99-01, 1999.
- [19] Mittal, R., Venkatasubramanian, S., and Najjar, F.M., “Large-Eddy Simulation of Flow Through a Low-Pressure Turbine Cascade”, AIAA 2001-2560.

- [20] Raverdy, B., Mary, I., Sagaut, P., and Liamis, N., “High-Resolution Large-Eddy Simulation of Flow Around Low-Pressure Turbine Blade”, *AIAA Journal*, Vol. 41, No. 3, March 2003, pp. 390-397.
- [21] Sekar, S., and Voke, P.R., “Large-Eddy Simulation of Unsteady Surface Pressure Over a Low-Pressure Turbine Blade due to Interaction of Passing Wakes and Inflexional Boundary Layer”, *Journal of Turbomachinery*, Vol. 128, April 2006, pp 221–231.
- [22] Dorney, D.J., Lake, J.P., King P.I., and Ashpis, D.E., “Experimental and Numerical Investigation of Losses in Low Pressure Turbine Blade Rows”, AIAA 2000-0737.
- [23] Suzen, Y.B., Huang, P.G., Volino, R.J., Corke, T.C., Thomas, F.O., Huang, J., Lake, J.P., and King, P.I., “A Comprehensive CFD Study of Transitional Flows in Low-Pressure Turbines Under a Wide Range of Operating Conditions”, AIAA Paper No. 2003-3591.
- [24] Praisner, T.J., and Clark, J.P., “Predicting Transition in Turbomachinery, Part I – A Review and New Model Development”, ASME Paper No. GT-2004-54108.
- [25] Praisner, T.J., Grover, E.A., Rice, M.J., and Clark, J.P., “Predicting Transition in Turbomachinery, Part II – Model Validation and Benchmarking”, *Journal of Turbomachinery*, Vol. 129, January 2007, pp 14 – 22.
- [26] Menter, F.R., Langtry, R.B., Likki, S.R., Suzen, Y.B., Huang, P.G., and Volker, S., “A Correlation-Based Transition Model Using Local Variables- Part I: Model Formulation”, *Journal of Turbomachinery*, Vol. 128, July 2006, pp 413 – 422.
- [27] Langtry, R.B., Menter, F.R., Likki, S.R., Suzen, Y.B., Huang, P.G., and Volker, S., “A Correlation-Based Transition Model Using Local Variables- Part II: Test Cases and Industrial Applications”, *Journal of Turbomachinery*, Vol. 128, July 2006, pp 423 – 434.
- [28] Moore, J.G. and Moore, J., “High Turbulence Turbine Cascade Performance Using the MARV Reynolds Stress Model”, AIAA 2009-1322.
- [29] Holloway, D.S., Walters, D.K., and Leylek, J.H., “Prediction of Unsteady, Separated Boundary Layer over a Blunt Body for Laminar, Turbulent, and Transitional Flow”, *International Journal for Numerical Methods in Fluids*, Vol. 45, March 2004, pp 1291-1351.
- [30] Walters, D.K., and Leylek, J.H., “Prediction of Boundary-Layer Transition on Turbine Airfoil Profile Losses”, ASME Paper No. IMECE 2003-41420.
- [31] Walters, D.K., and Leylek, J.H., “Computational Fluid Dynamics Study of Wake-Induced Transition on a Compressor-Like Flat Plate”, *Journal of Turbomachinery*, Vol. 127, January 2005, pp 52–63.
- [32] Yocum, A.M., O’Brien W.F., “Separated Flow in a Low Speed Two-Dimensional Cascade: Part I- Flow Visualization and Time-Mean Velocity Measurements. *Journal of Turbomachinery*, Vol. 115, 409-420, 1993.
- [33] Hill P., and Peterson C, “Mechanics and Thermodynamics of Propulsion” 2nd edition, Addison-Wesley Publishing Company Inc., 1992.
- [34] McQuilling, M., “Design and Validation of a High-Lift Low-Pressure Turbine Blade”, PhD Dissertation, Wright State University, Dayton, OH, August 2007.
- [35] Marks, C., Sondergaard, R., Wolff, M., and Estevadeordal, J., “PIV Investigation of a Highly-Loaded LPT Blade Using a Curved Laser-Sheet”, AIAA 2009-301.
- [36] Garmoe, T.L., “Characterization of the GH1R Low Pressure Turbine” *Master Thesis*, Air Force Institute of Technology, AFIT/DS/ENY/05-S02, 2005.

- [37] Nessler, C., Marks, C., Sondergaard, R., and Wolff, M., "Investigation of Losses on a Highly Loaded Low Pressure Turbine with Unsteady Wakes", AIAA 2009-302.
- [38] Bons, J.P., Sondergaard, R., and Rivir, R.B., "Control of Low-Pressure Turbine Separation Using Vortex Generator Jets", AIAA 1999-0367.
- [39] Woods, N., Sondergaard, R., McQuilling, M., and Wolff, M., "Investigation of Separation Control in Low Pressure Turbine using Pulsed Vortex Generator Jets", AIAA 2006-4450.
- [40] Casey, J.P., "Effect of Dimple Pattern on the Suppression of Boundary Layer Separation on a Low Pressure Turbine Blade", *Master's Thesis*, Air Force Institute of Technology, 2004. AFIT/GAE/ENY/04-M05.
- [41] Estevadeordal J., Gorrell S., Copenhaver W., "PIV study of wake-rotor phenomena in a transonic compressor under various operating conditions", *Journal of Propulsion and Power*, Volume 23, No. 1, pp. 235-242, Jan-Feb 2007.
- [42] Curtis, E., Hodson, H., Banieghbal, M., Denton, J., Howell, R., and Harvey, N., "Development of Blade Profiles for Low-Pressure Turbine Applications", *Journal of Turbomachinery*. Vol. 119, 531-538, 1997.
- [43] Clark, J. and Koch, P. "Benchmark Turbines for the Guidance of Design System Improvements", 2006 Turbine Engine Technology Symposium, Dayton, OH., September 14, 2006.
- [44] Sondergaard, R., Rivir, R., Bons, J., "Control of Low-Pressure Turbine Separation Using Vortex Generator Jets", *Journal of Propulsion and Power*, Vol. 18, No. 4, pp. 889-895, 2002.
- [45] Rizzetta, D.P., and Visbal M.R., "Numerical Investigation of Transitional Flow through a Low Pressure Turbine Cascade", AIAA 2003-3587.
- [46] ANSYS Fluent® User's Manual Version 6.3.26, 2006.
- [47] Visbal, M.R., "High Fidelity Simulations of Transitional Flows Past a Plunging Airfoil", AIAA 2009-391.
- [48] Nessler, C., Marks, C., Sondergaard, R., and Wolff, M., "PIV Investigation of Periodic Unsteady Wakes over a Highly Loaded LPT Blade", AIAA 2009-5107.
- [49] Schlichting, H., "Boundary Layer Theory", 6th Edition, McGraw-Hill Book Company Inc., 1968.
- [50] Meyer R.X., "The Effect of Wakes on the Transient Pressure and Velocity Distribution in Turbomachines", *AMSE Journal of Basic Engineering*. Vol. 80, pp. 1544-1552, 1958.
- [51] Hodson, H.P. and Howell, R.J., "Bladerow Interaction, Transition, and High-Lift Aerofoil in Low-Pressure Turbines", *Annual Review of Fluid Mechanics*. Vol. 37, pp. 71-98, 2005.
- [52] Sanders, D.D., O'Brien, W.F., Sondergaard, R., Polanka, M.D., and Rabe, D.C., "A Mixing Plane Model Investigation of Separation and Transitional Flow at Low Reynolds Numbers in a Multistage Low Pressure Turbine", AIAA Paper No. 2009-1467.
- [53] Sanders, D.D., O'Brien, W.F., Sondergaard, R., Polanka, M.D., and Rabe, D.C., "Turbulence Model Comparisons for Mixing Plane Simulations of a Multistage Low Pressure Turbine Operating at Low Reynolds Numbers", AIAA Paper No. 2009-4928.
- [54] Thompson C.T., "Investigations and Simulation of Ion Flow Control over a Flat Plate and Compressor Cascade", M.S. Thesis, Virginia Tech, May 2009.

Appendix I. Comparisons of the Fluent Formulations of Walters and Leylek's Transitional Flow Model

As previously discussed in Section 4.3.1, an updated version of the $k-k_L-\omega$ model has been fully integrated in the newest software release as Ansys® Fluent 12.0. All of the Aft-Loaded L1A blade simulations were completed with the Fluent 12.0 $k-k_L-\omega$ model because Fluent 6.3 version was not implemented as to be used in combination with the sliding mesh model. This model was needed for the Aft-Loaded L1A blade with upstream wake generators simulation. The Lightly Loaded and the Highly Loaded blade airfoil were completed using the Fluent 6.3 $k-k_L-\omega$ model because it was the only version of the model that was available at the time of those simulations.

It was discovered through private conversations with Prof. Walters that the main difference between the two versions of the $k-k_L-\omega$ model was a tuning of the model constants and reformulations of some of the secondary equations. The model was reformulated because the Fluent 12.0 $k-k_L-\omega$ model consistently performed better for several of his CFD test cases. So, flowfield comparisons of the Aft-Loaded L1A blade were made using the different versions of the Walters and Leylek [2] $k-k_L-\omega$ model in order to understand the differences in the prediction flow transition and separation at low Reynolds numbers. Two-dimensional simulations were completed at $Re = 50,000$ at high and low inlet turbulent intensities and compared to experimental results of Marks *et al.* [35] and Clark *et al.* [25] CFD results.

A.1 Fluent Formulations of the k - k_L - ω Model

This section describes the two formulations of the k - k_L - ω model inherent in the Fluent CFD software. Walters and Leylek [2] k - k_L - ω model was first implemented as a beta addition to the Fluent 6.3 CFD software. It was learned that the k - k_L - ω model was not programmed to function in conjunction with the sliding mesh or mixing plane numerical methods. The k - k_L - ω model was fully integrated in the Fluent 12.0 release of the CFD software. The sliding mesh numerical method was needed for Aft-Loaded L1A blade simulations using the passing wake generators so the Fluent 12.0 formulation was used for Aft-Loaded L1A blade airfoil simulations. The next section presents the transport equations for each of the k - k_L - ω model formulations.

A.1.1 Fluent 6.3 k - k_L - ω Model

The transport equations for the Fluent 6.3 model for the turbulent kinetic energy (k_T), laminar kinetic energy (k_L), and the specific dissipation rate (ω) which were given as

$$\frac{Dk_T}{Dt} = P_{k_T} + R + R_{NAT} - \omega k_T - D_T + \frac{\partial}{\partial x_j} \left[\left(\nu + \frac{\alpha_T}{\sigma_k} \right) \frac{\partial k_T}{\partial x_j} \right] \quad (A.1)$$

$$\frac{Dk_L}{Dt} = P_{k_L} - R - R_{NAT} - D_L + \frac{\partial}{\partial x_j} \left[\nu \frac{\partial k_T}{\partial x_j} \right] \quad (A.2)$$

$$\frac{D\omega}{Dt} = P_\omega + C_{\omega R} \frac{\omega}{k_T} (R + R_{NAT}) - C_{\omega 2} \omega^2 - C_{\omega 3} f_\omega \alpha_T \left(\frac{\lambda_{eff}}{\lambda_T} \right)^{4/3} \frac{\sqrt{k_T}}{d^3} + \frac{\partial}{\partial x_j} \left[\left(\nu + \frac{\alpha_T}{\sigma_\omega} \right) \frac{\partial \omega}{\partial x_j} \right] \quad (A.3)$$

A detailed description of all the model variables and dependencies was given in Walters and Leylek [2]. The constants for the Fluent 6.3 formulation of the k - k_L - ω model are given in Table A.1.

Summary of Model Constants		
$A_0 = 4.04$	$C_{INT} = 0.75$	$C_{\omega 1} = 0.44$
$A_s = 2.12$	$C_{TS,crit} = 1000$	$C_{\Delta P} = 0.15$
$A_v = 6.75$	$C_{R,NAT} = 0.04$	$C_{\omega 3} = 0.3$
$A_{BP} = 3$	$C_{11} = 3.4 \times 10^{-6}$	$C_{\lambda} = 2.495$
$A_{NAT} = 60$	$C_{12} = 1.0 \times 10^{-9}$	$C_{\mu,std} = 0.09$
$A_{TS} = 200$	$C_R = 0.08$	$Pr_{\theta} = 0.85$
$C_{BP,crit} = 12$	$C_{a,0} = 0.035$	$\sigma_k = 1$
$C_{NAT,crit} = 440$	$C_{\tau,1} = 4360$	$\sigma_{\omega} = 1.17$

Table A.1. Fluent 6.3 k - k_L - ω model constants

A.1.2 Fluent 12.0 k - k_L - ω Model

The transport equations for the Fluent 12.0 model for the turbulent kinetic energy (k_T), laminar kinetic energy (k_L), and the specific dissipation rate (ω) which were given as

$$\frac{Dk_T}{Dt} = P_{k_T} + R + R_{NAT} - \omega k_T - D_T + \frac{\partial}{\partial x_j} \left[\left(\nu + \frac{\alpha_T}{\sigma_k} \right) \frac{\partial k_T}{\partial x_j} \right] \quad (A.4)$$

$$\frac{Dk_L}{Dt} = P_{k_L} - R - R_{NAT} - D_L + \frac{\partial}{\partial x_j} \left[\nu \frac{\partial k_T}{\partial x_j} \right] \quad (A.5)$$

$$\frac{D\omega}{Dt} = C_{\omega 1} \frac{\omega}{k_T} P_{k_T} + \left(\frac{C_{\omega R} \lambda_T}{\lambda_{eff}} - 1 \right) \frac{\omega}{k_T} (R + R_{NAT}) - C_{\omega 2} \omega^2 - C_{\omega 3} f_{\omega} \alpha_T \left(\frac{\lambda_{eff}}{\lambda_T} \right)^2 \frac{\sqrt{k_T}}{d^3} + \frac{\partial}{\partial x_j} \left[\left(\nu + \frac{\alpha_T}{\sigma_{\omega}} \right) \frac{\partial \omega}{\partial x_j} \right] \quad (A.6)$$

A detailed description of all the model variables and dependencies was given in the Fluent 12.0 User Manual [46]. The constants for the Fluent 12.0 formulation of the k - k_L - ω model are given in Table A.2.

Summary of Model Constants		
$A_0 = 4.04$	$C_{INT} = 0.75$	$C_{\omega 1} = 0.44$
$A_s = 2.12$	$C_{TS,crit} = 1000$	$C_{\omega 2} = 0.92$
$A_v = 6.75$	$C_{R,NAT} = 0.02$	$C_{\omega 3} = 0.3$
$A_{BP} = 3$	$C_{11} = 3.4 \times 10^{-6}$	$C_{\omega R} = 1.5$
$A_{NAT} = 200$	$C_{12} = 1.0 \times 10^{-10}$	$C_\lambda = 2.495$
$A_{TS} = 200$	$C_R = 0.12$	$C_{\mu,std} = 0.09$
$C_{BP,crit} = 1.2$	$C_{a,0} = 0.035$	$Pr_\theta = 0.85$
$C_{NC} = 0.1$	$C_{SS} = 1.5$	$\sigma_k = 1$
$C_{NAT,crit} = 1250$	$C_{\tau,1} = 4360$	$\sigma_\omega = 1.17$

Table A.2. Fluent 12.0 $k-k_L-\omega$ model constants

Both Table A.1 and A.2 showed that the model constants are significantly different for the both formulations of the $k-k_L-\omega$ model. Also, the transport equation for the specific dissipation rate (ω) has changed which indicates that distribution of specific dissipation should be different for each of the formulations. The next section compared the flowfield predictions obtained from both the Fluent 12.0 and 6.3 formulations of the $k-k_L-\omega$ model at high and low inlet turbulent intensities.

A.2 CFD Predictions at Low Inlet Turbulence intensity

The two-dimensional cascade CFD model of Aft-Loaded L1A blade airfoil (Fig. 3.5(c)) was simulated at an inlet Reynolds number of 50,000. Unsteady simulations were ran using both Fluent versions of the $k-k_L-\omega$ model at $Tu = 0.5\%$ with an inlet turbulent length scale, $l_m = 50mm$. The next sections present the comparisons of the static pressure coefficient, boundary layer profiles, and total pressure loss coefficient with the experimental measurements taken by Marks *et al.* [35] in the LSWT. Also comparisons were made with CFD result of Clark *et al.* [25] which used the Prasnier and Clark [24] correlation based transitional flow model. A total of

D. Sanders

191,589 and 221,549 time-steps were used for averaging of mean flow quantities with the Fluent 6.3 and 12.0 version of the $k-k_L-\omega$ model using time step of $2 \mu\text{sec}$.

A.2.1 Mean Surface Static Pressure Coefficient

In Figure A.1, the mean static pressure coefficient distributions were compared to the measurements of Marks *et al.* [35] and CFD results of Clark [25]. At the $\text{Re} = 50,000$, both Fluent versions of the $k-k_L-\omega$ model results showed good agreement to the 55% and 42% axial chord suction surface location with Clark's [25] CFD and experimental results, respectively. There was only a slight difference in the predicted static pressure distribution to the 80% axial chord location using both versions of the $k-k_L-\omega$ model. The Fluent 6.3 $k-k_L-\omega$ model predicted a higher local pressure peak at the approximately 82% axial chord location compared to the Fluent 12.0 $k-k_L-\omega$ model. The difference was attributed to the behavior of the vortices created from the separated shear layer as they moved downstream to the wake region. Both $k-k_L-\omega$ model formulations predicted a lower peak pressure than the Clark [25] CFD result but both over-predicted the peak pressure compared to the experimental results. The results indicated the prediction of the blade loading using the $k-k_L-\omega$ model was independent of the Fluent model formulation at low turbulent intensities.

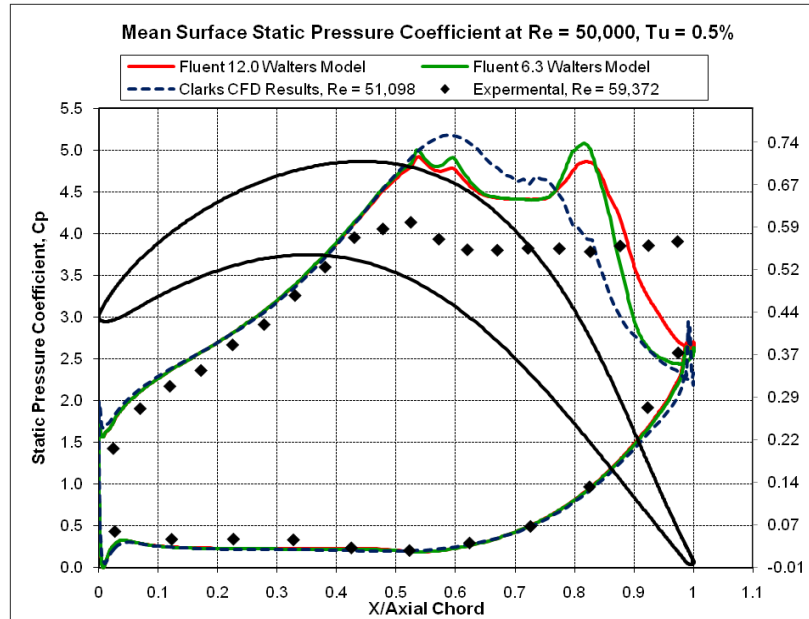


Figure A.1. The $k-k_L-\omega$ model formulation comparison of surface static pressure coefficient with Clark *et al.* [25] CFD simulations and experimental results [35] at $Re = 50,000$, $Tu = 0.5\%$ for the Aft-Loaded L1A blade airfoil

A.2.2 Velocity Contours and Boundary Layer Profiles

Mean velocity magnitude contour plots from both version of the $k-k_L-\omega$ model were compared to the PIV contour plots taken by Marks *et al.* [35] in Figure A.2. All contour plots showed flowfields on the suction surface of the blade starting at approximately 50.0 - 94% axial chord location. Both of the $k-k_L-\omega$ model formulations predicted separated flow on the suction surface trailing edge as in the experimental [35] PIV result. The mean flow characteristics were very similar in both $k-k_L-\omega$ model predictions, but the Fluent 12.0 version did predict a slightly larger separation region. The contours plots indicated the size of the suction surface separation region was significantly under-predicted compared to the experimental [35] PIV result.

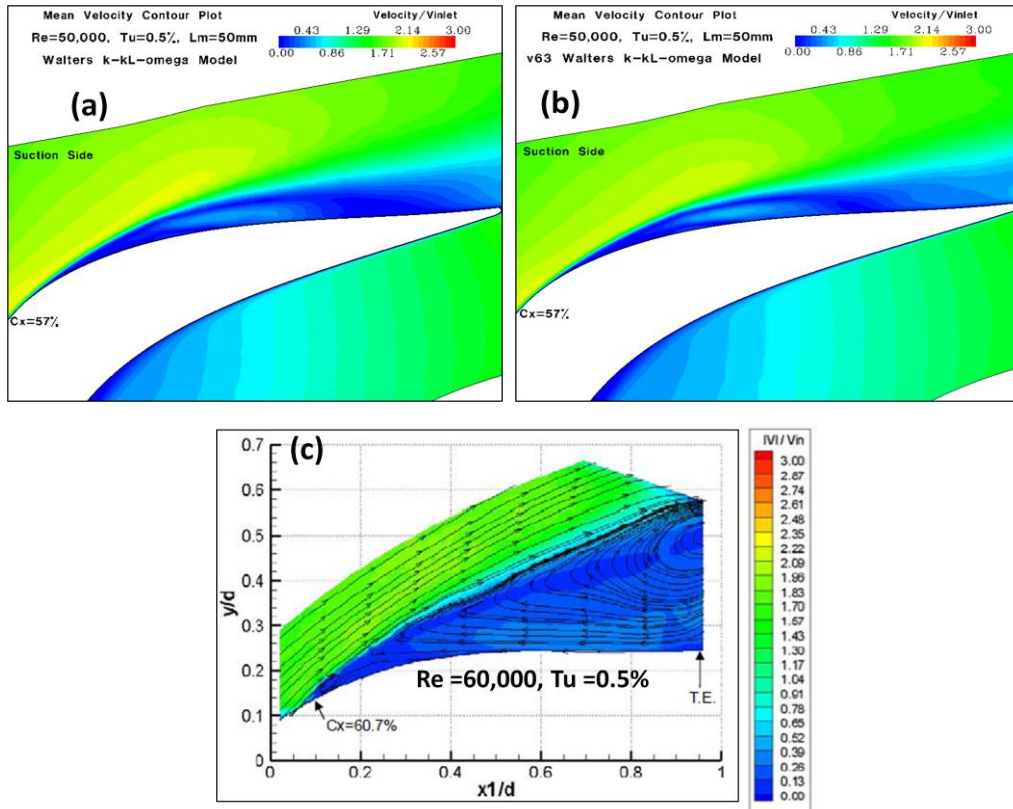


Figure A.2. Mean velocity contours plots of the (a) Fluent 12.0, and (b) Fluent 6.3 formulation of the $k-k_L-\omega$ model at $Re = 50,000$, and (c) PIV results [35] at $Re = 60,000$, $Tu = 0.5\%$ for the Aft-Loaded L1A blade airfoil

The mean axial velocity boundary layer profiles confirmed the trends observed in the blade suction surface contour plot comparisons. Figure A.3 shows identical boundary layer profiles using both $k-k_L-\omega$ model formulations to the 60.4% axial chord location. The separation location for the Fluent 6.3 model result at 64.4% axial chord was more downstream than the Fluent 12.0 version of the $k-k_L-\omega$ model which was located at the 62.8% axial chord location. This resulted in a larger separation region starting at the 65.5% axial chord location (Fig A.3(a)) in the Fluent 12.0 $k-k_L-\omega$ model prediction. Figure A.3(b) shows the reversed flow present in the boundary layer extended to the 95% axial chord location in the Fluent 12.0 $k-k_L-\omega$ model prediction. This indicated that the Fluent 12.0 model formulation predicted a larger influence of the adverse pressure gradient on the aft portion of the blade, causing more reversed flow. Both

model formulations under-predicted the separation region compared to the experimental results starting at the 60.4% axial chord location and continued for every downstream location (Fig. A.3(a)-(b)).

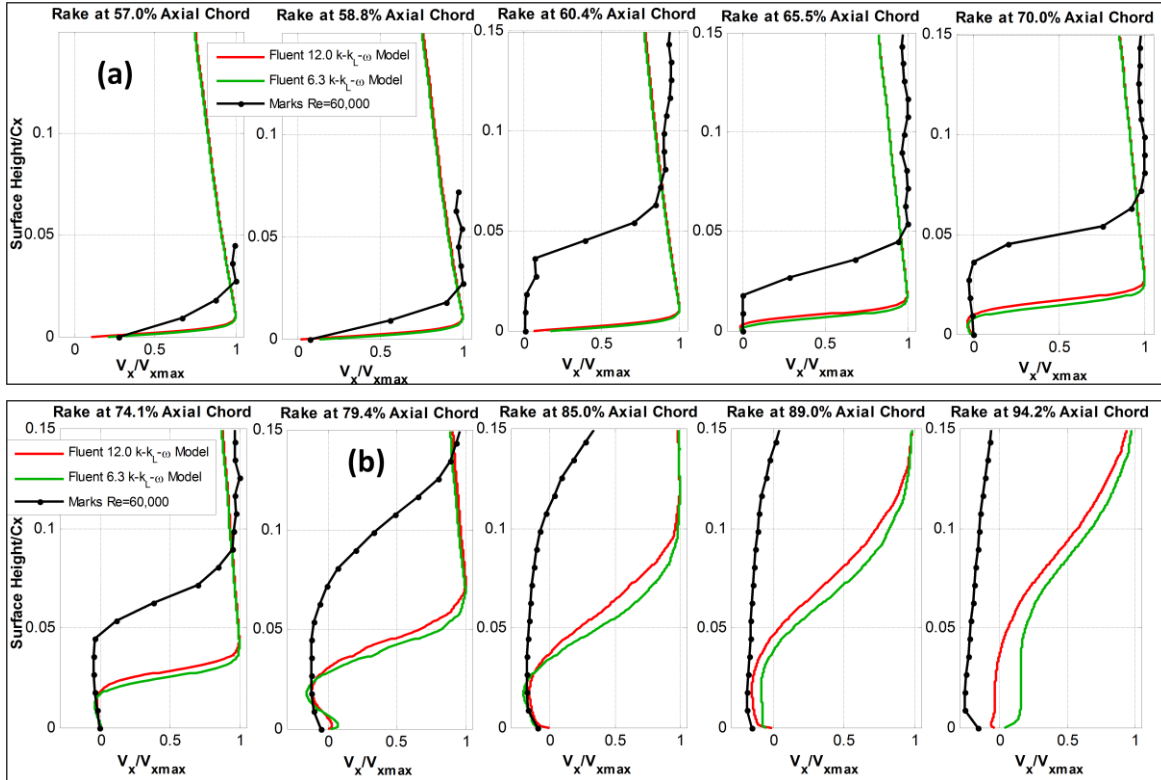


Figure A.3. The $k-k_L-\omega$ model formulation comparison of the mean axial velocity boundary layer profiles with experimental ($Re=60,000$) results [35] at inlet $Re = 50,000$, $Tu = 0.5\%$ for the Aft-Loaded L1A blade airfoil

A.2.3 Unsteady Features of the Flowfield

The $k-k_L-\omega$ model formulation comparisons were made in the prediction of the unsteady features of the flowfield. Instantaneous contour plots of vorticity were used to visualize the features of the flowfield as shown in Figure A.4. The overall unsteady vortex shedding behavior was similar for both the Fluent 12.0 and 6.3 versions of the $k-k_L-\omega$ model. The separated shear layer on blade suction surface consistently produced a clockwise vortex, while smaller counter-clockwise vortices were present beneath main vortex produced by the separated shear layer. The

Fluent 12.0 $k-k_L-\omega$ model consistently produced slightly larger vortices from the suction surface shear layer. Also, the behavior of the small counter-clockwise vortices shed at the trailing edge was similar in both $k-k_L-\omega$ model formulations. The main difference between both $k-k_L-\omega$ model formulation was that the Fluent 12.0 $k-k_L-\omega$ model prediction extended the vortices across the wake region compared to the Fluent 6.3 $k-k_L-\omega$ model prediction.

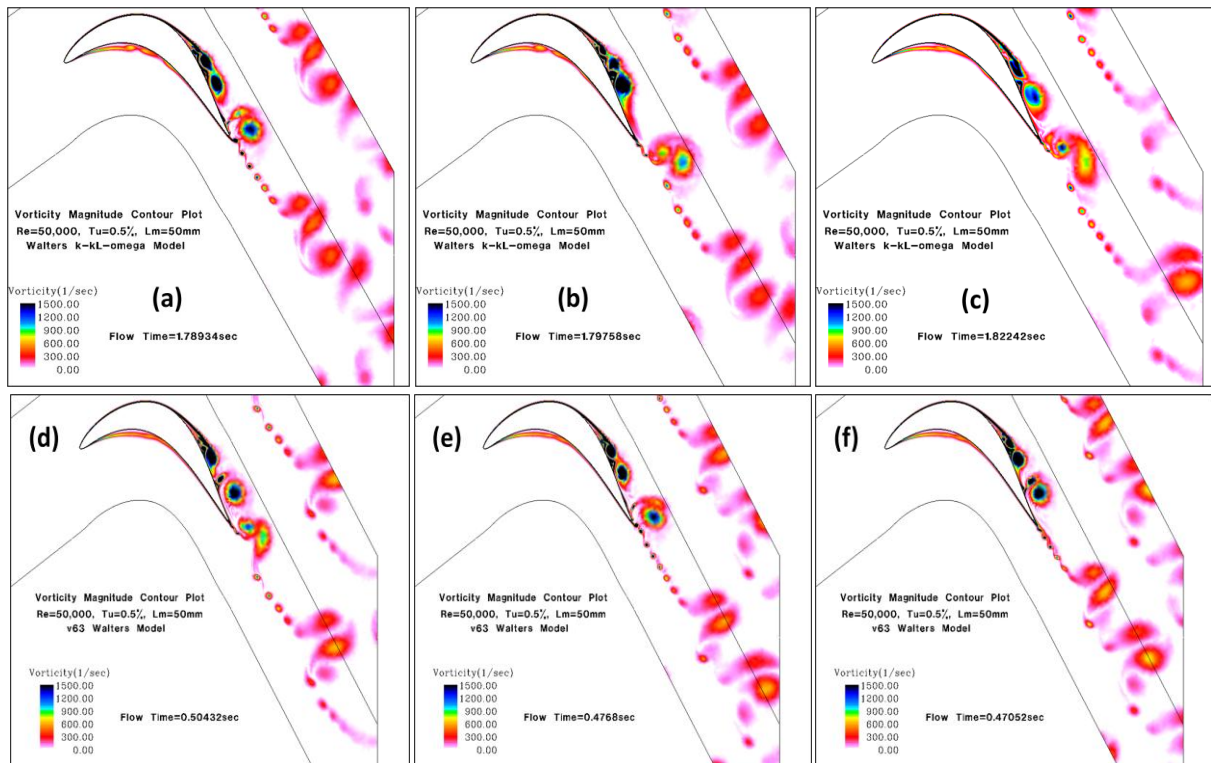


Figure A.4. Instantaneous vorticity contours at $Re = 50,000$, $Tu = 0.5\%$ for (a)-(c) Fluent 12.0 and (d)-(f) Fluent 6.3 of the $k-k_L-\omega$ model for the Aft-Loaded L1A blade airfoil

The time signal and the FFT of the drag coefficient were calculated for each simulation completed with the two $k-k_L-\omega$ model formulations. The frequency resolution was 2Hz and 3Hz for the Fluent 12.0 and Fluent 6.3 formulation of the $k-k_L-\omega$ model, respectively. Figure A.5(a) shows the unsteady behavior of the drag coefficient differed depending on which version of the $k-k_L-\omega$ model was implemented, which was attributed to the behavior of the vortex shedding. Yet

when comparing the FFT calculation, it showed that each $k-k_L-\omega$ model formulations was in good agreement on the frequency peaks present in the FFT calculation, given the frequency resolution. This quantitatively confirmed the finding observed in the vorticity contour plots in Fig. A.4 that the prediction of the overall unsteady behavior of the vortex shedding at $Re = 50,000$ was similar for both $k-k_L-\omega$ model formulations.

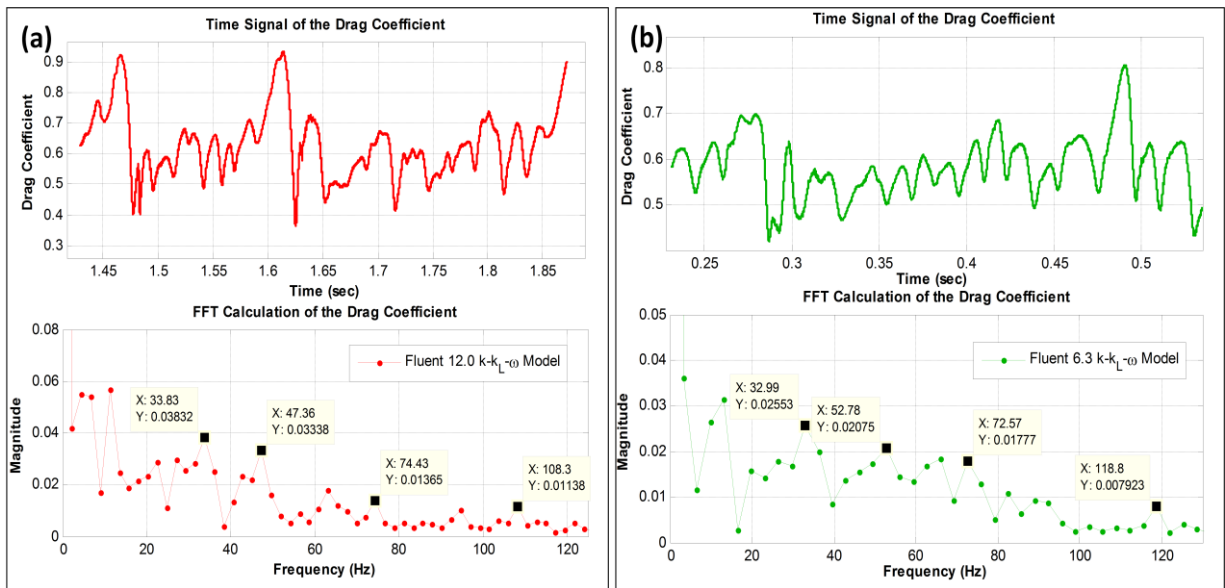


Figure A.5. Time signal and FFT calculation of the drag coefficient for the Aft-Loaded L1A blade airfoil using the (a) Fluent 12.0 and (b) Fluent 6.3 formulation of the $k-k_L-\omega$ model

A.2.4 Total Pressure Loss Coefficient

The total pressure loss coefficient obtained from both $k-k_L-\omega$ model formulations was compared to the experimental results of Marks *et al.* [35] as shown in Figure A.6. Both the formulations of the Walters and Leylek [2] $k-k_L-\omega$ transitional model significantly under-predicted the maximum value of the loss coefficient compared to the experimental results due to the over-prediction of the dissipation from the unsteady vortices in the wake region. The Fluent 6.3 $k-k_L-\omega$ model predicted a 14% higher value of the peak loss coefficient achieving 49% agreement with the experimental results compared to the Fluent 12.0 $k-k_L-\omega$ model prediction

with 43% agreement. The distribution of the loss coefficient indicated that the Fluent 12.0 $k-k_L-\omega$ model predicted the effect of the wake to extend further across the wake region than the Fluent 6.3 $k-k_L-\omega$ model prediction. Table A.1 shows that 81% agreement was achieved with the Fluent 12.0 $k-k_L-\omega$ model when comparing the integrated loss coefficient to the experimental results. This indicated that the Fluent 12.0 $k-k_L-\omega$ model predicted an adequate amount of viscous losses, but the distribution of the viscous losses across the wake region was inaccurate.

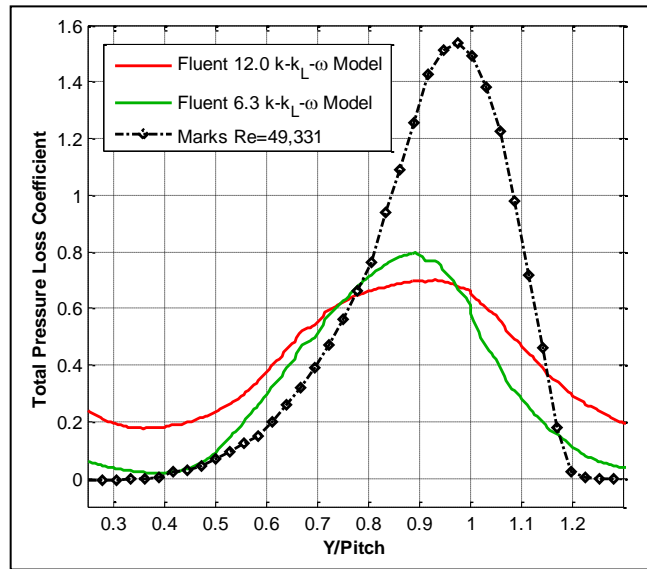


Figure A.6. The $k-k_L-\omega$ model formulation comparison of total pressure loss coefficient with experimental [35] result at inlet $Re = 50,000$, $Tu = 0.5\%$ for the Aft-Loaded L1A blade airfoil

Re	Fluent Model	$l_m(mm)$	Integrated Loss Coefficient		Maximum Loss Coefficient	
			CFD	Marks <i>et al.</i> [35]	CFD	Marks <i>et al.</i> [35]
50,000	12.0	50	0.4131	0.5099	0.7001	1.5974
50,000	6.3	50	0.3434		0.7955	

Table A.3. Maximum and integrated total pressure loss coefficient comparison with the experimental [35] results at $Re = 50,000$, $Tu = 0.5\%$ for the Aft-Loaded L1A blade airfoil

A.3 CFD Predictions at High Inlet Turbulence intensity

Unsteady simulations were completed at an inlet $Tu = 3.4\%$ using both formulations of the $k-k_L-\omega$ model at $Re = 50,000$. The inlet turbulent length scale was set as $l_m = 4mm$ for both simulations. Similar to the low turbulence intensity cases, comparisons were made using the static pressure coefficient, boundary layer profiles, and total pressure loss coefficient with the experimental measurements and Clark *et al.* [25] CFD results. A total of 11,000 time-steps using $t_{step} = 10\mu sec$ were used for averaging of mean flow quantities with the Fluent 6.3 $k-k_L-\omega$ model simulation whereas the Fluent 12.0 simulation used a total 50,000 time-steps with $t_{step} = 40 \mu sec$.

A.3.1 Mean Surface Static Pressure Coefficient

The mean surface static pressure coefficient shown in Figure A.7 compared the blade loading predicted with the Fluent 12.0 and 6.3 formulations of the $k-k_L-\omega$ model at high inlet turbulence intensity. The Fluent 12.0 $k-k_L-\omega$ model predicted a similar pressure distribution due to flow separation and turbulent reattachment which was comparable to Clark's [25] CFD and the experimental [35] results. The closed separation region was indicated to be larger in the Fluent 12.0 formulation results as compared to the experimental [35] and Clark's [25] CFD results. The Fluent 6.3 $k-k_L-\omega$ model predicted a fully turbulent flow static pressure distribution with no indication of a separation bubble which was not observed in the experimental results. So, this indicated the Fluent 12.0 $k-k_L-\omega$ model provides more effective prediction of the Aft-Loaded L1A blade loading at this inlet turbulence intensity.

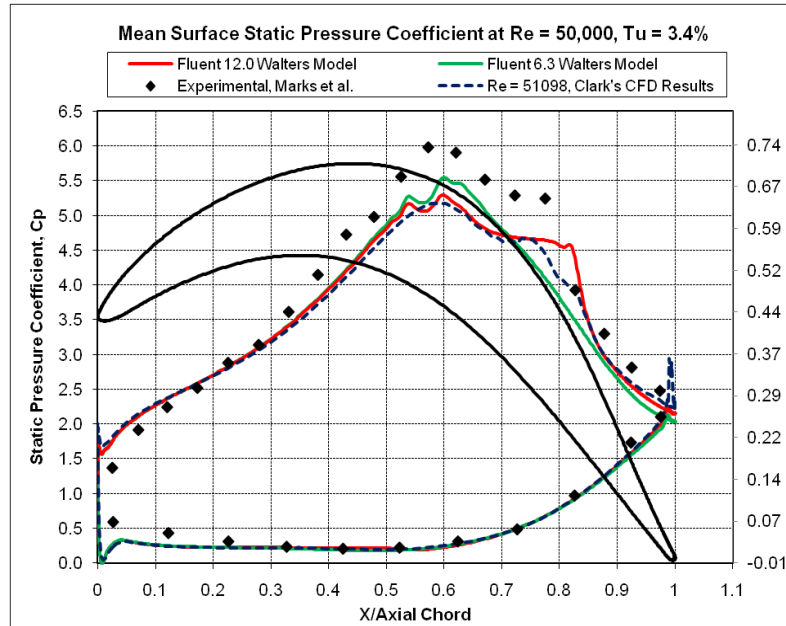


Figure A.7. The $k-k_L-\omega$ model formulation comparison of surface static pressure coefficient with Clark *et al.* [25] CFD simulations and experimental results [35] at $Re = 50,000$, $Tu = 3.4\%$ for the Aft-Loaded L1A blade airfoil

A.3.2 Velocity Contours and Boundary Layer Profiles

The velocity contours and boundary layer profiles were compared at high inlet turbulence intensity obtained from both formulations of the $k-k_L-\omega$ model. The velocity contours in Figure A.8(a) confirmed the presence of a closed separation region starting at approximately the 60% axial chord location in the Fluent 12.0 prediction which was observed in the experimental PIV contour plot in Figure A.8(c). The Fluent 6.3 $k-k_L-\omega$ model indicated an attached turbulent boundary layer which was not observed in the experimental results (Fig. A.8(b) & Fig. A.9). The boundary layer profiles for the Fluent 12.0 version of the $k-k_L-\omega$ model predicted the separation point at the 65.9% axial chord location and reattaching by the 89% axial chord location as shown in Figure A.9. The separation region was under-predicted in the Fluent 12.0 prediction compared to the experimental result [35]. The separation point was reported to be near 62% axial chord location. Reattachment occurred between the 79.4 and 85% axial chord

position in the experimental [35] result, which was predicted to be more downstream in the Fluent 12.0 formulation of the $k-k_L-\omega$ model.

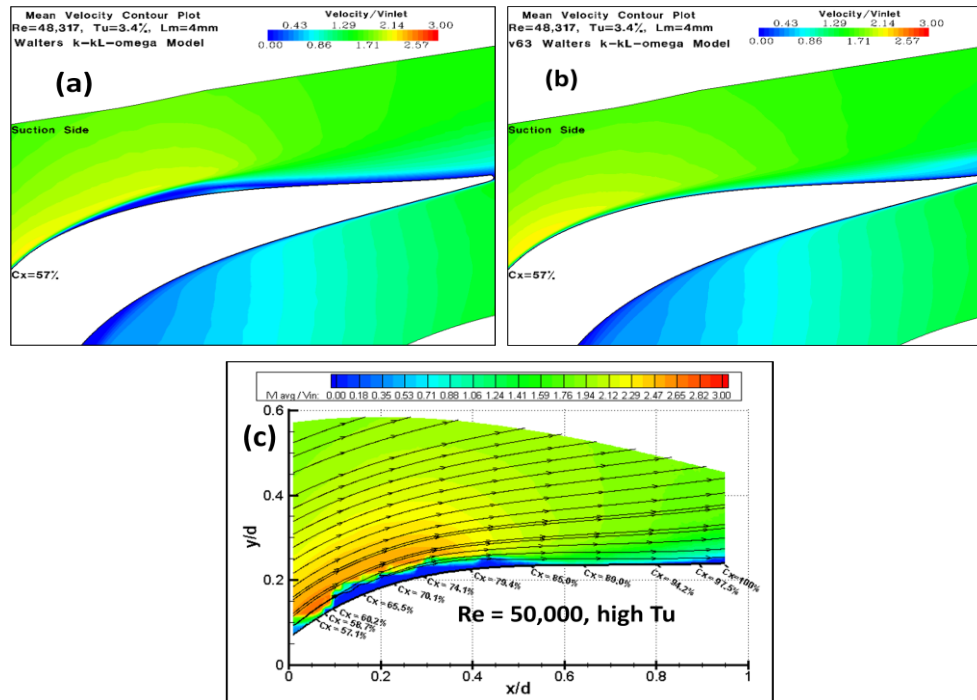


Figure A.8. Mean velocity contours plots of the (a) Fluent 12.0, (b) Fluent 6.3 formulation of the $k-k_L-\omega$ model and (c) PIV [35] results at $Re = 50,000$, $Tu = 3.4\%$ for the Aft-Loaded L1A blade airfoil

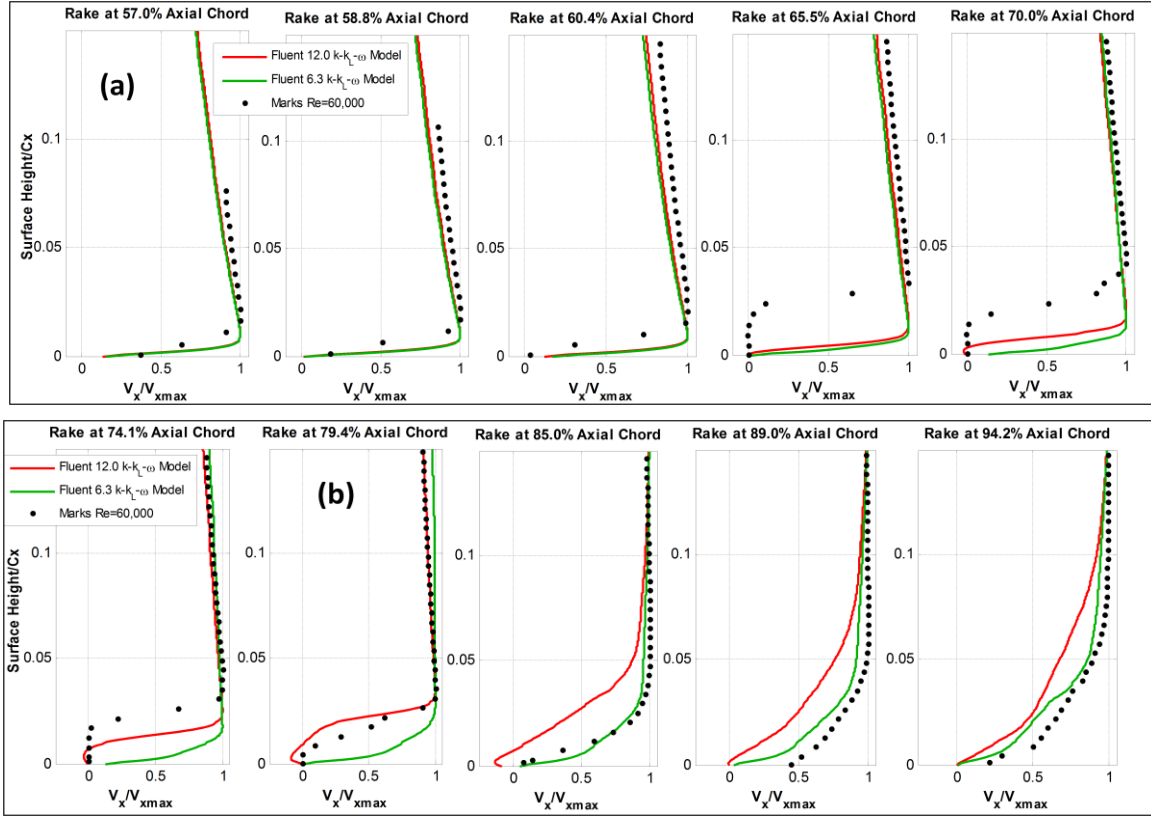


Figure A.9. The $k-k_L-\omega$ model formulation comparison of the mean axial velocity boundary layer profiles with experimental results [35] at inlet $Re = 50,000$, $Tu = 3.4\%$ for the Aft-Loaded L1A blade airfoil

A.3.3 Total Pressure Loss Coefficient

The total pressure loss coefficient obtained from both $k-k_L-\omega$ model formulations was compared to the experimental results of Marks *et al.* [35] as shown in Figure A.10. Both the formulations of the Walters and Leylek [2] $k-k_L-\omega$ transitional model significantly under-predicted the maximum value of the loss coefficient compared to the experimental results. The Fluent 6.3 $k-k_L-\omega$ model predicted a 34% higher peak loss coefficient and a narrower wake region compared to the Fluent 12.0 $k-k_L-\omega$ model. Better agreement to the experimental results of 63% was achieved in the integrated loss coefficient prediction with the Fluent 12.0 $k-k_L-\omega$ model.

In summary, the Fluent 12.0 $k-k_L-\omega$ model was used in the Aft-Loaded L1A blade airfoil simulations because it gave similar flow predictions at the lower inlet turbulence intensity, and better agreement with the experimental results at the high inlet turbulence intensity. The difference in the prediction in the Fluent 12.0 and 6.3 the $k-k_L-\omega$ model was attributed to the formulation of the transport equations in the $k-k_L-\omega$ model. The Lightly and Highly Loaded blade airfoil simulation completed with the Fluent 6.3 $k-k_L-\omega$ model were still considered valid because those simulations were done at a low inlet turbulence intensity where the Fluent 12.0 and 6.3 formulation of the $k-k_L-\omega$ model obtained similar results in the prediction of the flowfield.

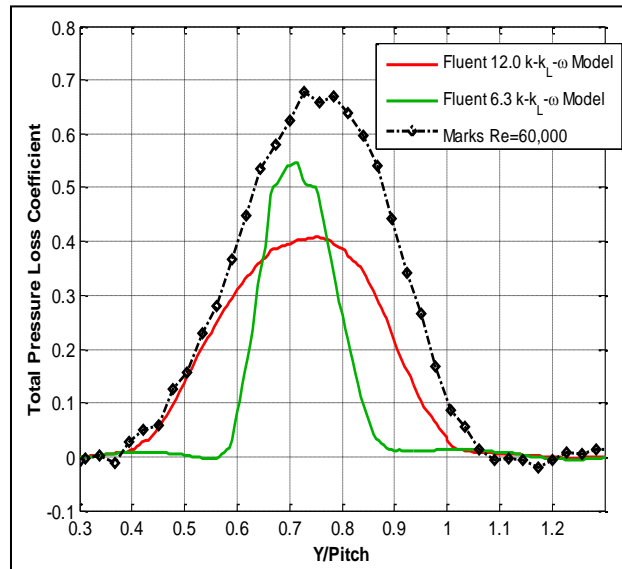


Figure A.10. The $k-k_L-\omega$ model formulation comparison of total pressure loss coefficient with experimental [35] result at inlet $Re = 50,000$, $Tu = 3.4\%$, for the Aft-Loaded L1A blade airfoil

Re	Fluent Model	$l_m(mm)$	Integrated Loss Coefficient		Maximum Loss Coefficient	
			CFD	Marks <i>et al.</i> [35]	CFD	Marks <i>et al.</i> [35]
50,000	12.0	4	0.1502	0.2397	0.4083	0.6791
50,000	6.3	4	0.0944		0.5475	

Table A.4. Maximum and integrated total pressure loss coefficient comparison with the experimental [35] results at $Re = 50,000$, $Tu = 3.4\%$ for the Aft-Loaded L1A blade airfoil

APPENDIX H

DESIGN AND VALIDATION OF A HIGH-LIFT LOW-PRESSURE TURBINE BLADE

A dissertation submitted in partial fulfillment of the
requirements for the degree of
Doctor of Philosophy

By

MARK WAYNE MCQUILLING
B.S.M.E., University of Kentucky, 2002
M.S.M.E., University of Kentucky, 2004

2007
Wright State University

WRIGHT STATE UNIVERSITY

SCHOOL OF GRADUATE STUDIES

July 13, 2007

I HEREBY RECOMMEND THAT THE DISSERTATION PREPARED UNDER MY SUPERVISION BY Mark Wayne McQuilling ENTITLED Design and Validation of a High-Lift Low Pressure Turbine Blade BE ACCEPTED IN PARTIAL FULFILLMENT OF THE REQUIREMENTS FOR THE DEGREE OF Doctor of Philosophy.

Mitch Wolff, Ph.D.
Dissertation Director

Ramana Grandhi, Ph.D.
Director, Ph.D. Program
Mechanical and Materials Engineering

Joseph F. Thomas, Jr., Ph.D.
Dean, School of Graduate Studies

Committee on
Final Examination

Mitch Wolff, Ph.D.

Scott Thomas, Ph.D.

Joseph Shang, Ph.D.

Rolf Sondergaard, Ph.D.

John Clark, Ph.D.

Richard Branam, Ph.D., Major USAF

ABSTRACT

McQuilling, Mark Wayne. Ph.D. Engineering Ph.D. Program, Department of Mechanical and Materials Engineering, Wright State University, 2007. Design and Validation of a High-Lift Low-Pressure Turbine Blade.

This dissertation is a design and validation study of the high-lift low-pressure turbine (LPT) blade designated L2F. High-lift LPTs offer the promise of reducing the blade count in modern gas turbine engines. Decreasing the blade count can reduce development and maintenance costs and the weight of the engine, but care must be taken in order to maintain turbine section performance with fewer blades. For an equivalent amount of work extracted, lower blade counts increase blade loading in the LPT section. The high-lift LPT presented herein allows 38% fewer blades with a Zweifel loading coefficient of 1.59 and maintains the same inlet and outlet blade metal angles of conventional geometries in service today while providing an improved low-Reynolds number characteristic. The computational design method utilizes the Turbine Design and Analysis System (TDAAS) developed by John Clark of the Air Force Research Laboratory. TDAAS integrates several government-funded design utilities including airfoil and grid generation capability with a Reynolds-Averaged Navier-Stokes flow solver into a single, menu-driven, Matlab-based system. Transition modeling is achieved with the recently developed model of Praisner and Clark, and this study validates the use of the model for design purposes outside of the Pratt & Whitney (P&W) design system where they were created. Turbulence modeling is achieved with the Baldwin and Lomax zero-equation model.

The experimental validation consists of testing the front-loaded L2F along with a previously designed, mid-loaded blade (L1M) in a linear turbine cascade in a low-speed wind tunnel over a range of Reynolds numbers at 3.3% freestream turbulence. Hot-wire anemometry and pressure measurements elucidate these comparisons, while a shear and stress sensitive film (S3F) also helps describe the flow in areas of interest. S3F can provide all 3 components of stress on a surface in a single measurement, and these tests extend the operational envelope of the technique to low speed air environments where small dynamic pressures and curved surfaces preclude the use of more traditional global measurement methods. Results are compared between the L1M and L2F geometries along with previous data taken in the same wind tunnel at identical flow conditions for the P&W Pack B geometry.

Table of Contents

Abstract	iii
List of Figures	vii
List of Tables	x
Nomenclature	xi
Acknowledgements	xiii
1 Introduction	1
1.1 Importance of the Work	2
1.2 The Low-Pressure Turbine	3
1.3 Instability and Transition	4
1.4 Current Direction of Low-Pressure Turbine Design	6
1.5 What is a High-Lift Design?	7
1.5.1 The Pack B Low-Pressure Turbine	8
1.5.2 Previous Design and Higher-Lift Efforts	8
1.6 Current Study	13
2 L2F Design	15
2.1 Turbine Design and Analysis System (TDAAS)	15
2.2 Airfoil Generation	16
2.3 Grid Generation	16
2.4 Flow Solver	18
2.5 Design of Experiments	21
2.6 The Result: L2F	26
2.7 Chapter Summary	28

3	Experimental Arrangement	29
3.1	Low-Speed Wind Tunnel	29
3.2	Techniques and Data Processing	31
3.2.1	Pressure Measurement	31
3.2.2	Thermal Anemometry	31
3.2.3	Particle Image Velocimetry	40
3.2.4	Shear and Stress Sensitive Film (S3F)	41
3.3	S3F Development for Low-Speed LPT Use	42
3.3.1	Experimental Setup	42
3.3.2	Results	44
3.4	Chapter Summary	50
4	Results	51
4.1	Reynolds Lapse	51
4.2	Boundary Layer Contours and Profiles	55
4.3	S3F Measurements	78
4.4	Transition Model Validation	84
4.5	Chapter Summary	90
5	Discussion	93
5.1	Conclusions	93
5.2	Future Work	95
A	More on Higher-Lift Design Efforts	97
B	AFRL's LSWT Turbulence Characterization	102
C	Background on Pressure and Skin Friction Measurement	107
D	Operation of S3F	111
E	Uncertainty Analysis	117
F	Short History of Gas Turbine Engine Development - DRAFT	125
G	LPT Aerothermodynamics and Flow Physics - DRAFT	128
H	Boundary Layers, Skin Friction, and Separation - DRAFT	138

I More on Instability and Transition - INCOMPLETE, needs significant revision...	142
References	155
Vita	166

List of Figures

1.1	The gas turbine industry.	2
1.2	Laminar separation.	4
2.1	Screen shots of airfoil shape generation.	17
2.2	Typical O-H grid mesh for Pack B profile.	18
2.3	Transition model databases, from [Praisner and Clark 2007].	19
2.4	Design process flow chart.	22
2.5	Variation in profiles generated by DOE.	24
2.6	L2F-like profiles generated by DOE.	25
2.7	Geometric comparison of Pack B, L1M, and L2F profiles.	26
2.8	Coefficient of Pressure for Pack B, L1M, and L2F.	27
3.1	AFRL's Low-Speed Wind Tunnel.	30
3.2	Example of Clark intermittency algorithm.	35
3.3	L1M and L2F boundary profile locations.	37
3.4	Method for determining attainable profile locations.	37
3.5	PIV setup with laser arm.	40
3.6	Pack B LPT test setup at ISSI.	43
3.7	Front cavity, $U=13.5\text{m/s}$, $h=1\text{mm}$, $\mu=150\text{Pa}$	44
3.8	Rear cavity, $U=13.5\text{m/s}$, $h=1\text{mm}$, $\mu=150\text{Pa}$	45
3.9	Shear displacement vectors and streamlines, $U=7\text{m/s}$, $h=1.5\text{mm}$, $\mu=25\text{Pa}$	46
3.10	Sequential series of displacement fields taken at 0.5Hz , $U=13.5\text{m/s}$, $h=1.5\text{mm}$, $\mu=25\text{Pa}$	47
3.11	Displacement fields, $h=1.5\text{mm}$, $\mu=25\text{Pa}$	48
3.12	S3F-oil film combined measurement regions of interest.	49
3.13	Oil film measurements.	49
4.1	Reynolds lapse for Pack B, L1M, and L2F airfoils.	52

4.2	L1M Umean/Uin, contours and profiles.	57
4.3	L1M turbulent profile similarity comparisons, $Re = 50k$	59
4.4	L1M turbulent profile similarity comparisons, $Re = 75k$	60
4.5	L2F Umean/Uin, contours and profiles.	61
4.6	L2F comparison to Falkner-Skan; $\beta = -0.199$, $Re = 25k$	62
4.7	L2F turbulent profile similarity comparisons.	63
4.8	L1M urms/Uin contours.	65
4.9	L1M skew and kurtosis contours.	66
4.10	L2F urms/Uin contours.	68
4.11	L2F skew and kurtosis contours.	69
4.12	L1M and L2F intermittency contours.	71
4.13	L1M unsteady development.	74
4.14	L2F unsteady development.	76
4.15	S3F round 1: Force distributions near L2F leading edge, 5-35%SSL.	80
4.16	S3F round 1: Force distributions near L2F trailing edge, 67-100%SSL.	81
4.17	S3F round 2: Friction force distributions on L2F, flow left to right, 42-100%SSL.	82
4.18	Transition model experimental validation.	89
B.1	Wind tunnel cross-section turbulence measurement locations.	103
B.2	LSWT FSTI development.	103
B.3	LSWT turbulence scale development.	106
C.1	Cartoon of typical floating-type shear sensor with multiple linkage possibilities.	108
D.1	Simplified S3F responses.	112
D.2	S3F response functions on loads for 1Pa force applied on the interval $[-0.1, 0.1]$	115
D.3	3D presentation of $\tilde{\mathbf{G}}$ matrix.	116
D.4	Amplitude-Frequency Characteristics of normal component (blue), shear component (red), and crosstalk (green) components of response function, $\omega = \Omega/\omega_0$; the spatial frequency referenced to $\omega_0 = 1/h$. Planar FEA model for S3F with $\mu=100\text{Pa}$ and $\nu=0.99$	116
E.1	Distributions of pressure measurements about the means $[\text{inH}_2\text{O}]$	120
E.2	L2F Reynolds lapse with error bars at low and high Re	124
G.1	Ideal Brayton cycle.	129

G.2	T-s diagram of a typical LPT stage.	130
G.3	Complex unsteady LPT environment.	132
G.4	Low <i>Re</i> effects, from [Sharma 1998].	134
G.5	Schematic of a typical separation bubble, from [Sharma 1998].	135
H.1	Boundary layer velocity distributions and derivatives.	140

List of Tables

1.1	Recent Design Efforts Summary, Part 1.	11
1.2	Recent Design Efforts Summary, Part 2.	12
3.1	Clark intermittency algorithm parameters.	34
4.1	Measured conditions across L1M cascade.	53
4.2	Measured conditions across L2F cascade.	53
4.3	Wake conditions.	54
4.4	U _{mean} /U _{in} maxima and minima.	56
4.5	L2F separation onset locations [%SSL].	81
4.6	Attached-flow transition model experimental conditions.	85
4.7	Separated-flow transition model experimental conditions.	86
4.8	Transition onset locations [%SSL].	87
E.1	Druck LPM5481 differential pressure transducer uncertainty [in H ₂ O].	119
E.2	TSI 1240-20 x-wire and 1211-20 hot-film uncertainties [m/s].	121
E.3	Influence coefficients for loss definition uncertainties.	122
E.4	Theoretical uncertainty in loss coefficients.	122
E.5	Repeatability-based standard deviation in L2F loss coefficients at low <i>Re</i>	123

Nomenclature

AL	aft-loaded
BL	boundary layer
B_x	axial chord length
C_f	skin friction coefficient, $C_f = \frac{\tau_w}{q}$
EXP	experiment
FL	front-loaded
$FSTI$	freestream turbulence intensity
GSM	gradient search methods
L_{area}	area-averaged loss coefficient, $L_{area} = \frac{(P_{t,in} - P_{t,ex})}{(P_{t,in} - P_{s,in})}$
L_{flux}	flux-averaged loss coefficient, $L_{flux} = \frac{[\sum u_{ex,i} \cdot (P_{t,in} - P_{t,ex})_i] / \sum u_{ex,i}}{(P_{t,in} - P_{s,in})}$
LE	leading edge
LPT	low-pressure turbine
ML	mid-loaded
NN	neural networks
PS	pressure surface
q	dynamic pressure, $q = \frac{1}{2} \rho U_\infty^2$
R_0	Hot-wire sensor resistance at 0°C [Ω]
R_{100-0}	Difference in hot-wire resistances between 0 and 100 °C [Ω]
R_{op}	Hot-wire sensor operating resistance [Ω]
$RANS$	Reynolds-averaged Navier-Stokes
Re	Reynolds number, $Re = \frac{U_\infty c}{\nu}$, $Re_x = \frac{\rho U_\infty x}{\mu}$, $Re_\theta = \frac{U_\infty \theta}{\nu}$
Re_θ	momentum thickness Re , $Re_\theta = \frac{U_\infty \theta}{\nu}$
S	suction surface area
SS	suction surface
SSL	suction surface length
T	temperature

T_{dew}	Dew-point temperature [K]
T_m	Mean hot-wire temperature [K]
T_{wire}	Hot-wire sensor temperature [K]
$TDAAS$	Turbine Design and Analysis System
TR	transition
TU	turbulence
Tu	local turbulence intensity
u	streamwise velocity
U_∞	freestream velocity
$VGJs$	vortex generator jets
WIT	wake-induced transition
x	streamwise direction
y	surface-normal direction
Zw	Zweifel loading coefficient, $Zw = 2 \frac{S}{B_x} \cos^2 \beta_2 \left[\frac{u_1}{u_2} \tan \beta_1 + \tan \beta_2 \right]$
<i>Greek</i>	
β	gas flow angle
δ	boundary layer height, $u(\delta) = 0.99U_\infty$
λ	integral length scale
ν	kinematic viscosity of fluid, $\nu = \frac{\mu}{\rho}$
ρ	density of air
τ	shear stress, $\tau = \mu \frac{\partial u}{\partial y}$
θ	boundary layer momentum thickness, $\theta = \int_0^\delta \frac{u}{U_\infty} (1 - \frac{u}{U_\infty}) dy$
<i>Subscript</i>	
∞	freestream condition
in	inlet condition
ex	exit condition
w	wall condition

Acknowledgements

I once thanked my wife and daughter, Kylie and Madison, for giving me so much support and so many reasons to succeed, and still today I can't begin to explain how much they've contributed to my understanding of life itself. I'll always owe them my greatest loyalty and support, because that's what they've constantly given me.

Sometimes at the graduate level, it's difficult for professors to take time and become involved with their students. I've been lucky enough to have such an advisor and friend in Dr. Mitch Wolff. He has been a constant beacon of support and guidance, being as truthful and concerned as he could have been, and without his help there's no chance I would have made it this far.

I've also learned that any job can only be as good as the people you work with, and the people of the Turbines Branch of AFRL's Propulsion Directorate at WPAFB are definitely world-class. I've been extremely fortunate to have Drs. John Clark and Rolf Sondergaard work with me on a daily basis, and I owe them a great deal of thanks for their willingness to teach, their professionalism, support, and guidance. I consider them friends, and I hope our relationships continue in the future.

I also owe a great deal of thanks to Drs. Jim Crafton and Sergey Fonov of Innovative Scientific Solutions, Inc. Having the chance to work with engineers who are pioneering a developing technology has been a challenging and very rewarding experience, and I thank them for their tolerance of a grad student's unending questions. I'd also like to thank Drs. Jeff Bons and Ralph Volino for their helpful insights into transition measurement techniques. The Dayton Area Graduate Studies Institute (DAGSI) also has my sincere gratitude for allowing me the opportunity to achieve my educational and professional goals.

I would also like to thank my dissertation committee members for making this a more complete work. Drs. Mitch Wolff, Joseph Shang, Scott Thomas, Richard Branam, John Clark, and Rolf Sondergaard have spent a great deal of energy in their critiques, and I sincerely thank them all.

And last but not least, I'd like to thank my lab partners and WizFriends Nate Woods and Ernest Thompson, and Josh Norris and sometimes Scott Stanfield for routinely stealing my treasure and stopping me from getting home.

1

Introduction

We don't know a millionth of one percent about anything.

– Thomas Edison

Modern gas turbine engines provide propulsion for many aircraft in service today. A cross-section of a modern gas turbine engine, the Pratt & Whitney PW4000, is shown in Figure 1.1(a). Air entering the engine is compressed by several rows of axial flow compressor blades before the combustion chamber in order to generate enough stagnation pressure in the flow to produce sufficient thrust. The compressor section is normally divided into two different groups: high-pressure and low-pressure; some recent designs even include a third spool for intermediate-pressure compressor and turbine sections. Each group consists of one or more stages of blades that pressurize the incoming flow of air. Following the compressor is the combustor, where fuel and air are mixed and burned, producing very high energy flow which exits into the turbine section. The turbine section extracts energy from the flow to drive the fan and compressor. The turbine section mirrors the compressor section with its high- and low-pressure sections, each with one or more rows of blades. The high-pressure turbine section is located directly behind the combustor. Its function is to extract energy from the highly pressurized hot gases and power the high-pressure compressor section through a shaft connecting the two. Likewise, the low-pressure turbine section extracts energy and drives the low-pressure compressor section. Due to the extremely hot exhaust gases from the combustor, intricate cooling mechanisms are required to keep the high-pressure turbine blades from melting. High-pressure turbine blade geometries house inner passages so cooling air can circulate through them, dumping heat out through hundreds of tiny holes in the blade surface. The thin trailing edges are also actively cooled with low temperature air relative to the blade metal temperature. Films of cooler air can also be injected near the leading edge of the blade that serve to coat the surface and protect it from the hot gases.

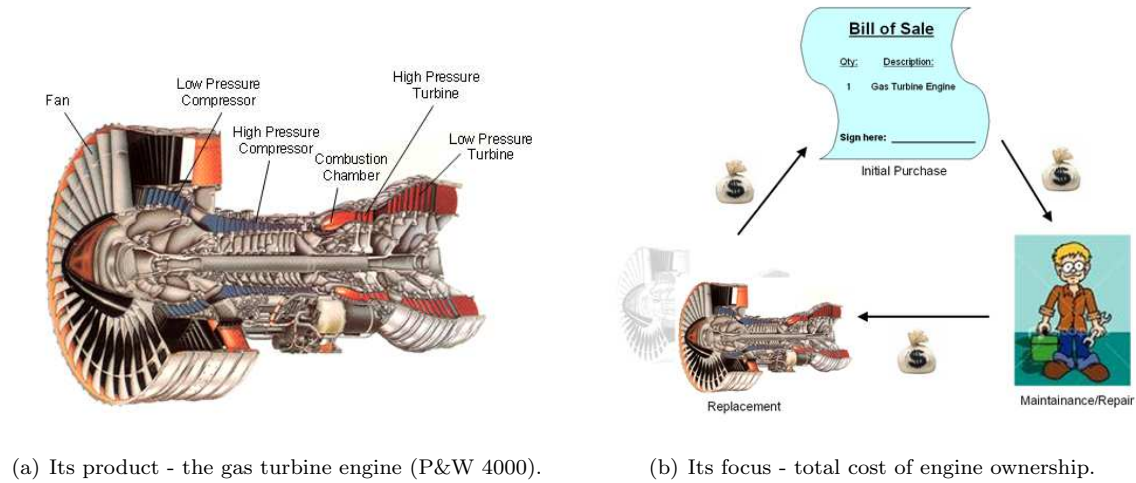


Figure 1.1: The gas turbine industry.

The mature gas turbine industry has become more cost-driven with its focus on the total cost of engine ownership, from initial purchase through maintenance and repair to replacement [?], as illustrated in Figure 1.1(b). This means the technology employed in the engine has reached such a developed state that some incremental improvements, however beneficial to performance, may no longer be cost-effective. Instead, the industry is focusing more on ways to reduce the current total cost of engine ownership.

1.1 Importance of the Work

This dissertation seeks to illustrate the design process and result when developing a front-loaded LPT airfoil with a loading characteristic higher than any previously published design. This work is part of an ongoing US Air Force Research Laboratory initiative which seeks to find the limits of the LPT design space. In other words, we want to find out what loading characteristics and loading levels provide optimal LPT designs over the varied flow conditions which occur in modern gas turbine engines.

The high-lift design presented herein promises a reduced low-pressure turbine blade count with an improved Reynolds lapse characteristic over current LPT blades in service today. The Reynolds lapse characteristic is the measure of total pressure loss across the LPT as the Reynolds number is decreased. Current LPTs suffer a dramatic increase in losses with decreasing Reynolds number, and this is usually due to the effects of separation [Sharma 1998]. A reduced turbine blade count can lower part counts, maintenance, and weight of an engine, thus lowering the overall system cost. The improved low- Re performance promises increased efficiency, reduced fuel consumption, longer loiter

times, and higher maximum altitudes over current designs in service today. Through the course of this study, a recently developed separated-flow transition model by Praisner and Clark was used to design the new LPT airfoil. Its validation proves the model's general utility in RANS-based turbomachinery design systems outside of the Pratt & Whitney design system where it was created. Thus the design of the new LPT dubbed "L2F" both expands the turbomachinery designer's current design space with higher-lift options and proves to the research community the general utility of a new transition modeling tool for RANS-based design and analysis purposes. The extensive bank of experimental data obtained in this work also provides a wealth of information useful for CFD code validation purposes.

In addition, this dissertation will illustrate the development of a shear and stress sensitive film (S3F) for low-speed applications, particularly in the LPT environment. A major difficulty with measuring surface shear in air flow environments is the small friction forces limited by the low density of air; these difficulties grow exponentially as flow velocity is decreased. This problem is addressed in this research by properly tuning the properties of the film such as elastic modulus and thickness. These low-speed tests provide the opportunity for S3F technology development, accomplished by Innovative Scientific Solutions, Inc., of Dayton, OH. Highly curved surfaces on the LPT blades in this study also present challenges to overcome. These issues have been addressed in order to bring to the experimental low-speed fluids community a non-intrusive diagnostic technique to obtain regional skin friction and normal pressure maps in low-speed air flow environments.

1.2 The Low-Pressure Turbine

LPT design is a tricky game to play. On one hand, the LPT must perform optimally at high- Re conditions near sea level where maximum loading is required for take-off. On the other hand, the majority of flight time is spent in higher altitude cruise conditions, where the lower air density results in a lower Re and lower momentum flow in the LPT section. Low- Re conditions can be particularly troublesome, as the lower momentum flow is prone to separation and transition effects due to the adverse pressure gradient experienced on the suction surface of the blade. Off-design operating conditions in the LPT section result in performance degradation due to this flow separation. There are several parameters that must be studied in order to develop a comprehensive understanding of the flow behavior around the LPT blade, including Reynolds number, freestream turbulence intensity (FSTI) and length scale, blade geometry, and pressure gradient.

A turbine section can have multiple stages typically consisting of two rows of airfoils, a vane and a blade; some designs employ counter-rotating blades which eliminate the vane. The vane row is

fixed and guides the incoming flow into the tangential direction of rotation. The row of blades turn the flow, resulting in a net torque on the shaft. The effect of the entire turbine section is to expand the gas (increase the velocity) while extracting energy to power the compressor.

There are two primary phenomena dictating the flow environment in the low-pressure turbine section: unsteadiness and low-Reynolds number effects (flow separation). Unsteadiness in the turbine section is caused by two principle mechanisms: secondary flows generated by a single blade row and the interaction of upstream disturbances (wakes and secondaries) with downstream blade rows as they convect with the bulk fluid. This high degree of unsteadiness also complicates the modeling of the transition process as the flow around the turbine blades changes from laminar to turbulent. At low Reynolds

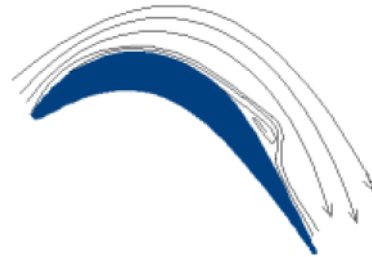


Figure 1.2: Laminar separation.

numbers, the turbine performance may be dictated by the laminar flow's poor resistance to separation. This flow separation in turn causes reduced efficiencies of the LPT section, and can significantly degrade turbine blade performance resulting in a loss of thrust and increased consumption of fuel. Gad-el-Hak [Gad-el-Hak 1990] suggests that for external aerodynamics, an airfoil shape experiencing a Reynolds number less than $5 \cdot 10^4$, based on freestream velocity and chord length, will experience laminar separation with no reattachment. Internal aerodynamics may react differently, however, as wall proximity effects and upstream disturbance convection may not allow the flow to expand and separate as easily as on airplane wings. Laminar separation in particular, as seen in Figure 1.2, leads to significant degradation of engine performance due to the presence of large re-circulation zones, with their attendant high degree of blockage, large wakes, and reduced flow turning. A turbulent boundary layer is much less likely to separate, and previous work has shown turbulent separation bubbles over turbine blades are smaller and have less effect on performance. The high-lift design presented herein seeks to increase the loading achieved by the LPT section rotor while simultaneously producing an airfoil with an improved low- Re characteristic.

1.3 Instability and Transition

Problems involving stability and transition exist in internal aerodynamics (turbomachinery) and external aerodynamics (air vehicles), as well as with hydrodynamics (submarines). Transition studies have been performed on flat plates as well as turbine geometries over a wide variety of flow conditions. Knowing the locations and length of transition are extremely important for design purposes; for

example, turbulent heat transfer levels are generally 3 to 5 times higher than in laminar conditions [Mayle 1991]. Several studies point to the need for improved transition modeling in order to advance the design of turbomachinery [Lakshminarayana 1991; Simon and Ashpis 1996; Dunn 2001]. The exploitation of transition and turbulence features in LPT flows both allows the high-lift design and complicates the flow structure around the airfoil. The difficulty in studying transition comes from the variety of factors which influence its evolution: development of freestream turbulence intensity and length scale, pressure gradient, surface curvature, wall roughness, heating and cooling, three-dimensionality, and unsteadiness, as well as other, perhaps less important effects. These non-linear growth mechanisms complicate the use of stability theory when an accurate prediction of transition is desired [Mayle 1991].

There are generally five basic modes of transition in gas turbine engines: natural, bypass, separated-flow, periodic-unsteady, and reverse [Mayle 1991]. Natural transition is the mode most thought of when “transition” is mentioned, and this occurs as a weak instability grows in a laminar boundary layer until subsequent breakdown and formation of turbulence. The most likely form occurring in gas turbine engines is *bypass transition*, wherein some or all of the laminar breakdown process does not occur, and is instead driven by freestream unsteadiness. Separated-flow transition occurs when a laminar boundary layer separates and transitions in the free shear layer above the bubble. This type of transition can occur near the leading edges of blades and near the point of minimum pressure on the suction surface sides. Of all of the modes, separated-flow transition is the most crucial for compressor and LPT design. Periodic-unsteady transition occurs due to the nature of turbomachinery flows: they are inherently periodic and unsteady, so the transition processes taking place are also unsteady and periodic. Reverse transition, often called “relaminarization”, occurs where a previously turbulent or transitional region is affected, usually by a strong favorable pressure gradient, so it becomes laminar. An instantaneous snapshot of the flow over a single airfoil may include laminar flow near the leading edge, followed by a wake- or shock-induced transition which is in turn replaced by a relaminarization with subsequent transition to turbulence occurring at multiple locations simultaneously. Mayle points out that one of the unresolved issues is whether or not the linear instabilities show up in regions of wake and shock interaction or strong adverse pressure gradient such as that occurring over the suction surface of the LPT. Halstead *et al.* have considered the effects of wakes so important to transition in turbomachinery as to define only two modes: wake-induced, and everything else (non-wake-induced) [Halstead et al. 1997a].

In 2004, Praisner and Clark published a transition model for RANS solvers using a two-equation turbulence model with sufficient accuracy for use in an airfoil design system [Praisner and Clark 2007; Praisner et al. 2007]. Using Wilcox’s $k - \omega$ turbulence model, they constructed a CFD-supplemented

experimental database of 57 attached-flow and 47 separated-flow with turbulent reattachment test cases using actual turbine geometries. Dimensional analyses led to the appropriate laminar boundary layer quantities for both flow situations. Two new transition models were developed - one for attached-flow and one for separated-flow with turbulent reattachment. The attached-flow model is based on a correlation between the local turbulence intensity, turbulent length scale, and momentum thickness Reynolds number at transition onset, which can be recast into a critical ratio of the boundary layer diffusion time to turbulent time scale. The separated-flow model was a correlation based on the momentum thickness Reynolds number at separation onset. The separated-flow transition model of Praisner and Clark is used in the current study to design the L2F geometry.

1.4 Current Direction of Low-Pressure Turbine Design

The gas turbine industry has achieved a high degree of maturity, which means it is becoming more of a cost-driven business rather than a technology-driven business. With increasing regularity, gas turbine design is focusing on the total cost of engine ownership, from initial purchase through maintenance and replacement. At the *Minnowbrook II 1997 Workshop on Boundary Layer Transition in Turbomachines*, Wisler explained how the lack of ability to accurately predict the transition process has seriously hampered the turbine engine designer's ability to gain maximum benefit from the design process [?]. This is especially crucial for compressor and turbine design, as the relative motion between adjacent stator and rotor blade rows cause high frequency disturbance patterns to propagate through the engine and influence the boundary layer behavior. Modern computational fluid dynamics (CFD) techniques can easily handle the Reynolds-Averaged Navier-Stokes equations (RANS) for both 2D and 3D configurations, but are typically only as accurate as the turbulence and transition modeling capability. Wisler continues to define the heart of the problem:

...what's missing is an adequate turbulence model, one that provides a practical, CFD design tool that will consistently and accurately predict transition and other boundary layer features for arbitrary flows. This missing link impedes designers in their efforts to tailor airfoil shapes to achieve increased loading and/or increased efficiency.

Two major design outcomes are desired here - increased loading and increased efficiency. Increasing the airfoil loading allows the reduction of engine part count, thereby reducing the cost, maintenance, and weight of the engine. Care must be taken when reducing the blade count, however, as it can lead to an increased chance for larger separation bubbles and increased loss [Gier and Ardey 2001]. Increasing the efficiency reduces the fuel consumption of the engine. Wisler estimates that a 1% gain in LPT efficiency will provide nearly \$52,000 per year per aircraft in operational savings for

most commercial and military aircraft. Another possible benefactor from the extra work provided by high-lift LPT designs include extra power generation for auxilliary systems such as air conditioning, radar and other electrical requirements, as well as for directed energy weapon systems. A current concern in their development and use is finding the tremendous amount of extra power needed to operate these systems; current concepts also include the addition of a reheat to the Brayton cycle in the form of an inter-turbine burner [Zelina 2006]. Wisler’s comment above illustrates how both of the current objectives of the gas turbine engine design community can be better achieved with improved turbulence and transition modeling.

1.5 What is a High-Lift Design?

The term “high-lift” in itself signifies an increased loading, which is one of the desired design features for the gas turbine industry as mentioned in the previous section. High-lift designs offer the promise of lower blade counts by extracting a greater amount of work per blade, thereby requiring fewer blades for an equivalent overall power extraction. Multiple studies have used the terms “high-lift” and “ultra-high-lift” to describe their “high performance” profiles, but with no standard descriptor by which to compare designs it is difficult to globally quantify a “high-lift” design. Several studies have called the Pack B profile a high performance blade, and as such a “high-lift” airfoil. One common measure of the amount of available work which can be extracted from a turbine blade is the Zweifel loading coefficient, Zw , defined in this study as Equation 1.1:

$$Zw = 2 \frac{S}{B_x} \cos^2 \beta_2 \left[\frac{u_1}{u_2} \tan \beta_1 + \tan \beta_2 \right] \quad (1.1)$$

where S is the suction surface length of the blade, B_x is the axial chord, β_1 and β_2 are the inlet and exit gas flow angles, respectively, and u_1 and u_2 are the inlet and exit streamwise velocity components, respectively. The Zweifel loading coefficient was originally developed to determine the number of blades and solidity needed for optimal turbine performance [Zweifel 1945; Hill and Peterson 1992]. Unfortunately, not all published work adheres to any standard guideline such as including their Zweifel loading coefficient with other results. As this work produces a new low-pressure turbine blade with a loading characteristic higher than any previously published design, it is somewhat abstract and silly to come up with a “*really-really-high-lift*” LPT designation, although other studies would lead one to consider such a designation. Therefore in this study, a “high-lift design” will be considered a nominal $Zw > 1.15$.

1.5.1 The Pack B Low-Pressure Turbine

Pratt & Whitney introduced the Pack B LPT design in order to provide a then-current higher-lift design with an improved low- Re efficiency in the LPT section [Clark 2005]. The Pack B turbine is an incompressible Mach-number scaled version of a conventional geometry used in commercial aircraft, and results in a nominal $Zw = 1.15$. The Pack B geometry has been used as a baseline LPT for many researchers over many topics, and this trend will continue here. Overall LPT performances presented in this dissertation will be compared to the Pack B as a baseline.

1.5.2 Previous Design and Higher-Lift Efforts

Previous design efforts have included derivatives of the Pack B as well as completely new airfoils. Concepts have included front-loaded, mid-loaded, and aft-loaded designs. Some studies have included LPT-relevant phenomena such as disturbances or wakes generated by upstream blade rows which convect through the engine and disturb the flow around the LPT. Wakes are an important viscous phenomena as they can (but not always) dissipate over longer time scales than inviscid pressure gradients [Dring et al. 1982], and therefore can propagate and cause more interactions than inviscid pressure waves alone. The generated wakes attempt to mimic the actual LPT environment by providing frequent, localized concentrations of disturbance energy which affect the boundary layer in two distinct fashions: an immediate inviscid Kelvin-Helmholtz vortex roll-up due to the wake penetration and roll-up in the boundary layer, and a subsequent diffusion of turbulent kinetic energy brought by the convecting wake [Stieger and Hodson 2004]. The term “wake-induced transition” has been used to label the effects of such phenomena [Mayle and Dullenkopf 1989]. For brevity, only the LPT design studies most relevant to the current work will be described here. More information on other recent LPT design research is included as Appendix A.

In 1997, Curtis *et al.* studied various blade profiles with $Zw \approx 1$ for LPT applications by changing the suction surface pressure distribution with flaps and inserts over inlet Reynolds number from 70,000 to 400,000 [Curtis et al. 1997]. Noting a great need for higher loaded designs, their study found wakes affect the suction surface loss much more than the trailing edge or pressure surface losses. They proposed the two most significant factors to determine the suction surface velocity distribution are the degree of deceleration along the surface and the location of the velocity peak. This is important since it gives us two distinct properties of an airfoil design to examine closely:

1. “degree of deceleration”: this is the pressure gradient, specifically the magnitude of adverse pressure gradient along the suction surface of an LPT design.
2. “location of velocity peak”: this is the loading characteristic, i.e. where the maximum or

minimum pressure is located on the airfoil. Choices include front- (L2F), mid- (L1M), and aft-loaded (Pack B) designs.

González *et al.* in 2002 experimentally studied the redesign for high lift of a civil engine LPT, where the LPT section accounted for 20% of the total engine weight and 15% of the total engine cost [González et al. 2002]. They found that profile loss, or the loss generated by viscous effects around the airfoil's cross-section, accounted for up to 80% of the total LPT losses. Their work supports the idea of an optimum location for the Mach number peak, or point of minimum pressure. Results show as Reynolds number is increased, the suction surface transition length decreases while reattachment moves upstream towards the leading edge. As Reynolds number was decreased, the stagnation pressure loss increased. Their investigation of an unsteady environment by introducing periodic wakes generated by moving bars across the inlet showed an earlier reattachment due to wake-induced transition. While unsteady results were unclear for aft-loading versus front-loading, González's steady results did in fact show the overall loss increased for an aft-loaded design.

Praisner *et al.* recently used their attached-flow and separated-flow transition models to develop two new LPT designs based on the Pack B profile [Praisner et al. 2004]. Using optimization techniques, they designed two $Zw = 1.4$ LPTs: one front-loaded (Pack D-F), and the other aft-loaded (Pack D-A). Compared to the performance of the original $Zw = 1.15$ aft-loaded Pack B, steady results showed the aft-loaded Pack D-A suffered greater losses over a range of Reynolds numbers while the front-loaded Pack D-F enjoyed decreased losses. The front-loaded design has an earlier suction peak compared to the aft-loaded designs, and this allows the adverse pressure gradient experienced by the front-loaded design to be spread out over a longer suction surface distance. Thus the adverse pressure gradient for the Pack D-F is not strong enough to cause separation before transition as with the aft-loaded designs, but will instead promote transition before separation. The authors also illustrated the inability of the Wilcox $\kappa - \omega$ turbulence model to accurately capture the effects of secondary flows near blade endwalls. With adequate transition modeling, they propose that front-loaded designs do not require the use of flow control (such as vortex generator jets) to maintain efficiency. In addition, later work found that a front-loaded LPT experiences a "row-loss augmentation" (decrease in losses) due to turning the flow earlier and encountering a less mixed-out wake [Praisner et al. 2006].

In 2005, Clark and Koch designed a mid-loaded LPT with $Zw = 1.34$, a 17% increase over the Pack B [Bons et al. 2005]. Their mid-loaded design reduced the adverse pressure gradient in the latter uncovered turning portion of the blade. Their work also examined the feasibility of designing LPTs with integrated flow control, in their case vortex generator jets (VGJs). VGJs allow an equivalent loading with a reduced axial chord, an increased loading at constant chord and solidity,

or a decreased solidity (increased pitch) at constant loading. Sondergaard *et al.* have shown that the use of VGJs on the Pack B profile allows an equivalent loading with 50% fewer blades [Sondergaard *et al.* 2002]. Both experimental and numerical studies have agreed that VGJs can effectively control separation with pulsed blowing at a duty cycle as low as 10% [Sondergaard *et al.* 2002; ?; Postl *et al.* 2004].

In 2006, Reimann *et al.* experimentally studied the Pack B and L1M profiles at a chord Reynolds number of 20,000 and $FSTI = 0.3\%$ with hot-film anemometry in order to investigate the efficacy of VGJs with different loadings and separation characteristics [Reimann *et al.* 2006]. VGJs were placed at 9% axial chord upstream of the respective separation onset locations, and were pulsed at 5 Hz with blowing ratios of 2 for the L1M and 3 for the Pack B. Their baseline no flow control tests found the L1M transitions before the Pack B due to the more forward (upstream) loading characteristic, with minimum C_p occurring at 47% and 63% axial chord for the L1M and Pack B, respectively. The L1M transition length was also longer than the Pack B; this was attributed to a closer proximity to the wall where the transition in the shear layer took place. Their work also showed earlier reattachment than previous MISES CFD results using Praisner and Clark's separated-flow transition model [Bons *et al.* 2005]. The recent studies highlighted above, as well as those included in Appendix A, have been organized into two tables which summarize some important conclusions regarding LPT design. Tables 1.1 and 1.2 list the researcher(s), year of publication, airfoil shape(s), test or simulation flow conditions, method of examination, and highlighted results. A quick glance over these two tables gives one some insight into the motivation and philosophy behind the current design study.

Examining the summary of recent design efforts presented in Tables 1.1 and 1.2, it appears that there is support for both front-loaded and aft-loaded LPT designs. The inclusion of wakes seems to be the dividing factor which determines whether or not the aft-loaded design will be beneficial. The pros and cons of wakes have been well-documented, and the front-loaded design performs well in both situations. This suggests the most robust LPT design over all flight conditions should be a front-loaded design. It has also been pointed out that only improved transition modeling will allow the high-lift solution to the low-Reynolds number LPT lapse in efficiency. By using Dan Dorney's (NASA Marshall) Wildcat flow solver [Dorney and Davis 1992] with Praisner and Clark's transition model to design a front-loaded, higher-lift LPT with an improved low- Re characteristic, the current study validates the transition model for turbomachinery design purposes and answers the call of the gas turbine industry for well-behaved higher-lift airfoils which can decrease the required blade count in modern gas turbine engines.

Table 1.1: Recent Design Efforts Summary, Part 1*.

Researcher(s)	Year	Airfoil(s)	Conditions	Method	Remarks
Cicatelli & Sieverding	1997	FL LPT	$Re = 2 \cdot 10^6$ FSTI=1.15%	EXP	PS dominance in shedding spectrum; TR'l BL has 2 maxima in spectra
Curtis <i>et al.</i>	1997	$Zw \approx 1$ LPT	$Re = 7 \cdot 10^4$ to $4 \cdot 10^5$	EXP	wakes primarily affect SS
Wolff <i>et al.</i>	2000	Pack B-like LPT cascade		hot-wire, wakes	wakes allow greater dp/dx , increase local τ_w ; calmed region benefits
Dennis <i>et al.</i>	2001	FL, ML, AL LPTs	optimization: GA,SQP for min P-loss	2D NS, $\kappa - \epsilon$ TU	thicker LE and FL design has lowest loss
Howell <i>et al.</i>	2001	AL, $Zw \approx 1$ LPTs	$Re = 1 \cdot 10^5$ to $2.1 \cdot 10^5$, FSTI=0.5%	EXP hot-wire wakes	$Re_\theta \sim 250$ for WIT; AL = increased losses when separated
Howell <i>et al.</i>	2002	$Zw \approx 1.05$ BR710 & BR715 LPTs	$Re = 6 \cdot 10^4$ to $1.2 \cdot 10^5$	EXP hot-wire wakes	$Re_\theta \sim 250$ for WIT; WIT occurs <i>only</i> if already separated
González <i>et al.</i>	2002	high-lift civil LPT, AL & FL		EXP wakes	$Re \uparrow = TR_{length} \downarrow$, RE upstream, loss \downarrow ; AL = \uparrow loss
Sieverding [†] <i>et al.</i>	2004	compressor blade	optimization: range and performance	3D MISES	GAs w/ mutation better than GSM, NN
Sonoda [†] <i>et al.</i>	2004	compressor blade	optimization: min P-loss	low- Re NS w/ Chien's $\kappa - \epsilon$ TU	FL blade = earlier TR = separation resistance

* Abbreviations defined in Nomenclature.

† Compressor optimization, not turbine.

Table 1.2: Recent Design Efforts Summary, Part 2*.

Researcher(s)	Year	Airfoil(s)	Conditions	Method	Remarks
Houtermans <i>et al.</i>	2004	$Zw = 1.47$ FL LPT	$Re = 5 \cdot 10^4$ to $2 \cdot 10^5$, FSTI=0.6%	EXP	$Re \uparrow = \uparrow$ loss; accurate TR modeling difficult for varied loading
Stieger <i>et al.</i>	2004	$Zw \approx 1$ AL T106 LPT	low Re	EXP	wake-BL interactions different inside separation bubble
Praisner <i>et al.</i>	2004	high-load $Zw = 1.4$ FL & AL LPTs	low- Re , 3D RANS sims	apply new TR model in design process	FL LPT outperforms ML and AL profiles; intermittency not considered for LPT design
Zhang & Hodson	2005	$Zw = 1.19$ T106C ML LPT	$Re = 1.3 \cdot 10^5$ to $2.6 \cdot 10^5$	EXP wakes trips	Re -dependent wire diameter; AL only with trips/wakes
Bons <i>et al.</i>	2005	$Zw = 1.34$ ML LPT (L1M)	low Re	EXP LPTs w/ VGJs	VGJs allow \downarrow chord, \uparrow loading, or \downarrow solidity; L1M stall-free down to $Re = 2 \cdot 10^4$
Reimann <i>et al.</i>	2006	$Zw = 1.34$ L1M and $Zw = 1.15$ Pack B	$Re = 2 \cdot 10^4$ $FSTI = 0.3\%$	EXP hot-wire VGJs	L1M TR's before Pack B with longer TR length; VGJ lag & effectiveness is blade-dependent; VGJ calming effect

* Abbreviations defined in Nomenclature.

1.6 Current Study

The current design study is part of an ongoing research plan undertaken by the US Air Force Research Laboratory (AFRL) at Wright-Patterson Air Force Base in Ohio. The research plan seeks to find the limits of stall-free loading by exploring and expanding the current design space for low-pressure turbine airfoils using state-of-the-art design codes and modeling capability. The previous research summarized in Tables 1.1 and 1.2 has used both computational and experimental methods to determine which type of LPT blade profile performs the best over a range of Reynolds number and relatively low freestream turbulence. The current transition modeling employed in this work, which allowed the aggressive loading levels of the L2F, is also currently being utilized for other platforms [Clark and Koch 2006]. These platforms include a transonic high-pressure turbine for advanced government cycles, a single-stage high-pressure turbine developed as an integral part of a supersonic UAV, LPT airfoils designed for Notre Dame's experimental transonic rig, a low heat load vane geometry available for code validation, and a high-pressure turbine designed for a DARPA (Defense Advanced Research Projects Agency) study on fluidic control with MIT and Lockheed. What's missing from the current literature is an answer to the call from the gas turbine industry for improved transition modeling to push the boundaries of the LPT design space and in doing so create an LPT design which allows the higher loading while maintaining or improving the low-Reynolds number lapse in efficiency. In addition to the new LPT design, this study provides the optimization needed for application of a shear and stress sensitive film to low-speed air flow environments on a curved surface, effectively providing the experimental fluids community with another non-intrusive measurement tool which can provide simultaneous regional maps of surface pressure and tangential stress on a surface. In summary, the current study accomplishes the following goals:

1. **Expand gas turbine engine industry's current LPT design space by validating the use of Praisner and Clark's transition modeling in the design cycle of a higher-lift LPT airfoil with an improved low-Reynolds characteristic.**

The current design study shows a well-behaved LPT with very high lift can be produced without the use of unsteady modeling or flow control. The experimental validation of the L2F also compares its performance to the previously-designed Pack B and L1M over a range of Reynolds numbers at a freestream turbulence level of 3.3%. The aft-loaded $Zw = 1.15$ Pack B profile has a lower lift and high Re lapse; the mid-loaded $Zw = 1.34$ L1M has a high lift and lower lapse; the front-loaded $Zw = 1.59$ L2F has an even higher lift with better low- Re lapse. For each test blade, total pressure measurements in the wake define the midspan loss behavior over several chord Reynolds numbers. Thermal anemometry allows the determination of wind tunnel

freestream turbulence level and length scale at the inlet of the cascade. Its use also provides velocity profiles and turbulence spectra in and around the boundary layer, providing a means to validate the transition modeling used in this study.

2. Demonstrate the use of a shear and stress sensitive film (S3F) for low-speed experimental applications.

S3F provides skin friction measurements which can be used to determine separation bubble physics such as separation onset and reattachment for a range of Reynolds number. These locations are necessary for the validation of the transition modeling used in this study.

The current study was performed in the Air Force Research Laboratory's Propulsion Directorate at Wright-Patterson Air Force Base in Ohio. The experimental validation is accomplished in the Low-Speed Wind Tunnel cascade testing facility in Building 252 on base. S3F development occurred in ISSI's wind tunnel in Dayton, Ohio and in Building 252 on base. This dissertation is divided into 5 chapters and 5 appendices. Chapter 2 describes the computational framework, methodology, and results of the L2F profile design. Chapter 3 contains the experimental arrangement and techniques used in Building 252 as well as the initial low-speed development of S3F conducted at ISSI. The experimental results taken on base are presented in Chapter 4, while a discussion summarizing this work is given in Chapter 5. Appendix A contains more on higher-lift LPT design efforts not included in the introduction. The measurements taken to characterize the AFRL LSWT turbulence scale and decay are presented and discussed in Appendix B. Appendix C contains background information related to pressure and skin friction measurement techniques, while Appendix D describes the operation and data reduction of the S3F technique. Appendix E presents an uncertainty analysis for the experimental techniques and results presented in this study.

2

L2F Design

A designer knows he has achieved perfection not when there is nothing left to add, but when there is nothing left to take away.

– Antoine de Saint-Exuptry

As mentioned in Chapter 1, the mature gas turbine industry concentrates much of its design effort in the reduction of the overall cost of the engine. The high-lift LPT promises a higher loading per blade, providing a greater amount of work extracted per blade. This could be useful in higher-loading take-off or climbing flight situations, as well as in the reduction of the engine cost by lowering the required blade count for a given total loading. This chapter describes the tools used to design the L2F profile, and compares the L2F to two previous designs, the L1M and the Pack B low-pressure turbines.

2.1 Turbine Design and Analysis System (TDAAS)

The computational system used to design and analyze the LPT profiles is the *Turbine Design and Analysis System* (TDAAS) developed by John Clark of AFRL. The TDAAS is a menu-driven, Matlab-based turbine development system which can optimize both low- and high-pressure turbines. This system incorporates Frank Huber's *Huberfoil* airfoil generation system together with Dan Dorney's *Wildgrd* grid generator and Wildcat flow solver [Dorney and Davis 1992] into a single graphical user interface configured for Matlab. Once an airfoil (turbine blade) shape is generated, a grid is mapped around the surface and the flow solver can then be executed. TDAAS provides all pre-processing and setup as well as all post-processing required for analysis.

2.2 Airfoil Generation

For airfoils of equal flow turning, the percent change in the pitch-to-chord ratio is approximately equal to the percent change in the Zweifel loading coefficient:

$$\frac{\left(\frac{pitch}{chord}\right)_{old} - \left(\frac{pitch}{chord}\right)_{new}}{\left(\frac{pitch}{chord}\right)_{old}} = \frac{(Zw)_{old} - (Zw)_{new}}{(Zw)_{old}} \quad (2.1)$$

Starting with the Pack B geometry at $Zw = 1.15$ and design pitch-to-chord of 0.885, Equation 2.1 was used to create the nominal L2F design at $Zw = 1.59$ resulting in a pitch-to-chord of 1.22. This results in a 38% increase in Zw over the Pack B geometry and will therefore allow a 38% decrease in blade count. All airfoils generated in this work have fixed inlet and exit blade metal angles to allow direct comparison.

Using the design and optimization capability within TDAAS, the Pack B geometry was easily translated into the nominal L2F geometry. The Pack B geometry was previously reverse-engineered to fit the *Huberfoil* profile construction [Clark 2005]. Subsequent design changes were then required to optimize the performance of the new design. New candidate profiles were generated using Frank Huber's *Huberfoil* airfoil shape generation algorithm which is internally executed from within TDAAS. The airfoil is defined using 6 Bezier curves and 13 other shape parameters for the candidate profile including: leading- and trailing-edge diameters and metal angles, axial chord length, height to length ratio, and uncovered turning. The user can choose between a graphical user interface (GUI), text, or graphical editing of up to 16 design parameters. The candidate profile is updated real-time in a viewing window along with curvature, thickness, and area distributions. These features are illustrated in screen shots of TDAAS for the Pack B profile in Figure 2.1.

2.3 Grid Generation

Any numerical CFD solver needs a set of grids over which the governing equations are solved. Dan Dorney's grid generation program *Wildgrd* was specifically developed to create grids for axial turbomachinery blade rows for use with Dorney's Wildcat flow solver [Dorney and Davis 1992]. Several different grid clusterings and spacings can be implemented depending on the type of turbine analysis desired, i.e. a supersonic grid vs a heat transfer grid vs a standard LPT grid. All results presented herein have used the standard LPT grid option as developed by John Clark. *Wildgrd* is externally executed from within TDAAS and produces 2D zonal H- and O-grids. The use of O- and H-grids was specifically developed for the design of linear turbomachinery cascades using 3D viscous flow codes [Lee and Knight 1989]. Dorney's *Wildgrd* generates algebraic H-grids that are

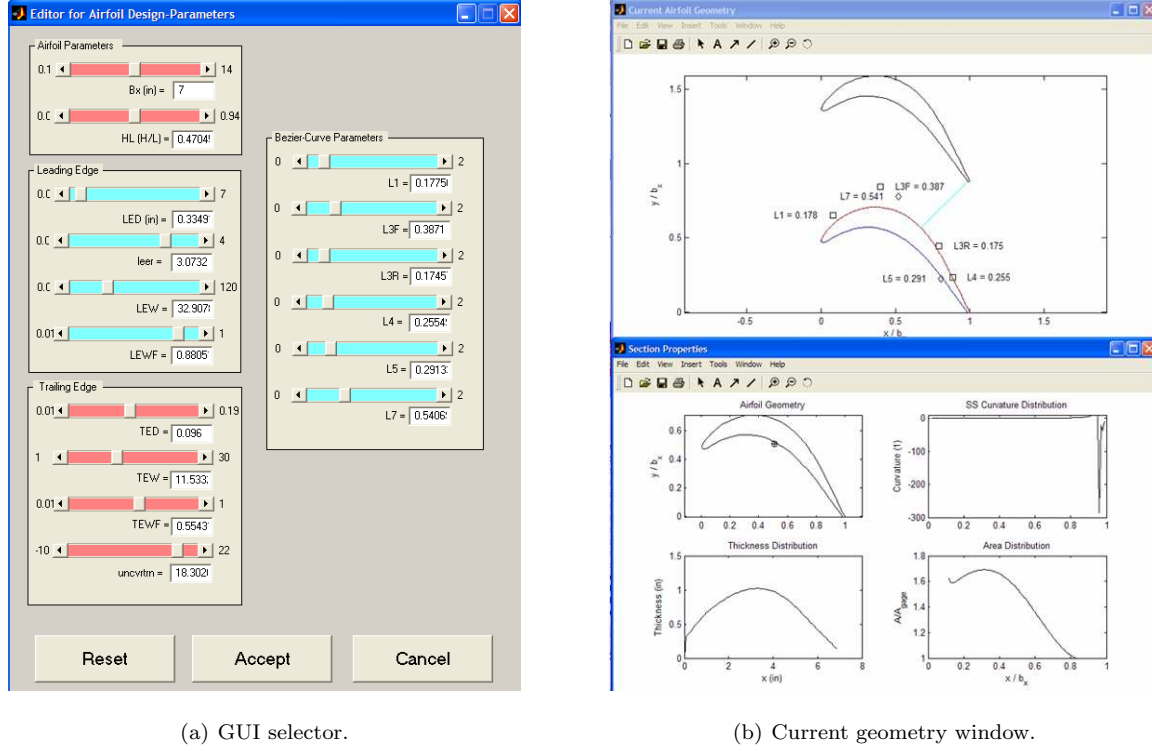


Figure 2.1: Screen shots of airfoil shape generation.

used upstream of the leading edge, downstream of the trailing edge, and in the blade passages. The H-grids are based on the airfoil mean camber line. H-grid lines can be clustered in both the axial and circumferential directions upstream of the leading edge and downstream of the trailing edge. The body-fitted O-grids are generated after the H-grids with an elliptic equation solver and are used to resolve the viscous flow along the surface. *Wildgrd* then solves the elliptic equations (2.2 and 2.3) using a successive line over-relaxation technique to produce the orthogonal O-grids:

$$\alpha x_{\xi\xi} - 2\beta x_{\xi\eta} + \zeta x_{\eta\eta} = -J^2(Px_{\xi} + Qx_{\eta}) \quad (2.2)$$

$$\alpha y_{\xi\xi} - 2\beta y_{\xi\eta} + \zeta y_{\eta\eta} = -J^2(Py_{\xi} + Qy_{\eta}) \quad (2.3)$$

with

$$\alpha = x_{\xi}^2 + y_{\eta}^2 \quad (2.4)$$

$$\beta = x_{\xi}x_{\eta} + y_{\xi}y_{\eta} \quad (2.5)$$

$$\zeta = x_{\eta}^2 + y_{\xi}^2 \quad (2.6)$$

where J is the Jacobian of the transformation matrix and P and Q are functions used to control clustering and orthogonality near walls. The blade-normal direction is stretched to provide fine grid

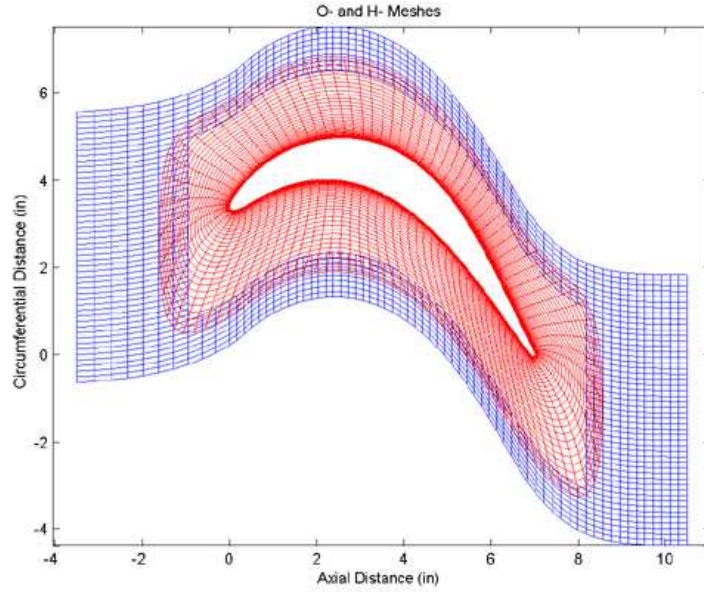


Figure 2.2: Typical O-H grid mesh for Pack B profile.

spacing at the wall with y^+ values less than unity. There are typically around 7,000 grid points per blade passage for the 2D model, and approximately 7 grid points per momentum thickness in airfoil boundary layers. The grid densities and spacings used for this study are consistent with industry design practices to capture thermal fields, surface heat transfer, and transition-related streamwise gradients in gas turbines (see, e.g. [Praisner and Clark 2007]). In addition, two four-point coordinate sets define the overlap between the O- and H-grids. These sets of coordinates help define the inner and outer boundaries of the O-H overlap. The points inside the overlapped inner boundary of the H-grid are not used to solve the governing equations. The governing equations are solved on both grids in the region between the inner and outer specified boxes, each box being defined by its respective four-point set of coordinates. Overlap of the grids helps ensure stability of the solution but can add computation time due to the calculation of redundant grid locations. A screen shot of a typical O-H grid mesh around the Pack B profile is shown in Figure 2.2.

2.4 Flow Solver

Wildcat is a quasi-3D, time-marching, implicit, zonal-grid, unsteady multiple blade row flow solver [Dorney and Davis 1992]. It solves the full or thin-layer Reynolds-Averaged Navier-Stokes equations by using a dual-time-step, linearized, approximate factored, upwind finite difference scheme. The upwind formulation, which inherently possesses dissipation that controls numerical instabilities

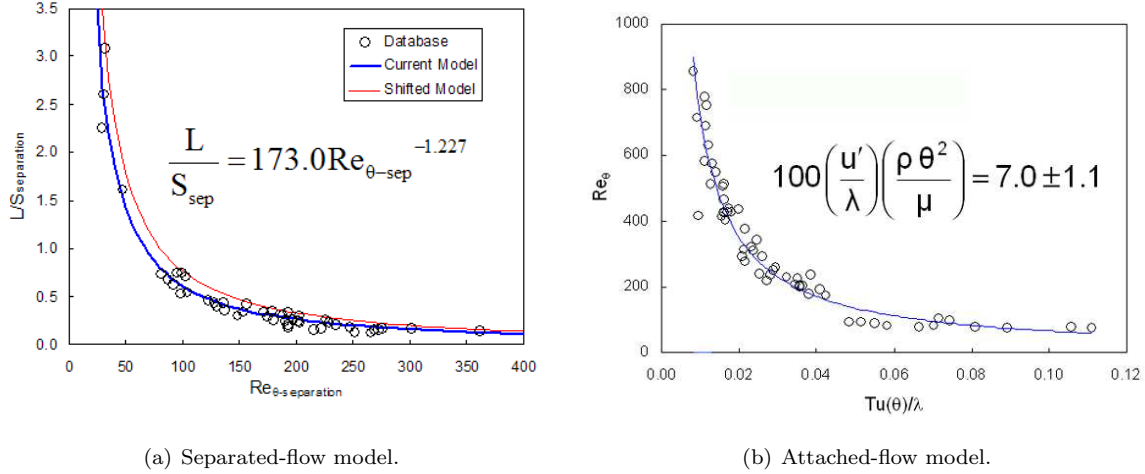


Figure 2.3: Transition model databases, from [Praisner and Clark 2007].

[Tannehill et al. 1997], is third order accurate in space and second order accurate in time.

The separated-flow transition model developed by Praisner and Clark [Praisner and Clark 2007] is used in this work to design the L2F. It is an empirically based model for RANS solvers intended for use in airfoil design systems. The model was constructed from a CFD-supplemented database of 47 separated-flow transition with turbulent reattachment experimental cascade test cases. The separated-flow model was developed in conjunction with an attached-flow model based on 57 experimental test cases. Dimensional analyses led to the appropriate parameters in each situation. The separated-flow model is a correlation relating the momentum thickness Reynolds number at separation onset with the length of the separation bubble from onset to transition in the bubble's shear layer. The separated model equation is presented below:

$$\frac{L}{S_{sep}} = C Re_{\theta-sep}^D \quad (2.7)$$

where L is the length along the bubble from onset to transition, S_{sep} is the suction surface distance from the leading edge to the onset of separation, $C = 173.0$, and $D = -1.227$.

The attached-flow model implies transition onset occurs when a ratio of a boundary layer diffusion time to a timescale of local large-eddy turbulent fluctuations (integral time scale) reaches a critical level. This relationship can be cast as Equation 2.8 below:

$$Re_{\theta} = A \left(Tu \cdot \frac{\theta}{\lambda} \right)^B \quad (2.8)$$

where the momentum thickness Reynolds number is equal to the RHS at transition; in the model $A = 8.52$, $B = -0.956$, and Tu , θ , and λ are the turbulence intensity, momentum thickness, and integral length scale at the boundary layer edge at the transition location. Data from the

development of the models is presented in Figure 2.3. Validation of the models is provided in [Praisner et al. 2007]. Here, turbulent eddy viscosity is calculated using the zero equation Baldwin-Lomax algebraic model [Baldwin and Lomax 1978].

Running a transitional case in Wildcat requires a previously converged laminar run in order to extract the model parameters at separation onset required for the separated-flow transition model. Thus, the transition trip location is determined based on laminar predictions. Turbulent eddy viscosity is then applied after a short transition zone of pre-specified length. It should also be noted the current implementation of the transition model is somewhat conservative. The original development within the Pratt & Whitney design system included the use of the attached-flow model up to the point of separation, the separated-flow model after separation, and the use of an additional quasi-laminar (QL) model which accounted for the effects of freestream turbulence on pre-transitional laminar boundary layers. The exclusion of the attached-flow and QL models results in an over-prediction of reattachment locations, translating into a longer bubble length and an increased loss prediction than that obtained through experiment. The previous use of the separated-flow transition model in creating the L1M profile [Bons et al. 2005] illustrates this phenomenon. The L1M was designed without the attached-flow or QL modeling, and their experimental verification found an under-prediction of onset and separation values of momentum thickness by 15% or more. Regarding the inverse relationship between Re and bubble length, this causes an over-prediction of the bubble length resulting in a conservative prediction; for $Re = 20,000$, the L1M predicted reattachment was 12% chord downstream of the experimental location.

As of 1997, the majority of CFD solvers designed for compressible flows experienced lowered efficiency or decreased accuracy in low Mach number regimes [Tannehill et al. 1997]. These difficulties are believed to be due to the stiff matrices of the ill-conditioned algebraic problem and round-off errors which are amplified due to differing magnitudes of flow variables. As Wildcat is a compressible code, simply changing the Mach number to survey the low Reynolds number range of interest in this study would not produce converged results. Therefore, an alternate method of changing the Reynolds number was employed. Instead of changing the velocity to reduce the Reynolds number, the density was instead modified (and therefore pressure by the ideal gas equation of state) to achieve the desired Reynolds numbers. The former approach of changing the velocity (Mach number) allowed converged results down to a chord inlet Reynolds number of $1.5 \cdot 10^5$, while the latter method allowed converged results down to $2 \cdot 10^4$, a difference of nearly an order of magnitude. Pressure fields converge faster than entropy fields due to different event time scales associated with pressure waves and diffusion [Clark and Grover 2006], and as such convergence in this study was achieved once the pressure field downstream of the trailing edge became periodic. Thus, changing the density and pressure allowed

Wildcat to converge in the lower range of Reynolds number desired for this study.

2.5 Design of Experiments

After the nominal L2F profile was created, further exploration of the design space was required to tailor the blade geometry for optimal performance. The methodology used to find the final L2F profile is outlined in the flow chart of Figure 2.4. First, the nominal design was constructed according to section 2.2. Baseline results were computed from Wildcat, and runs were then executed to find which of the 19 design variables had the most influence on the desired outcome: a front-loaded design with a good low-Reynolds number characteristic. Initially, a Monte-Carlo exploration of the design space was employed in order to find which parameter ranges led to reasonable performance. This first exploration narrowed the 19 variables down to 9, which included the leading edge diameter, leading edge wedge angle, degree of uncovered turning, leading edge ellipse ratio, and the 5 Bezier curve control handles L1, L3F, L3R, L4, and L7. In order to explore this reduced design space, a Matlab Design of Experiments (DOE) algorithm available within TDAAS was employed. This DOE algorithm uses the latin hyper square method which randomly distributes and permutes through the given variable ranges of each selected input variable. The DOE generated 250 variations within the selected design space, and each profile was examined for overall loading coefficient (Zw), total loss ($\Delta Pt/Q_{in}$), degree of front-loading (location of minimum pressure), and the magnitude and smoothness of the adverse pressure gradient along the suction surface.

Profiles generated by the DOE include thin as well as thick variations, some more front-loaded than others and some with smoother curvature and pressure gradient distributions. The exit Mach number for these design runs was held constant at 0.2; although this is considered a high-Reynolds number flow and our design intent is to produce a well-behaved airfoil at lower Reynolds numbers, this design philosophy successfully produced a mid-loaded airfoil (L1M) which was reported stall-free down to $Re = 20,000$ [Bons et al. 2005], and is therefore employed in the current work with confidence. Figures 2.5 and 2.6 show examples of selected shapes generated from the latin hyper square DOE. These figures present the selected profile attributes (shape and loading) in red with a blue dotted line background showcasing the final L2F for comparison. A loss parameter defined as the integrated change in total pressure normalized by the inlet total pressure is included in the title of the loading plot; this loss value for the L2F is 0.08969. Various selected profiles generated by the DOE will now be described in order to give the reader an idea of the reasoning behind the L2F selection.

Figures 2.5(a) and 2.5(b) show examples of thin profiles generated by the DOE, one with a lower

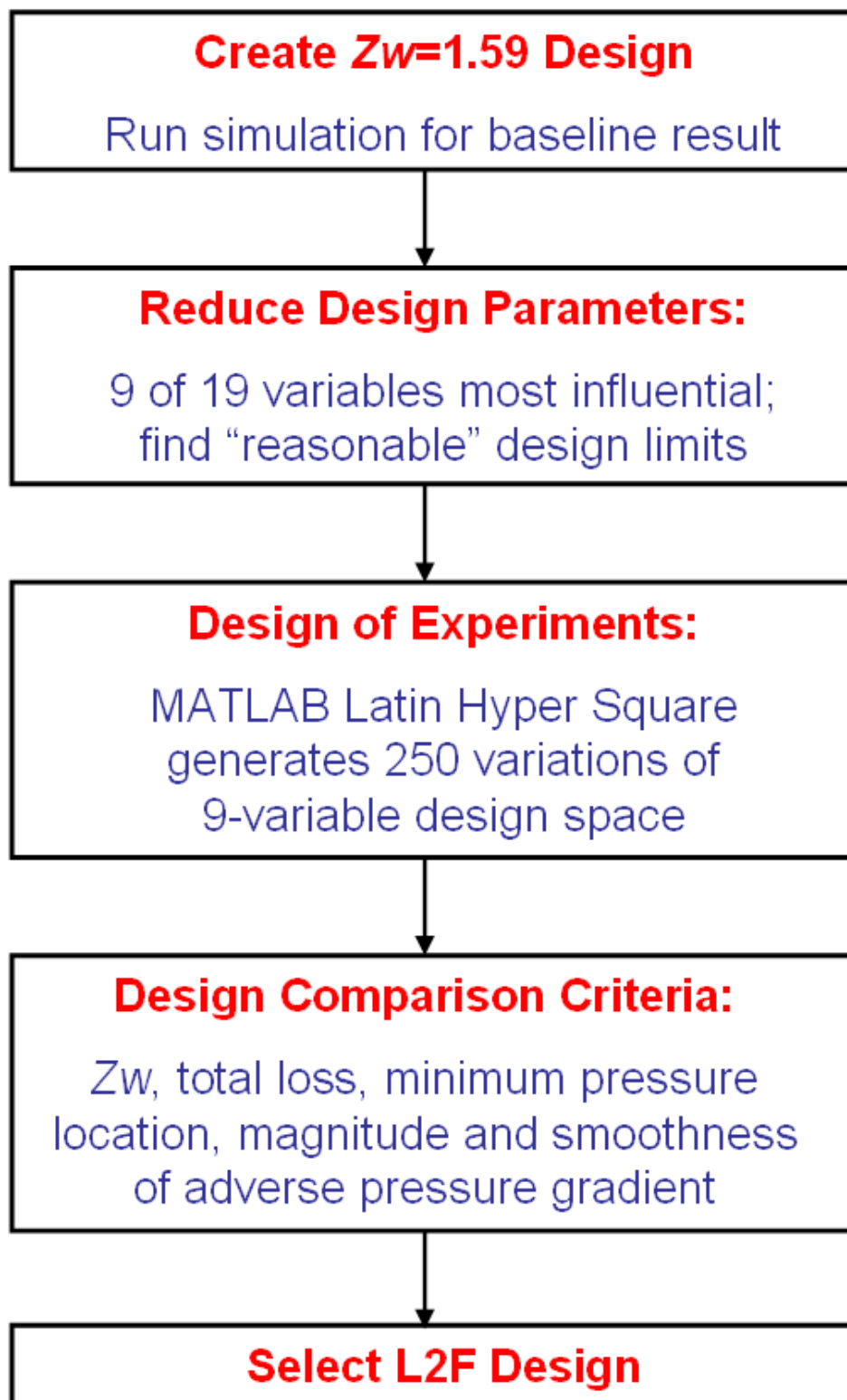


Figure 2.4: Design process flow chart.

loss and one with a higher loss value compared to the L2F. Both profiles also exhibit a more front-loaded characteristic with their respective pressure minimums in front of the L2F. Profiles such as these were not selected due to the non-smooth pressure gradient along the suction surface. A non-smooth pressure gradient such as in 2.5(b) induces oscillating forces on the flow, first decelerating from the pressure minimum to nearly 38% axial chord, then accelerating as the pressure gradient decreases until nearly 58%, then again decelerating the flow as the pressure rises to meet the trailing edge. In addition, these profiles induce a more severe magnitude of adverse pressure gradient (as evidenced by the slope of the pressure loading curve) which is known to cause separations to occur in lower Reynolds situations. Therefore, profiles which exhibit a less degree of adverse pressure gradient are favorable. Thicker designs, such as those in Figures 2.5(c) and 2.5(d), can allow a smaller magnitude pressure gradient but often induce a greater loss possibly due to the increased flow area blockage. Again, care must be taken with respect to where the point of pressure minimum is located - a more front-loaded design inherently spreads the adverse pressure gradient out over a longer suction surface distance, thus reducing the likelihood of separation. As some have suggested [Dennis et al. 2001], global shape optimizations work better to achieve the desired performance characteristics over inverse design methods, and Figure 2.5(d) may lend some support evidence to this argument. The loading achieved with this profile is very similar to the final L2F profile, but much more material is required for this blade over the L2F due to its thicker cross-section. Keeping in mind that an objective of this design should be the minimization of engine weight, the L2F is clearly superior (as long as the material density is the same for both cases). Perhaps an inverse design method used in conjunction with additional DOE or optimization studies could do better than either alone. Figures 2.5(e) and 2.5(f) show profiles which are more front-loaded and have an increased height-to-length ratio than the final L2F design. Again, these results are for an exit Mach number of 0.2, while a desired outcome is for improved low-Reynolds performance which dictates the adverse pressure gradient be as small as possible. Therefore, designs with gradients towards the upper end of the spectrum were not considered for the final design.

Figures 2.6(a) through 2.6(f) show examples of designs which are similar to the final L2F design. Again, attention was paid to the integrated loss values as well as the pressure minimum peaks and magnitude and smoothness of the adverse pressure gradients. These plots, in particular Figures 2.6(b) and 2.6(d), show how very small changes to the suction surface of the blade can result in significant differences in performance. A smooth curvature is also required when considering available manufacturing methods, which undoubtedly become increasingly difficult when adding more complexity to the design.

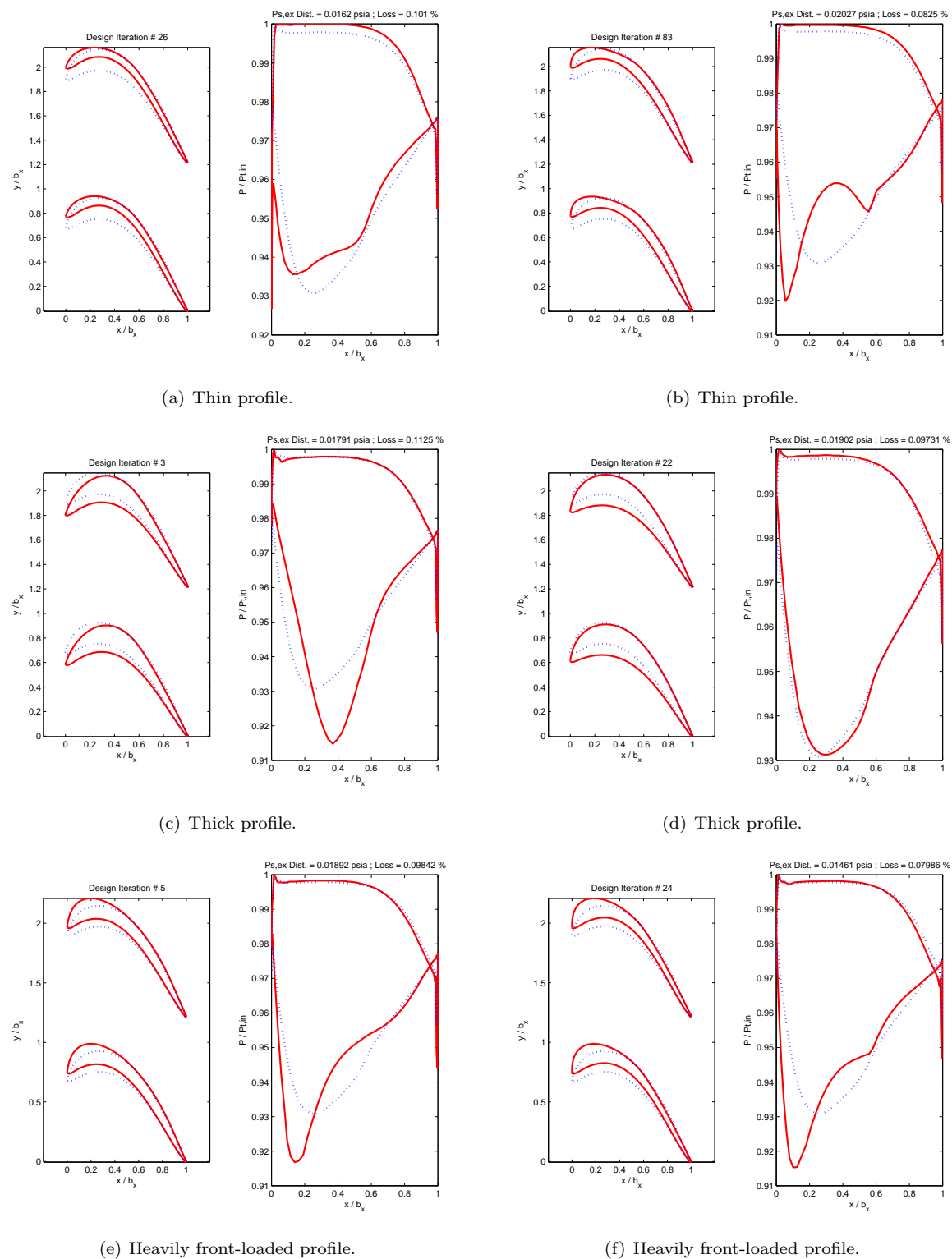


Figure 2.5: Variation in profiles generated by DOE.

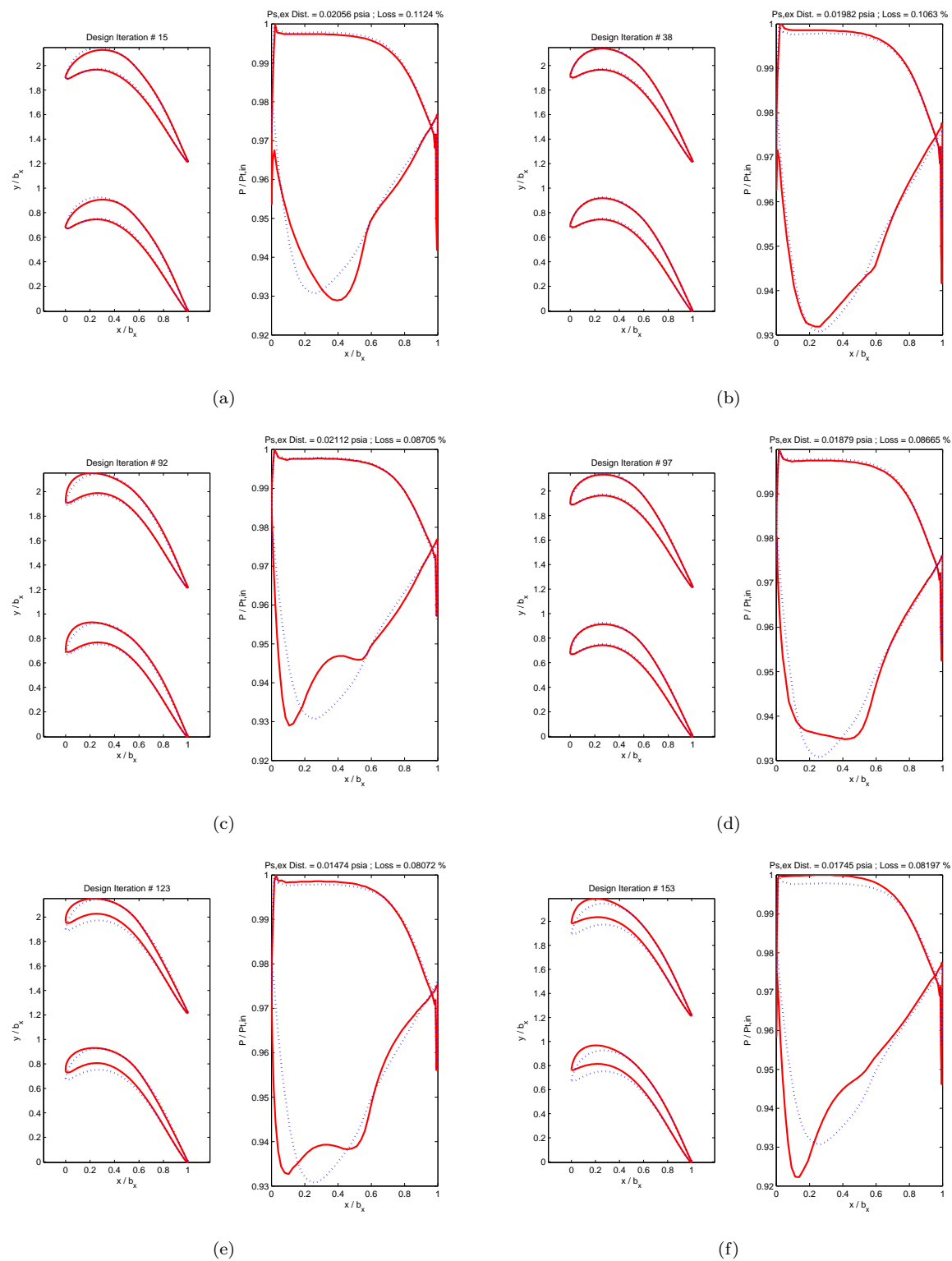


Figure 2.6: L2F-like profiles generated by DOE.

2.6 The Result: L2F

The design intention was to produce a front-loaded LPT with a nominal Zweifel loading coefficient near 1.6. By tailoring the leading edge and suction surface design parameters, the LPT should perform better than the Pack B LPT in the low Reynolds flow regime, thus answering the gas turbine industry's call for a higher-lift LPT with an improved low- Re characteristic. The latter portions of the resulting L2F profile is presented and compared to the Pack B and L1M geometries in Figure 2.7. The Pack B profile was developed by Pratt & Whitney in the 1990s and has a moderate lift ($Zw = 1.15$) and high Re -lapse; the L1M blade developed by Clark and Koch in 2005 has lower Re -lapse while producing higher lift ($Zw = 1.34$), allowing a 17% decrease in blade count and weight; the L2F profile designed herein has a lower Re -lapse at an even higher lift ($Zw = 1.59$), which allows a 38% reduction in blade count and weight. Again, the blade metal angles were held fixed to allow direct comparison of results. Figure 2.7 also gives the reader an idea of the different blade spacings achieved with the advanced blades.

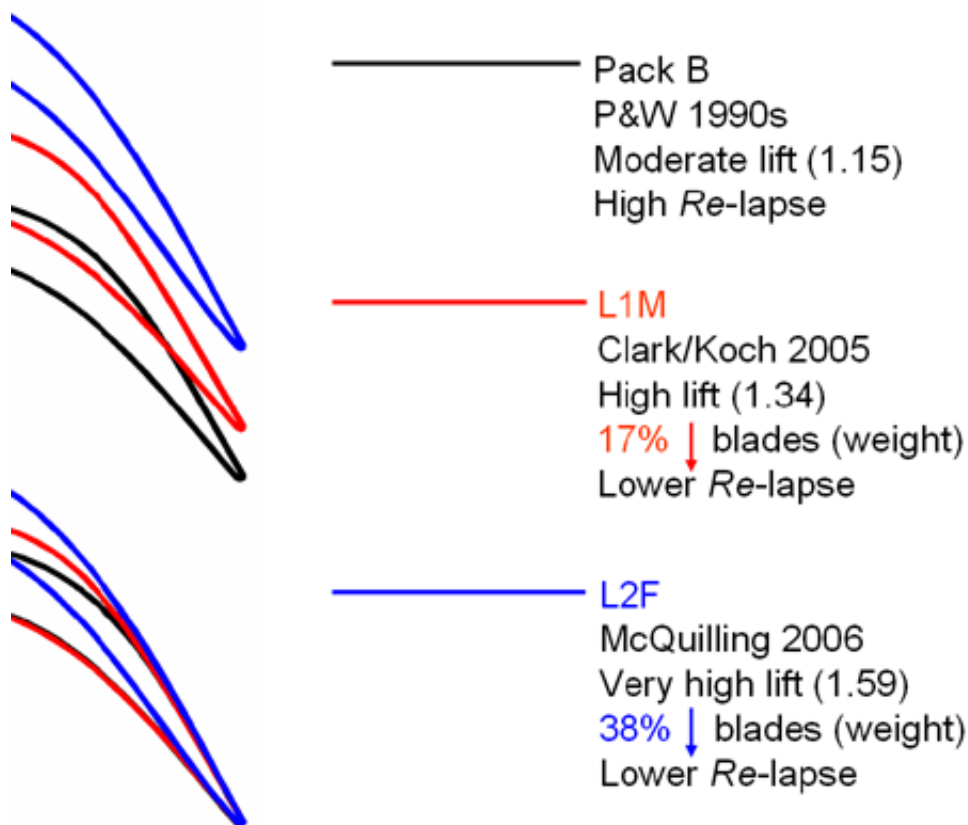


Figure 2.7: Geometric comparison of Pack B, L1M, and L2F profiles.

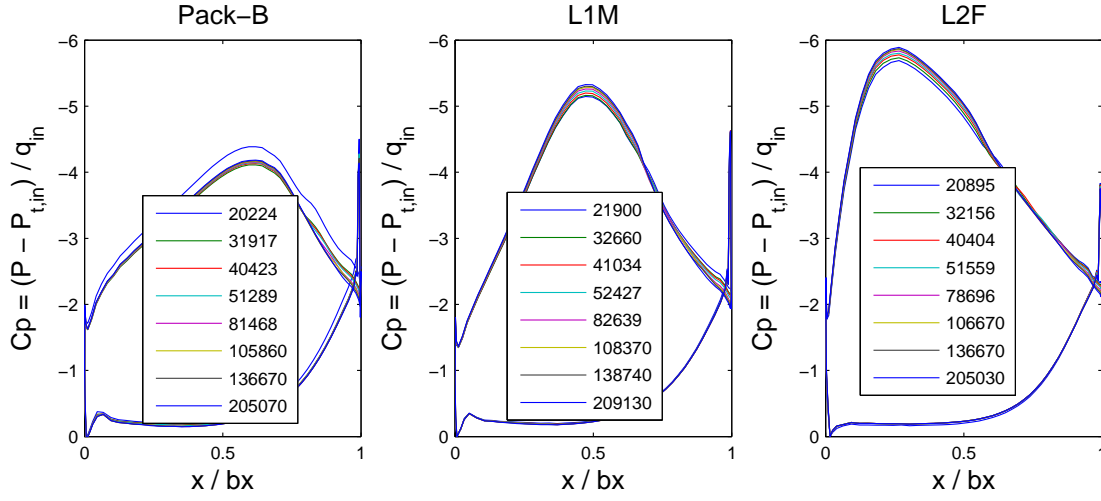


Figure 2.8: Coefficient of Pressure for Pack B, L1M, and L2F.

As mentioned in the introduction, Curtis *et al.* suggested two important characteristics of an LPT suction surface that we should consider during the design cycle: the location of the pressure minimum and the magnitude of adverse pressure gradient along the suction surface. Figure 2.8 presents Wildcat's transitional predictions of the coefficient of pressure distributions for the Pack B, L1M, and L2F profiles over various values of Re . This figure plots the difference between the local surface pressure and total inlet pressure, normalized by the inlet dynamic pressure, and is plotted with the classical inverse y-axis so the suction surface is on top. The Pack B, L1M, and L2F axial chord locations of pressure minimums are 62%, 48%, and 27%, respectively. Although not calculated, the magnitude of pressure gradient along the suction surface (slope of C_p curve) can also be seen in Figure 2.8, and shows that pushing the loading towards the leading edge allows a milder distribution of adverse pressure gradient along the suction surface by spreading out the total pressure change from the pressure minimum to the trailing edge over a greater distance. Therefore, front-loaded designs are more intrinsically separation-resistant due to the reduction of the adverse pressure gradient, which is known to be a primary factor in generating separation zones. It is interesting to note these pressure distributions do not exhibit the pressure plateau commonly associated with separation bubbles. We'll see later that these flows are in fact separated, but may have very thin separation bubbles.

2.7 Chapter Summary

Chapter 2 presented the computational design of the L2F airfoil. The *Turbine Design and Analysis System* in use at AFRL was outlined, including airfoil and grid generation, the Wildcat RANS flow solver, and the transition modeling developed by [Praisner and Clark 2007]. The two models, one for attached-flow and one for separated-flow transition, were intended for use in RANS-based airfoil design systems and were created by examining 47 experimental test cases of separated-flow transition with turbulent reattachment and 57 cases of attached-flow transition. Dimensional analyses led to the appropriate model representations, where the separated-flow model predicts the length along the separation bubble from separation onset to transition, and the attached-flow model defines the ratio of a boundary layer diffusion time to a local turbulent timescale which must match a critical level for transition to occur. The L2F design of experiments implemented a latin-hyper square method which randomly permuted through the design variables to create 250 variations of the design space. These variations included thick and thin designs with various degrees of front-loading and adverse pressure gradient. It was also shown how inverse design methods may possibly miss optimal designs, as thicker designs achieved similar pressure distributions as the final L2F, but with much more material these thicker designs were not chosen due to the requirement for reduced weight. The final L2F design was not chosen from the generated 250 variations; these variations instead provided insight into which levels of design variables produced the intended design: a high-lift front-loaded airfoil which performed well in the low Reynolds regime. The final design therefore became a mix of those generated by the DOE, resulting in a nominal $Zw = 1.59$ airfoil with its suction peak at 27% axial chord. This front-loaded profile provided a 38% increase in Zweifel loading coefficient, representing a 38% reduction in blade count over an airfoil typical of those in service today (e.g., the Pack B). This increase in lift also came with an improved Reynolds lapse characteristic which promises longer loiter times, a higher altitude flight ceiling, and reduced fuel consumption, all of which decrease the total cost of the gas turbine engine over its life cycle.

3

Experimental Arrangement

The satisfaction derived from solving a problem with an experiment is a very heady experience, almost addicting.

– Paul Berg

Several experimental measurement techniques are used in this work in order to validate L1M and L2F airfoil performance as well as verify the transition modeling used in the design process. All results presented in Chapter 4 were taken in AFRL's Low-Speed Wind Tunnel (LSWT) facility in Building 252 at Wright-Patterson Air Force Base in Ohio. This chapter briefly describes this facility along with the experimental techniques employed. In order to generate approximately 3.3% freestream turbulence intensity at the test section, a turbulence-generating grid was placed upstream of the test section. Appendix B describes the measurements taken in order to characterize the turbulence decay and length scale generated by the upstream grid. In addition, this chapter contains the initial development of the S3F technology accomplished in the Innovative Scientific Solutions, Inc. wind tunnel in Dayton, Ohio. This initial development helped set the framework for S3F application in low-speed air flow tests on a curved surface.

3.1 Low-Speed Wind Tunnel

The AFRL Low-Speed Wind Tunnel (LSWT) is inductively driven by a 125-hp electric motor powering an axial flow fan located downstream of the 0.85m tall by 1.22m wide test section. The test section is constructed of clear polycarbonate (Lexan) for optical access and is arranged to allow quick interchange of test cascades. This configuration can produce air inlet velocities up to 80 m/s. Honeycomb flow straighteners follow the 3.0m by 2.7m rectangular bell-mouth inlet with a gradual 8:1 area contraction which produces a uniform, low-turbulence velocity profile at the cascade test

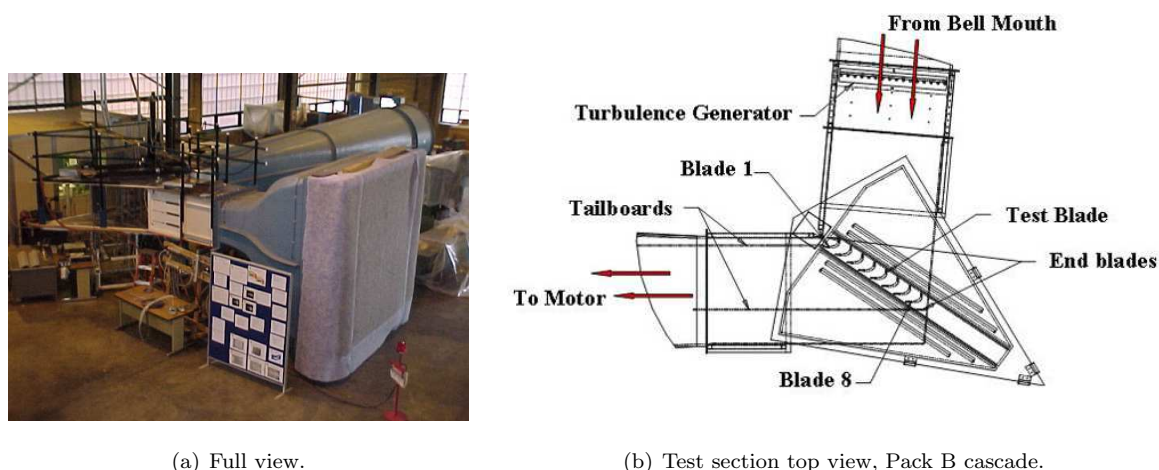


Figure 3.1: AFRL's Low-Speed Wind Tunnel.

section inlet. Figure 3.1(a) shows the full view of the AFRL LSWT tunnel while Figure 3.1(b) shows the top view of the test section for the Pack B cascade with 8 blades. The test section is constructed to accommodate interchangeable packs of blades which can slide into and out of the main section, and it contains adjustable tailboards to set proper periodicity. These tailboards can be slid toward or away from the cascade and can be angled to accommodate various inlet and exit angles. The L1M and L2F cascades were fitted with 7 blades to achieve periodicity, and the axial chords of the airfoils were 7in and 6in, respectively. Both airfoils have a 0.876m span with an inlet gas angle of 35 degrees and an exit gas angle of 60 degrees. A turbulence-generating grid can be placed 2.3m upstream of the test blade leading edge in order to generate 3.3% freestream turbulence at the cascade inlet. The grid is a square-mesh array of 2.54cm diameter tubes spaced 7.6cm apart, producing unsteady uniformity of $\pm 0.3\%$. Over the Reynolds number range from 25,000 to 75,000, the grid produces an integral length scale between 3.51 and 4.19cm, a Taylor microscale between 0.38 and 0.81cm, and a Kolmogorov length scale between 0.08 and 0.05cm at the entrance to the cascade. Details of the turbulence characterization can be found in Appendix B. Upstream flow diagnostics include a thermocouple for inlet temperature, an inlet hot-wire to determine the test Reynolds number, and a pitot-static reference probe. There are also four 1.5m long traverse slots located atop the cascade both upstream and downstream of the linear cascade. A three-axis traverse can be placed atop the tunnel to measure a planar section of the wind tunnel through these slots; its position is accurate to within $\pm 0.5\text{mm}$. A smaller 3-axis traverse can be placed inside the tunnel and is accurate to within $\pm 0.01\text{mm}$; this smaller traverse is used to position the hot-film probe in the boundary layer. Loss coefficients across the the wake of a cascade are measured with a Kiel probe containing a 1.5mm diameter sensor head plumbed to a differential pressure transducer with range of -0.2 to 0.8 inches

of water (-50 to 200 Pa).

3.2 Techniques and Data Processing

The standard flow diagnostic capability used in the AFRL LSWT includes pressure probes, hot-wire anemometry, and particle image velocimetry. An instrumentation demonstration was also conducted using a shear and stress sensitive film (S3F) developed by Innovative Scientific Solutions, Inc.

3.2.1 Pressure Measurement

Pressure probe measurements give the pressure at a single point in the wake of the turbine blades. All pressure data was taken at 1kHz for 30,000 samples with a 5s settling time in between successive measurements. The pressure probe setup uses a Druck LPM5481 differential transducer with a range of -0.2 to 0.8 in of water (-50 to 200 Pa) with output of 0 to 5 Volts, powered by a GW Instek GPS 3303 3-channel DC power supply. The pressure data is digitized and transferred to a PC through an 8-slot National Instruments PXI-1010 chassis with 16-bit A/D conversion; the chassis supports both PXI and SCXI connections. The probe is traversed across the wake in order to quantify the losses caused by the airfoil. Loss is generally defined as the deficiency in total pressure between the exit and inlet. As the instruments used herein offer differential pressure data, the following definitions are used to define area-averaged and flux- or mass-averaged losses:

$$L_{area} = \frac{\overline{(P_{t,in} - P_{t,ex})}}{\overline{(P_{t,in} - P_{s,in})}} \quad (3.1)$$

$$L_{flux} = \frac{[\sum u_{ex,i} \cdot (P_{t,in} - P_{t,ex})_i] / \sum u_{ex,i}}{(P_{t,in} - P_{s,in})} \quad (3.2)$$

The wake loss measurements are compared to predictions from Wildcat in Chapter 4.

3.2.2 Thermal Anemometry

Thermal anemometry is a point velocity measurement commonly used in contaminant-free, nearly isothermal gas flows where the mean velocities and turbulence intensities are not extremely high [Bernard and Wallace 2002]. The physical principle used by hot-wire anemometry is that the rate of cooling experienced by a thin heated wire can be nonlinearly related to the local flow velocity through King's Law. The algorithm which uses King's Law in this study to convert hot-wire signals to velocity has been developed over many years at WPAFB and is different from the four-constant model presented in [Bernard and Wallace 2002]. Therefore, it is described in more detail here. First,

the temperature of the wire, T_{wire} [K], is calculated using the sensor operating resistance, R_{op} [Ω], resistance at 0°C, R_0 [Ω], and difference in resistances between 100 and 0 °C, R_{100-0} [Ω]:

$$T_{wire} = \frac{R_{op} - R_0}{R_{100-0}} \times 100 + 273.15 \quad (3.3)$$

The mean sensor film temperature, T_m [K], is then calculated using T_{wire} and the freestream temperature, T_∞ [K], as measured by an upstream thermocouple:

$$T_m = \frac{T_{wire} + T_\infty}{2} \quad (3.4)$$

Next the density of air, ρ [$\frac{kg}{m^3}$], dynamic viscosity, μ [$\frac{kg}{m \cdot s}$], thermal conductivity, k [$\frac{W}{m \cdot K}$], and Prandtl number, Pr , are calculated using T_m , the atmospheric pressure read by a local barometer, and the dew-point temperature read with a hand-held hygrometer made by Control Company. The power dissipated by the wire is then calculated according to Equation 3.5:

$$power = volt^2 \times \frac{R_{op}}{(R_{op} + 10)^2} \quad (3.5)$$

where *volt* is the voltage reading from the anemometer. The local Nusselt and Reynolds numbers are then calculated according to Equations 3.6 and 3.7, respectively:

$$Nu = \frac{power \times (\frac{T_m}{T_\infty})^{TempPowRatio} \times Pr^{-1/3}}{\pi \times L_{wire} \times k \times (T_{wire} - T_0)} \quad (3.6)$$

$$Re = \left(\frac{Nu - C_{int}}{D_{slope}} \right)^{(1/Re_{exp})} \quad (3.7)$$

where *TempPowRatio* is a factory-set value used to account for differences between calibration and operation temperatures, L_{wire} is the length of the sensor, C_{int} and D_{slope} are the calibration constants of the sensor, and Re_{exp} is the experimentally determined Reynolds number of the bulk fluid flow. Finally, the local flow velocity, Vel [m/s], is determined from Equation 3.8:

$$Vel = \frac{Re}{(\rho \times d_{wire})/\mu} \quad (3.8)$$

where d_{wire} [m] is the diameter of the sensor. The local flow temperature, T_{flow} [K], can also be calculated with Equation 3.9:

$$T_{flow} = \frac{T_0}{((\frac{1}{2}\rho Vel^2 + P)/P)^{(\gamma-1)/\gamma}} \quad (3.9)$$

When using the X-wire, a distinct calibration technique is employed in order to gain the additional velocity component. First, the probe is calibrated over the full range of velocity at zero degrees incidence with the probe wires angled approximately 45° to the flow. Next, the probe is rotated through $\pm 30^\circ$ yaw for high, medium, and low velocities in order to construct interpolation curves which effectively produce a calibrated response good over $\pm 30^\circ$ yaw for the second velocity component. An

8-channel IFA 300 constant temperature anemometer made by TSI controls the sensor and supplies the voltage data to a PC through the NI PXI-1010 chassis with 16-bit A/D conversion. Two separate sensors are used with the anemometer, a single normal hot-film (model 1211-20) and a cross-flow X-wire hot-film (model 1240-20), both manufactured by TSI. The hot-film sensors are 3.2mm in length and 0.5mm in diameter and consist of a thin film of platinum on a quartz cylinder which does not lengthen or bend when heated. Data with the single normal hot-film was taken at 50kHz for 250,000 samples while data with the x-wire was taken at 2kHz for 40,000 samples. These sensors are used to obtain turbulence spectra in the wind tunnel, flow characteristics in the boundary layer, and flux-averaged loss coefficients over the wake of the linear cascade. Bons *et al.* have previously used hot-film anemometry to describe the turbulent character of separated flow above the Pack B and L1M blade profiles [Reimann et al. 2006], providing information such as locations of separation onset, transition onset and length, turbulent reattachment, and intermittency (percentage of time the flow is turbulent). An intermittency of one denotes a turbulent flow while an intermittency of zero indicates a laminar flow. The intermittency algorithm developed by Clark [Clark et al. 1994a] is employed in this work.

The Clark intermittency algorithm was developed for surface-mounted heat-flux gauges in order to track the leading and trailing edges of passing turbulent spots, and uses the first derivative of the time-resolved, measured quantity of interest with weighting and criterion functions as turbulence discriminators. Although this algorithm was not developed specifically for anemometry signals, it is expected to work equally as well away from the wall since the algorithm operates on signal derivatives which are indicative of transitional activity both on and away from the wall. The discriminator function is defined as:

$$D_i = m_i (q'_i)^2 \quad (3.10)$$

where q is the measurement signal (velocity in this case) and m is the relative signal magnitude defined by:

$$m_i = \frac{q_i - q_{min}}{q_{max} - q_{min}} \quad (3.11)$$

The first derivative q' is found from the central difference formula:

$$q'_i = \frac{q_{i+1} - q_{i-1}}{2h} \quad (3.12)$$

The original implementation used the sampling period for h ; here, h is chosen as the time step in between data points. The criterion function Cr is an exponentially-weighted, centered moving-average based on the detector function:

$$Cr_i = \frac{h^2}{1 + (\tau_s/h)} \sum_{j=i-(\tau_s/h)}^{j=i+(\tau_s/h)} w_j D_j \quad (3.13)$$

where w_j is the weighting factor defined by:

$$w_j = \exp\left(-\frac{0.625}{\tau_s/h}|j-i|\right) \quad (3.14)$$

Here, τ_s is the smoothing period, and was originally set to 10 μs based on the smallest detectable turbulent spot as determined by the upper limit of the bandwidth of the heat-flux instrumentation. In this study, τ_s is set to an integer multiple of the time step in order to maintain proper indices in the summation of the criterion function; this integer is chosen to select the number of surrounding data points used for the summation. Intermittency is determined by evaluating the criterion function against an appropriate threshold found by a trial and error approach. Table 3.1 presents the parameters used for intermittency calculation following Clark's algorithm, where n is the smoothing period integer, $\tau_s = n\Delta t$, and CT is the Clark intermittency threshold.

Table 3.1: Clark intermittency algorithm parameters.

Re	L1M			L2F		
	25	50	75	25	50	75
n	9	9	9	9	9	9
CT	9.40e-5	1.95e-4	2.75e-4	1.25e-4	3.25e-4	3.75e-4

There is some subjectivity in selecting these parameters. In the present work, three guiding principles were used as follows, in order of consideration:

1. Maintain the maximum intermittency at the wall in the downstream portion of the blade, subsequent to the establishment of fully turbulent flow.
2. Maintain an intermittency value less than 0.02 at the wall in the upstream, pre-transitional portion of the blade.
3. Maintain an intermittency value less than 0.02 in the freestream over the entire blade.

The guiding philosophy was to select a set of parameters which forced the intermittency to be less than 0.02 in the freestream and upstream of the transition location near the wall, while producing the highest possible intermittency downstream of transition. In fact, a range of parameters in the neighborhood of those in Table 3.1 produced somewhat consistent results, as shown in Figure 3.2(a) for the L2F airfoil near-wall values at $Re = 25k$ with $n = 5$. The figure legend contains various values for the intermittency threshold which show how a certain range, here between $1.5e-4$ and $5e-5$, produces a similar intermittency shape. The sudden increase in intermittency near 55% of the suction surface length (SSL) signals transition has occurred, and this trend was sought after

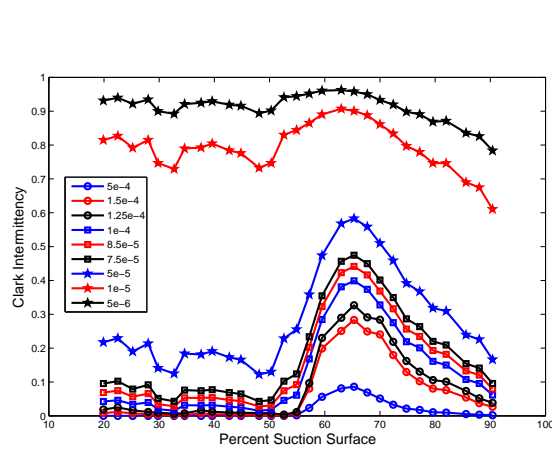
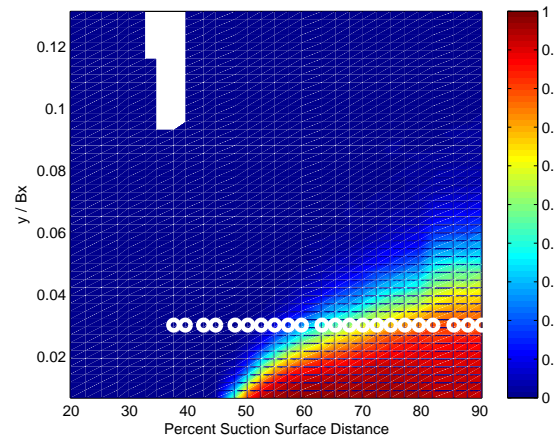
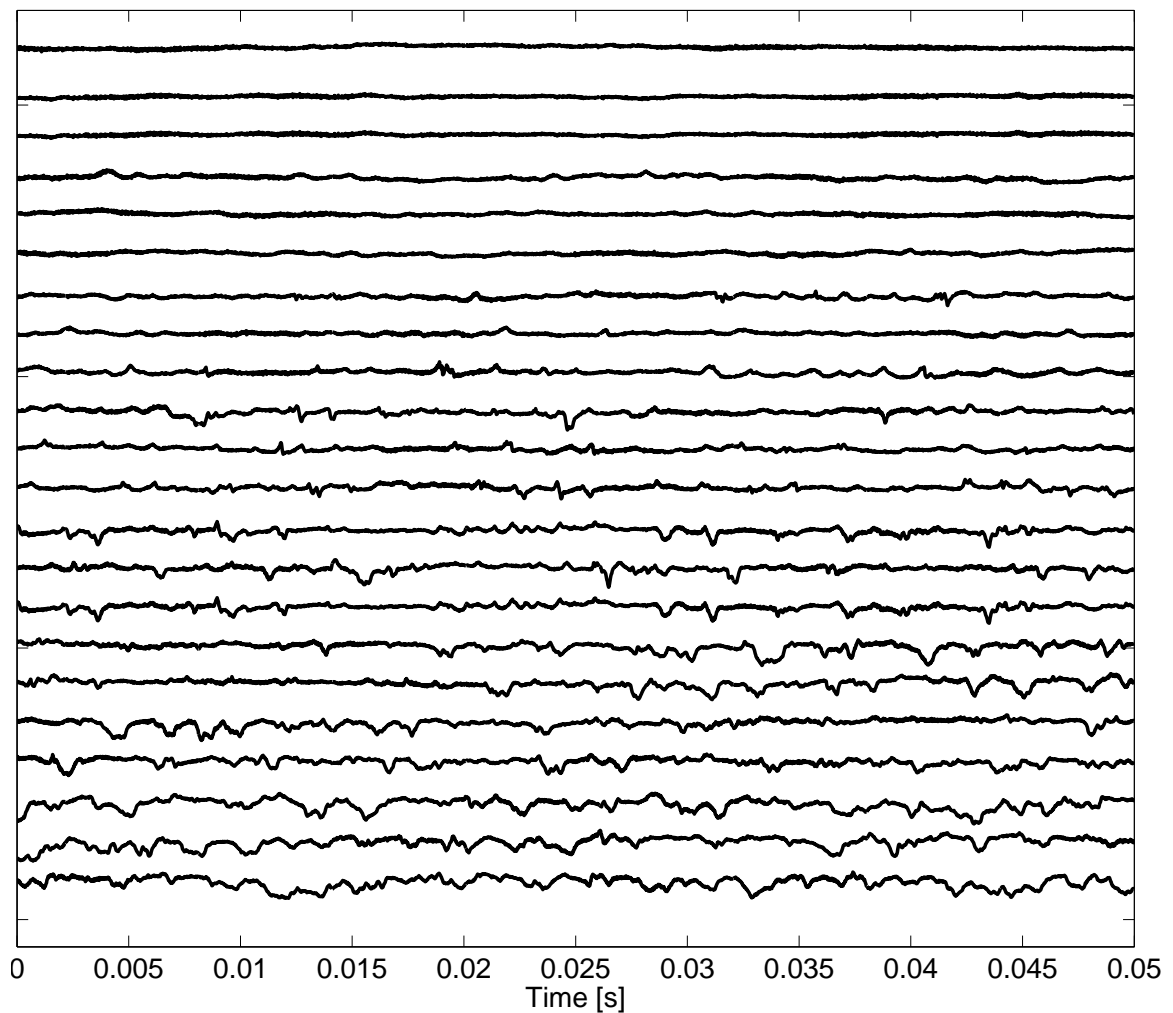
(a) Parameter selection, L2F $Re = 25k$, $n = 5$.(b) Sample locations, L2F $Re = 75k$.(c) Velocity traces, L2F $Re = 75k$.

Figure 3.2: Example of Clark intermittency algorithm.

for each test case. The smoothing integer n was selected equal to 9 in every case; as n increases the intermittency obviously increases, but it was found to be a good fit for highest possible intermittency after the sudden increase while maintaining low intermittency before the sudden increase. Clark's intermittency algorithm was used in this manner with confidence since a definite spike in intermittency occurred for all cases which produced a region which was shaped as expected. Visual inspection of data signals also gave confidence in the algorithm. An example sequence of velocity trace signals is presented in Figure 3.2(c) for the locations marked by white circles in Figure 3.2(b) of intermittency for the L2F airfoil at $Re = 75k$; these locations are 4.8mm (3% chord) up from the surface. In Figure 3.2(c), the first profile at the top corresponds to 37.6%SSL and each successive profile is plotted until the bottom profile at 90.4%SSL. By the 7th location (52.6%SSL) there is evidence of turbulent bursts when the intermittency in Figure 3.2(b) begins to ramp up. Continuing downstream, the random bursts increase in frequency until the flow is more turbulent than not, as indicated in Figure 3.2(b) as well. It is therefore believed that Clark's algorithm works well for determining the intermittency away from the wall, and intermittency results produced from this algorithm will be presented later in Chapter 4.

Higher-order turbulence statistics including the skew and kurtosis of the fluctuating velocity have also previously been used to identify the turbulent nature of a flow, and are calculated according to Equations 3.15 and 3.16 (from [Bernard and Wallace 2002]):

$$skew = \frac{\overline{u'^3}}{(\overline{u'^2})^{3/2}} \quad (3.15)$$

$$kurtosis = \frac{\overline{u'^4}}{(\overline{u'^2})^2} \quad (3.16)$$

These quantities have previously been used by [Reimann et al. 2006] and others to help identify regions of separated and transitional flow. In particular, Bons' group identified regions of reversed flow with negative skew, and regions containing both negative skew and positive kurtosis with those undergoing transitional events. This logic will be used in the current results of Chapter 4. In addition, a parameter using the velocities at the edge of the boundary layer will be used to determine the acceleration throughout the passage above the turbine blades. The acceleration parameter, K , is presented as Equation 3.17 below:

$$K = \frac{\nu}{U_e^2} \frac{dU_e}{dSSL} \quad (3.17)$$

where ν is the kinematic viscosity, U_e is the velocity at the boundary layer edge, and $dSSL$ is the change in streamwise distance across the suction surface. Using experimental data, the derivative is calculated with a 2nd order central difference using the change in suction surface length as the distance variable.

In order to position the hot-film probe accurately in the boundary layer, a Matlab code was written which takes into account the test section geometry, the cascade position within the test section, the airfoil surface geometries, and the probe and stand positions. This code outputs coordinates of surface-normal test points in the boundary layer for any suction surface location which can be directly input into the traverse control for data acquisition. Figure 3.3 shows the selected

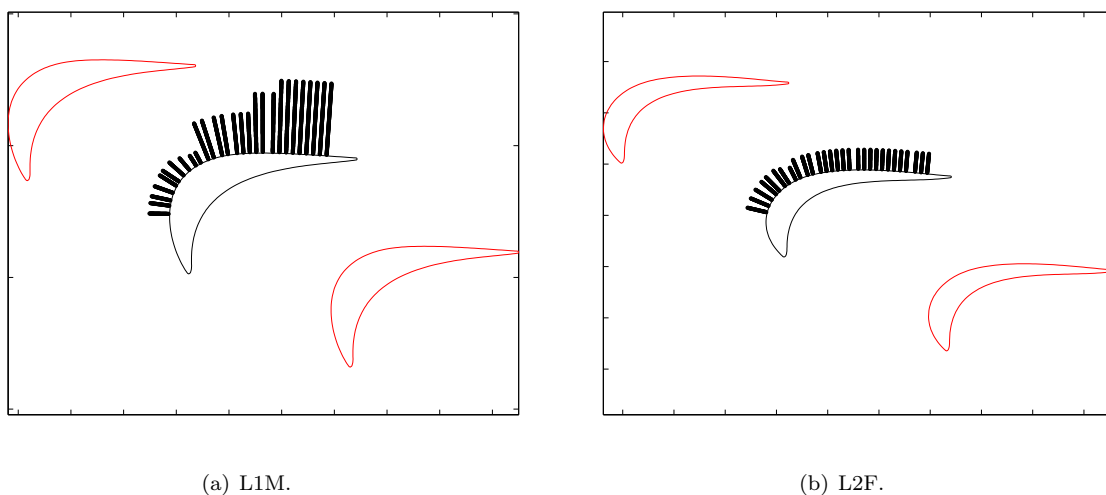


Figure 3.3: L1M and L2F boundary profile locations.

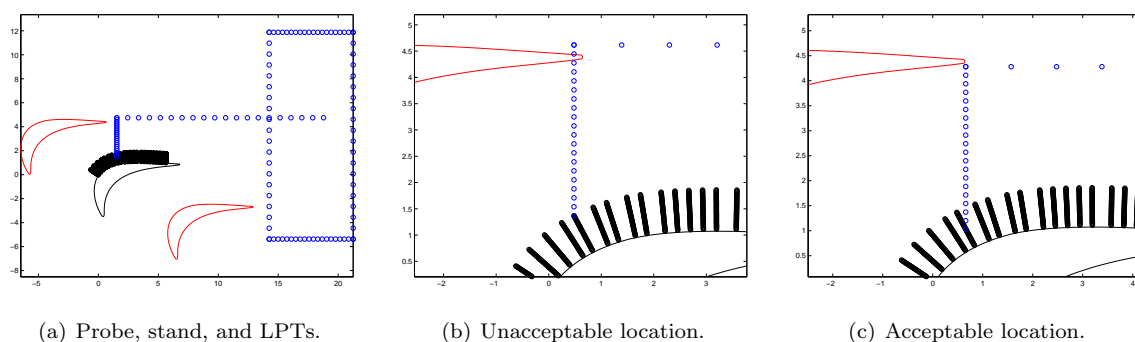


Figure 3.4: Method for determining attainable profile locations.

profile locations for each blade. These locations were selected based on the traverse and probe range of motion. The L1M is surveyed from 22.5 to 89.5%SSL, while the L2F is surveyed from 19.9 to 90.4%SSL. The profile locations were selected based on a 200pt coordinate set for each blade and a streamwise spacing of approximately 2.5%SSL. L2F profiles contain 50 evenly distributed surface-normal points from 1mm to 20mm up from the surface where possible; the L1M profiles contain from 50 locations to 184 locations, each assigned based on initial findings of boundary layer behavior in order to resolve the boundary layer height. In order to position the hot-film probe around the curva-

ture of each blade, a 90 degree bend adaptor was required between the probe holder and the probe. Figure 3.4 illustrates the process used to determine which profile locations were accessible in and around the test section using this adaptor. Figure 3.4(a) depicts the probe with 90 degree adaptor and probe holder, probe stand, and 3 relevant LPT blades for the L1M cascade. The probe device could be translated to any profile location in order to ensure none of the device conflicted with blade surfaces. Figure 3.4(b) shows an example of an outer location of a profile which is unattainable due to interference from the adjacent blade, while Figure 3.4(c) shows an acceptable location. The locations where data can not be obtained with this setup show up as void spots in contour maps such as those presented later in Figure 4.2.

The production of mean velocity profiles from thermal anemometry also allows shape comparison for laminar and turbulent similarity using boundary layer similarity laws selected from [White 2006]. In this work laminar profiles are considered those with a maximum intermittency value less than 0.02, even though the inlet freestream turbulence is 3.3%. The laminar profiles will be compared to Falkner-Skan wedge flows, which are a single parameter family of non-separating flows which solve the equation:

$$f''' + ff'' + \beta(1 - f'^2) = 0 \quad (3.18)$$

where $f' = u/U_{edge}$ and

$$\beta = \frac{2m}{m+1} \quad (3.19)$$

with boundary conditions

$$f(0) = f'(0) = 0 \quad f'(\infty) = 1 \quad (3.20)$$

The parameter β is a measure of the pressure gradient, and is positive for favorable gradients and negative for adverse gradients. This parameter is equal to zero for Blasius flow and has a limit of -0.19884 just prior to separation; thus the β parameter is a measure of the deviation from flat-plate Blasius flow. Profiles are normally plotted with f' on the ordinate axis and the dimensionless variable η on the abscissa:

$$\eta = y \sqrt{\frac{m+1}{2} \frac{U_{edge}}{\nu x}} \quad (3.21)$$

Turbulent profiles are analyzed for similarity by iterating upon the surface shear, τ_w , which produces similar shapes. In this work turbulent profiles are compared to the linear-law, the log-law, Spalding's law of the wall, and Clauser's similarity law [Clauser 1954] with Coles' addition of the "PI" term which accounts for pressure gradients [Coles 1956], hereafter referred to as Coles' law of the wake. All of these turbulent similarity were developed for fully developed turbulent flows, and all except Coles' law were intended for use under zero pressure gradient. These comparisons require the

transformation of velocity and surface-normal location into the wall coordinates given below:

$$u^+ = \frac{u_{mean}}{v^*} \quad y^+ = \frac{yv^*}{\nu} \quad (3.22)$$

where v^* is the friction velocity defined as:

$$v^* = \sqrt{\frac{\tau_w}{\rho}} \quad (3.23)$$

with τ_w being the wall shear stress and ρ the density of the fluid. The linear law, given by

$$u^+ = y^+ \quad (3.24)$$

is typically applicable for $y^+ \leq 5$ and governs the region where viscous (molecular) shear dominates the flow field near the wall. The log-law is given by:

$$u^+ = \frac{1}{\kappa} \ln(y^+) + B \quad (3.25)$$

where κ is the von Kármán constant equal to 0.41 and B is set equal to 5.0. The log-law region governs the overlap area of the flow where turbulent shear begins to dominate over molecular shear, and is normally applicable in the range $35 \leq y^+ \leq 350$. The third turbulent similarity comparison used in this work is Spalding's law of the wall given by:

$$y^+ = u^+ + e^{-\kappa B} \left[e^{\kappa u^+} - 1 - \kappa u^+ - \frac{(\kappa u^+)^2}{2} - \frac{(\kappa u^+)^3}{6} \right] \quad (3.26)$$

This similarity law used fully-developed turbulent pipe flow through its development, and is normally applied from the wall into the outer layer defined as $y^+ > 300$. The final turbulent similarity profile used in this work is Coles' law of the wake, given by Equation 3.27:

$$u^+ = \frac{1}{\kappa} \ln(y^+) + B + \frac{2PI}{\kappa} f\left(\frac{y}{\delta}\right) \quad (3.27)$$

where PI is the term which accounts for the pressure gradient, and δ is the boundary layer thickness. The last term includes a function of surface normal height approximated by:

$$f\left(\frac{y}{\delta}\right) = 3\left(\frac{y}{\delta}\right)^2 - 2\left(\frac{y}{\delta}\right)^3 \quad (3.28)$$

This function produces the 'S' shape experienced by turbulent boundary layer profiles under the influence of an adverse pressure gradient. Since the wall shear must be iterated upon to match these profiles, and this wall shear determines the wall coordinates used for all turbulent comparisons, all will be compared using the current data sets in case the data falls into one or more of the applicable ranges.



Figure 3.5: PIV setup with laser arm.

3.2.3 Particle Image Velocimetry

Particle image velocimetry (PIV) is a two-dimensional velocity measurement technique which uses the light scattering property of small tracer particles injected into a flow. The seed particles should be small enough (on the order of microns) to follow the flow without disturbing it, and are illuminated with a laser as they pass through the flow plane of interest. The scattered light in the 2D plane is recorded by a CCD camera, and computer algorithms correlate the scattered patterns between two back-to-back images. The correlation produces the distance traveled of each scattered light group between the images, and knowing the time in between successive images produces the vector velocity field in a 2D plane of the flowfield. A more detailed description of the PIV technique can be found in [Raffel et al. 1998]. The PIV system in building 252 uses a 120mJ Solo 120XT PIV Nd:YAG laser from New Wave Research together with a Rosco 4500 fog generator which creates particles on the order of a few microns in diameter out of propylene glycol seeding material. The laser sheet is constructed using a spherical then cylindrical lens setup and is directed into the test section using a laser arm from Dantec. The image is recorded with a 14bit PCO.1600 CCD camera with 1200x1600 pixel resolution, and data reduction is carried out using DPIV software from ISSI. Figure 3.5 shows the PIV setup for the leading edge of the L2F cascade with the laser arm and optics. In this work, PIV data is only used to verify the boundary layer height obtained from the single normal hot-film results.

3.2.4 Shear and Stress Sensitive Film (S3F)

The shear and stress sensitive film (S3F) provides regional surface maps of tangential shear and normal pressure in a single measurement, and is a new addition to the experimental capability at AFRL implemented by Innovative Scientific Solutions, Inc. of Dayton, OH. The S3F technique originated in the 1990s as a direct sensor to measure surface shear forces [Tarasov and Orlov 1990]. Detailed description of how the technique works can be found in [McQuilling et al. 2007], so only a brief summary will be presented here for convenience. The technique relies on the response of a thin elastomer film impregnated with luminescent molecules and doped with tracer particles on its surface. The film deforms under normal and tangential loads, and the tangential displacement measurement is achieved by tracking the movement of the titanium oxide tracer particles between a “wind-off” non-loaded state and a “wind-on” loaded state. The images are recorded by a CCD camera, and cross-correlation algorithms and optical flow techniques determine the displacements. During both states, the film is also illuminated with a light source of a specific wavelength that excites the luminescent molecules within the film. The molecules emit a different wavelength photon in order to relax back to its more stable ground state, and this emission is picked up by the same optically filtered CCD camera. The intensity of the emission is proportional to the thickness of the film, thus providing a regional measurement of normal deformation between the same “wind-off” and “wind-on” states. A ratio between the two conditions also provides a means to cancel out sources of error such as unequal illumination and uneven luminophore dispersion. This ratio calculation effectively makes the S3F a differential pressure gauge with tunable dynamic range calibration by modifying the film thickness, modulus of elasticity, and Poisson ratio. The normal pressure and tangential surface stresses which caused the three-dimensional deformations are determined from an inverse finite element model, whose inputs are the film thickness-sensitive luminescent intensity and the tracer translations between flow-off and flow-on conditions.

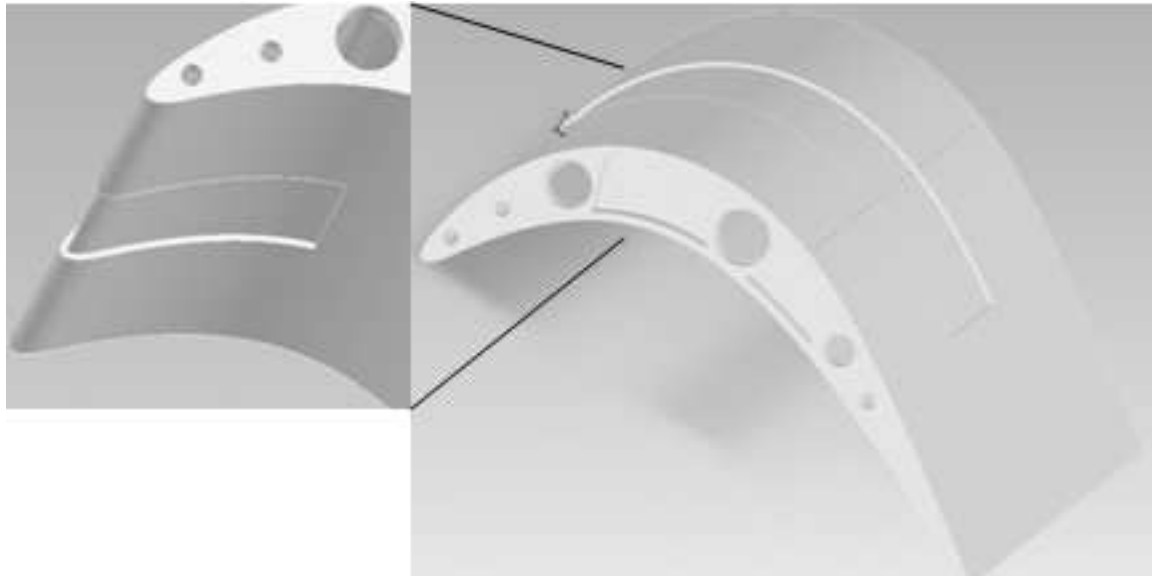
S3F was developed in order to measure two-dimensional static pressure on a surface without some of the drawbacks of pressure sensitive paints (PSPs) based on oxygen quenching, such as the need for oxygen in the flow environment and the limited pressure sensitivity, dynamic range, and frequency response [McQuilling et al. 2007]. More background information on pressure and skin friction measurement can be found in Appendix C, while more detail on the S3F data reduction process can be found in Appendix D.

3.3 S3F Development for Low-Speed LPT Use

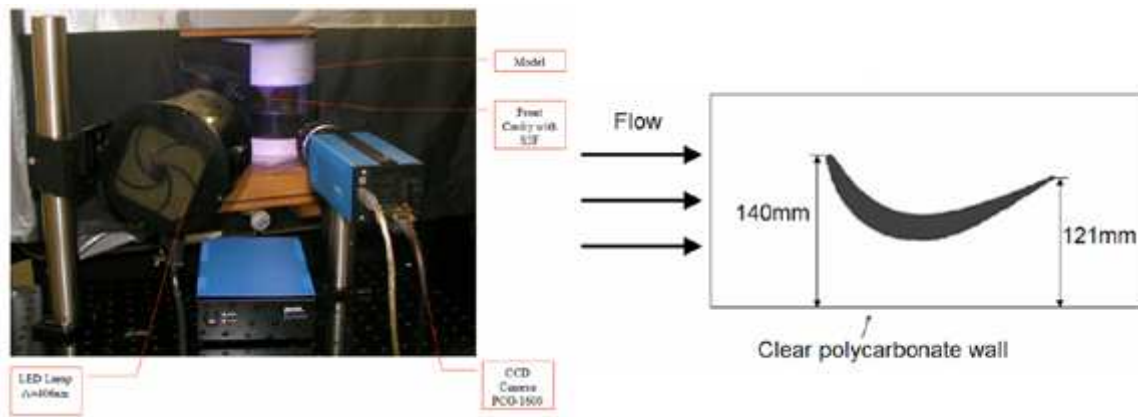
Initial work carried out in order to assess the efficacy of using S3F in a low-speed environment is now described. The complications of using S3F arise because the low-speed environments result in minimal surface shearing forces due to the passing fluid. Thus, the film properties must be meticulously calibrated for this difficult environment. Indeed, the calibration and reduction methodology which determines the surface forces are still under development for the low-speed regime. All experiments described in this section were conducted in the low-speed wind tunnel (LSWT) located at ISSI in Dayton, Ohio. The ISSI LSWT is a low-turbulence, open-circuit wind tunnel. Screens upstream of the test section condition the flow and one wall of the test section is made of clear polycarbonate to allow optical access.

3.3.1 Experimental Setup

The LPT geometry used herein is the Pack B profile with a 190.5mm axial chord and 203.2mm span. The blade, with a wrap-around 1.5mm deep \times 50.8mm wide S3F cavity, was made using the rapid-prototyping capability at WPAFB, and is shown in Figure 3.6(a). The orientation of the blade in the straight ISSI LSWT test section did not allow for proper inlet and exit angles typically used for LPT studies. Here it is necessary to remember the goals of this study. First, the current operational envelope of S3F has previously been restricted to water environments or higher speed air environments. These tests will push that envelope by extending the air flow use to very low speeds on the order of 1-7 m/s in order to investigate such phenomena as the low- Re lapse in efficiency. Second, issues specific to the LPT geometry, such as the varying gradient levels along the suction surface, were investigated and handled before further testing in realistic LPT orientations. Therefore, all results in this section are presented with respect to the camera point of view and are only referenced to regions along the suction surface where maximum gradient changes are expected, such as the leading edge and near the locations of maximum curvature. The blade with S3F inserts and black Mylar strips applied for oil film measurements is shown in Figure 3.6(b). The suction surface of the LPT blade is illuminated with an ISSI LM4 lamp and detected by a 14-bit PCO.1600 CCD camera with 1600×1200 pixel resolution. A single low-pass filter is used to distinguish the fluorescent emission while an ISSI timing box controls the excitation-detection sequence. Data is collected and stored on a PC.



(a) Pack B LPT with S3F cavity.



(b) Side and top views of LPT orientation.

Figure 3.6: Pack B LPT test setup at ISSI.

3.3.2 Results

Multi-dimensional skin friction measurement is not a new accomplishment, and as such previous work has developed the proper theory and terminology used to describe such results. Therefore, the terminology as presented in [Tobak and Peake 1982] will be used to aid the description of presented results. The S3F cavity was filled by two separate pieces of elastomer, one for the leading edge region and one for the trailing edge region (as seen in Figure 3.6(a)). Filling the cavity with multiple films instead of one long continuous film was desirable in order to wrap the film around the leading edge and maintain as flush as possible S3F with the blade surface.

$h=1\text{mm}$, $\mu=150\text{Pa}$ Film

Results at $U = 13.5\text{m/s}$ ($Re = 1.83 \cdot 10^6$) for a film thickness of 1mm and shear modulus of 150Pa are presented for the front cavity in Figure 3.7. A negative spike in streamwise skin friction (τ_x) near the leading edge, indicating surface tension facing upstream, reaches just below -21Pa and is a result of the blade orientation in the straight test section. As the oncoming flow is split between the pressure and suction sides near the nodal line of attachment around $x=10\text{mm}$, the flow heading towards the pressure side pulls on the film in the opposite (negative) direction with respect to the suction side. This negative spike region produces a local absolute maximum τ_x -gradient of $\sim 6.4\text{Pa/mm}$. After recovery to positive τ_x , the remainder of the leading edge strip encounters a mean streamwise friction level near 7.5Pa, with local gradients between 0-4Pa/mm. The cross-stream skin friction (τ_z) along section A-A fluctuates around zero, indicating a mostly two-dimensional flow field. The observed 3D influence is believed to be generated by the mounting plates above and below the turbine blade. Waves in the $-dC_p$ plot along Section A-A in Figure 3.7(c) indicate that the 1mm-150Pa S3F used near the leading edge was too sensitive for a 13.5m/s flow velocity in the current orientation. Further tests will implement an S3F with a better tuned shear modulus for this region.

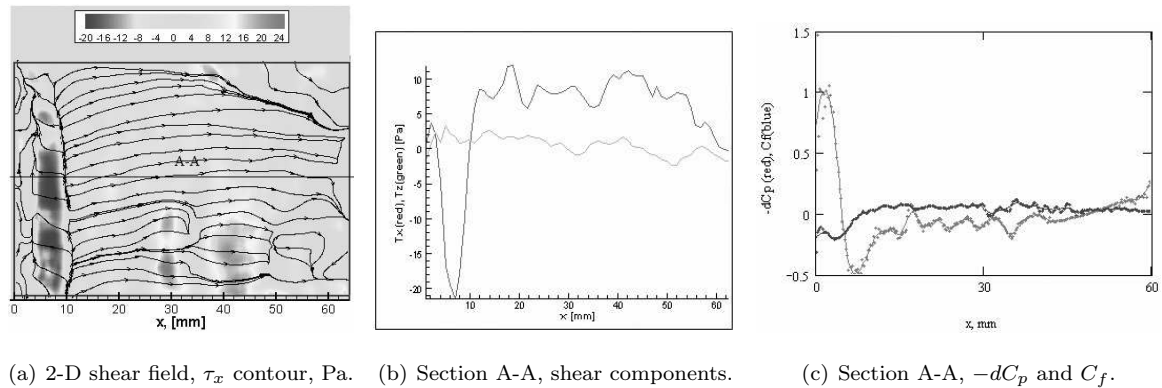
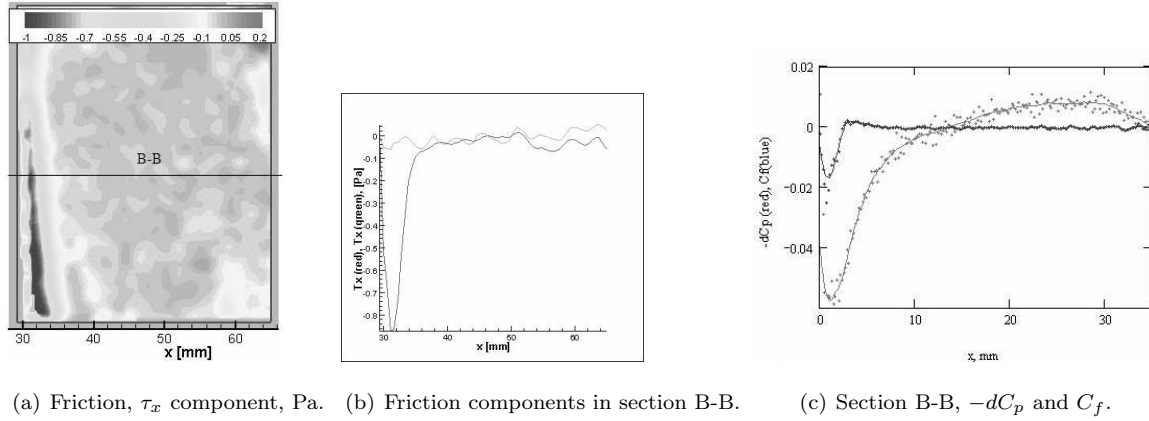


Figure 3.7: Front cavity, $U=13.5\text{m/s}$, $h=1\text{mm}$, $\mu=150\text{Pa}$.

Figure 3.8: Rear cavity, $U=13.5\text{m/s}$, $h=1\text{mm}$, $\mu=150\text{Pa}$.

Results for a similar 1mm-150Pa film in the rear cavity are shown in Figure 3.8 for 13.5m/s flow velocity. Again a negative spike is noticed around $x=30\text{-}36\text{mm}$, but is now due to a surface discontinuity near the upstream edge of the S3F. The rear cavity observes a negative mean τ_x of less than a tenth of a Pascal, indicating a flow separation on the latter part of the suction surface. The streamwise friction gradients in this region are significantly smaller than the front cavity, with absolute values less than 0.04Pa/mm . The cross-stream skin friction τ_z remains in a similar range as τ_x . The difference in skin friction between the front and rear cavities varies by more than an order of magnitude, and illustrates the need for separate S3Fs in each region. The larger mean and gradient levels near the leading edge require a film with smaller sensitivity than the trailing edge. From these preliminary results, the goal was set to develop an S3F with a shear modulus near 30-50 Pa in order to better resolve the expected magnitudes of pressure and shear.

$h=1.5\text{mm}$, $\mu=25\text{Pa}$ Film

The next film developed had a shear modulus of 25Pa at a thickness of 1.5mm. Skin friction results for this S3F are presented in Figure 3.9 for a flow velocity of 7m/s. Here, a focus of separation can be seen in the lower right portion of the plot, indicating a swirling motion of the fluid above. The streamwise shear component for the region of interest encompassed by the box on the left side is shown on the right of the figure in 3-D space. From these tests, the need became clear to apply a black Mylar strip beneath the S3F in order to reduce reflected excitation light and glare from the white material. This reduced the noise collected with the data, but increased the complexity of model setup since the S3F is difficult to glue to the black strip material. The increased noise levels for speeds lower than 7m/s increased the difficulty of the second data reduction step of transforming the deformation fields and luminescent intensities into shear and pressure fields. It was also found that

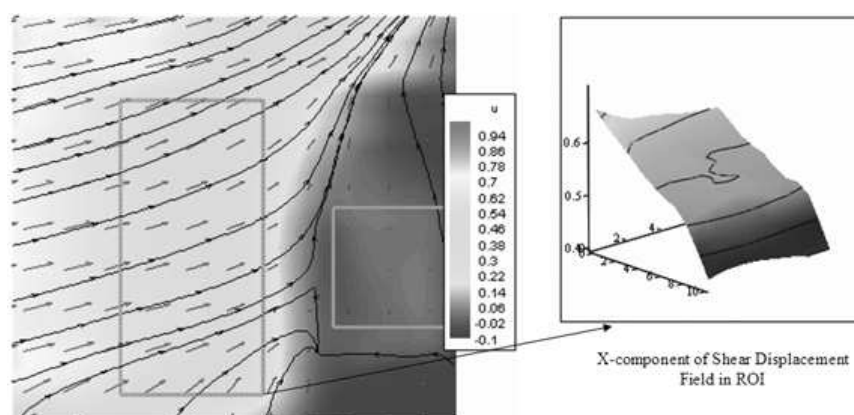


Figure 3.9: Shear displacement vectors and streamlines, $U=7\text{m/s}$, $h=1.5\text{mm}$, $\mu=25\text{Pa}$.

in order to best resolve the expected flow features it may be necessary to apply the S3F in small 5-10mm wide strips in the flow direction with 1-2mm gaps in between successive strips, running any length along the span. Since the pressure and shear stress gradient levels change so rapidly along the flow direction due to the LPT curvature, the S3F applied in strips would allow different composition and sensitivity S3F pieces to be placed in appropriate regions to better resolve the occurring levels in their respective locations. A sequential series of displacement fields taken at 0.5Hz with the same 1.5mm-25Pa S3F for a flow velocity of 13.5m/s is shown in Figure 3.10. The x-axis (streamwise direction) and y-axis (spanwise direction) are scaled to the pixel distribution of the camera only in order to show the ability of the S3F to track unsteady events. In Figure 3.10(a), a nodal line of separation appears near $x \approx 230$ highlighted by the ellipse, with an accompanying quasi-steady nodal line of attachment near $x \approx 1150$ highlighted with a box, indicating the presence of an unsteady separation bubble. Although the topological structure remains relatively preserved, the frame capture rate does not exceed the separation frequency and therefore cannot properly resolve the unsteadiness of the event.

Displacement fields for $U = 0.7$ to 4.4m/s are presented in Figure 3.11 for another 1.5mm-25Pa S3F. Evidence of an interaction with the uneven edge of the S3F on the top side of the cavity can be seen here. Similar topological structure can be seen in Figures 3.11(b) through 3.11(e), while in Figure 3.11(f) we see the emergence of a focus of separation near $(x,y)=(400,900)$ highlighted by an ellipse, and a saddle point of attachment near $(x,y)=(700,850)$ highlighted with a five-sided polygon, indicating the swirling 3D flow above. The top edge interaction eventually influences a nodal line of separation near $x \approx 1150$ highlighted with a rectangle, and a larger separation as the flow velocity approaches 4.4m/s in Figure 3.11(f), as seen by the upstream directed deformations occurring in the left half of the plot. The attainment of these displacement fields at low speeds, along with oil film

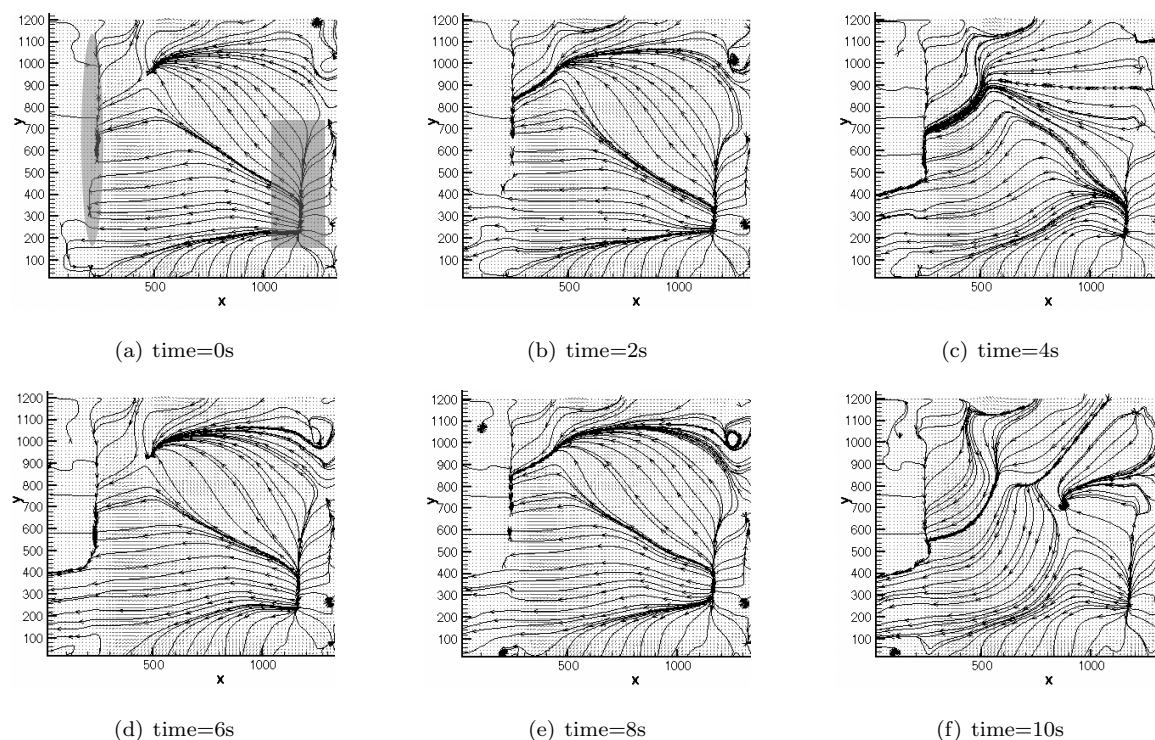
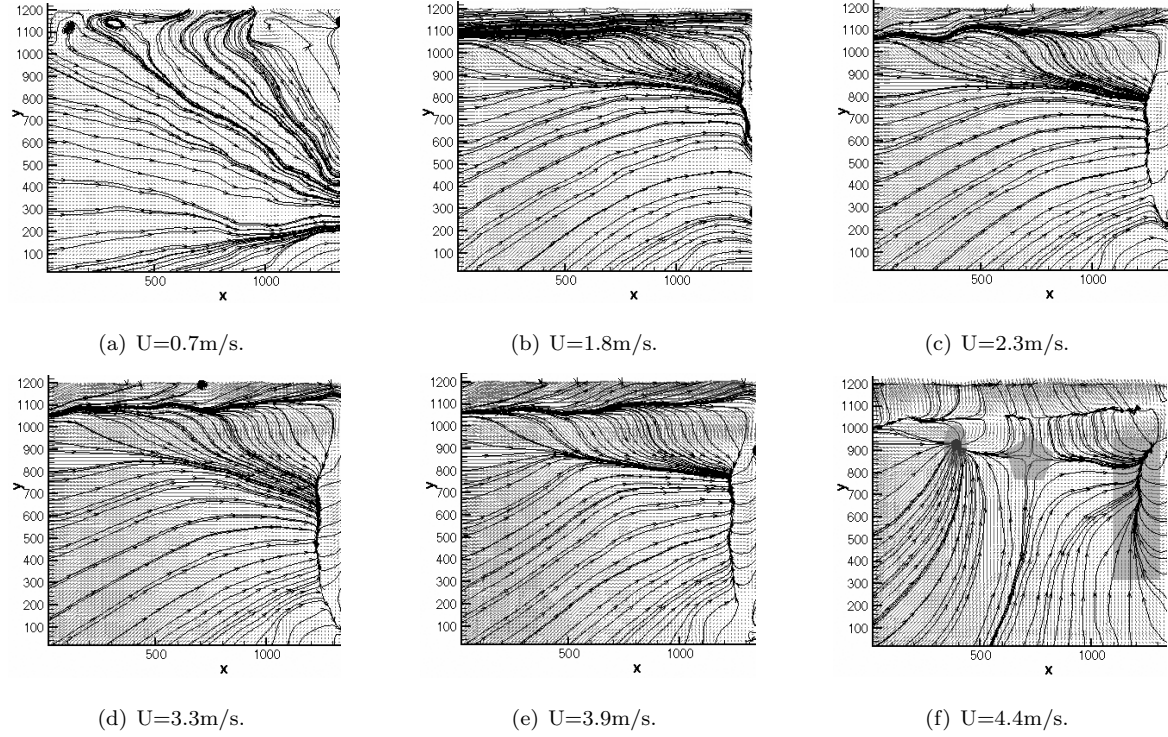


Figure 3.10: Sequential series of displacement fields taken at 0.5Hz, $U=13.5\text{m/s}$, $h=1.5\text{mm}$, $\mu=25\text{Pa}$.

verifications, signifies that a proper formulation and implementation of the S3F sensor will be able to produce shear and pressure fields in a flow speed range of 1-7m/s after an adequate amount of noise reduction is accomplished. Additionally, diminishing the region of interest (zooming in) can provide up to 10 times the current sensitivity level used in this paper, providing another means to reduce the noise and increase the signal- to-noise ratio for lower speed tests.

Oil-film Comparison

As mentioned earlier, the lowered signal-to-noise ratio at flow velocities below 7m/s complicated the attainment of shear and pressure fields. Therefore, in order to better trust the small translations indicated in the S3F displacement fields, oil film measurements were made directly below the S3F strip near the front cavity. The combined S3F-oil film setup was presented in Figure 3.6(b). The regions of interest for combined measurement are shown in Figure 3.12. For luminescent oil film skin friction measurements, the skin friction is determined by Equation C.1. Oil film results showing dx/dh as a function of time for dynamic pressures of 4.6 and 29.6Pa are shown in Figures 3.13(a) and 3.13(b). These figures illustrate the linear response of the oil film technique over the dynamic range of interest. The combined S3F-oil film measurements are shown in Figure 3.13(c), where the

Figure 3.11: Displacement fields, $h=1.5\text{mm}$, $\mu=25\text{Pa}$.

S3F measurements are comparable to the oil film results within $\frac{1}{4}$ to $\frac{1}{3}\text{Pa}$.

Conclusions

The S3F technique has successfully produced two-dimensional shear fields for flow velocities from 7 to 13.5 m/s on the Pack B low-pressure turbine blade geometry, corresponding to a Reynolds number range of $9.48 \cdot 10^5$ to $1.83 \cdot 10^6$. The goal of applying the S3F technique in a low-speed LPT environment and optimizing geometry related issues has been accomplished in this work. Due to significant differences of over an order of magnitude in mean shear and over two orders of magnitude in shear gradients between the leading and trailing edges, the use of separate S3F strips for each region is recommended. The leading edge region will require a smaller sensitivity S3F than the trailing edge due to the higher mean and gradient levels near the leading edge. An S3F with a shear modulus of 25Pa and a film thickness of 1.5mm has been successfully used to produce deformation fields at flow velocities from 0.7-4.4m/s, corresponding to an Re range of $8.90 \cdot 10^4$ to $5.97 \cdot 10^5$. In order to accurately resolve shear and pressure fields at these lower speeds below 7m/s, the signal-to-noise ratio must be increased above current levels.

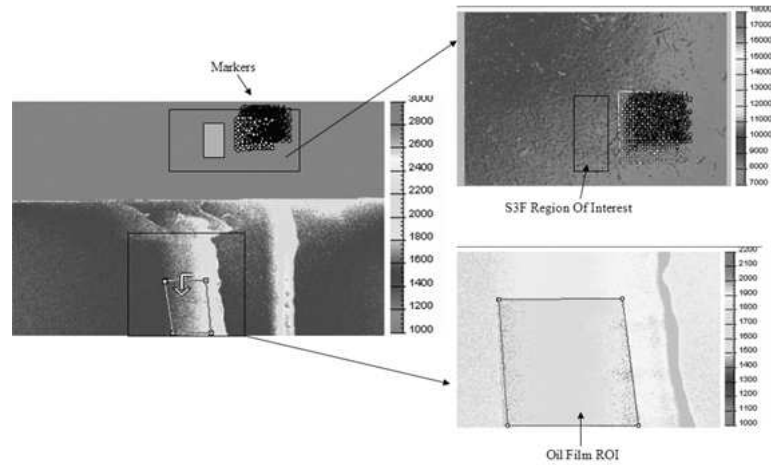


Figure 3.12: S3F-oil film combined measurement regions of interest.

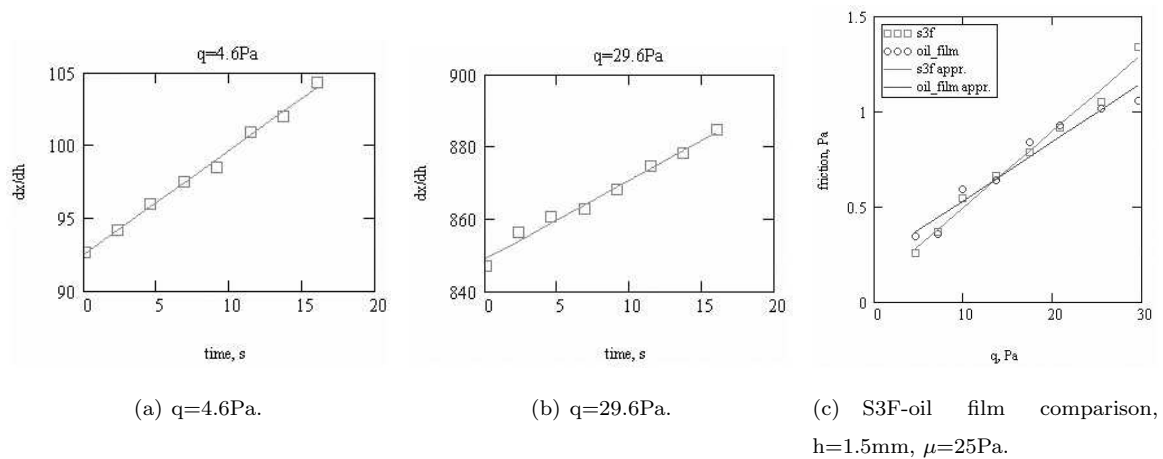


Figure 3.13: Oil film measurements.

3.4 Chapter Summary

Chapter 3 presented the experimental arrangement and data processing used for the tests both on base and at Innovative Scientific Solutions in Dayton, OH. The techniques included pressure measurement, thermal anemometry, particle image velocimetry (only for verification of boundary layer heights), and the S3F surface stress film. The hot-film data reduction routine employed in this work is different than the standard polynomial fit, and was developed at WPAFB over many years. The intermittency algorithm developed by Clark for use with surface-mounted heat flux gauges is found to work equally well away from the wall. This algorithm uses two parameters which are somewhat subjective in their selection, i.e. a set of these two parameters (the smoothing period and threshold) in a neighborhood of those chosen in this study could produce similar results, while not changing the overall conclusions. These parameters varied with Reynolds number, and were chosen in this work based on examining velocity traces and constructing an overall intermittency which made physical sense. The initial development of S3F which enabled its use in the low-speed air environment on the curved surface of a turbine blade was also presented. These initial S3F tests concluded that film compositions could in fact be formulated to fit the range of dynamic pressures desired for tests on base in the large subsonic wind tunnel. The biggest hurdle to overcome is harvesting enough of the reduced signal magnitude to overcome the noise in the system. And as air velocity is decreased, the signal magnitude decreases as the square of velocity, since that is the quantity upon which dynamic pressure depends.

4

Results

It doesn't matter how beautiful your theory is, it doesn't matter how smart you are. If it doesn't agree with experiment, it's wrong.

– Richard P. Feynman

This chapter presents and compares Wildcat predictions with experimental results. The performance data of greatest relevance to turbine designers, the Reynolds lapse curve, is presented first, followed by boundary layer contours and profiles for L1M and L2F which shed some light onto why each blade performs as it does. Next the S3F surface film results are presented, followed by the transition model validation.

4.1 Reynolds Lapse

Pressure and velocity measurements taken across the wake approximately one chord length downstream of the test blades provide a means to measure the available energy lost from the bulk fluid flow as it is turned by the linear cascade. The regions of lost available energy show up as deficiencies in velocity (or pressure), and constitute loss levels which can be integrated to form a Reynolds lapse curve. Figure 4.1 compares Wildcat predictions of L1M and L2F to previous experimental data on the Pack B and current results for the L1M and L2F airfoils plotted against inlet chord Reynolds number. Both area-averaged and mass-averaged losses are presented as defined by Equations 3.1 and 3.2; mass-averaged losses are slightly lower than area-averaged due to their accounting of the lower velocities in the wake regions. It should also be noted that the Wildcat CFD predictions were essentially run laminar with a turbulent trip at the model-predicted separated-flow transition onset location. Tables 4.1 and 4.2 present the L1M and L2F experimental results in tabular form for use in CFD validation; the units are [m/s] for velocity and [in H₂O] for the pressure measurements.

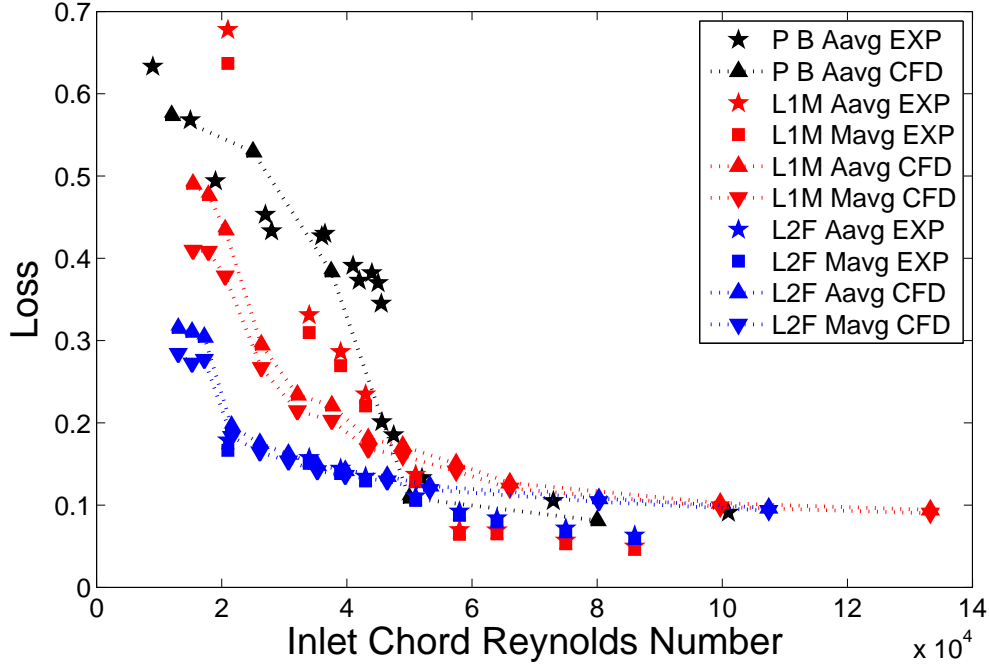


Figure 4.1: Reynolds lapse for Pack B, L1M, and L2F airfoils.

At first glance it is obvious the L2F blade outperforms the L1M and Pack B in the lower Reynolds number regime. Remembering that the aggressive L2F loading allows a 38% reduction in blade count and weight over the Pack B, the L2F answers the call of the gas turbine industry for reduced weight and improved low Reynolds performance, both of which decrease the overall cost of the turbine engine throughout its life cycle. Although the laminar with trip CFD predictions show the L2F stalls below $Re = 1.9 \cdot 10^4$, this result was not duplicable by the facility.

The Pack B is historically notorious for massive separation at lower Re , which begins to grow near $Re = 4.5 \cdot 10^4$ as evidenced by the steep rise in loss in both the experiment and CFD. The L1M loss knee begins below $Re = 5.8 \cdot 10^4$, although it is not as steep as the Pack B. This can be attributed to the mid-loading and earlier transition as noted in other work [Bons et al. 2005]. Even so, the L1M does eventually stall somewhere below $Re = 3.4 \cdot 10^4$, a trend also noticed in the CFD results. The increased losses over the CFD are believed to be a result of the increased turbulent-wetted area from an earlier transition, as well as enhancement of the local laminar shear due to interaction with the turbulence in the freestream which is not accounted for in the predictions. The L2F, however, does not stall at low Re and its experimental loss behavior does not show the loss knee associated with turbines that experience increased low- Re losses due to separation bubbles. The loss knee is formed as the losses dramatically increase with decreasing Reynolds number. We'll see later this

flow is in fact separated, but the bubble may be so thin that it behaves as if it is attached (without the loss knee). Comparisons drawn later with boundary layer contours obtained through thermal anemometry help explain this behavior. A very encouraging trend is that both the L1M and L2F enjoy reduced losses compared to the Pack B at the higher Re tested in this work; it was initially suspected the attached-flow losses may be higher than the Pack B due to the earlier transitions, but at least up to $Re = 8.6 \cdot 10^4$ the experimental losses remain below the Pack B levels. Somewhere between $Re = 5.1 \cdot 10^4$ and $Re = 5.8 \cdot 10^4$ the L2F losses increase over the L1M; again, this can be attributed to the increased turbulent-wetted area of the L2F.

Table 4.1: Measured conditions across L1M cascade.

Re_{in}	Re_{ex}	$\overline{u_{in}}$	$\overline{u_{ex}}$	$\overline{P_{t,in} - P_{s,in}}$	$\overline{P_{t,in} - P_{t,ex}}$	L_{area}	L_{flux}
$2.1 \cdot 10^4$	$3.4 \cdot 10^4$	2.0	3.2	0.0097	0.0066	0.6777	0.6369
$3.4 \cdot 10^4$	$5.6 \cdot 10^4$	3.1	5.1	0.0214	0.0071	0.3310	0.3097
$3.9 \cdot 10^4$	$6.5 \cdot 10^4$	3.5	5.8	0.0277	0.0079	0.2862	0.2695
$4.3 \cdot 10^4$	$7.2 \cdot 10^4$	3.9	6.5	0.0347	0.0081	0.2348	0.2206
$5.1 \cdot 10^4$	$8.4 \cdot 10^4$	4.7	7.7	0.0498	0.0068	0.1369	0.1285
$5.8 \cdot 10^4$	$9.5 \cdot 10^4$	5.2	8.5	0.0545	0.0038	0.0697	0.0644
$6.4 \cdot 10^4$	$1.0 \cdot 10^5$	5.8	9.4	0.0700	0.0049	0.0694	0.0650
$7.5 \cdot 10^4$	$1.2 \cdot 10^5$	6.9	11.1	0.1048	0.0060	0.0570	0.0529
$8.6 \cdot 10^4$	$1.4 \cdot 10^5$	7.7	12.4	0.1293	0.0064	0.0498	0.0461

Table 4.2: Measured conditions across L2F cascade.

Re_{in}	Re_{ex}	$\overline{u_{in}}$	$\overline{u_{ex}}$	$\overline{P_{t,in} - P_{s,in}}$	$\overline{P_{t,in} - P_{t,ex}}$	L_{area}	L_{flux}
$2.1 \cdot 10^4$	$3.7 \cdot 10^4$	2.3	3.9	0.0116	0.0021	0.1788	0.1665
$3.4 \cdot 10^4$	$5.7 \cdot 10^4$	3.6	5.9	0.0260	0.0041	0.1575	0.1508
$3.9 \cdot 10^4$	$6.4 \cdot 10^4$	4.0	6.7	0.0347	0.0050	0.1444	0.1383
$4.3 \cdot 10^4$	$7.0 \cdot 10^4$	4.6	7.5	0.0446	0.0060	0.1346	0.1292
$5.1 \cdot 10^4$	$8.4 \cdot 10^4$	5.4	8.9	0.0627	0.0069	0.1108	0.1057
$5.8 \cdot 10^4$	$9.5 \cdot 10^4$	6.1	10.0	0.0770	0.0071	0.0922	0.0875
$6.4 \cdot 10^4$	$1.1 \cdot 10^5$	6.6	10.9	0.0908	0.0076	0.0841	0.0795
$7.5 \cdot 10^4$	$1.2 \cdot 10^5$	7.9	12.9	0.1356	0.0097	0.0717	0.0675
$8.6 \cdot 10^4$	$1.4 \cdot 10^5$	8.8	14.4	0.1678	0.0106	0.0632	0.0592

Examining the average inlet and exit velocities from Tables 4.1 and 4.2 more closely, we see both the L1M and L2F airfoils accelerate the flow through the cascade to nearly the same level over the range of Re surveyed, where u_{ex} is approximately equal to $1.6 \cdot u_{in}$. Later it will be noted that these accelerations occur at different levels in different regions which lead to different boundary layer physics between the two airfoils.

Table G.3(b) presents measured wake conditions for the L1M and L2F airfoils including average percent exit turbulence level, wake width to the nearest 0.5cm, and wake depth defined as the maximum total pressure drop ($P_{t,in} - P_{t,ex}$) [in H₂O] in the wake. Remembering the inlet freestream turbulence is 3.3% for both airfoils, we see the effects of the L1M separation bubble in generating an increased level of unsteadiness as the bubble periodically convects downstream. As Reynolds number increases and the bubble size is reduced, the exit unsteadiness and wake width are reduced. The smaller level of exit unsteadiness and width seen in the L2F wake supports the idea of a very thin separation bubble which does not generate as much periodic unsteadiness as the L1M. Comparing the wake depths and widths, we see the L1M creates a wider and deeper wake than the L2F until somewhere after $Re = 6.4 \cdot 10^4$, where the L2F depth surpasses the L1M even though it remains thinner. Although this study proves unsteady effects are not necessary to design a well-behaved airfoil at aggressive loading levels, numerous higher-lift studies have touted the benefits of wake disturbance energy in re-energizing the separated boundary layer of downstream blade rows. Depending on the design point and heat load considerations of a given turbine engine, the larger L1M wakes may be more beneficial in a given situation especially at lower Reynolds numbers due to their increased turbulence levels.

Table 4.3: Wake conditions.

Re_{in}	L1M			L2F		
	$\overline{Tu_{ex}}$	Width	Depth	$\overline{Tu_{ex}}$	Width	Depth
$2.1 \cdot 10^4$	13.5	20.5	0.0125	5.0	13.0	0.0071
$3.4 \cdot 10^4$	8.8	20.0	0.0184	4.0	13.0	0.0144
$3.9 \cdot 10^4$	7.5	20.0	0.0221	3.8	13.0	0.0186
$4.3 \cdot 10^4$	6.8	19.5	0.0259	3.7	13.0	0.0235
$5.1 \cdot 10^4$	5.7	19.0	0.0416	3.6	13.0	0.0328
$5.8 \cdot 10^4$	4.4	19.0	0.0470	3.5	12.5	0.0402
$6.4 \cdot 10^4$	3.9	19.0	0.0502	3.5	12.0	0.0457
$7.5 \cdot 10^4$	3.6	18.5	0.0437	3.3	12.0	0.0674
$8.6 \cdot 10^4$	3.5	18.5	0.0518	3.3	11.5	0.0805

4.2 Boundary Layer Contours and Profiles

This section presents boundary layer contours and profiles obtained through thermal anemometry of $U_{\text{mean}}/U_{\text{in}}$, contours of $u_{\text{rms}}/U_{\text{in}}$, skew and kurtosis of the velocity signal, and contours and profiles of intermittency for the L1M and L2F airfoils at Re equal to $2.5 \cdot 10^4$, $5.0 \cdot 10^4$, and $7.5 \cdot 10^4$. It should be noted here that two distinct behaviors were noticed in the previous work which developed the Praisner and Clark attached-flow and separated-flow transition models. While flows remained attached, transition onset occurred where the ratio of a boundary layer diffusion time to the turbulent eddy time scale reached a critical level. The attached-flow model requires the momentum thickness, an integral boundary layer quantity which loses its physical meaning once the flow is separated. Models based on physical quantities are preferred over those that are empirically based due to the extra information provided about the physics involved. Since the attached-flow model can only be applied up to the point of separation, an additional model was necessary for those flows that separate before transition occurs. Therefore, the separated-flow model is instead based on the momentum thickness Reynolds number just before incipient separation, where the momentum thickness remains physically meaningful. This section presents thermal anemometry results with a minimum surface-normal position of 1mm up from the surface of the airfoil. Since this minimal distance may preclude the resolution of a very thin separation bubble, the current data sets are examined with both models in mind, where both transition models will be constructed where available data permits.

Table 4.4 shows the maximum and minimum velocities throughout the measured data zones for the L1M and L2F airfoils for all 3 Re . Previous research from the open literature [Reimann et al. 2006] employing single normal hot-wire sensors to determine separation zones have used a separation zone criteria defined as those regions having mean velocities less than $0.4 \times \max(U_{\text{mean}})$. If there are no regions where the velocity is under this threshold, the flow may react as an attached flow. This table shows the L1M airfoil contains separated flow for $Re = 2.5 \cdot 10^4$ and $5.0 \cdot 10^4$. Since the minimum mean velocity for the L1M at $Re = 7.5 \cdot 10^4$ is greater than the threshold, the flow must either be attached or have a very thin separation bubble below the first measurement point just 1mm up from the surface. This is supported by the Reynolds lapse plot of Figure 4.1, where the L1M losses level off into the gradual decreasing slope somewhere between $Re = 5.1 \cdot 10^4$ and $5.8 \cdot 10^4$ as an attached flow would do. The L2F airfoil is seen without reversed flow (up to 1mm), again agreeing with the behavior reported in Figure 4.1 and associated low wake widths and turbulence levels of Table G.3(b). The S3F measurements presented later in this chapter indicate the L2F blade does in fact separate; the bubble therefore must be thinner than 1mm or 0.7% of the axial chord. An interesting possibility now exists that the shear layer above a very thin separation bubble may transition as if attached and not separated. In order to clarify this response, both the attached-flow

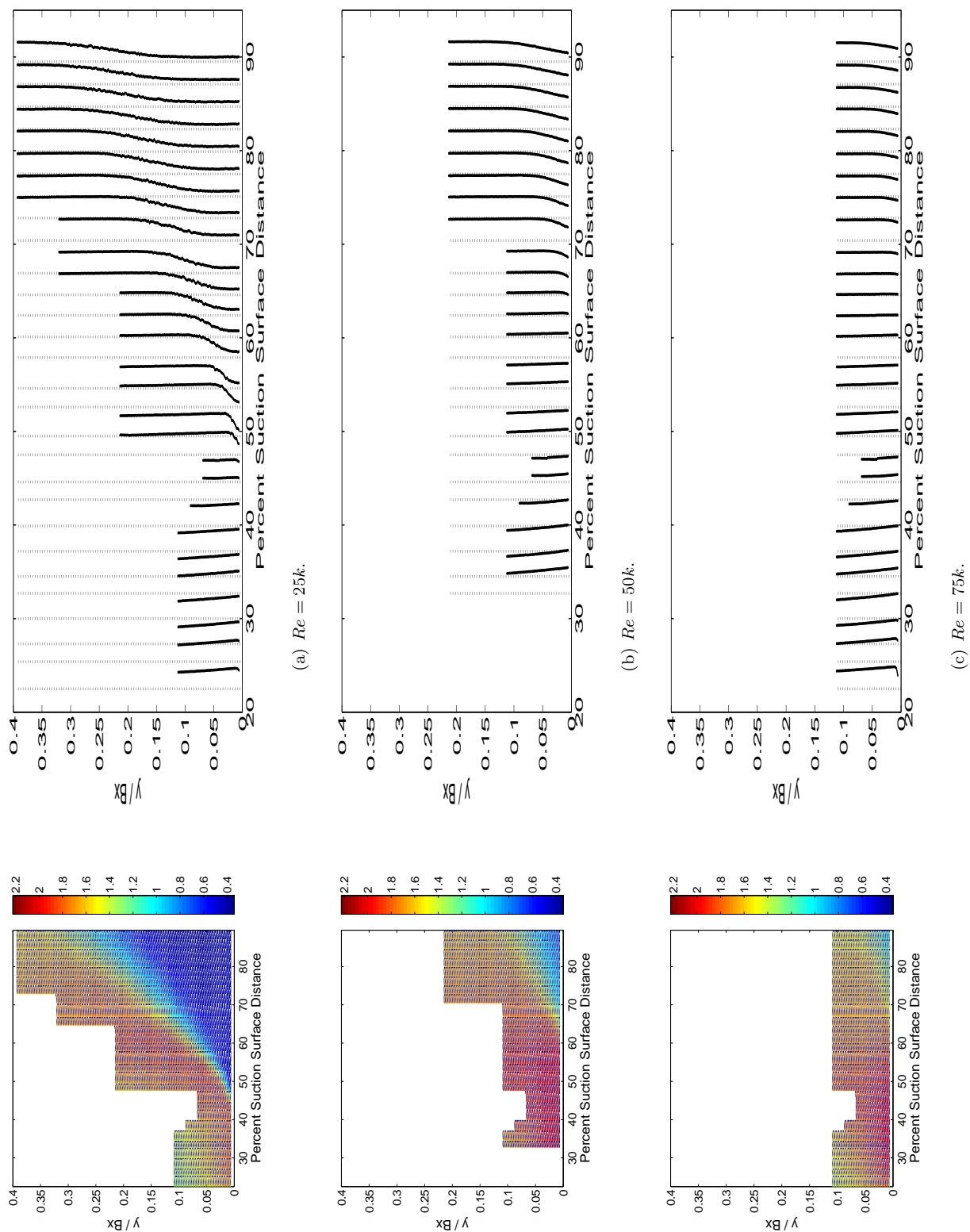
and separated-flow transition models will be constructed where data is available and compared to the model databases as presented in Figure 2.3(a) for the separated-flow model and in Figure 2.3(b) for the attached-flow transition model. As Table 4.4 gives a qualitative way to describe separation zones, the $0.4 \times \max(U_{mean})$ criteria is unable to provide separation onset locations which are upstream of the transition locations. Thus, the separated-flow transition model cannot be validated using this criteria for separation.

Table 4.4: U_{mean}/U_{in} maxima and minima.

Re_{in}	L1M			L2F		
	max	$0.4 \times \max$	min	max	$0.4 \times \max$	min
$2.5 \cdot 10^4$	4.2	1.7	0.8*	5.7	2.3	2.5
$5.0 \cdot 10^4$	9.5	3.8	3.0*	11.1	4.4	5.9
$7.5 \cdot 10^4$	13.9	5.6	7.3	17.6	7.0	8.8

* Separated condition defined by $0.4 \cdot \max(U_{mean})$.

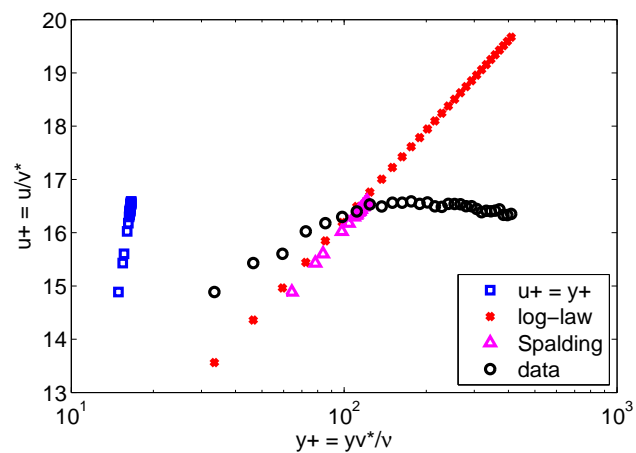
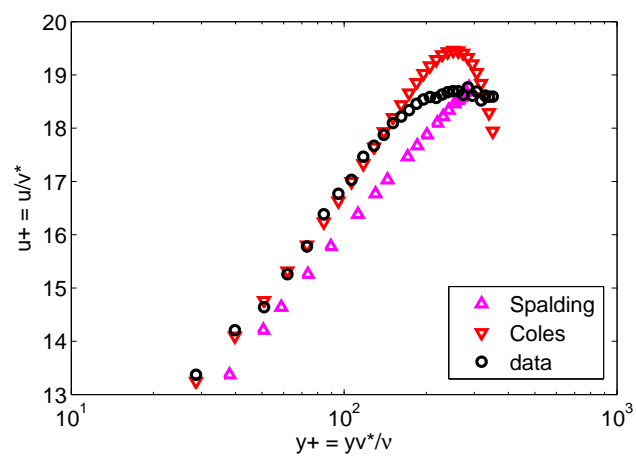
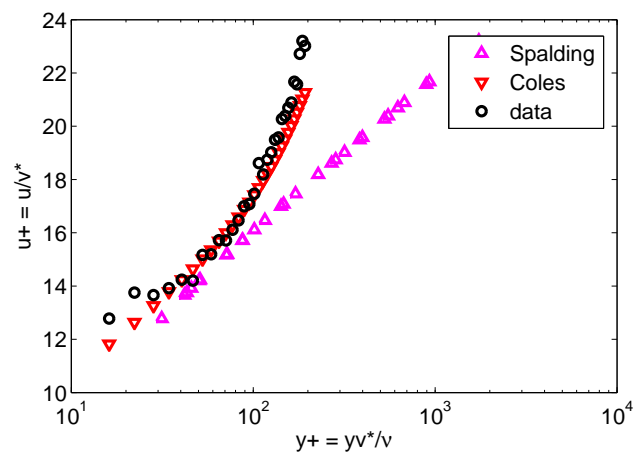
Figure 4.2 presents L1M U_{mean}/U_{in} contours and profiles for all three Re ; the contour scaling is identical for all three Re . Also note the differences in contour and profile heights, as the lower Re flows required a higher profile height to resolve boundary layer features. The blanked white areas of the contours represent the locations where data was not acquired as explained earlier with Figure 3.3. The influence of the passage acceleration can be seen by an increase in near-wall velocity from the first profile at 22.5%SSL up to the fifth profile at 32.7%SSL, after which the near-wall flow decelerates under the adverse pressure gradient. Noting that Wildcat predicted the point of minimum pressure at 47% axial chord (38.5%SSL), we see an earlier velocity peak in the experimental results than predicted. The accelerated profiles resemble those of a jet flow with higher velocities just up from the wall than in the freestream. The eventual deceleration squeezes the near-wall profiles into the familiar boundary layer shapes. By 47.5%SSL, the flow has decelerated enough to detach into a separated free shear layer. The L1M stalls at $Re = 25k$, as the sharp change in mean velocity beginning near 47.5%SSL and $y/Bx = 0.006$ grows progressively away from the wall in an unbounded fashion with downstream distance. The stall behavior can be seen more clearly in the profiles of Figure 4.2(a), where the velocities in the upper portion of the profile slow to minimal magnitudes less than 0.2 of the maximum velocity near the surface. In fact, this drastic change in the mean velocity continues to nearly 35% axial chord up, or a full 6.2cm up from the surface at the last profile acquired at 89.5%SSL. Under the shear layer a region of fluid with a momentum

Figure 4.2: L1M U_{mean}/U_{in} , contours and profiles.

deficiency recirculates and causes a flow blockage extending far out into the main passage.

As expected, the passage acceleration increases with Re as indicated by the increase in velocity in Figures 4.2(b) and 4.2(c) for $Re = 50k$ and $75k$, respectively. At $Re = 50k$, the near-wall velocity increases until 37.2%SSL where the adverse pressure gradient begins to slow the fluid, 4.5%SSL downstream of the $Re = 25k$ location. For $Re = 75k$, the near-wall fluid accelerates until 42.7%SSL, 10%SSL further downstream than for $Re = 25k$. The L1M then experiences its shear layer detachment near 60.1%SSL at $Re = 50k$, which gives way to a turbulent separation bubble. After this detachment, a mix of turbulent-like near-wall profiles continue to fade into more laminar-like shapes, suggesting the separation bubble remains below 1mm up from the surface. At $Re = 75k$, no such detachment is noticed after the maximum near-wall velocity as the profiles (and contour) appear turbulent and resemble an attached flow. The shape of the shear layer, as detected by the region of changing mean velocity with a knee-like curvature, is different for $Re = 75k$, also lending support to the idea of an attached flow versus a separated one.

Turbulent similarity comparisons for selected L1M mean velocity profiles at $Re = 50k$ are presented in Figure 4.3 plotted in wall coordinates with the log base 10 of y^+ on the abscissa. These comparisons were constructed by iterating upon the wall shear (τ_w) until a best fit was obtained between the similarity profiles and current experimental data using the applicable range of y^+ . The selected profiles presented in this figure illustrate the typical trends seen by all test cases for both airfoils except the stalled L1M at $Re = 25k$ which exhibits no turbulent similarity for any section of the surveyed suction surface. Significant differences include the first “good fit” location, the terminal shape of the data fit to Coles’ law of the wake (Equation 3.27), and the final suction surface location where the terminal shape occurs. A “good fit” location is where the data in the appropriate y^+ range is fit to Coles’ law with less error than to Spalding’s law; Coles’ law was chosen due to its accounting of the pressure gradient with the “PI” term. The terminal shape is considered as the earliest location which continues to closely resemble its followers as one progresses downstream. As expected, at no time do any of the profiles match the linear law which is only applicable extremely close to the wall (closer than 1mm). Comparison to the linear law in Figure 4.3(a) at 62.4%SSL for $\tau_w = 0.30\text{Pa}$ shows how the acquired data are located out of the viscous sublayer, an expected result since the closest wall data point is 1mm from the surface. Initially, and at different suction surface locations for each Reynolds number and airfoil, the data do not compare well with Spalding’s law or the log-law, with the lower y^+ data points residing above Spalding’s law and the higher y^+ points falling below, as illustrated in Figure 4.3(a) for the L1M $Re = 50k$ case at 62.4%SSL with $\tau_w = 0.30\text{Pa}$. Minimal to no agreement is found between data and the log-law or Spalding’s formula, which can be attributed to the transitional flow experiencing a pressure gradient, both of which were

(a) 62.4%SSL, $\tau_w = 0.30\text{Pa}$.(b) 66.9%SSL, $\tau_w = 0.22\text{Pa}$, $\text{PI}=0.24$.(c) 89.5%SSL, $\tau_w = 0.07\text{Pa}$, $\text{PI}=1.52$.Figure 4.3: L1M turbulent profile similarity comparisons, $Re = 50k$.

unaccounted for in the Spalding and log-law development. Instead, the profile begins stretching towards the 'S' shape described by Coles' law of the wake. By 66.9%SSL in Figure 4.3(b), the experimental data can be fit to Coles' profile with reasonable success using $\tau_w = 0.22\text{Pa}$ and a PI term equal to 0.24. A further increase to 89.5%SSL in Figure 4.3(c) using $\tau_w = 0.07\text{Pa}$ and $\text{PI}=1.52$ shows the terminal shape for the L1M at $Re = 50k$, where the lower and higher y^+ locations still in the applicable range exhibit higher u^+ values. Also as expected, the wall shear required to fit the data decreases with suction surface distance, while the PI term is seen to increase with downstream distance. The terminal shapes for other test points vary between those seen in Figures 4.3(b) and 4.3(c), illustrating how no profiles acquired during this work completely resemble fully developed turbulent flow.

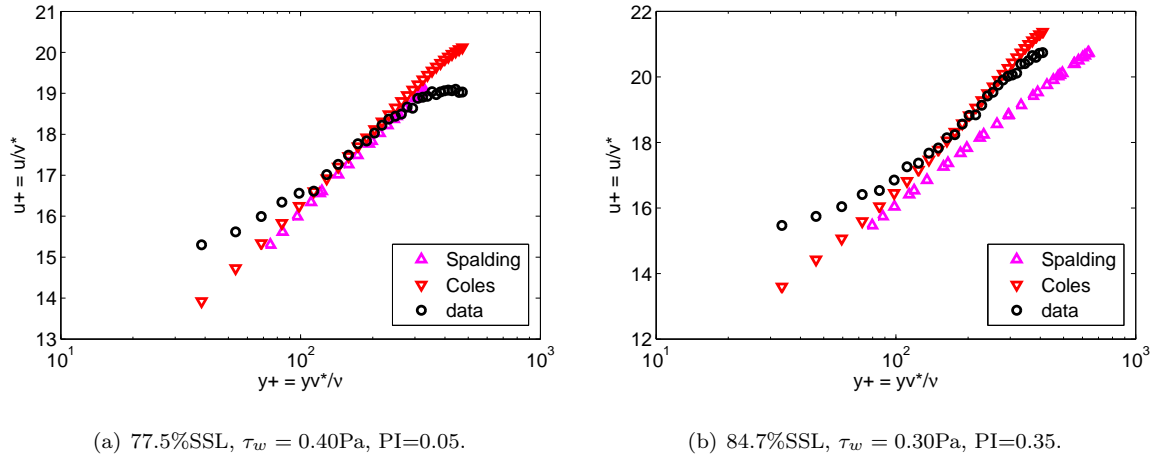
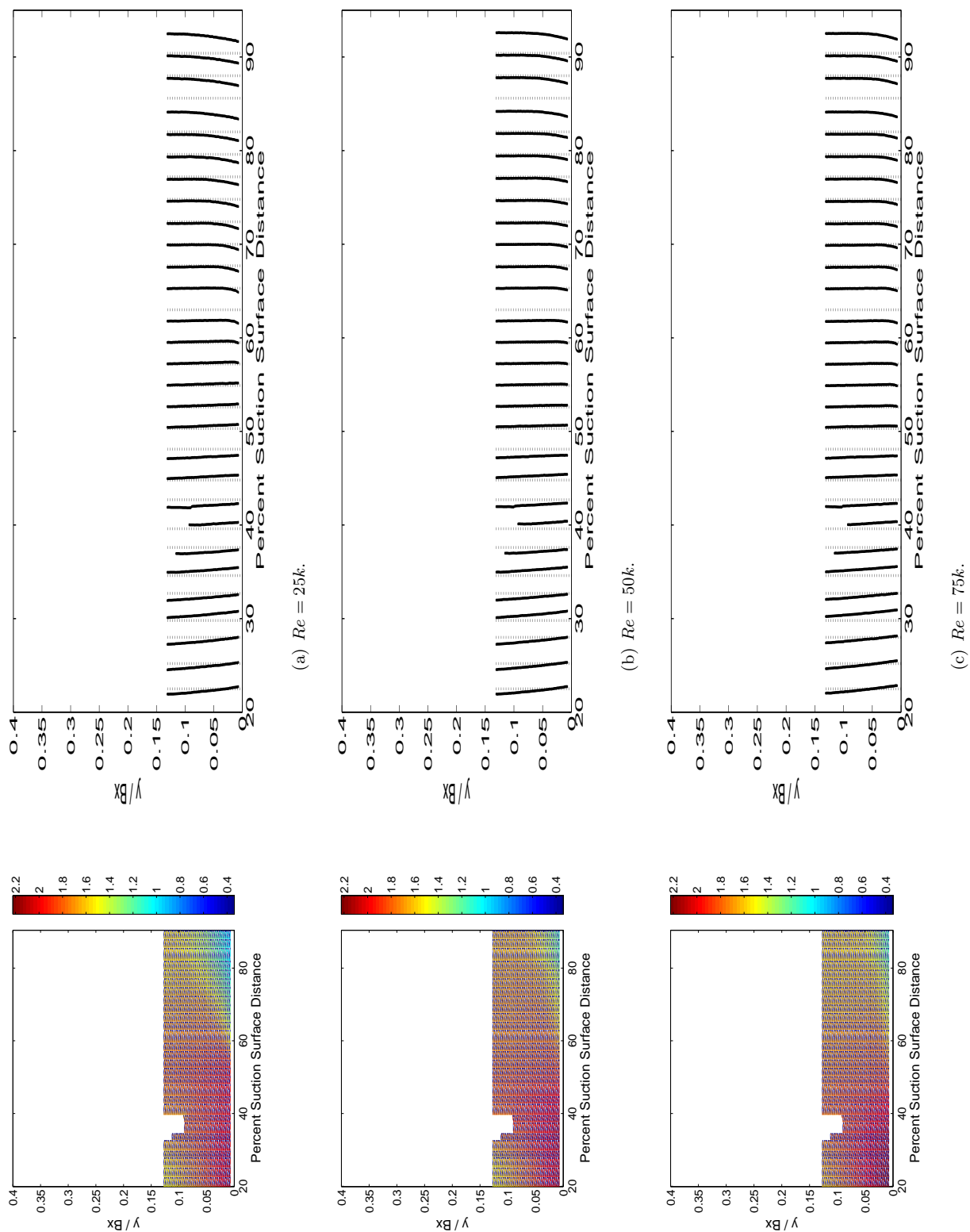


Figure 4.4: L1M turbulent profile similarity comparisons, $Re = 75k$.

Figure 4.4(a) shows the initial good fit for $Re = 75k$ occurs at 77.5%SSL using $\tau_w = 0.40\text{Pa}$ and $\text{PI}=0.05$. The terminal shape for the L1M is observed by 84.7%SSL in Figure 4.4(b) using $\tau_w = 0.30\text{Pa}$ and $\text{PI}=0.35$, where the higher y^+ locations never rise above Coles' law. Comparing Figures 4.3 and 4.4 shows how the first occurrence of a good fit moves downstream with increasing Reynolds number. This trend is also typical for the L2F airfoil. The PI term increases with downstream distance but decreases with increasing Reynolds number, trends also observed with the L2F data.

Figure 4.5 presents L2F $U_{\text{mean}}/U_{\text{in}}$ contours and profiles for all three Re where the contour scaling is the same as the L1M scaling. The topology for all three Re remains similar, resembling that of the attached L1M $Re = 75k$ case with a knee-like curvature in Figure 4.2(c). The height for the L2F contours and profiles remains at 20mm (11.2% axial chord) since this was sufficient to resolve the boundary layer features. In contrast to the L1M, the bulk of the L2F passage acceleration has already occurred further upstream than the first profile, here at 19.9%SSL for the L2F.

Figure 4.5: L2F U_{mean}/U_{in} , contours and profiles.

As a result, the profile point 1mm up from the surface experiences relatively constant deceleration throughout the entire flowfield for all three Re . This is due to the forward loading characteristic of the L2F, where the pressure minimum occurs further upstream and the remaining pressure increase to the trailing edge is spread out over a longer surface distance. Remembering Wildcat predicted the pressure minimum to occur at 27% axial chord (24%SSL), we again see an earlier velocity peak in the experimental results than predicted with Wildcat. This constant deceleration gradually retards the jet-like profiles of upstream locations into those more similar to zero pressure gradient boundary layer profiles of downstream locations. These downstream profiles also resemble turbulent attached flow profiles, which agree with the Reynolds lapse behavior of Figure 4.1.

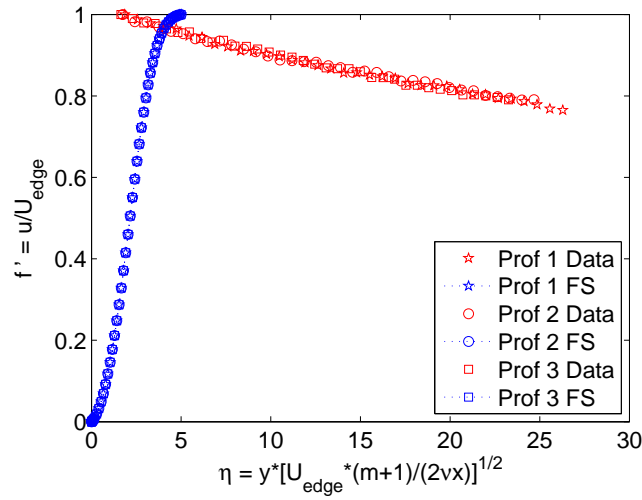


Figure 4.6: L2F comparison to Falkner-Skan; $\beta = -0.199$, $Re = 25k$.

Laminar comparisons against the Falkner-Skan family of similarity laws with $\beta = -0.199$ are presented in Figure 4.6 for L2F airfoil profiles which are upstream of separation at $Re = 25k$. The maximum adverse pressure gradient before separation is defined by $\beta = -0.199$, and this figure shows how the near-wall region's jet-like shape, where the velocity increases going towards the wall from the freestream, does not match the wedge flows represented by the Falkner-Skan solutions. This result is typical of all laminar profiles for all three Reynolds numbers upstream of separation where Falkner-Skan would be applicable. L2F turbulent similarity comparisons against Spalding's and Coles' laws are presented in Figure 4.7 for all three Reynolds numbers. For $Re = 25k$ in Figure 4.7(a), the first good fit location occurs at 70.0%SSL using $\tau_w = 0.08\text{Pa}$ and $PI=0.22$, and the terminal shape seen in Figure 4.7(b) at 90.4%SSL using $\tau_w = 0.05\text{Pa}$ and $PI=0.42$ matches Coles' law of the wake extremely well for $y^+ > 50$. Increasing the Reynolds number moves the initial good fit downstream to 82.0%SSL for both $Re = 50k$ and $75k$, as seen in Figures 4.7(c) and 4.7(e)

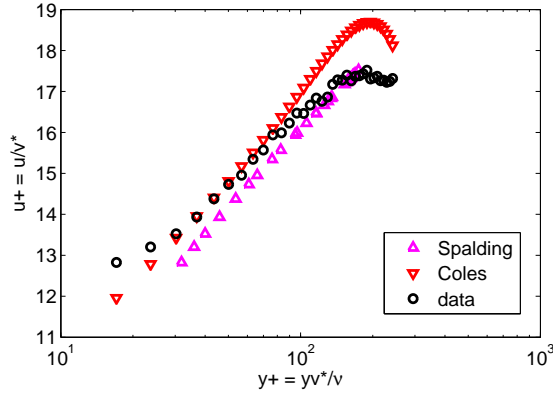
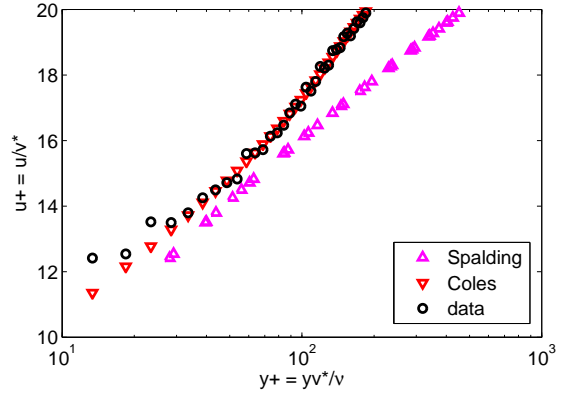
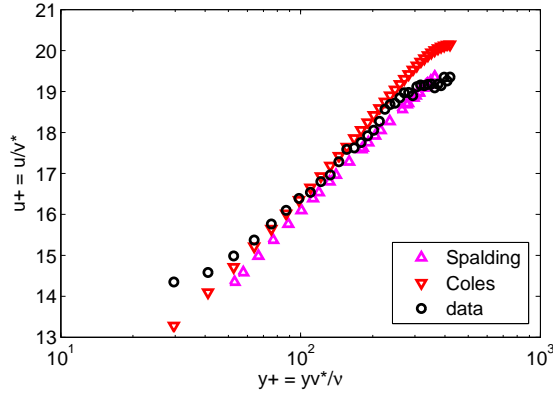
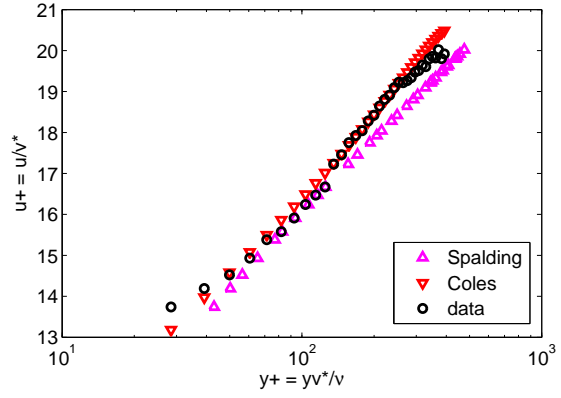
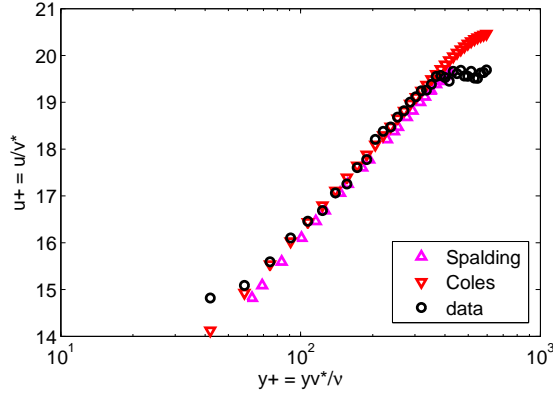
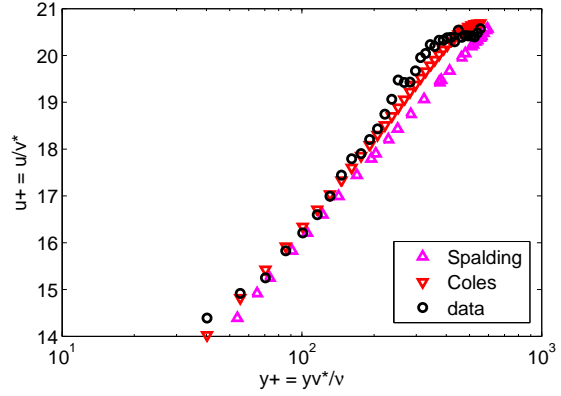
(a) 70.0%SSL, $Re = 25k$, $\tau_w = 0.08\text{Pa}$, $PI=0.22$.(b) 90.4%SSL, $Re = 25k$, $\tau_w = 0.05\text{Pa}$, $PI=0.42$.(c) 82.0%SSL, $Re = 50k$, $\tau_w = 0.24\text{Pa}$, $PI=0.14$.(d) 90.4%SSL, $Re = 50k$, $\tau_w = 0.22\text{Pa}$, $PI=0.19$.(e) 82.0%SSL, $Re = 75k$, $\tau_w = 0.47\text{Pa}$, $PI=0.04$.(f) 90.4%SSL, $Re = 75k$, $\tau_w = 0.43\text{Pa}$, $PI=0.12$.

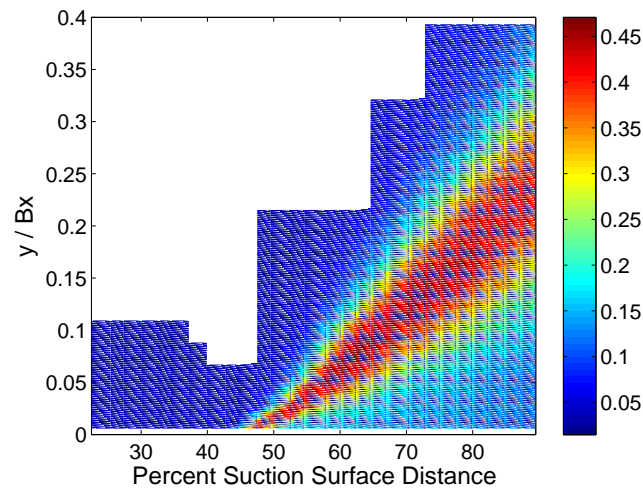
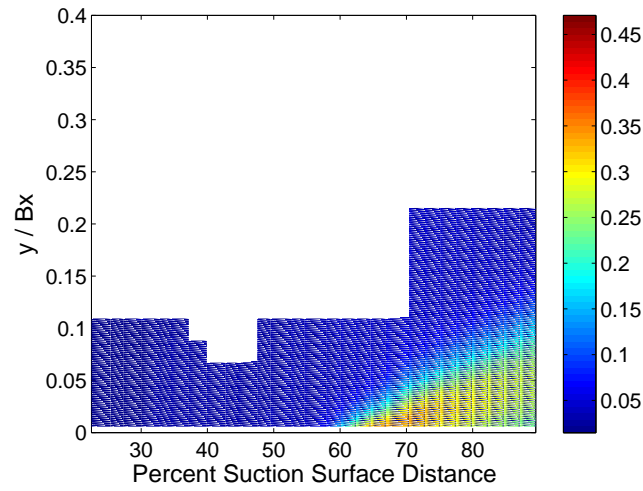
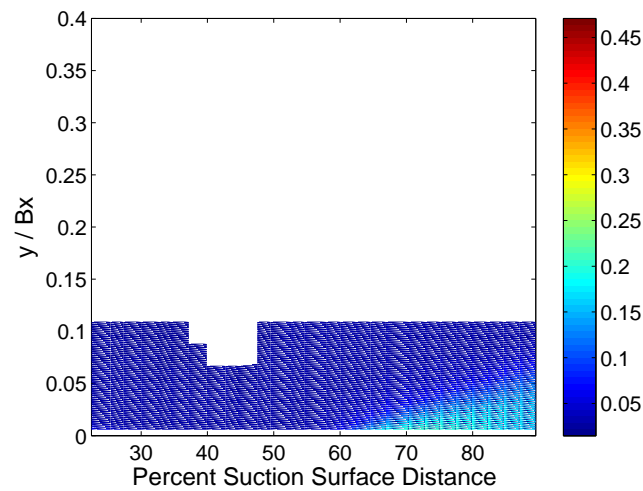
Figure 4.7: L2F turbulent profile similarity comparisons.

using $\tau_w = 0.24\text{Pa}$ and $PI=0.14$ for $Re = 50k$ and $\tau_w = 0.47\text{Pa}$ and $PI=0.04$ for $Re = 75k$. The terminal shapes are slightly different, however, as the $Re = 50k$ case remains below Coles' law with

increasing y^+ while the $Re = 75k$ case first shifts above and then falls below Coles' law. Again the similar L1M trends are noticed where the PI terms increase with downstream distance and decrease with increasing Reynolds number, while the shear stress follows the opposite trends. In addition, the higher y^+ data points in the L2F profiles do not lie above Coles' law as often as the higher y^+ points of the L1M. As only the near-wall 30 to 35 data points were used in these comparisons, it is quite possible that the L2F profiles deviate from Coles' law in a similar manner to the L1M further out into the freestream. As with the L1M, the deviation from the similarity laws are believed to be caused by an incomplete transition to turbulence and varying pressure gradients.

Figure 4.8 presents contours of $urms/U_{in}$ for all three Re for the L1M. The same heights over the various Re used for the mean velocity are presented in these figures as well in order to resolve the boundary flow features. Immediately we notice the severe degree of unsteadiness ($urms/U_{in}$) in the separated and stalled free shear layer for $Re = 25k$ in Figure 4.13(a). The first sign of near-wall unsteadiness occurs at 42.7%SSL. As expected from the mean velocity contours, the unsteadiness begins to sharply increase near the detachment location of 47.5%SSL, spreading very rapidly in the downstream and cross-stream directions, reaching a peak of 47.1% unsteadiness in the core near 62.4%SSL and as low as 7.3%Bx up from the surface. Again the unsteadiness continues unbounded with downstream distance, matching the rapid change seen in the mean velocity contours. Although this high level of unsteady flow convects downstream into the wake producing the average exit turbulence of 13.5% as reported earlier in Table G.3(b), it is still not enough turbulent mixing to force a reattachment of the separation. This means the adverse pressure gradient experienced by the mid-loaded L1M is too severe for its boundary layer to overcome without massive separation at low Re . Increasing Re to 50k in Figure 4.13(c) greatly reduces the unsteadiness compared to $Re = 25k$, where $urms/U_{in}$ begins to grow further downstream at 52.6%SSL now, with a peak value of only 34.1% occurring near 66.9%SSL at 1mm (0.6%Bx) up from the surface. A further increase to $Re = 75k$ in Figure 4.13(e) also sees the initial rise of unsteadiness at 52.6%SSL and reduces the peak unsteadiness to just 20.7% near 72.8%SSL at 1mm up from the surface. The L1M $Re = 75k$ case is considered attached (Table 4.4), while at lower Re the flow is considered separated, which corroborates with the loss behavior as noted in Figure 4.1. However, the maximum unsteadiness location for both the $Re = 50k$ and $Re = 75k$ cases are at the lowest profile point acquired nearest the wall, thus suggesting an attached-flow transition as opposed to transition atop a separation bubble. This contradiction supports the idea that separated-flow transition in the shear layer atop a very thin separation bubble may in fact behave like attached-flow transition.

Examining the skew and kurtosis of the L1M velocity signals in Figure 4.9 lend some insight into the transition process. The contour scales for all three Reynolds numbers are the same for

(a) $Re = 25k$.(b) $Re = 50k$.(c) $Re = 75k$.Figure 4.8: L1M u_{rms}/U_{in} contours.

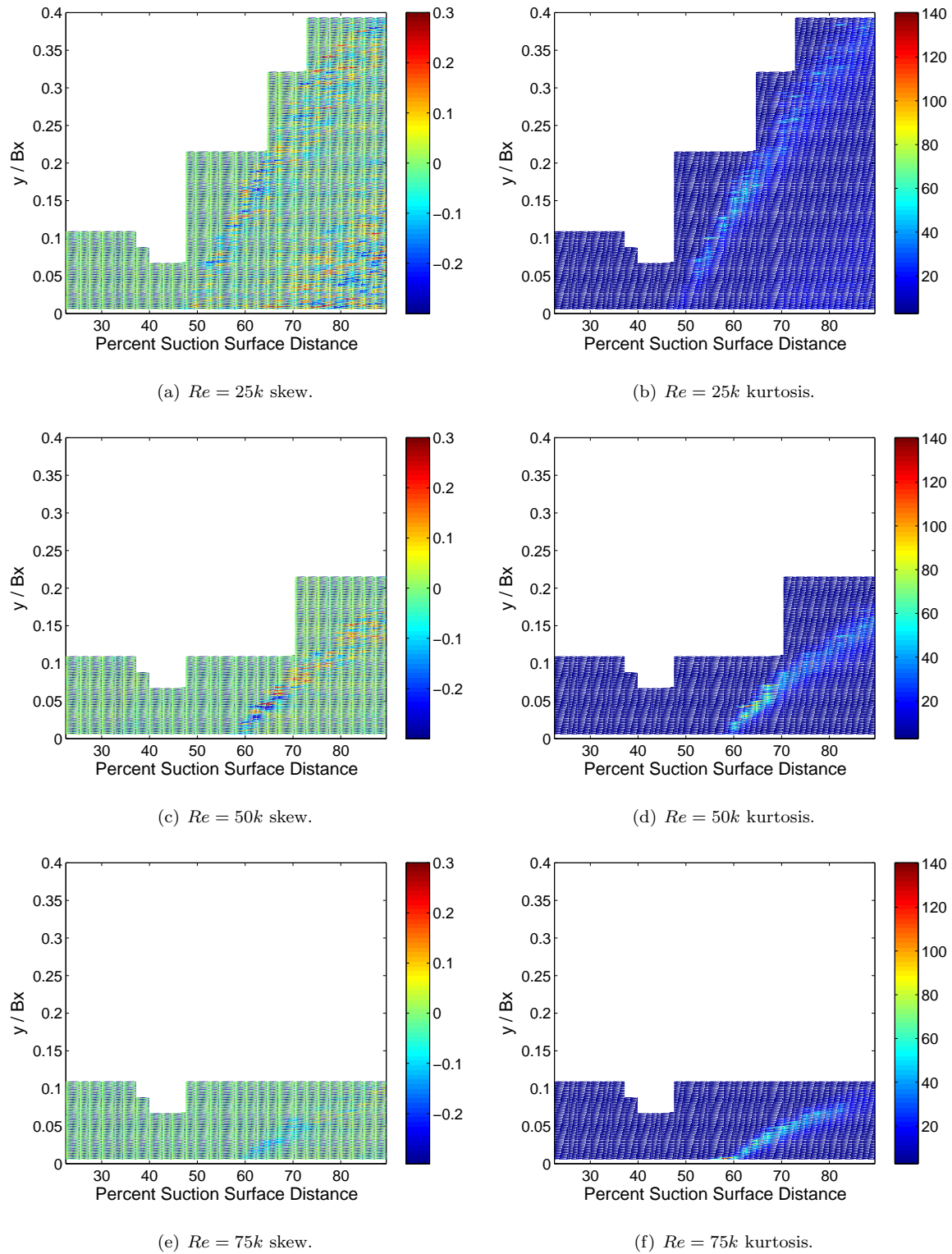
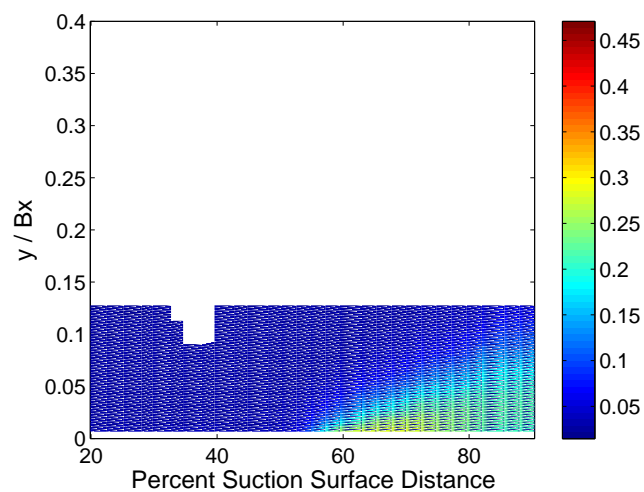
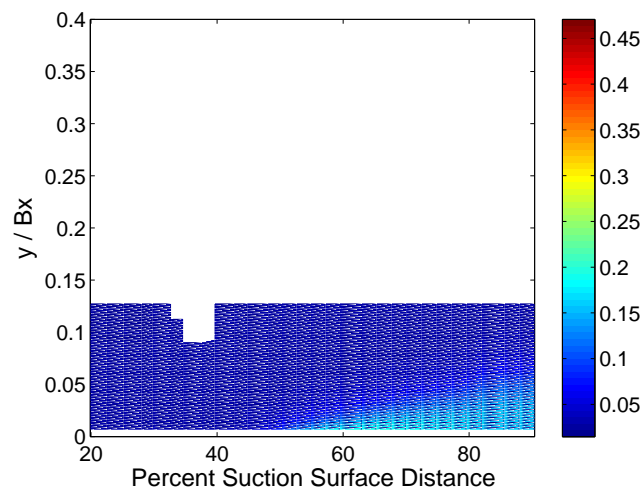
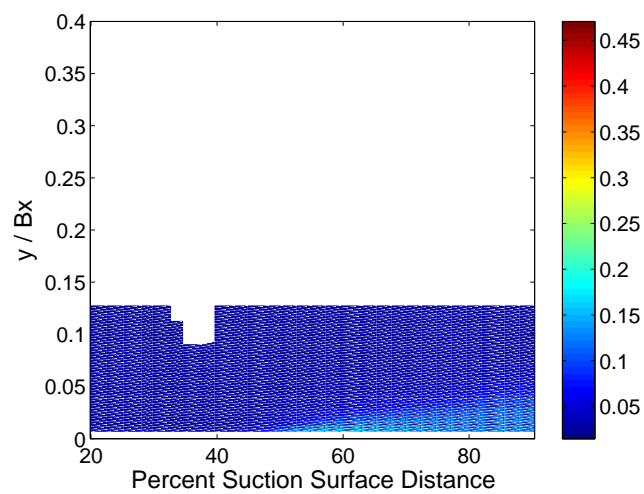


Figure 4.9: L1M skew and kurtosis contours.

skew and the same for kurtosis for ease of comparison. As explained earlier in Chapter 3, regions of both negative skew and positive kurtosis have been identified as transition indicators. This combination of skew and kurtosis first occurs near 47.5%SSL just 3.3%Bx up from the surface for the L1M at $Re = 25k$, suggesting the beginnings of a separated-flow transition away from the surface. Following the separated free shear layer downstream and away from the surface after 47.5%SSL, regions of alternating sign skew are tied with low magnitude kurtosis, suggesting a weakly intermittent transition process which never fully matures into turbulence, a trend also seen later with intermittency contours of Figure 4.12(a). Bons' description of the alternating sign skew in regions of positive kurtosis indicates the merging of smaller momentum laminar packets with higher energy turbulent pockets [Reimann et al. 2006]. As Reynolds number is increased to $50k$, levels of alternating sign skew and positive kurtosis are noticed at the near-wall profile location near 57.9%SSL. But in this case, the larger magnitude values of skew and kurtosis occur away from the wall, slightly downstream at 62.4%SSL and up 4.1%Bx from the surface, again suggesting a mixture between attached-flow and separated-flow transition. In order to construct the transition models for the next section, the transition location will be identified as the first streamwise location where the negative skew and positive kurtosis condition applies, in this case near the wall at 57.9%SSL. As Re is further increased to $75k$, the skew remains slightly negative but growing progressively positive downstream and away from the wall. The kurtosis, however, indicates a burst near 57.9%SSL, the same streamwise location of the $Re = 50k$ increase in kurtosis. The variation of kurtosis follows that of skew in reducing magnitude with downstream and surface-normal distance. The transition location indicated by skew and kurtosis for the L1M at $Re = 75k$ is therefore 57.9%SSL.

Figure 4.10 presents contours of u_{rms}/U_{in} for all three Reynolds numbers for the L2F airfoil. The contours for all three quantities are scaled the same as the L1M for ease of comparison. Again, the boundary layer physics were resolved with the smaller profile height, so surface-normal scale must be kept into consideration for full appreciation of the differences between the L1M and the L2F. At first glance, the L2F aerodynamics significantly reduce the amount of unsteadiness when compared to the L1M airfoil. For $Re = 25k$ in Figure 4.14(a), the unsteadiness first begins to increase near 52.6%SSL, compared to 42.7%SSL of the stalled L1M at $Re = 25k$. Therefore, the stronger acceleration of the front-loaded L2F pushes downstream the initial growth of unsteadiness compared to the mid-loaded L1M. The maximum unsteadiness of 28.7% occurs in the near-wall at 65.3%SSL, suggesting an attached-flow transition even at the lower Reynolds number value of $25k$. The intermittency contours presented later corroborate the appearance of near-wall transition for all three Re , again suggesting attached-flow instead of separated-flow transition. Initial growths of unsteadiness for $Re = 50k$ and $Re = 75k$ begin near 48.1%SSL and 44.8%SSL, respectively. As Re is

(a) $Re = 25k$.(b) $Re = 50k$.(c) $Re = 75k$.Figure 4.10: L2F u_{rms}/U_{in} contours.

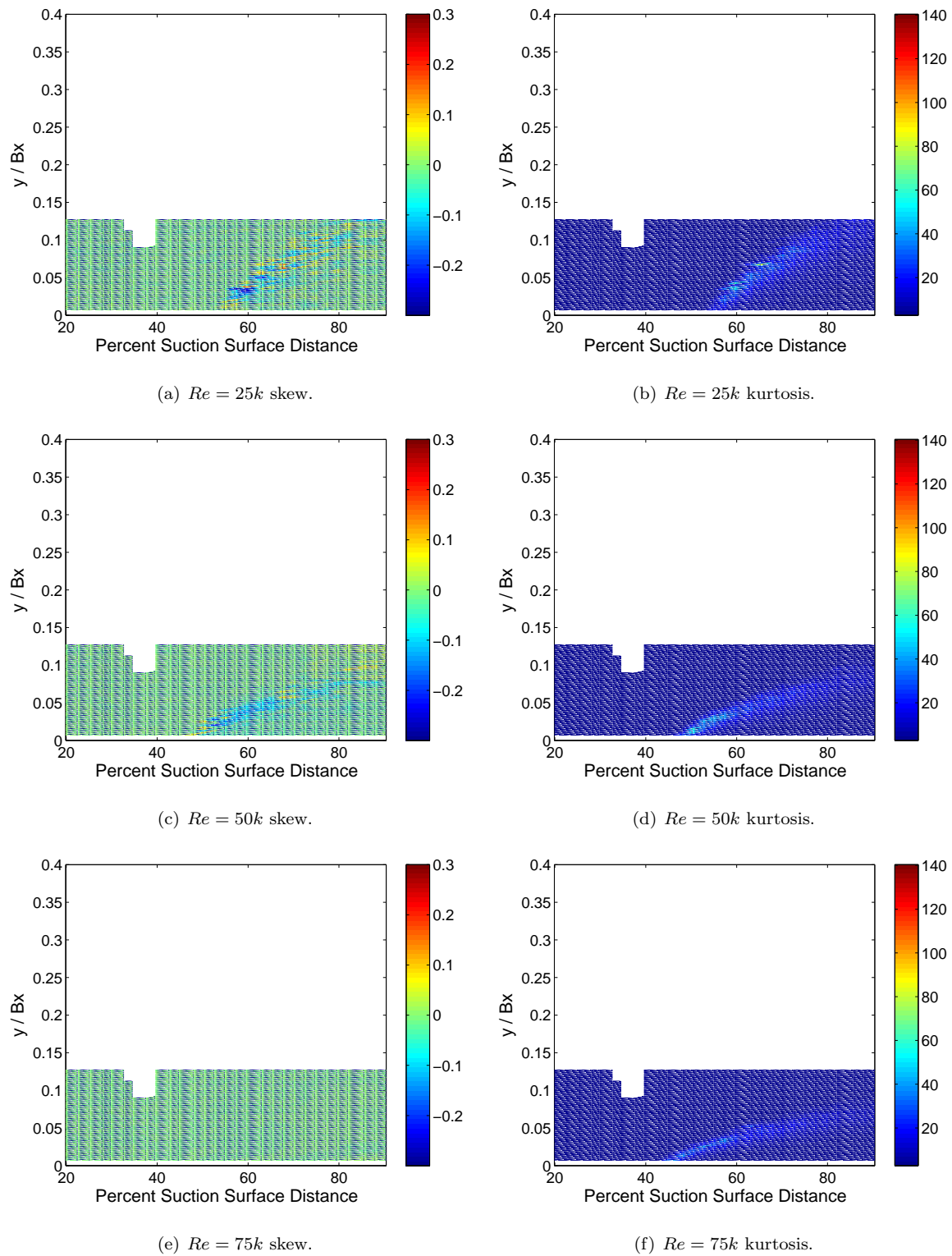


Figure 4.11: L2F skew and kurtosis contours.

increased beyond $25k$, the overall area of unsteadiness decreases significantly with Re and maximum levels remain in the near-wall locations, 19.5% at 65.3%SSL for $Re = 50k$ and 17.4% at 57.2%SSL for $Re = 75k$. Thus we see an increase in Re causes an earlier appearance of unsteadiness.

Examining the skew and kurtosis of the velocity signal in Figure 4.11, we can gain some insight into the transition process for the L2F airfoil. The contour scales for all three Re are the same as the L1M for ease of comparison. For $Re = 25k$, the combination of negative skew and positive kurtosis occurs near 54.9%SSL not in the near-wall location but just above at 1.4% axial chord above the surface. This location even so slightly away from the wall suggests a separated-flow transition, even though the maximum unsteadiness suggests an attached-flow transition. This contradiction again lends support to the argument that very thin bubble separated-flow cases may transition as if attached. Again we notice regions of alternating sign skew progressing downstream and away from the surface with downstream distance, signaling the interplay between the laminar and turbulent pockets. Increasing Re to $50k$ sends the skew-kurtosis condition upstream to 48.1%SSL in the near-wall location, signaling an attached-flow transition. The same trend applies to $Re = 75k$, where the skew-kurtosis condition appears at 44.8%SSL, even though now the skew has reached minimal levels when compared to the other 5 cases. Both skew and kurtosis continue to occur away from the wall with downstream distance.

Figure 4.12 presents intermittency contours obtained through Clark's algorithm for both airfoils at all three Re . The L2F regions of intermittency remain below the regions for the L1M for all three Re tested, even though the L1M $Re = 75k$ case approaches the lower height of the L2F $Re = 75k$ case. For example, the maximum surface-normal height of the intermittency distributions for the L2F at $Re = 25k$ is nearly 10% axial chord, while the L1M reaches above 30% of its axial chord. This trend is expected since previous discussion has concluded the L2F Reynolds characteristic behaves more like attached-flow transition while the L1M may experience a low Reynolds regime of clearly separated-flow transition with its increased losses seen back in Figure 4.1. Classical methods of transition identification normally consider the first appearance of intermittency as the location of transition onset, and this trend will continue here. As this work considers two separate methods of transition onset identification (skew-kurtosis criterion and intermittency), both methods will be used later in their own constructions of transition parameters and compared against the models presented in Figure 2.3.

At $Re = 25k$ for the L1M, the first appearance of intermittency occurs at 52.6%SSL, just 9.9%SSL downstream of where unsteadiness (u_{rms}/U_{in}) first appears. Figure 4.12(a) shows this occurs away from the wall in the separated shear layer of the stalled L1M. Transition to turbulence never fully completes, and the intermittency eventually dies out by 89.5%SSL. The L2F in Figure 4.12(b)

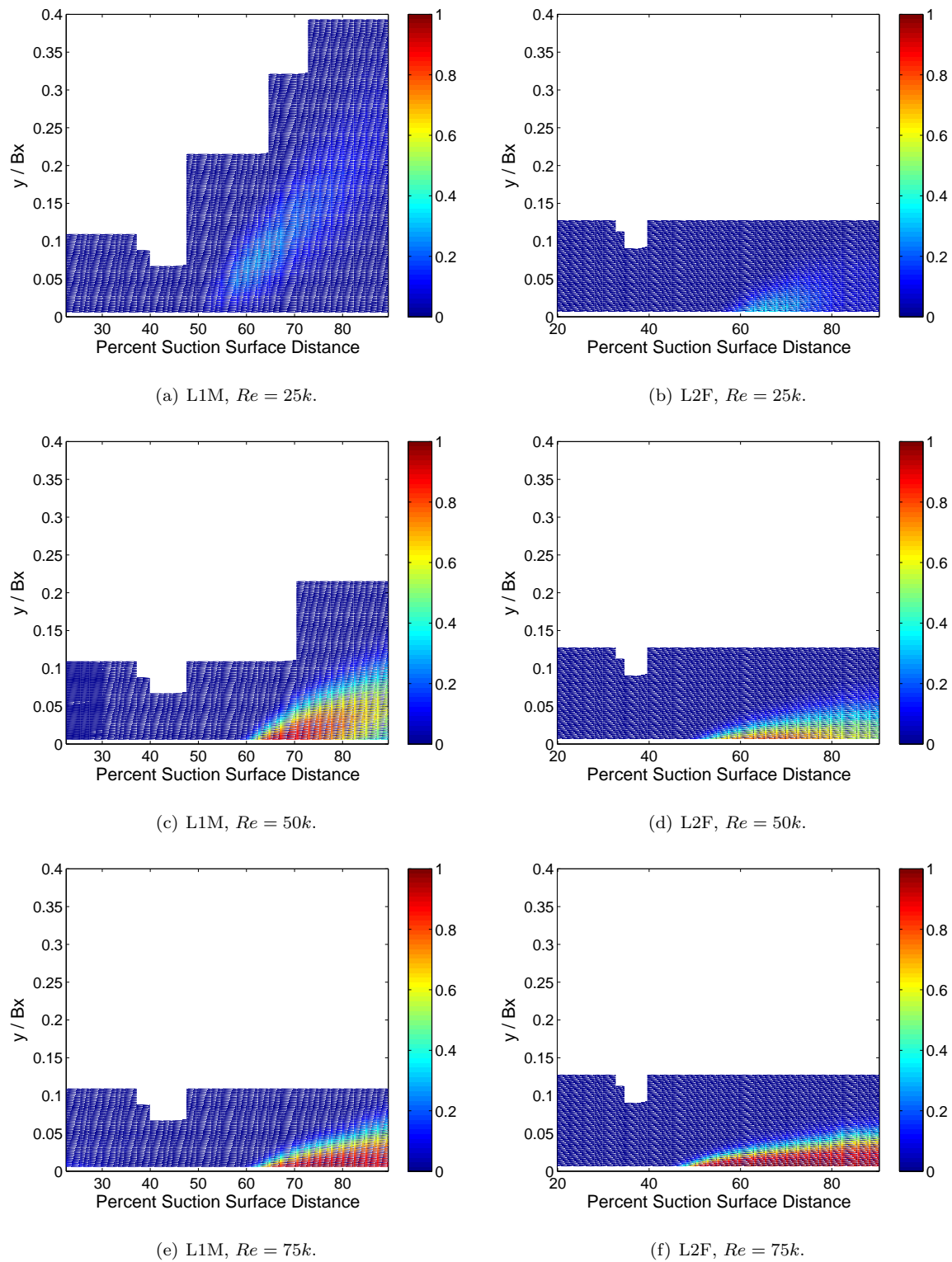


Figure 4.12: L1M and L2F intermittency contours.

resembles an attached flow intermittency pattern with its core closer to the wall than the L1M at $Re = 25k$. Intermittency first increases near 54.9%SSL, just 2.3%SSL downstream of where *urms* does the same. This distance from initial unsteadiness to the start of transition (intermittency) is shorter for the L2F than the L1M, suggesting the L2F forces a stronger bursting of turbulent energy when the flow finally begins to transition. Increasing Re to 50k, the L1M intermittency now resembles that of an attached flow where the maximum intermittency follows the *urms* location near the wall. Here intermittency first occurs near 60.1%SSL, 7.5%SSL downstream of the initial unsteadiness. Figure 4.12(c) shows the intermittency peaks near 66.9%SSL at 0.91 and then begins to drop with downstream distance. The turbulence spreads away from the wall, mixes with the freestream and then experiences some level of decay where the intensity decreases. Remembering the L1M loss knee in Figure 4.1 begins to level out around $Re = 50k$, we see the transition helps the L1M re-energize the boundary layer for higher Re , providing a reduced overall loss than the massively separated condition. The L2F at $Re = 50k$ in Figure 4.12(d) sees the first burst of intermittency near 48.1%SSL in the near-wall location, the same profile location where unsteadiness was first noticed. Again the L2F aerodynamics reduces the surface-normal extent of turbulence over the L1M, and again we notice an incomplete transition after the peak intermittency of 0.79 at 65.3%SSL. Since the L1M peak value is higher than the L2F peak at $Re = 50k$, the L1M experiences a slightly greater degree of turbulent bursting than the L2F, although the L2F transitions well before the L1M. Increasing Re to 75k in Figures 4.12(e) and 4.12(f) shows intermittency patterns which are classically thought of when transition to turbulence completes: a laminar flow begins to transition and eventually goes fully turbulent to remain turbulent thereafter. Intermittency increases near 60.1%SSL for the L1M, a distance of 7.5%SSL downstream of initial *urms*; the L2F again sees intermittency at the same location as *urms* at 44.8%SSL. This trend again suggests the L2F transition mechanism is much more efficient at promoting transition than the L1M, where initial *urms* takes longer to initiate transition (intermittency).

Another way of looking at the unsteady development for each airfoil is to examine the centroids of *urms*/*Uin* and intermittency at each profile location and examine where the maximums occur compared to the centroid locations, which provide information such as where the core of unsteady activity is located at each profile. The centroids are constructed with the non-dimensional surface-normal distance as the y-axis and the non-dimensional parameter value as the x-axis. Using this methodology, the area of *urms*/*Uin* and intermittency (γ) at each profile location can be thought of as the total activity at that location. The *xbar* components represent the strength of the core defined by the centroid, while the *ybar* components represent the non-dimensional surface-normal distance of the core. The *y*max tag identifies the non-dimensional surface-normal distance where the

maximum value is located. Figures 4.13 and 4.14 present this data against percent suction surface distance along with boundary layer and momentum thicknesses for the L1M and L2F airfoils. The y-axis of these graphs represents y/Bx for the $ybar$, y_{max} , δ , and θ plots, and is the total area value or $xbar$ of the centroid for the area and $xbar$ plots.

In Figure 4.13(a) for the L1M at $Re = 25k$, the $urms/U_{in}$ area increases at 42.7%SSL where the first sign of unsteadiness appeared in Figure 4.8. A sharp jump is seen before the shear layer detachment at 47.5%SSL both in the $urms/U_{in}$ area and now $xbar$, or magnitude of the core location. This location also marks where transition onset occurs using the skew-kurtosis condition. The strength of the core continues to rise until nearly 60%SSL, where it levels off through to the last profile at 89.5%SSL. This leveling off location corresponds roughly to where the width of the most turbulent portions of the $urms/U_{in}$ profiles slow their streamwise growth. The area, or total activity, continues to grow unbounded just as expected from earlier $urms$ contours. The $ybar$ and y_{max} locations appear to remain congruent throughout the measured zone, indicating the unsteady activity is mostly centralized. Figure 4.13(b) shows the small burst in intermittency appears in the regions which grow just after where the $urms$ begins, with a resulting increase in boundary layer height and momentum thickness. Near 39.9%SSL the maximum intermittency bursts away from the surface near $0.05 y/Bx$, vanishes after 42.7%SSL, and has another brief burst again at the same approximate height near 54%SSL. The onset of transition obtained with an intermittency level above 0.02 (above the threshold using Clark's algorithm) occurs at 49.5%SSL for the L1M at $Re = 25k$. The maximum intermittency occurs below the core intermittency. Progressing downstream increases the boundary layer thicknesses with continuing unsteadiness and dying intermittency. The core and maximum $urms$ occur under the boundary layer until 52.6%SSL, after which the core and maximum $urms$ lie outside the boundary layer and into the freestream. Core intermittency lies inside the boundary layer over the entire length surveyed. It's interesting to note that unsteadiness continues unbounded while intermittency levels off and then decreases. The maximum unsteady core activity occurs at the same location as the maximum intermittency core near 62.3%SSL, after which the total intermittency activity begins to decline. The core intermittency strength then declines at a much faster rate than the total activity (area), while the total unsteady activity ($urms$ area) continues to grow unbounded. This may support the argument that there is no re-laminarization as intermittency falls off since the unsteadiness continues to grow.

Increasing Re to $50k$ for the L1M in Figure 4.13(c) causes a small jump in total unsteady activity away from the wall around $0.1 y/Bx$ and 30%SSL which dips at 37.2%SSL then resurges at 44.6%SSL. The total activity continues to increase gradually until the skew-kurtosis transition onset location of 57.9%SSL, where it grows until nearly 70%SSL. A small dip at profile locations 8,

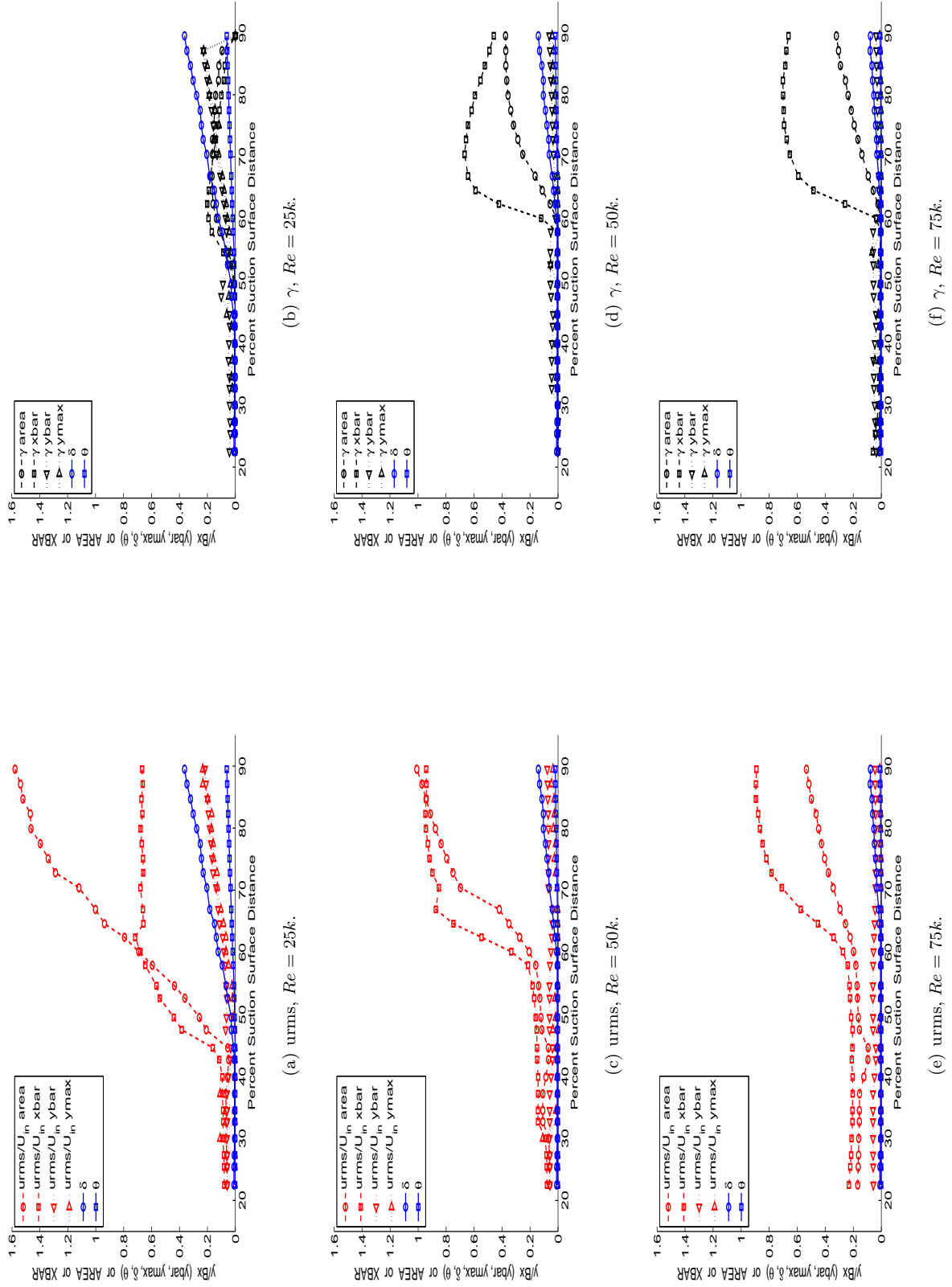


Figure 4.13: L1M unsteady development.

9, and 10 can be seen and is a result of the limited profiles available in those locations; the data in these areas is believed to remain consistent with surrounding points. The same trend is seen in the L1M case at $Re = 75k$, and with all L2F cases at profile locations 7 and 8. The core strength (\bar{x}) of urms activity follows the total activity, again suggesting a centralized distribution of unsteady activity which remains near the same height away from the surface all along the blade, as seen with the near-constant \bar{y} location. This \bar{y} location is outside of the boundary layer until 66.9%SSL, where it remains under the boundary for the duration of suction surface tested. The maximum unsteadiness remains below the core location all along the surface. Figure 4.13(d) shows transition onset by intermittency occurs at 60.1%SSL where the total activity far surpasses that at $Re = 25k$, while the core intermittent activity strengthens and then decreases after 70.0%SSL. This core intermittency (greater than 0.02) remains below the boundary layer at all times. This decrease in core strength is accompanied by an increase in total strength, suggesting the turbulence spreads more rapidly than it weakens, covering a greater physical area with downstream distance at the expense of core strength. Again the boundary layer thicknesses begin to grow near the point where intermittency increases instead of where unsteadiness or the skew-kurtosis condition occurs.

As Re is increased to $75k$ in Figures 4.13(e) and 4.13(f) for the L1M, another jump in total and core urms and intermittency is seen over $Re = 25k$ and $50k$ as expected due to the higher freestream velocity. The gradual buildup in total urms activity begins near 54.6%SSL and continues to the last profile at 89.5%SSL. The core of urms activity continues growing more rapidly after the skew-kurtosis transition onset at 57.9%SSL, while core intermittent activity is seen to rise after the intermittent transition location of 60.1%SSL up to its maximum strength at 70.4%SSL. Again the trend where the total intermittency grows while the core strength declines suggests a spreading of intermittent influence while trading off strength. The maximum unsteady and intermittent behavior continues to lie inside the core locations as evidenced by comparison of the \bar{y} to y_{max} plots. The maximum urms and maximum and core intermittency remain below the boundary layer, while the core urms is generated in the freestream until somewhere between 72.8 and 75.1%SSL where it shifts under the boundary layer. The boundary layer thicknesses again grow with intermittency instead of with unsteadiness. This trend suggests the Clark intermittency algorithm picks up on the activity that is somehow linked to growth in boundary layer thicknesses. This makes physical sense as well, since intermittency is associated with turbulent eddies which by their nature expand and mix the local fluid, resulting in the increase in boundary layer height. The original purpose of the algorithm was to track turbulent spots, which have been observed to cause increases in displacement and momentum thicknesses [Clark et al. 1994a]. It is encouraging that the current data sets and the previous development of the algorithm show increases in boundary layer thicknesses both on and

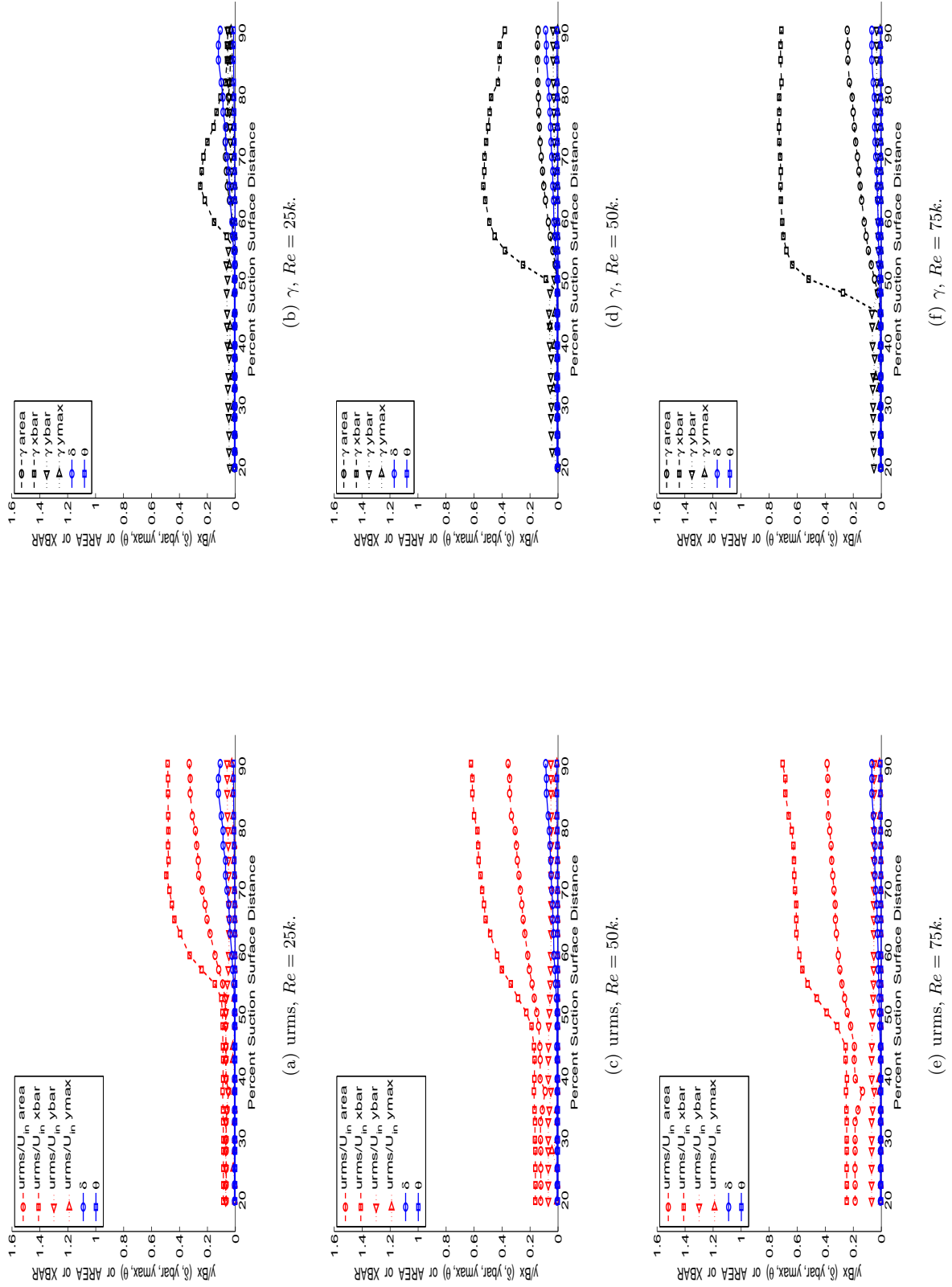


Figure 4.14: L2F unsteady development.

away from the wall as intermittency increases.

The centroids of urms and intermittency for the L2F airfoil are presented in Figure 4.14 for all three Reynolds numbers. At $Re = 25k$ in Figures 4.14(a) and 4.14(b), we immediately notice a lower range of parameter values when compared to any of the L1M cases. Compared to the L1M at $Re = 25k$, the L2F has a reduced total urms activity which begins to rise near 52.6%SSL, just before the skew-kurtosis transition at 54.9%SSL. The core strength also begins to rise near 52.6%SSL and continues to increase while the total activity levels off after its peak at 70.0%SSL. This trend suggests the L2F unsteady activity becomes more compact after 70.0%SSL since the total activity remains constant while the core strength increases. The maximum unsteadiness remains under the boundary layer for most of the blade, while the core urms remains outside the boundary layer until 65.3%SSL where it shifts underneath. Again we see the rise of the boundary layer thicknesses with intermittency near 54.9%SSL, while soon after the core of intermittent activity falls significantly lower to remain under the boundary layer. Just as with the L1M, the L2F core intermittency falls under the boundary layer just as it begins to grow. It's interesting to note the L2F urms activity continues to rise while the intermittency total activity peaks near 72.4%SSL and then begins to decline as the core shifts under the boundary layer. This intermittency core however peaks slightly earlier than the total activity around 65.3%SSL, suggesting an expansion of influence at the expense of core strength. After that, both core and total strength decline. The maximum urms and intermittency locations remain relatively coincident under the boundary layer at all times.

As Reynolds number is increased to $50k$ in Figures 4.14(c) and 4.14(d), there is an increase in core and total urms activity over $Re = 25k$, which is again expected since the faster freestream supplies more energy to the unsteadiness. Again we see a rise in core urms activity at the skew-kurtosis onset location of 48.1%SSL, which is immediately followed by a rise in core intermittent activity at the intermittency onset location of 50.3%SSL. Unlike $Re = 25k$ however, this time the core and total unsteadiness continue to rise to the last profile at 90.4%SSL, suggesting a continual growth in unsteady energy. This is not true for intermittency, as its core gains strength until 63.0%SSL and then slightly decreases, while the total intermittent activity seems to grow until the last profile location. Again this indicates a spreading influence of turbulence as it loses strength for coverage. The maximum and core intermittency remains under the boundary layer, while the core unsteadiness remains outside until 72.8%SSL where it falls under the boundary layer.

A further increase to $Re = 75k$ in Figures 4.14(e) and 4.14(f) again shows the expected increase in total and core urms activity with the increased levels over the $Re = 25k$ and $50k$ cases. Here the initial unsteady growth is seen at 44.8%SSL, the same location as the intermittency rise and transition onset location defined by both skew-kurtosis and intermittency. Here again the total

and core urms activity continue to increase through the measured region. The intermittency core strength levels off after 63.0%SSL while the total activity remains growing until the end. This again suggests a spreading of turbulent influence as core strength remains constant, a trend also seen back in the contour of Figure 4.12(f). The core and maximum intermittency remains below the boundary layer again, while the core unsteadiness falls under the boundary layer only after 79.6%SSL.

As expected from these plots, we notice the boundary layer height decreases in size with increasing Re for both airfoils. The total urms and intermittency activities (areas) also increase with Re due to the faster fluid pumping more energy into the unsteady processes. The L2F levels remain below the L1M however, even though transition initiates earlier. We also see that the core of urms is closely tied to the skew-kurtosis onset condition. This makes physical sense, because the skew and kurtosis are measures of the quality of the velocity signal, i.e. they measure the departure from the unfluctuated state. So as variation is introduced in velocity due to a transition or unsteady process, the core urms also reflects this change. We also see that the core urms remains outside of the boundary layer for longer distances before falling under as Re is increased; these occurrences are at 52.6, 66.9, and 72.8%SSL for the L1M and 65.3, 72.8, and 79.6%SSL for the L2F. This is because the faster freestream initiates unsteadiness earlier while simultaneously forcing the lower boundary layer height. Thus we see a more forward-loaded blade maintains its core unsteady activity outside of the boundary layer further downstream than the mid-loaded airfoil, even though the total unsteadiness is not greater in the wake (Table G.3(b)). This difference may help explain why an earlier transition with a lower amount of total unsteadiness can still maintain a well-behaved flowfield even at lower Reynolds numbers. The maximum urms remains under the core urms at all times, signalling that unsteadiness is connected to the presence of the wall boundary, either generated or at least amplified in the near wall region. The core intermittency decreases its strength (\bar{x}) faster than the intermittent total activity (area), signalling that the turbulent activity spreads away from the wall at the expense of core strength. The boundary layer growth is connected with the rise in intermittency and not the rise in urms. Therefore the mixing caused by the turbulent eddies is responsible for the boundary layer growth instead of general flow unsteadiness (urms). It is also interesting to note that unsteady activity can increase while turbulent activity decreases, showing unsteadiness and intermittency are not direct functions of each other.

4.3 S3F Measurements

As mentioned earlier, thermal anemometry requires the positioning of a probe throughout the flow-field in order to acquire information. This technique is limited near surfaces, since the thin sensor

element cannot touch any object or it will immediately be destroyed. The anemometry results presented in the last section illustrate how thin the separation bubbles in this study truly are - less than 1mm in the surface-normal direction. As such, thermal anemometry was unable to identify the separation dynamics needed to validate the separated-flow transition model. S3F can provide just this, as it measures the forces directly on the surface instead of the flowfield above. The S3F tests conducted at AFRL were completed in two rounds; the first placed separate patches of S3F for the leading and trailing edges, and the second round placed one continuous patch from the trailing edge to nearly 42%SSL. Round 1 results were intended to check the formulations of the S3F sensor and make sure the stiffness was properly selected for the local stress levels. The separation onset locations obtained in round 1 for the leading edge are used in the next section to validate the separated-flow transition model. Round 2 examines the trailing edge region with another S3F patch, and these results were to be compared with the round 1 trailing edge data to gain more insight into the data reduction process, thus helping ISSI obtain a better feel for the film's performance over two test points with the same flow conditions. We'll see later that obtaining results with S3F in these low flow speeds is still a challenging task, as round 1 produces different magnitude friction forces on the trailing edge than round 2. In fact, the friction patterns are also different.

Figure 4.15 presents round 1 S3F results for the leading edge region of the L2F blade. These results cover approximately 5 to 35%SSL. Figures 4.15(a), 4.15(b), and 4.15(c) show the displacement maps with magnitude as the colorbar, and are oriented with the flow coming from the right and going to the left. These figures show the L2F blade indeed separates, as the nodal line of separation can be seen for all three Re where the downstream (left) facing vectors converge with the upstream (right) facing vectors. The $Re = 25k$ case shows a separation line which is a function of airfoil span (y-direction), indicating an unsteady separation onset location. The other two Re maps display a separation line more consistent with span, and is located slightly further downstream than $Re = 25k$. Figure 4.15(c) also indicates a small separation closer to the leading edge, as seen with the nodal line of reattachment where the vectors diverge away from the line. During the course of the S3F round 2 tests, we found the blades slightly twist under the wind-on loaded state, and this may explain why the nodal line of reattachment seen in the bottom portion does not exist in the upper portion. This twisting may in fact cause the slight separation seen in this figure. Figure 4.15(d) presents the information which will be used in validating the separated-flow transition model. This figure presents the streamwise (x-dir) and transverse (y-dir) surface shear results averaged over the span for the maps presented in Figures 4.15(a), 4.15(b), and 4.15(c). Here the flow is coming from the left going to the right, so positive friction is directed downstream and negative friction is directed upstream, indicating the reverse flow inside of a separation bubble. The small magnitude transverse

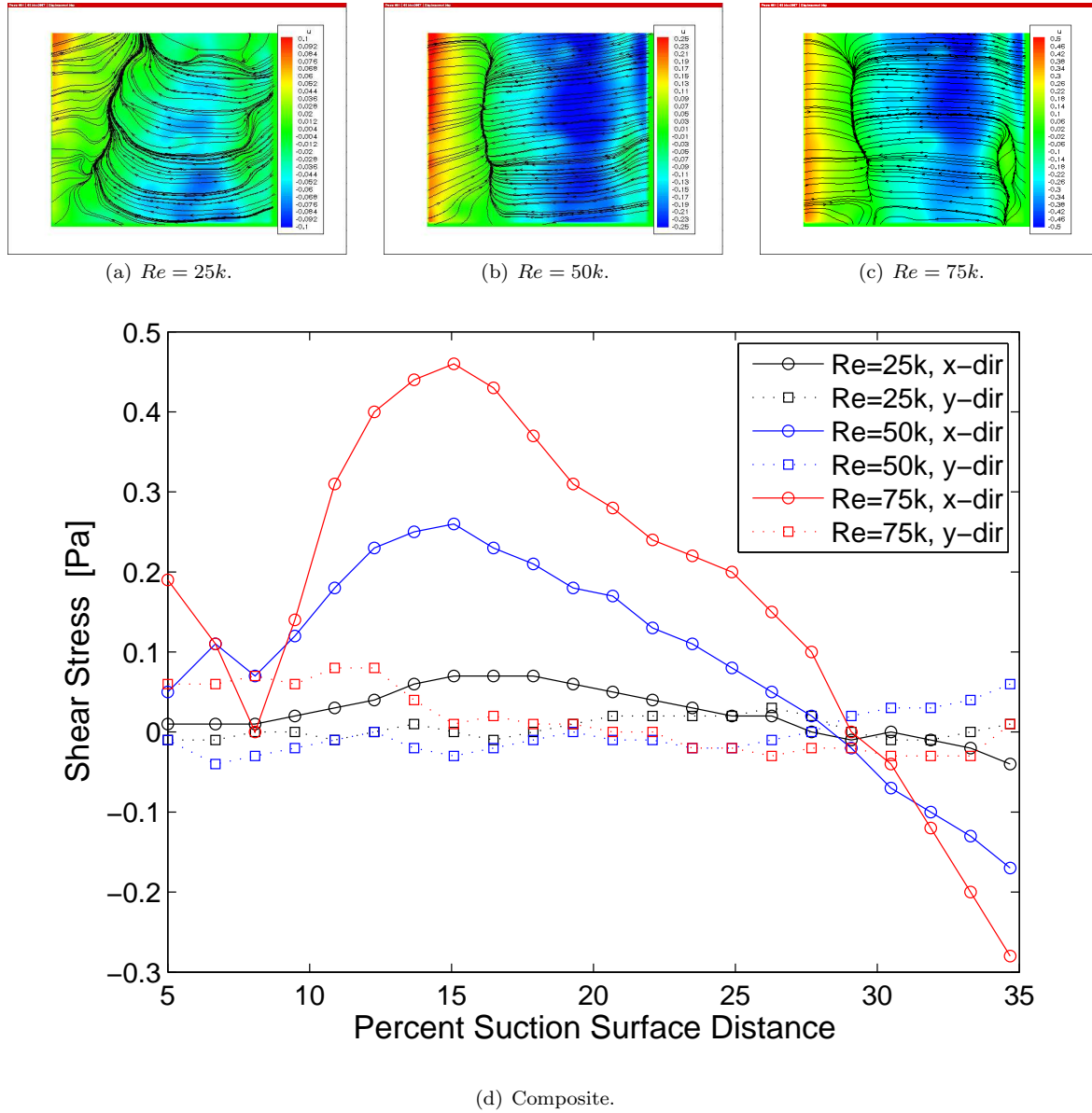


Figure 4.15: S3F round 1: Force distributions near L2F leading edge, 5-35%SSL.

friction (y-dir) indicates a mostly two-dimensional flow for all three Reynolds numbers with slight variation possibly due to the slight twisting of the blade under the applied load. The streamwise surface shear (x-dir) for $Re = 25k$ indicates a separation at approximately 26%SSL where the friction changes sign from positive (downstream) to negative (upstream). This location will be used later to validate the separated-flow transition model, where the model information will be taken from the nearest boundary profile at 25.2%SSL. Increasing Re moves this separation location slightly further downstream, where the $Re = 50k$ case is just upstream of the 75k case. Model validation for

these two latter cases will require boundary information from their nearest profile, both selected as 28.0%SSL. Also as expected in this figure we see that friction is proportional to and increases with Re . Table 4.5 shows the experimental separation onset locations along with Wildcat predictions in percent suction surface distance. All predicted onset locations occur further downstream than those found by experiment, although the proximity of the two methods is encouraging.

Table 4.5: L2F separation onset locations [%SSL].

Method	$Re = 25k$	$Re = 50k$	$Re = 75k$
S3F	25.2	28.0	28.0
Wildcat	27.5	29.0	29.0

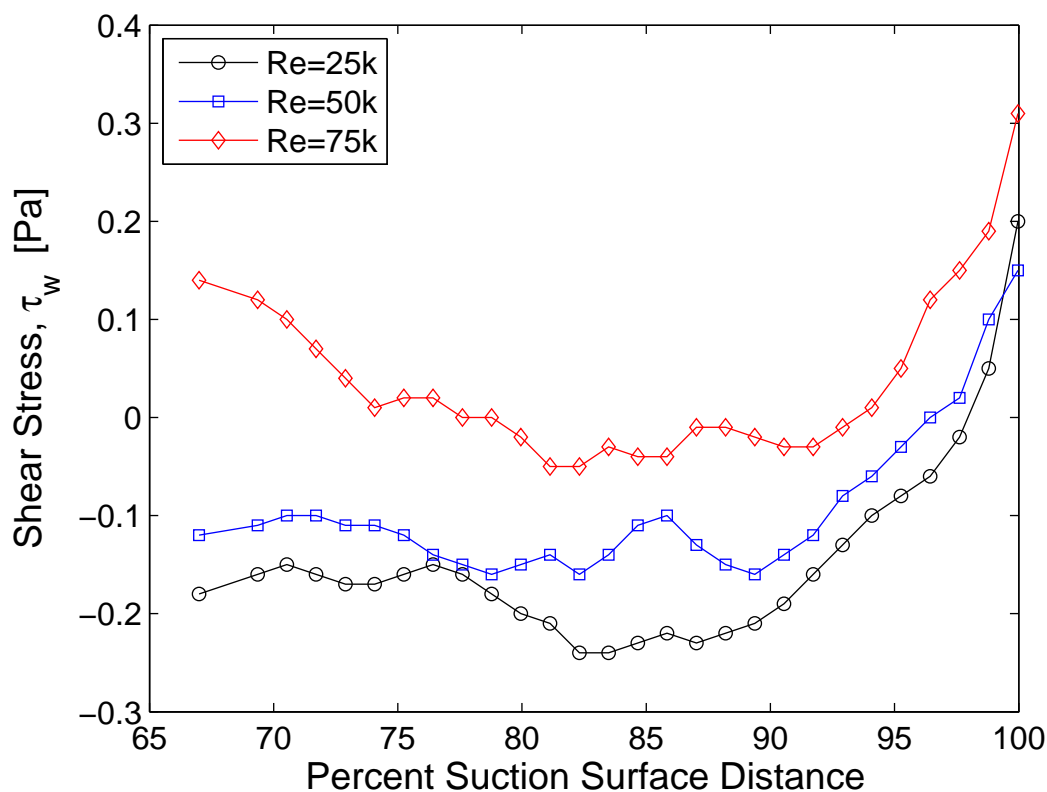


Figure 4.16: S3F round 1: Force distributions near L2F trailing edge, 67-100%SSL.

Figure 4.16 presents the round 1 streamwise S3F results for all three Re from 67%SSL to the trailing edge of the L2F airfoil. Again the flow is left to right, so a positive shear stress indicates downstream flow while a negative stress indicates upstream flow (separation). This figure shows the

friction forces experienced in this flow at the trailing edge are less than 1 Pascal. We also see that the $Re = 25k$ and $50k$ cases are separated by the beginning of the patch, and both reattach near 92-94%SSL. It is not clear whether or not the separation noticed here is continued from the leading edge or if it caused by a disturbance of the film's upstream edge. The $Re = 75k$ case appears attached as the patch begins, signalling that the separation near 28%SSL must have reattached somewhere before 67%SSL. The flow again briefly separates near 77%SSL and then quickly reattaches before the end of the blade near 92%SSL. This flow description will be contradicted by the round 2 results, again showing the difficulty experienced when resolving friction forces on the order of 1 or less Pascals. Again we must remember we are trying to not only resolve such low differences in friction which is a great achievement in its own right, but we are also simultaneously cancelling model and tunnel movement.

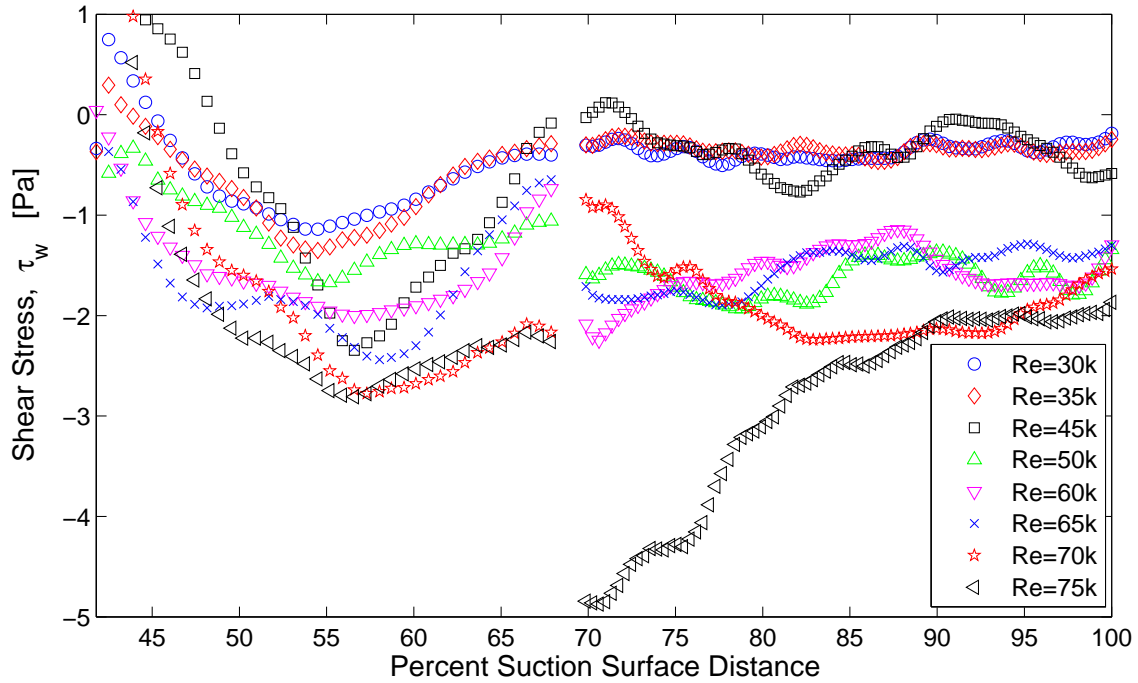


Figure 4.17: S3F round 2: Friction force distributions on L2F, flow left to right, 42-100%SSL.

Figure 4.17 presents the second round of S3F results for the L2F airfoil using the single continuous patch on the latter portion of the airfoil. In this figure, two data sets have been combined into one global picture, each data set separated by a small distance in the middle of the plot. Breaking up the data set into two areas was necessary to maintain proper camera resolutions and focusing over the large patch covering a substantial length of the trailing edge region. This figure shows time-averaged friction force distributions for the L2F airfoil over Reynolds numbers from $30k$ to $75k$ covering 41.8

to 100%SSL. Again the flow is from left to right, so positive shear indicates downstream flow and negative shear indicates reverse flow in a separation bubble. During this round of S3F tests, it was initially found that the tunnel vibration induced inaccuracies in the data reduction due to excess pixel movement. The sensitivity of S3F dictates that even a few pixels of model or tunnel movement registered by the CCD camera must be cancelled out in order to provide accurate results. In addition, it was further found that the blades twist under the applied wind load, which further complicates the reduction routine. In order to alleviate these problems, the camera and LED apparatus were bolted to the tunnel and a strip of marker dots were applied to the blade surface under the S3F patch, providing a means to cancel model movement during data reduction.

It should again be noted these round 2 results show a different flow pattern than the earlier round 1 results. This discrepancy illustrates the reduction process still needs more development before accurate skin friction can be obtained at the flow speeds encountered in this work. Looking at the trailing data set (right side), an obvious difference between round 1 and 2 results is how the L2F airfoil remains separated through to the trailing edge, since the friction forces at the trailing edge (right side) remain negative, indicating an upstream-directed friction force on the surface. In fact, the flow must remain separated at the trailing edge more often than not or the time-averaged friction would be positive (facing downstream). This is in direct contradiction to round 1 S3F and to Wildcat's CFD predictions. For Re equal to $30k$, $35k$, and $45k$, the L2F experiences lower friction levels on the order of 0 - 1 Pascals; again, these levels do not agree with round 1 results. The $Re = 45k$ case also sees higher amplitude frequency content compared to $30k$ and $35k$, seen by the waviness of the friction profile. There is also an abrupt reattachment that almost immediately returns separated near 72%SSL, as seen by the positive hump in friction. Friction levels again increase for Re equal to $50k$, $60k$, and $65k$, averaging nearly a 1.5 Pascal difference between the loaded (wind-on) and unloaded (wind-off) states. This could be due to an earlier transition with increased Reynolds number causing a more turbulent flow to inflict a heavier degree of friction on the surface. Increasing to $Re = 70k$ increases the overall friction as expected, but we see some discrepancy for the $Re = 75k$ case where the negative friction force increases its magnitude as you progress upstream. This result seems non-physical since the friction due to an increase in turbulent activity should increase over lower Reynolds numbers, and maintain a gradual decrease with distance to the trailing edge of the airfoil. The pattern seen in Figure 4.17 shows a different story where the surface shear under the separation bubble decreases magnitude much differently than the other flow speeds.

The left side of Figure 4.17 shows the upstream portion of the S3F patch along 41.8 to 67.9%SSL, where separation onset locations can be seen as the shear stress goes from positive (facing down-

stream) to negative (facing upstream). For comparison reasons, the separation onset locations for Re equal to $25k$ and $75k$ will also be constructed for model validation in the next section. For $Re = 25k$, the friction peaks near 57.8%SSL, and separation onset is seen to occur at 42.6%SSL. As Re increases to $30k$, the friction peak migrates upstream to nearly 52.6%SSL, and the separation onset moves downstream as expected to 43.8%SSL. A further increase to $Re = 35k$ moves separation onset to 41.8%SSL, a trend which suggests an unsteady separation onset location which varies with Reynolds number. Moving ahead to $Re = 75k$, separation onset occurs at the same location as for $Re = 25k$, at 42.6%SSL. Two anomalies are noticed in this figure, where the magnitude of friction for $Re = 40k$ and $45k$ surpass $25k$ and $75k$, an unexpected result. These anomalies suggest the round 2 results are not as accurate as the round 1 results. Oil-film measurements are planned to verify these trends and other traces to ensure they are not a result of the S3F patch disturbances and to see if they truly represent physical phenomena.

4.4 Transition Model Validation

This section collects data presented in earlier sections in order to test the validity of the separated-flow and attached-flow transition models. Wildcat predictions of transition model quantities are also included for comparison where appropriate. It was initially intended that this study would validate the separated-flow transition model used during the design process of the L2F airfoil. Wake traverse and thermal anemometry results presented earlier suggest the L2F flow behaves more like attached flows instead of separated flows, but the S3F friction measurements (and Wildcat predictions) clearly indicate a separated flow. As such, both situations will be formulated with available data and compared to model equations. Wildcat predictions showed separation bubbles which should have been resolved by examining the flowfield 1mm up from the surface of the blade (as close as this author was comfortable going next to the surface with a boundary layer traverse which was manually positioned). However, during the course of this work, these separation bubbles are found to be much thinner than expected, and as such the behavior of the airfoils resembled that of attached flow and attached-flow transition. In addition, the separated-flow transition model requires knowledge of the separation onset location, and thermal anemometry using the $0.4 * \max(U_{mean})$ criterion to judge separation locations as used by other published work when employing single normal hot-film sensors (which provide only magnitude, not direction) to resolve the boundary layer was insufficient to provide the required information. This criterion proved unsuccessful in identifying an onset location more upstream of the transition locations for the L1M $Re = 25k$ and $50k$ tests. Therefore, transition locations identified by the skew-kurtosis condition and intermittency, along with separation onset

locations obtained through the S3F technology will be used for comparison to the model equations.

Table 4.6: Attached-flow transition model experimental conditions*.

Variable	Original Range	L1M			L2F		
		$Re = 25k^\dagger$	$Re = 50k$	$Re = 75k$	$Re = 25k$	$Re = 50k$	$Re = 75k$
Re_θ	73 - 856	171/217	87/89	157/154	54/70	97/95	148
$K \cdot 10^6$	-1.9 - 4.8	-2.8/-1.6	-3.2/-4.0	-2.5/-3.0	-7.3/-7.5	-3.6/-3.6	-2.3
$K \cdot Re_\theta^2$	-0.15 - 0.06	-.08/-.08	-.02/-.03	-.06/-.07	-.02/-.04	-.03/-.03	-.05
M	0.05 - 1.24	< 0.2	< 0.2	< 0.2	< 0.2	< 0.2	< 0.2
Tg/Tw	1.0 - 1.41	1.0	1.0	1.0	1.0	1.0	1.0
$Tu[\%]$	0.11 - 5.09	3.3/7.0	3.9/7.4	2.6/4.3	5.4/6.4	3.3/5.2	2.4
λ/θ	4.26 - 66.2	117/59.2	26.3/33.6	38.3/31.4	44.5/30.6	37.3/28.4	34.5
Pr	0.71 - 0.71	0.71	0.71	0.71	0.71	0.71	0.71

* Some boxes contain two values separated by ‘/’, the first using the skew-kurtosis condition to identify transition onset, the second using intermittency.

[†] Stalled condition.

Tables 4.6 and 4.7 present the range of experimental conditions over which the attached-flow and separated-flow transition models were originally formulated, as well as the experimental conditions of the current study. The attached-flow conditions are taken where transition onset occurs, and include the momentum thickness Reynolds number, the K acceleration parameter (Equation 3.17), the Pohlhausen pressure gradient parameter defined as $K \cdot Re_\theta^2$, the local Mach number M , the gas to wall temperature ratio Tg/Tw , local percent turbulence Tu , the ratio of integral length scale to momentum thickness λ/θ , and the Prandtl number, Pr . The separated-flow conditions are taken at the location of separation onset, and include the momentum thickness Reynolds number $Re_{\theta-sep}$, the ratio of the length from separation to transition divided by the suction surface distance to separation onset $L/S_{separation}$, M , Tg/Tw , Tu , Pr , the ratio of turbulent eddy integral length scale to momentum thickness $(\lambda/\theta)_{separation}$, and $K \cdot Re_\theta^2$.

Except for the stalled L1M at $Re = 25k$, all tests exhibit boundary layer characteristics similar to those used during the attached-flow model development, as seen by the ranges of Re_θ and λ/θ in Table 4.6. The levels of acceleration are a different matter, however, as all cases except the $Re = 25k$ L2F using the skew-kurtosis condition for transition onset exceed the acceleration or deceleration used for initial model development. The degree of deceleration far exceeds initial levels, as these airfoils experience a greater total adverse pressure change on the suction surface which must be

overcome. Thwaites' separation criterion [White 2006] says any flow experiencing a deceleration greater (more negative) than -0.09 based on $K \cdot Re_\theta^2$ will undergo separated flow; the decelerations experienced by these airfoils at transition onset are approaching but remain less than this value, so separation can not be guaranteed solely on the basis of deceleration. This is a direct result of the spreading of the adverse pressure gradient over the L1M and L2F airfoils. The low loss levels seen in Figure 4.1 for these airfoils at the transition onset decelerations seen in this table are a good indication of the effectiveness of the current design philosophy (move loading and transition upstream) and modeling capability to extend the design space for higher-work turbomachinery blade designs. The levels of local boundary edge turbulence also extend beyond the initial range, which would be a welcome addition considering the higher levels of localized turbulence seen in a real gas turbine engine.

Table 4.7: Separated-flow transition model experimental conditions*.

Variable	Original Range	L2F		
		$Re = 25k$	$Re = 50k$	$Re = 75k$
$Re_{\theta-sep}^\dagger$	29 - 360	54.6 (86.3)	107.2 (130.1)	140.0 (161.3)
$L/S_{separation}^\dagger$	0.1 - 3.1	1.2/1.3 (0.8)	0.7/0.8 (0.5)	0.6 (0.4)
M	0.1 - 0.8	< 0.2	< 0.2	< 0.2
Tg/Tw	1.0 - 1.1	1.0	1.0	1.0
$Tu[\%]$	0.14 - 2.9	1.8	1.6	1.7
Pr	0.71	0.71	0.71	0.71
$(\lambda/\theta)_{separation}$	13 - 540	333	565	688
$K \cdot Re_\theta^2$	-0.98 - -0.03	-0.004	-0.004	-0.014

* Some boxes contain two values separated by '/', the first using the skew-kurtosis condition to identify transition onset, the second using intermittency.

[†] Wildcat predictions for $Re_{\theta-sep}$ and $L/S_{separation}$ are included in parentheses.

Table 4.7 shows the experimental conditions for the L2F are mostly within those used for the separated-flow transition model development; since the S3F sensor was only applied to the L2F airfoil, no separation onset location was identified for the L1M. The first variant is the ratio of integral length scale to momentum thickness for $Re = 50k$ and $75k$, which exceeds the upper bound used for model development. This implies one of three conditions: either the eddy lengths are larger

than found in development, the momentum thicknesses are smaller due to a more energy-preserved boundary layer, or a combination of the two. The second variant is the range of the Pohlhausen pressure gradient parameter ($K \cdot Re_\theta^2$), where all three Reynolds numbers experience less deceleration than cases used for model development. This is due to the forward loading characteristic of the L2F, where a higher total pressure change from the leading edge to the trailing edge was spread over more suction surface distance, allowing the smaller pressure gradient at separation onset. This table also shows Wildcat predictions of momentum thickness remain above the experimentally determined values. This means Wildcat predicts more lost momentum by separation onset than found by experiment, a trend opposite than expected since the predictions do not account for the effects of freestream unsteadiness on pre-transitional boundary layers. Remembering the separated-flow model (Equation 2.7), this greater momentum thickness causes a shorter length from separation to transition onset, a trend also observed in Table 4.7. Overall, the current tests extend the validation of the separated-flow transition model for airfoils with higher loading levels at similar conditions with less deceleration at separation onset compared to those test cases used for model development.

Table 4.8: Transition onset locations [%SSL].

	L1M			L2F		
	$Re = 25k$	$Re = 50k$	$Re = 75k$	$Re = 25k$	$Re = 50k$	$Re = 75k$
s/k	47.5 [†]	57.9	57.9	54.9	48.1	44.8
γ	49.5 [†]	60.1	60.1	57.2	50.3	44.8
Wildcat	70.4	61.2	55.7	51.3	42.7	40.1

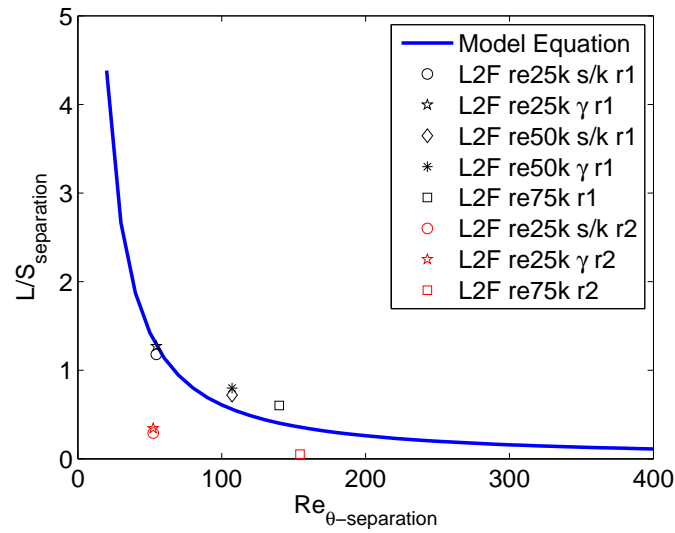
[†] Stalled condition.

Experimental transition locations have been defined by two distinct methods in this work: the skew-kurtosis condition and with intermittency. These two experimental locations along with Wildcat predictions are presented in Table 4.8 in percent suction surface for the L1M and L2F airfoils at all three Re . This table shows that negative skew with positive kurtosis occurs ahead of intermittency or at best remains coincident; model comparisons will be presented for both locations. The skew-kurtosis condition may reflect the behavior of laminar boundary layers before the onset of transition, which was accounted for in the “quasi-laminar” modeling used in model development. For the L1M, transition occurs at the same location for the un-stalled cases (at least within 2.5%SSL, the approximate distance between each profile) using both identification methods. The L2F airfoil transitions just after the mid-surface distance at 54.9 or 57.2%SSL for $Re = 25k$. As expected, the onset location moves upstream with Reynolds number, and the L2F transitions ahead of the

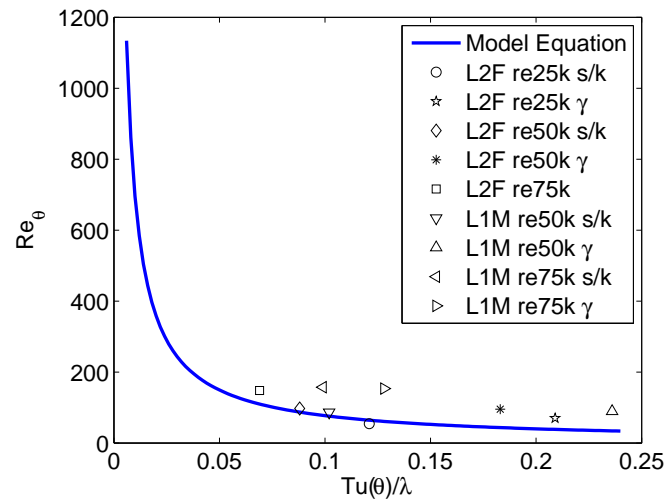
L1M. Again, this is due to the more forward loading of the L2F. For the L1M, Wildcat using the separated-flow transition model predicts transition onset relatively close to the experimental locations, except for the unpredicted stall at $Re = 25k$. Wildcat predicts earlier transition locations for the L2F, probably due to the over-prediction of the momentum thickness at separation onset used to construct the transition model, which leads to the shorter lengths between separation and transition onset.

Figure 4.18 presents both transition model equations plotted along with the experimental comparisons constructed with available data. Figure 4.18(a) shows the separated-flow model (Equation 2.7) and current data points for the L2F airfoil where separation onset information was available from the S3F. This figure shows both model constructions using round 1 S3F data on the leading edge region of the L2F airfoil along with round 2 data. Here we notice the model equation only agrees with the separation onset locations obtained through the round 1 S3F data, and we see the L2F matches the curve nearly exactly for $Re = 25k$, suggesting an accurate prediction of the length between separation and transition onset atop the bubble. The model is seen to under-predict this length for both $Re = 50k$ and $75k$ using both the skew-kurtosis and intermittency conditions. The front-loaded L2F sees the brunt of its acceleration before the first profile at 19.9%SSL, so the flow speed is near its highest when it separates around 28%SSL. This could explain why the $Re = 50k$ and $75k$ cases see a longer length from separation to transition than predicted with the model. Using the round 2 S3F data on the trailing edge region causes a severe over-prediction by the model for both $Re = 25k$ and $75k$. It is therefore suspected the onset locations obtained through the S3F round 2 data may in fact be artifacts of an upstream S3F patch disturbance; if this is the case, the true separation onset locations would be further upstream than those cited earlier, resulting in an increased length than plotted in the figure, which would in turn improve the agreement between the model and the experimental results. Thus, the round 1 S3F data along with boundary anemometry results provide more than satisfactory agreement with the separated-flow transition model, validating its use for turbomachinery design purposes.

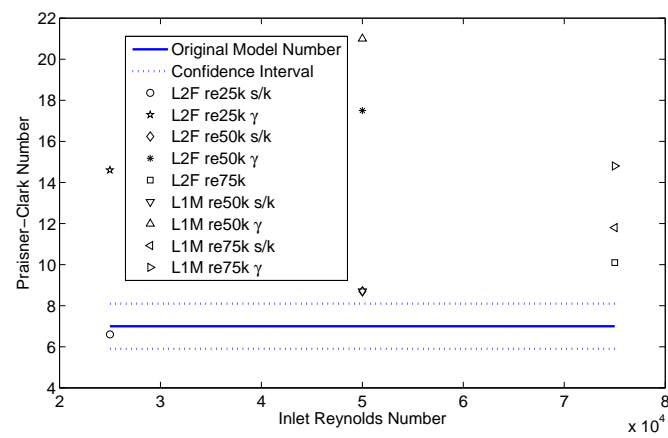
Several observations presented earlier in this chapter have suggested airfoils with very thin separation bubbles may transition as if attached. In order to clarify this response, all non-stalled cases have been plotted along with the attached-flow model in Figure 4.18(b). This figure shows very close agreement between the experimental data using the skew-kurtosis condition for transition onset, and the intermittency cases are not far off either. This trend suggests very thin separation bubbles may transition as if attached, since the proper ratios of flow quantities necessary for attached-flow transition are not far off from those in the database used for model construction. Examining Figure 4.18(b) more closely, we see certain flow cases and transition onset criteria produce closer agreement



(a) Separated-flow comparison.



(b) Attached-flow comparison.



(c) Praisner-Clark number.

Figure 4.18: Transition model experimental validation.

with the model curve. For example, the L2F at $Re = 25k$ and $50k$ match the curve closer using the skew-kurtosis condition, and at $75k$ the two onset criteria matched. The L1M data using the skew-kurtosis condition are also closer to the model than using the first sign of intermittency as the transition onset location. If one imagines removing the data using the intermittency onset criteria, then all experimental data using the skew-kurtosis method fit the curve very well. This trend also suggests separated flows with very thin bubbles may transition as attached flows.

Slight manipulation of Equation 2.8 leads to the following relationship from the attached-flow model which holds at the onset of transition [Praisner and Clark 2007]:

$$100 \frac{u' \theta^2}{\lambda \nu} = 7.0 \pm 1.1 \quad (4.1)$$

The relationship on the left-hand side is found to equal 7.0 ± 1.1 for all cases in the database used for model construction. The left-hand side is plotted for all experimental test cases in Figure 4.18(c) along with the original model database and confidence interval. The only test case which fits inside the confidence interval is the L2F at $Re = 25k$ using the skew-kurtosis transition onset. The S3F measurements presented earlier show the L2F is in fact separated at $Re = 25k$, which lends support to the idea that very thin separation bubbles may transition in the shear layer similar to attached-flow transition. To the contrary, all other test cases lie outside of the confidence intervals. Since separation bubbles decrease their height with increasing Reynolds number, the $Re = 50k$ and $75k$ L2F cases should have a separation bubble which is thinner than the $Re = 25k$ case. Furthermore, if separated cases can transition as if attached, the thinner separated cases should behave more like attached-flow transition unless bubble thickness is not the only factor which influences the change between separated-flow and attached-flow transition behavior. However, the $Re = 75k$ tests and those using intermittency for transition onset are clearly not within the confidence intervals for the Praisner-Clark number. This tells us there are still significant differences between flows that transition atop separation bubbles and those that remain attached.

4.5 Chapter Summary

Chapter 4 presents the detailed experimental results obtained in the low-speed wind tunnel on base, and it serves to provide an extensive database which can be used for CFD validation and further model development. This chapter begins with the Reynolds lapse performance curves of the Pack B, L1M, and L2F airfoils. Here it is seen the L2F outperforms both the L1M and Pack B in the low Reynolds regime. Unlike the Pack B and L1M airfoils, the L2F remains stall-free in the low Reynolds number regime, and the loss behavior resembles more of an attached flow rather than separated as it gradually increases with decreasing Re . Also surprising was the reduced losses at higher Reynolds

number, as it was initially suspected that the earlier transition may cause increased losses due to an increased turbulent-wetted surface area. Thus we have a higher-lift airfoil with an improved Reynolds lapse characteristic. The L2F also enjoys smaller wakes with decreased turbulence levels which lend support to the idea of a very thin separation bubble. Other observations corroborate this idea, where boundary layer traverses just 1mm up from the surface fail to capture the separation bubble. Several indicators in this work support the idea that very thin separation bubbles may transition as if attached. For example, u_{rms}/U_{in} and intermittency contours show unsteadiness and intermittency can build in the profile locations nearest to the wall, while the skew-kurtosis transition indicators can occur away from the wall; this mix of locations marking transitional activity suggests a mixture of attached-flow and separated-flow transition. In support of separated-flow transition, the alternating skew and higher kurtosis levels seem to occur only in the separated shear layer extending away from the wall with downstream distance. In fact, the Reynolds lapse curve in Figure 4.1 shows L2F behavior that appears attached (gradual decrease in loss with increasing Reynolds number) even though the S3F measurements clearly indicate a reversed flow at the surface of the blade. The skew-kurtosis transition onset criteria was found to coincide with a rise in core u_{rms} activity, and this core activity remains outside of the boundary layer until a critical distance when it falls below. This critical distance moves downstream with increasing Reynolds number, and the more forward-loaded L2F allows this unsteady core to remain outside of the boundary layer for longer distances. This trend may help explain why the earlier but lower levels of turbulent activity with the L2F can sustain a more well-behaved, non-massively separated boundary layer, as core activity below the boundary layer may be somewhat dampened. The boundary layers are also connected to the intermittency, as it is seen that Clark's algorithm picks up on the activity which causes the boundary layer growth mechanisms. The core and maximum intermittencies for all cases remain under the boundary layer once growth begins at the intermittent transition onset location. Intermittency transition onset is found to follow the skew-kurtosis condition, so the skew-kurtosis condition may in fact be the first indicator of transitional activity which is damped in the boundary layer until a level when intermittency increases, signalling a fluid motion that is dominated by turbulent spot growth which in turn causes the enhanced growth of the boundary layer.

As far as transition model validation, the separated-flow model was validated using a combination of S3F and thermal anemometry results. The goal of producing a higher-lift well-behaved airfoil was achieved using the separated-flow model, and its subsequent experimental validation proves the general utility of the model in RANS-based turbomachinery design systems. The attached-flow model was also constructed where possible, and it was seen that separated-flow cases with thin bubbles using the skew-kurtosis transition onset criteria do in fact fit reasonably well onto the

attached-flow model curve of Figure 4.18(b). The second form of the attached-flow model presented in Equation 4.1, which relates physical time scales at the onset of transition, shows that the separated flows which appear to transition as attached flows in Figure 4.18(b) do not in fact truly transition as attached, i.e. the time scales required for attached-flow transition are not in the proper ratios as found in the database used for model development. It was also seen that bubble thickness is not the only factor which changes the attached-flow behavior to separated-flow transition.

The time-averaged S3F measurements obtained in this work were a substantial achievement considering the difficulties associated with a low-speed air environment on a curved surface which deforms under the applied wind load. The data reduction routine for lower-speed tests, where the system noise tends to match or overtake the strength of the sensor signal, still requires development to produce accurate skin friction and normal pressure results. For example, the two rounds of S3F results taken in the trailing edge region of the L2F airfoil produce two different magnitudes of forces, when they should have concurred with each other. Another method of obtaining skin friction data is still required for satisfactory confidence in the technique at these low flow speeds, although initial development of the S3F sensor at ISSI showed agreement with oil-film results within less than a Pascal.

5

Discussion

Remember, then, that science is the guide of action; that the truth it arrives at is not that which we can ideally contemplate without error, but that which we may act upon without fear; and you cannot fail to see that scientific thought is not an accomplishment or condition of human progress, but human progress itself.

– William Kingdon Clifford

The current study sought to produce a high-lift low-pressure turbine blade while validating the use of Praisner and Clark's transition modeling used in the design cycle. The L2F turbine was produced that allows a 38% decrease in blade count over the Pack B geometry which is representative of airfoils used in current gas turbine engines. The L2F also enjoys an improved Reynolds lapse characteristic, which will allow higher altitude flight, longer loiter times, and reduced fuel consumption. All of the above improvements will lower the total cost of the gas turbine engine, a trend highly sought after from the mature gas turbine industry.

In addition, a shear and stress sensitive film was employed in a very difficult test environment, in hopes to give information useful for transition model validation. The S3F sensor was previously used in water and higher speed air flow environments where the dynamic pressures induce a high level of stress on the surface. In this work, S3F was employed in flow speeds as low as 2 m/s on a curved surface which deforms and twists under the loaded state. The goal was set to acquire time-averaged measurements on the suction surface of the L2F blade in a linear cascade.

Conclusions for this work are now given, followed by recommendations for future work.

5.1 Conclusions

This work has successfully used Clark's *Turbine Design and Analysis System* to develop the high-lift LPT designated "L2F". The separated-flow transition model of Praisner and Clark was used in the

design cycle, and the resulting $Zw = 1.59$ L2F airfoil provides 38% more lift per blade over an LPT similar to those currently in service today (the Pack B). This increase in lift provides two main options to the turbine engine designer: reduce the required blade count by 38% (which reduces the weight and fuel consumption of the engine), or increase the power extracted from the turbine section by 38%. Through this work, we see the aerodynamic effect of pushing the loading forward, as an earlier transition allows a greater suction surface adverse pressure gradient to be overcome without massive separation even at low Reynolds number. In fact, the improved Reynolds lapse characteristic of the L2F significantly decreases the separation losses, thereby reducing the fuel consumption and overall cost of the engine while providing a higher altitude flight ceiling. The earlier and increased passage acceleration of the L2F also delays the growth of bulk unsteadiness and pushes it towards the wall, a trend which increases with Reynolds number. The earlier transition also forces thinner boundary layers and narrower wakes, effectively leaving more of the passage to enjoy the lower losses associated with inviscid flows.

The separated-flow transition model used in the design cycle was validated in this work with thermal anemometry and S3F measurements. The model was formulated inside the Pratt & Whitney design system which also employs additional modeling not utilized in the current study. Therefore, this work also validates the general utility of the model for RANS-based turbomachinery design systems. Although the acquired experimental data suggests that airfoils with very thin separation bubbles may transition as if attached, comparisons of the experimental data to the separated-flow model and its associated attached-flow model show that the boundary layer properties required for attached-flow transition are generally not in the proper ratios when separated. Therefore, separated-flow cases with thin separation bubbles do not in fact transition as if attached. It was also found that separation bubble height is not the only factor which switches the attached-flow transition mechanism to separated-flow transition.

This work also proves that steady CFD with adequate transition modeling can still produce a well-behaved airfoil. Unsteady modeling techniques such as wakes and blade interactions were not necessary even at the incredibly high loading levels in this work. This was only possible due to the separated-flow transition modeling of Praisner and Clark employed in the design cycle.

The extensive database of experimental data produced in this work on the L1M and L2F airfoils can also be used for CFD code validation. Boundary layer data has been collected at various profile locations along the suction surface of each blade at 50kHz for 5 second records starting 1mm up from the surface and extending far enough into the freestream to resolve the boundary layer heights. Traverses in the wakes of both airfoils provide wake widths and depths along with pressure loss characteristics. The S3F technique has provided surface friction data which gives locations of

separation onset and bubble reattachment locations.

The S3F technology developed by ISSI has undergone substantial development in this work. The operational envelope of the technique has been extended to low-speed air environments on curved surfaces, and the time-averaged friction measurements presented in this work are the first of their kind. Simply obtaining the time-averaged surface friction results in this work is a monumental achievement when considering the decreased signal levels surrounded by relatively larger noise levels. New composition films have also been developed for this regime, and data reduction techniques are being improved which can account for the difficulties encountered in this work, namely low-speed environments on curved surfaces which translate and deform under the wind-on loaded state. As S3F uses optical data acquisition methods which are highly sensitive to even a few pixels in model movement, the issues being discovered and addressed in this work will undoubtedly open the door for the technique to be applied in a wider range of tests than previously possible. At the end of this work however, oil-film interferometry is still required to validate the magnitudes of friction forces measured with the S3F sensor, highlighting the need for further data reduction development in this flow regime.

5.2 Future Work

The fact that separated flows with thin bubbles have been observed to transition similar to attached flows begs several questions: if thin bubble separated flows can transition as if attached, what are the critical flow physics that switches attached-flow behavior to separated-flow behavior? Bubble thickness cannot be the only factor which influences this change, so what are the other important factors? What could knowing this critical situation do for designers? Is this merely a result of a higher magnitude pressure gradient forcing a transition near a reattachment location? Further study with a range of airfoil shapes producing a range of bubble thicknesses, although exhaustive, could shed some light onto the answers to these questions. In addition, techniques such as PIV taken at a fast enough rate could answer the question of whether or not flows with very thin separation bubbles transition in the shear layer above the bubble or instead inside of the bubble. If they do in fact transition above the bubble, perhaps the correct amount of momentum thickness for the attached-flow model would be obtained by integrating over the distance from the top of the bubble to the boundary layer height.

It has been suggested that profile loss accounts for 1/3 of the total pressure loss experienced by the airfoil [Denton 1993]. The aggressive loading levels achieved with front-loaded designs force a higher magnitude pressure gradient to push the flow in the upstream portions of the airfoils. This

increased upstream pressure may change the amount of loss production in the upstream portion of the blade, and further study could provide information to help tailor the profile geometry for lower loss generation in the presence of higher pressure gradients, thus producing an improved leading edge design critical for front-loading and the associated benefits explained in the current study.

In addition, the current modeling produced a well-behaved airfoil at extremely large loading levels compared to current designs. But what is the maximum loading we can achieve in a subsonic environment without massive losses? Further design work using the current philosophies and modeling capability could tell the turbine designer how much bigger his design space has become. In addition, further study of the highly-loaded designs in environments more realistic to the turbine engine, such as annular cascades and rotating rigs, could provide more realistic results including the effects of endwalls, compressibility, secondary flows, and wake-blade interactions.

A

More on Higher-Lift Design Efforts

This appendix includes other LPT design work which was not described in the Introduction, but was included in Tables 1.1 and 1.2.

In 1997, Cicatelli and Sieverding experimentally studied the effects of vortex shedding with a front-loaded LPT with low suction surface flow turning at an exit isentropic Mach number of 0.4, $Re = 2 \cdot 10^6$, and FSTI=1.15% [Cicatelli and Sieverding 1997]. They found that the shape of the shedding frequency spectrum is influenced by both the pressure and suction sides, but the difference in the transverse transport of fluid causes the pressure side vortex component to dominate the suction side contribution. They also found that their transitional boundary layer spectra contained a dominant bandwidth with two distinct maxima instead of a single dominant frequency.

In 2000, Wolff *et al.* employed hot-wire anemometry to study the boundary layer behavior on a high-lift LPT cascade similar to the Pack-B profile [Wolff et al. 2000]. They found that the becalmed region after the wake impingement combines laminar and turbulent benefits of the full velocity profile. The addition of wakes allows the flow to withstand a larger adverse pressure gradient without separation. They found that wakes initially increase the boundary layer thickness followed by a decrease in thickness caused by the accelerated flow before the next wake hits. The wakes also increase the local wall shear stress while shifting the region of loss production upstream of the impingement location.

In 2001, Dennis *et al.* used a 2D Navier-Stokes finite volume flow solver with a $k - \epsilon$ turbulence model to optimize an airfoil for minimal pressure loss [Dennis et al. 2001]. In this work they incorporated a tournament selection genetic algorithm (GA) using elitism together with sequential quadratic programming (SQP) techniques to optimize the airfoil geometry. Their fitness function was dependent on the outlet dynamic pressure, total lift, exit flow angle, mass flow rate, blade cross-sectional area, and a maximum thickness criterion which provided for mechanical and thermal feasibility. They found that the global aerodynamic objectives are better met through shape op-

timization instead of inverse design, where the airfoil geometry is modified until a pre-determined pressure distribution is achieved. Although near-wall accuracy is left to be desired with the $k - \epsilon$ turbulence model, Dennis *et al.* found the best overall design to be thicker and more loaded in the leading edge region.

Howell *et al.* in 2001 experimentally studied high lift profiles with $Zw \approx 1$ for aft-loaded LPTs over Re from 100,000 to 210,000 at a FSTI of 0.5% [Howell et al. 2001]. With hot-wire anemometry, they compared their losses to Thwaites' approximation for a laminar flow [White 2006] in order to assess the separation-induced effects. They found that as the loading increased, the bubble reattached earlier with a decreased length, while the bubble height and overall losses increased. The authors suggest these trends are due to an increase in the deceleration caused by the separation which in turn increases the receptivity of the boundary layer to disturbances. Additionally, the authors studied wake effects and found that the boundary layer is most receptive to wake-induced transition if the Reynolds number based on momentum thickness (Re_θ) is near 250 at the point of separation onset. Howell *et al.* also found that the pressure distribution is not particularly sensitive in determining the value of Re_θ just before separation. The authors found that aft-loading the LPT decreases the losses unless the flow is separated, in which case the losses are substantially increased. They found wakes to be beneficial for aft-loaded profiles, with proper wake frequencies always causing reattached flow, resulting in lower losses with a 15% increase in lift. Interestingly enough they found that doubling the wake frequency actually increased the losses sustained in their cascade. Their results suggest a reduction in blade count by 15%.

In 2002, another group including Howell experimentally studied the so-called "high-lift" and "ultra-high-lift" concepts of the Rolls-Royce Deutschland BR710 and BR715 LP turbines with $Zw \approx 1.05$ over Re from 60,000 to 120,000 [Howell et al. 2002]. They found that turbulent flow features in the boundary layer traveled around 90% of the freestream velocity near the leading edge, slowing to around 50% near the trailing edge. This difference was attributed to the changing pressure gradient along the suction surface of the blade. Again generating wakes upstream of the test section, they also found that the wake generates a turbulent spot on the surface and then quickly overtakes the leading edge of that spot, subsequently generating a new turbulent spot ahead of the previously generated spot on the surface. This process excites the shear layer and causes a roll-up into vortices which shed downstream. Thus a single wake can influence multiple locations along the surface through this "leap-frogging" effect. They found that this process can give the wake (which is now "convecting" inside the boundary layer) a region of influence which at times can locally travel faster than the freestream. Each of these turbulent spots eventually subside into a calmed region which is in turn subjected to the next incoming wake. The calmed regions have a full velocity profile and low entropy

generation which can itself inhibit spot generation and withstand a larger adverse pressure gradient than laminar boundary layers alone [Schulte and Hodson 1996; 1998]. A nice visual observance of turbulent spots can be found in the work of Anthony *et al.*, where fast-response heat flux gauges were employed to track a turbulent spot and its surface shape development during bypass transition [Anthony et al. 2005]. Howell *et al.* also found that the boundary layers of higher-lift LPTs do not exhibit as much of a becalmed effect after a wake passing as was found on lower lift profiles. Again this group found that $Re_\theta \sim 250$ was optimal for wake-induced transition in a separated laminar boundary layer, and additionally they found that wake-induced transition can *only* occur if the flow is already separated. This implies that there is some mechanism in the separated condition which allows the amplification of the wake disturbances into transition. They also conjectured that low-speed tests exhibit all the important features of higher-speed, rotating rig tests only when wakes are introduced.

In 2004, Sieverding *et al.* used a 3D flow solver (MISES) which coupled the Euler (inviscid) and integral boundary layer equations with the Abu-Ghannam and Shaw turbulence model at a freestream turbulence level of 5% to optimize a compressor blade for optimal range and performance [Sieverding et al. 2004]. The geometry was specified by 4th order Bezier curves with 2 linear patches, and they found that GAs with elitism and mutation worked better to define the optimal shape than gradient search methods and neural networks. Their constraints included the exit flow angle, moment of inertia, cross-sectional area, and the number of turning points used to define the geometry. They also found that the boundary layer shape factor, H , rises through transition but flattens when encountering the favorable pressure gradient along the compressor blade. Other recent compressor design work includes that of Sonoda *et al.*, where they attempted to optimize an airfoil for low- Re conditions using a modified Navier-Stokes solver with Chien's $k - \epsilon$ turbulence model [Sonoda et al. 2004]. Trying to minimize the total pressure loss and deviation gas flow angle, they found that a front-loaded compressor blade leads to an earlier boundary layer transition which delays or eliminates the separation creeping up from the trailing edge.

In 2004, a group at the von Karman Institute for Fluid Dynamics investigated the performance of a “very high lift” LPT blade with an emphasis on the prediction of separation [Houtermans et al. 2004]. Their experimental study focused on a front-loaded blade with a quoted $Zw = 1.47$ over Re from 50,000 to 200,000 at a FSTI=0.6%. Their blade suffered increased losses as Re was increased. The separation bubble investigations attempted to verify prediction methods presented in other works for locations of separation onset, maximum bubble displacement, bubble length, point of pressure recovery in the bubble, transition onset, and transition length. Models of [Mayle 1991], [Roberts 1975], [Walker 1993], [Hatman and Wang 1999], and [Yaras 2001; 2002] among others

were compared, but none successfully matched the experimental data for the high-lift blade. This illustrates the difficulty of constructing a transition model which can consistently and accurately predict separation bubble and transition phenomena for a low-pressure turbine blade over varied loading. A goal of the current work is to assess the accuracy of Praisner and Clark's transition model which was constructed for use over varied loading characteristics in a design capacity. Houtermans *et al.* also suggest that the position of the suction side velocity peak (pressure minimum) strongly influences the overall performance, similar to others' findings [Curtis *et al.* 1997].

In 2004, Stieger *et al.* experimentally studied wake-induced transition in a laminar separation bubble in a cascade of their aft-loaded "ultra-high-lift" $Zw \approx 1$ T106 LPT blade [Stieger *et al.* 2004]. They found that the wake-boundary layer interaction was much different once inside the separation bubble, and that large amplitude pressure fluctuations arise within the bubble which are indicative of coherent flow structures within the bubble. Their wake-induced flow structures traveled at nearly half the freestream velocity, but were not found to be solely a function of the wake passing frequency, which suggested evidence of non-linear interactions within the boundary layer. They also found that only a select band of frequencies can be amplified in the boundary layer to form coherent structures which may lead to a Kelvin-Helmholtz vortex roll-up.

In 2005, Zhang and Hodson experimentally studied the boundary layer development of their "ultra-high-lift" $Zw = 1.19$ mid-loaded T106C LPT when subjected to surface trips and unsteady wakes for Re from 134,000 to 255,000 [Zhang and Hodson 2005]. They found that the optimal wire diameter needed to decrease the separation-induced losses changed with Re , but was effective over both steady (no wakes) and unsteady (wake perturbations) environments. Ironically, as Re was increased beyond a limit, the separation bubble size decreased but the unsteadiness created by the trip wire caused a greater turbulence-wetted surface area which increased the overall losses. Placing the trip near the bubble also increased the losses when compared to an upstream placement due to the small separation bubble created by the trip wire merging with the pressure-gradient-induced bubble. Their suggestion for LPT design, which surprisingly agrees with Howell's observation, was to aft-load the profile only if trips could be used to enforce disturbances which would control the separation. Their data also suggests that a Kelvin-Helmholtz vortex roll-up is only possible when the separation bubble reaches a minimum height. This minimum height allows for more pressure peak variation in the unsteady bubble pressure. A successful surface trip mitigates the effect of the Kelvin-Helmholtz roll-up encountered in the separated boundary layer. The combined effect of trips and wakes reduced the losses because of the absence of strong roll-up vortices and the smaller separation bubble in between wakes. The authors believe the loss reduction is a compromise between the positive effects of a reduced separation bubble and the full boundary layer velocity profile of the

calmed region and the negative effects of a larger turbulent-wetted area. The optimum trip location was found to be midway between the velocity peak and the onset of separation.

Closed-loop separation flow control methods using the L1M profile were computationally studied by Brehm *et al.* in 2006 for $Re = 20,000$ and $FSTI = 0.3\%$ [Brehm et al. 2006]. In order to get a computational baseline flow on the L1M, they employed a 5th order accurate upwind Roe scheme for the convective fluxes, a 4th order accurate viscous discretization, and a 2nd order accurate Adams-Moulton time integration for their 2D finite volume implicit solver. A normal blowing slot was chosen for the flow control method as it is easier to implement in CFD codes (compared to, say, a VGJ hole angled and skewed to the freestream). They conducted an open-loop parameter study which was compared to two closed-loop methods, a proportional-differential (PD) feedback controller and a neural network trained by the open-loop parameter study which models the L1M flow (downstream pressure signal) and adjusts the forcing signal as necessary. The open-loop control most effective frequency changed from 8 to 7 Hz as the blowing amplitude was increased, but above a critical blowing ratio the jet acted as more of an obstruction than a separation controller. The closed-loop PD controller achieved a 21% reduction in the ratio of normal-to-axial aerodynamic forces (current goal). Their neural network showed a promising ability to model flow control conditions inside the open-loop parameter study box. All control methods resulted in smaller-than-separation rollers which propagated off of the suction surface. Future work will focus on real-time feedback control using modified neural networks.

B

AFRL's LSWT Turbulence Characterization

This section presents the measurements taken in AFRL's Low-Speed Wind Tunnel in order to characterize the turbulence development in the test section inlet along the wind tunnel streamwise direction when a turbulence generating grid is placed upstream of the test section. The nominal background turbulence intensity without the grid was measured to be less than 0.5%, but a higher degree of turbulence is required for the cascade tests in order to simulate the low-pressure turbine environment. The grid is located 90.5 inches (2.3m) upstream of the leading edge of the test blade. Figure B.1 shows the locations of the measurement points within the wind tunnel streamwise cross-section, including the centerline (CL) and 4 additional points each 1.5 inches (0.04m) horizontally and vertically away from the center. The additional points were taken in order to ensure the results were not biased by a probe position behind or in between one of the grid bars. When using grids to generate turbulence, two events compete to determine the eddy scales - a spectra manipulation effect whereby the grid chops and redistributes the existing background turbulence scales proportional to the grid size, and a wake effect which can decrease the length scales with high frequency fluctuations [Roach 1986]. Given enough time, the wake effect smoothes out after approximately 10 bar diameters downstream and the spectra manipulation effect dominates with scales increasing with distance in the downstream direction.

Figure B.2 shows the freestream turbulence development along the wind tunnel from the grid to the cascade face. As expected, an exponential is observed which decays down to approximately 3.4% just 5 inches (0.13m) before the leading edge of the test blade. Roach's streamwise turbulence intensity correlation for a square-mesh grid with round bars is also plotted in the figure and is shown

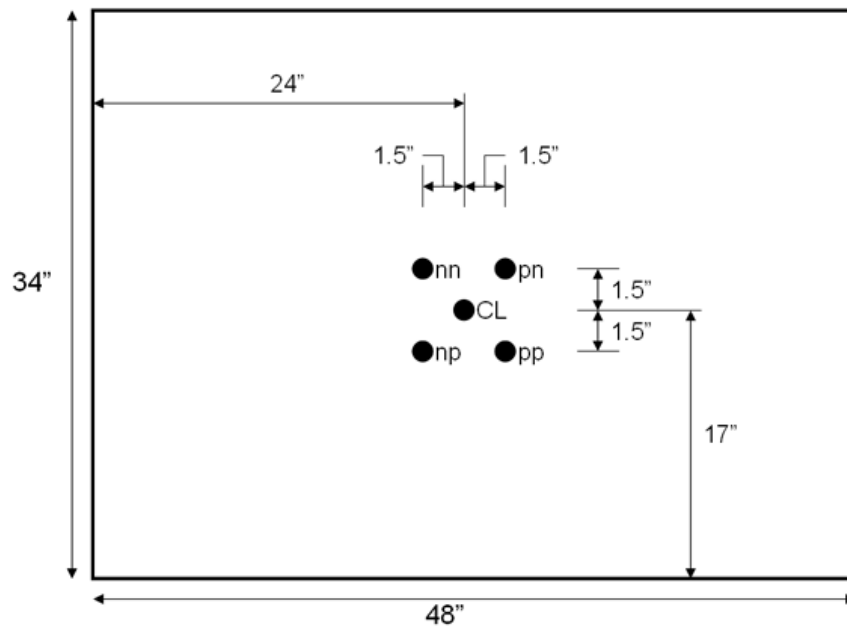


Figure B.1: Wind tunnel cross-section turbulence measurement locations.

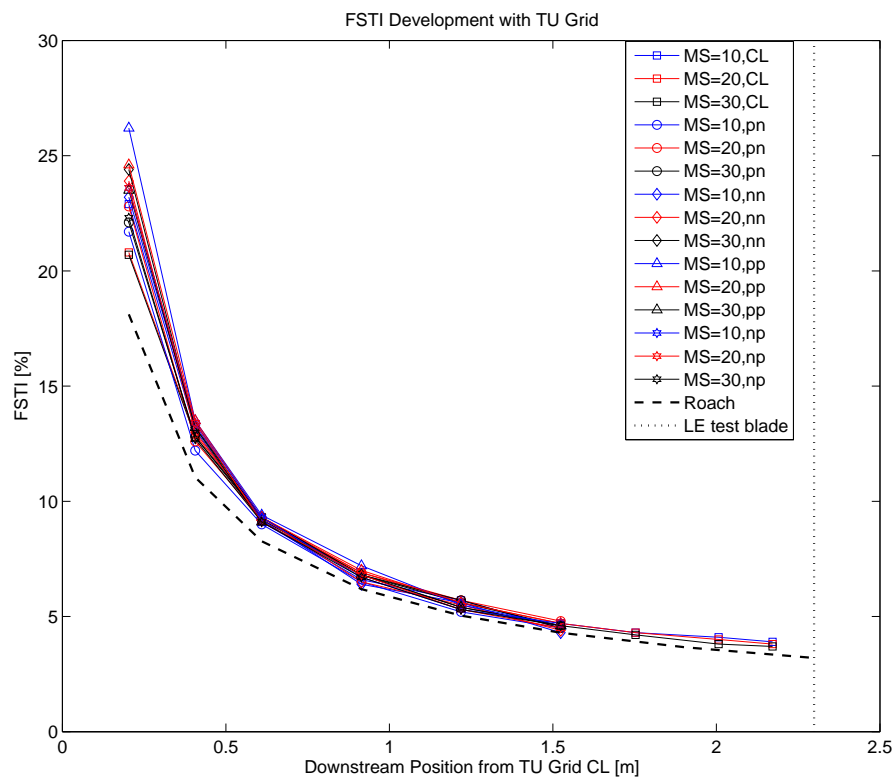


Figure B.2: LSWT FSTI development.

in Equation B.1:

$$FSTI = 0.80 \left(\frac{x}{d} \right)^{-5/7} \quad (\text{B.1})$$

where x is the downstream distance and d is the bar diameter. For the current setup, the correlation estimates $FSTI = 3.3\%$ at this location, within 2.9% of the measured value. Roach suggests that the normal components of turbulence, although not measured here, follow the ratio $(\overline{u'^2}/\overline{v'^2}) \sim (\overline{u'^2}/\overline{w'^2}) \sim 1.25$ resulting in normal FSTI of approximately 3.0% .

Turbulence scales are computed according to the methods described by Bernard and Wallace 2002, and these are briefly described here for convenience. The integral scale is computed by first computing the autocorrelation of the hot-wire signal:

$$\mathcal{R}_\tau = \frac{\overline{u(t)u(t+\tau)}}{\overline{u^2(t)}} \quad (\text{B.2})$$

This autocorrelation function is then integrated from the origin to the first zero crossing resulting in an integral time scale. Using Taylor's frozen turbulence assumption, one can multiply the time scale by the freestream velocity and produce a length scale which serves as the integral length scale, Λ . The Taylor microscale, λ , is derived using the slope and curvature of the autocorrelation function, f , at the origin:

$$0 = 1 + \lambda \frac{\partial f}{\partial r}(0) + \frac{\lambda^2}{2} \frac{\partial^2 f}{\partial r^2}(0) \quad (\text{B.3})$$

The slope at the origin is assumed zero since the sampling frequency was more than adequate to provide a smooth origin, and the second order partial derivative is approximated with a second order accurate central difference. The Kolmogorov length scale, η , is derived using the rms fluctuating velocity, integral scale, isotropic dissipation rate, ϵ [energy/s], and the kinematic viscosity of air, ν [m^2/s]:

$$\epsilon = \frac{u'_{rms}{}^3}{\Lambda} \quad (\text{B.4})$$

$$\eta = \frac{\nu^{3/4}}{\epsilon^{1/4}} \quad (\text{B.5})$$

The turbulent scale developments are presented in Figure B.3, with an integral scale approximately between 1.38 and 1.65 inches ($3.5\text{e-}2$ and $4.2\text{e-}2$ m), a Taylor microscale between 0.15 and 0.32 inches ($3.8\text{e-}3$ and $8.1\text{e-}3$ m), and a Kolmogorov length scale between 0.03 and 0.02 inches ($7.6\text{e-}4$ and $5.1\text{e-}4$ m) just 5 inches (0.13m) upstream of the leading edge of the test blade. For a scale resolution within 1% accuracy, Roach suggests a minimum sampling frequency, f_m , according to Equation B.6:

$$\frac{f_m \lambda}{U_\infty} > 5.0 \quad (\text{B.6})$$

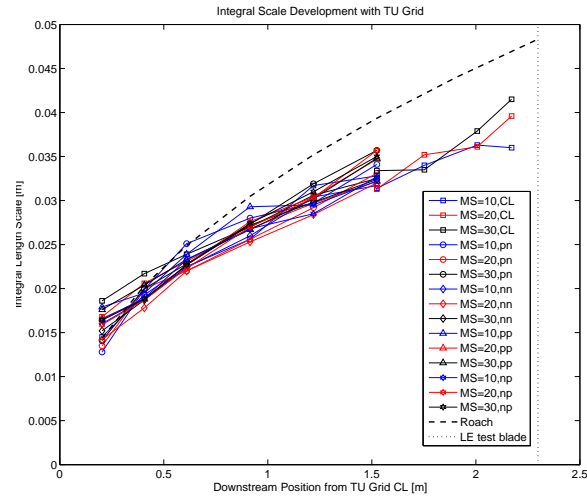
where λ is the scale of interest. To resolve the lowest measured Kolmogorov scale in this work, this requires a minimum sampling frequency of approximately 23kHz, well below the current sampling

frequency of 50kHz. Roach also suggests that the integral scale is independent of Reynolds number while the microscales are dependent on Reynolds number, trends also observed in the current data of Figure B.3. Roach's correlations for the streamwise integral and Taylor scales are presented in Equations B.7 and B.8 below:

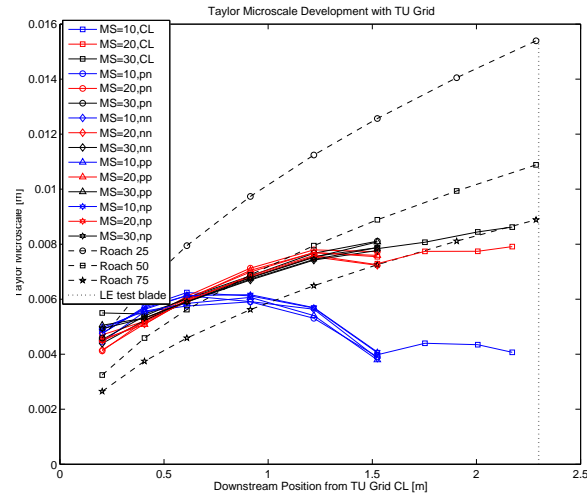
$$\Lambda_x/d = 0.20 \left(\frac{x}{d} \right)^{1/2} \quad (\text{B.7})$$

$$(\lambda_x/d)^2 = \frac{17.0}{Re_d} \frac{x}{d} \quad (\text{B.8})$$

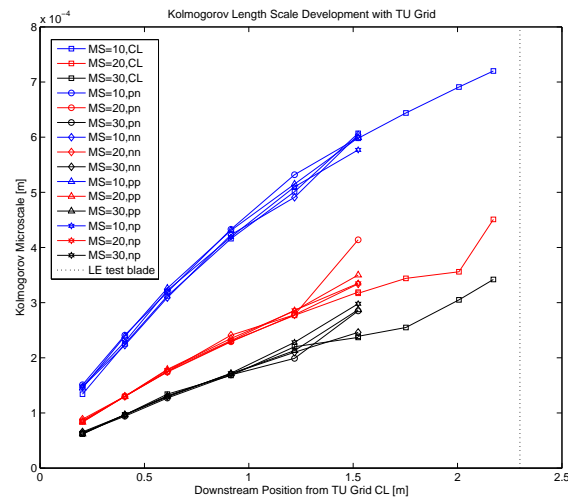
where Λ_x is the streamwise integral scale, λ_x is the Taylor microscale, and Re_d is the Reynolds number based on bar diameter. These correlations produce integral and Taylor scales of 1.85 and 0.64 inches (4.7e-2 and 1.6e-2 m), respectively, within 12-34% and 100-327% of the measured values, respectively. It is noted in Roach's paper that the integral scale correlation is more accurate than the Taylor scale correlation since the integral scales are mainly dependent on the grid bar diameter while the Taylor scales are more dependent on the instrumentation setup and the complex energy cascade of turbulence, which is difficult to match over distinct experimental configurations.



(a) Integral scale.



(b) Taylor microscale.



(c) Kolmogorov length scale.

Figure B.3: LSWT turbulence scale development.

C

Background on Pressure and Skin Friction Measurement

By understanding the past capability and limitations of surface force measurements, one can better understand and appreciate the development of new technologies. Probably the first recorded skin friction measurement apparatus was that described by William Froude in 1872, which measured the skin friction experienced by planks dragged across water, as mentioned in recent skin friction reviews [Hakkinen 2004; Plesniak and Peterson 2004]. There are basically two types of skin friction sensors: direct and indirect. Direct sensors are advantageous because they do not rely on theoretical or empirical correlations, but they can be very delicate and susceptible to system mechanical noise. Indirect skin friction sensors infer the skin friction from other quantities and are typically more robust. Indirect sensors are advantageous because the measured quantity is typically easy to obtain, although the correlation dependence can impose a limit on the applicability range. Surface pressure measurement is classically accomplished by pressure taps or transducers, but these only provide information at discrete locations. More advanced techniques such as pressure sensitive paint (PSP) can provide non-intrusive, two-dimensional surface pressure data with significantly less model preparation [Liu and Sullivan 2005].

Direct Skin Friction

Direct skin friction sensors are typically based on a floating element design as seen in Figure C.1, an oil film technique, or shear-sensitive liquid crystals. Floating element sensors and associated error correction schemes received great advancement at the California Institute of Technology in the 1950s, and these relate the translation of the floating element under an applied shear stress to the skin

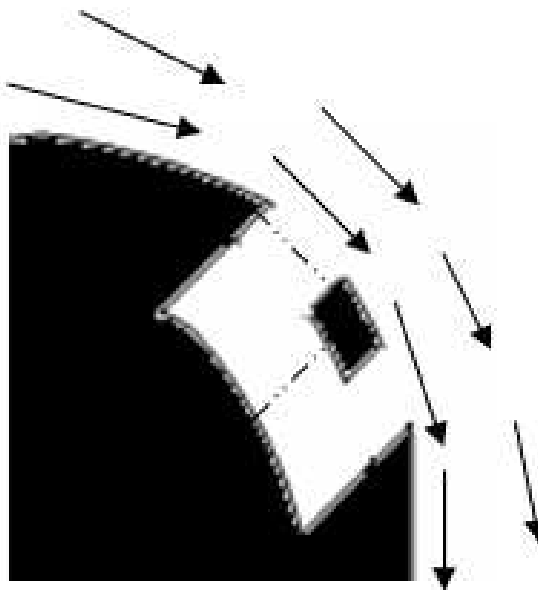


Figure C.1: Cartoon of typical floating-type shear sensor with multiple linkage possibilities.

friction. The accuracy of these direct sensors was mainly limited by their sensitivity to streamwise pressure gradients which create gap forces between the floating element, linkage mechanisms, and housing cavity. Adverse pressure gradients, such as those encountered in the LPT section, were particularly troublesome. The accuracy in 1969 was quoted within 10-15% of the actual skin friction value. Some potential drawbacks when using floating element sensors can be sensor spatial and force resolution trade-offs, misalignment errors, pressure gradient effects, and sensitivity to acceleration, vibration, and thermal expansion effects.

Oil film techniques use the proportionality of shear stress with the thinning rate of an oil film according to Equation C.1:

$$\tau = \eta \cdot \frac{d}{dt} \left(\frac{dx}{dh} \right) \quad (\text{C.1})$$

where τ is the skin friction, η is the oil's viscosity, x is the streamwise thinning and h is the thickness of the oil. There are two types of oil film skin friction techniques: interferometric and non-interferometric [Tyler et al. 2004]. Interferometric oil films work because the oil thickness is less than the coherence length of the light source, and the rays reflected from the thinning oil surface interfere with the rays reflected from the model surface, producing alternating regions of light and dark bands known as “interference fringes” [Plesniak and Peterson 2004]. Liu and Sullivan in 1998 used the level of luminescence of oil seeded with fluorescent molecules to determine the oil thickness. This method eliminates interferometry but requires additional calibration. All oil film

skin friction techniques require additional measurement of surface temperature and knowledge of the temperature-oil viscosity relationship [Plesniak and Peterson 2004].

A third common direct sensor are shear-sensitive liquid crystals, which had significant development in the 1960s [Plesniak and Peterson 2004]. This technique relies on the change in optical properties of liquid crystals applied to a test surface as they undergo a change in phase. This phase change can be temperature, heat transfer, or shear stress dependent. The optical property changes can be temperature, color, or intensity based. Drawbacks using liquid crystals can be the complicated calibration and optical access issues, temperature-sensitivity of liquid crystals, the need to apply a new coat after each test, crystal roughness effects on the flow, and limited availability and cost of the liquid crystals.

Indirect Skin Friction

Classical indirect skin friction sensors include the Stanton tube developed in 1920 and the Preston tube developed in 1954 [Plesniak and Peterson 2004]. These techniques use Pitot tube-like probe heads which are located very close to the surface. These methods assume a region of flow similarity close to the wall, which is only generally acceptable for turbulent flow conditions. The Clauser correlation also developed in 1954 is a classical indirect skin friction method based on the law of the wall analysis wherein the skin friction is related to the measured velocity profile in a turbulent boundary layer. Surface and sublayer fences designed to remain in the sublayer have been used since the 1960s. These record shear stress perpendicular to the fence and can be used in strong pressure gradients and compressible flows. This discrete point attainment of surface shear stress supplied the needed empirical information for low- Re computational turbulence modeling routines using sublayer wall functions for closure. Recent techniques using micro-electromechanical systems (MEMS) are based on fence deflections and can have responses up to 1 kHz, as reported in 2004.

Heat transfer analogies which relate the heat transfer obtained with hot-wire or hot-film devices to the skin friction can be used in any fluid where the conductivity of the fluid is greater than the conductivity of the wall (which does not include air) [Plesniak and Peterson 2004]. The underlying assumption with these techniques is that the thermal boundary layer lies entirely in the inner region of the velocity profile, which is why the sensors are placed in the viscous sublayer. Advanced probes use multiple-wire configurations to provide direction-independent, time-dependent wall shear stress. Another indirect skin friction sensor is an optical sensor which detects the Doppler shift of light scattered from particles passing through divergent fringes in the viscous sublayer. This technique, using what are termed Laser-based or “Fan Fringe” sensors, suffers from the interaction between

low data acquisition rates and low seed densities near the wall. As a result, the method has poor resolution of the sublayer in high Re flows due to turbulent boundary layers.

Surface Pressure Measurement

The first global aerodynamic surface pressure measurement was accomplished with pressure sensitive paints (PSPs) in the 1980s [Liu and Sullivan 2005]. PSP offers accurate, non-intrusive pressure measurement with increased spatial resolution when compared to conventional taps and pressure transducers. PSP systems use optical techniques to detect the pressure-sensitive luminescence of chromophores suspended in an oxygen-permeable binder. As the intensity is a function of the oxygen concentration in the binder, the surface partial pressure of oxygen is related to the luminescent emission. The surface pressure can be obtained from Henry's Law knowing the concentration of oxygen in the main flow. It is generally accepted that PSP techniques for air flow environments must have a velocity greater than ~ 15 m/s for accurate quantitative results.

The work of Liu and Sullivan in 1998 may pre-figure S3F development in 1998 when they published their work using luminescent oil films to measure skin friction. S3F uses the same luminescence technique to obtain film thickness measurements, but additionally provides about 25 times the pressure sensitivity of PSP and comparable signal-to-noise ratio with less data averaging, allowing more measurements for a given area in lower dynamic ranges unsuitable for PSP [Fonov et al. 2005]. S3F also combines a particle tracking algorithm for tracer particles applied on the surface of the luminescent elastic polymer film. The tracer particle translations and film thicknesses (luminescent intensities) are fed into an inverse finite element code which produces the surface normal pressure and tangential surface stress contours that caused the deformations. More information on the S3F technique is presented in the Experimental Arrangement chapter. Recently, this technique was applied to plasma flows in a Mach 5 tunnel at Wright-Patterson Air Force Base in Dayton, OH, alongside temperature- and pressure-sensitive paints [Crafton et al. 2005]. Since these techniques are optical and require no electrical equipment on the test surface, they are ideal for plasma environments where electrical equipment on the surface would interfere with the plasma kinetics. Information about the science behind or acquisition of PSP, TSP, PIV, or S3F systems can be found on the Innovative Scientific Solutions, Inc. website at www.innssi.com.

D

Operation of S3F

S3F is an elastic polymer film impregnated with luminescent molecules and doped with tracer particles on its surface [Fonov et al. 2005]. The origin of the S3F technique began in the early 1990s as a direct method to measure surface shear force [Tarasov and Orlov 1990]. Upon application of a force, the film's deformations in all three dimensions are recorded simultaneously using a single CCD camera. The luminescent molecules are excited at one wavelength and emit at another wavelength, and the intensity of the emission wavelength is proportional to the thickness of the film. Both a "flow-off" and "flow-on" image are required in order to track the surface deformations indicated by the movement of the tracer particles between the two conditions. A ratio between the two conditions also provides a means to cancel out sources of error such as unequal illumination and uneven luminophore dispersion. This ratioing effectively makes the S3F a differential pressure gauge with tunable dynamic range calibration by modifying the film's modulus of elasticity and Poisson ratio. The normal pressure and tangential surface stresses which caused the three-dimensional deformations are reconstructed from an inverse finite element model, whose inputs are the film thickness-sensitive luminescent intensity and the tracer translations between flow-off and flow-on conditions.

Some insight into the operation of the S3F technique can be gained by considering the simplified response of the film to normal and tangential loads. The response to a purely normal load is shown in Figure D.1(a). As mentioned above, the film will deform under the normal load but will not compress or yield. The local thickness of the film will be modified by the presence of the load near the point of application, and will return to its original shape upon its removal. Maximum surface displacement is a function of the material properties and the applied normal load. Materials are typically formulated in order to ensure a deflection less than 5% of the total film thickness under maximum anticipated loading, and can be produced to provide less than 1% deflection. The issue of concern is to ensure the film displacement does not introduce flow changes due to the surface deflection. The stressed film thickness is a function of the applied normal force, the original thickness

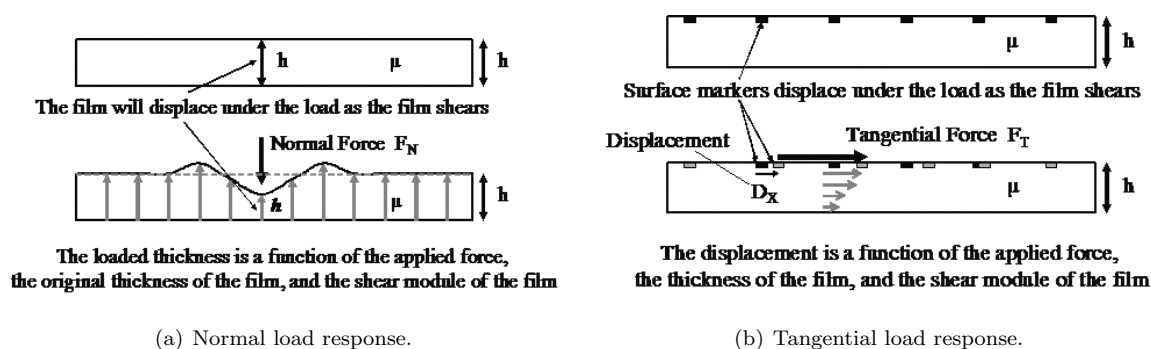


Figure D.1: Simplified S3F responses.

of the film, and its shear modulus, $h=f(F_N, h, \mu)$. The film responds to gradients in pressure and not to changes in static pressure. This can be a significant advantage for several reasons. First, the sensor is a differential rather than an absolute gauge and thus can be tuned for applications that require larger or smaller sensitivity. Furthermore, the result is a shear sensor that is insensitive to static pressure changes.

The response of the film to a purely tangential force is depicted in Figure D.1(b). Here, the surface of the film will undergo a tangential displacement due to the load but again will not yield or compress. The response of the film may be visualized by considering a series of markers on the surface of the film. The markers will be displaced as the film shears and this displacement is a function of the film properties. Again, upon removal of the load the film will return to its original shape. The actual response of the film is more complex as the responses are mildly coupled; a pure tangential load will generate a slight change in film thickness and a pure normal load will generate a slight tangential displacement. These simplified examples however demonstrate the basic operation of the S3F.

There are several ways for films to be applied to a surface including spraying with an airbrush, allowing the film to polymerize in a cavity on the model surface, and forming the film in a cavity on a flexible layer which can be glued onto a model surface. Forming films in cavities provides good control of the film thickness and physical properties and control of these parameters is necessary for quantitative measurements of pressure and shear stress. Film formation consists of pouring the polymer components into a flat cavity with a smooth or polished bottom. The film thickness can be estimated by direct measurements using either optical absorption or a capacitive thickness gauge. The film calibration procedure involves applying a specified load to the film surface and measuring the corresponding normal and tangential deformation of the film.

A final property of interest is the film's frequency response and their potential as a high-frequency probe for both shear stress and pressure. The range of the linear frequency response of such an

elastomer is limited by the natural frequency of the shear oscillation, and can be estimated by Equation D.1:

$$f_o = \frac{1}{2\pi} \sqrt{\frac{\mu}{\rho h^2}} \quad (\text{D.1})$$

where μ is the shear modulus of the film, ρ is the film density, and h is the film thickness. Previous composition variations with $\mu \in (10 - 1000)\text{Pa}$ and $h \in (0.1 - 1)\text{mm}$ have produced films with frequency responses from 0.3 to 10kHz. A detailed description of the technique along with proof of concept tests are now presented.

Measurement Concept Let's consider a cavity V having length L and depth h filled with elastic material with known shear modulus μ and Poisson ratio ν . The upper contact surface is submerged in the flow creating a pressure distribution $p(x)$ and friction force $f(x)$. Surface loads provide elastic deformations and we can measure normal u_y and tangential u_x, u_z displacement fields of the surface points. In the absence of volume forces, the homogeneous elastic material and small deformations equations of equilibrium can be represented as Lamé equations [Braess 2002]:

$$(\lambda + \mu)\theta_k + \mu\Delta u_k = 0 \quad (\text{D.2})$$

which are based on the Cauchy estimation for the deformation tensor:

$$\epsilon_{k,l} = \frac{1}{2}(u_{k,l} + u_{l,k}) \quad (\text{D.3})$$

Here, the volume deformation $\theta = \epsilon_{11} + \epsilon_{22} + \epsilon_{33}$, and $\lambda = (2\mu\nu)/(1 - 2\nu)$. The three equations D.2 are accompanied by boundary conditions. On the contact surface S , displacements u_k are described as measured functions of coordinates:

$$u_i = u_{oi}(x_i) \quad \text{on} \quad S \quad (\text{D.4})$$

and $u_i = 0$ on the other cavity boundaries. Thus, the described equation system is elliptic in the cavity for all values of Poisson ratio excluding 0.5 and 1 and therefore has a single solution. For the cavity occupying a half-space this is known as the Boussinesq problem and the equation of equilibrium can be integrated.

S3F is a material with a very low compressibility like rubber. S3F is essentially a rarefied polymeric matrix filled with an incompressible fluid. It requires a great deal of energy to produce a small change in density. It simplifies measurements of normal displacement component (see below) but provides an additional problem in the mathematical model - a large difference in the magnitude of Lamé constants:

$$\lambda \gg \mu$$

For the sake of simplicity, let's limit our consideration by a plane strain case, then u_z is zero on the total contact surface. Lamé equations D.2 can be rewritten in variational form as [Danaila et al. 2003]:

$$\int_V [2\mu\epsilon_{ij}(\mathbf{u})\epsilon_{ij}(\mathbf{v}) + \lambda\epsilon_{ii}(\mathbf{u})\epsilon_{jj}(\mathbf{v})]dx = \int_{S_{ii}} \mathbf{g}\mathbf{v}dx, \quad \mathbf{v} \in V \quad (\text{D.5})$$

where $\mathbf{g}=(f,p)$ are the loads acting on contact surface S and $\mathbf{v} = (v_x, v_y)$ is the probe vector. Substituting $\lambda\epsilon_{ij} = p$, we are led to the following problem: Find (\mathbf{u}, p) such that

$$\begin{aligned} \int_V [2\mu\epsilon_{ij}(\mathbf{u})\epsilon_{ij}(\mathbf{v}) + p\epsilon_{ii}(\mathbf{v})]dx &= \int_{S_{ii}} \mathbf{g}\mathbf{v}dx, \quad \mathbf{v} \in V \\ \int_V [\epsilon_{ii}(\mathbf{u})q - \frac{1}{\lambda}p(\mathbf{u})q]dx &= 0, \quad q \in L_2 \end{aligned} \quad (\text{D.6})$$

It is shown in [Danaila et al. 2003] that problem D.6 has a finite element solution that converges uniformly in λ . The system D.6 provides the possibility to create a system of functions of influence or Green's functions as FEA solutions for surface loads \mathbf{g} which model delta-type functions. In this case, the surface displacements are a convolution of the matrix of influence \mathbf{G} and loads \mathbf{g} applied on the contact surface S :

$$u(\mathbf{x}) = \int_S \mathbf{G}(\mathbf{x} - \mathbf{x}')\mathbf{g}(\mathbf{x}')d\mathbf{x}' \quad (\text{D.7})$$

where

$$\mathbf{G} = \begin{pmatrix} r_{xx} & r_{xy} \\ r_{yx} & r_{yy} \end{pmatrix}$$

is the matrix of Green functions or matrix of influence. The FEA approximation of functions of influence is presented in Figure D.2, where constant loads were applied on the interval $[0.1h, 0.1h]$ of an elastic test strip having $\mu = 100$ and $\nu = 0.4999$, with thickness $h=1\text{mm}$ and length $[-10h, 10h]$. Red lines present the surface displacement reaction on the shear load in the shear (1) and normal (2) directions, while the blue lines present the reaction on the normal load in the normal (3) and tangential (4) directions. The normal displacement due to the action of a normal force can be approximated by the function:

$$\tilde{r}_{yy}(x) = \frac{1}{\mu}[(a_0 + a_1\exp(-|x|/k_1) + a_2\exp(-|x|/k_2))] \quad (\text{D.8})$$

where parameters $(k_1, k_2, \text{ and } a_i)$ are obtained by fitting the FEA data. The shear (tangential) displacement due to the action of an applied normal force can be approximated by the function:

$$\tilde{r}_{yx}(x) = \frac{1}{\mu}(a_3\exp(-|x|/k_3)) \quad (\text{D.9})$$

Similarly for the case of an applied shear load, the approximations for normal and shear displacements are given by:

$$\tilde{r}_{xy}(x) = \frac{1}{\mu}(a_4\exp(-|x|/k_4)) \quad (\text{D.10})$$

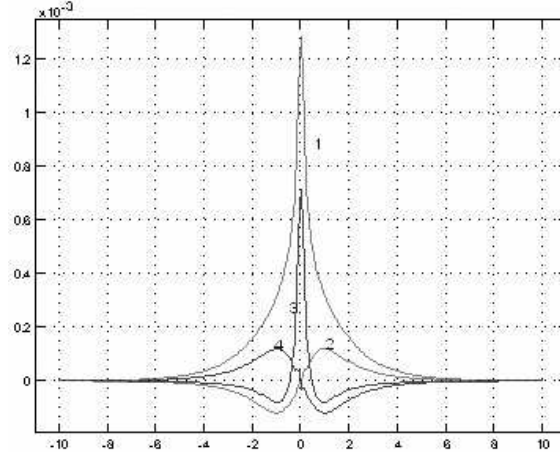


Figure D.2: S3F response functions on loads for 1Pa force applied on the interval $[-0.1, 0.1]$.

$$\tilde{r}_{xx}(x) = \frac{1}{\mu} a_5 \exp[a_6 + a_7 \exp(-|x|/k_5) + a_8 \exp(-|x|/k_6)] \quad (\text{D.11})$$

Rewriting (D.7) in discrete form the reaction to an arbitrary load $L_{ij} = (L_{xi}, L_{yi})$ applied at surface location $[x_0, x_N]$ can be presented as:

$$R_{xj} = \Delta x \sum_{k=0}^N L_{xk} \tilde{r}_{xx}(x_j - x_k) + L_{yk} \tilde{r}_{yx}(x_j - x_k) \quad (\text{D.12})$$

$$R_{yj} = \Delta x \sum_{k=0}^N L_{xk} \tilde{r}_{xy}(x_j - x_k) + L_{yk} \tilde{r}_{yy}(x_j - x_k) \quad (\text{D.13})$$

This system of linear equations (D.12 and D.13) with unknown L_k has the diagonally dominant matrix:

$$\tilde{\mathbf{G}}_{jk} = \begin{pmatrix} \tilde{r}_{xxjk} & \tilde{r}_{xyjk} \\ \tilde{r}_{yxjk} & \tilde{r}_{yyjk} \end{pmatrix} \quad (\text{D.14})$$

which can be inverted and used to solve for the applied loads. Figure D.4 presents amplitude-frequency characteristics of the response functions, which were estimated using their approximation of FEA results. The workable region of spatial frequencies is located in the interval $[0.05..0.5]$ where the AFC of normal and cross-talk component reveals differential properties; the AFC of the shear component is integrative and at least 10 to 100 times larger which explains the possibility to resolve a comparatively small friction force in the presence of high pressure gradients.

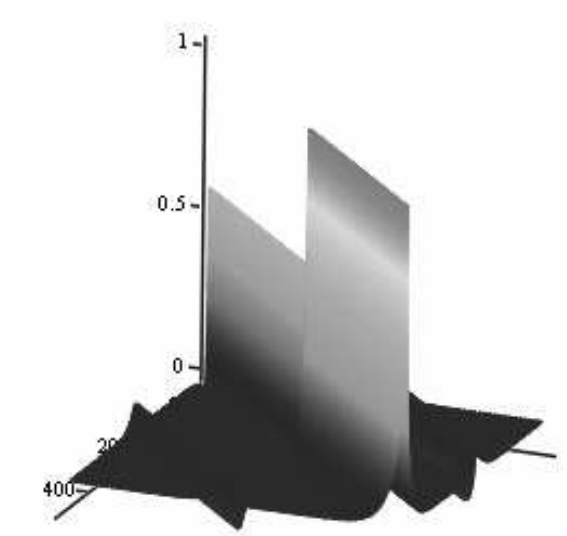


Figure D.3: 3D presentation of $\tilde{\mathbf{G}}$ matrix.

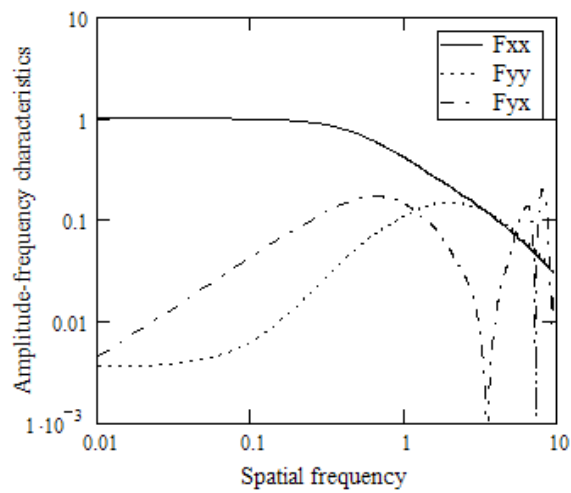


Figure D.4: Amplitude-Frequency Characteristics of normal component (blue), shear component (red), and crosstalk (green) components of response function, $\omega = \Omega/\omega_0$; the spatial frequency referenced to $\omega_0 = 1/h$. Planar FEA model for S3F with $\mu=100\text{Pa}$ and $\nu=0.99$.

E

Uncertainty Analysis

“Who can comprehend errors?”

– Psalm 19, verse 13

There are two basic types of errors in measurement: random and systematic [Dieck 2002]. Random errors affect results to cause scatter in test data; systematic errors remain relatively constant over an experiment and cause bias in the results. Both types of errors cause deviation from the true value and are always present in every experiment measuring any type of quantity. Uncertainty analysis seeks to classify these errors and determine their overall effects on the test result in order to gain an appreciation of “how good” the measurement is. This appendix presents a rigorous theoretical uncertainty analysis for the thermal anemometry and pressure measurement techniques employed in this dissertation, as well as a repeatability-based analysis based on test data acquired over a small time interval respective of the time scale used for the results presented in Chapter 4. As the surface stress film is a developing technology and the reduction methodology is under development, no uncertainty analysis is presented for S3F. The total uncertainty definition used in this work is the U_{95} uncertainty model which produces uncertainty intervals at 95% confidence. All terminology presented in this Appendix can be found in [Dieck 2002].

Definitions and Methodology

Several definitions are required to understand uncertainty terminology. The standard deviation of a measurement, S_x , is defined as:

$$S_x = \left[\frac{\sum (X_i - \bar{X})^2}{N - 1} \right]^{1/2} \quad (\text{E.1})$$

where X_i is the value of the i th X in the sample, \bar{X} is the sample average, and N is the sample size. The random uncertainty of a sample, $S_{\bar{x}}$, uses the standard deviation as follows:

$$S_{\bar{x}} = \frac{S_x}{\sqrt{N}} \quad (\text{E.2})$$

The systematic uncertainty of a sample, $B_{\bar{x}}$, is taken from manufacturer specifications of accuracy for a given instrument. There are also errors in measurement due to uncertainties in the instrument calibration process, which are also divided into random and systematic components. The random calibration uncertainty, $S_{\bar{x},cal}$, is defined as:

$$S_{\bar{x},cal} = \left[\frac{\sum (Y_i - Y_{i,c})^2}{N - K} \right]^{1/2} \quad (\text{E.3})$$

where Y_i is the i th data point in a calibration corresponding to X_i , $Y_{i,c}$ is the value of the curve fit corresponding to X_i , and K is the number of calibration coefficients used in the curve fit. The systematic calibration uncertainty, $B_{\bar{x},cal}$, is determined by the process used to calibrate the instrument. In this work, a Ruska 7250lp low-pressure calibrator was used to calibrate the pressure transducer, and its systematic calibration uncertainty was obtained from the manual provided with the calibrator. The hot-film sensors were then calibrated against the pressure transducer, and the hot-film systematic calibration uncertainties were obtained by propagating the pressure transducer uncertainty through the Bernoulli equation:

$$V = \sqrt{\frac{2P}{\rho}} \quad (\text{E.4})$$

where P is the pressure at the measurement point of interest and ρ is the density of air (1.168 kg/m³). The influence coefficient, which determines the sensitivity of the hot-film test result to the pressure transducer's uncertainty, is found by taking the partial derivative of the velocity with respect to pressure:

$$\frac{\partial V}{\partial P} = (2\rho P)^{-1/2} \quad (\text{E.5})$$

The systematic calibration uncertainty for the hot-film results is then determined by:

$$B_{\bar{x},cal,HF} = \left[\left(\frac{\partial V}{\partial P} \right)^2 (U95_{pr})^2 \right]^{1/2} \quad (\text{E.6})$$

where $U95_{pr}$ is the total uncertainty of the pressure measurement at 95% confidence given by:

$$U95 = \pm t \left[(S_{\bar{x}})^2 + (S_{\bar{x},cal})^2 + (B_{\bar{x}}/2)^2 + (B_{\bar{x},cal})^2 \right]^{1/2} \quad (\text{E.7})$$

where t is the proper value of the Student's t -distribution. The individual instrument uncertainties must then be propagated into the loss definitions presented as Equations 3.1 and 3.2 and root-sum-squared similar to Equation E.6 above. The resulting influence coefficients (partial derivatives)

are:

$$\frac{\partial L_{area}}{\partial(\overline{P_{t,in}} - \overline{P_{t,ex}})} = \frac{1}{(\overline{P_{t,in}} - \overline{P_{s,in}})} \quad (E.8)$$

$$\frac{\partial L_{area}}{\partial(\overline{P_{t,in}} - \overline{P_{s,in}})} = -\frac{(\overline{P_{t,in}} - \overline{P_{t,ex}})}{(\overline{P_{t,in}} - \overline{P_{s,in}})^2} \quad (E.9)$$

$$\frac{\partial L_{flux}}{\partial u_{ex}} = \frac{\sum(\overline{P_{t,in}} - \overline{P_{t,ex}}) / \sum u_{ex} - [\sum u_{ex} \cdot (\overline{P_{t,in}} - \overline{P_{t,ex}})] / (\sum u_{ex})^2}{(\overline{P_{t,in}} - \overline{P_{s,in}})} \quad (E.10)$$

$$\frac{\partial L_{flux}}{\partial(\overline{P_{t,in}} - \overline{P_{t,ex}})} = \frac{1}{(\overline{P_{t,in}} - \overline{P_{s,in}})} \quad (E.11)$$

$$\frac{\partial L_{flux}}{\partial(\overline{P_{t,in}} - \overline{P_{s,in}})} = -\frac{[\sum u_{ex} \cdot (\overline{P_{t,in}} - \overline{P_{t,ex}})] / \sum u_{ex}}{(\overline{P_{t,in}} - \overline{P_{s,in}})^2} \quad (E.12)$$

Measurement Uncertainties

The uncertainty in this appendix is determined by two distinct methods: the first being a rigorous treatment of the applicable equations for the loss coefficient following the methodology presented in [Dieck 2002], and the second being a repeatability-based uncertainty determined by comparing multiple sets of test data taken on different days at the same Reynolds numbers.

Theoretical Determination

All pressure measurement data are acquired with a Druck LPM5481 low-pressure differential transducer with range from -0.2 to 0.8 inches of H₂O and a measurement face diameter of 1.5mm. Table E.1 presents the uncertainty breakdown for the Druck transducer at two dynamic pressures, 7.5e-3 and 1.3e-1 inches H₂O (or 1.8 and 7.3 m/s). These flow speeds correspond to the L1M test case Reynolds numbers of 21,000 and 86,000, the lower and upper Reynolds number bounds of the acquired experimental test data for the L1M and L2F airfoils. At both dynamic pressures, the un-

Table E.1: Druck LPM5481 differential pressure transducer uncertainty [in H₂O].

Pressure	$S_{\bar{x}}$	$B_{\bar{x}}/2$	$S_{\bar{x},cal}$	$B_{\bar{x},cal}$	U95
7.5e-3	6.6e-3	1.0e-3	0.0e0	4.5e-13	1.3e-2
1.3e-1	3.7e-4	1.0e-3	0.0e0	1.3e-10	2.2e-3

certainty is dominated by the random and systematic components based solely on the transducer's response and not on the calibration process. The high levels of random uncertainty, $S_{\bar{x}}$, is believed to be due to two physical phenomena occurring during the uncertainty data acquisition. First, one

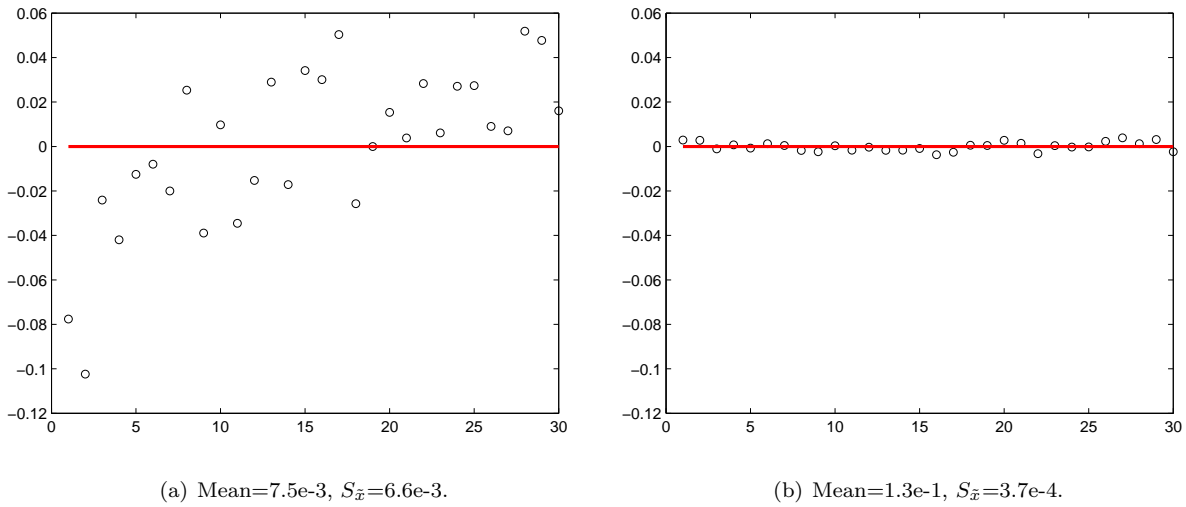


Figure E.1: Distributions of pressure measurements about the means [inH₂O].

end of the differential transducer was plumbed to the inlet freestream where the random uncertainty was affected by the freestream unsteadiness generated by the upstream turbulence grid. Second, the other end of the transducer was plumbed to a position behind the cascade close to the inside wall where wake effects should be minimal but still affect the reading. It is suspected that these unsteady mechanisms (turbulence grid and wake effects) induced fluctuations read by the transducer which is wrongly cited as random uncertainty. Figure E.1 shows the distributions of measurements about the mean for both flow speeds, where the x-axis corresponds to each of the 30 measurements taken for uncertainty calculations, the y-axis corresponds to the amount over or under the mean, and the red line represents the respective mean. Each measurement is an average of data taken at 1kHz for 30,000 samples, with an average time of 2 minutes in between successive measurements. In Figure E.1(a) for the mean pressure of 7.5e-3 inH₂O, the standard deviation is equal to 0.00663 inH₂O. In Figure E.1(b) for a mean pressure of 1.3e-1 inH₂O, the standard deviation is equal to 0.00037 inH₂O, which illustrates how increasing the flow speed dramatically decreases the fluctuation about the mean value. For purposes of completeness, this theoretical treatment of uncertainty will continue to use the random uncertainty for the pressure transducer as presented in Table E.1, although it is believed that the low Re random error assessment contains systematic error which renders its use invalid. Therefore, estimates using both the high- Re and low- Re uncertainty will be used at low- Re , since it is believed that the true random error of the pressure transducer was that obtained at the higher Reynolds number.

Throughout this work, two different hot-film sensors were used to acquire velocity data. The first is a TSI 1240-20 x-wire hot-film probe and the second is a single normal 1211-20 hot-film sensor.

Table E.2 presents the uncertainty breakdown for both sensors at the same flow speeds as reported for the Druck pressure transducer. In this table, no entry was supplied for the systematic uncertainty,

Table E.2: TSI 1240-20 x-wire and 1211-20 hot-film uncertainties [m/s].

1240-20					
Speed	$S_{\bar{x}}$	$B_{\bar{x}}/2$	$S_{\bar{x},cal}$	$B_{\bar{x},cal}$	U_{95}
1.8	2.3e-2	N/A	7.4e-3	1.5e-0	3.0e0
1.8*	2.3e-2	N/A	7.4e-3	2.7e-1	5.4e-1
7.3	9.5e-3	N/A	7.4e-3	6.4e-2	1.3e-1
1211-20					
Speed	$S_{\bar{x}}$	$B_{\bar{x}}/2$	$S_{\bar{x},cal}$	$B_{\bar{x},cal}$	U_{95}
1.8	3.5e-3	N/A	6.2e-3	1.5e0	3.0e0
1.8*	3.5e-3	N/A	6.2e-3	2.7e-1	5.4e-1
7.3	8.9e-3	N/A	6.2e-3	6.4e-2	1.3e-1

* Calculations using pressure uncertainty of 2.2e-3 inH₂O.

$B_{\bar{x}}$, since there is no straight-forward way to assess the systematic uncertainty present in the complex hot-wire data reduction scheme. In these situations, the uncertainty reference [Dieck 2002] suggests making an (absolutely dangerous!) educated guess as to the magnitude of the unknown systematic uncertainty if one is comfortable and experienced with such measurements. As this author is not comfortable doing so, the entry is left blank as a “best chance” determination. This table shows how the uncertainties for both the 1240-20 x-wire and the 1211-20 hot-film are dominated by the propagated uncertainty of the pressure transducer. As expected, comparison of the uncertainties for the flow speed of 1.8 m/s using the propagation of low- Re and high- Re pressure uncertainties shows how using the lower random uncertainty for the pressure transducer results in lower uncertainty in the flow speed.

Table E.3 shows the influence coefficients defined by Equations E.8 through E.12 for both Reynolds numbers analyzed. This table shows how the uncertainty in both area-averaged and flux-averaged loss is more heavily influenced by the pressure uncertainty, while the velocity uncertainty does not contribute a significant effect. As expected, the influence of the pressure uncertainty decreases with Reynolds number, as the magnitudes of the influence coefficients at $Re = 86k$ drop significantly compared to those at $Re = 21k$.

Table E.3: Influence coefficients for loss definition uncertainties.

Reynolds #	$\frac{\partial L_{area}}{\partial (P_{t,in} - P_{t,ex})}^*$	$\frac{\partial L_{area}}{\partial (P_{t,in} - P_{s,in})}^*$	$\frac{\partial L_{flux}}{\partial u_{ex}}^\dagger$	$\frac{\partial L_{flux}}{\partial (P_{t,in} - P_{t,ex})}^*$	$\frac{\partial L_{flux}}{\partial (P_{t,in} - P_{s,in})}^*$
21k	57.47	-49.55	0.00	57.47	-49.55
86k	3.36	-2.93	0.00	3.36	-2.93

* Units equal to $[\text{inH}_2\text{O}]^{-1}$.

† Units equal to $[\text{m/s}]^{-1}$.

Table E.4: Theoretical uncertainty in loss coefficients.

Reynolds #	L_{area}	L_{flux}
21k	0.3786	0.3786
21k*	0.2361	0.2361
86k	0.0072	0.0072

* Calculations using pressure uncertainty of 2.2e-3 inH₂O.

The resultant effect of the instrument uncertainties on the experimental loss coefficients are presented in Table E.4 for both Reynolds numbers. Here, both values of random uncertainty for the pressure transducer are included. This table shows an uncertainty in loss of 0.3786 or 0.2361 at $Re = 21k$ and 0.0072 at $Re = 86k$, again showing that the uncertainty decreases with Reynolds number. However, the large value of uncertainty at $Re = 21k$ must be an extremely conservative estimate using either random uncertainty for the pressure transducer, since a true uncertainty of this magnitude would preclude the attainment of the well-correlated Reynolds lapse trends seen in Figure 4.1. In fact, the correlation between data points, which were taken over multiple days for each airfoil, as well as the agreement of trends seen with the L2F CFD predictions and experimental findings suggest the accuracy of the experimental results must be better than the theoretical uncertainty obtained through the rigorous treatment of propagated uncertainties. Therefore, another method of determining the accuracy of the experimental results based on multiple data sets of the same Reynolds number is presented in the next section to provide an uncertainty based upon the repeatability of loss coefficient determination.

Repeatability-Based Determination

For an estimation of experimental uncertainty based on repeatability, multiple data sets of the same test condition using the L2F airfoil were compared to determine standard deviations of loss coefficients at three Reynolds numbers: 3 sets at $21k$, 2 sets at $34k$, and 3 sets at $39k$. These sets include those presented earlier in Figure 4.1, and give a total of 8 sets upon which an average standard deviation can be produced which represents a repeatability-based uncertainty. Table E.5 shows the calculated area- and flux-averaged loss coefficients and standard deviations of those loss coefficients for each of the three Reynolds numbers. The first entry for each Reynolds number were plotted in the Reynolds lapse plot of Chapter 4.

Table E.5: Repeatability-based standard deviation in L2F loss coefficients at low Re .

Reynolds #	L_{area}				L_{flux}			
	1	2	3	stdev	1	2	3	stdev
$21k$	0.1788	0.1889	0.1695	0.0097	0.1665	0.1813	0.1572	0.0122
$34k$	0.1575	0.1594	—	0.0013	0.1508	0.1529	—	0.0015
$39k$	0.1444	0.1478	0.1469	0.0018	0.1383	0.1422	0.1408	0.0020

As the standard deviations provided above in Table E.5 represent actual test data, they are believed to be more realistic and representative of the true uncertainty in the loss coefficients. Therefore, the above standard deviations for each of the low Reynolds number cases are accepted for the true uncertainty of the loss coefficients at those Reynolds numbers. The experimental L2F loss coefficients of Figure 4.1 with error bars representing the standard deviations at low Reynolds number found in Table E.5 are plotted along with the theoretical uncertainty for $Re = 86k$ in Figure E.2. This figure shows how the trends described in Chapter 4 remain valid after repeatability-based uncertainty is applied. It is also believed that the amount of uncertainty at $Re = 86k$ represented by the error bars in this figure is greater than what could be expected if multiple data sets were taken for this Reynolds number and a repeatability-based uncertainty was performed.

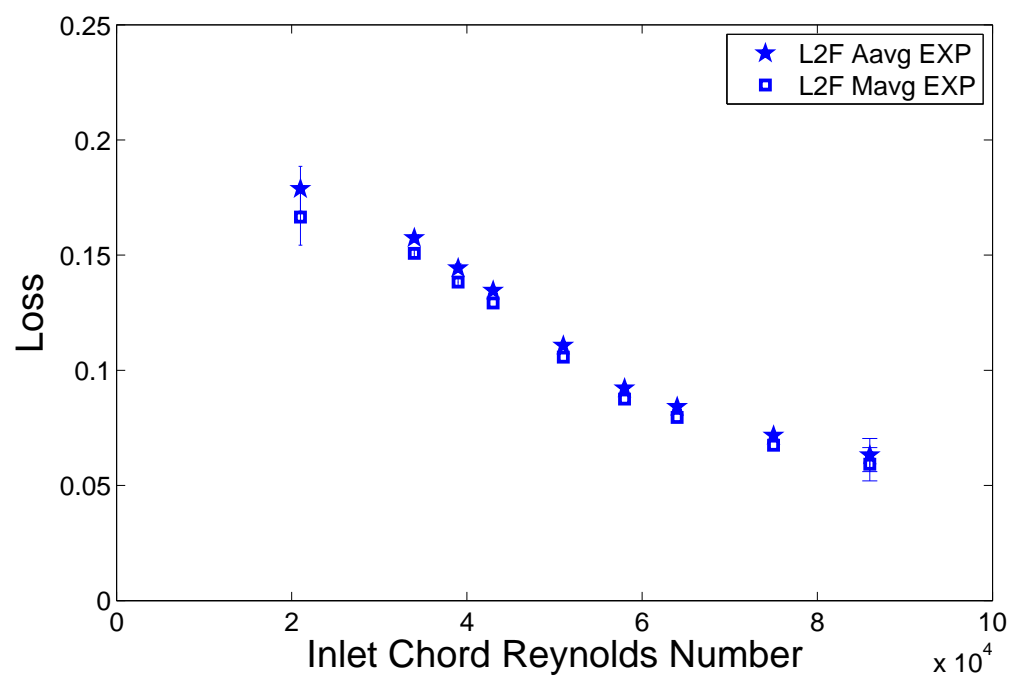


Figure E.2: L2F Reynolds lapse with error bars at low and high Re .

F

Short History of Gas Turbine Engine Development - DRAFT

In 1909, the United States government commissioned the Wright brothers to build the first military aircraft, powered by a piston engine and a propeller. In 1921, the propulsion system of modern aircraft achieved its first breath of life in the patent of Guillaume [Mattingly 1996]. This new design would use turbomachinery to create a large jet of fluid exiting the engine, providing the basis for the term “jet engine”. In this design, the intake air was first compressed by an axial-flow compressor before entering a radial combustor. An axial-flow turbine followed the combustor, extracting just enough energy to drive the compressor. This design soon became shelved as then-current propeller-driven aerovehicles could not exceed 200 mph; a flight speed of nearly 400 mph would be necessary to be compatible with Guillaume’s jet engine exhaust speeds.

Fortunately enough, the gas turbine engine idea would see another avenue into existence through the work of Sir Frank Whittle in the UK. In December of 1929, Whittle came up with the idea of increasing the fan pressure ratio and adding a turbine to existing reciprocal engines. Just a month later in January of 1930, Whittle applied for a patent of the first turbojet engine: a multi-stage, axial-flow compressor followed by a radial compressor stage, then the combustor, then an axial-flow turbine to drive the compressor, followed by an exhaust nozzle. He considered the turbojet as a hybrid of “propeller gas turbine” and “rocket” principles. In 1936, he then conceived the idea of a *bypass engine* or *turbofan*, which diverts air flow pathways to achieve better efficiencies. By April of 1937, Whittle accomplished the first bench-test of a jet engine using liquid fuel.

Simultaneous with Whittle, a German scientist was making great headway into gas turbine engine development. In 1936 Hans von Ohain, the so-called father of German jet propulsion technology, started working on a new combustor design using hydrogen as the fuel. Incredibly, he completed a

working prototype of the hydrogen combustor in just 2 months! By February of 1937, von Ohain completed the hydrogen jet engine prototype and by 1938 had a functioning annular combustor now using gasoline as the fuel. On August 27, 1939, Hans von Ohain's annular combustor design helped power the first flight of a turbojet aircraft (German He-178) anywhere in the world. The flight in itself was remarkable, but it also had about 2-3 times the net power output to engine weight ratio than the best propeller/piston engines of equal thrust, and for the first time the combustion chambers could be made small enough to fit inside the engine envelope as determined by the required sizes of compressor and turbine blading.

In that same year of 1939, a retired German patent examiner found and published the early jet engine patents. By the 1940s, the US company Pratt & Whitney gained an interest in jet propulsion, but wartime policies restricted their involvement. After World War II, P&W went full steam ahead into jet propulsion using turbomachinery, and with US government support started constructing their own facility for design and testing. In September of 1941, the US bought some of Whittle's plans from the British Air Commission, and by 1945 Lockheed's single engine P80A Shooting Star powered by General Electric's 4000-lb thrust I40 engine reached 620 mph; the jet age had officially begun.

In the 1960s, Whittle's original idea of a bypass engine received greater attention. The high-bypass-ratio fanjets and turbojets emerged, which allowed the "2nd generation" of commercial jet aircraft, the so-called *widebody* such as the Boeing 747 with a passenger capacity of around 400. The advantages of these new gas turbine engines included higher overall efficiencies which provided longer flight times and range (the 1939 German He-178 had an engine life of around 20 operational hours), shorter travel times which increased passenger enjoyment, and quieter and cleaner emissions. Much of the work following the end of World War II focused on improving the compressors and combustors, as these components are the basis for the power output of the engine.

Even with superior thrust/weight ratios, the early turbojets were not suitable for applications where greatest fuel economy, highest reliability, and long endurance and service life were required. Newer developments therefore focused on an ever-increasing overall efficiency, larger power output engines, larger power output to engine weight ratios, and greater service life, endurance, and reliability. A first step to accomplish these goals was to again focus on the compressor and increase its pressure ratio in order to increase overall engine efficiency. A 1940s turbine engine may have a compressor pressure ratio of 3:1 with efficiencies near 80%, whereas modern engines can exceed 40:1 with efficiencies greater than 90%. This increase was in part due to multiple rotor and variable stator arrangements coupled with variable front-stage bleeding to minimize the compressor-combustor mismatchings which killed the efficiencies of early turbojets. An improved compressor efficiency and

increased mass flow were the big players which reduced engine length, frontal area, and the power-to-weight ratio. Much of the above improvements were only possible through combined efforts of industry and government with private research companies and universities.

After compressor efficiency and mass flow increases, the next big development was to increase turbine inlet temperatures, which led back to improving combustors for higher efficiency and lower pollution. A major development for turbine component improvement came with cooled, hollow blades which provided some defense against the hot combustor exhaust gases and allowed those higher turbine inlet temperatures. Heat-resistant materials also improved the turbine section. With these new efforts, the bypass ratio exceeded 8:1, where up to 8 times the massflow going through the turbine now was diverted straight into the exhaust mixing chamber so that proper exit exhaust velocities could be maintained. These higher bypass ratios allowed longer flight ranges, more thrust at lower speeds (good for takeoff and climbing), lower jet velocities which lowered the noise, and lower fuel consumption and reduced chemical emissions.

A next logical step in gas turbine design is to increase the loading of each individual turbine blade. This will be achieved only with the use of improved transition modeling, and provides a means to extract more power from existing arrangements or to decrease the required number of blades for an equivalent overall loading of existing arrangements. A decrease in blade count will also decrease the overall investment cost of the engine from initial purchase through maintenance and replacement. This thesis serves to illustrate how much more lift is available from the low-pressure turbine section when modern modeling and design strategies are employed.

G

LPT Aerothermodynamics and Flow Physics - DRAFT

As mentioned earlier in Chapter 1, flow in the low-pressure turbine section is dictated by a high degree of unsteadiness and flow separation at low Reynolds numbers. This Appendix describes the aerothermodynamics and flow physics which govern the performance of the entire section as well as the individual blade rows.

Low-Pressure Turbine Aerothermodynamics

The gas turbine engine thermodynamic process is governed by the Brayton cycle, which inherently produces low efficiencies in the LPT section due to the large variation in blade velocity with radius moving outward from root to tip [El-Wakil 2002]. In order to increase efficiency, designers use a higher degree of curvature for the low-pressure turbine blades than the high pressure turbine blades. This higher degree of curvature helps regulate the large change in blade velocity with radius. The ideal Brayton cycle is comprised of four processes: an isentropic compression (1 to 2), a constant-pressure heat addition (2 to 3), an isentropic expansion through the turbine (3 to 4), and a constant-pressure heat rejection (4 to 1) [Mattingly 1996]. These processes are shown in Figure G.1. Step 1 to 2 is where the compressor isentropically increases the pressure of the gas. Fuel is then added and burned in the combustor from 2 to 3. The gas then expands through the turbine and exhaust nozzle while the turbine isentropically extracts energy from the flow from 3 to 4. Finally, heat is dumped externally to get back to 1 from 4. For an ideal cycle, the compressor and turbine processes are considered to be both reversible and adiabatic (therefore *isentropic*), and the heating and cooling processes are considered to be constant-pressure. For a calorically perfect gas ($\gamma = \text{constant}$), the

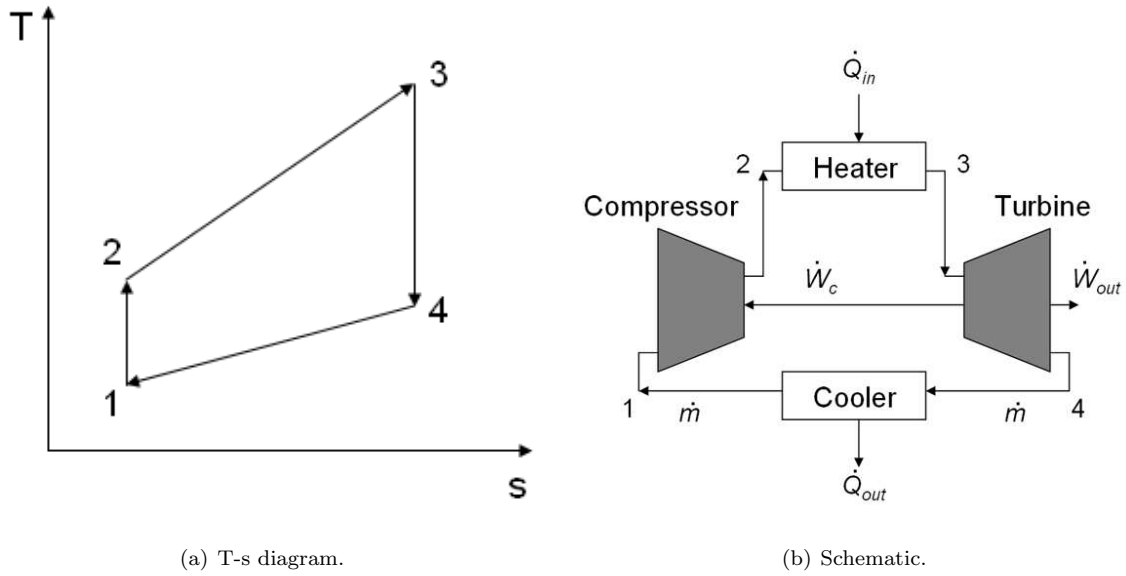


Figure G.1: Ideal Brayton cycle.

ideal Brayton cycle gives the following results:

$$\dot{W}_c = \dot{m}c_p(T_2 - T_1) \quad (\text{G.1})$$

$$\dot{W}_t = \dot{m}c_p(T_3 - T_4) \quad (\text{G.2})$$

$$\dot{Q}_{in} = \dot{m}c_p(T_3 - T_2) \quad (\text{G.3})$$

$$\dot{Q}_{out} = \dot{m}c_p(T_4 - T_1) \quad (\text{G.4})$$

$$\dot{W}_{out} = \dot{W}_t - \dot{W}_c = \dot{m}c_p[(T_3 - T_4) - (T_2 - T_1)] \quad (\text{G.5})$$

where \dot{m} is the massflow and c_p is the constant pressure specific heat. The thermal efficiency of the cycle, η_{th} , is given by:

$$\eta_{th} = \frac{\dot{W}_{out}}{\dot{Q}_{in}} \quad (\text{G.6})$$

For an ideal cycle with $\gamma = \text{constant}$, $(P_2/P_1)^{(\gamma-1)/\gamma} = T_2/T_1 = T_3/T_4$, so that the thermal efficiency can be written as:

$$\eta_{th} = 1 - \left(\frac{P_1}{P_2}\right)^{(\gamma-1)/\gamma} \quad (\text{G.7})$$

Now let's look closer at the turbine section. A turbine section can have multiple stages, each of which consists of two rows of blades, a stator and a rotor. The stator row is fixed and guides the incoming flow into the tangential direction of rotation. The row of rotor blades is pushed by the flow, resulting in a net torque on the shaft. Although the flow is slowed by viscous friction across the stator and rotor components, the overall effect of the entire turbine section is to expand

the gas (increase the velocity) until its exit through the exhaust nozzle while extracting energy to power the compressor. The ideal process described above is not accurate due to energy losses which occur in the real process. These losses can be illustrated better with the aid of another T-s diagram for a typical low-pressure turbine stage, as shown in Figure G.2. Locations 1 and 2 correspond

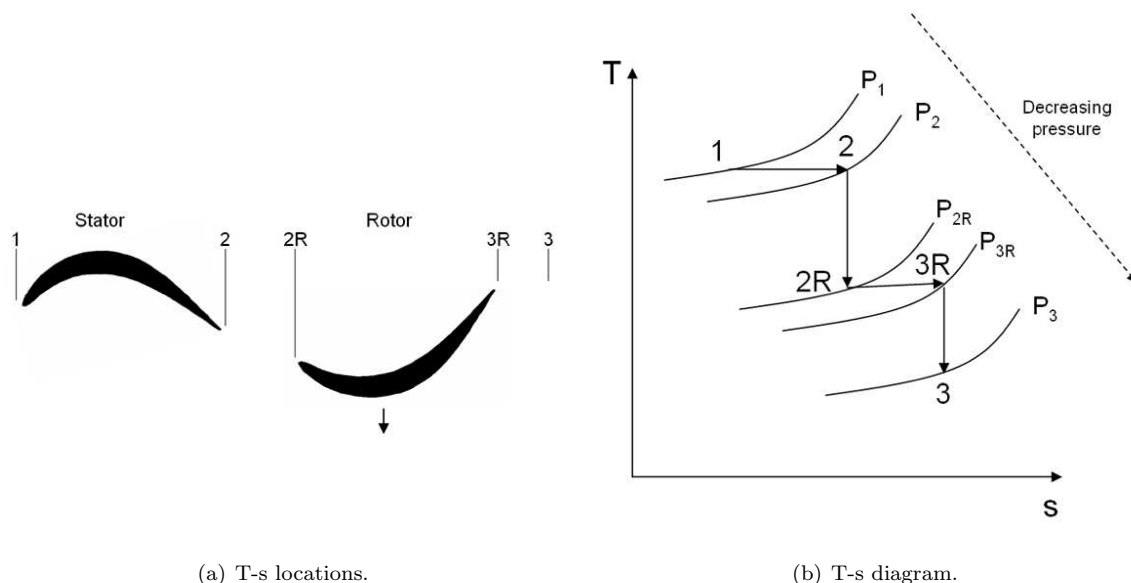


Figure G.2: T-s diagram of a typical LPT stage.

to the stator inlet and exit, respectively, while 2R and 3R correspond to the rotor inlet and exit, respectively. Location 3 marks the beginning of the next stator, and the passages between stators and rotors (2 to 2R and 3R to 3) are considered isentropic. The rotor work is achieved from 2R to 3R. Constant pressure lines are shown on the T-s diagram in Figure G.2(b). As seen in the figure, a pressure drop occurs over both the stator and rotor as the entropy is increased. These pressure drops decrease the efficiency of the stage, η_t , as related by [Mattingly 1996]:

$$\eta_t = \frac{1 - \frac{T_3}{T_1}}{1 - \left(\frac{P_3}{P_1}\right)^{(\gamma-1)/\gamma}} \quad (\text{G.8})$$

Since a pressure drop ($P_3 < P_1$) increases the denominator in Equation G.8, a larger P_3/P_1 (reduced pressure drop) will increase the efficiency of the stage and therefore of the overall engine. The high-lift design presented herein seeks to increase the loading achieved by the LPT section rotor while simultaneously producing an airfoil with an improved low- Re characteristic. Flow separation is a phenomenon which under low- Re conditions can significantly increase the pressure drop across the rotor, thereby causing a reduced efficiency of the LPT section.

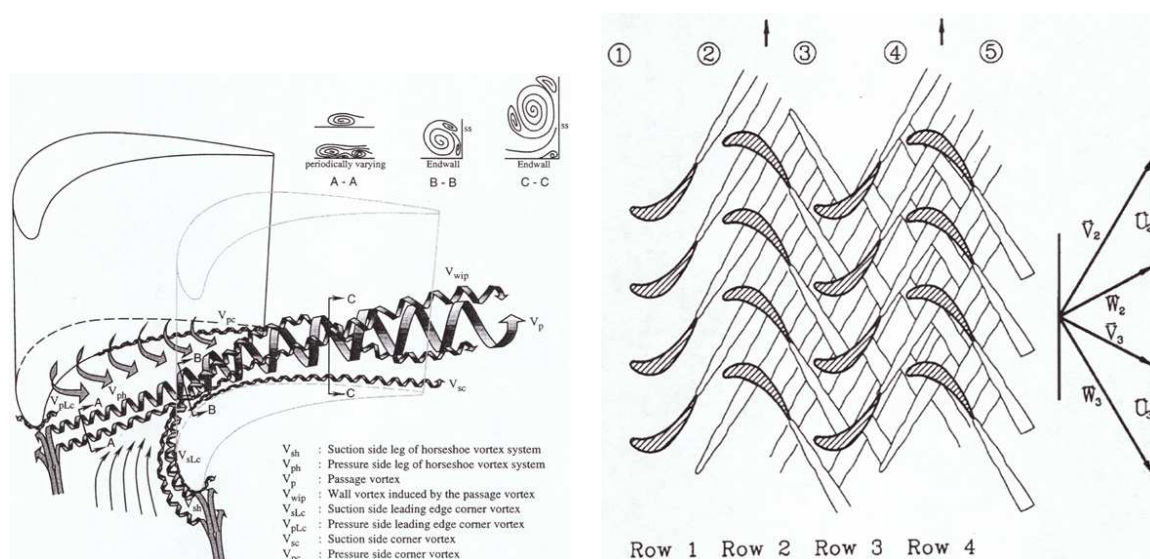
Low-Pressure Turbine Flow Physics

Low-pressure turbines have a tough life; they are subjected to periodic disturbances from upstream blade rows including inviscid pressure waves and viscous wake interactions. The combination of a low Reynolds number and high loading make separation effects extremely important. Coupled with a high level of transition and turbulence phenomena, the LPT environment is extremely harsh.

LPT Unsteadiness

The flow around a low-pressure turbine is highly unsteady, with freestream turbulence levels reaching as high as 20% [Volino and Simon 2000]. In their 1990 overview of unsteadiness in turbine flows, Sharma *et al.* found that unsteady losses account for 25% - 100% of the energy losses in a steady environment [Sharma et al. 1990]. These unsteady effects include inviscid waves, shocks, and wakes generated from upstream blade rows which convect into downstream blade rows. They found that hub secondary flows are strongly affected by the wakes while tip secondaries are not. These upstream structures migrate to the suction side of the LPT as they convect downstream. In general, the initial 3/4 of the airfoil experience the majority of 3D unsteady and rotational effects which play a significant role in pressure distribution and temperature segregation, while the last 1/4 of the blade is mainly dominated by unsteady viscous flow mechanisms (separation). Adamczyk explains that the inability of current 3D CFD models using no empirical correlations to resolve these unsteady flow features in multistage turbomachinery flows is not within the designer's required level of accuracy [Adamczyk 2000].

In 1997, Wang *et al.* experimentally studied the secondary flows in a 4-blade high-performance Pack-B-like LPT cascade at $Re = 27,000$ and $FSTI < 0.2\%$ [Wang et al. 1997]. Their resultant interpretation of LPT secondary flows are illustrated in Figure G.3(a). The horseshoe vortex at the stagnation point is a periodic, multi-vortex structure which splits off into pressure and suction side vortices. The upwash and downwash of these vortices can influence local minimums and maximums of pressure along the blade surface. The pressure leg of the horseshoe vortex becomes the main passage vortex as the strong adverse pressure gradient forces its migration toward the suction surface, eventually interacting with the suction leg of the horseshoe vortex. These two vortices finally mix back together after the exit plane of the LPT. Along the way, the main passage vortex influences the formation of a counter-rotating wall vortex whose fluid is taken from the inlet boundary layer upstream of the cascade. This wall vortex has significant impact on the mass transfer throughout the main passage. A major consequence of the vortex formation and interaction described above is that the passage vortex leads to much of the pressure loss across the cascade and can lead to high



(a) Secondary flows, from Wang et al. 1997.

(b) Wake propagation, from Schobeiri et al. 2003.

Figure G.3: Complex unsteady LPT environment.

heat transfer rates to the blade endwall. The above unsteady effects are generated by the presence of only a single cascade. In reality, LPT sections of modern gas turbine engines house multiple blade rows, so that all of the above disturbances of a single blade row are shed downstream and are coupled with other wakes and disturbances which are themselves convecting into downstream blade rows. Figure G.3(b) provides a glimpse of how complex LPT flow environments really are; each wake or disturbance shed from one row migrates downstream where it is continually disrupted and transformed into other disturbances, creating a high level of freestream turbulence [Schobeiri et al. 2003]. Passing wakes can have a positive benefit for low- Re flows where separation is a problem, but can increase losses in higher- Re flows where transition has already begun [Coton et al. 2003]. Proper consideration of wake mixing effects in CFD simulations and experiments with rod-generated wakes also require consideration of the local pressure gradient's influence on the mixing process [Praisner et al. 2006]; accounting for up to 1.5% of the total lost efficiency in turbines, evidence shows a hastened mixing process in adverse and a reduced mixing process in favorable gradients. Praisner *et al.* also suggest that front-loading causes an increased “row-loss augmentation” (loss reduction) due to its earlier diffusion of a less-mixed out wake. The wakes also manipulate the secondary flows by decreasing the pressure side separation bubble enough to curb its contribution to the main passage vortex [Schobeiri et al. 2003]. The secondary flow pattern then spreads out more along the span, smearing out the smaller fluctuations. These wakes are dominantly fed from the pressure side of the blade and typically shed somewhere between 10 to 60 Hz in LPT flows [Cicatelli and Sieverding 1997].

This frequency becomes deterministic as rotation is introduced. The increased FSTI due to wakes has its greatest influence in the low-loss outer boundary layer due to dampening effects near the wall [Griffin and Davies 2004]. As you progress through stages, the flow loses some momentum due to the work being extracted out by previous blade rows, thereby decreasing the Reynolds number. These wakes and disturbances can sometimes be beneficial in later stages for delaying or prohibiting separations caused by the reduction in Reynolds number [Howell et al. 2001]. Recent full scale rotating rig experimental results on a single-stage turbine show that the vane-blade interactions significantly modify the cooling flows as well; even the cooling channels internal to the blade see some effects [Haldeman and Dunn 2006]. Properly locating wakes by circumferentially adjusting the relative position of adjacent guide vanes and rotors, termed “airfoil clocking” or “indexing”, has also proven beneficial in the design of turbomachinery blading [Huber et al. 1996; Griffin et al. 1996].

It has been suggested that the tip leakage loss, endwall loss, and profile loss equally account for 1/3 of the total loss through the turbine section [Denton 1993]. Loss mechanisms included viscous friction in the boundary layer and free shear layer, heat transfer across a finite ΔT such as core flow to coolant flow, and non-equilibrium processes such as rapid expansions and shock waves with high entropy generation due to heat conduction and high viscous stress within the waves. Denton suggests that transition to turbulence in turbomachines will occur when the momentum thickness Reynolds number is within $300 < Re_\theta < 1000$. This range is reduced to $200 < Re_\theta < 500$ for the high turbulence flows encountered in the LPT section.

Low Reynolds Number Effects

The measured turbine efficiencies at takeoff can be up to 2 points higher than at cruise conditions [Simon and Ashpis 1996]. The loss experienced at higher altitudes (lower Reynolds numbers) is primarily due to laminar flow separations on the turbine blading. Flow separations cause most of their damage in the aft 25% of vane and rotor suction surfaces and the first 40% of rotor pressure surfaces [Dorney and Ashpis 1998]. The turbulence intensity in wakes also lose their effectiveness as Re drops [Halstead et al. 1997b]. Roberts defines four categories of flow regimes over an airfoil [Roberts 1980]:

1. high enough Reynolds number (based on axial chord) to force the flow into transition before separation can occur.
2. lower Re flow where a small, laminar separation bubble can occur. This short bubble’s influence remains on the suction surface and only minimally perturbs the inviscid pressure distribution.
3. lower Re where the short bubble “bursts” into a longer one. The longer bubble’s influence

substantially alters the pressure distribution in the outer (and therefore inner) flow.

4. complete separation without reattachment.

Progression down the list, or decreasing the chord Reynolds number, increases the loss experienced by the turbine section. The Re -dependent loss is illustrated by Sharma in Figure G.4 [Sharma 1998]. When the airfoil chord Reynolds number is low enough, the laminar boundary layer reaches

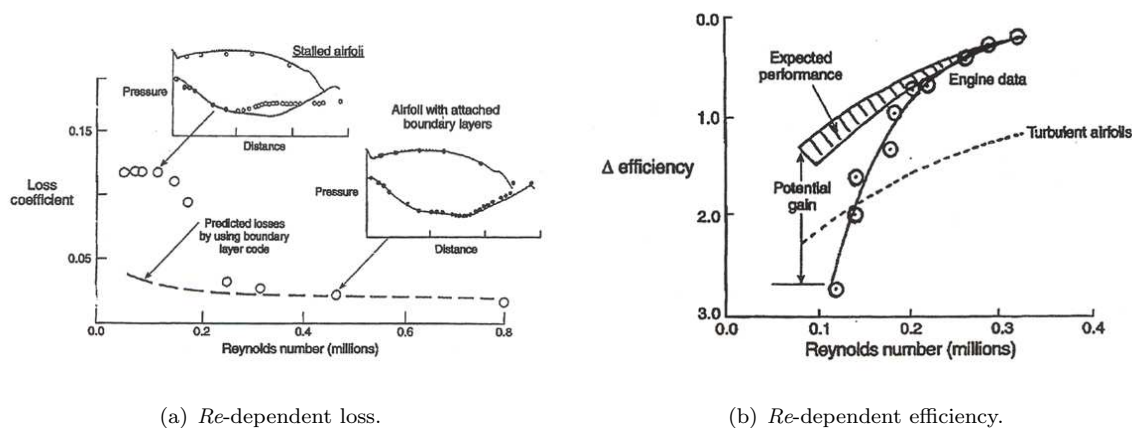


Figure G.4: Low Re effects, from [Sharma 1998].

separation before transition can occur. The bubble then forms a laminar free shear layer that eventually transitions to turbulence. The turbulent free shear layer can then diffuse enough higher energy fluid by entrainment to reattach as a turbulent boundary layer. As Re drops, the laminar shear layer grows in length, and turbulent entrainment can no longer bring enough high-energy fluid to cause reattachment at an inviscid non-separating pressure level. Roberts continues to define two necessary conditions for a laminar bubble formation:

1. an adverse pressure gradient of sufficient strength to cause laminar separation.
2. flow conditions for a laminar state.

The second item requires a smooth surface, low FSTI, and a momentum thickness Reynolds number below that where transition occurs. A schematic showing the pressure distribution throughout a typical separation bubble is shown in Figure G.5. The flow separation causes a sudden increase in the local pressure which decreases the velocity peak and total circulation. This in turn creates a pressure plateau throughout the laminar portion of the bubble. Transition in the shear layer atop the bubble forces a pressure increase until turbulent reattachment. The net effect of the bubble is to decrease the overall lift obtained from the airfoil. Gier and Ardey suggest the viscous losses inside the bubble can be neglected, and the real loss comes from pushing the shear layer into the

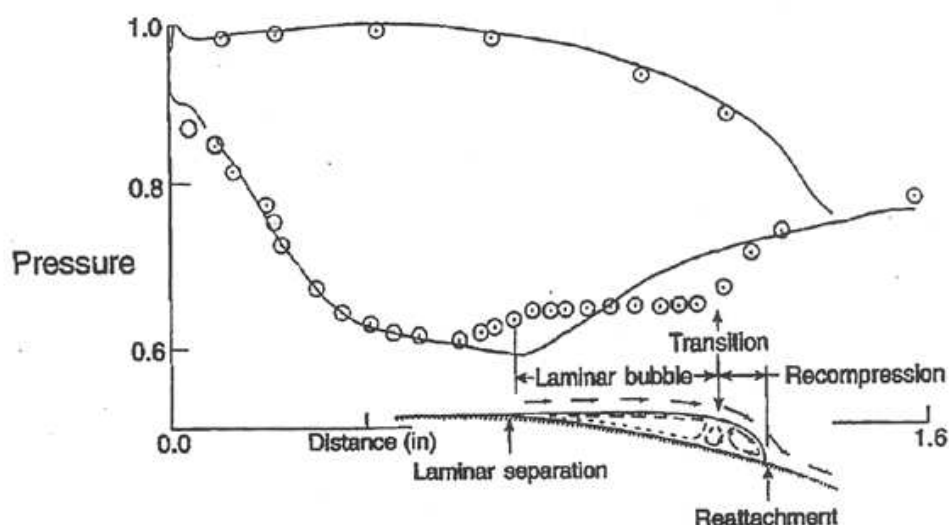


Figure G.5: Schematic of a typical separation bubble, from [Sharma 1998].

freestream causing additional mixing losses; they also suggest an increased loading can compound this effect [Gier and Ardey 2001]. Unsteady separation bubbles can also themselves induce periodic pressure waves or shocks that cause extra interactions and wear and tear on machine parts, and these waves can travel circumferentially around the wheel as well as longitudinally both upstream and downstream in the axial flow path [Clark and Grover 2006; Davis 2006]. In compression systems, the two major sources of instability (surge and rotating stall) are highly influenced by and coupled to flow separations, and can lead to a decreased operational pressure rise 15%-35% less than optimal in order to maintain a safe distance away from the surge line [Paduano et al. 2001]. In fact, some compressor instabilities are only amplified when individual blades are stalled; once a single blade is stalled however, compressor dynamics can force this “stall-cell” to leap-frog onto adjacent blades all the way around the circumference of the annulus.

In 1996, Malkiel and Mayle studied transition in a separation bubble on a flat plate with a semi-circular leading edge at a $Re = 29,000$ at $FSTI=0.3\%$ [Malkiel and Mayle 1996]. They found that the streamwise progression of intermittency in the shear layer is very similar to attached boundary layer transition, except that transition in a separated shear layer occurs much quicker than in the attached case. The separated shear layer begins in a laminar state and grows slowly. Without much entrainment, the laminar shear layer remains stagnant at a nearly constant pressure and cannot support any transverse pressure gradient (dp/dy), so the streamlines of the upstream flow lose their curvature. As a result, the shear layer travels along a straight line which makes an angle to the surface at the point of separation. The straightening of the shear layer stretches the

boundary layer into less stable velocity profiles, allowing a greater receptivity to instabilities which can trigger transition. When the fundamental Kelvin-Helmholtz shear layer instability reaches a critical strength, the instability waves acting like spanwise vortices interact with its neighboring waves and create subharmonics due to the rolling over and pairing of the Kelvin-Helmholtz vortices. The direction of the shear layer changes after transition occurs, and the shear layer renews its growth which causes an increased mass entrainment leading to the reversed flow of a separation bubble. In the transitional separated bubble, the production of turbulence is normally associated with the appearance of these varying-harmonic instabilities. The shear layer vortices can also entrain turbulent fluid from downstream areas and force it back upstream to interact with the Kelvin-Helmholtz instability development.

Lou and Hourmouziadis recently studied a flat plate with a contoured upper wall which simulated the LPT pressure gradient [Lou and Hourmouziadis 2000]. Their separated bubble transitioned in the shear layer before reattachment and was dominated by the shear layer instabilities. As they progressed down the blade surface into the separated shear layer, they found a dominant frequency of 480 Hz with an amplified super-harmonic at 960 Hz. They found that a free shear layer has less damping ability than an attached boundary layer, and that the maximum vorticity line connecting the inflection points of the velocity profiles trigger the shear layer instabilities, providing energy to them via momentum transfer until transition occurs, followed rapidly by reattachment and turbulence. They also found that the momentum thickness Re at separation increased with freestream Reynolds number. By forcing at 7 Hz they found that an unsteady inflow produces a smaller bubble than steady conditions at the same Re , but the shear layer instabilities were now amplified at 350 and 700 Hz. Their oscillations affected every aspect of the separation bubble except the onset location. Unsteady flow also produced non-harmonic frequencies in the spectrum as well, attributed to the trailing edge vortex shedding. Their work suggests a strong dependence on the momentum thickness when describing flow which encounters separation bubbles.

Breare *et al.* experimentally studied pressure surface separations with a thin LPT for $1 \cdot 10^5 < Re < 3 \cdot 10^5$ [Breare et al. 2002; Breare et al. 2002]. They found that the incident flow angle was the dominant factor in determining the extent of pressure side separation bubbles, with wakes, FSTI, and Re only having a secondary influence – these effects are fundamentally due to the loading characteristic. The separation bubble effectively causes a blockage with high viscous shear which increases the mixing losses. Their 2D RANS simulations showed that wakes had little effect on the pressure side separation bubble length but did in fact produce deterministic behavior in the bubble [Breare and Hodson 2004]. They also found that increasing the thickness of the blade causes the main passage vortex to impinge the suction surface farther downstream, as well as reducing the strength

of secondary flows.

In 2003 and 2005, Schobeiri *et al.* experimentally studied LPT suction side flow separation in a 5-blade cascade under unsteady conditions [Schobeiri et al. 2003; Schobeiri et al. 2005]. Using conditional sampling and wavelet analysis techniques, they found that the wake-generated temporal periodicity remained deterministic throughout the outer inviscid flow but was essentially destroyed once inside the boundary layer. Their emerging picture of wake-disturbed LPT flow is that only a few turbulent spots can evolve on the surface due to the constant buffeting of the boundary layer with wakes. The wakes and turbulent spots convect at different speeds and their interaction induces non-regular velocity fluctuations throughout the boundary layer. They also found that despite the injection of turbulent kinetic energy into the boundary layer by the wakes, transition does not occur instantaneously due to the strong adverse pressure gradient on the suction surface. Their work suggests that LPT blades should be designed with a minimum local adverse pressure gradient. They also propose that the temporal gradient of the turbulence fluctuation ($\partial v_{rms}/\partial t$) is responsible for higher momentum transport into the boundary layer which can control the separation.

In 2005, Dris and Johnson presented work describing transition on concave surfaces at FSTI of 1% and 4% [Dris and Johnson 2005]. A concave curvature, such as that of an LPT suction side, excites a Taylor-Görtler instability leading to a spanwise migration of vortical energy. The upwash and downwash of these vortices cause thickness variations along the span by enhancing the momentum transport in the boundary layer. The upwash portion reduces the skin friction and is less stable in the boundary layer, leading to an earlier transition than in the downwash region. The skin friction increases with curvature while the shape factor decreases due to the fuller velocity profiles. The Taylor-Görtler vortices induced by the curvature also effectively increase the FSTI level and promote an earlier transition. These observations were also used to adapt an intermittency-based attached flow transition model for separated flow conditions [Redford and Johnson 2005].

H

Boundary Layers, Skin Friction, and Separation - DRAFT

In 1904, Ludwig Prandtl showed that the effects of viscosity in a fluid in motion around a body or surface can not be neglected near the surface. The outer fluid away from the wall experiences a region where viscous effects are negligible, called the *inviscid* or *potential* flow. At the wall, the fluid velocity slows from that in the outer potential flow to zero at the surface, a so-called *no-slip condition*. The layer where this deceleration due to viscous effects and larger wall-normal velocity gradient $\partial u/\partial y$ occurs is called the *boundary layer*. It is generally accepted that the boundary layer has a finite height, δ , defined as the wall-normal distance from a surface where the velocity equals 99% of the freestream flow:

$$u(\delta) = 0.99U_\infty \quad (\text{H.1})$$

where U_∞ is the freestream velocity. Any value of viscosity and velocity gradient in the boundary layer is important due to its contribution to the shear stress, τ , defined by Newton's law of friction:

$$\tau = \mu \frac{\partial u}{\partial y} \quad (\text{H.2})$$

where μ is the dynamic viscosity, u is the streamwise velocity, and y is the wall-normal direction. The shear stress defined by Equation H.2 is responsible for momentum transport perpendicular to the main flow direction. At the wall ($y = 0$), the shear stress (τ_w) is related to the skin friction, C_f , on the surface through Equation H.3:

$$C_f = \frac{\tau_w}{\frac{1}{2}\rho U_\infty^2} \quad (\text{H.3})$$

where ρ is the fluid density and U_∞ is the freestream velocity. The skin friction is a non-dimensional measure of the tangential forces acting on the surface due to the viscous fluid passing above, and can be integrated over the surface to provide the friction drag. The heat transfer is also affected by

the wall shear stress through the Reynolds analogy [White 2006]:

$$\frac{|q_w|}{\tau_w} = \frac{|k(\partial T/\partial y)_w|}{\mu(\partial u/\partial y)_w} \approx \frac{k}{\mu} \left| \frac{dT}{du} \right|_w \quad (\text{H.4})$$

where q_w is the heat transfer at the wall and k is the thermal conductivity. Reynolds developed the above analogy to estimate heat transfer in shear layers, and it is only applicable in flows where u and T are similar. The nondimensional form typically relates the skin friction to the Stanton number, C_h , in the following ratio:

$$\frac{C_h}{C_f} = fcn \left(Pr, \frac{x}{L}, geometry \right) \quad (\text{H.5})$$

with

$$C_h = \frac{Nu_x}{Re_x Pr} = \frac{\bar{q}_w}{\rho c_p (T_w - T_\infty) U_\infty} \quad (\text{H.6})$$

$$Nu_x = \frac{q_w x}{k(T_w - T_\infty)} \quad (\text{H.7})$$

$$Re_x = \frac{\rho U_\infty x}{\mu} \quad (\text{H.8})$$

$$Pr = \frac{\mu c_p}{k} \quad (\text{H.9})$$

where T_w and T_∞ are the wall and freestream temperatures, respectively. The Nusselt number, Nu_x , is a dimensionless heat transfer parameter. The dimensionless Reynolds number, Re_x , relates the momentum to viscous forces. The Prandtl number, Pr , is the dimensionless ratio relating the viscous to thermal diffusion rates. Other important boundary layer parameters include the displacement thickness, δ^* , and the momentum thickness, θ , defined as:

$$\delta^* = \int_0^\delta \left(1 - \frac{u}{U_\infty} \right) dy \quad (\text{H.10})$$

$$\theta = \int_0^\delta \frac{u}{U_\infty} \left(1 - \frac{u}{U_\infty} \right) dy \quad (\text{H.11})$$

The displacement thickness is a measure of how far the outer inviscid flow is displaced away from the wall due to the drop in velocity in the viscous boundary layer, while the momentum thickness is a measure of how much momentum is lost from the inviscid flow due to the same velocity drop.

Applying the boundary layer concept and a proper order of magnitude analysis simplifies the governing equations for continuum fluid flow, the *Navier-Stokes* equations. One such simplified equation is the boundary layer x -momentum equation for an incompressible fluid, which can be found from any standard fluid mechanics text, as presented in Equation H.12:

$$u \frac{\partial u}{\partial x} + v \frac{\partial u}{\partial y} = -\frac{1}{\rho} \frac{dp}{dx} + \nu \frac{\partial^2 u}{\partial y^2} \quad (\text{H.12})$$

where x is the streamwise direction, v is the wall-normal velocity, ρ is the density of the fluid, dp/dx is the streamwise pressure gradient, and ν is the kinematic viscosity. Applying the x -momentum boundary layer equation at the wall produces the compatibility condition shown in Equation H.13:

$$\mu \left(\frac{\partial^2 u}{\partial y^2} \right)_w = \frac{dp}{dx} \quad (\text{H.13})$$

since $u(x, 0) = 0$ and $v(x, 0) = 0$ at $y = 0$. The compatibility condition shows that the curvature, or second derivative, of the velocity profile at the wall is a function of the streamwise pressure gradient, and the curvature changes sign as the pressure gradient changes sign. Figure H.1 illustrates the boundary layer velocity profiles and first and second derivatives for a favorable ($dp/dx < 0$) and an adverse pressure gradient ($dp/dx > 0$). For flows with a favorable pressure gradient, i.e. the pressure

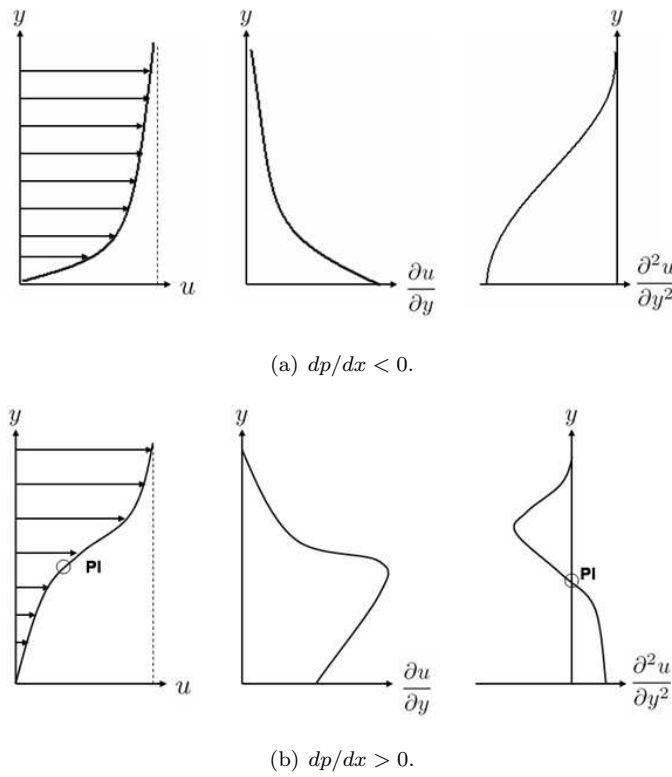


Figure H.1: Boundary layer velocity distributions and derivatives.

decreases with x as in Figure H.1(a), Equation H.13 at the wall gives $(\partial^2 u / \partial y^2)_w < 0$, and therefore $\partial^2 u / \partial y^2 < 0$ over the entire boundary layer thickness. In flows with adverse pressure gradients as in Figure H.1(b), Equation H.13 gives $(\partial^2 u / \partial y^2)_w > 0$. But since at a distance away from the wall $\partial^2 u / \partial y^2 < 0$, there must be a point in the boundary layer where $\partial^2 u / \partial y^2 = 0$. This location is called an *inflection point*, denoted by PI in Figure H.1(b). This has important consequences for flows that are separated.

Separation is a flow condition which arises due to the combination of an adverse pressure gradient and viscous friction forces slowing down the fluid in the boundary layer. In a gas turbine engine, separation effects are most prevalent in the high aspect ratio blading (compressors and LP turbines) where endwall generated turbulence does not reach the midspan, allowing a laminar flow more prone to separation. By again applying boundary layer theory and a proper order of magnitude analysis to the Navier-Stokes equations, the y -momentum equation for an incompressible fluid reveals:

$$\frac{dp}{dy} = 0 \quad (\text{H.14})$$

This shows that the surface-normal pressure gradient does not change throughout the boundary layer, which implies that the boundary layer and surface will experience the same streamwise pressure distribution as the outer inviscid flow. In separated flow, fluid in the boundary layer loses enough kinetic energy due to viscous friction that its reduced momentum cannot overcome the increasing pressure, thereby decreasing the velocity enough to cause a reversal in the flow direction at the surface. The reversed flow near the wall results in a thickening of the boundary layer, which in turn causes an increase in the massflow transported away from the surface and into the outer flow. Since the velocity profile at separation must have a point of inflection, it follows that separation can only occur when the outer flow experiences an adverse pressure gradient. In low- Re LPT environments, separated flow is caused by the adverse pressure gradient encountered on the suction surface due to the curvature of the blade. The location of separation onset is also associated with a zero skin friction at the wall, i.e.

$$\tau_w = \mu \left(\frac{\partial u}{\partial y} \right)_w = 0 \quad (\text{H.15})$$

For low- Re conditions, the LPT performance is completely dictated by the extent of flow separation.

The point of inflection in the velocity profile also has important implications for the stability of such flows. Using an inviscid perturbation form of the governing equations [Schlichting 2001], Lord Rayleigh (1880-1913) was able to show that the presence of an inflection point is a *necessary condition* for the appearance of unstable waves, the so-called *point of inflection criterion*. In 1935 W. Tollmien proved that the presence of an inflection point is a *sufficient condition* for the presence of unstable, amplified waves. Keeping in mind our earlier discussion about pressure gradients, the above conditions imply that pressure drops are stabilizing while pressure increases are destabilizing. This in turn implies that the point of the pressure minimum on a body has a fundamental influence on the laminar to turbulent transition in a boundary layer flow.

I

More on Instability and Transition - INCOMPLETE, needs significant revision...

The problem of the transition from laminar to turbulent flow in the boundary layer is unparalleled in having attracted the interest of investigators for so many years. Despite the enormous amount of research effort devoted to it, our understanding of the problem is still far from complete.

That was a statement made by Itiro Tani in 1969 when he published an article detailing then-current philosophy regarding the transition of laminar flow into turbulent flow [Tani 1969]. As mentioned before, the location and extent of the transition region is affected by many factors: development of freestream turbulence intensity and length scale, pressure gradient, surface curvature, wall roughness, heating and cooling, three-dimensionality, and unsteadiness, to name the biggest players.

Langtry and Menter recently classified the current available methods used in CFD applications for predicting the transition to turbulence into 3 different categories: low- Re turbulence models, e^N methods, and the use of experimental correlations [Langtry and Menter 2005]. Low- Re turbulence models are used to calibrate wall damping functions and are based on reproducing the viscous sublayer behavior. These models attempt to predict the onset of turbulence, which is not technically a transition model, and are only applicable to bypass transition situations. It is also generally accepted now that turbulence modeling without transition modeling is unreliable. The second class of methods, developed in the 1950s, use an e^N parameter and rely on local linear stability theory and a parallel flow assumption to calculate the growth of a disturbance amplitude from a “neutral point”

inside the boundary layer to the point of transition. The onset of transition is assumed to occur once the e^N parameter exceeds some prescribed value, which is usually determined from wind tunnel tests or other experiment, making the e^N methods at least semi-empirical. Since the e^N methods are based on linear stability theory, they fail to account for non-linear growths such as surface roughness or high freestream turbulence, and this is why Navier-Stokes codes using e^N prediction techniques typically require a coupling to another boundary layer code. The e^N method has enjoyed most of its success in external aerodynamics such as the flow around airplane wings. As no model has achieved a desired level of accuracy, the gas turbine industry prefers the third class of transition prediction methods: the use of experimental correlations. These methods usually correlate levels of turbulence, intermittency, or pressure gradient with a momentum thickness Reynolds number, and may require boundary layer search algorithms with interpolation methods in some modern CFD codes using unstructured grids or parallel computing.

Stability Theory

As mentioned above, transition and turbulence modeling is very difficult to accomplish within a certain degree of accuracy. The difficulty lies in the myriad of factors influencing the transition from laminar to turbulent conditions, as well as the fact that many of those factors are not independent of each other. Therefore, no singular theory has been able to accurately describe the breakdown from laminar flow into turbulence. Consequently, most modeling methods have included empirical correlations in order to remain effective. Classical methods of analyzing instability in fluid dynamics have focused on analyzing the equations of motion with linear stability theory.

The basic idea behind linear stability theory is to superimpose small *linear* disturbances onto a local, undisturbed boundary layer state and determine if the perturbations grow or decay [Reed et al. 1996]. The analysis is performed by linearizing the complete, unsteady Navier-Stokes equations about the basic state. To obtain the Orr-Sommerfeld linearized equations, substitute the perturbed quantities ($x_j = X_j + x_j'$) into the Navier-Stokes set, neglect all products of the primed disturbance quantities, and then subtract out the basic flow state (X_j). Using the separation of variables technique can further simplify the set into ordinary differential equations. Linear stability theory provides information about the fundamental linear modes of instability, but fails to account for nonmodal growth and interaction, characteristics which are a rule of thumb for low-pressure turbine flows. Due to the eigenvalue nature of this process, results give the frequencies which amplify in the boundary layer but gives no account for the initial amplitudes of those frequencies.

In spite of its shortcomings, linear stability theory can provide useful information. Theory pre-

dicts for incompressible streamwise instabilities there is only one mode of interest as the least stable, the Tollmien-Schlichting (T-S) instability. Compressibility and centrifugal instabilities (Taylor-Görtler) also add modes. For 2D subsonic flows, the inviscid instability proves to be the inflection point or *Rayleigh instability*. As mentioned before, this is a fundamental instability in low-pressure turbine flows. Viscosity is mostly stabilizing until it lowers the Re too significantly. Viscosity also imposes the no-slip condition which creates the Reynolds stresses that can also agitate subsonic instabilities. Reed *et al.* suggests that natural transition along the T-S mode occurs over a short distance. Concave curvature (suction side of LPT) has a destabilizing effect while convex curvature (pressure side of LPT) is stabilizing. In 3D boundary layers, such as those in actual turbomachinery, the largest shear stress at the inflection points presents the most unstable location for the adverse pressure gradient to excite instabilities. In 2000, Schmid analyzed linear stability theory in wall-bounded shear flows and concluded that bypass transition, which is the mode of transition most often experienced in low-pressure turbine flows, results from nonmodal growth of disturbances not relying on the least stable mode (T-S) of the flow [Schmid 2000]. Schmid explained how the nonlinear terms in the Navier-Stokes equations do not directly contribute to energy growth or decay, but rather distribute energy between different spatial scales. This scale redistribution has an influence in the growth of the nonmodal transition process. In 2003 and 2005, Rist, Augustin, and Wagner chose the vorticity-velocity formulation of the Navier-Stokes equations to study the effects of instability waves on a flat plate laminar separation bubble using direct numerical simulation (DNS) coupled with linear stability analyses [Augustin et al. 2003; Rist and Augustin 2005]. They found that the laminar separation bubble decreases the local skin friction while it creates a thick wake, increasing the drag. They also found that 2-3 times less amplitude was needed with unsteady sinusoidal disturbances than steady at eliminating the separation bubble. The unsteady forcing also directly provided the initial amplitudes for the Orr-Sommerfeld prediction for laminar to turbulent transition. Their analysis also suggested an optimal disturbance injection location for separation control (using sinusoidal disturbances) well upstream of the onset position. Their 3D analysis showed an optimal disturbance location 10 times more upstream than the 2D prediction.

Govindarajan and Narasimha applied coordinate transformation to the standard Orr-Sommerfeld stability equations in order to correct for non-parallel flows under pressure gradients [Govindarajan and Narasimha 1995]. They found that non-parallelism, as occurring in LPT flows, causes a growth in higher frequency fluctuations, especially in low Re situations; this effect is mitigated in favorable pressure gradients but agitated under adverse pressure gradients. Overall results show that stability in non-parallel flows is a strong function of the streamwise variation in surface-normal distance between walls.

Modes of Transition

There are five basic modes of transition in gas turbine engines: natural, bypass, separated-flow, periodic-unsteady, and reverse [Mayle 1991]. Natural transition is the mode most thought of when “transition” is mentioned, and occurs as a weak instability grows in a laminar boundary layer until amplification into turbulence. Tollmien and Schlichting were the first to describe this process, and as such the instability waves causing natural transition are usually called Tollmien-Schlichting, or T-S waves [Schlichting 2001]. The T-S waves begin as 2D velocity variations, and soon become three-dimensional, interacting with and producing 3D variations in the mean flow. The 2D velocity variations can be caused by an adverse pressure gradient, as occurring with the flow around low-pressure turbine blades. The 3D variations grow until they mature into local regions of very high shear, creating small localized regions of turbulence in a quasi-laminar flow. These localized regions of turbulence develop into hairpin-shaped vortices, which continue to grow in their influence until transition of the mean flow begins. Although the LPT environment is highly disturbed, evidence of T-S frequencies in transitioning shear layers over separation bubbles have been found, although its multiple frequency peak nature suggests a Kelvin-Helmholtz instability [Volino 2002b]. Nonetheless, Walker estimates the period of the most unstable T-S frequency for flows in adverse pressure gradients to follow Equation I.1:

$$period = 2.0(\nu/u_c^2)Re_\theta^{3/2} \quad (I.1)$$

The above equation was formulated while examining the velocity profiles of Falkner-Skan flows and assumes that the T-S waves force the transition process once per cycle [Walker 1989]. Others have more recently used derivatives of Equation I.1 to identify T-S spectral content in transitioning regions upstream of separation bubbles and in the shear layer above [Zhang et al. 2002].

The term *bypass* was originally coined by Morkovin circa 1969, where it represented several things including the production of turbulent spots. Mayle’s review considers bypass transition as that which is characterized by large disturbances in the freestream and therefore *bypasses* the T-S instability growth of the natural transition process [Mayle 1991]. Here, linear stability theory is irrelevant. Since the first few stages of natural transition have been bypassed, theories for bypass transition have classically included turbulent spots and their production, growth, and convection. Separated-flow transition occurs when a laminar boundary layer separates and transitions in the free shear layer above the bubble. Turbulence can force a reattachment which forms the bubble. This type of transition can occur near the leading edges of blades and near the point of minimum pressure on the suction surface sides. The bubble length is process dependent, and all stages of the natural transition can occur in the shear layer; T-S instabilities have been observed to occur in

a long enough separation bubble. Long bubbles produce large losses and change the gas exit flow angles, which should be avoided. Short bubbles have less effect, and have actually been thought of as a control mechanism since they can induce transition. Of all of the modes, separated-flow transition is the most crucial for compressor and LPT design.

Periodic-unsteady transition occurs due to the nature of turbomachinery flows: they are inherently periodic and unsteady, so the transition processes taking place are also unsteady and periodic. Wake-induced transition is one example; shocks can also cause periodicity. These unsteady modes of transition also bypass the first few stages of natural transition and are so disruptive that they coalesce into turbulent spots and strips which grow and propagate downstream. Between these spots and strips, other modes of transition can occur simultaneously. Reverse transition, often called “relaminarization”, occurs where a previously turbulent or transitional region is affected so that it becomes laminar, similar to the events occurring after a wake or turbulent spot has recently convected from an area. An instantaneous snapshot of the flow over a single airfoil may include laminar flow near the leading edge, followed by a wake- or shock-induced transition which is in turn replaced by a relaminarization with subsequent transition to turbulence occurring over multiple modes all at once. Mayle points out one of the unresolved issues is whether or not the linear instabilities show up in regions of wake and shock interaction or strong adverse pressure gradient such as that occurring over the suction surface of the LPT. Halstead *et al.* have considered the affects of wakes so important to transition in turbomachinery as to define only two modes: wake-induced, and everything else (non-wake-induced) [Halstead et al. 1997a].

Transition Modeling

One of the first early transition models was due to Liepmann in 1945, which correlated a ratio of the fluctuating component of velocity to the local friction velocity via $u'/u_* = 7.5$ at transition. Later work would modify the value from 7.5 to 3.0 or include the range from 3.0 to 7.4, but these types of correlations may be more indicative of turbulent spot activity rather than transition onset location, and may require the use of conditional sampling techniques [Praisner and Clark 2004]. The behavior of u' and v' in the transitioning boundary layer should be viewed as the distribution of turbulent kinetic energy in the shear flow [Tennekes and Lumley 1972]. The u' component will be larger than v' since it receives the kinetic energy production from the mean flow. The transfer of energy is accomplished by the nonlinear pressure fluctuation, $\overline{p'\partial u'_i/\partial x_i}$. As transition completes, the turbulent eddies are becoming smaller until viscous dissipation equals the amount of turbulent energy production in the freestream.

Another leap for transition modeling was due to Emmons in 1951 when he proposed his turbulent spot theory [Emmons 1951]. Using water channel flow visualization, he showed that transition occurs through a random production of turbulent spots within the laminar boundary layer. As the spot travels over the surface, flow conditions alternate between turbulent and laminar. Initial findings of turbulent spots were triangular in shape and grew as they convected downstream, spreading at nearly 11 degrees at an average velocity of $0.7U_\infty$ until the flow was fully turbulent. Later work would find a dependence of the spreading angle and convection speed on the pressure gradient, and modified the average velocity to $0.667U_\infty$ for zero pressure gradient flows [Clark et al. 1994b]. Using fast-response heat flux gauges, Clark *et al.* have verified that the lateral spreading of spots is due to the “local destabilization of the laminar boundary layer at their edges” [Clark et al. 1992]. Emmons believed that transition is a stochastic, 3D, unsteady process that occurs where both laminar and turbulent conditions coexist. Previously transition was considered a 2D phenomenon. Emmons first treated transition by grouping laminar and turbulent solutions together at a transition location which was found by matching the two momentum thicknesses, or where $\theta_L(x_{tr}) = \theta_T(x_{tr})$. This method worked for total loss and heat transfer when transition was short, but was too inaccurate with shear stress and heat transfer at x_{tr} . Numerical methods using Emmons’ philosophy normally extrapolated back turbulent information into the transition zone. Emmons then presented a statistical theory of transition which depended on an expression for the fraction of time the flow is turbulent, given the label “intermittency” (γ_{int}):

$$\gamma_{int} = 1 - \exp[-\iiint g dx_o dz_o dt_o] \quad (\text{I.2})$$

where $g = g(x, z, t)$ is a turbulent spot production parameter. When the intermittency equals 1, the flow is fully turbulent. Flow quantities (Q) are then determined as a combination of laminar and turbulent values:

$$Q = (1 - \gamma)Q_L + \gamma Q_T \quad (\text{I.3})$$

Schubauer and Klebanoff would soon correct Emmons’ uniform distribution of spot production theory and instead propose a localized, concentrated inception of spots, possibly the precursor to Narasimha’s concentrated breakdown hypothesis [Schubauer and Klebanoff 1956]. They also added that turbulence always moves downstream followed by laminar flow which remains in a state of calm for a period of time before transition begins again. This phenomena would soon be called “relaminarization” or “reverse transition”. Schubauer and Klebanoff also found the leading and trailing edges of the spots in a zero-pressure gradient flow travel at $0.88U_\infty$ and $0.5U_\infty$, respectively. The calmed region following a turbulent spot is identified with an elevated but decreasing shear stress which suppresses instabilities and remains resistant to flow separation due to its fuller laminar-like velocity profile [Halstead et al. 1997a]. This calmed region can be terminated by subsequent

passing of turbulent spots or other transitional phenomena (including natural breakdown), can significantly extend the length of transition, and is the link between the transitional events occurring in turbomachinery boundary layers. The effectiveness of calmed regions in suppressing separation between wakes is a function of the freestream turbulence level [Halstead et al. 1997b].

Equation I.3 has been shown to be a good approximation for δ , δ^* , and H , while exact for θ [Dhawan and Narasimha 1958]. This could be why many transition theories use θ for their correlation parameter. In 1957 and 1985, Narasimha and coworkers showed that the streamwise mean velocity through transition to turbulence on a flat plate collapse onto a single curve governed by a one-parameter family based on intermittency [Dhawan and Narasimha 1958; Narasimha 1985]. This was defined as:

$$\gamma_{int} = 1 - e^{-A\xi^2} \quad (\text{I.4})$$

where

$$\xi = \frac{x - x_{tr}}{x_{\gamma_{int}=0.75} - x_{\gamma_{int}=0.25}} \quad (\text{I.5})$$

and $A = 0.412$. Thus, no matter the cause, all transitioning regions on a flat plate with zero pressure gradient fit a single universal intermittency distribution, Equation I.4. They presented a method to measure intermittency from hot-wire anemometry signals, and when γ_{int} was measured, the best way to determine x_{tr} was to plot the data in the form:

$$F(\gamma_{int}) = [-\ln(1 - \gamma_{int})]^{1/2} \quad (\text{I.6})$$

Their “concentrated breakdown” hypothesis defined transition as the streamwise location where all turbulent spots are formed randomly in time and cross-stream (spanwise) position. Together with the concentrated breakdown assumption, they developed another expression for Emmons’ turbulent spot production parameter g :

$$g(x) = n\delta(x - x_{tu}) \quad (\text{I.7})$$

where n is the turbulent spot production rate per unit time and unit distance, $\delta(x)$ is the Dirac delta function, and x_{tu} is the location where turbulent spots are formed. The corresponding “universal” intermittency distribution is:

$$\gamma_{int}(x) = 1 - \exp\left[-\frac{n\sigma}{U_\infty}(x - x_{tr})^2\right], (x \geq x_{tu}) \quad (\text{I.8})$$

where σ is Emmons’ dimensionless spot propagation parameter, originally estimated at 0.1. Equation I.8 could also be represented in nondimensional form according to:

$$N = \frac{n\sigma\theta_{tr}^3}{\nu} \quad (\text{I.9})$$

where θ_{tr} is the momentum thickness at transition and ν is the kinematic viscosity. Gostelow *et al.* later correlated the nondimensional breakdown parameter N by plotting the $F(\gamma_{int})$ function and using the Pohlhausen pressure gradient parameter (λ_θ) to account for different levels of turbulence (Tu) and pressure gradient [Gostelow et al. 1994]:

$$N = \begin{cases} 0.86 \cdot 10^{-3} \exp[2.134\lambda_\theta \ln(Tu) - 59.23\lambda_\theta - 0.564\ln(Tu)] & \lambda_\theta \leq 0 \\ 0.86 \cdot 10^{-3} \exp[-0.564\ln(Tu)] & \lambda_\theta > 0 \end{cases} \quad (\text{I.10})$$

Using the nondimensional breakdown parameter recasts the universal intermittency distribution:

$$\gamma_{int} = 1 - \exp \left[- \left(\frac{x - x_{tr}}{\theta_{tr}} \right)^2 \frac{N}{Re_{\theta_{tr}}} \right] \quad (\text{I.11})$$

Narasimha showed that the breakdown rate scales with boundary layer thickness and viscous diffusion time δ_t^2/ν . Their work also led to transition location and length predictions based on the intermittency concept, as well as corrections for pressure gradients and compressibility. Simple uses of intermittency modeling typically modify the eddy viscosity μ_t according to the intermittency. Sharma soon developed a similar thermal intermittency factor ($\gamma_{int,h}$) using the Pohlhausen pressure gradient parameter, although this approach implies two different types of spots, one for a “momentum turbulence” and one for a “thermal turbulence”:

$$\gamma_{int,h} = 1 - \exp[-(\hat{n}\sigma)_h (Re_x - Re_{x,tr})^2] \quad (\text{I.12})$$

with $(\hat{n}\sigma)_h = \hat{n}\sigma[1 + (21 \text{ or } 7.25)\lambda_\theta]^{-2.68}$ [Sharma 1987]. Common approaches with the intermittency concept use experimental correlations for transition onset and length.

Most methods of modeling transition have used some sort of empirical correlation, sometimes together with the intermittency concept, to determine transition onset and length. In 1969 the most accurate way to predict transition was to assume a range of values for the local momentum thickness Reynolds number at transition onset, $Re_{\theta,tr}$, and compare this with the local value until a match occurred, signalling transition [Tani 1969]. The range was typically constructed from experimental correlations. The main factors back then were believed to be FSTI and pressure gradient.

In 1980, Abu-Ghannam and Shaw studied a flat plate with FSTI from 0.3 to 5% under typical turbomachinery pressure gradients without separation [Abu-Ghannam and Shaw 1980]. They produced a set of empirical relationships for the start and end of transition over various conditions using the Pohlhausen pressure gradient parameter, λ_θ . Their method essentially compares laminar skin friction to local values to determine the location of transition onset, which was a change from intermittency-based models. For zero pressure gradients, the start and end of transition is given by:

$$\begin{aligned} Re_{\theta S} &= 163 + \exp(6.91 - FSTI) \\ Re_{\theta E} &= 2.667 Re_{\theta S} \end{aligned} \quad (\text{I.13})$$

For non-zero pressure gradients, or $\lambda_\theta \neq 0$, transition is signalled when the momentum thickness Re is equal to:

$$Re_\theta = 163 + \exp \left[F(\lambda_\theta) - \frac{F(\lambda_\theta)}{6.91} FSTI \right] \quad (I.14)$$

with

$$F(\lambda_\theta) = \begin{cases} 6.91 + 12.75\lambda_\theta + 63.64(\lambda_\theta)^2, & \lambda_\theta < 0 \\ 6.91 + 2.48\lambda_\theta - 12.27(\lambda_\theta)^2, & \lambda_\theta > 0 \end{cases} \quad (I.15)$$

$$\lambda_\theta = \frac{\theta^2}{\nu} \frac{dU_\infty}{dS} \quad (I.16)$$

Their natural transition model was considered applicable in flows up to a freestream turbulence level of 10%. Presenting detailed quantitative development of the boundary layer, they suggested that the past history of the pressure gradient affects transition more than the local value at transition onset. The start and end of transition is mainly a function of the turbulence level and the pressure gradient, and the boundary layer parameters ($\theta, H, C_f, \gamma_{int}$) are related by correlations to the distance from the start of transition.

In 1991, Mayle compiled an extensive review of transition in turbomachinery and showed how transition information obtained at low freestream turbulence levels is useless for the gas turbine designer since FSTI levels in real turbomachines is quite high [Mayle 1991]. Primary factors influencing transition in turbomachines include FSTI, pressure gradient, and the periodic, unsteady passing of wakes. Mayle says the onset of transition is a function of the level and scale of freestream turbulence, wakes and shock waves, and the amount of acceleration occurring in the flow, while transition length mainly depends on FSTI and the pressure gradient. Secondary factors influencing transition include surface roughness, surface curvature, compressibility, and heat transfer. Transition on gas turbine airfoils can be a combination of types, which implies that different locations of the same blade can experience different modes of transition all at the same time. Also, transition and separation can occur within the same area of a surface, showing up as alternating turbulent spots and laminar separation bubbles both interrupted by wakes, which lends at least some conceptual support to the modeling of transition by intermittency. In general, $Re_{\theta tr}$ increases with an increase in acceleration or a decrease in FSTI. In gas turbines, the magnitude of FSTI forces acceleration to have a secondary effect. To model transition and separation correctly for design purposes, Mayle suggests a high inlet turbulence level with appropriate length scales. Turbulent heat transfer levels are generally 3 to 5 times higher than in laminar conditions. Mayle suggests that if transition occurs before the pressure minimum it will be stretched by the acceleration while after the pressure minimum results in a shorter transition due to the adverse pressure gradient. Borrowing the intermittency concepts from Emmons and Narasimha (particularly $F(\gamma_{int})$), Mayle then constructed several correlations for transition onset, turbulent spot generation rates, and transition length, although the transition

onset correlation has been shown to overpredict Re_θ at transition onset [Simon and Ashpis 1996]. Mayle's 1991 correlations have also been updated by others [Gostelow et al. 1994].

By 1993, Walker identified 4 main uses of intermittency to identify the location of transition: derivatives of Mayle's 1991 correlation of $n\sigma$ with the turbulence level and a pressure gradient parameter, $K = \lambda_\theta/Re_\theta^2$ for both short and long bubbles; correlations of $N = n\sigma Re_{\theta,t}^3$ with the turbulence level and the Pohlhausen pressure gradient parameter λ_θ ; correlations based on linear stability theory and a minimum transition length; and correlations of $N = n\sigma Re_{\theta,t}^3$ in terms of turbulence only, which is a subset of the second use [Walker 1993]. Alternate approaches solving a separate transport equation for the intermittency have been developed by several groups. In 1992, Cho and Chung presented a hybrid $\kappa - \epsilon - \gamma_{int}$ turbulent transport model for free shear flows used to provide accurate cross-stream intermittency distributions [Cho and Chung 1992]. Steelant and Dick later proposed their own intermittency transport model for near-wall flows and was developed to match the streamwise distributions using the correlations of Abu-Ghannam and Shaw [Steelant and Dick 1996]. They used a conditioned form of the Navier-Stokes equations whereby the intermittency of transition was handled by conditioned averages which are taken during the fraction of time the flow is turbulent or laminar. This type of technique, labeled "conditional sampling", is not uncommon in transition studies [Qiu and Simon 1997], and filters a data set to only examine the portion which contains transitional or turbulent events as judged by a predefined condition of transition or turbulence [Antonia 1981]. Volino used conditional sampling and wavelet analysis for a transitional boundary layer and found that nonturbulent and turbulent regions of the flow both exhibit self-similarity in their respective velocity profiles, lending support to the modeling of transition with intermittency [Volino 2003; 2005]. Steelant and Dick's intermittency transport equation is applicable for zero, favorable and adverse pressure gradients, and was later modified for high freestream turbulence environments [Steelant and Dick 2001].

In LPT flows, the onset and end of transition are typically in different regions where the pressure gradient may change sign. Solomon *et al.* suggests that rapid pressure gradient changes, such as those encountered in the LPT section, cause deviations from Narasimha's universal intermittency distribution [Solomon et al. 1996]. Solomon *et al.* therefore developed a method to calculate intermittency in regions of changing pressure gradients by forcing the turbulent spot spreading half-angle α and spot propagation parameter σ to be functions of the Pohlhausen pressure gradient parameter:

$$\sigma = 0.03 + \frac{0.37}{0.48 + 3.0\exp(52.9\lambda_\theta)} \quad (\text{I.17})$$

and

$$\alpha = 4 + \frac{22.14}{0.79 + 2.72\exp(47.63\lambda_\theta)} \quad (\text{I.18})$$

This is an obvious step since it has been shown experimentally that these parameters do in fact depend on pressure gradient [Clark et al. 1994b]. Using Gostelow's relation (I.10), the spot generation rate, n , is assumed to depend only on the conditions at transition onset. The resulting intermittency expression developed by Solomon *et al.* is presented below:

$$\gamma_{int} = 1 - \exp \left[-n \int_{x_t}^x \frac{\sigma}{\tan \alpha} \frac{dx}{U} \int_{x_t}^x \tan \alpha dx \right] \quad (I.19)$$

A next step in intermittency transport equation modeling came with Suzen and Huang, who combined Cho and Chung's model with Steelant and Dick's [Suzen and Huang 1999]. Taking the best from each model, they blended Abu-Ghannam and Shaw's development of streamwise intermittency from Cho and Chung (Abu-Ghannam and Shaw) with the cross-stream modeling afforded by Steelant and Dick's model. This method seems to work across a wide variety of transitional operating conditions [Suzen et al. 2003]. To gain an appreciation of how an additional intermittency transport equation functions with the standard set of Navier-Stokes equations, the model of [Suzen et al. 2003] is presented below:

$$\begin{aligned} \frac{\partial \rho \gamma_{int}}{\partial t} + \frac{\partial \rho u_j \gamma_{int}}{\partial x_j} = & (1 - \gamma_{int}) \left[(1 - F) 2 C_0 \rho \sqrt{u_k u_k} f(s) f'(s) \right. \\ & + F \left(\frac{C_1 \gamma_{int}}{k} \tau_{ij} \frac{\partial u_i}{\partial x_j} - C_2 \gamma_{int} \rho \frac{k^{2/3}}{\epsilon} \right. \\ & \times \left. \frac{u_i}{\sqrt{u_k u_k}} \frac{\partial u_i}{\partial x_j} \frac{\partial \gamma_{int}}{\partial x_j} \right] + C_3 \rho \frac{k^2}{\epsilon} \frac{\partial \gamma_{int}}{\partial x_j} \frac{\partial \gamma_{int}}{\partial x_j} + \frac{\partial}{\partial x_j} \\ & \times \left([(1 - \gamma_{int}) \gamma_{int} \sigma_{\gamma l} \mu + (1 - \gamma_{int}) \sigma_{\gamma t} \mu_t] \frac{\partial \gamma_{int}}{\partial x_j} \right) \end{aligned} \quad (I.20)$$

with the distributed breakdown function

$$f(s) = \frac{as'^4 + bs'^3 + cs'^2 + ds' + e}{gs'^3 + h} \quad (I.21)$$

where $s' = s - s_{tr}$, s is the distance along the streamwise coordinate, and s_{tr} is the transition location. The coefficients are:

$$\begin{aligned} a &= 50 \sqrt{\frac{n\sigma}{U}} & b &= -0.4906 & c &= 0.204 \left(\frac{n\sigma}{U} \right)^{-0.5} \\ d &= 0.0 & e &= 0.04444 \left(\frac{n\sigma}{U} \right)^{-1.5} \\ h &= 10e & g &= 50 \end{aligned} \quad (I.22)$$

The shear stress is

$$\tau_{ij} = \mu_t \left[\frac{\partial u_i}{\partial x_j} + \frac{\partial u_j}{\partial x_i} - \frac{2}{3} \frac{\partial u_k}{\partial x_k} \delta_{ij} \right] - \frac{2}{3} \rho k \delta_{ij} \quad (I.23)$$

The blending function F uses the turbulent kinetic energy, k , and the vorticity, W :

$$F = \tanh^4 \left[\frac{k/W\nu}{200(1 - \gamma_{int}^{0.1})^{0.3}} \right] \quad (I.24)$$

The remaining model constants for Suzen and Huang's intermittency transport model are:

$$\begin{aligned} \sigma_{\gamma l} &= \sigma_{\gamma t} = 1.0 & C_0 &= 1.0 & C_1 &= 1.6 \\ C_2 &= 0.16 & C_3 &= 0.15 \end{aligned} \quad (I.25)$$

The intermittency is incorporated by multiplying the eddy viscosity (μ_t) obtained through a turbulence model by the intermittency:

$$\mu_t^* = \gamma_{int}\mu_t \quad (\text{I.26})$$

Suzen and Huang chose Menter's SST (shear stress transport) turbulence model, which is touted as combining the $k-\epsilon$ model developed for freestream independence together with Wilcox's $k-\omega$ model developed with wall accuracy in mind [Menter 1993]. This method of assigning the effective eddy viscosity (μ_t^*) is accurate as long as the Reynolds stresses in the nonturbulent part can be neglected [Simon and Stephens 1991]. For attached flow, transition onset is determined by a modified version of Abu-Ghannam and Shaw's momentum thickness Reynolds correlation, as presented in [Huang and Xiong 1998]:

$$Re_{\theta_{tr}} = (120 + 150Tu^{-2/3})\coth[4(0.3 - K_t \cdot 10^5)] \quad (\text{I.27})$$

where K_t is the minimum value of the acceleration parameter in the downstream deceleration region. A more involved model, which adds an additional equation for the transition momentum thickness Reynolds number, has also been recently developed [Menter et al. 2006]. The newer model combines intermittency development with empirical correlations for transition onset and length, which allows other users to incorporate their own proprietary models for use in 3D design codes.

In the mid to late 1990s, Mayle and co-workers again studied the effects of various levels and scales of turbulence on laminar and pre-transitional boundary layers [Dullenkopf and Mayle 1995; Mayle and Schultz 1996; Mayle et al. 1998]. First, they showed that an increased freestream turbulence level on the suction side resulted in an earlier transition, while on the pressure side it results in a greatly increased laminar heat transfer. They constructed several correlations for turbulence effects and categorized them by scale into two categories: large eddies and small eddies. Others have also found length scale important [Moss and Oldfield 1992; Rivir 1996]. Volino found that an increased length scale adds separation resistance [Volino 2002a], while others have found that length scale has no effect on transition location [Butler et al. 2001]. From linear stability calculations, Mayle *et al.* found a representative band of frequencies which optimally disrupt the laminar boundary layer to fluctuate around the value given by $f\lambda = \text{constant} \cdot U_\infty/\delta$, where the length scale of the correlating eddies is nearly 16δ . The *constant* took values of 0.02 - 0.03. Next, they showed that any fluctuation in the freestream produces a proportional one in the boundary layer that initially grows linearly with distance. This means that turbulence in the boundary layer is not only produced by freestream diffusion, but also by pressure fluctuations. Volino and Simon call this effect "buffeting", whereby freestream pressure fluctuations push the boundary layer fluid in the wall-normal direction, resulting in u' and v' perturbations that cause varying levels of frequencies in the boundary layer [Volino and Simon 2000]. Volino and Simon also found that the boundary layer fluctuations are

associated with larger scale eddies in higher FSTI cases, while they are attributed to streamwise unsteadiness in lower FSTI environments; others have agreed [Graveline and Sjolander 2005]. Mayle *et al.* also found that the higher frequency turbulence is damped out in the boundary layer, while lower frequency turbulence penetrates and promotes transition; thus the boundary layer acts as a low-pass filter. Finally, they showed that the effects of increased turbulence on turbines include increased laminar heat transfer in the stagnation region near the leading edge of the pressure side as well as earlier transition and increased turbulent heat transfer on the suction side. A representative wave number of effective turbulence range correlates to $k_\delta = 0.11/\delta$. They found the turbulence that affects heat transfer the most is not the integrated (measured) level of turbulence in the freestream, but rather the turbulence corresponding to a band of wave numbers around k_δ selected by the boundary layer. The scales of turbulence most effective on triggering pre-transitional boundary layers is that centered around the Kolmogorov dissipative range.

References

- ABU-GHANNAM, B. AND SHAW, R. 1980. Natural Transition of Boundary Layers - The Effects of Turbulence, Pressure Gradient, and Flow History. *Journal of Mechanical Engineering Sciences* 22, 5, 213–228.
- ADAMCZYK, J. 2000. Aerodynamic Analysis of Multistage Turbomachinery Flows in Support of Aerodynamic Design. *ASME J. Turbo.* 122, 189–217.
- ANTHONY, R., JONES, T., AND LAGRAFF, J. 2005. High Frequency Surface Heat Flux Imaging of Bypass Transition. *Journal of Turbomachinery* 127, 2, 241–250.
- ANTONIA, R. 1981. Conditional Sampling in Turbulence Measurement. *Annual Review of Fluid Mechanics* 13, 131–156.
- AUGUSTIN, K., RIST, U., AND WAGNER, S. 2003. Investigation of 2D and 3D Boundary-Layer Disturbances for Active Control of Laminar Separation Bubbles. AIAA Paper No. AIAA-2003-0613.
- BALDWIN, B. AND LOMAX, H. 1978. Thin Layer Approximation and Algebraic Model for Separated Turbulent Flows. AIAA Paper AIAA-78-257.
- BERNARD, P. AND WALLACE, J. 2002. *Turbulent Flow: Analysis, Measurement, and Prediction*. John Wiley and Sons, Inc., Hoboken, New Jersey.
- BONS, J., HANSEN, L., CLARK, J., KOCH, P., AND SONDERGAARD, R. 2005. Designing Low-Pressure Turbine Blades with Integrated Flow Control. ASME Paper GT2005-68962.
- BRAESS, D. 2002. *Finite Elements.*, 2nd ed. Cambridge University Press.
- BREAR, M. AND HODSON, H. 2004. The Effect of Wake Passing on a Flow Separation in a Low-Pressure Turbine Cascade. *ASME J. Turbo.* 126, 250–256.

- BREAR, M., HODSON, H., GONZÁLEZ, P., AND HARVEY, N. 2002. Pressure Surface Separations in Low-Pressure Turbines - Part 2: Interactions With the Secondary Flow. *ASME J. Turbo.* 124, 402–409.
- BREAR, M., HODSON, H., AND HARVEY, N. 2002. Pressure Surface Separations in Low-Pressure Turbines - Part 1: Midspan Behavior. *ASME J. Turbo.* 124, 393–401.
- BREHM, C., GROSS, A., AND FASEL, H. 2006. Closed-Loop Control of Low-Pressure Turbine Laminar Separation. AIAA Paper No. AIAA-2006-3021.
- BUTLER, R., BYERLEY, A., VANTREUREN, K., AND BAUGHAN, J. 2001. The Effect of Turbulence Intensity and Length Scale on Low-Pressure Turbine Blade Aerodynamics. *International Journal of Heat and Fluid Flow* 22, 123–133.
- CHO, J. AND CHUNG, M. 1992. A $\kappa - \epsilon - \gamma$ Equation Turbulence Model. *Journal of Fluid Mechanics* 237, 301–322.
- CICATELLI, G. AND SIEVERDING, C. H. 1997. The Effect of Vortex Shedding on the Unsteady Pressure Distribution Around the Trailing Edge of a Turbine Blade. *ASME J. Turbo.* 119, 810–819.
- CLARK, J. 2005. Personal communication.
- CLARK, J. AND GROVER, E. 2006. Assessing Convergence in Predictions of Periodic-Unsteady Flowfields. ASME Paper GT2006-90735.
- CLARK, J., JONES, T., AND LAGRAFF, J. 1994a. On the Propagation of Naturally-Occurring Turbulent Spots. *J. Engr. Math.* 28, 1–19.
- CLARK, J., JONES, T., AND LAGRAFF, J. 1994b. Turbulent-Spot Propagation in Favorable and Adverse Pressure Gradients. *Proceedings of the ASME 1994 International Mechanical Engineering Congress and Exposition* Chicago, IL, Nov. 6–11, 137–145.
- CLARK, J. AND KOCH, P. 2006. Benchmark Turbines for the Guidance of Design System Improvements. 2006 Turbine Engine Technology Symposium, September 14, Dayton, OH.
- CLARK, J., LAGRAFF, J., MAGARI, P., AND JONES, T. 1992. Measurement of Turbulent Spots and Intermittency Modelling at Gas-Turbine Conditions. *Heat Transfer and Cooling in Gas Turbines* NATO/AGARD CP-527, 7.1–7.14.
- CLAUSER, F. 1954. Turbulent Boundary Layers in Adverse Pressure Gradients. *J. Aeronaut. Sci.* 21, 91–108.

- COLES, D. 1956. The Law of the Wake in the Turbulent Boundary Layer. *J. Fluid Mech.* 1, 191–226.
- COTON, T., ARTS, T., LEFEBVRE, M., AND LIAMIS, N. 2003. Unsteady and Calming Effects Investigation on a Very High-Lift LP Turbine Blade - Part I: Experimental Analysis. *ASME J. Turbo.* 125, 281–290.
- CRAFTON, J., FONOV, S., JONES, G., AND FONOV, V. 2005. Optical Measurements of Pressure and Shear in a Plasma. AIAA Paper No. AIAA-2005-5006.
- CURTIS, E., HODSON, H., BANIEGHBAL, M., DENTON, J., HOWELL, R., AND HARVEY, N. 1997. Development of Blade Profiles for Low-Pressure Turbine Applications. *ASME J. Turbo.* 119, 531–538.
- DANAILA, I., HECHT, F., AND PIRONNEAU, O. 2003. *Simulation numerique en C++*. Dunod: Paris, France.
- DAVIS, R. 2006. A Novel Means for Predicting Stall in Axial Compressors. Turbine Engine Technology Symposium, Dayton, OH, September 11–14.
- DENNIS, B., DULIKRAVICH, G., AND HAN, Z.-X. 2001. Optimization of Turbomachinery Airfoils with a Genetic/Sequential-Quadratic-Programming Algorithm. *AIAA J. Prop. and Power* 17, 5.
- DENTON, J. 1993. Loss Mechanisms in Turbomachines. *ASME J. Turbo.* 115, 4, 621–656.
- DHAWAN, S. AND NARASIMHA, R. 1958. Some Properties of Boundary Layer Flow During the Transition from Laminar to Turbulent Motion. *Journal of Fluid Mechanics* 3, 418–436.
- DIECK, R. 2002. *Measurement Uncertainty: Methods and Applications*, 3rd ed. ISA - The Instrumentation, Systems, and Automation Society.
- DORNEY, D. AND ASHPIS, D. 1998. Study of Low Reynolds Number Effects on the Losses in Low-Pressure Turbine Blade Rows. AIAA Paper No. AIAA-98-3575.
- DORNEY, D. AND DAVIS, R. 1992. Navier-Stokes Analysis of Turbine Blade Heat Transfer and Performance. *ASME J. Turbo.* 114, 795–806.
- DRING, R., JOSLYN, H., HARDIN, L., AND WAGNER, J. 1982. Turbine Rotor-Stator Interaction. ASME Paper No. 82-GT-3.
- DRIS, A. AND JOHNSON, M. 2005. Transition on Concave Surfaces. *ASME J. Turbo.* 127, 507–511.

- DULLENKOPF, K. AND MAYLE, R. 1995. An Account of Free-Stream-Turbulence Length Scale on Laminar Heat Transfer. *ASME J. Turbo.* 117, 401–406.
- DUNN, M. G. 2001. Convective Heat Transfer and Aerodynamics in Axial Flow Turbines. *ASME J. Turbo.* 123, 637–686.
- EL-WAKIL, M. M. 2002. *Powerplant Technology*. McGraw-Hill Primis Custom Publishing.
- EMMONS, H. 1951. The Laminar-Turbulent Transition in a Boundary Layer - Part I. *Journal of the Aeronautical Sciences* 18, 490–498.
- FONOV, S., GOSS, L., JONES, G., CRAFTON, J., FONOV, V., AND OL, M. 2005. New Method For Surface Pressure Measurements. AIAA Paper No. AIAA-2005-1029.
- GAD-EL-HAK, M. 1990. Control of Low-Speed Airfoil Aerodynamics. *AIAA Journal* 28, 1537–1551.
- GIER, J. AND ARDEY, S. 2001. On The Impact of Blade Count Reduction on Aerodynamic Performance and Loss Generation in a Three-Stage LP Turbine. ASME Paper No. 2001-GT-0197.
- GONZÁLEZ, P., ULIZAR, J., VÁSQUEZ, R., AND HODSON, H. 2002. Pressure and Suction Surfaces Redesign for High-Lift Low-Pressure Turbines. *ASME J. Turbo.* 124, 161–166.
- GOSTELOW, J., BLUNDEN, A., AND WALKER, G. 1994. Effects of Free-Stream Turbulence and Adverse Pressure Gradients on Boundary Layer Transition. *ASME J. Turbo.* 116, 392–404.
- GOVINDARAJAN, R. AND NARASIMHA, R. 1995. Stability of spatially developing boundary layers in pressure gradients. *Journal of Fluid Mechanics* 300, 117–147.
- GRAVELINE, S. AND SJOLANDER, S. 2005. Spectral Analysis of Measurements of Separated Flow Transition on a Turbine Airfoil. AIAA Paper No. AIAA-2005-4769.
- GRIFFIN, L., HUBER, F., AND SHARMA, O. 1996. Performance Improvement Through Indexing of Turbine Airfoils: Part II – Numerical Simulation. *ASME J. Turbo.* 118, 636–642.
- GRIFFIN, P. AND DAVIES, M. 2004. Aerodynamic Entropy Generation Rate in a Boundary Layer with High Freestream Turbulence. *Journal of Fluids Engineering* 126.
- HAKKINEN, R. 2004. Reflections on Fifty Years of Skin Friction Measurement. AIAA Paper No. AIAA-2004-2111.

- HALDEMAN, C. AND DUNN, M. 2006. Aerodynamic and Heat Flux Measurements in a Single-Stage Fully Cooled Turbine, Part 2: Experimental Results. Turbine Engine Technology Symposium, Dayton, OH, September 11–14.
- HALSTEAD, D., WISLER, D., OKIISHI, T., WALKER, G., HODSON, H., AND SHIN, H.-W. 1997a. Boundary Layer Development in Axial Compressors and Turbines: Part 1 of 4 - Composite Picture. *ASME J. Turbo.* 119, 114–127.
- HALSTEAD, D., WISLER, D., OKIISHI, T., WALKER, G., HODSON, H., AND SHIN, H.-W. 1997b. Boundary Layer Development in Axial Compressors and Turbines: Part 3 of 4 - LP Turbines. *ASME J. Turbo.* 119, 225–237.
- HATMAN, A. AND WANG, T. 1999. A Prediction Model for Separated-Flow Transition. *Journal of Turbomachinery* 121, 594–602.
- HILL, P. AND PETERSON, C. 1992. *Mechanics and Thermodynamics of Propulsion*. Addison Wesley Longman, Reading, MA.
- HOUTERMANS, R., COTON, T., AND ARTS, T. 2004. Aerodynamic Performance of a Very High Lift Low Pressure Turbine Blade With Emphasis on Separation Prediction. *ASME J. Turbo.* 126, 406–413.
- HOWELL, R., HODSON, H., SCHULTE, V., STIEGER, R., SCHIFFER, H.-P., HASELBACH, F., AND HARVEY, N. 2002. Boundary Layer Development in the BR710 and BR715 LP Turbines - The Implementation of High-Lift and Ultra-High-Lift Concepts. *ASME J. Turbo.* 124, 385–392.
- HOWELL, R., RAMESH, O., HODSON, H., HARVEY, N., AND SCHULTE, V. 2001. High Lift and Aft-Loaded Profiles for Low-Pressure Turbines. *ASME J. Turbo.* 123, 181–188.
- HUANG, P. AND XIONG, G. 1998. Transition and Turbulence Modeling of Low Pressure Turbine Flows. AIAA Paper No. AIAA-98-0339.
- HUBER, F., JOHNSON, P., SHARMA, O., STAUBACH, J., AND GADDIS, S. 1996. Performance Improvement Through Indexing of Turbine Airfoils: Part I – Experimental Investigation. *ASME J. Turbo.* 118, 630–635.
- LAKSHMINARAYANA, B. 1991. An Assessment of Computational Fluid Dynamic Techniques in the Analysis and Design of Turbomachinery. *Journal of Fluids Engineering* 113, 315–352.
- LANGTRY, R. AND MENTER, F. 2005. Transition Modeling for General CFD Applications in Aeronautics. AIAA Paper No. AIAA-2005-0522.

- LEE, D. AND KNIGHT, C. 1989. Evaluation of An O-H Grid Formulation For Viscous Cascade Flows. AIAA Paper AIAA-89-0207.
- LIU, T. AND SULLIVAN, J. 2005. *Pressure and Temperature Sensitive Paints*. Springer-Verlag, Berlin, Germany.
- LOU, W. AND HOURMOUZADIS, J. 2000. Separation Bubbles Under Steady and Periodic-Unsteady Main Flow Conditions. *ASME J. Turbo.* 122, 634–643.
- MALKIEL, E. AND MAYLE, R. 1996. Transition in a Separation Bubble. *ASME J. Turbo.* 118, 752–759.
- MATTINGLY, J. D. 1996. *Elements of Gas Turbine Propulsion*. McGraw-Hill, Inc.
- MAYLE, R. 1991. The Role of Laminar-Turbulent Transition in Gas Turbine Engines. *Journal of Turbomachinery* 113, 509–537.
- MAYLE, R. AND DULLENKOPF, K. 1989. A Theory for Wake-Induced Transition. ASME Paper No. 89-GT-57.
- MAYLE, R., DULLENKOPF, K., AND SCHULTZ, A. 1998. The Turbulence That Matters. *ASME J. Turbo.* 120, 402–409.
- MAYLE, R. AND SCHULTZ, A. 1996. The Path to Predicting Bypass Transition. ASME Paper No. 96-GT-199.
- MCQUILLING, M., WOLFF, M., FONOV, S., CRAFTON, J., AND SONDERGAARD, R. 2007. An Experimental Investigation of a Low-Pressure Turbine Blade Suction Surface Using a Shear and Stress Sensitive Film. *Experiments in Fluids* In Press.
- MENTER, F. 1993. Zonal Two Equation $k - \omega$ Turbulence Models for Aerodynamic Flows. AIAA Paper No. AIAA-93-2906.
- MENTER, F., LANGTRY, R., LIKKI, S., SUZEN, Y., HUANG, P., AND VÖLKER, S. 2006. A Correlation-Based Transition Model Using Local Variables - Part I: Model Formulation. *ASME J. Turbo.* 128, 413–422.
- MOSS, R. AND OLDFIELD, L. 1992. Measurements of the Effect of Free-Stream Turbulence Length Scale on Heat Transfer. ASME Paper No. 92-GT-244.
- NARASIMHA, R. 1985. The Laminar-Turbulent Transition Zone in the Boundary Layer. *Progress in Aerospace Sciences* 22, 29–80.

- PADUANO, J., GREITZER, E., AND EPSTEIN, A. 2001. Compression System Stability and Active Control. *Annual Review of Fluid Mechanics* 33, 491–517.
- PLESNIAK, M. AND PETERSON, S. 2004. Wall Shear Stress Measurements for Conventional Applications and Biomedical Flows (invited). AIAA Paper No. AIAA-2004-2301.
- POSTL, D., GROSS, A., AND FASEL, H. 2004. Numerical Investigation of Active Flow Control for Low-Pressure Turbine Blade Separation. AIAA Paper AIAA-2004-2204.
- PRAISNER, T. AND CLARK, J. 2004. Predicting Transition in Turbomachinery, Part I - A Review and New Model Development. ASME Paper No. IGTI-2004-54108.
- PRAISNER, T. AND CLARK, J. 2007. Predicting Transition in Turbomachinery, Part I - A Review and New Model Development. *ASME J. Turbo.* 129, 1–13.
- PRAISNER, T., GROVER, E., RICE, M., AND CLARK, J. 2004. Predicting Transition in Turbomachinery, Part II - Model Validation and Benchmarking. ASME Paper No. IGTI-2004-54109.
- PRAISNER, T., GROVER, E., RICE, M., AND CLARK, J. 2007. Predicting Transition in Turbomachinery, Part II - Model Validation and Benchmarking. *ASME J. Turbo.* 129, 14–22.
- PRAISNER, T., NASH, T., RICE, M., AND CLARK, J. 2006. Performance Impacts Due to Wake Mixing in Axial-Flow Turbomachinery. ASME Paper GT2006-90666.
- QIU, S. AND SIMON, T. 1997. An Experimental Investigation of Transition as Applied to Low Pressure Turbine Suction Surface Flows. ASME Paper No. 97-GT-455.
- RAFFEL, M., WILLERT, C., AND KOMPENHANS, J. 1998. *Particle Image Velocimetry: A Practical Guide*. Springer-Verlag, Berlin, Germany.
- REDFORD, J. AND JOHNSON, M. 2005. Predicting Transitional Separation Bubbles. *ASME J. Turbo.* 127, 497–501.
- REED, H., SARIC, W., AND ARNAL, D. 1996. Linear Stability Theory Applied to Boundary Layers. *Annual Review of Fluid Mechanics* 28, 389–428.
- REIMANN, D., BLOXHAM, M., CRAPO, K., PLUIM, J., AND BONS, J. 2006. Influence of Vortex Generator Jet-Induced Transition on Separating Low Pressure Turbine Boundary Layers. AIAA Paper AIAA-2006-2852.
- RIST, U. AND AUGUSTIN, K. 2005. Control of Laminar Separation Bubbles Using Instability Waves. ISABE Paper No. ISABE-2005-1041.

- RIVIR, R. 1996. Transition on turbine blades and cascades at low Re numbers. AIAA Paper. No. AIAA-1996-2079.
- ROACH, P. 1986. The generation of nearly isotropic turbulence by means of grids. *Heat and Fluid Flow*, 82–92.
- ROBERTS, W. 1975. The Effect of Reynolds Number and Laminar Separation on Axial Cascade Performance. *Journal of Engineering for Power* 97, 261–274.
- ROBERTS, W. 1980. Calculation of Laminar Separation Bubbles and Their Effect on Airfoil Performance. *AIAA Journal* 18, 1, 25–31.
- SCHLICHTING, H. 2001. *Boundary Layer Theory*, 8th ed. Springer Publishing.
- SCHMID, P. J. 2000. Linear stability theory and bypass transition in shear flows. *Physics of Plasmas* 7, 5, 1788–1794.
- SCHOBEIRI, M., ÖZTÜRK, B., AND ASHPIS, D. 2005. On The Physics of Flow Separation Along a Low Pressure Turbine Blade Under Unsteady Flow Conditions. *Journal of Fluids Engineering* 127.
- SCHOBEIRI, M., READ, K., AND LEWALLE, J. 2003. Effect of Unsteady Wake Passing Frequency on Boundary Layer Transition, Experimental Investigation, and Wavelet Analysis. *Journal of Fluids Engineering* 125, 251–266.
- SCHUBAUER, G. AND KLEBANOFF, P. 1956. Contributions on the Mechanics of Boundary-Layer Transition. NACA Report 1289.
- SCHULTE, V. AND HODSON, H. 1996. Unsteady Wake-Induced Boundary Layer Transition in High Lift LP Turbines. ASME Paper No. 96-GT-486.
- SCHULTE, V. AND HODSON, H. 1998. Prediction of the Recalmed Region for LP Turbine Profile Design. *ASME J. Turbo.* 120, 839–846.
- SHARMA, O. 1987. Momentum and Thermal Boundary Layer Development on Turbine Airfoil Suction Surfaces. AIAA Paper No. 87-1918.
- SHARMA, O. 1998. Impact of Reynolds Number on LP Turbine Performance. *Minnowbrook II 1997 Workshop on Boundary Layer Transition in Turbomachines*. NASA/CP-1998-206958.
- SHARMA, O., PICKETT, G., AND NI, R. 1990. Assessment of Unsteady Flows in Turbines. ASME Paper No. 90-GT-150.

- SIEVERDING, F., RIBI, B., CASEY, M., AND MEYER, M. 2004. Design of Industrial Axial Compressor Blade Sections for Optimal Range and Performance. *Journal of Turbomachinery* 126.
- SIMON, F. AND ASHPIS, D. 1996. Progress in Modeling of Laminar to Turbulent Transition on Turbine Vanes and Blades. NASA TM-107180.
- SIMON, F. AND STEPHENS, C. 1991. Modeling of the Heat Transfer in Bypass Transitional Boundary-Layer Flows. NASA Technical Paper 3170.
- SOLOMON, W., WALKER, G., AND GOSTELOW, J. 1996. Transition Length Prediction for Flows with Rapidly Changing Pressure Gradients. *ASME J. Turbo.* 118, 744–751.
- SONDERGAARD, R., BONS, J., AND RIVIR, R. 2002. Reducing Low-Pressure Turbine Stage Blade Count Using Vortex Generator Jet Separation Control. ASME Paper GT-2002-30602.
- SONODA, T., YAMAGUCHI, Y., ARIMA, T., OLHOFFER, M., SENDHOFF, B., AND SCHREIBER, H. 2004. Advanced High Turning Airfoils for Low Reynolds Number Condition - Part I: Design and Optimization. *ASME J. Turbo.* 126, 350–359.
- STEELANT, J. AND DICK, E. 1996. Modelling of Bypass Transition with Conditioned Navier-Stokes Equations Coupled to an Intermittency Transport Equation. *International Journal for Numerical Methods in Fluids* 23, 193–220.
- STEELANT, J. AND DICK, E. 2001. Modeling of Laminar-Turbulent Transition for High Free Stream Turbulence. *Journal of Fluids Engineering* 123, 22–30.
- STIEGER, R. AND HODSON, H. 2004. The Transition Mechanism of Highly-Loaded Low-Pressure Turbine Blades. *ASME J. Turbo.* 126.
- STIEGER, R., HOLLIS, D., AND HODSON, H. 2004. Unsteady Surface Pressures Due to Wake-Induced Transition in a Laminar Separation Bubble on a Low-Pressure Cascade. *ASME J. Turbo.* 126, 544–550.
- SUZEN, Y. AND HUANG, P. 1999. Modeling of Flow Transition Using an Intermittency Transport Equation. NASA/CR-1999-209313.
- SUZEN, Y., HUANG, P., HULTGREN, L., AND ASHPIS, D. 2003. Predictions of Separated and Transitional Boundary Layers Under Low-Pressure Turbine Airfoil Conditions Using an Intermittency Transport Equation. *ASME J. Turbo.* 125, 455–464.

- SUZEN, Y., HUANG, P., VOLINO, R., CORKE, T., THOMAS, F., HUANG, J., LAKE, J., AND KING, P. 2003. A Comprehensive CFD Study of Transitional Flows in Low-Pressure Turbines Under a Wide Range of Operating Conditions. AIAA Paper No. AIAA-2003-3591.
- TANI, I. 1969. Boundary-Layer Transition. *Annual Review of Fluid Mechanics*, 169–196.
- TANNEHILL, J. C., ANDERSON, D. A., AND PLETCHER, R. H. 1997. *Computational Fluid Mechanics and Heat Transfer*, 2nd ed. Taylor and Francis, Philadelphia, PA.
- TARASOV, V. AND ORLOV, A. 1990. Method for determining shear stress on aerodynamic model surface. Patent of Russia, 4841553/23/1990.
- TENNEKES, H. AND LUMLEY, J. 1972. *A First Course in Turbulence*, 2nd ed. MIT Press.
- TOBAK, M. AND PEAKE, D. 1982. Topology of Three-Dimensional Separated Flows. *Annual Review of Fluid Mechanics* 14, 61–85.
- TYLER, C., FONOVI, S., GOSS, L., CRAFTON, J., JONES, E., AND SARKA, B. 2004. Comparison of Computationally Predicted and Experimentally Measured Skin Friction. AIAA Paper No. AIAA-2004-2304.
- VOLINO, R. AND SIMON, T. 2000. Spectral Measurements in Transitional Boundary Layers on a Concave Wall Under High and Low Free-Stream Turbulence Conditions. *ASME J. Turbo.* 122, 450–457.
- VOLINO, R. J. 2002a. Separated Flow Transition Under Simulated Low-Pressure Turbine Airfoil Conditions: Part 1 - Mean Flow and Turbulence Statistics. ASME Paper No. GT-2002-30236.
- VOLINO, R. J. 2002b. Separated Flow Transition Under Simulated Low-Pressure Turbine Airfoil Conditions: Part 2 - Turbulence Spectra. ASME Paper No. GT-2002-30237.
- VOLINO, R. J. 2003. Conditional Sampling in a Transitional Boundary Layer Under High Freestream Conditions. *Journal of Fluids Engineering* 125, 28–37.
- VOLINO, R. J. 2005. An investigation of the scales in transitional boundary layers under high free-stream turbulence conditions. *Experiments in Fluids* 38, 516–533.
- WALKER, G. J. 1989. Transitional Flow on Axial Turbomachine Blading. *AIAA Journal* 27, 5, 595–602.
- WALKER, G. J. 1993. The Role of Laminar-Turbulent Transition in Gas Turbine Engines: A Discussion. *ASME J. Turbo.* 115, 207–217.

- WANG, H., OLSON, S., GOLDSTEIN, R., AND ECKERT, E. 1997. Flow Visualization in a Linear Turbine Cascade of High Performance Turbine Blades. *ASME J. Turbo.* 119, 1–8.
- WHITE, F. M. 2006. *Viscous Fluid Flow*, 3rd ed. McGraw-Hill, Inc.
- WOLFF, S., BRUNNER, S., AND FOTTNER, L. 2000. The Use of Hot-Wire Anemometry to Investigate Unsteady Wake-Induced Boundary-Layer Development on a High-Lift LP Turbine Cascade. *ASME J. Turbo.* 122, 644–650.
- YARAS, M. 2001. Measurements of the Effects of Pressure-Gradients History on Separation-Bubble Transition. ASME Paper 2001-GT-0193.
- YARAS, M. 2002. Measurements of the Effects of Freestream Turbulence on Separation-Bubble Transition. ASME Paper GT-2002-30232.
- ZELINA, J. 2006. The State of Inter-Turbine Burner Developments. 2006 Turbine Engine Technology Symposium, Dayton, OH, September 11–14.
- ZHANG, X. AND HODSON, H. 2005. Combined Effects of Surface Trips and Unsteady Wakes on the Boundary Layer Development of an Ultra-High-Lift LP Turbine Blade. *ASME J. Turbo.* 127, 479–488.
- ZHANG, X., MAHALLATI, A., AND SJOLANDER, S. 2002. Hot-Film Measurements of Boundary Layer Transition, Separation, and Reattachment on a Low-Pressure Turbine Airfoil at Low Reynolds Numbers. AIAA Paper No. AIAA-2002-3643.
- ZWEIFEL, O. 1945. Die Frage der optimalen Schaufelteilung bei Beschaukelungen von Turbomaschinen, insbesondere bei groer Umlenkung in den Schaufelreihen. *Brown Boveri Mitteilungen*, 32.

Vita

Mark McQuilling was born in Louisville, Kentucky in 1978. He graduated from Seneca High School in 1997 with Honors from the Advanced Liberal Arts Program. He received his B.S. and M.S. in Mechanical Engineering from the University of Kentucky in 2002 and 2004. He has presented multiple talks and papers on his research at conferences on both the national and international level. He was awarded a Dayton Area Graduate Studies Institute 3-year PhD Fellowship in 2004 and was therefore able to conduct his research at nearby Wright-Patterson Air Force Base in the Turbines Branch of the Propulsion Directorate of the Air Force Research Laboratory. He received his PhD in Engineering from Wright State University in Dayton, OH in 2007. He now lives with his wife, Kylie, daughter, Madison, and puppy, Sadie, near St. Louis, MO where he is beginning his faculty career as Assistant Professor in the Aerospace and Mechanical Engineering Department of Parks College of Engineering, Aviation, and Technology at Saint Louis University.

APPENDIX I

CHARACTERIZATION OF INTERNAL WAKE GENERATOR AT LOW REYNOLDS NUMBER WITH A LINEAR CASCADE OF LOW PRESSURE TURBINE BLADES

A thesis submitted in partial fulfillment
of the requirements for the degree of
Master of Science in Engineering

By

CHASE A. NESSLER
B.S., Wright State University, 2008

2010
Wright State University

WRIGHT STATE UNIVERSITY
SCHOOL OF GRADUATE STUDIES

April 5, 2010

I HEREBY RECOMMEND THAT THE THESIS PREPARED UNDER MY SUPERVISION BY Chase A. Nessler ENTITLED Characterization of Internal Wake Generator at Low Reynolds Number with a Linear Cascade of Low Pressure Turbine Blades BE ACCEPTED IN PARTIAL FULFILLMENT OF THE REQUIREMENTS FOR THE DEGREE OF Master of Science in Engineering.

J. Mitch Wolff, Ph.D.
Thesis Director

George P.G. Huang, P.E., Ph.D.
Chair of the Mechanical and Materials
Engineering Department

Committee on
Final Examination

J. Mitch Wolff, Ph.D.

James Menart, Ph.D.

Haibo Dong, Ph.D.

Rolf Sondergaard, Ph.D.

John A. Bantle, Ph.D.
Vice President for Research and
Graduate Studies and Interim Dean
of Graduate Studies

Abstract

Nessler, Chase A., M.S. Egr., Department of Mechanical and Materials Engineering, Wright State University, 2010. Characterization of Internal Wake Generator at Low Reynolds Number with a Linear Cascade of Low Pressure Turbine Blades.

Unsteady flow and its effects on the boundary layer of a low pressure turbine blade is complex in nature. The flow encountered in a low pressure turbine contains unstructured free-stream turbulence, as well as structured periodic perturbations caused by upstream vane row wake shedding. Researchers have shown that these conditions strongly influence turbine blade performance and boundary layer separation, especially at low Reynolds numbers. In order to simulate these realistic engine conditions and to study the effects of periodic unsteadiness, a moving bar wake generator has been designed and characterized for use in the Air Force Research Labs low speed wind tunnel. The layout is similar to other traditional squirrel cage designs, however, the entire wake generator is enclosed inside the wind tunnel, up-stream of a linear cascade. The wake shed from the wake generator was characterized by its momentum deficit, wake width, and peak velocity deficit. It is shown that the wakes produce a periodic unsteadiness that is consistent with other wake generator designs.

The effect of the periodic disturbances on turbine blade performance has been investigated at low Reynolds number using the highly loaded, AFRL designed L1A low pressure turbine profile. Wake loss measurements, pressure coefficient distribution, and

particle image velocimetry was used to quantify the L1A blade performance with unsteady wakes at a Reynolds number of 25,000 with 0.5% and 3.4% free-stream turbulence. Wake loss data showed that the inclusion of periodic wakes reduced the profile losses by 56% compared to steady flow losses. Previous pressure coefficient distributions showed that the L1A blade profile, under steady flow conditions, has non-reattaching separated flow along the suction surface. With the inclusion of the periodic wakes, the pressure coefficient profile revealed that the flow separation had been dramatically reduced to a small separation bubble.

The wake passing event was split into six phases and captured using two-dimensional planar PIV. The interaction between the passing wakes and the separation bubble was noted. The bubble was observed to grow in size between passing wakes, but was only able to achieve a fraction of the original level of separation. The streamlines through the unrestricted blade passage were able to better follow the blade profile, indicating an improved exit flow angle with lower losses. The data shows that the wake generator was successfully implemented into the wind tunnel and is able to properly simulate blade row interactions.

Table of Contents

Chapter 1	1
Introduction.....	1
1.1 Motivation	1
1.2 Literature Review	3
1.2.1 Boundary Layer Development, Transition, and Separation.....	3
1.2.2 Periodic Unsteady Flow and the use of Wake Generators.....	6
1.2.3 Wake Generating Mechanisms	11
1.2.4 The Flow Physics and Transition Mechanism of Unsteady Wakes.....	13
1.2.5 Affect of Periodic Unsteady Wakes on Flow Separation and Losses.....	18
1.3 Objective	23
Chapter 2	25
Wake Generator Design.....	25
2.1 Experimental Facility	25
2.2 Wake Generator Design Objectives and Constraints	26
2.3 Wake Generator Design	27
2.3.1 Wake Generating Mechanism.....	27
2.3.2 Track Configuration.....	28
2.3.3 Wake Generator Structure.....	31
Chapter 3	34
Characterizing the Periodic Wake Produced by the Wake Generator	34
3.1 Experimental Analysis	34
3.2 Experimental Setup	36
3.3 Wake Characteristics from a Partially Populated Chain	38
3.4 Wake Characteristics from a Fully Populated Chain	43

3.5	Wake Characteristics from an Airfoil Shape.....	49
3.6	Conclusions	56
Chapter 4	58
Low Pressure Turbine Blade Performance with Periodic Unsteady Wakes at Low Reynolds Number		58
4.1	Linear Cascade of Low Pressure Turbine Blades	58
Linear Cascade.....		59
4.2	Wake Loss Measurements of the L1A Blade Profile with Periodic Unsteady Wakes.....	60
4.2.1	Cascade Periodicity.....	60
4.2.2	Wake Loss Experimental Setup	62
4.2.3	Baseline Case of Wake Loss Measurements for Steady Flow Conditions .	64
4.2.4	Wake Loss Measurements with Periodic Unsteady Wakes	66
4.3	Pressure Coefficient Distribution on the L1A Blade Profile with Periodic Unsteady Wakes	69
4.3.1	Experimental Setup	69
4.3.2	Pressure Coefficient Distribution for the L1A Blade Profile.....	70
4.4	Phase Locked Particle Image Velocimetry Measurements on the Suction Surface of the L1A Blade Profile with Periodic Unsteady Wakes	73
4.4.1	Particle Image Velocimetry	73
4.4.2	PIV Experimental Setup	75
4.4.3	Baseline Data	79
4.4.4	Low FSTI Hot-Wire Study	81
4.4.5	Low FSTI PIV Results.....	83
4.4.6	High FSTI Hot-Wire Study.....	85
4.4.7	High FSTI PIV Results	88
Chapter 5	94
Conclusions.....		94
References		99
Appendix A		104
Wake Generator Operation and Maintenance.....		104

List of Figures

1.1	Current trend toward low pressure turbine blade count reduction [48].	3
1.2	Wake generator configuration at Cambridge University [13].	8
1.3	Schematic of wake generating system at Texas A&M University [13].	9
1.4	CAD drawing and schematic of wake generating system and test section at Ohio State University [15].	10
1.5	Schematic of high speed test facility wake generating system at the Universität der Bundeswehr München [16].	10
1.6	Schematic of annular cascade with rotating wake generating system at NASA Glenn Rotor-Wake Heat Transfer facility [11].	10
1.7	Sketch of the wake acting like a negative jet impinging upon the separation bubble [25].	16
2.1	(a) Top view schematic of wind tunnel test section (b) Wind tunnel setup at AFRL.	25
2.2	Examples of different track configurations considered and modeled in simulation program.	30
2.3	Visualization output of wake generator track produced in simulation program	30
2.4	3D CAD drawing of wake generator structure with chain tensioner, sprockets, and chain guides highlighted.	32
2.5	3D CAD drawing of wake generator structure installed in wind tunnel. Wake generator system is highlighted in red.	32
2.6	Wake generator system installed in low speed wind tunnel.	33
3.1	Description of parameters used in calculation of wake width and peak velocity deficit.	35
3.2	Control surface for momentum deficit of the generated wake.	35

3.3	Simulation of periodic unsteadiness by cylindrical rod generated moving wakes.	37
3.4	Complete cycle of ensemble average velocity data showing both primary wakes and secondary wakes. (Re = 25k, Top: FSTI 0.5%, Bottom: FSTI 3.4%).	40
3.5	Convergence study of the number of cycles needed for a fully developed time-averaged wake.	41
3.6	Complete cycle of ensemble average velocity data for a fully populated chain. (Re = 25k, $\phi = 0.8$, FSTI 0.5%).	45
3.7	Vector decomposition of the flow inside the wind tunnel.	48
3.8	Wake generator with airfoils installed.	50
3.9	Complete cycle of ensemble average velocity data using nine cylindrical rods followed by nine airfoil shapes. (Re = 50k, $\phi = 1.57$, FSTI 0.5%).	52
3.10	Ensemble average velocity of the primary wakes using nine cylindrical rods followed by nine airfoil shapes (Re = 50k, $\phi = 1.57$, FSTI 0.5%).	54
4.1	Schematic of linear cascade indicating where blade numbering begins.	59
4.2	Cascade Periodicity with and without the wake generator running (Re = 50k, $\phi = 0.8$, FSTI 3.4%).	62
4.3	Wake loss measurement showing steady flow L1A low pressure turbine blade performance at a Reynolds number of 25k and two levels of FSTI.	65
4.4	Wake loss measurement showing L1A profile performance with periodic unsteady wake flow at a Reynolds number of 25k and two levels of FSTI.	67
4.5	Pressure coefficient distribution with periodic unsteady wakes compared to steady flow for two different FSTI levels.	71
4.6	Block diagram of cross-correlation analysis procedure using fast Fourier transforms [54]	74
4.7	Schematic of PIV setup.	76
4.8	Seeding system used for PIV measurements.	77
4.9	Diagram of the different rod locations for each phase.	78
4.10	Non-dimensional velocity contour of steady flow baseline case with stream lines indicating a recirculation region.	80

4.11	Instantaneous PIV image demonstrating eddies forming in the separated shear layer.	81
4.12	100 ensemble averaged measurements of velocity within the blade passage during a complete cycle of the wake generator. ($Re = 25k$, FSTI 0.5%).	82
4.13	PIV contours of non-dimensional average velocity for six phases of wake passing. FSTI = 0.5%.	85
4.14	100 ensemble averaged measurements of velocity within the blade passage during a complete cycle of the wake generator. ($Re = 25k$, FSTI 3.4%).	86
4.15	Time location for each of the six phases as the wake passes the hotwire within the blade passage for the first three recorded wakes.	88
4.16	PIV contours of non-dimensional average velocity for six phases of wake passing. FSTI = 3.4%.	89
4.17	Non-dimensional phase average subtracted velocity contour.	92

List of Tables

3.1	Calculated wake characteristics based on hot-film measurements for a 36% duty cycle wake generator.	42
3.2	Calculated wake characteristics based on hot-film measurements for a 100% duty cycle wake generator.	46
3.3	Calculated wake characteristics based on hot-film measurements for a cylindrical rod and airfoil shape.	54
4.1	Summary of integrated wake total pressure loss scaled with the blade axial chord for baseline case with steady flow.	66
4.2	Summary of integrated wake total pressure loss scaled with the blade axial chord for periodic unsteady flow case.	69

Nomenclature

b	= Wake width
C	= Chord length
C_p	= Pressure coefficient
L_c	= Critical length
P	= Pressure
q	= Dynamic Pressure
Re	= Reynolds Number
u_p	= Peak velocity deficit
u_0	= Minimum velocity achieved inside wake
U_{axial}	= Flow velocity in the axial direction ($U_{\infty} \cdot \cos(35^\circ)$)
U_{rod}	= Rod speed
U_{wake}	= Velocity of propagating wake
U_{∞}	= Free-stream velocity
V	= Decomposed velocity
\mathbf{w}	= Velocity vector in rotating frame
Z_w	= Zweifel coefficient

Greek Symbols

α	= Absolute flow angle
β	= Flow angle relative to axial direction
ϑ	= Angle between resultant and free-stream velocity
ϕ	= Flow coefficient (axial velocity/bar speed)
γ_{int}	= Integrated wake total pressure loss coefficient

Subscripts

A	=	Axial component
cs	=	Control surface
d	=	Rod diameter
ex	=	Cascade exit conditions
F	=	Free-stream component
in	=	Cascade inlet conditions
R	=	Resultant component
S	=	Static property
t	=	Total/Stagnation property
T	=	Tangential component
x	=	Axial direction

Acronyms

AFRL	=	Air Force Research Laboratory
FFT	=	Fast Fourier Transform
FSTI	=	Free-Stream Turbulence Intensity
LSWT	=	Low Speed Wind Tunnel
HW	=	Hot-Wire
PIV	=	Particle Image Velocimetry

Acknowledgements

This research was funded by the United States Air Force Research Laboratory Propulsion Directorate. I am deeply indebted to my advisor, Dr. Mitch Wolff and Dr. Rolf Sondergaard, who gave me the opportunity to perform this work. I would like to thank Dr. Rolf Sondergaard for his mentorship, knowledge, and all of his help, especially with LabView. I would also like to thank Christopher Marks for teaching me how to do PIV and letting me constantly bounce ideas off of him. I would like to thank Charlie Stevens for his support and everyone at RZTT for making my experience there very enjoyable. I would also like to thank Derik Miller, for sweating it out with me during the construction of the wake generator inside the wind tunnel.

A special thanks to my wife, Krista, for supporting me through my education and believing in me.

Dedication

For my Father,

You were my inspiration to go into engineering, and my motivation to finish.

Chapter 1

Introduction

1.1 Motivation

Low Reynolds numbers are often encountered in low pressure turbines especially at high altitude cruise environments. The use of unmanned aerial vehicles has pushed the altitude limits even further, resulting in extremely low Reynolds number flows through the low pressure turbine. These conditions can result in a component efficiency drop on the order of 7 percent between takeoff and cruise environments for small military engines [1]. Current trends in gas turbine engine development have been toward utilizing larger bypass ratios resulting in a lower core flow, and decreasing the number of blades in the low pressure turbine while maintaining the same amount of stage work. As a consequence of these trends, the low pressure turbine can experience Reynolds numbers as low as 25,000 with fewer blades producing the same amount of stage work. Under these flow conditions, the development of a laminar boundary layer, coupled with a strong adverse pressure gradient on the suction surface of a low pressure turbine blade, can lead to blade stall, or boundary layer separation.

Due to the relatively large aspect ratios in a low pressure turbine, the profile loss, particularly with boundary layer separation, is the largest contributing factor of the

overall total loss. It has been shown that a conventional low pressure turbine blade can have up to 60 percent of the losses generated by the suction surface boundary layers [2]. Sharma [3] has shown that increasing low Reynolds number aerodynamic performance of low pressure turbine blades has the potential to increase low pressure turbine efficiency by over 1%. In high bypass ratio turbo fans, almost 80% of the total thrust comes from the low pressure turbine driven fan. Small increases in low pressure turbine efficiencies can therefore have large increases in specific fuel consumption [4].

Other improvements to the low pressure turbine can come from reductions in blade numbers for a given stage. Almost one third of the total engine weight in a modern high-bypass-ratio engine comes from the low pressure turbine [5]. Blade count reductions can have a substantial effect on weight due to the relatively large aspect ratios in the low pressure turbine. Reduced blade numbers also benefit the manufacturer as it results in a reduced part count, reduced manufacturing costs, and an increase in reliability.

In low Reynolds number flows, a laminar boundary layer typically develops on the suction surface of a low pressure turbine blade. As blade numbers are reduced and the blade loading is increased, the peak surface pressure also increases, which is followed by a stronger adverse pressure gradient. If the laminar boundary layer is unable to overcome the adverse pressure gradient that is present on the aft portion of a low pressure turbine blade, the boundary layer will separate. Ongoing efforts for improving the low pressure turbine performance have therefore been twofold; increasing the efficiency at low Reynolds number in which boundary layer separation is most likely to occur, and increasing the blade loading to reduce the blade count for a given stage.

Current research in low pressure turbine blade performance has been toward understanding boundary layer separation in low Reynolds number flows and the effect of a large adverse pressure gradient resulting from increased blade loading. As this research matures, new blade designs have been developed for the low pressure turbine that utilize the laminar boundary layer to reduce losses and withstand larger adverse pressure gradients resulting from increased blade loading. Figure 1.1 illustrates the current design trend of blade count reductions as a function of pressure ratio.

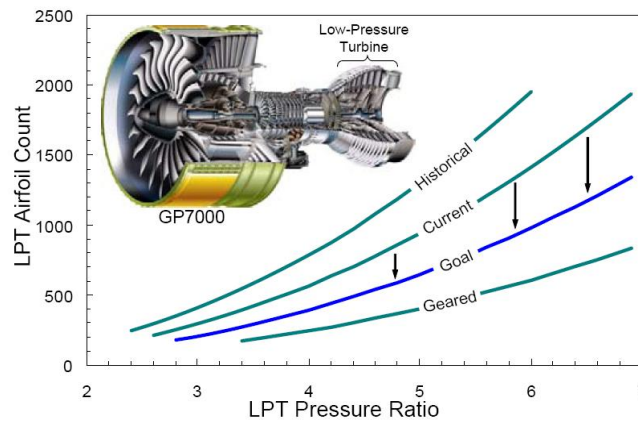


Figure 1.1 Current trend toward low pressure turbine blade count reduction [48].

1.2 Literature Review

1.2.1 Boundary Layer Development, Transition, and Separation

Many researchers have suggested that a reduction of profile loss and boundary layer separation at low Reynolds number can be accomplished by affecting the transition of the boundary layer. The three main modes of transition suggested by Mayle [6] in which a laminar boundary layer transitions to turbulent, are summarized by Öztürk and

Schobeiri [7]. The first mode is referred to as natural transition and occurs when a weak instability in the laminar boundary layer develops into two-dimensional Tollmien-Schlichting waves. These waves are amplified within the boundary layer until they become three-dimensional and eventually transition the flow to turbulent. This type of transition mode is described as only occurring in low free-stream turbulence environments and is said to be irrelevant to gas turbine flows which are considered to have high turbulence intensities. The second mode of transition is referred to as bypass transition and develops through large disturbances in the external flow, causing the first mode of transition to be bypassed. These large disturbances can be a source for a turbulent spot to develop in the boundary layer, effectively causing it to transition. The third transition mode is called separated flow transition, and is described as occurring in a separated free shear layer of a laminar boundary layer. A separated shear layer is said to originate when the flow close to the wall stagnates due to an adverse pressure gradient. This causes a flow blockage, forcing the rest of the flow to separate from the blade surface and a separated shear layer develops [8]. The transition process and its location in the separated free shear layer are explained as significantly affecting the separation bubble length and are often seen in the compressor and low pressure turbine [7].

Free-stream turbulence within a turbine engine can be on the order of 12-15 percent which, as stated above, can affect the behavior of the boundary layer and its transition. Researchers commonly use turbulence generating grids in wind tunnel testing to simulate this high free-stream turbulence seen in turbine engines. The effects of Reynolds number and turbulence intensity on boundary layer separation were investigated by Volino and Hultgren [1] using a flat plate subject to the same

dimensionless pressure gradient as the suction side of a low-pressure turbine airfoil. Detailed velocity measurements were made in the Reynolds number range of 50k to 300k, covering typical operating conditions for a low pressure turbine for cruise and take-off environments. It was found that Reynolds number and free-stream turbulence were not important factors on boundary layer separation as long as they are low enough to maintain a laminar boundary layer upstream of the separation location. However, the location and the extent of the transition zone were said to be strongly dependent on Reynolds number and free-stream turbulence. The reattachment process was observed to simultaneously occur with the onset of transition in both high and low free stream turbulence intensities. In low free stream turbulence, the laminar boundary layer begins to fluctuate at the separation point and continues to fluctuate in a finite frequency band in the separated shear layer. These fluctuations grow until a breakdown into turbulence occurs and the boundary layer would reattach. For the high free-stream turbulence conditions, the separation bubbles were described as being considerably thinner. For the higher Reynolds numbers of 200k and above, transition of the boundary layer was seen before the separation location and was often able to suppress the flow from separating. According to Volino and Hultgren, if separation were to occur at these high Reynolds numbers, the bubble was very small and did not affect the downstream development of the boundary layer.

In a continuation of this study, Volino [9] found that high free-stream turbulence intensity had competing effects in the evaluation of losses. The high turbulence was said to enhance mixing which tended to increase the boundary layer development along with

the losses. At high enough turbulence intensities, it was observed to cause an earlier transition and reattachment, which decreases the boundary layer thickness and losses.

In summary, Volino describes flow separation to be influenced by the state of the boundary layer and the location of transition. Laminar, rather than turbulent boundary layers are much more susceptible to separation, and the location of transition can prevent or reattach separated flow. In this study, according to Volino, if boundary layer transition occurs far enough upstream it can prevent separation, while if it occurs in the shear layer over a separation bubble, it will induce boundary layer reattachment. Low Reynolds number flow moves the transition location further downstream, and unsteady flow associated with the flow turbulence intensity moves the transition location upstream. Although higher turbulence intensities may prevent separation, the effect of a longer turbulent region increases losses compared to an attached laminar boundary layer.

1.2.2 Periodic Unsteady Flow and the use of Wake Generators

The flow inside a turbine engine is known to be unsteady and contain large scale structures that are not captured using turbulence grids in wind tunnels. According to Doorly [10], the unsteady flow in a turbine engine is produced by three main sources, some of which produce periodic flow disturbances. The first source is from the turbulence and instabilities generated in the combustion chamber. The second is due to the potential flow interactions between stages which contribute to periodic unsteadiness. And the third cause of the unsteady flow is said to arise from the periodic unsteadiness generated from wakes shed by the separated blade boundary layers of the trailing edge of one stage, which propagates downstream, impinging on the successive stages. Doorly

referred to this event as “wake-passing”. The effect of wake passing has been listed by Walker as one of four primary factors influencing transition in gas turbine blades [11]. Wake passing causes unsteady flow characteristics to develop through periodic perturbations caused by the passing rotor blades. This periodic unsteadiness can have dramatic effects on profile losses of highly loaded low pressure turbine blades with separated boundary layers [12].

Researchers have shown that small disturbances, including passing wakes, can affect transition on a laminar boundary layer or a separated free shear layer and therefore affect the losses generated. Over the past three decades researches have attempted to include the effect of passing wakes in conjunction with free-stream turbulence for a more accurate and realistic evaluation of loss on compressor and low pressure turbine blades. The overall goal of these Researchers is to simulate the rotor-stator flow interactions seen in multistage turbomachinery in a more controlled environment such as a wind tunnel.

The simulation of wakes shed from upstream stages in a wind tunnel environment has been performed in a number of different ways. Typically, the simulations consist of wake generating mechanisms that traverse upstream of a test article, shedding wakes as they pass. Although there is no set standard or theory for wake generating systems like there is for turbulence grids, researchers try to simulate a periodic wake passing that is consistent with what a turbine blade will see in a turbine engine. Usually, the size and shape of the wake generating mechanism is chosen, such that a velocity deficit, turbulence parameter, drag coefficient, or loss coefficient is matched to that of a turbine blade. Similarly, the spacing between the wake generating mechanisms and the distance upstream of the test article is also matched to what is found in a turbine engine. The

velocity that the wake generating mechanism is traversed across the test section is typically chosen to match the velocity triangles of a turbine engine.

One of the most famous wake generating systems is located in the Whittle Laboratory at Cambridge University and is shown in figure 1.2. This system uses cylindrical rods as the wake generating mechanism and the rods are fastened to rubber belts that traverse across a linear cascade of turbine blades in a low speed wind tunnel. The rods enter and exit through the sides of the wind tunnel and complete the loop downstream of the cascade. Various rod spacing and rod diameters have been used to match the typical spacing and loss coefficient of a stator vane.

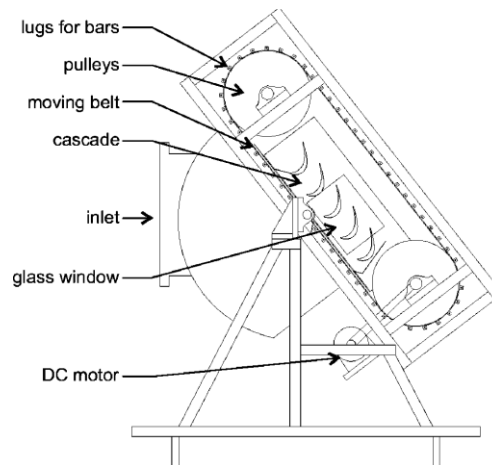


Figure 1.2 Wake generator configuration at Cambridge University [13].

The wake generating system at the Texas A&M University, shown in figure 1.3, also uses cylindrical rods as the wake generating mechanism. The size of the rods and distance upstream of the cascade is chosen so that the Reynolds stresses and velocity deficit of the wake from the rod are matched to the wake shed from a turbine blade. Similarly the rod spacing and bar velocity is chosen to match what is found for a stator row and stage velocity triangle in a turbine engine.

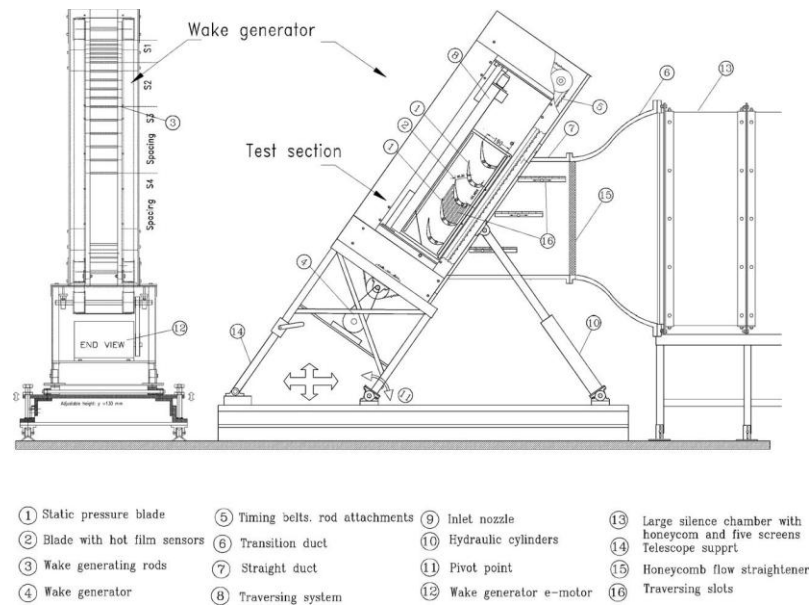


Figure 1.3 Schematic of wake generating system at Texas A&M University [14].

Other noteworthy wake generating systems include one designed by Bons et al. [15] at Ohio State University, shown in figure 1.4; the high speed system located at the Universität der Bundeswehr München and is upstream of a high-speed wind tunnel shown in figure 1.5; and a rotating rig in an annular cascade at NASA Glenn Rotor-Wake Heat Transfer facility shown in figure 1.6. The majority of wake generating systems that have been developed use cylindrical rods as the wake generating mechanism and wake parameters chosen to match what is found in a turbine engine.

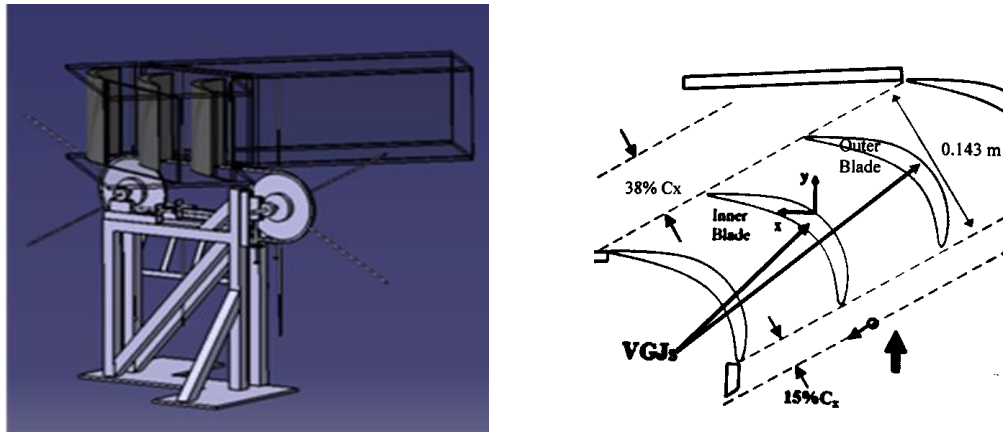


Figure 1.4 CAD drawing and schematic of wake generating system and test section at Ohio State University [15].

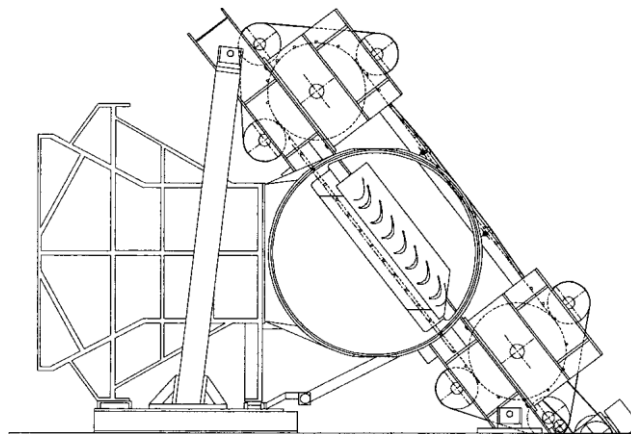


Figure 1.5 Schematic of high speed test facility wake generating system at the Universität der Bundeswehr München [16].

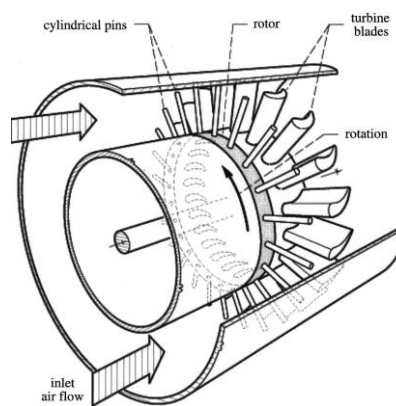


Figure 1.6 Schematic of annular cascade with rotating wake generating system at NASA Glenn Rotor-Wake Heat Transfer facility [17].

1.2.3 Wake Generating Mechanisms

The use of cylindrical rods as a wake generating mechanism is based on the similarities of the wake characteristics to a turbine blade. In an experimental study, a two-component laser Doppler velocimeter (LDV) was used to look at the time-varying characteristics of the turbulent near wake of a large scale turbine cascade [18].

Comparisons of the mean flow properties of the turbine blade wake were made to that of a wake shed from a circular cylinder. It was found that the kinematic structure of the periodic flow was qualitatively similar to an analogous study of the near wake from a circular cylinder. The magnitude of the velocity components, however, was much lower for the turbine blade and displayed slightly lower stream-wise and cross-stream Reynolds stresses. It was also found that the Strouhal number associated with vortex shedding frequency was higher for the turbine blade. Although the test was performed at a relatively high Reynolds number with a vortex shedding frequency of 1300 Hz, the authors state that the findings can be applied to lower Reynolds number flows with lower vortex shedding Strouhal numbers.

Schobeiri [19], who has done extensive research with wake flow through curved channels, states that the far wake ($x/d > 80$) from a cylindrical rod appropriately matches the Reynolds stress components of a wake from a turbine blade. According to O'Brien and Capp [20], who measured the two-component phase-average turbulence statistics downstream of cylindrical rods, found that cylinder wakes cannot simulate the boundary layer and the loading of an upstream blade. The authors state however, that the velocity deficit and turbulence production are simulated to some degree.

Researchers have found that even though the wake shed from a circular cylinder can not exactly match the wake from a turbine blade, the primary flow features of concern are adequately simulated. The differences between the two wakes are thought to arise from the interaction of the flow coming off of the suction side and the pressure side of the turbine blade [10]. Sieverding et al. [21] was able to show smoke visualizations of the suction-side and pressure-side vortices in the far wake of a turbine blade demonstrating these interactions.

Pluim et al. [22] performed a wake comparison study of four different shapes to be used in a wake generator in an effort to better simulate rotor-stator flow interactions. The wakes of the four different shapes were compared to that of a wake shed by a L1A low pressure turbine blade. Of interest to this current study were the results of the cylindrical rod, isosceles triangle (wedge), and a biconvex shape. The wedge shape was chosen to better match the known asymmetric wake of a turbine blade while the biconvex shape was chosen to compare the wake of an aerodynamic shape. By comparing individual parameters, such as the velocity deficit, RMS velocity, and Reynolds shear stress, a least squares analysis was performed to calculate the distance downstream (x/d) that the shape should be placed to best fit the profile obtained from the L1A turbine blade. The results show that the biconvex shape had the thinnest and quickest recovering wake of the shapes tested, which resulted in the worst fit to the L1A wake. The cylindrical rod had good similarities to the blade wake at an x/d distance of 8, but the wedge shape skewed at a 15 degree angle placed at an x/d distance of 6 was the best match and most like the turbine blade wake.

Extensive research has gone into the use of cylindrical rods as the wake generating mechanism because of the importance of accurately simulating upstream blade row wake shedding in wind tunnel testing. The simulation of upstream wake shedding needs to be representative of engine conditions so that once a blade design has been evaluated in the wind tunnel, the results will scale to full engine rig tests. The two wake characteristics of a stator or rotor most commonly chosen to match are the velocity deficit and turbulence quantities. These quantities and their interaction with a boundary layer are thought to be responsible for affecting transition and separation on the blade suction surface.

1.2.4 The Flow Physics and Transition Mechanism of Unsteady Wakes

The effect of wake passing has been stated as being a primary factor in the transition of the boundary layer on low pressure turbine blades. Understanding this effect on the transition process and on blade losses is desired if new blade designs are to have increased loading and improved low Reynolds number performance. Through an effort to better understand the transition process, researchers have studied the interaction between unsteady wakes and separated boundary layers. In an investigation of the development of a boundary layer with unsteady wakes, Schulte and Hodson [12] used hot-film sensors to determine the boundary layer characteristics at the onset and following the passing of an unsteady wake over a separation bubble. Their data showed that, for a given bar diameter and spacing, a turbulent event is triggered in front of the impinging wake and moves at 70 percent of the free-stream velocity. This turbulent patch, with its increased levels of shear stress, was observed to prevent the boundary

layer from separating and is followed by a laminar or “becalmed” region. The becalmed region is said to also prevent the boundary layer from separating due to its relatively elevated shear stress and more developed velocity profiles. This effect did not last as a small separation bubble formed between passing wakes. A predication of this becalmed region that follows the wake-induced turbulent patches was undertaken by Schulte and Hodson [23]. It was found that this phenomenon could be modeled by the laminar unsteady boundary layer equations, making it predictable and independent of any turbulence modeling.

Unsteady surface pressure measurements on a low pressure turbine blade in the presence of unsteady wakes were made by Stieger et al. [24] with fast response Kulite pressure transducers. Large amplitude fluctuations were seen in the measurements as the wake convected over the separation bubble. PIV measurements were used to identify vortices present in the boundary layer, and it was confirmed by reference to literature that these vortices were responsible for the pressure oscillations. The authors proposed that an instability mechanism from the passing wake amplified the fluctuations in the laminar shear layer. This amplification is said to lead to the formation of rollup vortices embedded in the boundary layer.

Stieger and Hodson [25] performed detailed two-dimensional Laser Doppler Anemometry (LDA) measurements on the suction surface of a low pressure turbine blade to further investigate the interaction between a convecting wake and a separation bubble. In this study, a new mechanism was observed that explains the boundary layer transition due to the interaction of a convecting wake.

The process of the interaction and the transition mechanism is broken down into a sequence of events that is repeated periodically, as wakes pass over the blade surface. Figure 1.7, reproduced from Stieger and Hodson [25], depicts this sequence of events. In this process, the authors build upon the concept proposed by Meyer [26], in which the convecting wake can be thought of as a negative jet within the flow field. The authors describe the process starting with the wake acting like a negative jet, which impinges upon the blade surface upstream of a developing separation bubble. The negative jet is said to split into two streams, one flowing upstream retarding the flow, and one flowing downstream accelerating the flow. As the wake approaches the separation bubble, the authors observed the outer region of the boundary layer accelerate and the separated shear layer becoming more intensified. As the wake convects over the separation bubble, the free shear layer becomes deformed as seen in Figure 1.7b. At this point, the separated shear layer is very unstable and it is proposed by the authors that the wake disturbance triggers an inviscid Kelvin-Helmholtz rollup as depicted in Figure 1.7c. It is said that as the wake continues to convect downstream, more rollup vortices are shed as shown in Figure 1.7d. These vortices are described as being formed by the inviscid rollup of the shear layer, which then rapidly breaks down into turbulence and causes the boundary layer to transition. The authors note that this transition mechanism requires a separated shear layer and only occurs if a separation bubble is present.

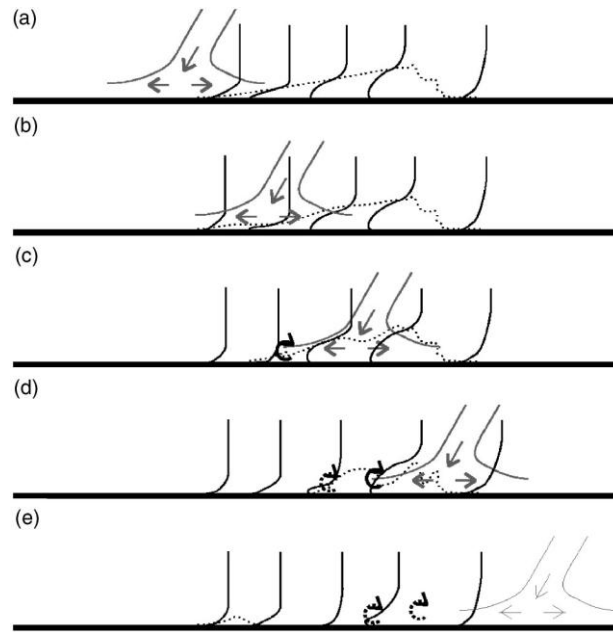


Figure 1.7 Sketch of the wake acting like a negative jet impinging upon the separation bubble [25].

Two-dimensional Particle Image Velocimetry (PIV) was used by Uzol et al. [27] to investigate the interaction between unsteady wakes and the separated boundary layer on the suction side of a high lift low pressure turbine blade. It was observed that before the wake impinged upon the blade, the separation bubble was large enough for the free shear layer to roll up into a vortex. The authors explain that the roll up of the free shear layer is possibly due to the inviscid mechanism explained by Stieger and Hodson [25]. From the PIV measurements, the separation bubble was seen to continually shrink in both height and length as the wake progressed through the blade passage. Once the bubble became too small and the free shear layer was unable to roll into a large vortex, smaller size eddies were identified by their swirl strength, and were observed to combine forming other eddies, or breakup into turbulence. Once the wake had passed, the separation

bubble was observed to grow in height and length but was never able to attain the size of the steady flow case.

In a detailed unsteady boundary layer measurement, the onset and extension of the separation zone with unsteady wake flow was identified [7]. The separation zone was observed to periodically contract and expand with the passing wake. The authors suggest that in conjunction with the pressure gradient and the passing wakes, the fluctuation acceleration (rate of change of RMS velocity with respect to time) offers a higher momentum and energy transfer into the boundary layer which energizes the separation zone and can cause it to partially or completely disappear. A condition in which the direction of the fluctuation acceleration determines the behavior of the separation zone is presented. The authors suggest if the fluctuation acceleration is greater than zero, the separation zone starts to contract and as it becomes less than zero, it gradually expands back to the shape before the contraction. It is concluded that the fluctuation gradient is a natural characteristic of the periodic wake and does not exist in a steady flow with high turbulence intensity.

The convection of a wake through a turbine passage was studied using two-dimensional LDA [13]. In this study the perturbation velocity vectors, calculated by subtracting the ensemble average velocity from the time average velocity, were used to visualize the wake convecting through the blade passage. The visualization showed the wake becoming bowed, stretched and elongated as it passed over the blade surface. Most importantly, turbulence measurements revealed turbulent kinetic energy production external to the boundary-layer flow and provided a method in which the convection of a turbulent wake through a blade row may increase the levels of turbulence.

1.2.5 Affect of Periodic Unsteady Wakes on Flow Separation and Losses

The inclusion of unsteady wakes in the flow around a low pressure turbine blade at low Reynolds number has been shown to be very beneficial, especially if the suction surface exhibits a separated boundary layer. Schobeiri [28] performed a study in which the Reynolds number and the wake passing frequency was varied and compared to steady flow conditions. It was shown that increasing the Reynolds number from 110k to 150k had little effect on the separation bubble and C_p distribution for the steady state case. For the unsteady case however, the C_p distribution displayed increased loading with a shorter separated region for the higher Reynolds number, indicating the separation bubble had been reduced in height and length. Boundary layer measurements confirmed these observations and revealed the separation bubble contracting and expanding as the wake passed.

The free-stream turbulence intensity (FSTI) can also play an important role in the extent of flow separation with passing wakes. Öztürk and Schobeiri [29] performed a turbulence study with passing wakes for four different FSTI and found that the effect of the wake can be washed out in the turbulence and the separation behavior is completely dominated by turbulence levels. It was found that the wake becomes absorbed in the free-stream turbulence when the level of the time-averaged turbulence fluctuations is above the maximum level of the wake fluctuations.

In a similar study using the same facility, the effects of periodic unsteady wake flow on boundary layer development, and separation along the suction surface of a low pressure turbine blade was investigated [14]. In this study, two unsteady and one steady

flow conditions were analyzed at a Reynolds number of 110k. Similar results were found in which the wakes periodically disturb the boundary layer with their high turbulence vortical core, and were effective in reducing the size of the separation bubble. A periodic contraction and expansion with a reduction in the separation bubble height was also observed.

Curtis et al. [2] used a loss-lift parametric study to design low pressure turbine blades based on the results from a datum profile. It was shown that the inclusion of wakes caused an attached transitional boundary layer to develop on the blade surface which was previously laminar for steady inflow. The addition of the wakes had modified the boundary layers on all three blades tested and it was a contributing factor in the loss measurements.

Utilizing this knowledge gained from increased blade loading with unsteady wake flow, a study was performed using newly designed “ultra high lift” blade profiles and compared to a previous generation of high lift profiles [5]. Experiments were performed in both a high speed and low speed cascade with unsteady wakes, and then validated using a high speed cold flow multi-stage turbine rig. The high lift profiles achieved a 20% blade count reduction from previous designs while the ultra high lift profiles attained an 11% further reduction in blade count from that of the high lift design.

In both the high speed and low speed cascade tests with unsteady wakes, a strong dependency on Reynolds number was shown with losses increasing with decreasing Reynolds number. The high speed cascade tests show that the ultra high lift profile had lower losses from a Reynolds number (based on suction surface length and isentropic exit velocity) of 300k to 105k, then increased dramatically and surpassed that of the high lift

profile down to the tested Reynolds number of 70k. The results were not as promising for both the low speed and cold flow rig tests. In both tests the high lift profile slightly out-performed the ultra high lift profile which showed higher losses and lower efficiency. Although the ultra high lift profile did not out-perform the high lift profile, a higher loading with decreased blade count and a significant reduction in weight was achieved. The authors note that further investigation is needed to identify the source of the loss in performance. However, they suggest it may be caused by increased secondary flow due to the higher loading and decreased wake passing frequency due to the decreased blade count.

Using the same cold flow test rig as in [5], Howell et al. [30] performed a boundary layer study using surface mounted hot-film sensors, in which wall shear stress was analyzed for both a high lift profile and an ultra high lift profile that had a 12 % reduction in blade count. The results showed that much of the flow physics seen in the low speed cascade tests with simulated wakes was present in the full size cold flow test rig. The cold flow test rig data showed the typical regions of wake induced transition followed by a calmed region, which further validates the usefulness and the ability to simulate rotor-stator flow interactions in low speed cascades with simulated upstream wakes.

A similar study by Howell et al. [4] showed that higher lift generating low pressure turbine profiles can be achieved when the inclusion of wake induced transition is taken into account at the design phase of the turbine blade. In this study, multiple mid-loaded profiles with increasing lift were tested and compared to a mid-loaded datum profile. Hot-film measurements showed that, for a fixed peak suction location, as the

loading was increased, unsteady flow reattachment of the boundary layer was shown to have moved upstream when compared to the datum profile with steady inflow. The authors cite Howell [8] as showing that, as the surface length of the bubble is reduced with increasing lift, the height of the bubble is increased along with the losses generated. The authors explain that this loss increase under steady flow conditions is partly due to the increased region of a turbulent boundary layer that develops downstream of reattachment. With the inclusion of simulated unsteady wakes, the data shows a significant reduction in losses. The authors state that the potential for obtaining a loss reduction with the use of wakes increases as the loading increases.

Using this information, and in an attempt to reduce the turbulent region downstream of reattachment, an aft-loaded blade design was produced with 15% increased loading over the datum profile. In an aft loaded blade, peak suction occurs further downstream along with the separation and reattachment locations, effectively reducing the post reattachment turbulent region. The results with simulated upstream wakes show that the aft loaded profile had slightly higher losses than the datum profile, but produced 15% more lift, which translates into a 15% blade count reduction. Howell et al. [4] concludes that understanding the unsteady effects of wake flow can change the design limits placed on the location of peak suction and separation as well as the deceleration level.

Periodic wakes have been shown to reduce profile losses at low Reynolds number due to a reduction of the separation bubble. At high Reynolds numbers, the reduced viscous effects along with the smaller boundary layer can prevent separation as discussed previously. In a study by Coton et al. [31] in which high Reynolds numbers were tested,

the advantages of unsteady wakes deteriorated with increasing Reynolds number. At high Reynolds number the boundary layer becomes thinner and transition was shown to occur without the inclusion of unsteady wakes. At these high Reynolds numbers, the inclusion of wakes slightly increased the losses as larger turbulent regions were present. Similar results were found in other studies at high Reynolds number [32] [12] where the unsteady wakes increased losses. In these studies it was concluded that the loss reduction at low Reynolds number was significant and outweighed the efficiency cost of the relatively small loss increase at high Reynolds number.

Periodic wakes have been shown to reduce the separation bubble, but in many of these studies the separation bubble was not completely removed and was shown to grow between passing wakes. Flow control studies with periodic wakes have attempted to further reduce the separation bubble and losses. Gompertz [33] performed a separation flow control study using vortex generating jets with simulated upstream wakes on the L1A low pressure turbine blade. It was found with periodic unsteady wakes, the separation zone was reduced, and the integrated wake total pressure loss was decreased by more than 75%. This however, was not enough to fully attach the flow and a small separation bubble remained. With the inclusion of the vortex generating jets, the flow became attached and the C_p distribution fully recovered its high Reynolds number performance. The author states that with vortex generating jets located at 72% C_x , pressure data indicated that the jet disturbance assumes a secondary role to the unsteady wakes, requiring more energy to penetrate through the separation zone. It is concluded that the actuation of the jet inside the separated zone increased the effectiveness by timing the jet induced calmed zone between wake passing events.

In a parametric study by Zhang and Hodson [34], the effect of surface trips on the profile losses of a low pressure turbine blade were examined and then applied with the presence of unsteady wakes. It was found that employing the optimized surface trip with unsteady wakes did not induce transition immediately, but sped up the transition process in the separated shear layer. This occurred underneath and between the wakes and further reduced the profile loss.

1.3 Objective

The role of wake generating systems in the research of flow separation on low pressure turbine blades has proven to be invaluable. Extensive research using wake generating devices has been ongoing for the past thirty years and will continue as more research is necessary to reach the goals of efficiency and blade loading industry desires (Figure 1.1). In an effort to help industry reach these goals, the Air Force Research Laboratory (AFRL) has been working to expand the design space and push the aerodynamic loading limits of low pressure turbine blades [35]. In a continuation of this effort, a wake generating system was desired for use in the AFRL low speed wind tunnel (LSWT) facility to further investigate the effects of periodic unsteadiness on low pressure turbine blade efficiency.

The subject of this thesis is the design and characterization of a wake generating system for the AFRL low speed wind tunnel. The design objective is to produce periodic unsteadiness in the flow impinging upon a linear cascade of low pressure turbine blades that properly simulates the effect of upstream blade row wake shedding. It was preferred

that the design have little to no modifications to the existing wind tunnel structure and the appropriate flow conditions be maintained across the test section. In accordance with these design constraints, a completely internal wake generating system was developed for the AFRL low speed wind tunnel.

The characterization of the wake generating system was a comprehensive study of the effect on the wind tunnel flow and the behavior of the cascade of low pressure turbine blades with periodic unsteady wakes. The effect on the wind tunnel flow was assessed by checking for proper flow velocities at various locations within the wind tunnel using hot-wire measurements, and verifying cascade periodicity with pressure measurements. The wake produced from the wake generating system was characterized with turbulence quantities and wake properties measured from the velocity deficit of two different wake generating shapes. Wake loss measurements were obtained for evaluation of blade losses with periodic unsteady wakes and compared to steady inflow data. Pressure taps were instrumented on the suction and pressure side of the blade profile to obtain surface pressure measurements and blade loading characteristics. Particle image velocimetry (PIV) was used on the flow along the blade suction surface for a complete analysis of the flow field within the blade passage with periodic unsteady wakes. The free-stream turbulence intensity (FSTI) was varied for each measurement from a low FSTI of 0.5% to a high FSTI of 3.4%. This characterization of the new wake generating system provides quantification of wake generating parameters and demonstrates the capabilities and limitations of the system for further investigations.

Chapter 2

Wake Generator Design

2.1 Experimental Facility

A wake generating system was designed for the low speed wind tunnel at AFRL Wright-Patterson Air Force Base. The dimensions and functionality of the wind tunnel were the primary design constraints for the wake generating system.

The wind tunnel is an open circuit type with a 0.85m tall by 1.22m wide test section containing a linear cascade of low pressure turbine blades. The test section contains adjustable tailboards to set cascade periodicity and is able to be angled for different inlet and exit angles. A 125hp variable frequency electric motor drives an axial flow fan located downstream of the test section and is capable of inlet velocities up to 80m/s. The inlet is a 3.0m by 2.7m rectangular bell-mouth with an 8:1 gradual reduction in cross-sectional area. Air enters through a series of honeycomb flow straighteners, which produce a flow uniformity of less than 1% and a free-stream turbulence intensity (FSTI) of approximately 0.5% at the test section inlet. An optional square bar mesh turbulence-generating grid can be placed upstream of the cascade yielding a free-stream turbulence intensity of about 3.4% to better match the flow field encountered in a turbine

engine. A schematic of the wind tunnel can be seen in figure 2.1(a) and the entire setup is shown in figure 2.1(b).

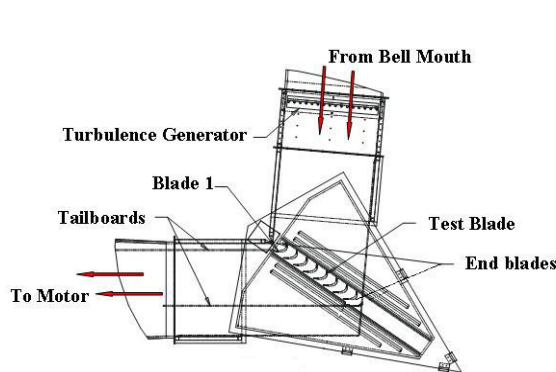


Figure 2.1 (a) Top view schematic of wind tunnel test section



(b) Wind tunnel setup at AFRL.

2.2 Wake Generator Design Objectives and Constraints

The overall design objective for the wake generating system was to produce periodic unsteadiness in the flow impinging upon a linear cascade of low pressure turbine blades, which properly simulates the effect of upstream blade row wake shedding. It was preferred that the design have little to no modifications to the existing wind tunnel structure and the appropriate flow conditions be maintained across the test section. Historically, installing a wake generating system in a wind tunnel consisted of cutting into the test section and separating it from the inlet and exit. This allows for the drive system to be mounted externally and the wake generating mechanism to enter and exit through the wind tunnel sides. Since cutting into the current test section was undesirable, a completely internal design was chosen for the wake generating system. The enclosed

design does not modify the current wind tunnel structure and keeps the internal flow contained without leakages, unlike other external wake generator designs.

In a typical design of a wake generating system, the wake generating mechanism traverses across the cascade upstream, and again downstream, in order to complete a cycle. With the entire system limited to inside the wind tunnel, certain design constraints became apparent. Cascade geometry in the test section would not allow for any part of the system to pass through, therefore limiting the entire structure to be placed upstream of the cascade. All functionality and adjustability of the wind tunnel was to be maintained, including the use of the optional turbulence grid. Based on these constraints, the entire wake generating system was to be confined between the cascade and turbulence grid in the approximately 2.3m long region with a constant cross-section of 0.85m by 1.22m (figure 2.1a). Since the entire system was to be placed inside the wind tunnel, the components of the system were to be small and low-profile so that the flow at the test section was not unintentionally disturbed. These requirements were feasible given the large scale of the wind tunnel and the relatively large wall boundary layers in which the wake generator components could be contained.

2.3 Wake Generator Design

2.3.1 Wake Generating Mechanism

The majority of wake generating systems use cylindrical rods as the wake generating mechanism. The validity of this was investigated in the literature review and it was shown that the wake shed from a cylindrical rod adequately matches the wake shed from

a turbine blade [10, 18, 19, 20-22]. Based on these studies, it was decided to also use a cylindrical rod as the wake generating mechanism for this system. Carbon fiber rods were chosen as the wake generating mechanism due to their relatively light weight and natural dampening characteristics to help suppress rod vibration. Following the same methodology of other wake generating systems, the rod diameter was chosen to match the trailing edge diameter of the cascade blade profiles, and the placement upstream of the cascade was chosen to be a half of an axial chord length. Although a typical vane count is 60-75% of the blade count in a low pressure turbine [36], the rod spacing was chosen to match the blade spacing of the cascade as this was thought to be a good starting point. This resulted in the rods traversing 8.9cm upstream of the cascade with a rod diameter of 3.2mm, and a rod spacing of 17.8cm.

As a second option, an airfoil shape was designed to be used as a wake generating mechanism to better match the wake shed from a turbine blade. A symmetric NACA 0025 airfoil was chosen as the wake generating shape for its relatively thick aerodynamic body which is thought to produce a more appropriate wake. A casting mold was designed so that the airfoil shape could be cast around a hollow aluminum rod, allowing easy installation overtop the existing carbon fiber rods. In an effort to minimize the flow disturbance of the airfoil as it travels around the track, the airfoil was designed to “weather-vane” around the carbon fiber rod. This allows the leading edge to always face the flow direction, minimizing the flow blockage.

2.3.2 Track Configuration

Based on the design configuration, it was determined that a squirrel cage design common in other wake generating systems would best suit the wind tunnel layout. The squirrel cage design consisted of the cylindrical rods oriented vertically and fastened to the drive mechanism running along the top and bottom of the wind tunnel.

A fully enclosed design with the entire system upstream of the cascade will inherently cause secondary wakes to be generated as the wake generating mechanism makes a second, upstream traverse, back across the wind tunnel completing the cycle. This is the drawback to an internal wake generating system, as wakes cannot be continuously produced due to the effect of secondary wakes. Instead, the cylindrical rods were only placed on a portion of the traversing track so that the generation of secondary wakes upstream does not interfere with the primary wakes. Different track configurations were conceived by Dr. Rolf Sondergaard of AFRL in an attempt to optimize the number of primary wakes generated in a single cycle. These configurations were based on the dimensions of the wind tunnel and also utilized a delay loop to achieve a suitable number of primary wakes shed during one cycle.

An optimization routine was developed by Dr. Sondergaard to quantify the track configurations based on maximizing the number of primary wakes while minimizing the cycle time. For each track configuration, the rod speed, rod spacing, and the number of rods were used as inputs to the optimization routine, and the track length, primary wake time, cycle time and efficiency were calculated. The optimal track configuration was chosen based on an efficiency parameter which was defined as the ratio of primary wake generating time to cycle time. Figure 2.2 shows an example of the different track configurations examined and figure 2.3 shows the optimization routine visualization.

The visualization is a time plot that demonstrates the time of primary (bottom region) and secondary (top region) wake shedding with the distance along the cascade face.

Parameters were adjusted so that the primary and secondary wakes did not overlap.

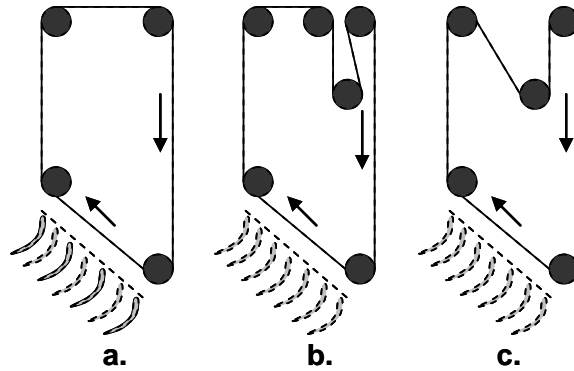


Figure 2.2 Examples of different track configurations considered and modeled in simulation program.

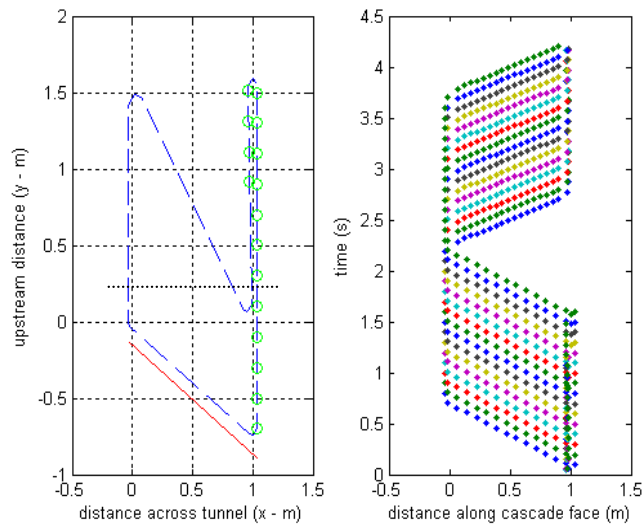


Figure 2.3 Visualization output of wake generator track produced in simulation program.

The optimal track configuration, shown in figure 2.2 (c), produced a track length of 8.407m with 18 cylindrical rods equally spaced across a 3.02m span. Based on these

dimensions the wake generator system has a 36% duty cycle for which primary wakes are generated.

A hollow pin roller-chain was chosen as the carrier mechanism and allowed easy attachment of the rods. A 3hp, 3450rpm variable frequency motor was selected to drive the system through a 1.59cm diameter shaft by means of a v-belt. The v-belt was used instead of a direct drive system as a safety precaution in case the chain locked up, the belt would slip and not cause any damage. The drive motor was to be mounted externally with the drive shaft penetrating through a hole on the top of the wind tunnel. The final design uses five sprockets on the top and bottom of the wind tunnel to guide the chain through directional changes and two chain tensioners located on the slack side of the drive pulley.

2.3.3 Wake Generator Structure

The low speed wind tunnel at AFRL is adjustable for various inlet and exit flow angles and it was necessary to have the wake generating system also be adjustable for various angles. Based on this need, UniStrutTM was selected for the wake generator structure so that all of the components are adjustable for different configurations of the wind tunnel. The wake generator structure, chain, sprockets, chain guides, and tensioners, were all designed to be compact and placed as close to the wind tunnel walls as possible. By keeping the majority of the structure within the approximately 10 cm thick wind tunnel wall boundary layers, the free-stream flow disturbances caused by the wake generator structure should be minimized. The final design was drawn using 3D CAD software and is shown in figure 2.4 and figure 2.5. A picture of the wake generating system installed in the wind tunnel is shown in figure 2.6.

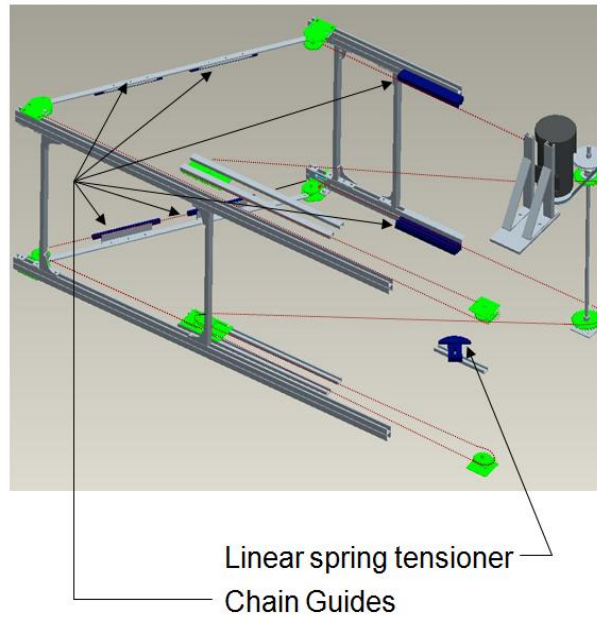


Figure 2.4 3D CAD drawing of wake generator structure with chain tensioner, sprockets, and chain guides highlighted.

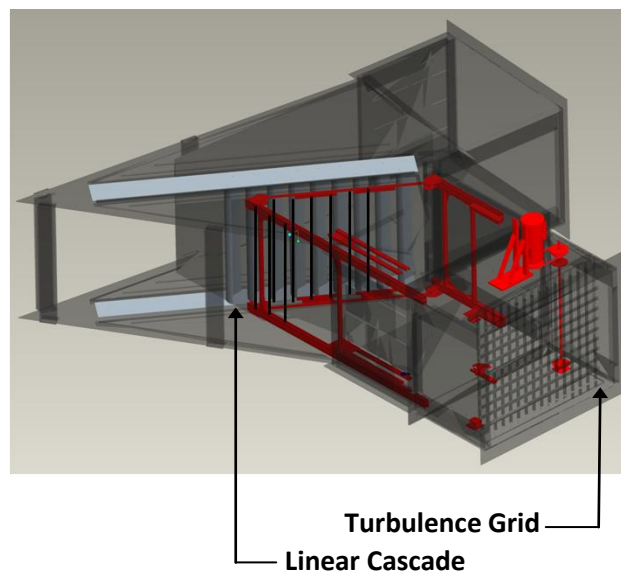


Figure 2.5 3D CAD drawing of wake generator structure installed in wind tunnel. Wake generator system is highlighted in red.

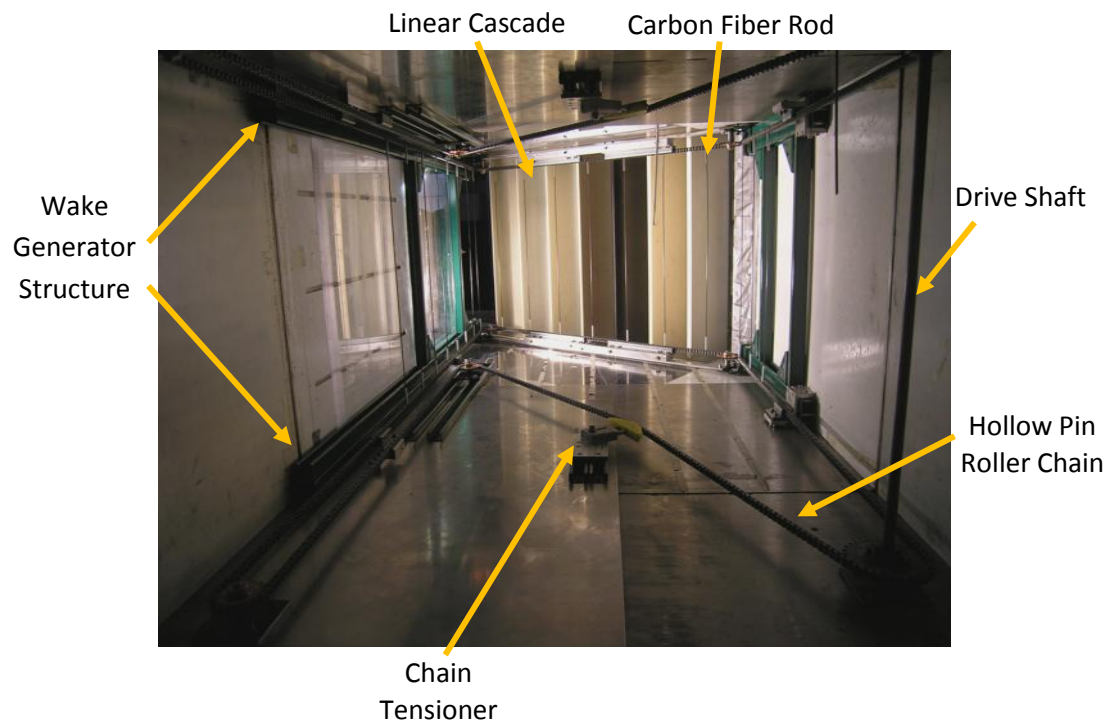


Figure 2.6 Wake generator system installed in low speed wind tunnel.

Chapter 3

Characterizing the Periodic Wake Produced by the Wake Generator

3.1 Experimental Analysis

Velocity and pressure measurements were performed downstream of the wake generating mechanisms to characterize the wakes impinging upon the cascade of turbine blades. The individual wake was quantified by wake width, peak velocity deficit, and momentum deficit. The wake width b , and values used to calculate peak velocity deficit u_p are defined in figure 3.2. The wake width as used here, was measured from 95% of the undisturbed velocity on either side of the wake velocity deficit. The peak velocity deficit u_p , was calculated using eqn. (3.1) for each wake generating mechanism.

$$u_p = \frac{U - u_0}{U} \quad (3.1)$$

In this equation, U is the average undisturbed free-stream velocity and u_0 is the minimum value of the velocity in the deficit. The momentum deficit of the generated wake can be derived from the linear momentum equation for a fixed, non-deforming control volume. The equation used for this calculation is given in eqn. (3.2).

$$\int_{cs} u^* (U - u) dx \quad (3.2)$$

The control surface used in the analysis of this equation is shown in figure 3.3. It is assumed that the boundaries of the control surface are located a distance away from the body so that the pressure across the control surfaces is constant. The surface at B is also assumed to be a distance downstream where the static pressure is equal to the free-stream static pressure [37].

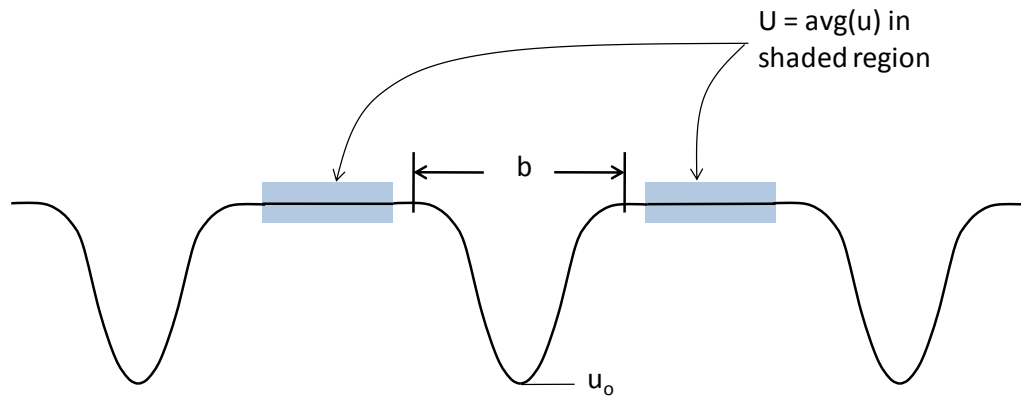


Figure 3.1 Description of parameters used in calculation of wake width and peak velocity deficit.

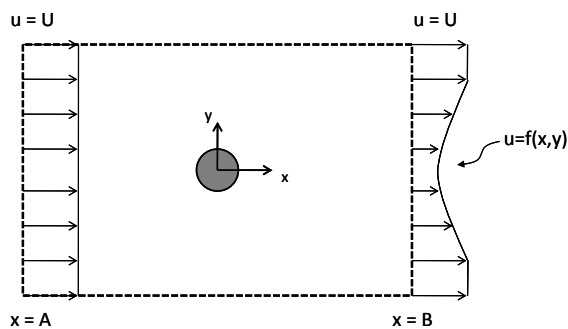


Figure 3.2 Control surface for momentum deficit of the generated wake

The integrated momentum deficit was also used in the evaluation of the number of cycles needed to fully develop the time-averaged wake. This parameter was used

since each individual wake produced by the cylindrical rod should contain about the same momentum deficit as a time averaged wake. Therefore, based on conservation of momentum, a converged momentum deficit should be obtained, given the appropriate amount of cycles. The number of cycles needed for a converged result will also be used in the evaluation of the integrated wake total pressure loss measurement. A fully developed time-averaged wake is needed for this measurement in order to properly evaluate the effectiveness of the periodic unsteadiness.

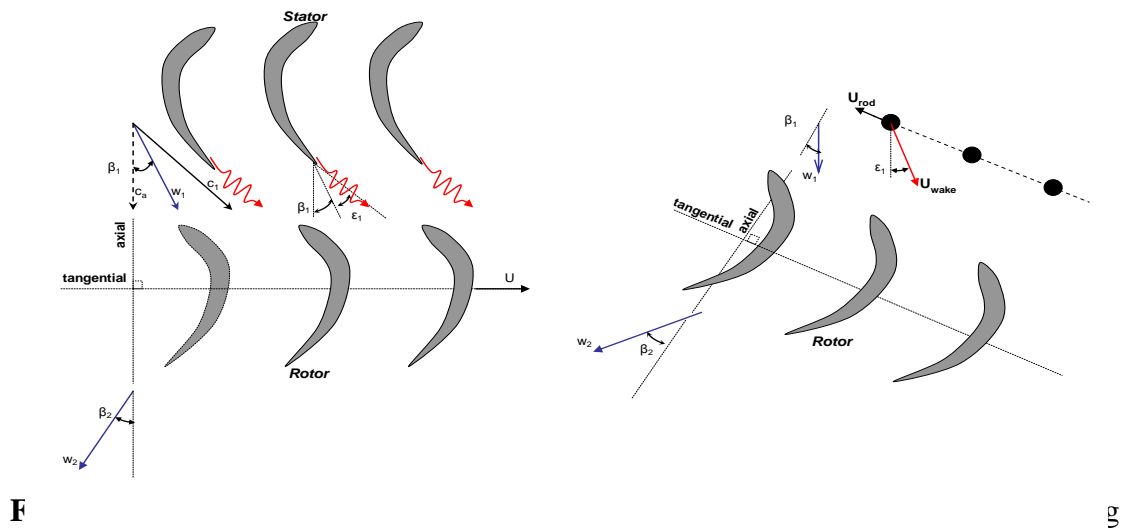
3.2 Experimental Setup

A characterization of the wakes shed from the two wake generating mechanisms was performed using pressure and velocity data at two different Reynolds numbers and two different free-stream turbulence intensities. Since low Reynolds number performance is of interest, a Reynolds number (based on inlet velocity and axial chord length) of 25,000 and 50,000 were used with a FSTI of 0.5% and 3.4%. For each of these flow conditions, two different traversing speeds were considered while rod diameter and rod spacing were held constant. A common parameter used in evaluating the traversing speed with respect to the flow speed is the flow coefficient. The flow coefficient is defined as the ratio of the axial flow velocity to the rod velocity and is shown in eqn. (3.3).

$$\phi = \frac{U_{axial}}{U_{Rod}} \quad (3.3)$$

For each Reynolds number and FSTI tested, data was taken with a flow coefficient of 0.7 and 0.8.

These values of flow coefficients are commonly used values to match velocity triangles of a rotor and stator blade row [12]. Figure (3.1) gives a geometrical representation of modeling a vane row with cylindrical rods and the respective flow interactions. In this figure, it is shown that as the rotor blades rotate, they are subject to periodic unsteadiness generated from upstream vane row wake shedding. Matching the rod velocity to the velocity triangle of the stage, and allowing the rods to traverse across a static cascade can effectively simulate the rotor stator interaction.



Pressure and velocity data was taken by placing a total pressure Kiel probe, along with a single element hot-wire probe, in an undisturbed region of flow upstream of the passing rods so that free-stream conditions could be obtained. The velocity probe was placed upstream of the primary wakes, but within the loop of the wake generator. The measuring probe needed to be placed here so that the inlet velocity to the cascade could be measured for the Reynolds number calculation. A second total pressure Kiel probe and a single element hot-film probe were mounted together, 6.35cm apart in the span-

wise direction, and placed just in front of the leading edge of the cascade between blades 3 and 4. The total pressure Kiel probes were connected to the high and low pressure side of a Druck LPM5481 differential pressure transducer with a range of -50 to 200 Pa. The output of this device was the difference in total pressure between the free-stream and the affected downstream total pressure. The upstream hot-film probe was used in setting the free-stream conditions of the wind tunnel, while the second probe was used to measure the velocity deficit of the wakes impinging upon the linear cascade. Data was taken with the measuring probes in a fixed position while the eighteen cylindrical rods passed by during a cycle.

Data was recorded using Lab ViewTM data acquisition software. The software was setup so that data was acquired at a sampling frequency of 2 kHz for both pressure and velocity. Data acquisition was phased locked, based on the location of a trigger sensor. This sensor was a fast response phototransistor optical sensor and was triggered by flags placed along the length of the chain. Two photoelectric sensors were used, one to trigger the phased locked data acquisition process, and another to measure the speed of the chain. Phase locking the data acquisition was needed since the cylindrical rods were only spaced out across 36% of the total chain length.

3.3 Wake Characteristics from a Partially Populated Chain

A complete cycle of ensemble average velocity data at a Reynolds number of 25,000 with a FSTI of 0.5% and 3.4% is shown in figure 3.4. The second smaller set of periodic wakes in this figure are the secondary wakes generated as the rods make a

second traverse across the wind tunnel completing the cycle. No interaction between primary and secondary wakes was observed, proving the effectiveness of the delay loop. The velocity trace at the low FSTI of 0.5% shows strong evidence of the secondary wakes for both the inlet probe and cascade wake probe. The magnitude of the velocity fluctuation in the secondary wakes was unexpected given the small rod diameter and the distance upstream the wakes are generated.

At the higher FSTI of 3.4%, the secondary wakes appear to be mostly washed out in the free-stream turbulence with little remnants of a periodic velocity deficit. The effect of the secondary wakes mixed with the primary wakes will be investigated further by using a chain fully populated with rods.

The data in figure 3.4 shows that as the cylindrical rods first pass by, it takes about three rod passes before a periodic wake is established. Therefore, it was decided to analyze the wake from the ninth rod for the characterization to eliminate any non periodic effects. The ensemble averaging was also observed to eliminate non-periodic effects due to rod vibration and random fluctuations in the wake.

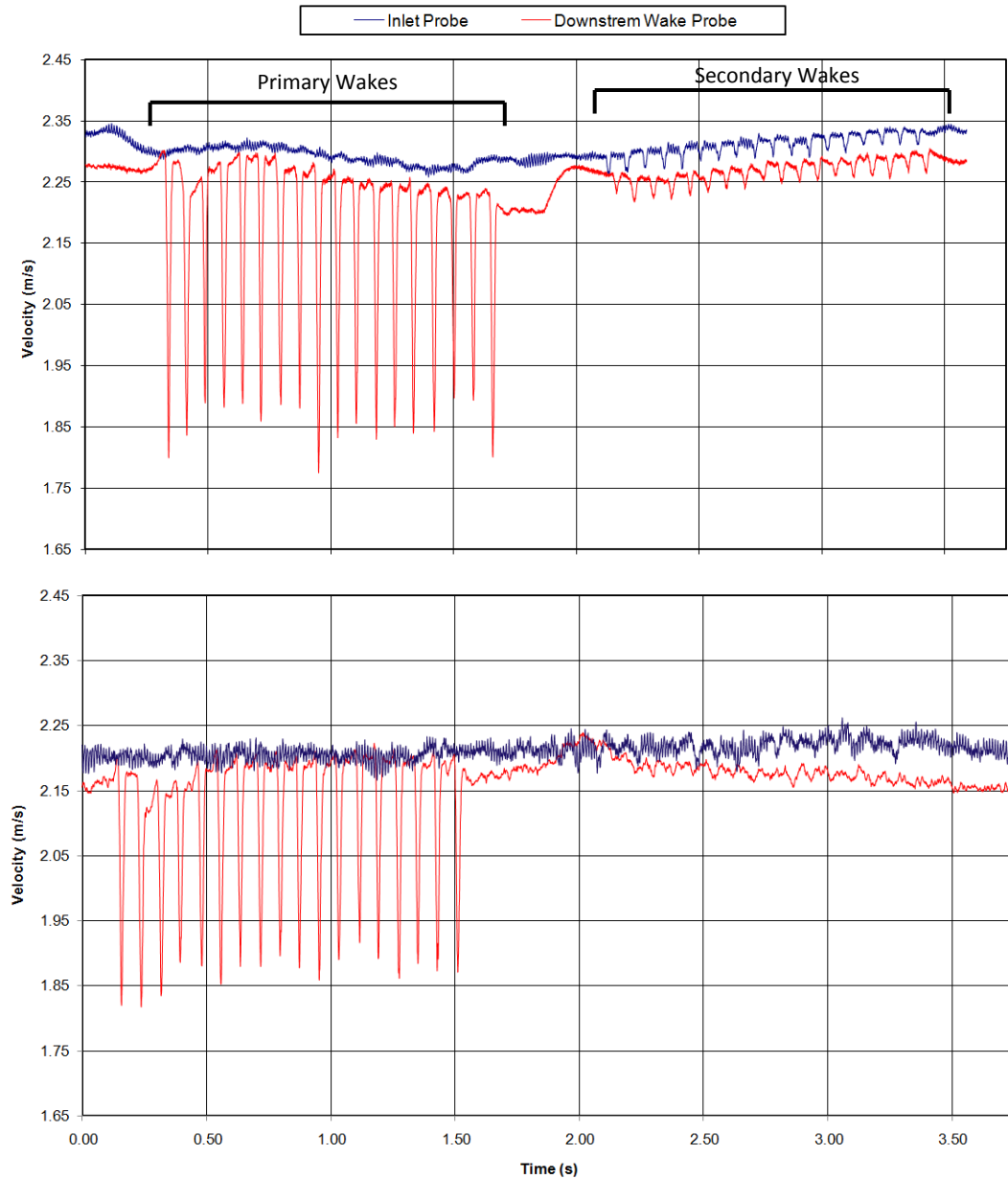


Figure 3.4 Complete cycle of ensemble average velocity data showing both primary wakes and secondary wakes. ($Re = 25k$, Top: FSTI 0.5%, Bottom: FSTI 3.4%)

Using the momentum deficit from the ninth wake, a convergence study was produced for evaluating the number of cycles needed for a fully developed time-average wake. A range of 50, 100, 200, and 400 cycles were averaged for two data sets at a Reynolds number of 25,000 with a flow coefficient of 0.8 and FSTI of 0.5%. Analogous

data was taken for the higher Reynolds number with similar results, but for simplicity, the 25,000 case will be considered here. Increasing from 50 to 100 cycles, the integrated momentum deficit saw a change of 3.5%, while going from 100 to 200 cycles averaged, the momentum deficit saw a 1.5% change. A similar trend is shown for 200 to 400 cycles averaged with a 3.2% change. These values are well within an acceptable change for experimental data and compared well to the instantaneous data. From these results, along with comparing values to the instantaneous raw data, it was decided to use 100 cycles to define a fully developed time averaged wake. A summary of this convergence data for every ensemble is shown in Figure 3.5.

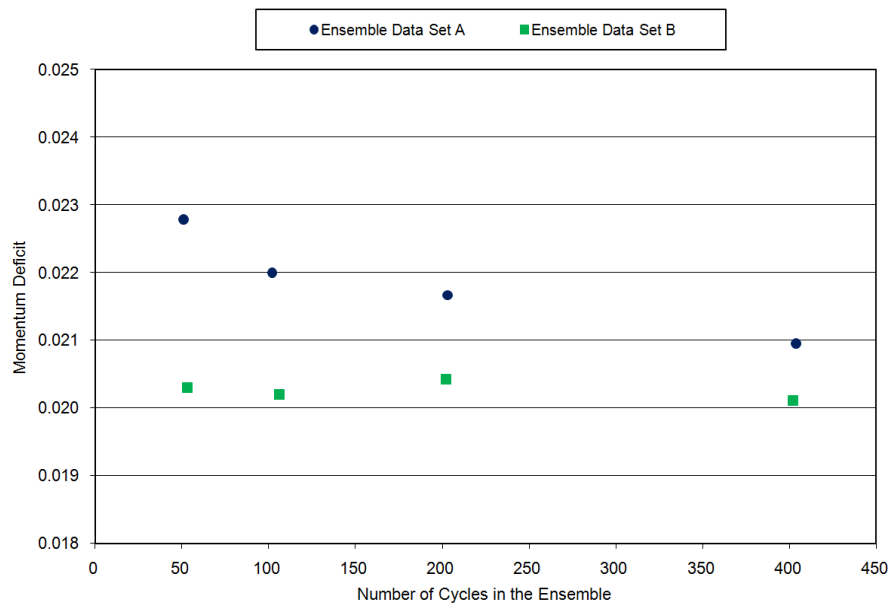


Figure 3.5 Convergence study of the number of cycles needed for a fully developed time-averaged wake

Using 100 cycles for an ensemble average and analyzing the ninth wake produced from the series of eighteen rods, the wake width, peak velocity deficit, and integrated momentum deficit was calculated for each case and summarized in Table 3.1.

Reynolds Number/FSTI	Flow Coefficient ϕ	Momentum Deficit	Wake Width (m)	Peak Velocity Deficit
25k/0.5%	0.817	0.0220	0.0861	0.2143
25k/0.5%	0.697	0.0246	0.0809	0.1816
25k/3.4%	0.810	0.0144	0.0715	0.1335
25k/3.4%	0.712	0.0158	0.0651	0.1254
50k/0.5%	0.821	0.0683	0.0624	0.1752
50k/0.5%	0.700	0.0982	0.0667	0.2047

Table 3.1 Calculated wake characteristics based on hot-film measurements for a 36% duty cycle wake generator.

As expected, for a constant FSTI the experimental results show increasing momentum deficit with increasing Reynolds number and decreasing flow coefficient. This agrees with the definition of flow coefficient that a lower value results in a higher wake passing frequency and a higher Reynolds number seen by the rod. The increase in FSTI results in a dissipation of the wake parameters as it affects both the convection of the wake and also the behavior in which it is shed from the rod. A net reduction in all of the parameters was observed as the wake became mixed in with the flow and had less of an effect on the free-stream compared to the low FSTI case.

The results for the wake width and peak velocity deficit did not show a trend with Reynolds number. This variation in the results is thought to be due to rod vibration and the distance downstream in which the wake was measured. At half an axial chord length downstream, the wake is being measured at 28 rod diameters downstream. For these low rod Reynolds numbers (400-1800), the wake properties at this distance are categorized as being in the near wake ($x/d < 80$) which is considered to be much more erratic. This is due to the fact that the wake of a blunt body such as a cylindrical rod creates a wake of

alternating shed vortical structures [38]. In the near wake these structures are very unsteady in nature and do not produce as consistent results, as compared to being in the far wake or similarity region. The rod vibration along with the rod not being a perfectly smooth cylinder, can lead to a turbulent wake being shed which would produce these inconsistencies.

The pressure measurements showed a decrease in total pressure from the location downstream of the turbulence grid to the cascade leading edge. Unfortunately, the pressure never attained a steady state value, as the 36% duty cycle of the wake generator was not long enough to produce a flow-field long enough to measure. This resulted in a sinusoidal behavior of the data as wakes are shed and then followed by a calm period during the cycle.

3.4 Wake Characteristics from a Fully Populated Chain

A continuous generation of wakes is very desirable, in that it would simplify the data acquisition process and speed up the measurement time. In addition, some measuring devices, particularly pressure measuring devices, have relatively slow response times and require a flow-field to be established for a certain duration of time. In some cases, a wake generator with a 36% duty cycle may not establish a flow-field long enough to accurately measure. Therefore, the feasibility and accuracy of a continuous generation of wakes with the current system was investigated.

In order for a continuous generation of wakes with the current system to occur, rods would have to be placed around the entire length of the chain. With this

configuration, the secondary wakes will affect the primary wakes and an unwanted disturbance in the wind tunnel flow may occur. In an effort to quantify this, the chain was populated with rods around the entire length, and wake characteristics were quantified by wake width, peak velocity deficit, and momentum deficit, in the same manner as in the previous section. Data was also acquired in the same way with hot-wire probes and ensemble averaging of the data. The results with the fully populated chain were then compared to the results with a partially populated chain.

For simplicity, a Reynolds number of 25,000 with both flow coefficients and both levels of FSTI were evaluated. Figure 3.6 shows a time trace for one case of the ensemble averaged velocity data for a complete cycle with the continuous generation of wakes. The velocity trace shown in this figure displayed small disturbances in-between passing wakes and was observed in all four cases. The first set of wakes in this figure show a larger disturbance in-between the passing wakes compared to the disturbances seen in the remaining wakes. When a more detailed analysis was done on the individual wakes, a similar observation was made at the peak of the deficit with larger fluctuations occurring in some wakes. These disturbances and random magnitude fluctuations are thought to be a function of the location in which the secondary wakes interact on the primary wakes. These fluctuations do not seem to be a large factor in affecting the shape of the wake.

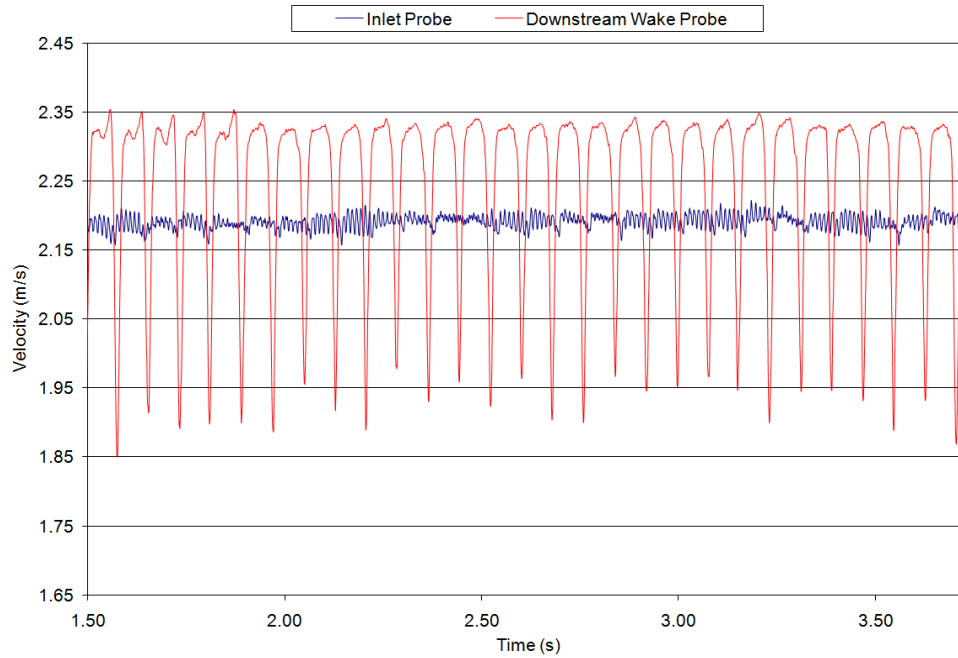


Figure 3.6 Complete cycle of ensemble average velocity data for a fully populated chain. ($Re = 25k$, $\phi = 0.8$, FSTI 0.5%)

Wake properties were measured in the same manner as the previous section with 100 cycles averaged in the ensemble. Since there is no delay in establishing periodic unsteady flow with the continuous generation of wakes, a random wake was selected for analysis. To make the analysis easier and more repeatable, a wake without large fluctuations from the secondary wakes was chosen from each data set. Table 3.2 summarizes the wake properties obtained from the analysis.

Reynolds Number/FSTI	Flow Coefficient ϕ	Momentum Deficit	Wake Width (m)	Peak Velocity Deficit
25k/0.5%	0.802	0.0222	0.0628	0.1849
25k/0.5%	0.695	0.0279	0.0652	0.2079
25k/3.4%	0.805	0.0220	0.0609	0.1735
25k/3.4%	0.714	0.0242	0.0596	0.1746

Table 3.2 Calculated wake characteristics based on hot-film measurements for a 100% duty cycle wake generator.

The trends in table 3.2 are similar to the ones shown in table 3.1. As the flow coefficient is decreased, the momentum deficit increased for both FSTI tested. Once again, there was no apparent trend for the wake width and peak velocity deficit with Reynolds number. This variation in the results is again thought to be due to rod vibrations resulting in a turbulent wake and the distance downstream in which the wake was measured.

Comparing the wakes from the 36% duty cycle wake generator to the 100% duty cycle wake generator showed a decrease in the effect of higher turbulence intensity. For the 36% duty cycle case, the momentum deficit decreased on average 35% from the low FSTI to the high FSTI, while the 100% duty cycle case only decreased 7%. The peak velocity deficit and wake width were within an expected experimental variation and the secondary wakes did not seem to have an overwhelming effect. In general the wake characteristics were similar for the partially populated chain and the fully populated chain.

It was observed for the 100% duty cycle case, in all four data sets, the velocity magnitude had increased from the inlet probe to the cascade probe. A slight change in

velocity was observed in the 36% duty cycle data, but was marginal. For the 0.8 flow coefficient, the velocity magnitude had increased by about 5.5%, while for the 0.7 flow coefficient, the velocity magnitude had increased by about 6.5%. This increase in velocity magnitude can be attributed to the addition of a swirl velocity caused by the rods as they traverse across the wind tunnel.

A single element hot-film probe, such as the one used in this experiment, only measures velocity magnitude and is insensitive to direction. Knowing the free-stream velocity from the inlet probe and the effective velocity measured by the cascade probe, the tangential component of velocity induced by the rods can be decomposed. An estimate of the tangential velocity magnitude along with the change in flow incidence can be made using vector decomposition shown in figure 3.7. Using this analysis, for a flow coefficient of 0.8, the tangential velocity induced by the traversing rods was estimated at 1.49 m/s, which changes the flow incidence angle by 4.7 degrees. Similarly, for a flow coefficient of 0.7, the tangential velocity was estimated at 1.52 m/s, which changed the flow incidence angle by 5.0 degrees. This change in the flow incidence angle is undesirable, as the cascade is no longer being tested at design conditions which can change the performance of the blade.

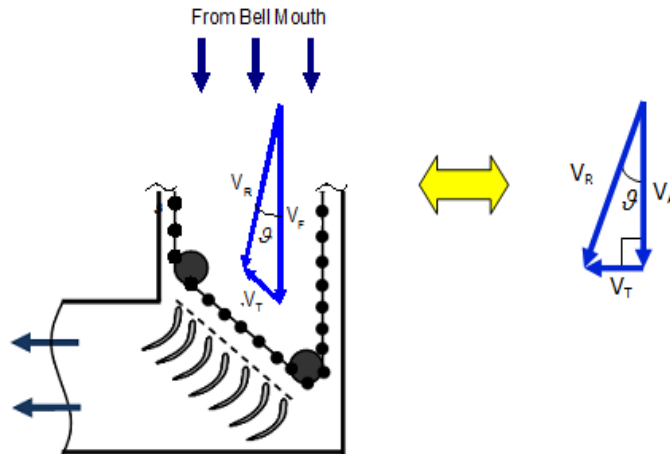


Figure 3.7 Vector decomposition of the flow inside the wind tunnel.

The effect of a change in flow incidence angle on turbine blade performance is dependent on the location of peak loading on the turbine blade [39]. Aft loaded turbine blades are inherently less affected by small flow incidence angle changes due to blade loading location. With peak loading occurring on the aft portion of the blade, the flow within the blade passage can correct itself before peak loading is reached. For front loaded blade profiles however, small variations in flow incidence angle can have a large effect on blade performance. At peak loading, the boundary layer is very susceptible to separation, and a small change in flow angle can cause a boundary layer to separate. This small change in flow incidence angle present in the wind tunnel with a 100% duty cycle wake generator was determined to be insignificant when testing aft loaded blade profiles. Further investigations will be needed when front loaded profiles are used with the 100% duty cycle wake generator.

3.5 Wake Characteristics from an Airfoil Shape

An airfoil shape was designed as an alternative wake generating mechanism to better match the wake shed from a turbine blade. A symmetric NACA 0025 airfoil was chosen as the wake generating shape for its relatively thick aerodynamic body, which is thought to produce a more appropriate wake. A casting mold was developed and the airfoil shape was cast around a hollow aluminum rod, which was then installed overtop the existing carbon fiber rod. In an effort to minimize the flow disturbance of the airfoil as it travels around the track, the airfoil was designed to “weather-vane”, or rotate according to the flow direction, around the carbon fiber rod. This allowed the leading edge to always face the flow direction, minimizing the flow blockage. For this initial quantification, nine airfoil shapes were made and the wake was evaluated along with the ability of the airfoil to weather-vane. Based on the results of this initial quantification, design changes, along with adjusted parameters, are suggested for better performance and improved production of a more appropriate wake.

Previous results show that with a 36% duty cycle chain, as the rods first pass by, a transient period exists before a periodic unsteady flow field is established. For this initial characterization, nine cylindrical rods were placed in front of the nine airfoils to initialize the flow field and establish the periodic unsteadiness. The spacing of the wake generating mechanisms, both the airfoils and the rods, was kept at the cascade blade spacing of 17.8 cm. The distance upstream to the center of the rods was also kept at 8.9 cm as before. The NACA 0025 airfoil scaled for this application resulted in a 6.8 cm chord with a maximum thickness of 1.7 cm. The airfoil pivoted around the carbon fiber rod 6 mm from the leading edge, resulting in an axial distance of 2.7 cm between the

cascade leading edge and the airfoil trailing edge. Figure 3.8 shows the setup in the wind tunnel using the airfoil shapes.



Figure 3.8 Wake generator with airfoils installed.

The wake shed from the airfoil was measured in the same manner as the previous sections with 100 cycles averaged in the ensemble. Hot-film probes were used to acquire the velocity data and were placed in the same locations of the cascade inlet and within the wake generator loop as before. The wake was characterized in the same manner with the quantification the wake width, peak velocity deficit, and momentum deficit.

The initial measurement was performed at a Reynolds number of 25,000 with a flow coefficient of 0.8 and both levels of FSTI. Under these flow conditions, the ability for the airfoil to weather-vane was marginal and inconsistent. At this low free-stream velocity, the lift on the airfoil was not enough to overcome the frictional resistance associated with rotating around the carbon fiber rod. About half of the airfoils were able to pivot freely while the other half exhibited an increased frictional resistance that was larger than what the lift force could overcome. This increased resistance was attributed to the hollow aluminum rod not being perfectly straight during the casting process.

In an effort to improve performance, the carbon fiber rods were lubricated and guides were placed around some of the flywheels to keep the airfoil oriented properly during the large directional changes. These modifications improved performance dramatically, but the inconsistency of the airfoil's ability to weather-vane during every cycle skewed the ensemble average results. Using a higher free-stream velocity by testing the airfoil shape at a Reynolds number of 50,000, increased the lift force to a level that consistently allowed the airfoils to weather-vane properly. This proved the concept of the airfoil's ability to weather-vane and further modifications should allow lower Reynolds numbers to be tested.

For the 50,000 Reynolds number test, a more conservative chain speed was used so that data could be acquired without damage to the airfoils or wake generator. Figure 3.9 shows the velocity trace for a complete cycle with nine cylindrical rods followed by nine airfoils at a Reynolds number of 50,000, with a flow coefficient of 1.57 and using a FSTI of 0.5%. Based on the current performance, further modifications would allow higher chain speeds to be obtained.

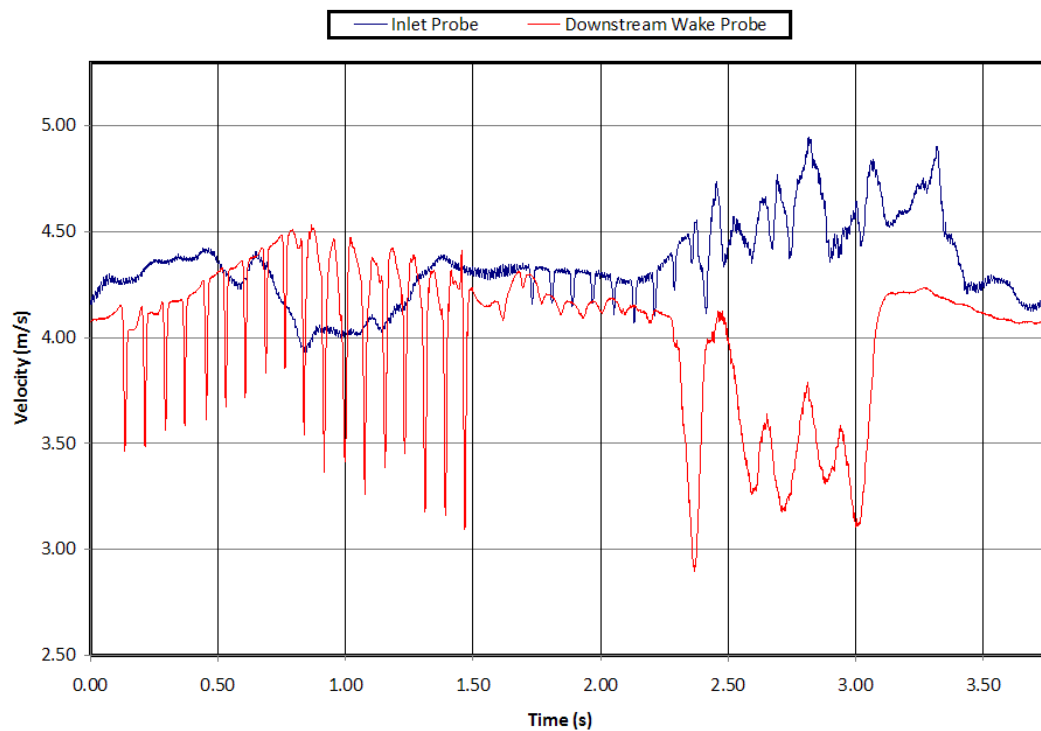


Figure 3.9 Complete cycle of ensemble average velocity data using nine cylindrical rods followed by nine airfoil shapes. ($Re = 50k$, $\phi = 1.57$, FSTI 0.5%)

For the plot in figure 3.9, the first nine velocity deficits are the wakes shed from the cylindrical rods, while the last nine deficits are from the airfoil shapes. The rise and drop of velocity indicates that the airfoils induce a tangential velocity as they pass the cascade. This is similar to what was seen previously in the 100% duty cycle chain. The

velocity deficit of the airfoil compared to the circular cylinders is much larger as expected with the trailing edge of the airfoil only 2.8 cm upstream of the cascade. This increase in the velocity deficit removed the calm period between the wakes that was seen with the circular cylinders. This calm period is present in actual engines as seen in Howell et al. [30], indicating the airfoil spacing should be increased or the airfoils moved upstream. The secondary wakes seen in the last half of this plot have a significant influence on the wind tunnel flow. This is due to the large angle in which the airfoils traverse across the delay loop, causing them to be skewed to the free-stream flow, resulting in a large flow blockage and disturbance. The inlet probe, which is used to set the wind tunnel Reynolds number, was also greatly affected by the airfoils. Further improvements will be needed to reduce this effect so that accurate tunnel conditions can be set.

Figure 3.10 gives a closed view of the primary wakes. Since data was taken at a different flow coefficient than before, the wake from the cylindrical rod of this data set was used for comparison to the wake of the airfoil. The wake of the fourth rod was used for the analysis to avoid effects from the tangential velocity induced by the airfoils. Similarly, the fifth airfoil wake was used in the analysis as it also was less affected by the tangential velocity. Table 3.3 gives a summary of the wake properties measured.

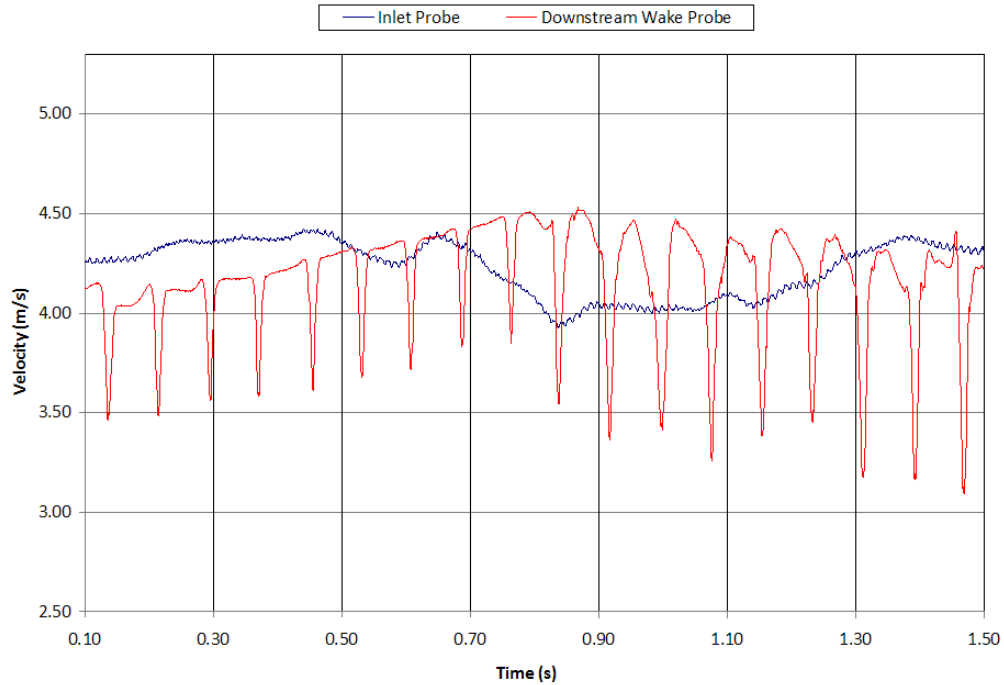


Figure 3.10 Ensemble average velocity of the primary wakes using nine cylindrical rods followed by nine airfoil shapes ($Re = 50k$, $\phi = 1.57$, FSTI 0.5%)

Reynolds Number/FSTI	Flow Coefficient ϕ	Momentum Deficit	Wake Width (m)	Peak Velocity Deficit
Rod 50k/0.5%	1.57	0.0343	0.0351	0.1442
Airfoil 50k/0.5%	1.57	0.0850	0.0517	0.2216

Table 3.3 Calculated wake characteristics based on hot-film measurements for a cylindrical rod and airfoil shape.

Comparing the wake of the cylindrical rod from this data set, to the previous data set at the same Reynolds number with a flow coefficient of 0.8 and 0.7, the wake properties are consistently lower for the higher flow coefficient of 1.57 as expected. This gives some insight into what the wake properties for the airfoil would be for the lower

flow coefficients of 0.8 and 0.7. The data in table 3.3 shows the wake of the airfoil contains higher values compared to the cylindrical rod. This was expected due to the difference in the distance to the cascade with the airfoils being much closer. The wake of the airfoil was much wider since the thickness was 1.7 cm compared to the diameter of the rod being 0.32 cm. This shows that the wake of a streamlined body will have a much slender wake for the same diameter of rod. The momentum deficit was more than twice that of the rod, but the peak velocity deficit and wake width were only about 50% larger. These differences in wakes can be used to better match a particular shape of wake that is to be simulated in future studies.

These initial results show that an airfoil with the ability to weather-vane, can be used as a wake generating mechanism for this system. Further improvements can be made so that the problems encountered during this test can be reduced to an acceptable level. In order to reduce the friction as the airfoil rotates, a thicker aluminum hollow rod is suggested for use during the casting process. A stiffer rod should help maintain the rods straightness during casting. Guides can be placed around directional changes to keep the airfoil oriented properly during the excessive g forces. Using the same airfoil dimensions, the spacing between airfoils and the spacing upstream of the cascade should be increased to better match the wakes seen in a real engine. Given the large flow disturbance caused by the airfoil traversing through the wind tunnel, it is suggested that the shape be reduced in size but maintain the current spacing. This will reduce the wake shape to a more appropriate level and minimize the flow disturbance in the wind tunnel. In addition, the foam used in the casting process worked well, but other lightweight materials could be used that would produce a smoother profile. This includes filler

materials such as micro-balloons mixed with resin, could produce the smooth profile desired.

3.6 Conclusions

The wake from two different wake generating mechanisms was quantified under various flow conditions using the wake generating system. Cylindrical rods were used as the first wake generating mechanism and the results were comparable to other wake generating systems. For the cylindrical rods, the rod diameter matched the trailing edge diameter of the blade set, the rod spacing matched the cascade spacing, and the rods were placed half an axial chord length upstream. These parameters are consistent with other wake generating systems and proved to produce similar wake properties. The momentum deficit, wake width, and peak velocity deficit were quantified under various flow conditions, such that the data can be referenced or compared in future wake generator studies.

The wake from a 100% duty cycle system was compared to the wake of 36% duty cycle system. A continuous generation of wakes is very desirable, in that it would simplify the data acquisition process and speed up the measurement time. The 100% duty cycle system induced a noticeable tangential velocity that was quantified. Based on the results, a 100% duty cycle chain is acceptable for use as it was shown to produce a comparable wake to the 36% duty cycle chain.

A symmetric NACA 0025 airfoil was used as the second wake generating shape in this study. The wake of this aerodynamic body was quantified and compared to the

cylinder wake, and differences in the wakes were noted. These differences in wakes can be used to better match a particular shape of wake that is to be simulated in future studies. The concept to allow the airfoil shape to weather vane was proven and design changes were suggested. More work is needed before an airfoil shape can be implemented, but the results were promising and showed potential. For the rest of this current study, only the cylindrical rods were used as the wake generating mechanism.

Chapter 4

Low Pressure Turbine Blade Performance with Periodic Unsteady Wakes at Low Reynolds Number

4.1 Linear Cascade of Low Pressure Turbine Blades

In the previous chapter, the wakes shed from the wake generator were quantified and shown to produce a periodic unsteadiness consistent with other wake generating systems. The effect of the periodic unsteadiness is now characterized on a cascade of low pressure turbine blades with loss measurements, surface pressure distribution, and full field velocity measurements. Since low Reynolds number is of interest, all measurements are taken at a Reynolds number of 25,000, based on inlet velocity and axial chord length.

The linear cascade consists of seven fully immersed L1A low pressure turbine blade profiles and two partial blade profiles on either end. These blades were designed by Clark and Koch [40] and were manufactured using cast polyurethane. The cascade blade profile has an axial chord (C_x) of 0.178m, a span of 0.88m, and a solidity of 0.99. This aft loaded blade has the same design inlet and exit angles as the Pack B blade profile of 55 and 30 degrees respectively. The L1A profile is a very highly loaded, low pressure

turbine blade with a calculated incompressible Zweifel coefficient of 1.23 based on Eq. (4.1).

$$Z_w = 2 \frac{s}{C_x} \cos^2 \alpha_{out} (\tan \alpha_{in} - \tan \alpha_{out}) \quad (4.1)$$

The L1A profile generates 17% more lift than the Pack B, which correlates to a 17% blade count reduction. The L1A profile is an aft loaded blade design making it prone to separation under steady flow conditions due to the axial location of the peak velocity and strong adverse pressure gradient on the blade suction surface. This blade was designed for use in flow control studies in which separation may be suppressed, while maintaining the benefits of both very high loading and aft loading [25]. In a previous study performed in the same facility, it was shown for Reynolds numbers less than 40,000 and a FSTI of 3.4%, the L1A profile exhibits a non-reattaching separation zone with high losses [41]. These characteristics were desired for the current study to demonstrate the capability of the wake generating system. A schematic of the linear cascade is shown in figure 4.1.

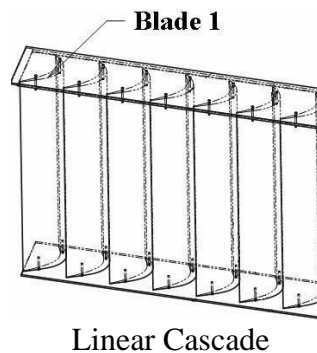


Figure 4.1 Schematic of linear cascade indicating where blade numbering begins

4.2 Wake Loss Measurements of the L1A Blade Profile with Periodic Unsteady Wakes

4.2.1 Cascade Periodicity

Before any blade measurements can be performed, the cascade periodicity must be checked so that the results are not skewed by improper wind tunnel flow. Although a wake generating system was installed inside the wind tunnel, the structure was kept to the wind tunnel walls and cascade periodicity was not expected to be affected.

Cascade periodicity for this facility is normally set at a Reynolds number of 100,000. Since the periodicity is to be checked with the wake generator running at an appropriate flow coefficient, a Reynolds number of this magnitude is mechanically unfeasible under the current configuration of the wake generator. Therefore, it was decided that adequate results could be obtained by checking the periodicity with and without the wake generator running at a Reynolds number of 50,000. Cascade periodicity was checked with a 36% duty cycle wake generator so that it could be compared to a case in which wakes were not being produced. For the case without the wake generator running, the rods are parked along the wind tunnel wall after the delay loop. At this location, the rods are not in the wind tunnel main flow and should have little effect on the wind tunnel performance.

Cascade periodicity is measured by plotting the difference in total pressure from the inlet to the exit of the cascade across blades 2, 3, 4, and 5. For this measurement, a static total pressure probe located upstream of the linear cascade and the primary wakes, was used to acquire the inlet total pressure. A second total pressure Kiel probe was located approximately one-half chord lengths downstream of the cascade and was used

for measuring the exit total pressure. Both probes were mounted to a dual axis traverse allowing the probes to accurately traverse across the entire cascade. Both measuring probes acquired data using Lab ViewTM data acquisition software, with a sampling frequency of 1 kHz. Data was taken at 0.5 cm increments, with each increment averaging 40 seconds of pressure data. The 36% duty cycle chain used for this measurement had the same rod parameters used in the wake characterization.

If the cascade has periodic flow across the blades of interest, each blade profile should have somewhat similar pressure peaks with similar pressure between them. Figure 4.2 shows the plot of the cascade differential total pressure across blades 2, 3, 4, and 5. Data was taken at a Reynolds number of 50,000 using a flow coefficient of 0.8 with a high FSTI of 3.4%. The plot shows that periodic flow has been maintained across the cascade with the installation of the wake generator system. Both with and without the wake generator running, the cascade flow periodicity is maintained and no adjustment to the tailboards was needed. Since no modifications were needed, this periodicity was assumed to translate to the lower FSIT of 0.5% and any other flow coefficient.

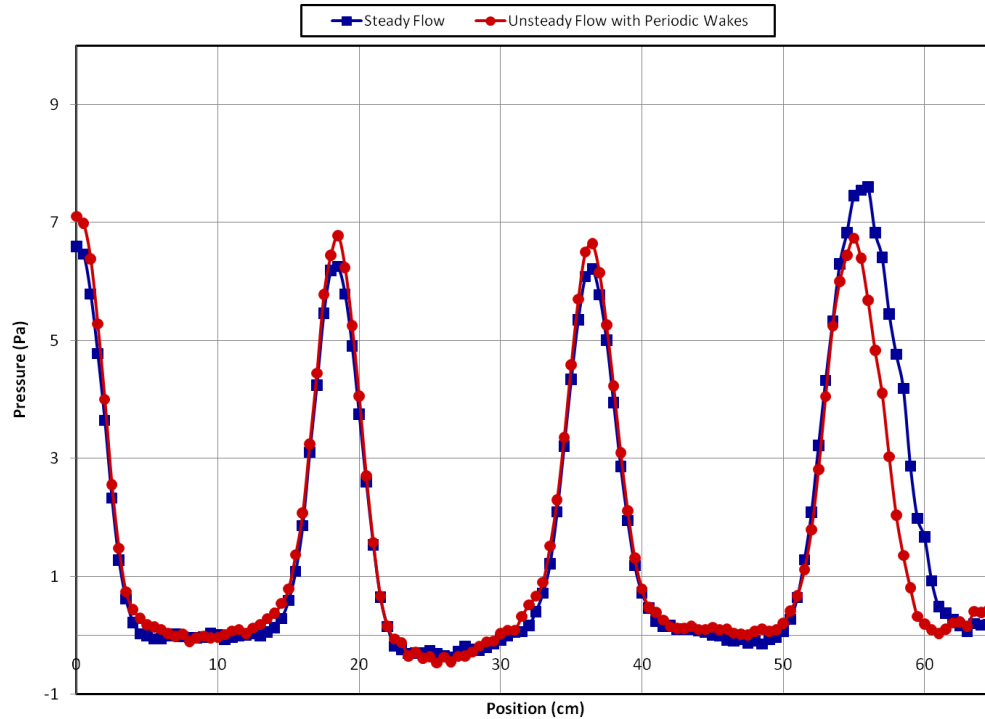


Figure 4.2 Cascade Periodicity with and without the wake generator running.
($Re = 50k$, $\phi = 0.8$, FSTI 3.4%)

4.2.2 Wake Loss Experimental Setup

Wake loss measurements were performed with steady and unsteady inflow at a Reynolds number of 25,000 with two levels of FSTI. The cylindrical rods were used in all unsteady flow experiments with the same rod parameters as were used before. The rod diameter matched the trailing edge diameter of the blade set; the rod spacing matched the cascade spacing, and the rods were placed half an axial chord length upstream. The rod diameter along with the rod spacing was held constant during this investigation.

Data was taken using a static total pressure probe located upstream of the linear cascade and the primary wakes, but within the track loop of the wake generator. A second total pressure Kiel probe, along with a dual element X hot-wire probe, were

located approximately one-half chord lengths downstream of the cascade. These two probes were mounted together in the same plane, 5.08cm horizontally apart. Both pressure probes were connected to the high and low pressure side of a Druck LPM5481 differential pressure transducer with a range of -50 to 200 Pa. All three probes were mounted to a dual axis traverse and fed into the wind tunnel through 1.25 cm wide slots, allowing the probes to traverse across the entire cascade. Pressure and velocity measurements were performed across the third blade of the cascade. A single element hot-film probe was located upstream of the cascade and within the wake generator loop. This fixed probe was used to set the wind tunnel conditions by measuring the free-stream velocity. All measuring probes acquired data using Lab ViewTM data acquisition software, with a sampling frequency of 1 kHz.

Wake total pressure loss was measured by scanning across the blade at 0.5 cm increment steps. At each increment, data was recorded for 60 seconds and averaged. Between each measurement, a 15 second settling period was used so that the probes could stabilize at each position. The long measuring period and settling time was used due to the unsteady flow associated with the L1A blade profile at this low Reynolds number.

The integrated wake total pressure loss was calculated based on the average pressure measurements at each increment. The equation used for this calculation is the same used in Bons et al. [15] and Marks et al. [41] as shown in equation (4.2).

$$\gamma_{\text{int}} = \frac{1}{s} \int_{-s/2}^{s/2} \left(\frac{P_{T,in} - P_{T,ex}}{P_{T,in} - P_{S,in}} \right) ds \quad (4.2)$$

This equation gives the area averaged integrated wake total pressure loss. A similar loss measurement, mass averaged wake loss, could also be used to quantify the blade performance. Since previous data on this blade taken at this facility was the area averaged wake loss, it was decided to use this wake loss measurement for comparison.

4.2.3 Baseline Case of Wake Loss Measurements for Steady Flow Conditions

The behavior of the L1A low pressure turbine blade was characterized under steady flow conditions in the same facility by Marks et al. [41]. As mentioned previously, in this study it was found that the L1A exhibits non-reattaching separated flow on the suction surface for Reynolds numbers less than 40,000 with a FSTI of 3.4%. For comparison of a baseline case under steady flow conditions, the results of the wake loss measurements from this previous study are summarized.

Data was acquired in the same manner as described above using the same equipment. Data was taken at various Reynolds numbers and two levels of FSTI. Of interest to this current study are the cases of a Reynolds number of 15,000 and 30,000 with a FSTI of 0.5%, and the case of a Reynolds number of 25,000 at a FSTI of 3.4%. Figure 4.3 is a plot of the measured wake loss coefficient across blade number three for each of these cases. The profile was shifted so that the center of the integration width was at zero.

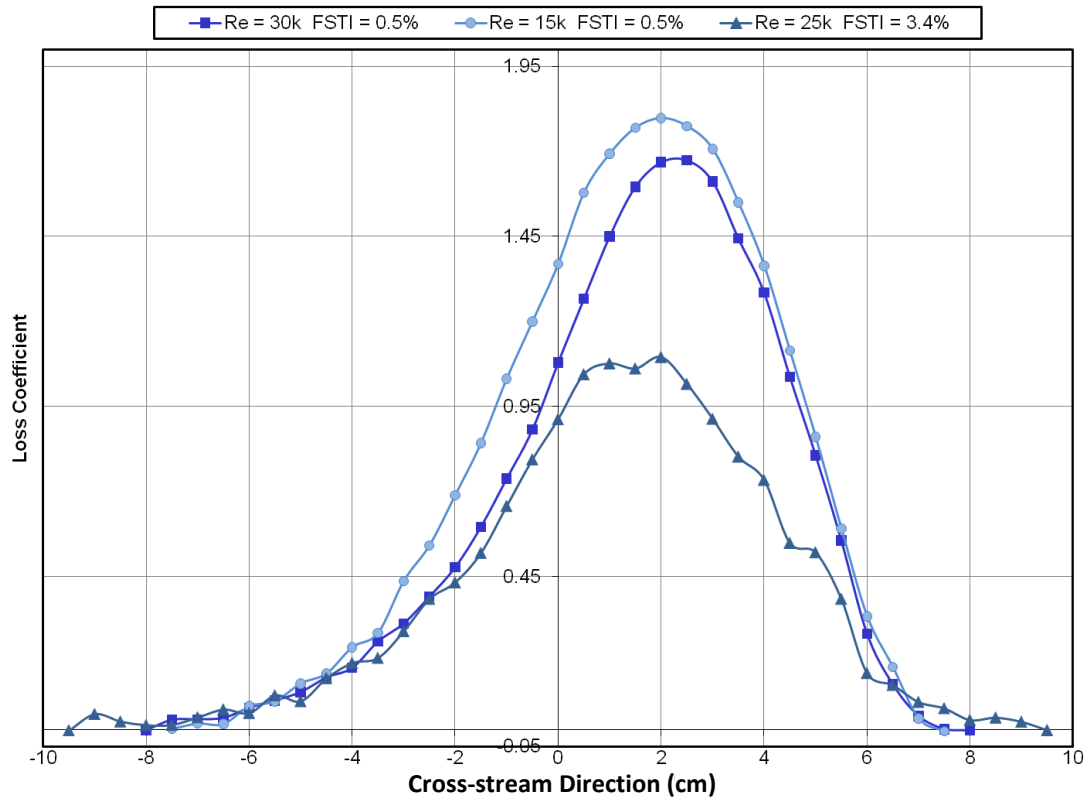


Figure 4.3 Wake loss measurement showing steady flow L1A low pressure turbine blade performance at a Reynolds number of 25k and two levels of FSTI.

The profiles shown in figure 4.3 are slightly skewed to the right with a gradual rise in loss coefficient followed by a steep decline. This type of behavior indicates separation is present on the suction surface of the blade. The increased FSTI is expected to energize the boundary layer along with the separated free shear layer, effectively reducing the profile loss. The effect of the increased FSTI of 3.4% is shown as a reduction in profile magnitude but a slight increase in the profile width. This resulted in a net reduction of the profile loss.

The integrated wake total pressure loss scaled with the blade axial chord for this baseline case is summarized in table 4.1. Using previous data from this study, from a Reynolds number of 15,000 to a Reynolds number of 50,000, based on the four data

points in this range, the baseline data showed a linear reduction in profile loss. Using this linear trend, a linear interpolation was performed to approximate the profile loss at a Reynolds number of 25,000. This interpolation resulted in an integrated total pressure loss coefficient of 0.581. Using this value and comparing the effect of FSTI on steady flow, the integrated profile loss was reduced by 29% by FSTI alone. Since unsteady wake flow is considered an extension of increased flow turbulence, significant reductions in the profile loss is expected with the inclusion of wakes.

Reynolds Number	FSTI	Integrated Wake Total Pressure Loss
15k	0.5%	0.638
30k	0.5%	0.553
25k	3.4%	0.413

Table 4.1 Summary of integrated wake total pressure loss scaled with the blade axial chord for baseline case with steady flow.

4.2.4 Wake Loss Measurements with Periodic Unsteady Wakes

Wake loss measurements were carried out on the linear cascade with periodic unsteady flow and the results were compared to the baseline case with steady flow. Measurements were performed using a chain fully populated with rods so that wakes are continuously generated, yielding a 100% duty cycle wake generator. Area averaged wake loss measurements are based on the inlet and exit pressures, which for this facility, are measured using a differential pressure transducer as stated in section 4.2.2. This type of pressure measuring device has a relatively slow response time and is not able to

accurately measure the flow field that is produced using a 36% duty cycle chain. Based on the results from the previous study, a 100% duty cycle wake generator will produce a consistent periodic flow field long enough to measure and should provide accurate results.

Wake loss measurements were performed with periodic unsteady wakes at a Reynolds number of 25,000 using a flow coefficient of 0.8 with two levels of FSTI. Figure 4.4 is a plot of the measured wake loss coefficient across blade number three for a FSTI of 0.5% and 3.4%. The loss profile was shifted so that the center of the integration width is at zero as before.

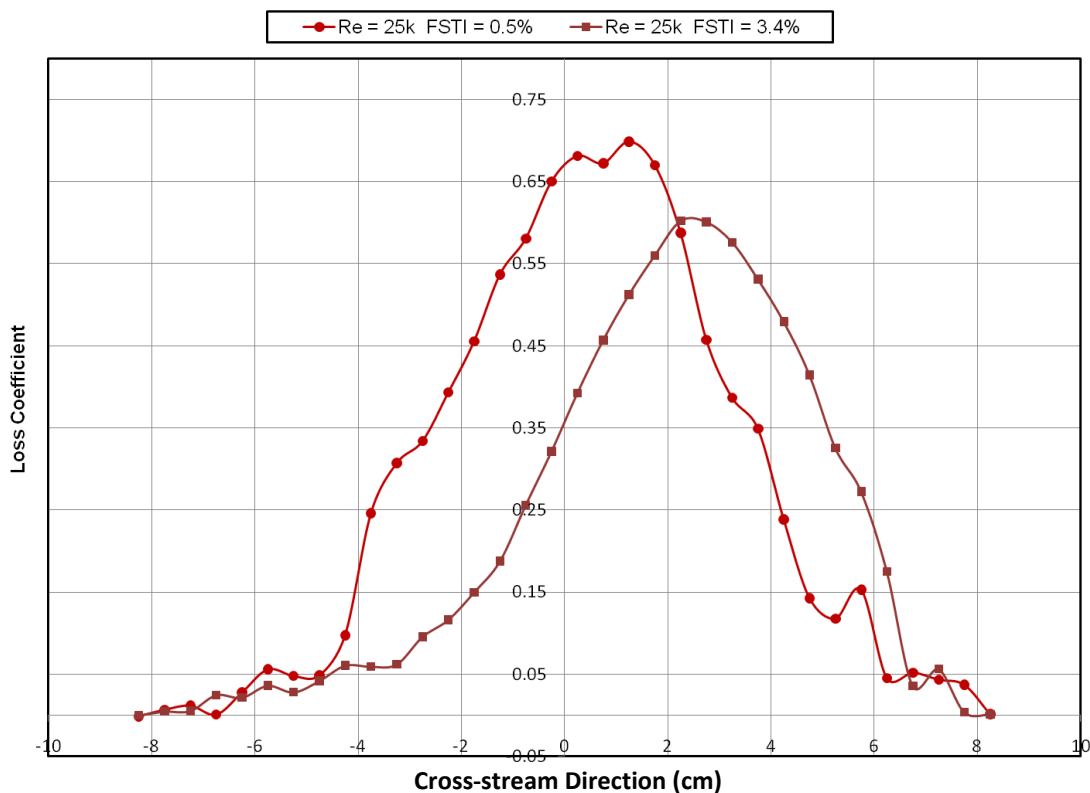


Figure 4.4 Wake loss measurement showing L1A profile performance with periodic unsteady wake flow at a Reynolds number of 25k and two levels of FSTI.

The loss profiles in figure 4.4 show a similar trend as the baseline case with the profiles slightly skewed, indicating flow separation is still present on the suction surface of the blade. The extent of this flow separation is not apparent in these profiles, but a large reduction in the loss magnitude indicates that the profile loss has been reduced significantly. The loss profiles with the inclusion of the periodic unsteady wakes are not as smooth as the steady flow case, indicating the flow is very unsteady. The effect of the increased FSTI is a further reduction in the loss magnitude and the overall profile loss. In both profiles, a small spike in the loss coefficient is observed at 5.75 cm for the low FSTI and 7.25 cm for the high FSTI case. This spike in the loss profile is believed to be due to vortices rolling off of the suction surface of the blade. This spike is more pronounced in the low FSTI data, which indicates a larger separation is present.

The area averaged integrated total pressure loss for the profiles shown in figure 4.4 was calculated and tabulated in table 4.2. As expected from what was observed in literature, the effect of the periodic passing wakes is a substantial reduction in profile losses. For a Reynolds number of 25,000 with a FSTI 0.5%, comparing the interpolated value for steady inflow, the profile losses with the inclusion of periodic wakes had been reduced by 56%. At this same Reynolds number with a higher FSTI, the inclusion of periodic wakes reduced the profile loss by almost 49%. The effect of FSTI between the unsteady flow cases was a reduction in the profile loss by 18%. The effect of FSTI on steady flow was on the same order of reduced profile losses. This indicates that the inclusion of FSTI with the unsteady wakes, further reduces profile losses even with the effect of the wake being slightly decreased.

Reynolds Number/ Flow Coefficient	FSTI	Integrated Wake Total Pressure Loss
25k / 0.8	0.5%	0.257
25k / 0.8	3.4%	0.210

Table 4.2 Summary of integrated wake total pressure loss scaled with the blade axial chord for periodic unsteady flow case.

4.3 Pressure Coefficient Distribution on the L1A Blade Profile with Periodic Unsteady Wakes

4.3.1 Experimental Setup

A pressure coefficient distribution gives a map of the pressure distribution on a blade profile and depicts blade loading with its relative location on the blade surface. Pressure coefficient distributions were obtained to quantify the flow behavior over the blade surface with periodic unsteady wakes and compared to steady flow data.

Pressure coefficient data was obtained using pressure taps, which had been previously installed on the surfaces of two L1A blade profiles. The pressure taps consisted of 1.3 mm diameter holes staggered along the blade surface so that any flow disturbance caused by the hole did not propagate downstream to another hole. Each pressure tap was individually plumbed with plastic tubing and fed through the bottom of the wind tunnel. A total of 30 pressure tap locations were used, with 19 placed on the suction surface of blade three, and 11 placed on the pressure side of blade four. The

plastic tubing was connected to a multi-port Scanivalve that allowed the use of a single pressure transducer for all thirty measurements.

The pressure was measured using a differential pressure transducer with a range of -50 to 200 Pa. At each pressure tap location, 60 seconds of data was acquired and averaged, resulting in the average pressure distribution over the blade surface. A settling time of 15 seconds was used between each measurement to allow the pressure transducer to equalize. Once again, due to the relatively slow response time of the pressure transducer, rods were placed around the entire length of the chain. The 100% duty cycle wake generator produced a continuous periodic unsteady flow field needed for the pressure coefficient measurement to be accurately measured. Pressure coefficient data was taken at a Reynolds number of 25,000 with a flow coefficient of 0.8 and two levels of FSTI. Data was compared to steady flow conditions taken previously by Marks et al. [41] using the same facility.

The pressure coefficient was calculated at each location on the blade surface using Eq. (4.3).

$$C_p = \frac{\overline{P_{0,i}} - \overline{P_s}}{\overline{q_i}} \quad (4.3)$$

where $\overline{P_{0,i}}$ was the average inlet total pressure, $\overline{q_i}$ was the average inlet dynamic pressure, and $\overline{P_s}$ was the average static pressure on the surface of the blade.

4.3.2 Pressure Coefficient Distribution for the L1A Blade Profile

Figure 4.5 is a plot of the pressure coefficient distribution with periodic wakes overlaid on a previous data set measured with steady flow from Marks et al. [41]. For steady flow

conditions, the profiles show that non-reattaching separated flow is present on the aft portion of the blade suction surface. This is more pronounced in the low 0.5% FSTI case, in which the profile flattens at approximately 62% axial chord (C_x), and continues to the trailing edge. At the higher FSTI of 3.4% with steady flow, the extent of the flow separation has been reduced, but is still present, indicated by the large pressure difference between the pressure and suction surfaces at the trailing edge. Steady flow data was not taken at a Reynolds number of 25,000 due to the small difference in flow behavior between a Reynolds number of 15,000 and 40,000.

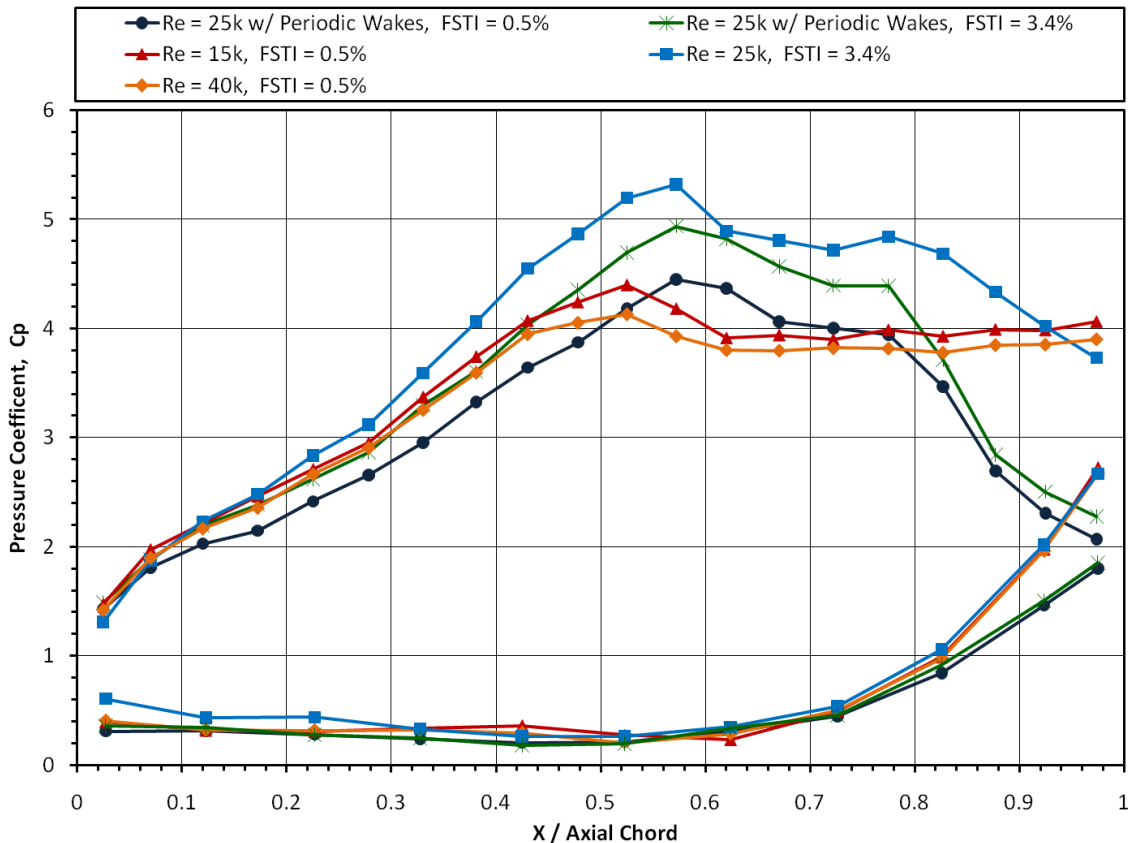


Figure 4.5 Pressure coefficient distribution with periodic unsteady wakes, compared to steady flow for two different FSTI levels.

For the low FSTI of 0.5% with steady flow, the peak pressure location for this case is at approximately 52.5% C_x , while the separation location is at approximately 62.0% C_x . Similarly, for the high 3.4% FSTI with steady flow, the peak pressure was moved slightly downstream to approximately 57.2% C_x , with separation occurring around 67% C_x . These results are consistent with what was observed in the wake loss measurements, with the profiles indicating separated flow with high losses.

In both FSTI cases with periodic unsteady wakes, the pressure profiles indicate the flow along the suction surface is attached, and contains a closed separation bubble. For the low FSTI of 0.5% with unsteady wakes, the profile shows the separation bubble beginning at approximately at 67% C_x and reattaching between 77.5% and 83% C_x . The overall peak pressure for this case was increased, compared to steady flow, and moved further downstream to 57.5% C_x . This increase in pressure level, along with the movement downstream, indicates higher blade loading was achieved.

The increased level of 3.4% FSTI with unsteady wakes had a similar effect on the blade performance with a further increase in blade loading. The pressure profile indicated a closed separation bubble was present, beginning at approximately 72% C_x and reattaching between 77.5% and 83% C_x . Although this reattachment point is similar to the low FSTI case, increased spatial resolution is thought to reveal earlier reattachment at the higher FSTI due to the shape of the profile at this location. Peak loading at this FSTI occurred at 57% C_x and had an increased magnitude, compared to the lower FSTI with unsteady wakes. These profiles agree with the wake loss data, showing a small closed separation is present with reduced losses at the higher FSTI. Comparing the four cases tested, the effect of the periodic wakes was an increase in blade loading through a higher

peak pressure located further downstream, and effectively reattaching the separated flow, forming a separation bubble on the blade surface.

Comparing steady and unsteady flow with wakes at the high FSTI of 3.4%, the profiles indicate that higher loading was achieved under steady flow conditions. This may not necessarily be the case and could be a result of the experimental data. In this measurement, the flow over the blade surface with unsteady wakes is averaged, and the velocity deficit produced by the passing wakes will reduce the result to some degree. The slow response time of the differential pressure transducer acts like a low pass filter on the data measured. This will produce a low frequency time average of the data as a result. In addition to this, the Reynolds number may not have been exactly matched during each measurement. Currently there is not enough data available to verify if the difference in profiles is valid or not.

4.4 Phase Locked Particle Image Velocimetry Measurements on the Suction Surface of the L1A Blade Profile with Periodic Unsteady Wakes

4.4.1 Particle Image Velocimetry

Particle image velocimetry (PIV) is a non-intrusive imaging technique used to measure instantaneous velocity fields. A typical PIV system consists of a flow seeding method, camera, high power light source, timing box, and computer. The general process of a 2D PIV measurement includes adding tracer particles to a fluid flow and illuminating them at two successive instants in time. The illumination of the particles is recorded to a camera

and the image pair is cross-correlated using analysis software. The cross-correlation determines the displacement of the particles between the two images. Knowing the time delay between the two image recordings, instantaneous velocity data can be calculated for the flow field.

The cross-correlation procedure used in standard PIV calculations is summarized in figure 4.6. The process starts with a correlation window, typically 128 x 128 pixels, that marches across the black and white raw images, performing the appropriate computation. Successive passes are usually made in the analysis, decreasing the correlation window by half each time. A velocity vector is then produced for every correlation window location using this process.

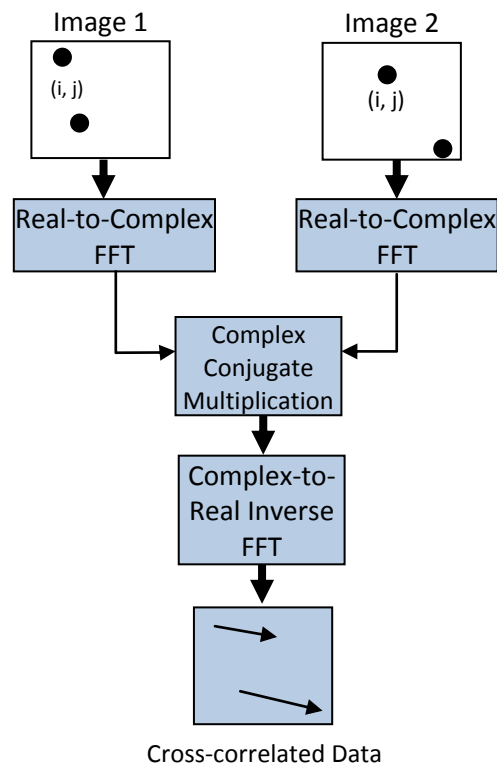


Figure 4.6 Block diagram of cross-correlation analysis procedure using fast Fourier transforms [42].

4.4.2 PIV Experimental Setup

Particle image velocimetry was used to investigate the effect of periodic wakes on the flow field around the L1A blade profile. An experiment was set up to investigate the flow field within the blade passage of the linear cascade, along with the separation behavior at the blade surface. In this experiment, the wake passing event was split into six phases and captured using 2-D planar PIV. The flow field was investigated at a Reynolds number of 25,000 with a flow coefficient of 0.8 using a high and low FSTI. Since data is captured relatively quickly, a partially populated chain with the previous rod parameters was used for this investigation.

The test section of the low speed wind tunnel, shown in figure 2.1, is composed of clear polycarbonate giving full optical access to the linear cascade from four different sides. Phase-locked two-dimensional planar PIV measurements were taken along the suction surface of the L1A profile for six different phases of wake passing. A dual-head 532-nm, frequency doubled, flash lamp-pumped Nd: YAG laser was used to illuminate the seed particles through a thin laser sheet along the flow direction of the suction surface at mid-span of blade three. Blade three had been previously painted a flat black to minimize reflections from the laser. The laser was capable of delivering dual 120 mJ pulses at repetition rates of up to 15Hz. An adjustable laser arm containing laser sheet-forming optics was mounted on an optical breadboard located outside of the wind tunnel.

Mie scattering from the seed particles was recorded on commercial, high-resolution cross-correlation digital camera sensors with a resolution of 1600 by 1200 pixels and a maximum framing rate of 30 frames per second (fps). The camera was fitted with a 35-70mm f2.8 lens set to a focal length of ≈ 40 mm, which provided a field of view

of approximately 140mm by 105mm. The camera was mounted underneath the test section looking up through a 1.25cm thick, clear polycarbonate plate. The field of view contained approximately 90% to 45% suction surface length of blade three. Timing of the camera exposure and laser pulses was controlled using an eight channel pulse generator. Figure 4.7 illustrates this setup and shows the relation between the laser, camera, and blade set.

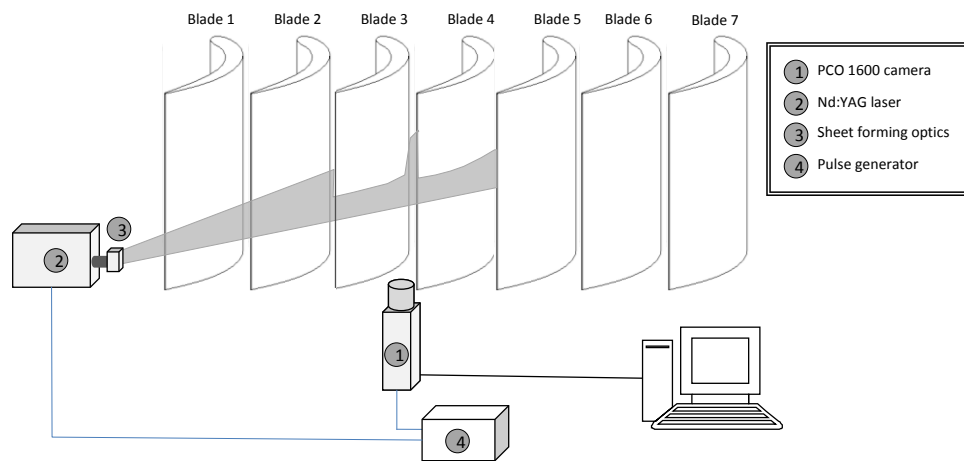


Figure 4.7 Schematic of PIV setup

Seeding of the flow was accomplished with a theatrical fog generator, which produced atomized particle sizes on the order of micrometers. A new adjustable seeding system was constructed for this measurement to allow for easier seeding of the flow. The seeding system consisted of a y-pipe that split the fog into two flexible tubes going up to an 11.5cm diameter PVC pipe that spanned across the bell-mouth inlet. Fog exited the pipe through numerous slots and entered the bell-mouth 1.22m away. This setup was to provide proper mixing while allowing enough time for the fog to cool and not induce any buoyancy driven flows. A picture of this setup is shown in figure 4.8.



Figure 4.8 Seeding system used for PIV measurements

Phase locking of the PIV measurements was done using quick response phototransistor optical sensors placed along the wake generator chain, which externally triggered the pulse generator. The wake passing event was split into six phases with the first phase notionally beginning with a rod positioned directly in front of the leading edge of blade four in the axial direction. The temporal delay between the two laser pulses was a function of flow velocity, optical magnification, and interrogation spot size. The delay for each phase however, was purely based on rod velocity and the distance the rod needed to travel from the sensor. A diagram of the different phases is shown in Figure 4.9. In this figure, the black filled rods demonstrate the placement for the first phase, while the dotted circles are rod locations for the next five phases.

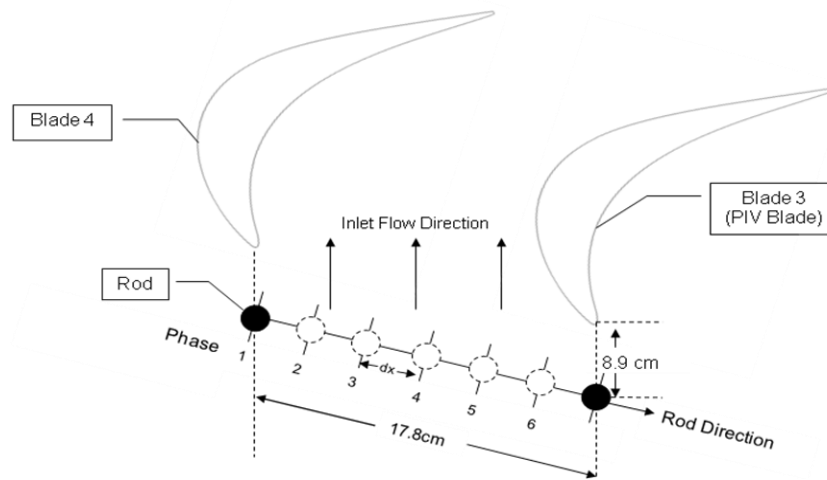


Figure 4.9 Diagram of the different rod locations for each phase

Once the PIV images were captured and digitized, the velocity field was obtained using cross-correlation techniques over interrogation domains of the images using PIV analysis software. Two different analysis software were used for the correlation. For the high FSTI data, images were processed using PPIV software developed by Innovative Scientific Solutions Inc. (ISSI). For the low FSTI data, images were processed using the commercial software Flow Manager. For consistency, the same correlation parameters were used in both analyses.

The present results were obtained with two and three passes using interrogation domains of 128, 64, and 32 pixels with an overlapping of 75%. Overlapping domains (by three-quarters the domain size) yields more vectors and is not merely interpolation, since it includes new particles in every domain sub-region [43, 44]. Accuracy is expected to be approximately 1% using a ten pixel displacement, and slightly higher close to the wall [44]. A parallel computing code for Linux clusters from ISSI was utilized for the PPIV software for added processing speed [45].

For each phase, 150 image pairs were correlated and averaged. A statistical vector filter was employed in the averaging routine to remove bad vectors from the average. The vector filter was needed due to the unsteady nature of the passing wakes and the occasional lack of seeding in the images. The PPIV statistical vector filter was set to include two standard deviations of variation in the analysis. The Flow Manager vector filter worked in a similar manner but used a moving average calculation across the entire vector map. In both cases, bad vectors were removed instead of being replaced by interpolation.

4.4.3 Baseline Data

The L1A low pressure turbine blade is a very highly loaded design that is prone to flow separation at low Reynolds numbers with steady inflow. Specifically, this blade profile has been shown to have a non-reattaching separation zone with high losses at Reynolds numbers less than 40,000 and a FSTI of 3.4% [41].

For a direct comparison of the effect the wakes have on the flow field around the L1A profile, a baseline case with no wakes is presented. In all cases, data was taken at a Reynolds number of 25,000, based on inlet velocity and axial chord length. Two levels of FSTI were investigated, a low level of 0.5% and a high level of 3.4%.

Figure 4.10 shows PIV data along the suction surface of the L1A blade for both levels of FSTI. The contours are of non-dimensional average velocity magnitude and streamlines of the velocity vectors are overlaid, indicating flow direction. This data agrees with previous results, in that a non-reattaching separation zone is present, implying high profile losses. The blue contour levels contain streamlines showing

reversed flow, characteristic of flow separation. At the higher FSTI, the extent of the flow separation is slightly reduced. This was also observed in both the wake loss and pressure coefficient measurements.

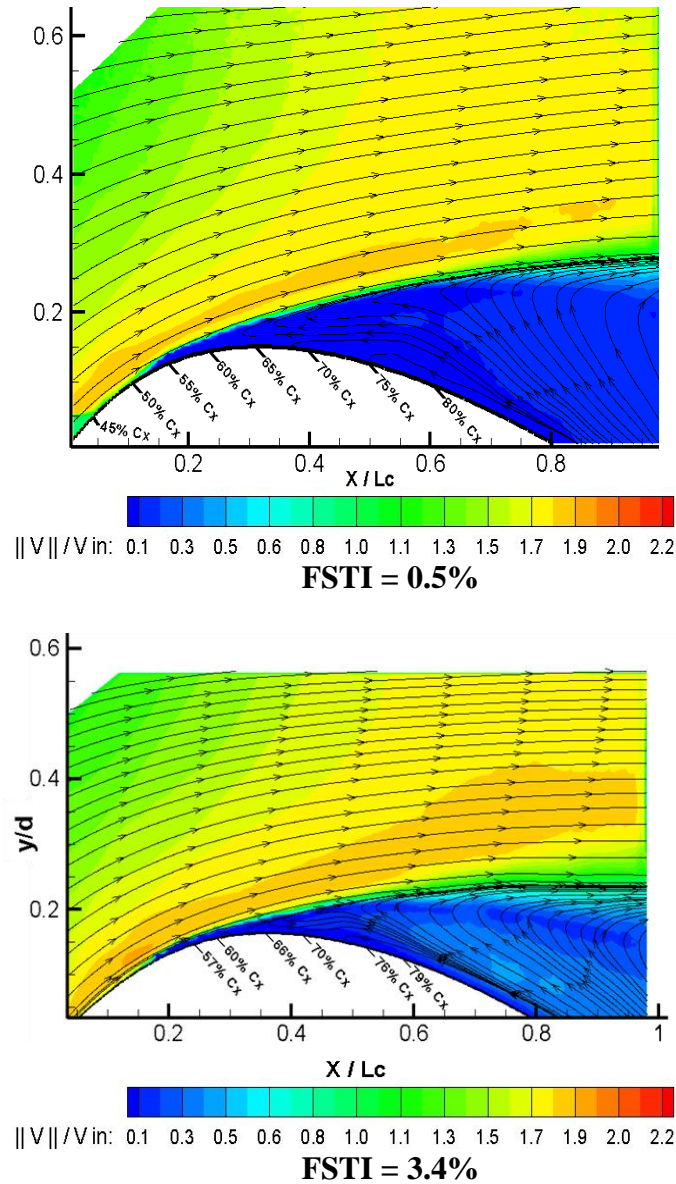


Figure 4.10 Non-dimensional velocity contour of steady flow baseline case with stream lines indicating a recirculation region.

An instantaneous PIV image of this separated flow at low FSTI is shown in figure 4.11. This image is used to show the separated shear layer that is present, and the eddies rolling off of it. These eddies are shown to transition into turbulence, however, this transition is not enough to reattach the flow at this Reynolds number. According to literature, eddies transitioning to turbulence in a separated shear layer typically results in reattachment of the flow. This demonstrates the extent of the separation, since the flow transitioned in the separated shear layer, but did not reattach.

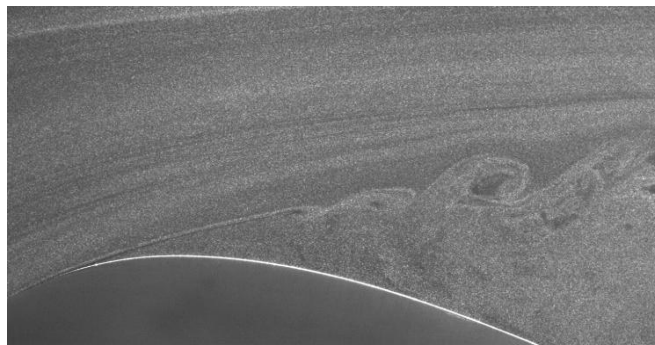


Figure 4.11 Instantaneous PIV image demonstrating eddies forming in the separated shear layer

4.4.4 Low FSTI Hot-Wire Study

An internal wake generator, with wakes being generated for only a fraction of the cycle time, will have an initial non-periodic unsteady effect, depending on the nature of the flow across the blade. For the current flow conditions, the large separated flow will interact with the incoming wakes in a transient manner until a periodic unsteadiness is established. In order to determine how many rod passes are needed to establish the periodic unsteadiness, a single element hot-film probe was used to acquire velocity-time traces within the blade passage at three different locations. Figure 4.12 is a plot of 100

ensemble averaged measurements of non-dimensional velocity during a complete cycle of the wake generator for the three locations. The placement of the probe was such, that velocity was acquired at two different locations in the free-stream and one location near the blade surface. The data from the hotwires indicates that approximately six wake passes are needed to establish periodic unsteadiness in the flow velocity. Based on this information, the first six wake passes were used to establish a periodic unsteadiness and the PIV data was recorded on the remaining wakes.

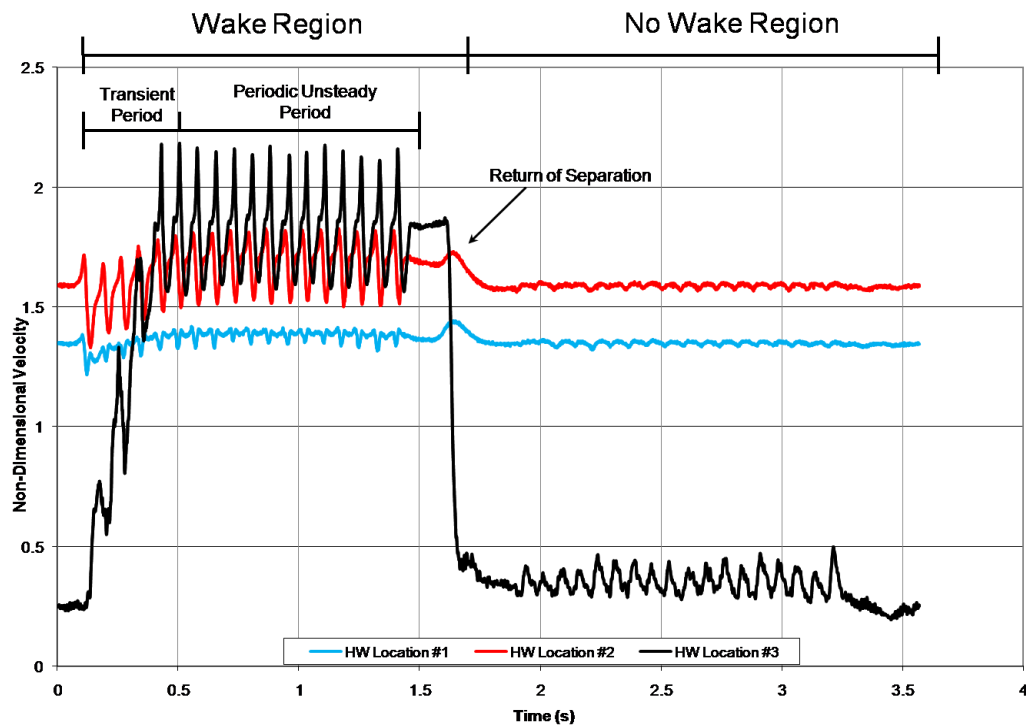


Figure 4.12 100 ensemble averaged measurements of velocity within the blade passage during a complete cycle of the wake generator. ($Re = 25k$, FSTI 0.5%)

The hotwire velocity time trace shows the return of the flow separation in the no wake region along with its effect on the flow velocity. Hotwire location number one and two were placed within the free-stream velocity, with location number one being the

furthest upstream. Hotwire location number three was placed close to the blade surface within the separated flow region and outside of the boundary layer. At this location, the hotwire shows a dramatic decrease in velocity when the flow is separated from the blade. As the wakes impinge upon the blade surface, the separated boundary layer is reduced in size until a periodic steady state is reached. The separated flow across the suction surface of the blade acts like a flow blockage within the blade passages, which appears as a reduction in the flow velocity.

4.4.5 Low FSTI PIV Results

PIV results for the low FSTI case are shown in figure 4.13. For the six phases of wake passing, velocity contours are plotted with overlaid streamlines of the velocity components. All velocity data has been made non-dimensional with respect to the inlet velocity. The wake passing event can best be described by beginning with Phase #3. In this phase a very small separation bubble is present, indicated by the dark blue color, starting around 70% C_x . In Phase #3, the wake has just entered the blade passage upstream, and is outside the field of view. Toward the end of the visible blade surface, the contour levels are showing increased velocity, indicating a closed bubble is present. This was verified with the surface pressure measurements. Progressing to Phase #4, the separation bubble has grown in height and the streamlines indicate a small recirculation region, or vortex, has formed. By Phase #5, the separation bubble has grown in height and length covering a much larger region of the suction surface. The center of the recirculation has moved further downstream, but the separation location has moved slightly upstream to about 67% C_x . Based on hotwire data, the wake is located roughly

between 60-65% C_x in Phase #6. In this phase, the separation bubble has grown to its full height and length, extending further down the suction surface. The center of the recirculation region has moved upstream from the previous phase and the separation point has appeared to move downstream to 70% C_x . A change of events occurs in Phase #1, as the separation bubble appears to have shed a vortex with the location of the wake trailing behind it. The vortex is observed to roll down the blade surface in Phase #2, with the vortex partially out of the field of view and a very small separation bubble remains as shown in Phase #3.

Compared to the baseline case, the flow through the blade passage with periodic wakes was less restricted and higher flow velocities were attained. The non-reattaching flow in the baseline case was dramatically reduced to a small separation bubble. The bubble was observed to grow in size between passing wakes, but was only able to achieve a fraction of the original size. The streamlines through the unrestricted blade passage better follow the blade profile, indicating an improved exit flow angle with lower losses.

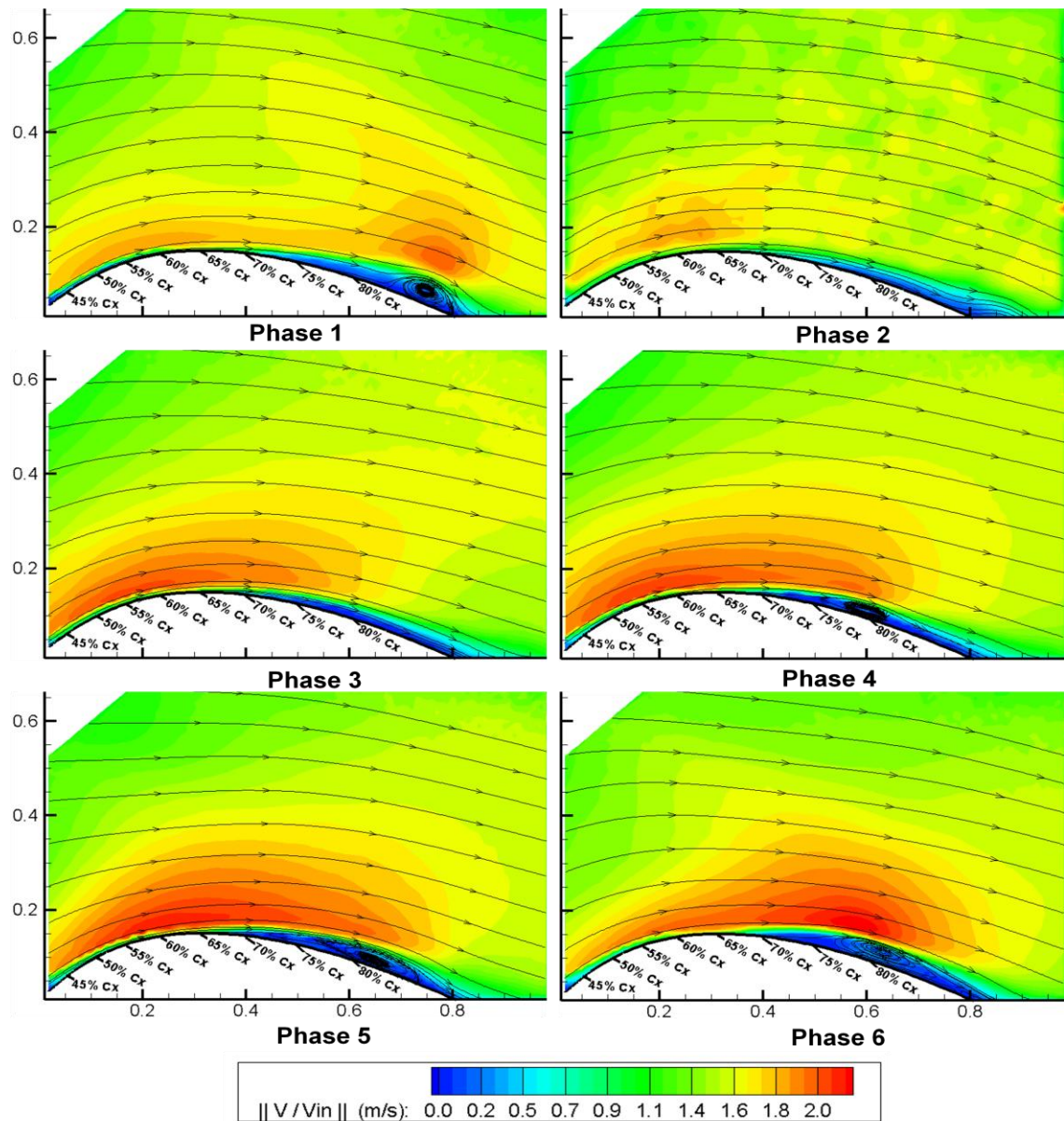


Figure 4.13 PIV contours of non-dimensional average velocity for six phases of wake passing. FSTI = 0.5%

4.4.6 High FSTI Hot-Wire Study

Following the same procedure as before, two single element hot-film probes were used to acquire velocity-time traces for evaluating the number of rod passes needed to establish a periodic unsteadiness at the higher FSTI. Figure 4.14 is a plot of 100

ensemble averaged measurements of velocity during a complete cycle of the wake generator. Data was acquired by placing two hotwires in the free-stream of the blade passage between blades 3 and 4, within the PIV field of view and measuring plane, set approximately 5cm apart in the flow direction. The data from the hotwires indicates that approximately eight wake passes are needed to establish periodic unsteadiness in the flow velocity. PIV data confirmed that the wake from rod eight left a small separation bubble on the suction surface that was slightly larger in size when compared to the remaining passing wakes. This is two more wake passes than what was required for the low FSTI case. From this data, it was determined to use eight passing wakes to establish a periodic unsteadiness and acquire data on the remaining wakes.

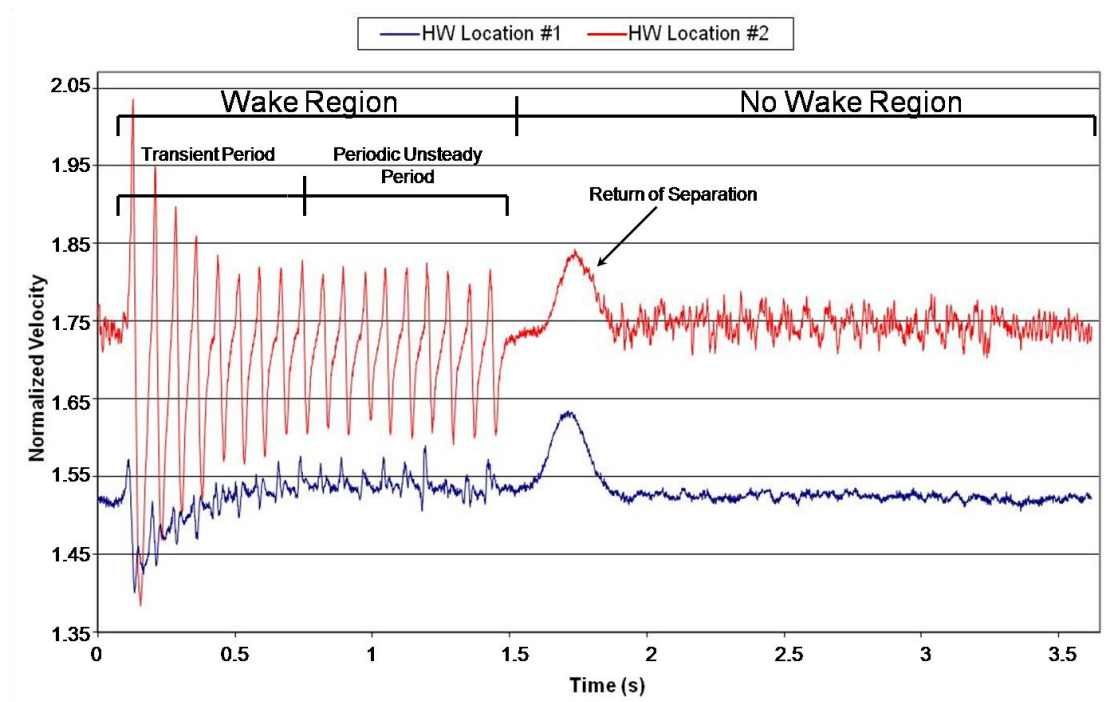


Figure 4.14 100 ensemble averaged measurements of velocity within the blade passage during a complete cycle of the wake generator. ($Re = 25k$, FSTI 3.4%)

In both velocity time traces from the two hotwires, the return of the flow separation is evident in the no wake region, along with its affect on the flow velocity. The separated flow across the suction surface of the blade acts like a flow blockage between the blade passages, which appears as a reduction in the flow velocity.

The placement of hotwire location #2 was such that, the impinging wakes were not as distorted as the wakes measured at location #1. Since wakes are continuously shed from the moving rod, the effect is a velocity deficit of a certain width that spans across the entire blade passage. As the wake convects downstream, it becomes distorted and strained, as can be seen by the two different hot wire measurements. Stieger et al. [13] was able to visually capture this event using Laser Doppler Anemometry (LDA) and analyzing the turbulent kinetic energy.

The hotwire data was also used in conjunction with the PIV data to track the location of the wake for the six different phases of the rod position. The wake location for a particular phase was calculated using the time trace of the voltage from the optical sensor, plus its respective delay for the particular phase. Figure 4.15 shows, for the first three recorded wakes, the time location for each of the six phases as the wake passes the hotwire within the blade passage. For each phase, the location on the velocity deficit from the wake was consistent and repeatable. Knowing the location of the hotwires with respect to the PIV field of view, the location, and the affect from the impinging wakes, can successfully be tracked in the velocity field data.

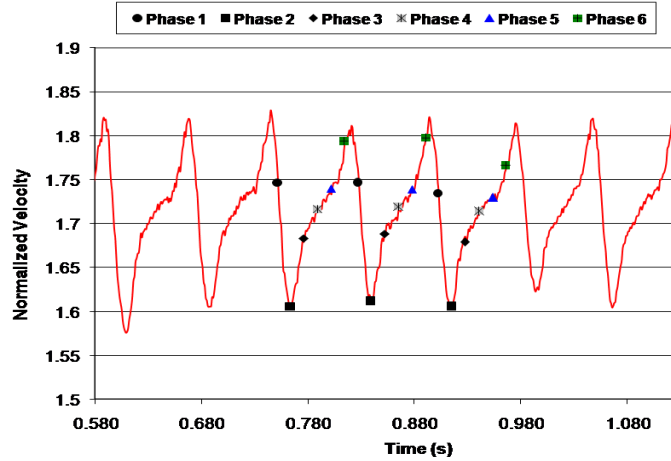


Figure 4.15 Time location for each of the six phases as the wake passes the hotwire within the blade passage for the first three recorded wakes.

4.4.7 High FSTI PIV Results

Non-dimensional velocity magnitude contour plots of the six different phases of rod position are presented in Figure 4.16. Streamlines of the vector components are overlaid, indicating the flow direction across the blade. The hotwire locations are depicted in all six phases and in the following figures. Velocity magnitude is non-dimensionalized with respect to the inlet velocity as before, and the axes are non-dimensionalized with respect to a characteristic length.

Using the data from hotwire location #2, shown in Figure 4.14, the approximate location of the wake can found in all six phases. The exact area of the velocity deficit from the wake is not specified due to the lack of information from point measurements of a hotwire.

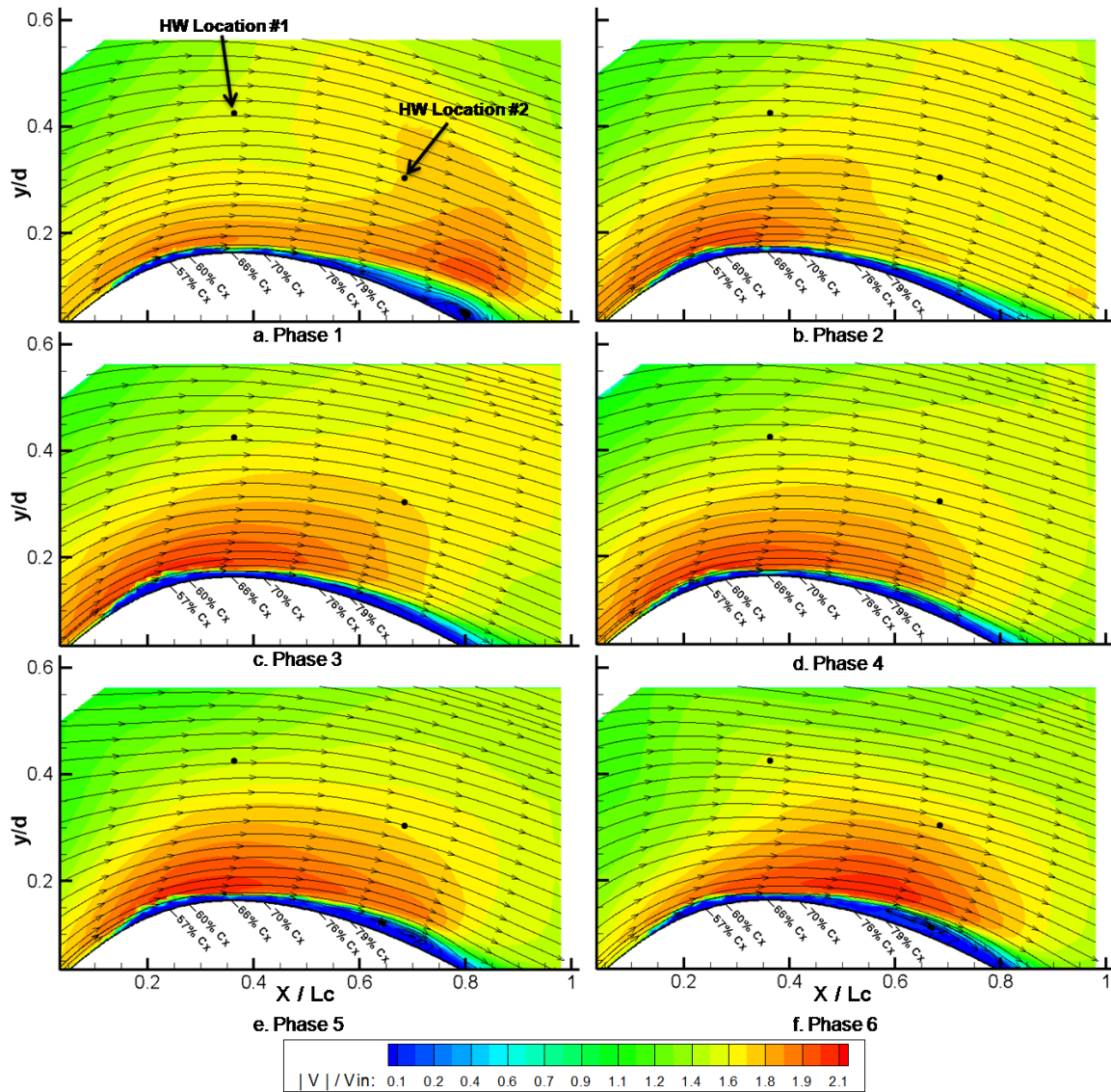


Figure 4.16 PIV contours of non-dimensional average velocity for six phases of wake passing. $FSTI = 3.4\%$

Figure 4.16a (Phase #1) shows attached flow with a small separation bubble toward the trailing edge of the blade. The location of the wake in this phase is just upstream of hotwire location #2, as it is pushing the high velocity region along with the separation bubble downstream. Figure 4.16b (Phase #2) has no recirculation region and attached flow across the visible length of the suction surface. The location of the wake is now on top of hotwire location #2 and is evident by the lower velocity contour level in

that area. Phase #3 of this figure shows more of a return of the high velocity area along the blade surface with the location of the wake being partly outside the field of view. In Phase #4 of this figure, the wake is thought to be mostly out of the field of view with the high velocity region showing signs of being pushed downstream, indicating a new wake moving into view. Hot wire data of the location of the wake for Phase #5 indicates the velocity is almost back to a steady state value at hotwire location #2. The high velocity region has moved further downstream, and a small separation bubble is starting to form in this phase at approximately 85% C_x . Phase #6 displays a growth in the size of the separation bubble along with the high velocity region being pushed further downstream, indicating the effect of the new wake progressing through the blade passage.

The growth of the separation bubble in Phase #6 has also moved the bubble upstream as the wake impinges upon the blade surface. This agrees with other researchers' claims that this movement of the separation bubble upstream triggers transition of the boundary layer earlier, which keeps the flow attached. The effect of the next time step (Phase #1), is then washing the separation bubble off, as it moves downstream with the wake.

The PIV results for the high FSTI of 3.4% are similar to the low FSTI of 0.5%. The difference between the two data sets is the size of the separation bubble. In the high FSTI data, the separation bubble appears much smaller in size. This agrees with the lower loss values measured and the pressure distribution data. Similarly, the vortice, observed to roll off of the blade surface in Phase #1, is much smaller compared to the vortice observed in Phase #1 of the low FSTI data. This data shows that the effect of a

higher FSTI is a reduction in losses and higher blade loading that is achieved through a reduction of the separation bubble on the suction surface of the blade.

Even though the wake does not completely stand out in the above plots, the effect of the impinging wakes is clear, in that the flow is attached with a very small separation bubble forming in-between the wake passing. Capturing the wake structure using PIV can be difficult, due to the relatively high turbulence intensities and unsteady nature of the wake. Since PIV averages together numerous image pairs, the wake structure gets washed out and the wake appears as a lower velocity region as shown in the above plots.

Certain flow features of the velocity field can be made apparent through the use of perturbation velocity. The perturbation velocity is defined as the difference between the ensemble averaged and time-averaged velocity fields [13, 25, 27, 46]. The perturbation velocity for this data set was calculated by averaging together the velocity magnitude of all six phases and then subtracting that average from the individual phases. The calculation of the perturbation velocity will remove the natural unsteadiness of the flow, due to the FSTI, and will show the flow structure that is unique to that phase.

The perturbation velocity contour plots for the six phases is presented in figure 4.17 with overlaid streamlines of the perturbation velocity vectors. The placement of the two hotwires is also superimposed on this plot for reference of the wake location. In this figure, large vortical structures are present and travel down the blade passage with increasing phase number. This flow behavior was also captured in a recent CFD study with periodic wakes [47]. Comparing the hotwire data with the location of the large vortical structures, the location of the vortices B and D, coincides with the stated location

of the passing wake. Although these vortices do not contain the complete structure of the wake, they give insight into the effect of the passing wake.

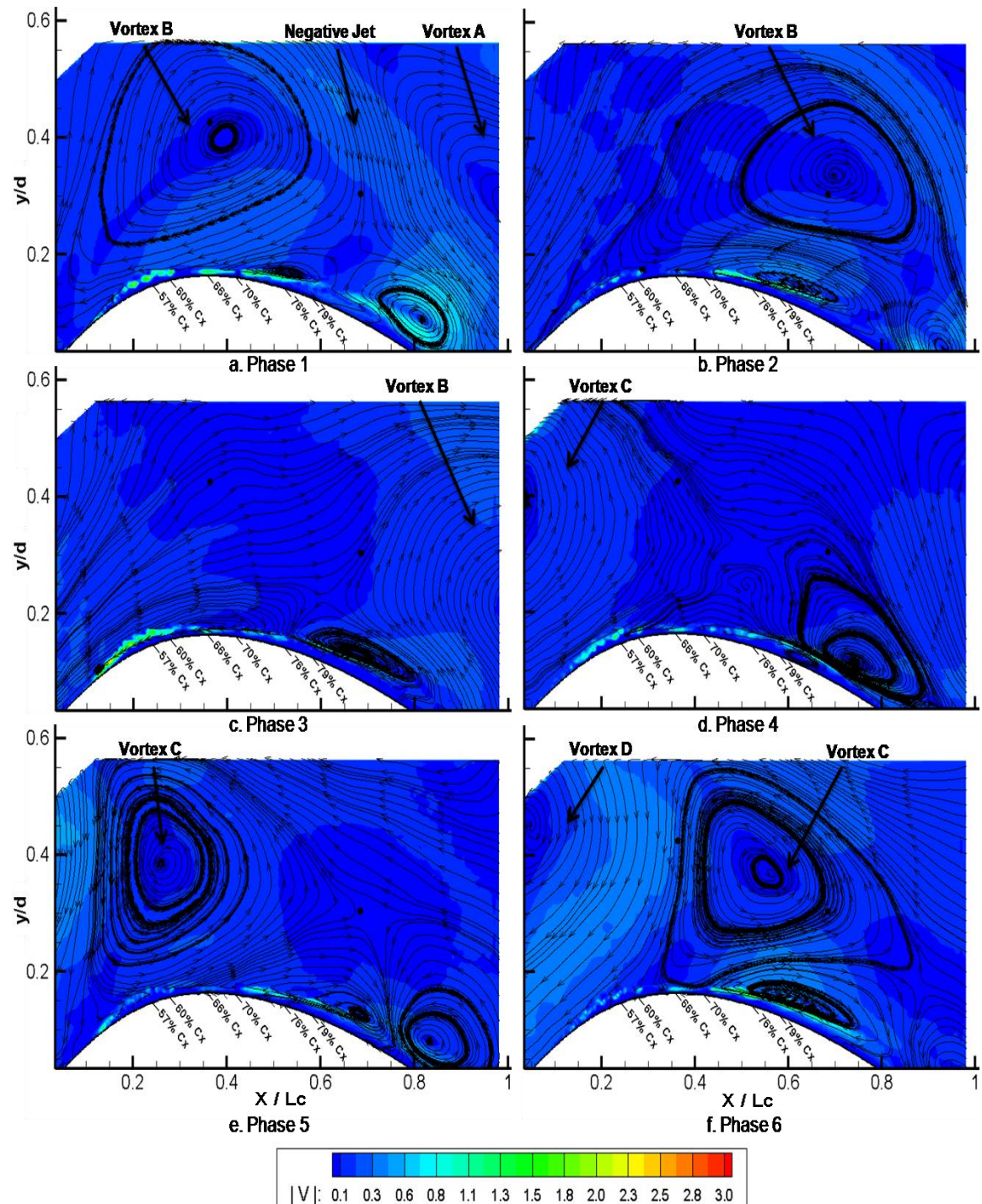


Figure 4.17 Non-dimensional phase average subtracted velocity contour

In phase 1 of this figure, two large vortices are present along with a much smaller vortex that is in the same location as the separation bubble in the previous figure. The interaction between the two large vortices appears as a negative jet, as described by other researchers [26]. In this phase, the negative jet is located just in front of the separation bubble, which effectively pushes it downstream. Tracking vortex B from Phase #1 to Phase #2, the center of this vortex is now on top of hotwire location #2, which agrees with the hotwire velocity time trace of figure 4.15. Figure 4.17c (phase 3) shows the back edge of vortex B with no new vortex structure coming into view. Phases #4 and #5 shows a new vortex structure, vortex C, moving into view and convecting through the blade passage. Smaller vortices at the location of the separation bubble are also apparent in these phases and grow in size. Phase #6 in this figure, shows yet another vortex coming into view, vortex D, which is starting to interact with vortex C. The interaction between the two large vortices, along with the interaction between the separation bubble vortex and vortex C, seems to cause the smaller separation vortex to roll upstream, based on the streamline directions.

Looking at Phases #6 and #1, the interaction between the two large vortices is what seems to cause the negative jet in this figure to form. This data agrees with other researchers' claims that the impinging wake can be thought of as a negative jet acting on the boundary layer, and by moving the separation location fractionally upstream, the boundary layer transitions earlier and keeps the flow attached to the blade surface [25].

Chapter 5

Conclusions

Researchers have used wake generating systems to demonstrate the affect of periodic passing wakes on low pressure turbine blade performance at low Reynolds numbers. Literature has shown that periodic passing wakes dramatically affects performance and the inclusion this effect in the design phase is a vital component of improving low Reynolds number performance and reducing losses.

Wakes shed from upstream vane rows have been shown to cause a periodic disturbance within the free-stream flow in the form of a momentum deficit. This periodic perturbation impinges upon the separated boundary layers of low pressure turbine blades and the interaction can have a profound effect on profile losses. Researchers have shown that the interaction can be used to improve low Reynolds number performance and allow higher lift generating profiles to be developed beyond the current design limits. These higher loading blade profiles have been shown to achieve the same losses of current blade designs while generating significantly more lift. This correlates to blade count reductions in the portion of the engine that can account for a third of the overall engine weight.

In an effort to aid industry in increasing low Reynolds number performance and increase efficiencies of the low pressure turbine, the Air Force Research Laboratory has

been working to expand the design space and push the aerodynamic loading limits of low pressure turbine blades [35]. In a continuation of this effort, a wake generating system was designed for use in the AFRL low speed wind tunnel facility to further investigate the effects of periodic unsteadiness on low pressure turbine blade performance.

The newly designed wake generator system was characterized and shown to produce a periodic unsteadiness that is consistent with other wake generator designs. The periodic wakes produced by cylindrical rods were characterized by momentum deficit, peak velocity deficit, and wake width. The wake of an aerodynamic body was also quantified and compared to the cylinder wake and differences in the wakes were noted. The concept to allow the airfoil shape to weather vane was proven and design changes were suggested. The effect of the internal wake generator on the internal wind tunnel flow was also investigated along with the ability of the wind tunnel to maintain cascade periodicity. From this investigation, the wake generator was shown to produce the desired periodic unsteadiness and is able to be used as an accurate simulator of blade row interactions.

The effect of the periodic wakes on a linear cascade of L1A low pressure turbine blades was investigated through the use of wake loss measurements, pressure coefficient distributions, and velocity field data. Low Reynolds numbers were of interest, so measurements were performed at a Reynolds number of 25,000 with two levels of FSTI.

A baseline case of data was obtained under steady flow conditions for comparison with the periodic wake data. Wake loss measurements showed that with steady flow and both levels of FSTI tested, the L1A blade profile has high losses at this low Reynolds number. Pressure coefficient distribution measurements showed that the blade profile

had non-reattaching separated flow on the suction surface of the blade profile. For the low FSTI of 0.5% with steady flow, the peak pressure location for this case was at approximately 52.5% C_x , while the separation location was at approximately 62.0% C_x . Similarly for the high 3.4% FSTI with steady flow, the peak pressure was moved slightly downstream to approximately 57.2% C_x , with separation occurring around 67% C_x .

PIV measurements gave a visualization of the extent of the separated flow through velocity contour plots. Streamlines overlaid on the PIV contour plots revealed the reversed flow present in the separation and the undesirable exit flow angle resulting from the separation. This flow separation was responsible for these high losses and the increased FSTI had little effect on reducing the separation at the Reynolds number tested.

Wake loss measurements with the inclusion of periodic wakes showed a dramatic reduction in losses. The profile losses with the inclusion of periodic wakes at a Reynolds number of 25,000 with low FSTI had been reduced by 56%. At this same Reynolds number with a higher FSTI, the inclusion of periodic wakes reduced the profile loss by almost 49%. The effect of FSTI between the unsteady flow cases was a reduction in the profile loss by 18%.

Pressure coefficient distributions showed increased loading with the inclusion of unsteady wakes. The pressure coefficient profile revealed a closed separation bubble was present on the suction surface of the blade. For the low FSTI of 0.5% with unsteady wakes, the profile shows the separation bubble beginning at approximately at 67% C_x and reattaching between 77.5% and 83% C_x . The overall peak pressure for this case was increased compared to steady flow, and moved further downstream to 57.5% C_x . This

increase in pressure level along with the movement downstream indicates higher blade loading was achieved.

The increased level of 3.4% FSTI with unsteady wakes had a similar effect on the blade performance with a further increase in blade loading. The pressure profile indicated a closed separation bubble was present, beginning at approximately 72% C_x and reattaching between 77.5% and 83% C_x . Peak loading at this FSTI occurred at 57% C_x and had an increased magnitude compared to the lower FSTI with unsteady wakes.

PIV measurements with unsteady wakes confirmed the presence of a closed separation bubble on the suction surface of the blade. The velocity contour plots indicated the velocity through the blade passage had increased and the streamlines showed a more appropriate exit flow angle was achieved.

The wake passing event was split into six phases and the affect of the periodic passing wake was observed. Between passing wakes, a separation bubble was observed to form and grow in size. As the wake approached, the wake began to interact with the separation bubble causing it to move along the blade surface. Once the wake moved overtop the separation bubble, a vortex was observed to roll out of the bubble. Once this vortex was shed, the separation bubble was significantly reduced in size. After the wake had passed, the separation bubble was observed to grow in size and the process started over.

Compared to the baseline case, the flow through the blade passage with periodic wakes was less restricted and higher flow velocities were attained. The non-reattaching flow in the baseline case was dramatically reduced to a small separation bubble. The bubble was observed to grow in size between passing wakes, but was only able to achieve

a fraction of the original size. The streamlines through the unrestricted blade passage better follow the blade profile indicating an improved exit flow angle with lower losses.

Perturbation velocity streamlines were calculated and shown for six phases of wake passing. The perturbation velocity was able to demonstrate the wake acting like a negative jet and agreed with previous studies [25, 13, 27, 55, 56]. The wake was observed through the negative jet, to stain and deform as it convected through the blade passage. The negative jet was observed to form counter rotating vortical structures on either side of the jet. As the jet convected through the blade passage, it was observed to move over top of the separation bubble, which agrees with previous observations and literature.

References

- [1] Volino, R. J., and Hultgren, L. S., 2001, “Measurements in Separated and Transitional Boundary Layers Under Low-Pressure Turbine Airfoil Conditions,” ASME J. Turbomachinery, Vol. 123, pp. 189–197.
- [2] Curtis, E. M., Hodson, H. P., Banieghbal, M. R., Denton, J. D., and Howell, R. J., 1997, “Development of Blade Profiles for Low-Pressure Turbine Applications,” ASME J. Turbomachinery, Vol. 119, pp. 531–538.
- [3] Sharma, O., 1998, “Impact of Reynolds Number on LP Turbine Performance,” Proceedings of 1997 Minnowbrook II Workshop on Boundary Layer Transition in Turbomachines, NASA/CP-1998-206958.
- [4] Howell, R. J., Ramesh, O.N., Hodson, H.P., Harwey, N. W., and Schulte, V., 2001, “High Lift and Aft-Loaded Profiles for Low-Pressure Turbines,” ASME, J. of Turbomachinery, Vol. 123, pp. 181–188.
- [5] Haselbach, F., Schiffer, H. P., Horsman, M., Dressen, S., Harvey, N., and Read, S., 2002, “The Application of Ultra High Lift Blading in the BR715 LP Turbine,” ASME J. Turbomachinery, Vol. 124, pp. 45–51.
- [6] Mayle, R. E., 1991, “The Role of Laminar-Turbulent Transition in Gas Turbine Engines,” ASME J. Turbomachinery, Vol. 113, pp.509–537.
- [7] Öztürk, B., and Schobeiri, M. T., 2009, “Experimental Study of the Effects of Periodic Unsteady Wakes on Flow Separation in Low Pressure Turbines,” NASA/CR-2009-214831.
- [8] Howell, R. J., 1999, “Wake Separation Bubble Interaction on Low Reynolds Number Turbomachinery,” Ph.D. Dissertation, Cambridge University, England.
- [9] Volino, R. J., 2002, “Separated Flow Transition Under Simulated Low- Pressure Turbine Airfoil Conditions—Part 1: Mean Flow and Turbulence Statistics,” ASME J. Turbomachinery, Vol. 124, pp. 645–655.

- [10] Doorly, D. J., 1984, "Study of the Effect of Wake-Passing on Turbine Blades," Ph.D. Dissertation, University of Oxford, England.
- [11] Walker, G., 1998 "Transition in Turbomachines-An Overview," Proceedings of 1997 Minnowbrook II Workshop on Boundary Layer Transition in Turbomachines, NASA/CP- 1998-206958.
- [12] Schulte, V., and Hodson, H. P., 1998, "Unsteady Wake-Induced Boundary Layer Transition in High Lift LP Turbines," ASME J. Turbomachinery, Vol. 120, pp. 28-35.
- [13] Stieger, R. D., and Hodson, H. P., 2005, "The Unsteady Development of a Turbulent Wake Through a Downstream Low-Pressure Turbine Blade Passage," ASME J. Turbomachinery, Vol. 127, pp. 388-394.
- [14] Schobeiri, M. T., and Öztürk, B., 2004, "Experimental Study of the Effect of Periodic Unsteady Wake Flow on Boundary Layer Development, Separation, and Reattachment Along the Surface of a Low Pressure Turbine Blade," ASME J. Turbomachinery, Vol. 126, pp. 663-676.
- [15] Bons, J. P., Pluim, J., Gompertz, K., Bloxham, M., and Clark, J. P., "The Application of Flow Control to an Aft-Loaded Low Pressure Turbine Cascade with Unsteady Wakes," Proceedings of 2008 IGTI ASME Turbo Expo, Berlin, Germany, GT2008-50864.
- [16] Wolff, S., Brunner, S., Fottner, L., 2000, "The Use of Hot-Wire Anemometry to Investigate Unsteady Wake-Induced Boundary-Layer Development on a High-Lift LP Turbine Cascade," ASME J. Turbomachinery, Vol. 122, pp. 644-650.
- [17] Heidmann, J. D., and Lucci, B. L., 2001, "An Experimental Study of the Effect of Wake Passing on Turbine Blade Film Cooling," ASME J. Turbomachinery, Vol. 123, pp. 214-221.
- [18] Ubaldi, M., and Zunino, P., 2000, "An Experimental Study of the Unsteady Characteristics of the Turbulent Near Wake of a Turbine Blade," Elsevier Science Inc., Experimental Thermal and Fluid Science, Vol. 23, pp.23-33.
- [19] Schobeiri, M. T., John, J., and Pappu, K., 1996, "Development of Two-Dimensional Wakes Within Curved Channels: Theoretical Framework and Experimental Investigation," ASME J. Turbomachinery, Vol. 118, pp. 506-518.
- [20] O'Brien, J. E., and Capp, S. P., 1989, "Two-Component Phase-Averaged Turbulence Statistics Downstream of a Rotating Spoked- Wheel Wake Generator," ASME J. Turbomachinery, 111, pp. 475-482.

- [21] Sieverding, C. H., Ottolia, D., Bagnera, C., Comadoro, A., Brouckaert, J. F., and Desse, J. M., 2004, "Unsteady Turbine Blade Wake Characteristics," ASME J. Turbomachinery, Vol. 126, pp. 551-559.
- [22] Pluim, J., Memory, C., Bons, J., and Chen, J. P., 2009, "Designing a High Fidelity Wake Simulator for Research using Linear Cascades," ASME Paper No. GT2009-59276.
- [23] Schulte, V., and Hodson, H. P., 1998, "Prediction of the Becalmed Region for LP Turbine Profile Design," ASME J. Turbomachinery, Vol. 120, pp.839-846.
- [24] Stieger, R. D., Hollis, D., Hodson, H. P., 2004, "Unsteady Surface Pressures Due to Wake-Induced Transition in a Laminar Separation Bubble on a Low-Pressure Cascade," ASME J. Turbomachinery, Vol. 126, pp. 544-550.
- [25] Stieger, R. D., and Hodson, H. P., 2004, "The Transition Mechanism of Highly Loaded Low-Pressure Turbine Blades," ASME J. Turbomachinery, Vol. 126, pp. 536-543.
- [26] Meyer, R. X., "The Effect of Wakes on the Transient Pressure and Velocity Distributions in Turbomachines," Transactions of the ASME, p.1544, 1958.
- [27] Uzol, O., Zhang, X.F., Cranstone, A., and Hodson, H., 2007, "Investigation of Unsteady Wake-Separated Boundary Layer Interaction Using Particle-Image-Velocimetry," ASME Paper GT2007-28099.
- [28] Schobeiri, M. T., Öztürk, B., and Ashpis, D. E., 2007, "Effect of Reynolds Number and Periodic Unsteady Wake Flow Condition on Boundary Layer Development, Separation, and Intermittency Behavior Along the Suction Surface of a Low Pressure Turbine Blade," ASME J. Turbomachinery, Vol. 129, pp. 92-107.
- [29] Öztürk, B., and Schobeiri, M. T., 2007, "Effect of Turbulence Intensity and Periodic Unsteady Wake Flow Condition on Boundary Layer Development, Separation, and Reattachment Along the Suction Surface of a Low-Pressure Turbine Blade," ASME J. Fluids Engineering, Vol. 129, pp. 747-763.
- [30] Howell, R. J., Hodson, H. P., Schulte, V., Stieger, R. D., Schiffer, H. P., Haselbach, F., and Harvey, N. W., 2002, "Boundary Layer Development in the BR710 and BR715 LP Turbines—The Implementation of High-Lift and Ultra-High-Lift Concepts," ASME J. Turbomachinery, Vol. 124, pp. 385-392.
- [31] Coton, T., Arts, T., Lefebvre, M., and Liamis, N., 2003, "Unsteady and Calming Effects Investigation on a Very High-Lift LP Turbine Blade—Part I: Experimental Analysis," ASME J. Turbomachinery, Vol 125, pp. 281-290.

- [32] Hodson, H. P., 1984, "Boundary Layer and Loss Measurements on the Rotor of an Axial Flow Turbine," ASME Journal of Engineering for Gas Turbines and Power, Vol. 106, No. 2.
- [33] Gompertz, K. A., 2009, "Separation Flow Control with Vortex Generator Jets Employed in an Aft-Loaded Low-Pressure Turbine Cascade with Simulated Upstream Wakes," Master's Thesis, Ohio State University.
- [34] Zhang, X. F., and Hodson, H. P., 2005, "Combined Effects of Surface Trips and Unsteady Wakes on the Boundary Layer Development of an Ultra-High-Lift LP Turbine Blade," ASME J. Turbomachinery, Vol. 127, pp. 479-488.
- [35] McQuilling, M., 2007, "Design and Validation of a High-Lift Low-Pressure Turbine Blade," Ph.D. Dissertation, Wright State University, Dayton, Ohio.
- [36] Bloxham, M., Reimann, D., Crapo, K., Pluim, J., and Bons, J. P., 2009, "Synchronizing Separation Flow Control With Unsteady Wakes in a Low-Pressure Turbine Cascade," ASME J. Turbomachinery, Vol. 131, pp.1-9.
- [37] White, F., 1991. "Viscous Fluid Flow," McGraw-Hill, Inc.
- [38] Roshko, A., 1954, "On the Development of Turbulent Wakes from Vortex Streets," National Advisory Committee for Aeronautics. NACA-TR-1191.
- [39] Sondergaard, R., 2010, personal correspondence.
- [40] Clark, J. and Koch, P. "Benchmark Turbines for the Guidance of Design System Improvement," 2006, Turbine Engine Technology Symposium, Dayton, OH, Sept. 14.
- [41] Marks, C., Sondergaard, R., Estevadeordal, J., Wolff, M., 2009, "PIV Investigation of a Highly-Loaded LPT Blade Using a Curved Laser Sheet," AIAA Paper No. 2009-301.
- [42] Raffel, M., Willert, C., Wereley, S., Kompenhans, J., 1998, "Particle Image Velocimetry, A Practical Guide," Springer.
- [43] J. Estevadeordal, S. Gorrell, W. Copenhaver, 2007, "PIV study of wake-rotor phenomena in a transonic compressor under various operating conditions," AIAA J. of Propulsion and Power, Volume 23, No. 1, pp. 235-242.
- [44] Hart, D., 2000, "Super-Resolution PIV by Recursive Local-Correlation," Journal of Visualization, Vol. 3, No. 2, pp.187-194.

- [45] McCray, T.W., Estevadeordal, J. and Puterbaugh, S. L., 2005, "Parallel Computing for Linux Clusters—Application to Particle Image Velocimetry", AIAA Paper 2005-1385.
- [46] Hodson, H.P. and Howell, R.J., "Bladerow Interaction, Transition, and High-Lift Aerofoil in Low-Pressure Turbines," Annual Review of Fluid Mechanics. Vol. 37, pp. 71-98, 2005.
- [47] Sanders, D.D., Nessler, C.A., Sondergaard, R., Polanka, M.D., Marks, C., Wolff, M., O'Brien, W.F., 2010, "A CFD AND EXPERIMENTAL INVESTIGATION OF UNSTEADY WAKE EFFECTS ON A HIGHLY LOADED LOW PRESSURE TURBINE BLADE AT LOW REYNOLDS NUMBER," ASME Paper No. GT2010-22977.
- [48] Praisner, T. J., Grover, E. A., Knezevici, D. C., Popovic, I., Sjolander, S. A., Clark, J. P., Sondergaard, R., and Koch, P. J., 2008, "Toward the Expansion of Low-Pressure-Turbine Airfoil Design Space," Proceedings of GT2008 ASME TURBO EXPO 2008: Power for Land, Sea, and Air June 9-13, 2008, Berlin, Germany GT2008-50898

Appendix A

Wake Generator Operation and Maintenance

Operation

The wake generator system is driven by a 3hp, 3450 rpm variable frequency electric motor. The motor is coupled to a 1.59cm diameter shaft by means of a v-belt. Various pulley sizes can be fitted to the motor and drive shaft, and the current configuration allows for 1100-2000 rpm (motor shaft) speeds to be operated. This range of rpm is desirable due to the shaft driven cooling fan located on top of the motor. Lower rpm is not recommended, as the motor will overheat during extended operation. The motor has two power shut off switches; one located on the side of the wind tunnel next to the motor, and one located next to the controller by the control room.

The motor is operated by a Baldor V-drive controller. This controller has various options and controls all functionality of the drive motor. For a complete description of the controller, refer to the operation manual. The controller has a front LCD screen that displays information about the controller. This screen will display the mode the controller is in along with the current motor rpm. The controller can be operated remotely through a handheld controller (sold separately) or a computer (not currently

hooked up). To use the front controller buttons, the controller must be in “local” mode as opposed to “remote”. If power is turned off to the controller, the default mode is “remote”.

The controller has a jog function that is useful to move the wake generator mechanisms to a different location on the track. To jog the motor, press the jog button and then hold down the reverse button to jog the chain. Release the reverse button when you want the chain to stop. The motor was wired backwards, and so the reverse button will move the chain in the proper direction. Due to the location of the chain tensioner the wake generator is only designed to move in one direction. Once the chain is located in the desired location, press the stop button to exit the controller out of jog mode. Note: you cannot manually drive the chain when the motor is in jog mode. The motor should not be left in jog mode as it is continuously receiving power from the controller.

Running the System

To turn the wake generator system on, first press the enter button on the front panel. The current motor rpm will be displayed. This is the rpm the motor start operating at. It is recommended that the initial rpm always be set to 500. This will allow the user to check the system and make sure everything is operating properly before a higher rpm is selected. Once enter is pressed the user can use the up, down, left, right buttons to select the desired starting rpm (should be set to 500). Once the desired rpm is entered, press the enter button again to enter this rpm into the controller. Once it is determined safe to turn the system on, press the reverse button (no need to hold it down). The wake generator should turn on and begin moving. Once it is determined that everything is operating properly, press the up arrow to increase the motor speed by 50

rpm. The current motor rpm is displayed on the LCD screen. Continue pressing the up arrow to keep increasing the speed until you have reached the desired value. Similarly, the down arrow button will decrease the motor speed by 50 rpm.

Stopping the System

In case of an emergency, the system can be shut off using the red stop button on the front panel, or by turning off power using the power shut off at any time. The method of stopping the system is to use the down arrow, decreasing the rpm till 500 rpm is displayed on the front panel. Once the system is turned down to 500 rpm, press the red stop button. Note: the controller maintains the last set rpm value and will return to this value if the reverse button is pressed. Make sure you check the set rpm value before running the system.

The acceleration time and deceleration time can be adjusted through the controller. It is currently set to safe acceleration times and is not recommended that these values be changed. Further options can be found in the operation manual.

Maintenance

The wake generator system needs routine maintenance for proper operation. For every 10 hours of operation, the system needs to be lubricated. The parts that need lubricated are the chains, sprockets, and drive shaft bearings. The chain is lubricated using spray grease located in the flammable cabinet. The sprockets are also lubricated with Teflon spray grease located in the flammable cabinet. The drive shaft bearings are located on top of the wind tunnel and need a single pump from the grease gun.

During lubrication, chain tension and rod couplers should be checked. Chain tension is adjusted by with the chain tensioners located on the slack side of the drive

sprocket. The chain tension should be such that the chain appears rigid between the tensioner and flywheel during operation. Excessive chain movement at this location is a sign that the chain should be tightened. The rod couplers should be checked for tightness. When the couplers become loose, they will begin to spin on the chain. If a coupler is loose, remove the bolt, apply locktite, and replace the bolt.

These are basic operating instructions and Dr. Rolf Sondergaard should be consulted for any modifications or maintenance to the wake generator system.